DOE/NASA/0179-1
NASA CR-165143
STDR-80-22

ANALYTICAL INVESTIGATION OF CRITICAL PHENOMENA IN MHD POWER GENERATORS

STD Research Corporation
Post Office Box "C"
Arcadia, California 91006

31 July 1980

Prepared for
NATIONAL AERONAUTICS AND SPACE ADMINISTRATION
Lewis Research Center
Under Contract DEN 3-179

for
U.S. DEPARTMENT OF ENERGY
Office of Magnetohydrodynamics
Assistant Secretary for Fossil Energy

DOE/NASA/0179-1
NASA CR-165143
STDR-80-22

ANALYTICAL INVESTIGATION OF CRITICAL PHENOMENA IN MHD POWER GENERATORS

STD Research Corporation
Post Office Box "C"
Arcadia, California 91006

31 July 1980

Prepared for
NATIONAL AERONAUTICS AND SPACE ADMINISTRATION
Lewis Research Center
Cleveland, Ohio 44135
Under Contract DEN 3-179

for
U.S. DEPARTMENT OF ENERGY
Office of Magnetohydrodynamics
Assistant Secretary for Fossil Energy
Washington, D.C. 20545
Under Interagency Agreement EC-77-AA-012674

ABSTRACT

Critical phenomena in the Arnold Engineering Development Center (AEDC) High Performance Demonstration Experiment (HPDE) and the U.S. U-25 Experiment, are analyzed. Also analyzed are the performance of a NASA-specified 500 MW(th) flow train and computations carried out by STD Research under Contract AC-01-79ET15501 concerning critical issues for the scale-up of MHD Generators.

The HPDE is characterized by computational simulations of both the nominal conditions and the conditions during the experimental runs. The steady-state performance is discussed along with the Hall voltage overshoots during the start-up and shutdown transients. The results of simulations of the HPDE runs with codes from the Q3D and TRANSIENT code families are compared to the experimental results. The results of the simulations are in good agreement with the experimental data.

Additional critical phenomena analyzed in the AEDC/HPDE are the optimal load schedules, parametric variations around the simulations of HPDE Run 006-014, the parametric dependence of the electrode voltage drops, the boundary layer behavior, near electrode phenomena with finite electrode segmentation, and current distribution in the end regions.

The U.S. U-25 experiment is characterized by computational simulations of the nominal operating conditions. The steady-state performance for the nominal design of the U.S. U-25 experiment is analyzed, as is the dependence of performance on the mass flow rate.

A NASA-specified 500 MW(th) MHD flow train is characterized for computer simulation and the electrical, transport, and thermodynamic properties at the inlet plane are analyzed.

Issues for the scale-up of MHD power trains are discussed. The AEDC/HPDE performance to date is analyzed to compare these experimental results to scale-up rules. The optimum Mach number distribution is analyzed with emphasis upon its effect on part-load and transient behavior. The effects of alternate cross-sectional shapes on channel performance are also evaluated.

TABLE OF CONTENTS

Table of Contents (cont'd)

Table of Contents (cont'd)

LIST OF TABLES

List of Tables (cont'd)

LIST OF FIGURES

List of Figures (cont'd)

List of Figures (cont'd)

List of Figures (cont'd)

List of Figures (cont'd)

List of Figures (cont'd)

List of Figures (cont'd)

List of Figures (cont'd)

List of Figures (cont'd)

List of Figures (cont'd)

List of Figures (cont'd)

List of Figures (cont'd)

List of Figures (cont'd)

List of Figures (cont'd)

List of Figures (cont'd)

List of Figures (cont'd)

List of Figures (cont'd)

List of Figures (cont'd)

ANALYTICAL INVESTIGATION OF CRITICAL PHENOMENA IN MHD POWER GENERATORS

1.0 INTRODUCTION

U.S. MHD technology for commercial power generation has made a significant transition in 1980. Test data is being obtained for MHD power trains of sufficient scale, interaction, and durability to bridge the gap between prior laboratory scale experiments and the requirements of commercial systems. In addition, detailed design studies are being initiated for advanced power train concepts which will ultimately lead to pilot-scale tests of a coal-fired MHD power plant. The significant power train projects in this transitional phase of MHD technology include the AEDC High Performance Demonstration Experiment (HPDE), the U.S. U-25 generator/diffuser; U.S. participation in the U-25B experiments, the UTSI Coal Fired Flow Facility (CFFF), the Advanced Power Train (APT) for the Component Development and Integration Facility (CDIF), and the Engineering Test Facility (ETF).

These projects each represent an important advance beyond previous laboratory experience. In contrast to past laboratory experiments, these projects test MHD power trains in which the interaction between the electrical forces and working fluid will be strong enough to cause important departures from classical internal duct gasdynamics. There are at present only limited experimental data to guide the prediction of the performance and behavior of MHD channels in such moderate-to-high interaction situations. Likewise, there is a lack of experimental data against which the test results of these programs might be compared. Under NASA Contract DEN3-179, STD Research Corporation has continued the application of its

comprehensive analytical capabilities to predict and interpret the behavior of high interaction MHD power trains. This Final Report for Contract DEN3-179 describes the results of analyses of high interaction experiments and designs carried out by STD during this transitional phase of MHD technology.

The planning, detailed analysis, and interpretation of the AEDC/HPDE and the U-25 experiments have been the subject of concern at STD Research Corporation from their initial conception [1-1]. During many years of contributions to the initiation and evaluation of these experiments, STD Research Corporation has analyzed many of the interim designs for the experimental hardware. Under U.S. Department of the Interior, and U.S. Department of Energy contracts since 1971, STD Research has made numerous specific recommendations for improved test parameters and procedures for the HPDE and U.S. U-25 tests. Many of the STD recommendations have resulted in changes in test hardware and/or procedures.

Under DOE contract AC-01-79ET15501 and NASA contract DEN3-179, STD Research has analyzed the "as-built" specifications of the HPDE and U-25 experiments under nominal operating conditions. These analyses have quantitatively predicted the effects of critical, nonideal processes which will control the performance of the HPDE and U-25 tests. Moreover, the work under these contracts has mapped the predicted nominal operating characteristics of those experiments over the likely ranges of mass flow rate, working fluid composition, diffuser recovery coefficient, wall temperature, and other operating conditions.

Under Contract DEN3-179, STD Research has carried out analysis of preliminary data from the first tests of the HPDE.

These experimental data confirm earlier analytical predictions by STD Research Corporation, such as the presence of large axial voltages during the start-up transient and the presence of much-larger-than design electrode voltage drops. This experimental confirmation of effects predicted by the STD analytical tools further validates the accuracy of these tools.

Studies of the nominal operation of the HPDE have yielded estimates of the relative importance of critical phenomena expected in the flow train tests. Unfortunately, the experiments can never run at precisely the nominal conditions. A significant test of an analytical tool is its capability to utilize inputs from instantaneous measurements taken during a test, and then to predict other quantities measured at the same instant during the same test. Such data are now available from the HPDE, and comparisons between such data and the STD/MHD code results are presented in this report.

Previous test data analyses at STD Research Corporation [1-2] have amply demonstrated the benefits of careful test data analysis for providing data consistency and understanding of the relative importance of the operative physical processes. As data have been received from the HPDE, STD Research Corporation has undertaken a detailed analysis of appropriate, self-consistent data sets which have led to (1) better understanding of the significance of each test and (2) recommendations for improved test procedures.

The survey of the nominal performance of the U-25 generator designed and constructed in the United States was carried to the point of evaluation of the "as-built" performance of the channel. The channel has not been operated to date, and therefore the analytical predictions of the

studies of nominal performance have not been checked against experimental data. Insights gained by the comparison between the analytical simulation of AEDC/HPDE experimental data were applied to the U-25 nominal operating conditions, however. These analyses focused on the implications of operating the U-25 channel with cold walls without modification of the original design loft. The results indicated that the electrode boundary layer voltage drops would assume a major role in the achievement of the 10 MW design goal with the "as-built" U-25 nominal operating conditions.

Perhaps the most important objective of analytical modeling of any physical process is the development of the ability to extend the results of experiments under one set of conditions to the conditions of other experiments. To do this, one must have the ability to exercise sufficiently rigorous and complete physical models which do not depend upon the application of adjustable, empirical factors in order to obtain agreement with experimental data. The use of such rigorous analytical tools, as are employed at STD Research Corporation, place a substantial burden on the experimentalist to provide precise, complete measurements for all of the physical data required as input to the calculation. Experience at STD Research Corporation [1-4] has shown that the combination of well diagnosed experimental data and rigorous analyses can pay dividends in understanding complex physical mechanisms and the experimental data itself. After the initial "shake down" phases of HPDE testing, the HPDE is beginning to produce such data. The simulations performed under Contract DEN3-179 have been fruitful as a consequence.

It is of interest to extrapolate the results of the AEDC/HPDE experimental data analyses to-date to conditions of

higher interaction. These conditions include operation of pilot scale and commercial scale MHD generators. Under Contract DEN3-179 and its predecessors, STD Research Corporation has characterized the behavior of MHD power trains from laboratory scale to commercial scale utilizing a self-consistent set of analytical tools. It was shown in [1-3] that the performance and fluid behavior of MHD power trains correlates well with the appropriate interaction parameters. The performance and interaction parameters of the AEDC/HPDE relative to generators of other scales are surveyed in the present report.

Utilizing the results of calculations carried out under Contract AC-01-79ET15501, the scale dependence of the performance of generators of alternate cross-sections (elliptical and hexagonal) also has been analyzed. The benefits of alternate cross-sectional geometries are strongly dependent on the boundary layer characteristics present at a particular station in a given channel. The power generation potential of each of three cross-sections in each of four channels ranging in scale from 20 MW thermal input to 2000 MW thermal input is compared. The comparison has been carried out between the power actually generated and (1) the power generation potential predicted by simplified electrical calculations, (2) power generation with rectangular geometry, and (3) ideal power generating capability based on center-line conditions at each axial station. While the analyses are indicative of the potential benefits of alternate cross-sectional configurations in MHD generators at various scales, the results do not represent optimum configurations. A number of additional computational degrees of freedom which were not considered in the previous study may also serve to improve the performance of generators of alternate cross-sections beyond the levels demonstrated.

Finally, an analytical study of the scale dependence of part load and transient behavior of MHD power generators is summarized in the present report. It is shown that a critical parameter for the successful part load operation of MHD power generation is the velocity or Mach number distribution in the MHD generator. The conclusion of this study has been that the key to successful off-design or part load operation of MHD generators is the maintenance of the Mach number distribution at or near the optimum value for the stagnation conditions existing at each station in the MHD generator.

This Final Report is organized according to the major topics addressed during the course of Contract DEN3-179. Section 2 presents a brief description of the codes utilized during the analytical investigations, and points out documents and literature in which fuller descriptions of the codes may be found. Section 3 focuses on the analysis of the "as-built" AEDC/HPDE, including the analysis of actual test data. Section 4 is devoted to special studies based upon the simulations of AEDC/HPDE experimental data described in Section 3. Section 5 describes the characteristics of the nominal, "as-built", operating conditions and specifications of the U.S. U-25 flow train. Section 6 describes the results of thermodynamic calculations of coal combustion products, including estimates of the electrical conductivity at the inlet of a NASA specified 500 MWth MHD generator. The purpose of Section 7 is to put the results of the present contract and Contract AC-01-79ET15501 into the context of the overall development program for MHD power generation. Sections 8 and 9 summarize the findings of the report and enumerate the major recommendations resulting from the studies presented.

2.0 DESCRIPTION OF THE STD/MHD CODES

The STD/MHD codes are constructed from a large collection of modules or subprograms which address various aspects of the MHD problem. Taken together, these codes define and solve the MHD problem, including, where applicable:

1. Viscosity and wall roughness
2. Volume viscous losses
3. Wall roughness effects on skin friction
4. Other skin friction effects
5. Compressibility
6. Turbulence, including MHD effects
7. Turbulence structure parameters and transport coefficients
8. Convective heat transfer
9. Radiative heat transfer
10. Anisotropic, nonuniform, fluctuating electrical transport properties
11. Nonuniform, fluctuating plasma/fluid properties
12. Nonequilibrium effects
13. Finite reaction rates, including ionization/recombination
14. Electron energy relaxation
15. Electron radiation losses
16. Electron thermal and concentration diffusion
17. Nonlinearity of the plasma as a conducting medium
18. Electrode surface and sheath phenomena
19. Electrochemical effects at the electrodes and slag layer
20. Finite electrode effects
21. Flow separation
22. Current leakage due to imperfect segmentation or slag layer leakages
23. Axial current leakage in the plasma and interelectrode arcing
24. Trans-boundary layer arcing
25. Shock waves and shock wave/boundary layer interactions
26. MHD instabilities (including magnetoaerothermal)
27. Ionization instability modes
28. Current streamer formation
29. Start-up transients, including sequencing of fuel, oxidizer, and seed valves, secondary injection of fuel, seed and oxidizer, and load circuit switching
30. Shut-down transients
31. Perturbations from steady state operation, including steam plant upsets, load circuit faults, part-load operation and load following transients
32. Generator/power conditioning system interactions
33. Generator end region losses
34. Slag layer dynamic phenomena

35. Channel geometry effects, including nonrectangular cross-sectional shapes
36. Transverse pressure gradients and nonuniformities
37. Secondary flows induced by MHD or viscous effects
38. Fundamental combustion processes, including particle burnout, particle trajectories, liquid layer formation on combustor walls, seed mixing and uniformity, pressure loss, etc.
39. Alfvèn waves
40. Hartmann flow
41. Nucleation effects
42. Electron capture by particles
43. Radiative ionization and recombination
44. Nonequilibrium radiation and coherent radiation
45. Effects of nonideal mixtures in condensed phase chemistry
46. "Faraday Catastrophe" load faults
47. Three-dimensional and time-dependent induced magnetic field effects
48. Ion slip effects
49. Nonideal plasma effects
50. Combustor-generated inlet swirl

The modules or subprograms describing these and other processes can be coupled in a variety of ways, depending upon the desired focus of a given calculation.

Detailed descriptions of the formulations, solutions, and applications of the appropriate STD/MHD codes are contained in Ref. [2-1] through [2-5]. A capsule description of each of the TRANSIENT, Q3D, PROPERTIES, FIN, INLET, BONDLAY, and GRAPHICS code families follows.

Code Family: TRANSIENT

Time-dependent magnetohydrodynamics, plasmadynamics, and compressible gasdynamics for internal flows with MHD power extraction and body forces. Comprehensive code family accounts for two-dimensional effects, wall effects (heat transfer and friction) and kinetics. Applicable to MHD power systems, gas-dynamic lasers, and other high temperature flow systems in which start-up, shutdown or unsteady operation are important. TRANDEE is one of the specialized codes within this family. The User's Guide to this code is available, Ref. [2-3].

Code Family: **Q3D**

Quasi-three-dimensional, steady MHD, electrical, and fluid mechanical effects in equilibrium (combustion-driven) or nonequilibrium (noble gas) MHD flow trains (combustor, nozzle, channel, and diffuser) of arbitrary cross section. This code family includes various cross sectional MHD generator performance calculations which may be coupled to predict three dimensional performance and behavior. While finite segmentation options exist, they were not utilized in the performance of the Q3D calculations described in this report. QUE3DEE is one of the specialized codes within this family. A User's Guide is available for this code, Ref. [2-4].

Code Family: **PROPERTIES**

Generalized transport and thermodynamic properties of equilibrium combustion flames. These codes consider reactions between more than 500 gas, liquid, or solid state species. Flexible inputs include initial fuel, oxidizer, and additive (seed, ash, etc.) compositions and states. Outputs include electrical and fluid transport coefficients and all thermodynamic state variables.

Code Family: **FIN**

Two-dimensional MHD electrode solutions with electron energy relaxation, electron ionization/recombination kinetics, effects of slag coatings, and finite electrode/insulator width. Codes in this family apply to the region of the MHD generator channel which may be considered "periodic"; i.e., regions in which changes from electrode pair to adjacent electrode pair are essentially negligible.

Code Family: **BONDLAY**

Integral boundary layer models with MHD body forces, Joule dissipation, wall roughness effects.

Code Family: **GRAPHICS**

General and customized graphics packages for post-processing raw data files generated by other code families. Includes codes for contour generation and three dimensional projection of bivariate data.

Code Family: **INLET**

Codes in this family solve the two- dimensional electrical part of the MHD problem in the part of the MHD generator which cannot be considered periodic. These codes take given gasdynamic variables and compute the two dimensional distributions of electron temperature, Ohm's law coefficients, current density, and electric field in the end regions of an MHD channel.

REFERENCES

[2-1] S. T. Demetriades, "Computer Analysis and Evaluation of MHD Systems," STD Research Corporation Final Report FE2243-22 prepared for ERDA, Divn. Magnetohydrodynamics, Fossil Energy Category UC-90g, January 1979

[2-2] "STD/MHD Codes - Overview and Catalogue of Some of the STD/MHD Code Families Available to the Public," STD Research Corporation Report No. STDR-104-79, July 1979

[2-3] "STD/MHD Codes - Introductory Users Guide; Code: TRANDEE, Family: TRANSIENT," STD Research Corporation Report No. STDR-101-79, July 1979

[2-4] "STD/MHD Codes - Introductory Users Guide; Code: QUE3DEE, Family: Q3D," STD Research Corporation Report No. STDR-102-79, July 1979

[2-5] "STD/MHD Code Descriptions for Computer Programs Utilized under Contract AC-01-79-ET15501," STD Research Corporation Final Report, Task 1, Contract No. AC-01-79-ET15501; Report No. STDR-79-3 prepared for ERDA, Divn. Magnetohydrodynamics, DOE/ET/15501-1, Fossil Energy Category UC-90g, January 1979

3.0 HPDE DATA ANALYSIS AND INTERPRETATION

STD Research Corporation has performed calculations to survey the power producing characteristics of the AEDC/HPDE over the nominal operating range as well as calculations to simulate actual experiments which have occurred to date. The results of these studies are discussed in this section.

3.1 Channel Characterization

Subsection 3.1.1 describes the physical parameters used for simulations of the nominal operation of the AEDC/HPDE. Descriptions of operating parameters which differed from these nominal conditions during actual tests are provided in subsequent subsections.

3.1.1 AEDC/HPDE - Nominal Conditions

The flow train of the Arnold Engineering Development Center High Performance Demonstration Experiment (AEDC/HPDE) consists of a combustor, transition nozzle, electrode test section, generator, generator/diffuser adapter section and diffuser. Fig. 3-1 is a schematic of the final, "as-built" internal dimensions of the device (axial locations are referenced from the combustor back plate).

3.1.1.1 Geometry

The combustor for the HPDE is based on renovation and modification of what was formerly the LORHO burner and is described in [3-1] through [3-4]. For the purpose of performance analysis, the combustor may be characterized as a

0.610 m diameter cylinder of 1.195 m length. The transition nozzle is a three-dimensional contraction from the 0.605 m diameter burner to a 0.264 m by 0.489 m rectangular electrode test section. The electrode test section is of no consequence during the MHD experiments and may be regarded simply as an unloaded portion of the generator. The MHD generator channel is constructed in 5 sections, the dimensions of which are shown in Fig. 3-1. In the STD computer codes the x-axis is located at the center of the channel cross-section. The y-axis is in the electrode-to-electrode direction with the positive direction being from cathode toward anode. The z-axis is in the sidewall-to-sidewall direction. The magnetic field vector is in the positive z direction. The channel height, width, area, and aspect ratio are plotted as a function of the axial coordinate in Fig. 3-2.

There are 485 pairs of electrically accessible electrodes, of which only 417 pairs spanning 7.15 m in the interior of the channel are loaded under the nominal operating load schedule.

The electrodes are electrically isolated from each other with refractory, and each electrode spans the transverse distance across the channel. The gap between electrodes is 1.52 m throughout the channel [3-5]. Graphite caps are attached to each electrode pair to allow operation at a high surface temperature.

The "pegwall" insulator walls are composed of 0.019 square conducting pegs which are spaced 1.58 mm apart and are insulated with refractory material [3-4].

The generator is fitted (via an adapter section) with a plane-walled diffuser with parallel sidewalls (extensions of

the electrode walls) and diverging top and bottom walls. The mechanical design [3-1] of the diffuser allows for setting the upper and lower walls at any angle between 0 and 3^{o}. Experiments to date have fixed the divergence angle at 1^{o} on both walls.

3.1.1.2 Magnetic Field

The magnet for the MHD High Performance Demonstration Experiment is designed to provide (at 27 MW and 16 kA) a peak field of 6 T when pulsed from 77 K (LN_2) and 5.5 T when operated continuously water-cooled. The magnet bore is 0.89 m wide by 0.71 m high at the entrance, 1.4 m wide by 1.17 m high at the exit, and the poles are 7.1 m long. The total length of the magnet is a 9.16 m. [3-6]

Fig. 3-3 shows the agreement between the predicted and measured magnetic field distributions. STD simulations of the AEDC/HPDE experiments to date have used, as input for the field distribution, the MEA design values [3]-[5]. These values are scaled by the measurement of Hall probe H9 for each particular run under analysis.

3.1.1.3 Loading

The nominal loading scheme for the HPDE generator is in a Faraday configuration. For purposes of performance survey calculations, the load distribution is given as follows [3-5].

x(m)	RL (ohm-m)
$2.735 \leq x \leq 8.875$	0.8
$8.875 < x \leq 9.885$	1.6

where x is measured from the burner backplate. The electrode

spacing is given in [3-7] and is included in Table 3-1 for convenience.

3.1.1.4 Working Fluid

The working fluid for the channel is composed of the products of the combustion of toluene and oxygen with nitrogen diluent. The seed is potassium hydroxide dissolved in methanol. The fuel/seed mixture is injected into the combustor as a liquid at ambient temperature. The nominal mass flow rates for the facility are 45 kg/s for operation between 2 and 3 T, 50 kg/s for operation between 3 and 4 T, and 53 to 54 kg/s for operation at 4 T and greater [3-5]. The nominal value for both the N_2/O_2 mole ratio and the stoichiometry is 1.0. Table 3-2 contains a list of the flow rates which describe the working fluid under nominal conditions (2 T, 45 kg/s).

3.1.1.5 Wall Conditions

The nominal values for the surface temperatures on both the insulating and electrode walls are shown in Fig. 3-4. These temperatures were determined by a one-dimensional transient heating analysis performed by AEDC personnel and described in [3-7]. For all calculations the duration of heating was taken to be 15 s, after which there was a cool-down cycle during which atmospheric air is forced through the channel. The temperature history for each wall is calculated at the channel inlet and exit, and the distribution of the wall temperatures along the channel were obtained by assuming a linear variation between these locations (for values corresponding to t = 15 s). The combustor operates with a wall temperature of 450 K, and the roughness of all walls is characterized by an equivalent sand roughness of 3 mm in the

electrode test section and channel, and as "smooth" in the combustor, nozzle, and diffuser [3-5].

3.1.1.6 Channel Inlet Conditions

The character of the flow as it enters the MHD generator is not completely defined by the experimental data. Ideally, one would prefer to know with confidence the complete distribution of mass, momentum, and energy at the inlet plane. Available data are sparse due to the experimental difficulty of obtaining these measurements. The heat loss to the water-cooled components of the burner is on the order of 3% [3-4]. The total heat loss to all components upstream of the first loaded electrode was calculated, as described in Section 3.1.2.5, by STD Research; the value of 5.7% was used for the nominal case. The original design calculations based on the nominal operating conditions indicated that the boundary layer thickness is approximately 12 mm at the inlet plane.

3.1.1.7 Other Conditions and Assumptions

The generator exit condition is determined by the fact that the HPDE flow train exhausts to the atmosphere. Hence, the static pressure in the exit plane of the diffuser is assumed to have the nominal value of one atmosphere.

3.1.2 AEDC/HPDE - Experimental Conditions

The HPDE experimental conditions are chosen according to experience learned from each successive test and a test plan which includes variation of the key test parameters. Consequently, the HPDE runs have not, to date, operated at exactly

the "nominal" conditions pr ,ented in the previous section. Post-experimental data analysis is the only way to determine the operating point of a particular experiment. It is the purpose of this section to set fo:.h as completely as possible, using the data at hand, the experimental conditions under which the AEDC/HPDE has actually operated to this date.

3.1.2.1 Magnetic Field

During power producing runs the magnetic field strength is monitored via Hall probes, the locations of which are shown in Fig. 3-5. All probes are located on the floor of the magnet bore. A measure of the variation of the magnetic field in the interelectrode direction is provided by probes H2A and H3A which are displaced above and below the midline (y = 0) by 0.014 m. The location of these probes with respect to the design magnetic field distribution is shown in Fig. 3-3. Note that they are near the peak magnetic field region. For the purpose of computer simulation of the experiments, the measured values of probes H2A and H3A are averaged over the time interval of interest. The resulting value of the magnetic field is then used to scale the design curve to yield the complete magnetic field distribution for the experiment under consideration. Table 3-3 contains the values of the magnetic field so obtained for the AEDC experiments to date.

3.1.2.2 Loading

The load bank is a series of liquid rheostats consisting of polypropylene buckets, each containing two copper plates. The plate spacing can be varied to achieve a resistance range from 10 to 60 ohms. Table 3-4 contains the

resistance of each electrode pair as set by AEDC personnel [3-8], [3-9]. These values have been normalized by a water conductivity of 150 μS/cm. Note that the reference resistances for electrode pairs numbered greater than 357 have been changed for runs subsequent to 006-007 and also that electrode pairs 401 and above are open circuited. Table 3-5 contains the water conductivity during the runs for all runs to date. To determine the resistance schedule for any particular run, the values from Tables 3-4 and 3-5 must be used in the following equation:

$$R_{run} = R_{ref} \, (150/K_{run})$$

The product of the above load resistance and the electrode pitch (width from Table 3-1 plus the insulator thickness of 1.52 mm) then uniquely specifies the loading of the channel in the Faraday configuration. It should be noted here that comparisons of the load resistances determined in the above manner and those determined from the voltage-current characteristics of the experimental data are not very good for Run 006-008, but were better for subsequent runs. Further discussion on this point is contained in Sections 3.6 and 3.7.

3.1.2.3 Working Fluid

Table 3-6 contains a list of the flow rates of the various constituents of the working fluid for two typical experimental runs (006-008 and 006-014). These flow rate data are input to codes from the STD THERMODYNAMICS family to generate a thermodynamic data base and other data. Input flow rates for oxidizer, seed, and fuel were obtained by averaging the experimental data over the time period $4.54 \leq T_2 \leq 5.21$ s for Run 006-014 and $9.5 \leq T_2 \leq 10.2$ s for Run 006-008.

3.1.2.4 Wall Conditions

Fig. 3-6 illustrates the results of a transient heating analysis performed by AEDC personnel for the electrode surface including the 1/2" graphite caps [3-11]. Experimental data have indicated that the heat transfer rates on the electrode surfaces at the inlet flange and at a station 5.59 m from the inlet flange are 450 Btu/ft^2-sec and 100 Btu/ft^2-sec, respectively. Several of the power producing runs to date have yielded their best data about 5 seconds into the run. Reading the curves of Fig. 3-6 (at t = 5 s) for the heat transfer rates mentioned above yields electrode surface temperatures of 1130 K and 540 K at the inlet flange and a point 5.59 m downstream, respectively. For the purpose of performance calculations, the complete temperature distribution is assumed to be linear along the channel between these two points. These data were the best available at the time these simulations were performed.

All simulations beginning with the simulations of Run 006-014 utilized the temperature profile described in the above paragraph. Simulations of runs prior to 006-014, which were carried out before this information became available, utilized the nominal temperature distribution, Fig. 3-4.

As the HPDE runs were analyzed, better wall temperature data became available. A further revision to the electrode surface temperatures has been published in [3-12] and is reproduced in Fig. 3.7. This estimate is based on a two-dimensional, fully viscous calculation including the effects of pressure gradient.

3.1.2.5 Channel Inlet Conditions

To determine the boundary layer thickness at the first loaded electrode, a series of computations have been made with a code from the STD BONDLAY Family. Several runs were made assuming various values for the equivalent sand roughness in the components upstream of the channel with the following results at the first loaded electrode:

Sand Roughness Height (mm)	δ(electrode wall) (mm)	δ(sidewall) (mm)
0.0 (smooth)	17.6	19.3
0.1	24.0	
1.0	34.9	38.4
2.0	40.0	44.3
3.0	43.6	48.4

These calculations also predict that the total enthalpy loss up to the first loaded electrode ranges between approximately 5.7% for the smooth wall calculation to approximately 7.2% for the 3.0 mm roughness calculation. The latter value compares well with the datum of 7.5% measured by AEDC [3-12].

density, integrated power output, and interelectrode voltages are determined from the primary measurements and other geometrical data.

3.2.3 STD Interface with HPDE Data Systems

The HPDE data acquisition system data are processed by codes from the STD GRAPHICS family and plotted as a function of both space and time. These codes allow the data and computational results to be displayed with any degree of time and space resolution necessary, contingent of course, on the ultimate density of the data, to examine events of importance. Fig. 3-8 is illustrative of the manner in which critical events can be followed throughout their lifetime using this type of display.

A plot of the data acquisition system data for a typical AEDC run (006-008) is given in Fig. 3-9. On this figure the time coordinate increases from left-to-right and starts at T_2 = 0 (T_2 is the time in seconds from combustor ignition). Also, the axial distance along the flow train is plotted from top-to-bottom. On this figure, the value of the data is plotted vertically above the corresponding point in the time-distance coordinate plane. It is possible to define and plot subsets or "windows" in the data as small as necessary to resolve an event of interest if the data are available. Such options have as yet gone unused for the HPDE data due to the relative coarseness of the experimental data in space and time. Much higher data rates will be required to resolve the space-time variation of critical phenomena such as MHD instability modes, electrical transients, etc.

3.3 Steady State Performance at the Nominal Operating Conditions

Prior to receiving the experimental data from the initial powered runs, a study was conducted in order to determine the probable performance range of the AEDC generator during the first phase of testing. The nominal operating conditions were defined by AEDC personnel and are documented in Section 3.1.1. During these computations the peak magnetic field was varied between 2.0 and 4.0 T and the mean flow rate was varied between 45 and 54 kg/s. Due to the unavailability of sophisticated FIN or ARRAY calculations in the early stages of te HPDE analysis, a variety of wall condition models were employed in Q3D for the initial calulations of the HPDE performance under the nominal operating conditions.

With the arc mode current transfer option, the current transverse through the boundary layer flows with negligible loss when the local electric field exceedes a critical value. Based on previous work, the critical value used for these computations is -12 kV/m. For the diffuse current mode option, the current transverse through the boundary layer is computationally forced to be uniform across the width and length of the electrodes.

Figs. 3-10 and 3-11 present the summary of the predicted performance of the HPDE at the nominal operating conditions for 2 T, 3 T, and 4 T operation. Performance predictions were carried out as a function of mass flow rate with the STD TRANSIENT family of codes in the quasi-steady mode of operation. The predicted values fall within the bounds of uncertainty defined by a series of more sophisticated, quasi-three-dimensional calculations with the Q3D family of

codes. Depending upon the relative importance of seed condensation and current transport mechanisms, the predicted power output was found to vary between 4.28 to 15.3 MW at 2 T and between 25.96 to 39.76 at 4 T. Fig. 3-11 indicates that the experiment should not be expected to obtain 15% enthalpy extraction at 4 T and the nominal operating conditions.

Figs. 3-12 to 3-24 are results of a calculation, COBQFXRIHU, with a code from the Q3D family for the 2 T nominal condition (Point A (2 T) in Fig. 3-10). These are axial profiles of certain key variables which are output from the calculation. The origin for the axial coordinate in these figures is located at the inlet flange (end of electrode test section in Fig. 3-1). Note how the sectioning in the channel construction (see Fig. 3-1) is directly reflected in the Mach number and velocity distribution of Fig. 3-13. The load factor decreases from 0.8 to 0.64 over the active channel (Fig. 3-15). Fig. 3-16 shows that approximately 15.3 MW are produced at the nominal 2 T conditions at an enthalpy extraction ratio of 0.059. Maximum normal current densities of approximately 0.5 A/cm^2 and maximum Hall fields of approximately 1.8 kV/m are present during operation as shown by Fig. 3-17. Maximum voltage drops* of approximately 750 V occur in the rear end of the generator (Fig. 3-21).

*Except as otherwise noted, voltage drops in this report are defined as the difference between the Faraday voltage and the voltage difference across the channel if the centerline transverse voltage gradient were extrapolated to the electrodes.

3.4 Hall Voltage Overshoots

The mechanism for the occurrence of Hall field overshoots during start-up and shutdown was described in Vol. I, pp. 5-12 to 5-16 of the STD Research Corporation report FE2243-17 under contract EX-76-C-01-2243 (May 1978). During periods in which the channel is operating at design mass flow rates, but is unseeded or slightly seeded, high velocities are experienced in the channel. In the presence of the magnetic field, B, these higher-than-design velocities can lead to much higher-than-design Hall fields:

$$E_x = \beta UB(1-K)/G$$

Taking note that $\beta \sim B/p$, we find that (1) $E_x \sim B^2$, and (2) every factor in the above expression (except the nonuniformity factor G) changes in the direction to increase the magnitude of E_x as the velocity increases. Such unseeded or slightly seeded conditions are present during the start-up and shutdown sequences because the seed valve is opened last and closed first.

In the calculations described in the forementioned report, Hall fields exceeding 20 kV/m locally were observed at the nominal 6 T condition during the start-up and shutdown events, and Hall fields exceeding 4 kV/m extended over more than half the channel. Scaling these fields by the square of the ratio of magnetic flux density in Run 006-008 to the value used in the previous study $(2.35\ T/6\ T)^2$, we might expect Hall fields of the order of 3 kV/m over the entire channel due to the increased extent of the supersonic flow region in AEDC/HPDE Run 006-008 (see Section 3.6 for a complete analysis of this run). Thus, instantaneous total Hall voltages up to 25 kV might be expected in the 006-008 start-up and shutdown events.

Fig. 3-25 is a plot of the anode-to-ground voltage for electrode pair number 336 during AEDC/HPDE Run 006-008 in which the diffuser became grounded during the run. Figs. 3-26 and 3-27 show the anode and cathode voltages at all instrumented electrodes (for the Data Acquisition System) over the entire duration of the run. It is clear that the overvoltages occurred throughout the channel. The reduced data acquisition system data, which are presented in all plots of data acquisition systems in this report, are averages over five acquisitions in order to filter the noise. Therefore, while voltages as high as 25 kV are not displayed in these figures, the high standard deviations associated with the peaks in the Fig. 3-25 data imply higher instantaneous voltages than the averaged values depicted in Fig. 3-25.

The sequence of events that took place during Run 006-008 are reasonably well understood and are depicted schematically in Fig. 3-28. This figure presents the actual measured diffuser-to-ground voltage along with a curve which represents the ideal generator voltage which would occur if there had not been an external arc from the diffuser to ground. Due to an approximate 2 s delay between fuel injection and seed injection into the combustor flow, sufficient time is available to establish steady, unseeded combustion flow in the MHD channel during start-up. If no electrical faults develop, the Hall voltage would have reached 25 kV as discussed above. This is indicated by the solid trace in Fig. 3-28. Instead, an electrical breakdown from diffuser to ground developed as the Hall voltage increased in Run 006-008. The exact breakdown voltage is not known from the experimental data due to the long averaging times of the data acquisition system and panel meter data. If sufficient information about the geometrical configuration of the region near the electrical breakdown were

known, the air breakdown voltage could be calculated. This is not a critical parameter because the breakdown problem at this location has since been corrected.

During the period between the electrical breakdown and the onset of seed flow to the combustor, the external arc is sustained by passage of a modest amount of current through the plasma from the combustor to the diffuser breakdown location. Independent assessments of the electrical conductivity in the plasma during the unseeded period yield an estimate of 0.03 S/m $\pm$ 0.02 S/m. These estimates were arrived at by (1) examination of the STD THERMODYNAMICS code family predictions for the electrical conductivity of the unseeded combustion flame, and (2) an analysis of the Faraday current and voltage measurements during the unseeded portion of Run 006-008 using calculated values of the gas velocity.

By assuming that the electrical conductivity is relatively constant in the generator during the unseeded portion of the run, by assuming that the conductivity is relatively uniform over the channel cross-section, and by taking note that the measured voltage to ground of anode 1 and anode 10 differ by 1000 volts (the corresponding difference on the cathode side is 1200 volts), it is possible to estimate a total current flow during the unseeded period of approximately 10 $\pm$ 5 A. Such a "trickle" of current would be sufficient to maintain the external arc from the diffuser to ground.

As the seed first enters the combustor, the bulk conductivity of the plasma increases, and the current available to the external arc increases substantially. The steady-state current in the external arc, corresponding to the time when the seed flow has reached its steady-state value, is estimated from

Q3D computations to be in excess of 850 A, and possibly as high as 1200 A (see Section 3.6). The burning voltage of the external arc decreases as the current increases, according to the standard V-I characteristic of electrical arcs. During the seed-on transient, the voltages to ground of the loaded electrodes in the generator undergo a voltage transient which is indicated in Figs. 3-25 to 3-27. Unlike these floating electrode circuits, the diffuser voltage is fixed by the arc burning characteristics; and, consequently, the diffuser does not experience this "seed-on" transient.

During the HPDE shutdown sequence, the seed valve is shut prior to fuel cut-off. As the seed is purged from the channel, the conductivity required to sustain the high current discharge gradually diminishes, and the diffuser voltage follows the V-I characteristics of the external discharge. Were there are no electrical faults present, the Hall voltage would again rise to approximately 25 kV. However, the burning voltage of the arc rises to some lower value, and then the external diffuser-to-ground discharge is extinguished. When the discharge is extinguished, the diffuser-to-ground voltage rises but is intercepted by the voltage trace which would be present without external electrical discharges. This trace falls as the fuel supply to the combustor diminishes and combustion ceases.

The practical lesson from all this: over-voltage protection for many tens of thousands of volts rather than hundreds or thousands of volts should be provided between power train and ground.

3.5 Shock Location

The range of possible mass flow rates and magnetic field strengths obtained in the AEDC/HPDE facility allow for operation in both the supersonic and subsonic flow regimes. The nominal operating conditions for the initial testing phase (described in Section 3.1.1) were designed to insure operation in the supersonic flow regime. Ideally, the shock-down to subsonic flow would occur downstream of the active channel. While surveying the nominal operating conditions with a code from the TRANSIENT family, particular attention was given to following the position of the shock as it varied with mass flow rate and magnetic field strength.

Figs. 3-29 and 3-30 are representative of the results of this study at the 2 T nominal condition. The origin of the axial coordinate for these plots is the burner backplate (channel exit is at 9.85 m). Fig. 3-31 summarizes the predicted location of the normal shock during operation at 2 T, 3 T, and 4 T with the nominal operating conditions and various mass flow rates. It is seen from these figures that the shock is predicted to lie outside the active portion of the generator, except during 4 T operation. The 4 T shock can be pushed out of the generator by a small increase of the mass flow rate within the facility limits. Also shown are the shock locations predicted for unseeded operation for the nominal N/O ratio and for a combustion mixture, designated N/O = 1.25, which simulates the off-design conditions for the first hot flow test of the generator. The data from this test show a pressure disturbance indicative of a shock system at approximately 9.1 m. The STD calculation based on the best available interpretation of experimental conditions predicts a normal shock to exist 1.6 m downstream of the pressure anomaly.

This is consistent with the empirically determined observation in supersonic flows that the duct stalls 2-3 diameters upstream of a normal shock computed by one-dimensional gas dynamics.

3.6 Analysis of Run 006-008

During start-up of Run 006-008 an electrical breakdown from diffuser to ground developed as the Hall voltage increased. Calculations were initiated with codes from the Q3D family to determine the leakage current from the diffuser to ground for this run and the associated power loss due to operating with the grounded diffuser. An input data set, which contains magnetic field and load resistance distributions and thermodynamic data from the AEDC Data Package [3-9], was constructed for use in these computations. These inputs are discussed more fully in Section 3.1.2.

It should be remarked here that this simulation was performed prior to receiving the revised wall temperature schedules of Figs. 3-6 or 3-7 and as such the calculation was done using the nominal electrode wall temperature schedule of Fig. 3-4. In addition, the assumption of smooth walls upstream of the gererator was made according to the nominal conditions. Subsequent simulations of the Run 006-014 data suggest that the upstream conditions are more accurately characterized by rough walls.

As a first approximation to simulate the effects of the grounded diffuser, a series of Q3D computations was performed in which a constant value of I_x is assumed to exist at each cross-section of the generator. The actual leakage current would be determined as that current which yields distributions of normal current density, power, Faraday voltage, and Hall potential most closely resembling those measured during the experiment.

At the time these calculations were performed, the data for the electrode potentials during the run appeared to contain a number of uncertainties. The data from the meter panel and data acquisition systems were each incomplete. Depending on how the data were combined, an estimate for the Hall potential difference across the active channel between 1100-1600 V might be obtained. In addition, calculations to check the load resistance at several electrode pairs indicated a few discrepancies between the data from the two systems. Many of the load resistances inferred from the measured currents and voltages differ substantially, particularly at the rear end of the generator, from the values used in the simulations. These input values were provided to STD on the basis of separate measurements of load resistance prior to the run and are documented in Section 3.1.2.

According to AEDC personnel [3-13] there were two causes of data inconsistencies in Run 006-008:

(1) The current measurements by the panel meters are subject to a large uncertainty because currents of the order of 24 A are being measured on a 200 A (full-scale) meter, resulting in approximately a $\pm$ 5 A uncertainty in the reading.

(2) The current transductors used in the data acquisition system were probably measuring such low currents as to be in a nonlinear range of the probe characteristics.

It is important to note that at the time of the STD Run 006-008 simulations, the HPDE might be considered to be in a "shake-down" mode in which the data acquisition and reduction procedures were being perfected. Some of the data utilized in this simulation have been confirmed by AEDC to be inconsistent.

These inconsistencies have been corrected by AEDC since the time of the STD simulations. When the data acquisition system data and the meter panel data for Run 006-008 were refined by AEDC, better agreement with the load resistances was obtained.

Two Q3D runs were made in an attempt to simulate this experiment: CMSIPUFIKW with $I_x = 0$ and CMSIQBEIKW with $I_x = 850$ A. The axial variation of the gasdynamic, plasma, and electrical parameters from CMSIPUFIKW are given in Figs. 3-32 through 3-43. The axial variation of these same parameters from computation CMSIQBEIKW are given in Figs. 3-44 through 3-55.

Comparison of the axial variations of the gasdynamic parameters presented in Figs. 3-32 and 3-44 indicates that the values are nearly the same with a slightly higher velocity, Mach number, stagnation temperature, and stagnation pressure from CMSIQBEIKW than for CMSIPUFIKW. Comparison of the axial variation of the plasma properties in Figs. 3-33 and 3-45 indicates that the Hall parameter is larger at the exit for CMSIQBEIKW. As seen by comparison of Figs. 3-35 and 3-47, the Faraday load factor and electrical conversion efficiency are not identical when there is a net I_x. For CMSIQBEIKW, the Faraday load factor decreases to about 0.4 at the back end of the channel.

Due to the large value of I_x and power dissipation in the arc from diffuser to ground, the values of the power extraction parameters are much smaller for CMSIQBEIKW, Fig. 3-48, than for CMSIPUFIKW, Fig. 3-36. The axial variations of the electrical field variables in Figs. 3-37 and 3-49 indicate that the net I_x causes the Hall field to be negative at the front and back ends of the channel. In addition, the Faraday

voltage and normal current density are lower with a net I_x. Comparison of the axial variation of the electrode potential from Figs. 3-38 and 3-50 shows the effects of a net I_x: the potentials decrease at the front end of the channel (due to negative E_x); potentials are smaller throughout the channel; and the differences from cathode to anode (Faraday voltage) are smaller throughout the channel.

Comparison of the electrode voltage drops in Figs. 3-39 and 3-51 indicates that the voltage drops are the same at the entrance, but peak at about a 20% lower value for CMIQBEIKW. Comparison of the electrode boundary layer parameters on Figs. 3-41 and 3-53 indicate that the net I_x causes an increase in the anode shape factor and a decrease in the cathode shape factor. Comparison of the sidewall boundary layer parameters on Figs. 3-42 and 3-54 indicates that the sidewall boundary, displacement, momentum, and enthalpy thicknesses are all greater with a net I_x.

Computation CMSIPUFIKW simulated the conditions which might have been obtained in the HPDE if the external short from diffuser to ground had not occurred. Computation CMSIQBEIKW is a first approximation to simulate the conditions of Run 006-008 at the time corresponding to T_2 of approximately 9.0 s. This computation is only a first approximation because the actual I_x caused by the shorted diffuser is not known. Therefore, precise correspondence between calculated and measured values cannot be expected.

Fig. 3-56 illustrates the static pressure distribution, both measured and predicted, in the active generator. The excellent agreement of theory and experiment indicates that there were no large-scale anomalous fluid mechanical phenomena

present in the channel during this portion of the run, and suggest that the differences between the experimental data and the computations described below may be mainly electrical in nature.

The measured and predicted potential of the cathode are depicted in Fig. 3-57. The experimental distribution from the AEDC meter panel data system was obtained from an AEDC plot, which is given in Fig. 3-58. It should be remarked here that the meter data for the potential is unreliable over the first 10 instrumented electrodes, since negative potentials could not be accurately measured at the time of the run. Also plotted in Fig. 3-57 is the cathode potential recorded by the data acquisition system. Both experimental distributions have been plotted with an offset from the recorded values such that the potential at electrode no. 168 is zero.

The Q3D calculations as originally planned would determine the constant value of I_x in the generator such that the Hall potential difference computed from entrance to exit compared well with the measured values. The unreliability of the meter data at the inlet and the sparsity of the data from the acquisition system at the exit prevents a precise determination of the potential difference. Simultaneous consideration of both sets of data indicate a Hall potential difference of about 1200 V as a reasonable target (see Fig. 3-57). The Q3D calculation CMSIQBEIKW was made with I_x = 850 A, nominal wall temperatures, and diffuse current transfer. The predicted Hall potential shows good qualitative agreement with the data. Further computations at an increased I_x would probably lower the potential difference to the target value.

Figs. 3-59, 3-60 and 3-61 are plots of the experimental and the calculated distributions of normal current density, Faraday voltage, and power respectively. The meter data distributions were obtained from an AEDC figure, which is reproduced as Fig. 3-62, while those for the data acquisition system were taken from [3-9]. Again, there is good qualitative agreement between theory and experiment for these quantities. Clearly, the theory and experiment lack quantitative agreement, especially in the rear-end region of the generator. Possible causes of this lack of agreement are (1) failure to match I_x, (2) unreliable electrical data, or (3) the presence of phenomena not revealed by the present computation.

Certainly, some of the discrepancy is expected since the Hall potential comparison of Fig. 3-57 indicates that a higher I_x should be used in the computation. in addition, there are discrepancies in the experimental data recorded by the two measuring systems. Perhaps this is best illustrated in the current and voltage graphs of Figs. 3-59 and 3-60. While the voltage measurements at T_2 = 8 s agree fairly well, the current distributions vary differently along the channel. In addition to the fact that the data is in some instances perhaps not yet well understood, the occurrence of additional phenomena such as internal shorting and current loops (resulting in nonconstant I_x) in the generator cannot be excluded. STD computation CMSIQBEIKW utilized a leakage current of I_x = 850 A to predict a Hall potential difference of approximately 1400 V. An additional estimate for the magnitude of I_x can be obtained from the equation

$$I_x = \frac{V\sigma}{A} L$$

where L is the length over which the short occurs and A is the cross sectional area occupied by the current. At the back end of the channel a typical cross sectional area is 0.8 m^2. The measurements from the data acquisition system at T_2 = 8 s indicate an anode to ground potential (V) of approximately 1400 V at 6.22 m from the first loaded electrode. The axial distance from this station to the diffuser (grounded) is 2.67 m. STD computations yield an electrical conductivity ( ) in this region of approximately 3 S/m. Assuming the leakage current fills the entire cross-sectional area of the channel, application of Eq. (1) yields I_x = 1300 A. Similarly, at the front end of the generator typical values of the cross-sectional area and gas conductivity are 0.14 m^2 and 11 S/m, respectively. The experimental data at T_2 = 8 s indicates an anode to ground potential of approximately 400 V at 1.82 m from the channel inlet. Using these values, application of Eq. (1) predicts a leakage current of 340 A.

To obtain a valid value of the leakage current and its effects, it is necessary to take into account the structure and location of the leakage current with sophisticated models. Although the bulk conductivity averaging presented in the previous paragraph is crude, the order of magnitude of the leakage current may be estimated.

3.7 Steady State Q3D Simulation of Run 006-014

AEDC Run 006-014 was a powered run of 8 seconds duration which arced in the breech at approximately 5.3 s after the seed entered the channel. The experimental data show two distinct performance regimes (see Figs. 3-63 to 3-72)

(1) A period between $4.5 \leq T_2 \leq 5.21$ s in which the channel is ungrounded and the data is relatively steady in time.

(2) A period between $5.5 \leq T_2 \leq 6.5$ s in which the channel is operating in a grounded condition.

The Q3D simulations performed under this contract have pertained only to the channel performance when in the ungrounded condition.

The input data for the Q3D simulations are fully described in Section 3.1.2. These data were obtained by averaging the experimental data over the time period $4.54 \leq T_2 \leq 5.21$ s. The effect of the bleed resistor was accounted for in the calculation with a constant axial current of 23.54 A. This value was obtained from the average diffuser-to-ground voltage (9416 V) and the known resistance of the #12 wire used as the bleed resistor (400 ohms).

Heat transfer measurements by AEDC personnel have resulted in a modified electrode surface temperature as shown in Fig. 3-6. The sparseness of the heat transfer data prohibits exact specification of the electrode surface temperature. The Q3D simulations have, at the suggestion of AEDC personnel, used temperatures corresponding to the 450 Btu/ft^2-sec and 50 Btu/ft^2-sec curves (at T = 5 s) at the inlet and exit flanges respectively. A linear variation of temperature with axial location was assumed between these points. The nominal temperature distribution was retained for the insulating walls (Fig. 3-4).

A list of the nominal load resistances, supplied by AEDC, is contained in Table 3-7 for runs subsequent to Run 006-006. These values of resistances have been normalized to, a

nominal water conductivity factor of 150 μs/cm. Also listed in Table 3-7 are the average load resistances obtained from the experimental data at these locations. To conform as closely as possible to the experimentally observed values of the load resistance, and yet retain the detailed electrode-by-electrode distribution provided by the nominal schedule, STD adjusted the nominal schedule with a conductivity factor of 159 μs/cm for these initial calculations. This agrees with the conductivity values derived from the data acquisition system values for Faraday voltage divided by Faraday current over the first 168 electrode pairs. The load schedule used in these simulations appears to be at variance with the experimentally indicated values in the downstream half of the generator, and the performance predictions may be expected to be less reliable toward the aft end of the generator. A plot of input load resistance schedule and the resistance as determined by the experimental data at each instrumented electrode pair is given in Fig. 3-86.

Three Q3D calculations have been made during the theoretical simulation of Run 006-014:

(1) STD Computation BTAYUYDJBE: assumes all walls prior to inlet flange can be characterized as smooth walls. Inlet boundary layer thickness is 18 mm. Enthalpy loss upstream of the generator inlet flange is 5.7%.

(2) STD Computation CHPQUUUJBQ: assumes roughness of all walls prior to generator inlet flange can be characterized by an equivalent sand roughness of 3 mm. Enthalpy loss upstream of generator inlet flange increases to 7.2% and inlet boundary layer thickness increases to 44 mm. (See Section 3.1.2.5).

(3) STD computation CHPQQFLJDV: Assumes roughness of all walls prior to generator inlet flange can be characterized as smooth walls. Inlet boundary layer thickness is 18 mm. Enthalpy loss upstream of the generator is increased to 7.2% to account for a 3% combustion inefficiency due to incomplete droplet-burnout, as discussed in [3-14]. The chemistry was maintained the same, however.

Figures 3-74 to 3-89 contain the results of a typical Run 006-014 simulation calculation (CHPQUUUJBO) in the form of axial profiles of the key gasdynamic and electrical variables. Fig. 3-75 shows that the Faraday load factor, K, decreases along the channel from approximately 0.7 to 0.6. Figs. 3-76 and 3-77 show that the interaction parameter based on velocity and the interaction parameter based on pressure achieve values at the end of the channel of approximately 2.3 and 0.95 respectively. This interaction is sufficiently high to cause noticeable electrode boundary layer asymmetries (e.g., the electrode shape factors in Fig. 3-79) and nearly zero blockage at the channel exit (Fig. 3-76). Fig. 3-86 shows that the generator power output under these conditions is approximately 22 MW. Maximum normal current densities and Hall fields of approximately 0.7 A/cm^2 and 2.0 kV/m respectively exist at steady-state conditions (Fig. 3-87). Fig. 3-89 indicates that boundary layer voltage drops in excess of 2000 V may exist at the end of the generator for this relatively cold wall operation.

The boundary layer voltage drop measurements are perhaps not sufficiently refined at the present time to discriminate between various models of current transport at the walls. The diffuse discharge model selected for the Q3D simulation of Run 006-014, has yielded voltage drops within the range of uncertainty of the data and has been approximately confirmed with the more sophisticated FIN and ARRAY calculations described in Section 4.5.

3.8 Steady-State TRANSIENT Simulation of Run 006-014

Under conditions of higher interaction than were studied with Q3D in the neighborhood of the Run 006-014 operating conditions, the flow will become transonic in the MHD generator. The Q3D family of codes requires additional computational resources to iterate on the downstream pressure condition in transonic or subsonic flows. To economize, the high interaction cases for the Run 006-014 parametric study were carried out with the TRANSIENT family of codes, with the quasi-steady option. The starting point for the TRANSIENT parametric variations is a simulation of Run 006-014 utilizing data generated by the Q3D simulationn CHPQUYDJBE to account for multidimensional phenomena. Figures 3-90 through 3-98 are plots of the results of a computation, BRCYTRCJEB, with a code from the TRANSIENT family to simulate AEDC Run 006-014. The origin of the axial coordinate in these graphs is the burner backplate. The first loaded electrode is at x = 2.7 m and the last is at x = 9.4 m (see Fig. 3-90). These calculations were made for conditions similar to those of CHPQUYDJBE (smooth walls upstream of generator and 100% efficient combustion), which were discussed in the previous section.

Most of the key parameters resulting from TRANSIENT simulations shown in Figures 3-90 through 3-98 are also quite comparable to the Q3D simulation CHPQUUUJBO, which was described in the previous section. In particular, Figure 3-96 shows that a maximum current density of 0.685 A/cm^2 and a maximum Hall field of 2.005 kV/m are predicted with the TRANSIENT code. This compares well with the $J_{y,max}$ of 0.7 A/cm^2 and the $E_{x,max}$ of 2.007 kV/m predicted with Q3D (see Fig. 3-87). Similarly, the exit Mach numbers predicted by TRANSIENT and Q3D are 1.73 and 1.74, respectively (Figs. 3-78 and 3-91).

These figures also show the shock is located 10.74 m from the burner backplate. The total heat loss to the wall predicted by TRANSIENT is 31.46 MW, while that predicted by Q3D is 30.97 MW. The TRANSIENT calculation yields 23.6 MW for the integrated power output while the Q3D calculation CHPQUUUJBO predicts 21.3 MW or a difference of approximately 10%. Most of this discrepancy is due to the pre-generator wall roughness characterization which was for smooth walls in the TRANSIENT calculations and for rough walls in CHPQUUUJBO. The power output from the TRANSIENT calculation is more comparable to the result of the Q3D simulation CHPQUYDJBE, 24.6 MW.

The simulation of the generator operation with the TRANSIENT code is useful because it gives a broader view, if with slightly less detail, of the entire flow train. It should be noted that the accuracy of TRANSIENT and the agreement between results from computations with the TRANSIENT and Q3D code families is due to inputs to TRANSIENT from Q3D calculations to account for fundamentally multidimensional phenomena such as wall losses and plasma nonuniformity factors. This is necessary to ensure the accuracy of any quasi-one-dimensional calculation.

3.9 Comparison of Run 006-014 Measurements with Q3D Simulations

The results from Q3D computations discussed in Section 3.7 were analyzed and compared to the experimental data from HPDE Run 006-014. In this section the results of this comparison are presented with emphasis placed on two Q3D calculations, CHPQUUUJBO and CHPQQFLJDV. The conditions and underlying assumptions for these separate computations (see Section 3.7) are identical except for the following:

(1) The inlet boundary layer thickness and enthalpy flux are determined by a smooth wall boundary layer calculation upstream of the generator for computation CHPQQFLJDV (rather than rough with 3 mm equivalent sand roughness assumed in CHPQUUUJBO).

(2) A 3% combustion inefficiency due to incomplete droplet-burnout is assumed for computation CHPQQFLJDV (rather than a 100% efficient combustor assumed in CHPQUUUJBO).

The experimental data for the static pressure, a primary measurement of the data acquisition data, during the time after ignition, $4.1 \leq T_2 \leq 5.2$ s is given in Fig. 3-99. The static pressure is a primary measurement of the data acquisition data. The axial coordinate in Fig. 3-99 is referenced to the generator inlet flange. Also given in Fig. 3-99 are the axial distributions of static pressure from computations CHPQUUUJBO and COBQQFLJDV. There is excellent agreement between the experimental and the computed values throughout the channel.

The experimental HPDE meter panel data from Run 00 014 at T_2 = 4.8 s are compared to the values obtained from computations CHPQUUUJBO and COBQQFLJDV in Figs. 3-100 through 3-111. The axial coordinate in these figures is referenced to the inlet flange. The Faraday voltage (Fig. 3-100) and the current per electrode (Fig. 3-101) are primary measurements of the meter panel data. The normal current density (Fig. 3-102) and the integrated power output (Fig. 3-105) are determined from the primary measurements and other geometrical data. The computed values from computations CHPQUUUJBO and COBQQFLJDV fall within the measurement tolerances of the experimental values. Some local discrepancies of up to 5% are evident, but it is our judgment that the accuracy of the input data, especially for load resistance, as well as the $\pm$ 2% fluctuations in current and voltage during the period 4.5 s $< T_2 <$ 5.21 s could explain such differences. As shown in Fig. 3-100,

the computations tend to underpredict the Faraday voltage in the front half of the generator. This can be explained by consideration of the uncertainty of the channel loading.

The difference between the voltage-current characteristics measured by the two data-gathering systems and the nominal values is discussed in Section 3.7. The calculated values of the load resistances from the meter panel data yield values that are typically 10% higher than those computed from the data acquisition system (see Fig. 3-103). This is especially true in the latter third of the generator. In addition, the value of a load resistance computed at a particular electrode pair can vary 3-5% with time.

A rough calculation, under the assumption that the fluid properties change only slightly at this rather low interaction level, indicates that if the downstream load resistance were matched more accurately, a lower current and a higher Faraday voltage could be expected, the differences being approximately 3-5%. The integrated power output, shown in Fig. 3-105 would be relatively unaffected (the difference is estimated to be less than 1%) by this adjustment to input load resistance.

The integrated power distribution for the meter panel data measurements can be regarded as approximate, but better than the distribution obtained from the data acquisition system measurements. These points were calculated by numerically integrating the power through the loads for the instrumented electrode pairs. To obtain a value for the integrated power, the power was assumed to vary linearly between each set of instrumented electrodes (10 electrode pairs apart). The scatter in the power per electrode measured by the meter panel data, and plotted in Fig. 3-104, indicates that such a regular behavior is probably a weak assumption.

Computation CHPQUUUJBO simulated a bleed resistor from the diffuser-to-ground with a net axial current of 24 A. The power dissipated in this bleed resistor was calculated to be 0.2 MW by CHPQUUUJBO. This is less than 1% of the power produced in the channel.

It should be reemphasized that these preliminary computations have assumed diffuse-mode current transfer. At the relatively cold electrode surface temperatures indicated by the experimental heat transfer measurements to this point, arc mode current transfer is a distinct possibility, particularly on the anodes, and should be considered. This will be discussed further in Section 4.5 This will be discussed further in Section 4.5. The results described in Section 4.5 further suggest the possibility of the existence of very small arcs, particularly on the anodes.

The axial distribution of total electrode voltage drop from computation CHPQUUUJBO is given in Fig. 3-106. Experimental values of total voltage drop, obtained from the HPDE program manager, at four axial locations are also given in this figure. The electrode voltage drops computed by STD Computation CHPQUUUJBO appear to agree with the measured voltage drops within the experimental tolerances.

The axial distributions of centerline, cathode, and anode electrical potential are given in Figs. 3-107, 3-108, and 3-109, respectively. The potentials have been adjusted to set ground (0.0 V) at the centerline of the first loaded electrode pair. There is excellent agreement between the meter panel and the results of computation COEQGFLJDV. Also given on Fig. 3-109 are the data obtained by the data acquisition system for the time period $4.1 \leq T_2 \leq 5.2$ s.

REFERENCES

[3-1] G. W. Garrison, et al, "Annual Report on the MHD Hi Report on the MHD High Performance Demonstration Experiment," ERDA Report FE-1542-1, July 1975

[3-2] H. J. Schmidt, et al, "Report on the MHD Performance Experiment of the Period May 1, 1975, to September 30, 1976," ERDA Report FE-1542-2, July 1977

[3-3] H. J. Schmidt, et al, "Report on the MHD Performance Experiment for the Period October 1, 1976, to September 30, 1977," DOE Report FE-1542-35, March 1978

[3-4] H J. Schmidt, et al, "Report on the MHD Performance Experiment for the Period October 1, 1977 to September 30, 1978," DOE Report FE-2895-3, April, 1979

[3-5] Meeting with R. Starr, J. Lineberry, H. Schmidt, and W. Milam of ARO, Inc., B. Phillips of NASA/Lewis Research Center, and T. Swean and A. Vetter of STD Research Corporation at AEDC, 9 August 1979

[3-6] R. J. Averill, et al, "Final Engineering Report on the Dual Mode Magnet for the High Performance Demonstration Experiment," ERDA Report FE-1542-3, July 1977

[3-7] H. J. Schmidt, "Final Report on the Design of the MHD Generator Channel for the High Perfo.mance Demonstration Experiment," ERDA Report FE-1542. August 1977

[3-8] R. L. Lowry, "High Performance Demonstration Experiment Supersonic Faraday Performance Evaluation," Data Package: Propulsion Wind Tunnel Facility, Arnold Engineering Development Center; Preliminary Data: Run MI-006-006, Sept. 1979

[3-9] R. L. Lowry, "High Performance Demonstration Experiment Supersonic Faraday Performance Evaluation," Data Package: Propulsion Wind Tunnel Facility, Arnold Engineering Development Center; Preliminary Data: Run MI-006-008, Oct. 1979

[3-10] R. L. Lowry, "High Performance Demonstration Experiment Supersonic Faraday Performance Evaluation," Data Package: Propulsion Wind Tunnel Facility, Arnold Engineering Development Center; Preliminary Data: Run MI-006-010, 31, Oct. 1979

[3-11] Preliminary Data received during meeting between R. Starr, R. Lowry, H. Schmidt, and W. Milan of AEDC and T. Swean and A. Vetter of STD Research Corporation at AEDC, January 1980

[3-12] R. L. Starr, et al., "Description, Performance, and Preliminary Faraday Power Production Results of the HPDE Facility," Paper presented at the 7th Int'l. Conference on MHD electrical Power Generation, MIT, June 1980

[3-13] Private Communication: telephone conversation with R.L. Starr 6 Dec. 1979

[3-14] S. T. Demetriades, "Analyses of Critical Transient Phenomena in the AEDC/HPDE, Vol. III, Initial Pre-experiment Combustor Analysis," STD Research Corporation Report FE-2243-17 prepared for ERDA, Division Magnetohydrodynamics, May 1978

[3-15] R. L. Lowry, "High Performance Demonstration Experiment Supersonic Faraday Performance Evaluation," Data Package: Propulsion Wind Tunnel Facility, Arnold Engineering Development Center; Preliminary Data: Run MI-006-013, 14 January 1980

[3-16] R. L. Lowry, "High Performance Demonstration Experiment Supersonic Faraday Performance Evaluation," Data Package: Propulsion Wind Tunnel Facility, Arnold Engineering Development Center; Preliminary Data: Run MI-006-014, 22 January 1980

TABLE 3-1

Channel Electrode Width

Electrode Reference No. *	Electrode Width** (m)	No. of Electrodes
-30 to 26	0.0254	57
27 to 58	0.01905	32
59 to 162	0.01588	104
163 to 394	0.0127	232
395 to 444	0.0254	50
445 to 454	0.02223	10

*Electrodes are numbered consecutively upstream and downstream from electrode 0 which is the first electrode connected to a load.

** The insulator thickness is 1.52 mm between adjacent electrodes

TABLE 3-2

Nominal Flow Rates of Combustion Gases

Component	Flow Rate
Fuel	5.649 kg/s
Oxidizer	37.247 kg/s
Seed	2.069 kg/s
N_2/O_2	1.0
Pilot (CH_4)	0.034 kg/s
Seed Concentration	0.454 kg KOH/kg CH_3OH

Total enthalpy of combustion gases (no losses) 271.7 MW

Specific enthaipy of combustion gases 6.04 MJ/kg (adiabatic conditions)

T_{flame} (6 atm) = 3021 K

0-4356

TABLE 3-3

Nominal Magnetic Field Used for AEDC Simulations

Run no.	$\frac{\langle B(H2A) + B(H3A) \rangle}{2}$*	Time Interval	Ref.
006-006	1.537	$4.5 \leq T_2 \leq 7.5$	[3-8]
006-008	2.327	$9.5 \leq T_2 \leq 10.2$	[3-9]
006-010	2.697	$4.0 \leq T_2 \leq 4.5$	[3-10]
006-013	2.810	$4.5 \leq T_2 \leq 5.5$	[3-11]
006-014	3.231	$4.5 \leq T_2 \leq 5.3$	[3-11]

*Due to nonlinear behavior of the instrumentation, the numbers presented in this table are slightly in error. Refined data, [3-12], were not available at the time these simulations were performed.

0-4357

TABLE 3-4.

A. HPDE Load Resistance Settings for Runs Prior to 006-008

Electrode No.	Reference Resis. Ω (K = 150)	Date 1979	Electrode No.	Reference Resis. Ω (K = 150)	Date 1979
-24	Open (∞)	Oct.10	17	28	Oct.10
-23	↓	↓	18	30	↓
-22	↓	↓	19	28	↓
-21	↓	↓	20	28	↓
-20	↓	↓	21	30	↓
-19	↓	↓	22	↓	↓
-18	↓	↓	23	32	↓
-17	↓	↓	24	30	↓
-16	↓	↓	25	↓	↓
-15	↓	↓	26	↓	↓
-14	↓	↓	27	39	↓
-13	↓	↓	28	37	↓
-12	↓	↓	29	39	↓
-11	↓	↓	30	41	↓
-10	↓	↓	31	39	↓
- 9	↓	↓	32	37	↓
- 8	↓	↓	33	39	↓
- 7	↓	↓	34	↓	↓
- 6	↓	↓	35	↓	↓
- 5	↓	↓	36	↓	↓
- 4	↓	↓	37	↓	↓
- 3	↓	↓	38	↓	↓
- 2	↓	↓	39	↓	↓
- 1	↓	↓	40	↓	↓
0	28	↓	41	↓	↓
1	30	↓	42	↓	↓
2	30	↓	43	38	Oct.11
3	28	↓	44	↓	↓
4	30	↓	45	↓	↓
5	↓	↓	46	↓	↓
6	↓	↓	47	↓	↓
7	↓	↓	48	↓	↓
8	↓	↓	49	↓	↓
9	28	↓	50	↓	↓
10	30	↓	51	↓	↓
11	↓	↓	52	↓	↓
12	↓	↓	53	↓	↓
13	↓	↓	54	↓	↓
14	↓	↓	55	↓	↓
15	28	↓	56	↓	↓
16	30	↓	57	↓	↓

0-4330

TABLE 3-4. (cont.)

Electrode No.	Reference Resis. Ω (K = 150)	Date 1979	Electrode No.	Reference Resis. Ω (K = 150)	Date 1979
58	48	Oct.11	102	53	Oct.15
59	47		103	51	
60			104		
61			105		
62			106	53	
63			107	56	
64	50		108	58	
65	47		109	53	
66	50		110	51	
67	47		111	50	Oct.16
68			112	50	
69			113	52	
70			114	50	
71	50		115		
72	47		116		
73			117		
74			118		
75			119	52	
76			120	50	
77			121		
78			122		
79			123		
80	50		124		
81	51	Oct.15	125		
82			126		
83			127		
84			128	52	
85			129	50	
86			130		
87	53		131		
88	51		132		
89			133	52	
90			134	52	
91			135	50	
92	53		136		
93	51		137		
94			138		
95			139		
96			140		
97			141		
98			142	48	
99			143	52	
100			144	50	
101			145	52	

0-4330-1

TABLE 3-4. (cont.)

Electrode No.	Reference Resis. Ω (K = 150)	Date 1979	Electrode No.	Reference Resis. Ω (K = 150)	Date 1979
146	50	Oct.16	190	67	Oct.17
147	52		191	69	
148	52		192		
149	50		193		
150	52		194	64	
151			195	67	
152			196		
153			197	69	
154	50		198	67	
155			199	69	
156			200	69	
157	52		201	67	
158	50		202	69	
159			203	67	
160			204		
161			205		
162			206	69	
163	67		207		
164			208		
165		Oct.17	209	67	
166			210	62	
167			211	69	
168	69		212	67	
169	67		213	67	
170			214	64	
171			215	69	
172	69		216	67	
173	67		217	63	Oct.18
174			218	65	
175			219		
176			220		
177	69		221		
178	67		222	63	
179	69		223	65	
180	67		224		
181	69		225		
182	67		226		
183	69		227	68	
184	67		228	65	
185			229	68	
186			230	68	
187			231	65	
188			232	65	
189			233	68	

0-4330-2

TABLE 3-4. (cont.)

Electrode No.	Reference Resis. Ω (K = 150)	Date 1979	Electrode No.	Reference Resis. Ω (K = 150)	Date 1979
234	68	Oct.18	278	69	Oct.18
235	65	↓	279	65	↓
236	65	↓	280	68	↓
237	63	↓	281	63	↓
238	65	↓	282	↓	↓
239	↓	↓	283	↓	↓
240	↓	↓	284	65	↓
241	↓	↓	285	↓	↓
242	↓	↓	286	↓	↓
243	↓	↓	287	68	↓
244	↓	↓	288	65	↓
245	63	↓	289	↓	↓
246	65	↓	290	↓	↓
247	↓	↓	291	63	↓
248	↓	↓	292	65	↓
249	↓	↓	293	↓	↓
250	68	↓	294	↓	↓
251	65	↓	295	↓	↓
252	68	↓	296	68	↓
253	65	↓	297	65	↓
254	↓	↓	298	68	↓
255	↓	↓	299	70	↓
256	↓	↓	300	68	↓
257	↓	↓	301	65	↓
258	↓	↓	302	65	↓
259	↓	↓	303	63	↓
260	↓	↓	304	63	↓
261	↓	↓	305	65	↓
262	↓	↓	306	63	↓
263	↓	↓	307	65	↓
264	↓	↓	308	68	↓
265	↓	↓	309	63	↓
266	↓	↓	310	65	↓
267	68	↓	311	68	↓
268	65	↓	312	70	↓
269	68	↓	313	65	↓
270	65	↓	314	↓	↓
271	↓	↓	315	↓	↓
272	↓	↓	316	67	↓
273	68	↓	317	67	↓
274	63	↓	318	63	↓
275	65	↓	319	68	↓
276	63	↓	320	63	↓
277	65	↓	321	65	↓

0-4330-3

TABLE 3-4. (cont.)

Electrode No.	Reference Resis. Ω (K = 150)	Date 1979	Electrode No.	Reference Resis Ω (K = 150)	Date 1979
322	70	Oct.18	367	70	Oct.19
323	65	↓	368	68	↓
324	68	↓	369	↓	↓
325	68	↓	370	↓	↓
326	65	↓	371	↓	↓
327	63	↓	372	↓	↓
328	68	↓	373	66	↓
329	65	↓	374	70	↓
330	65	↓	375	63	↓
331	70	↓	376	89	↓
332	68	↓	377	91	↓
333	65	↓	378	89	↓
334	63	↓	379	89	↓
335	65	↓	380	105	↓
336	65	↓	381	103	↓
337	↓	↓	382	108	↓
338	↓	↓	383	127	↓
339	↓	↓	384	152	↓
340	↓	↓	385	164	↓
341	↓	↓	386	176	↓
342	70	↓	387	Open (∞)	↓
343	68	↓	388	↓	↓
344	65	↓	389	↓	↓
345	68	↓	390	↓	↓
346	65	↓	391	↓	↓
347	65	↓	392	↓	↓
348	63	↓	393	↓	↓
349	68	↓	394	↓	↓
350	63	↓	395	↓	↓
351	68	↓	396	↓	↓
352	65	↓	397	↓	↓
353	68	↓	398	↓	↓
354	68	↓	399	↓	↓
355	65	↓	400	↓	↓
356	68	↓	401	↓	↓
357	65	↓	402	↓	↓
358	70	Oct.19	403	↓	↓
359	70	↓	404	↓	↓
360	68	↓	405	↓	↓
361	70	↓	406	↓	↓
362	70	↓	407	↓	↓
363	68	↓	408	↓	↓
364	↓	↓	409	↓	↓
365	↓	↓	410	↓	↓
366	70	↓	411	↓	↓

0-4330-4

TABLE 3-4. (cont.)

Electrode No.	Reference Resis. Ω (K = 150)	Date 1979
412	Open (∞)	Oct.19
413		
414		
415		
416		
417		
418		
419		
420		
421		
422		
423		
424		
425		
426		
427		
428		
429		
430		
431		
432		
433		
434		
435		
436		
437		
438		
439		
450		
451		
452		
453		
454		
455		

0-4330-5

TABLE 3-4. (cont.)

B. HPDE Load Resistance Settings for Runs Subsequent to 006-007

Electrode No.	Reference Resis. Ω (K = 150)	Date 1979	Electrode No.	Reference Resis. Ω (K = 150)	Date 1979
336	Open (∞)	Oct.18	377	142	Oct.18
337	↓	↓	378	↓	↓
338	↓	↓	379	↓	↓
339	↓	↓	380	↓	↓
340	↓	↓	381	↓	↓
341	↓	↓	382	↓	↓
342	↓	↓	383	↓	↓
343	↓	↓	384	↓	↓
344	↓	↓	385	↓	↓
345	↓	↓	386	↓	↓
346	↓	↓	387	↓	↓
347	↓	↓	388	↓	↓
348	↓	↓	389	↓	↓
349	↓	↓	390	↓	↓
350	↓	↓	391	↓	↓
351	↓	↓	392	↓	↓
352	↓	↓	393	↓	↓
353	↓	↓	394	↓	↓
354	↓	↓	395	112	↓
355	↓	↓	396	110	↓
356	↓	↓	397	112	↓
357	65	↓	398	↓	↓
358	101	↓	399	↓	↓
359	96	↓	400	↓	↓
360	100	↓	401	Open (∞)	↓
361	102	↓	402	↓	↓
362	102	↓	403	↓	↓
363	97	↓	404	↓	↓
364	100	↓	405	↓	↓
365	102	↓	406	↓	↓
366	102	↓	407	↓	↓
367	102	↓	408	↓	↓
368	100	↓	409	↓	↓
369	100	↓	410	↓	↓
370	102	↓	411	↓	↓
371	100	↓	412	↓	↓
372	142	↓	413	↓	↓
373	↓	↓	414	↓	↓
374	↓	↓	415	↓	↓
375	↓	↓	416	↓	↓
376	142	↓	417	↓	↓

0-4330-6

TABLE 3-4. (cont.)

Electrode No.	Reference Resis. Ω (K = ±50)	Date 1979
418	Open (∞)	Oct.18
419		
420		
421		
422		
423		
424		
425		
426		
427		
428		
429		
430		
431		
432		
433		
434		
435		
436		
437		
438		
439		
440		
441		
442		
443		
444		
445		
446		
447		
448		
449		
450		
451		
452		
453		
454		
455		

0-4330-7

TABLE 3-5

Water Conductivity in Load Buckets for AEDC Experiments

Run No.	K_{run} (μS/cm)	Ref.
006-006	178.0	[3-8]
006-008	175.4	[3-9]
006-010	178.6	[3-11]
006-011	approx. 180.0	[3-11]
006-012	172.4	[3-11]
006-013	150.0	[3-15]
006-014	160.0	[3-16]

0-4358

TABLE 3-6

Flow Rates of Combustion Gases and
Runs 006-008 and 006-014

Component	Run 006-008	006-014
Fuel (kg/s)	6.60	6.84
Oxidizer (kg/s)	40.99	39.82
Seed (kg/s)	1.84	2.54
Pilot (CH_4) (kg/s)	0.034	0.034
N_2/O_2 ratio	1.0	0.929
Seed Concentration (kg KCH/kg CH_3OH)	0.3	0.3
Equivalence Ratio (fuel lean)	1.5	1.11
Total enthalpy of combustion gases (no losses) (MW)	299.3	303.8
Specific enthalpy of combustion gases (MJ/kg)	6.05	6.16
T_{flame} (6 atm) (K)	3048	3063

0-4359

TABLE 3-7

Load Resistances for AEDC Run 006-014

Data Acquisition Station Number	Electrode Pair Number	Nominal Resistance (K_{con} = 150) (ohms)	Averaged Experimental Resistance $4.54 \leq T2 \leq 5.21$ (ohms)	Indicated Conductivity Factor (μS/cm)
1	42	39.1	36.64	160.0
2	84	50.9	48.19	158.4
3	126	50.0	47.97	156.3
4	168	69.1	65.63	157.8
5	210	61.9	61.25	151.6
6	252	67.8	66.02	154.0
7	294	65.5	65.82	149.3
8	336	65.5	65.70	149.5
9	376	141.6	153.71	138.2

0-4360

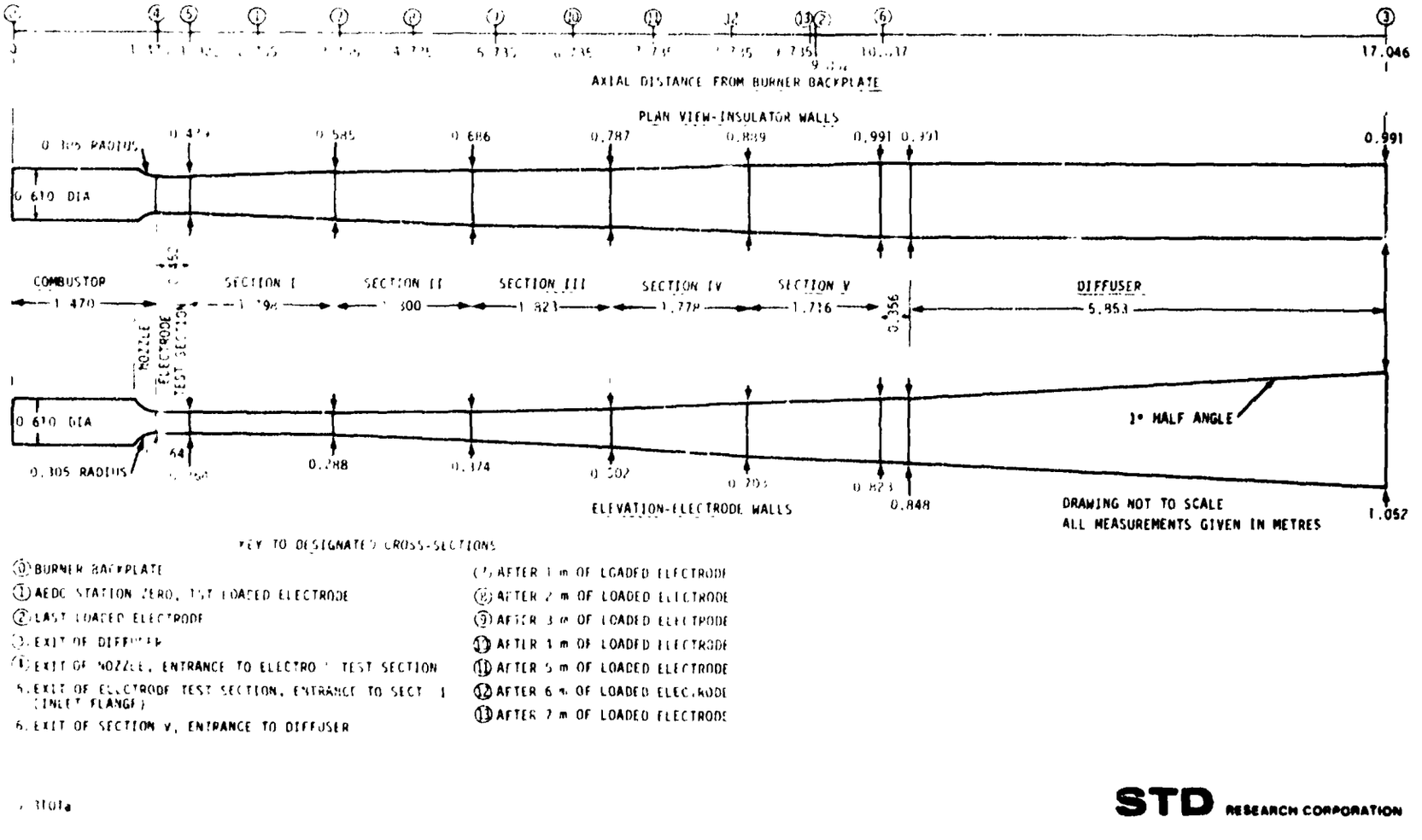

KEY TO DESIGNATED CROSS-SECTIONS

0. BURNER BACKPLATE
1. AEDC STATION ZERO, 1ST LOADED ELECTRODE
2. LAST LOADED ELECTRODE
3. EXIT OF DIFFUSER
4. EXIT OF NOZZLE, ENTRANCE TO ELECTRODE TEST SECTION
5. EXIT OF ELECTRODE TEST SECTION, ENTRANCE TO SECT I (INLET FLANGE)
6. EXIT OF SECTION V, ENTRANCE TO DIFFUSER
7. AFTER 1 m OF LOADED ELECTRODE
8. AFTER 2 m OF LOADED ELECTRODE
9. AFTER 3 m OF LOADED ELECTRODE
10. AFTER 4 m OF LOADED ELECTRODE
11. AFTER 5 m OF LOADED ELECTRODE
12. AFTER 6 m OF LOADED ELECTRODE
13. AFTER 7 m OF LOADED ELECTRODE

STD RESEARCH CORPORATION

Fig. 3-1. AEDC/HPDE internal geometry with designated cross sections

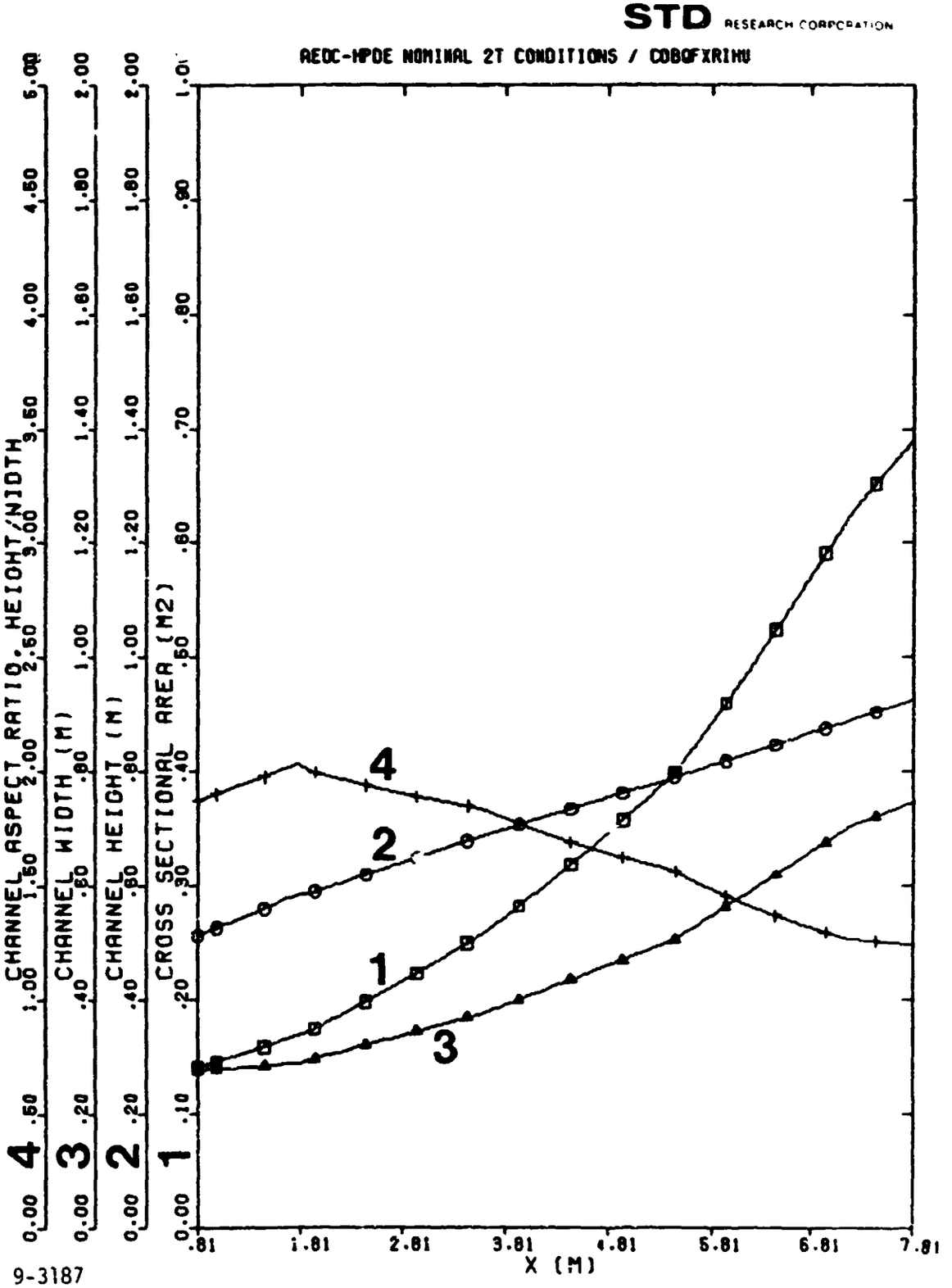

Fig. 3-2. Axial variation of the channel geometry in the AEDC/HPDE at the nominal 2 T operating conditions.

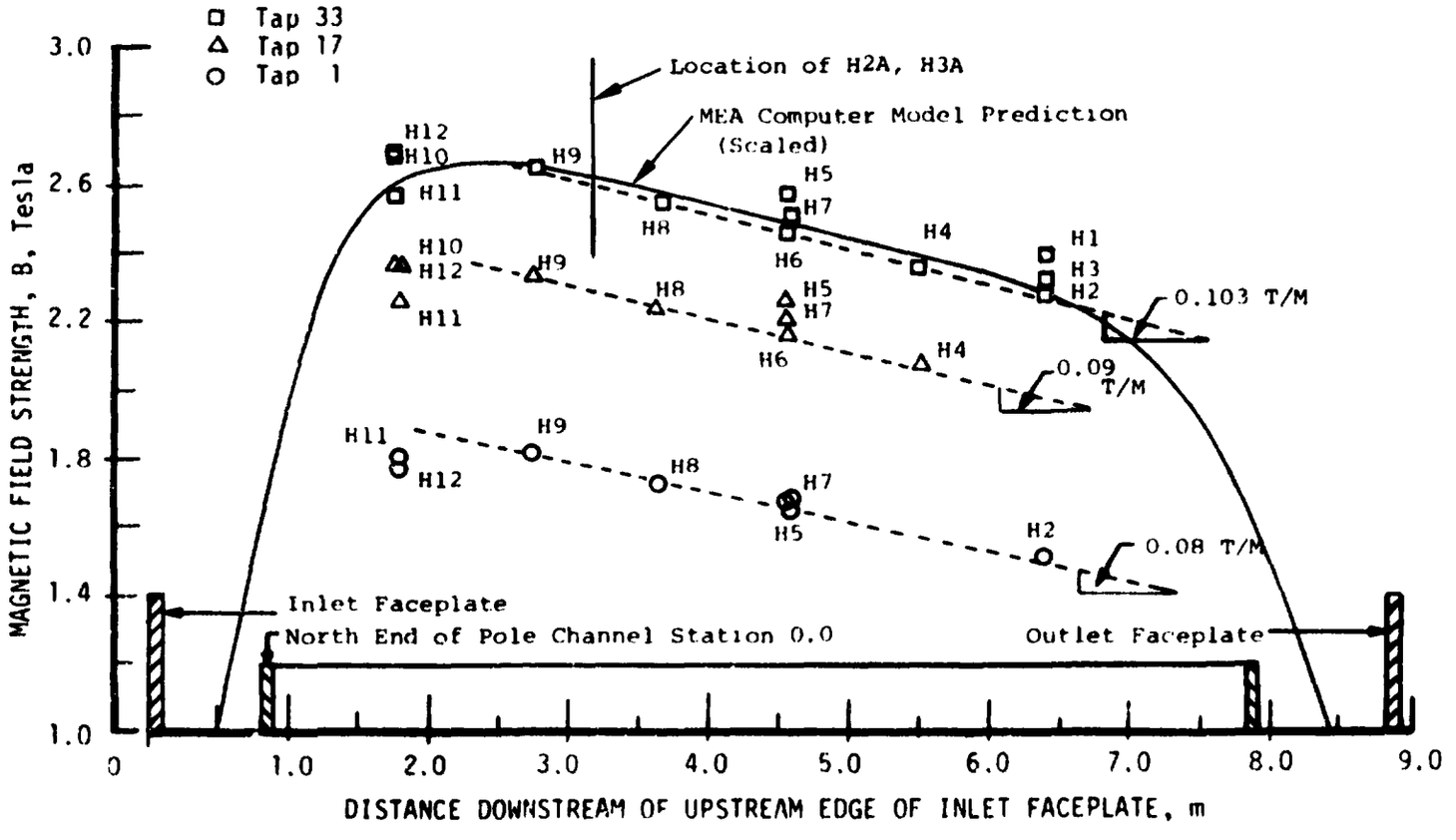

Fig. 3-3. Magnetic field strength distribution along magnet bore

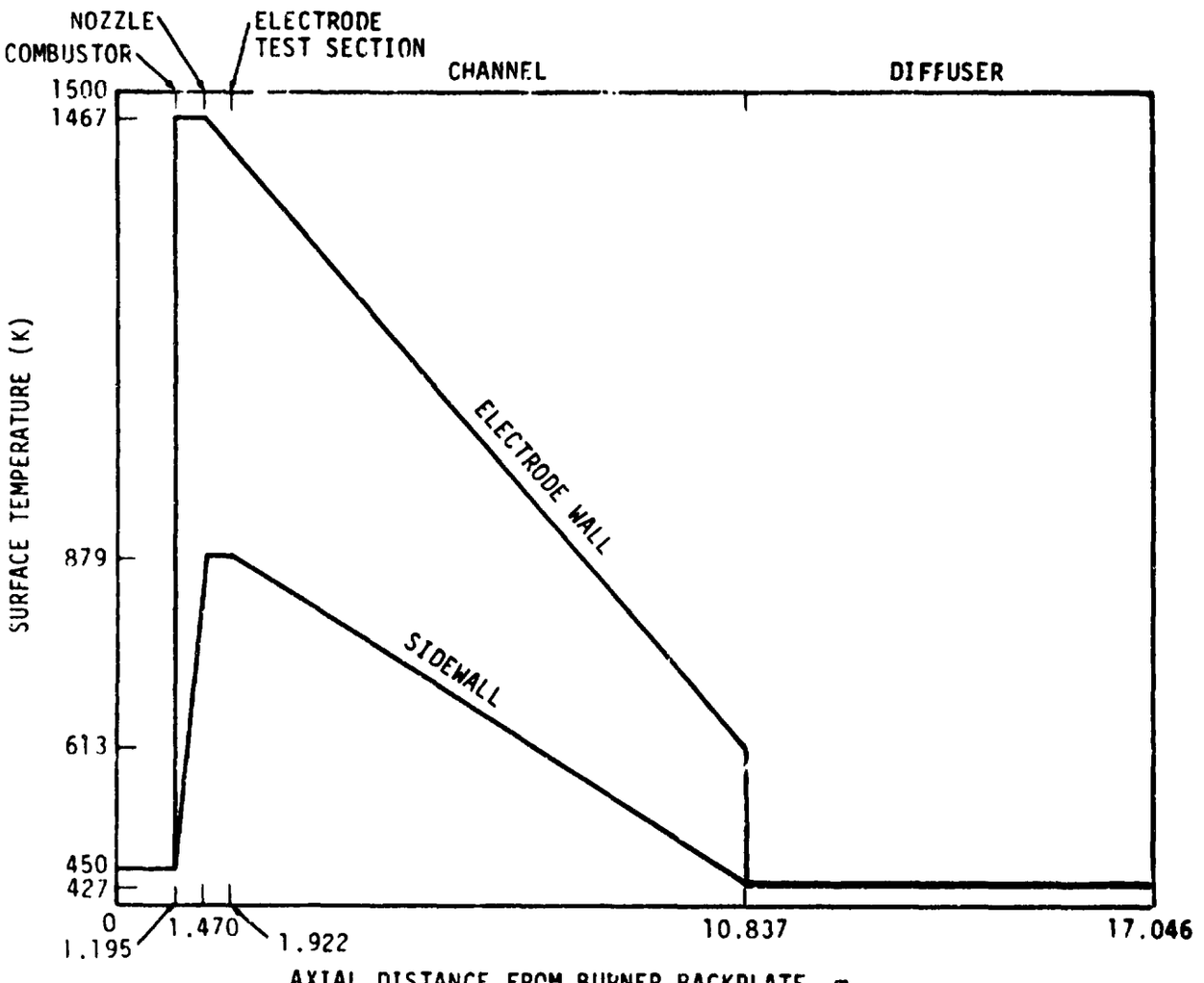

Fig. 3-4. AEDC/HPDE nominal wall surface temperature distribution.

9-3103b

STD RESEARCH CORPORATION

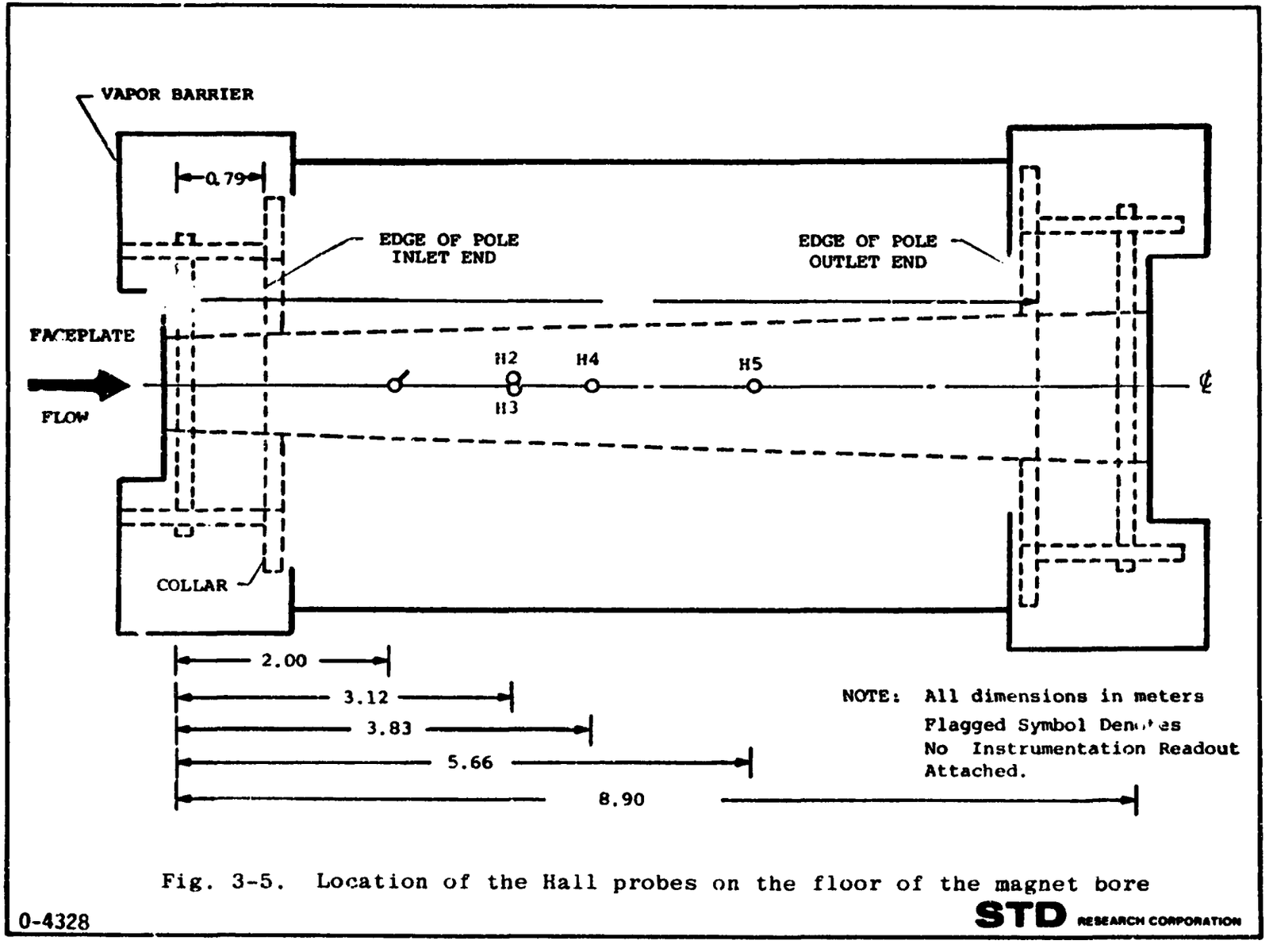

Fig. 3-5. Location of the Hall probes on the floor of the magnet bore

0-4328

STD RESEARCH CORPORATION

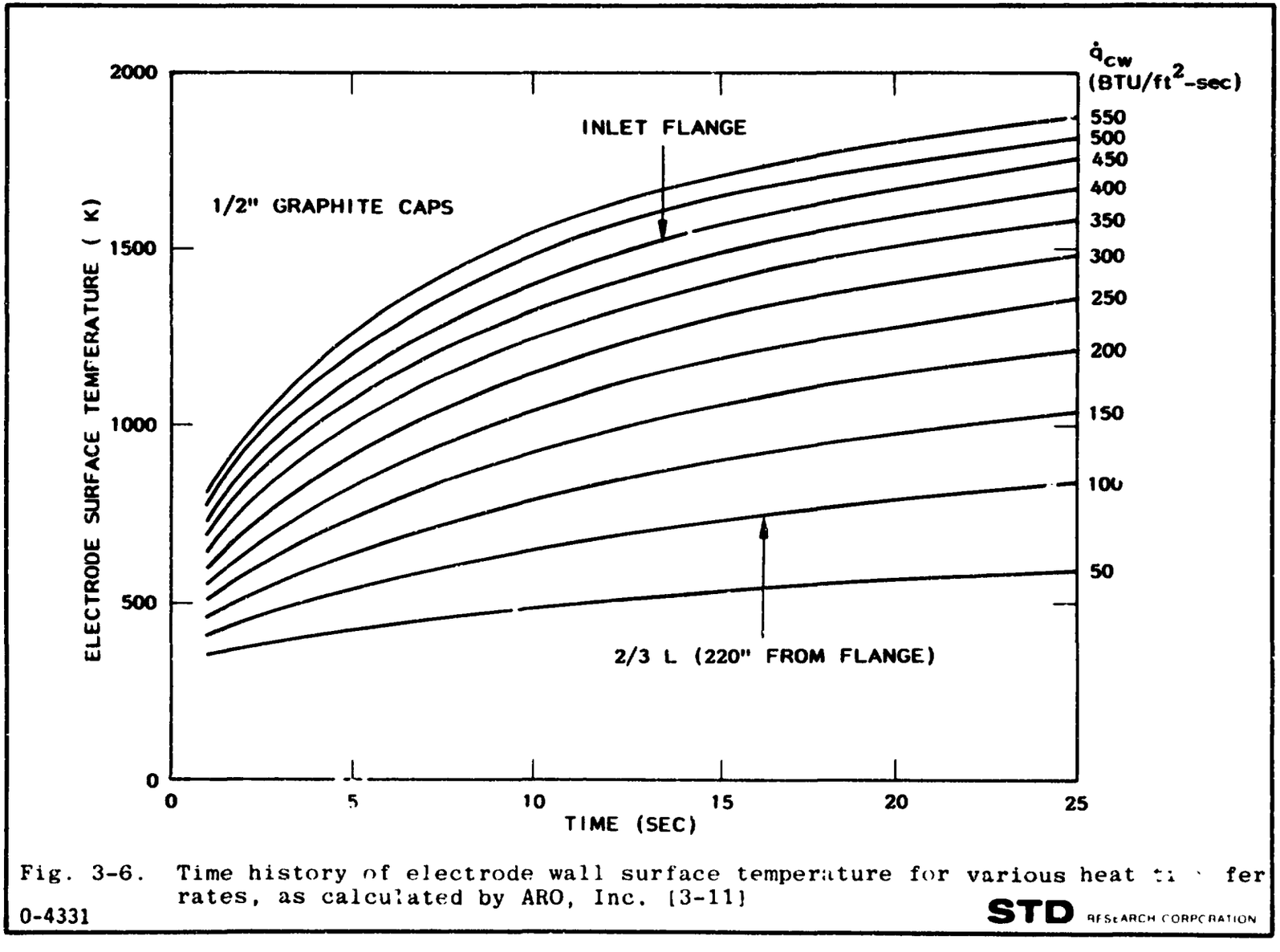

Fig. 3-6. Time history of electrode wall surface temperature for various heat transfer rates, as calculated by ARO, Inc. [3-11]

0-4331

STD RESEARCH CORPORATION

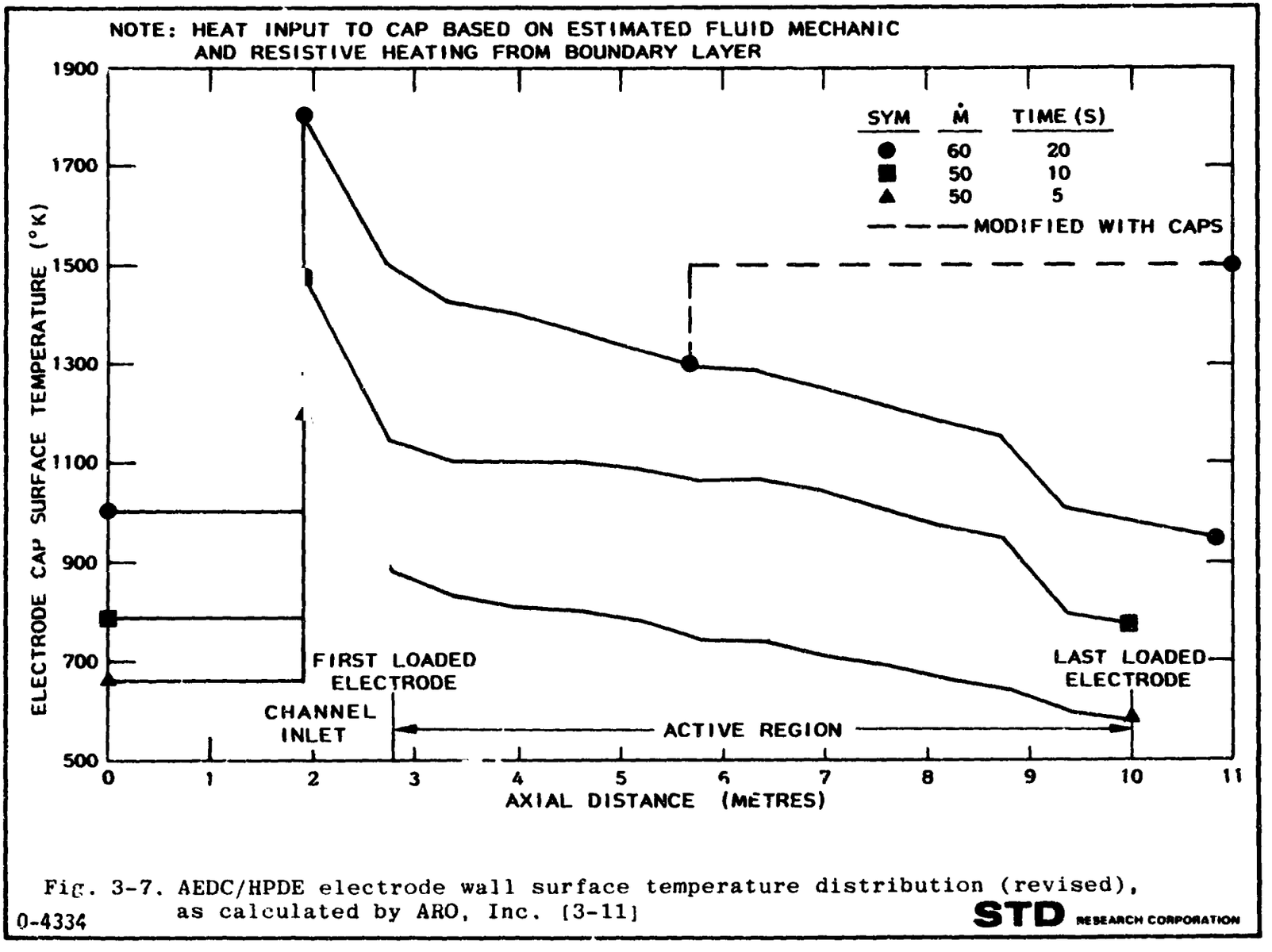

Fig. 3-7. AEDC/HPDE electrode wall surface temperature distribution (revised), as calculated by ARO, Inc. [3-11]

0-4334

STD RESEARCH CORPORATION

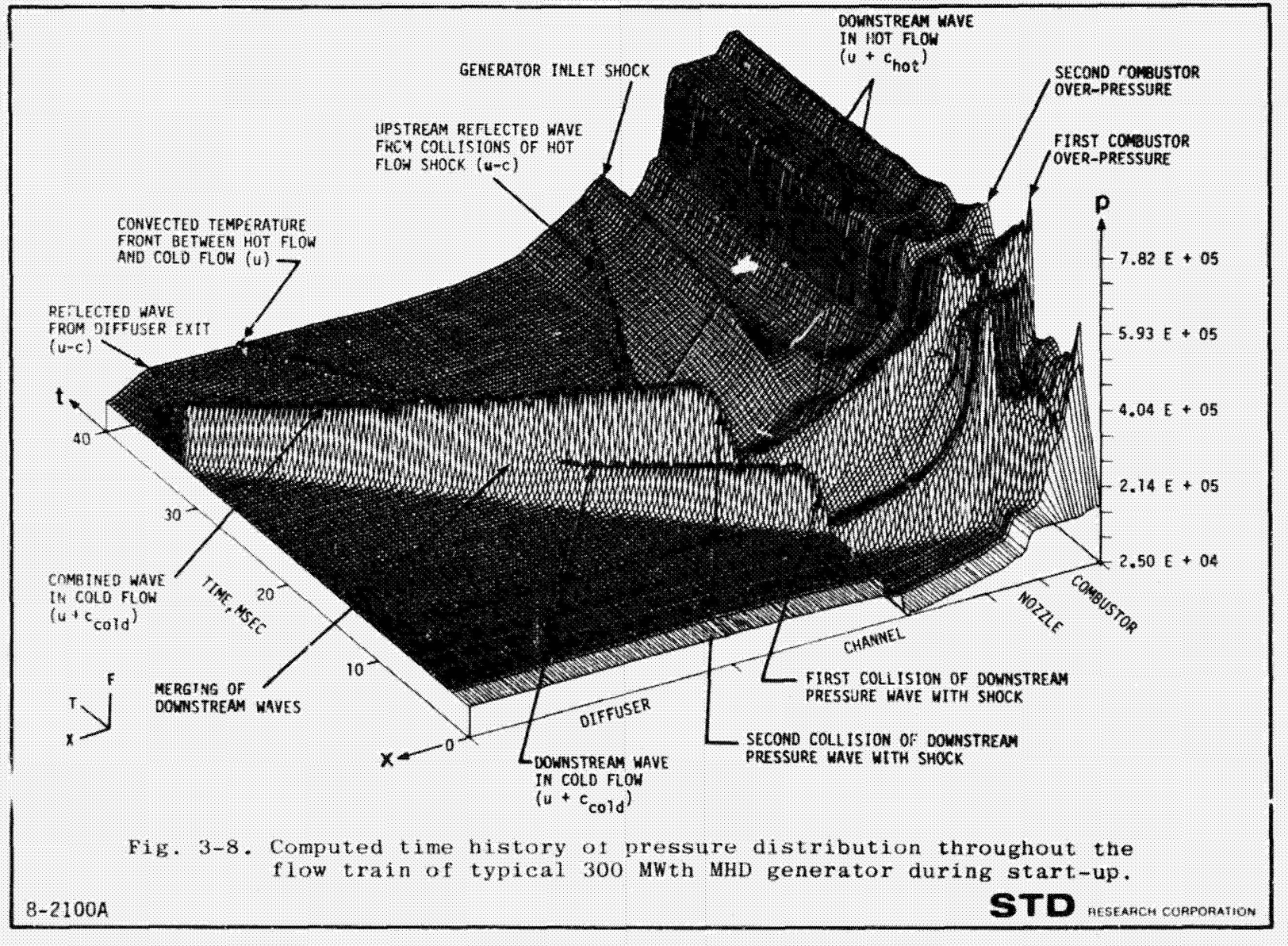

Fig. 3-8. Computed time history of pressure distribution throughout the flow train of typical 300 MWth MHD generator during start-up.

8-2100A

STD RESEARCH CORPORATION

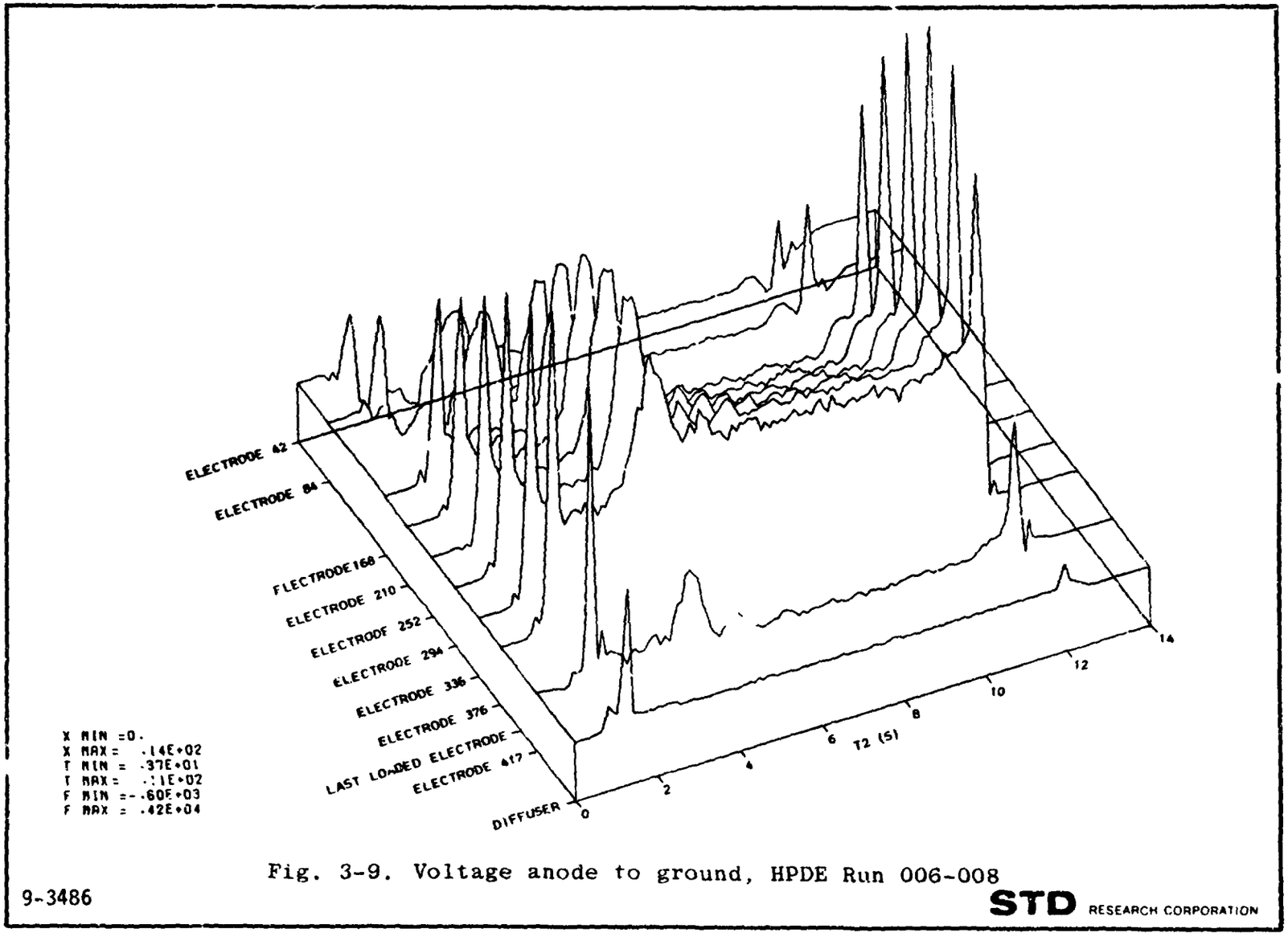

Fig. 3-9. Voltage anode to ground, HPDE Run 006-008

9-3486

STD RESEARCH CORPORATION

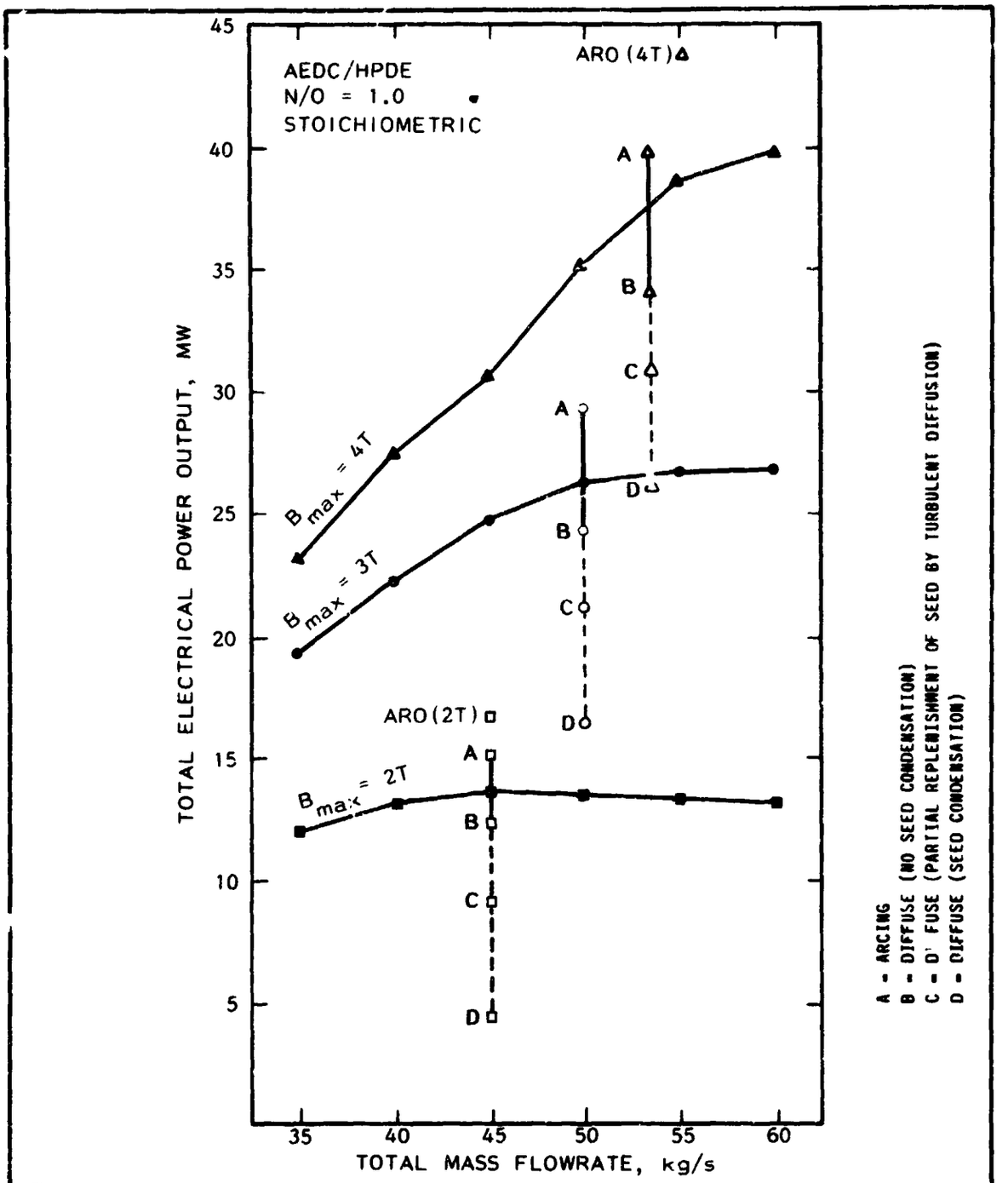

Fig. 3-10. Electrical power output as a function of mass flowrate and magnetic field for the nominal operating conditions of the AEDC/HPDE. Code families: TRANSIENT and Q3D. Codes: MQS (solid symbols) and Q3DXY & Q3DXZ (open symbols). All computations completed before 18 September 1979.

9-3323

STD RESEARCH CORPORATION

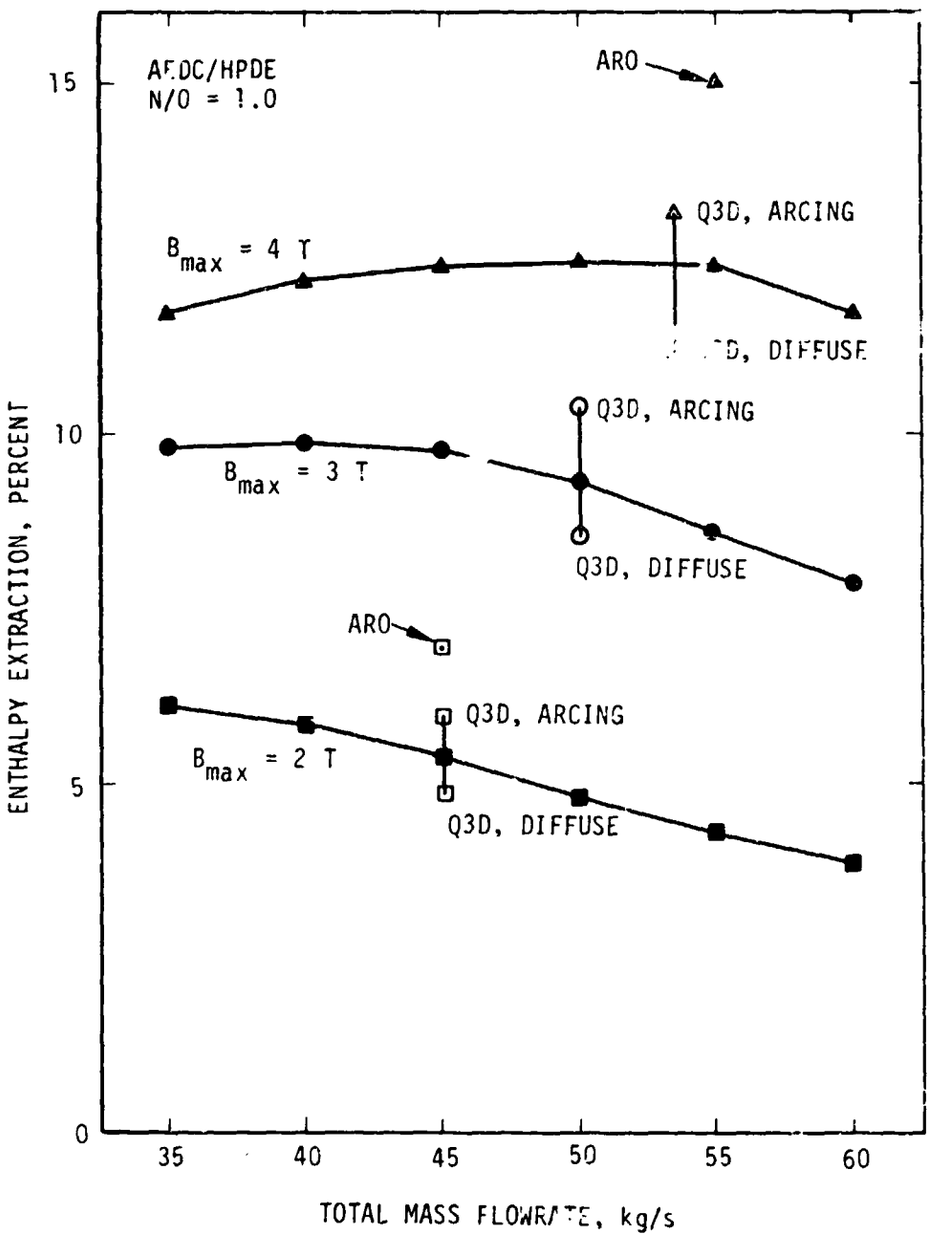

Fig. 3-11. Enthalpy extraction ratio as a function of mass flow rate and magnetic field for the nominal operating conditions of the AEDC/HPDE. Code families: TRANSIENT and Q3D. Codes: TQS and Q3DX4 + Q3DXZ (no condensation considered.)

9-3217

STD RESEARCH CORPORATION

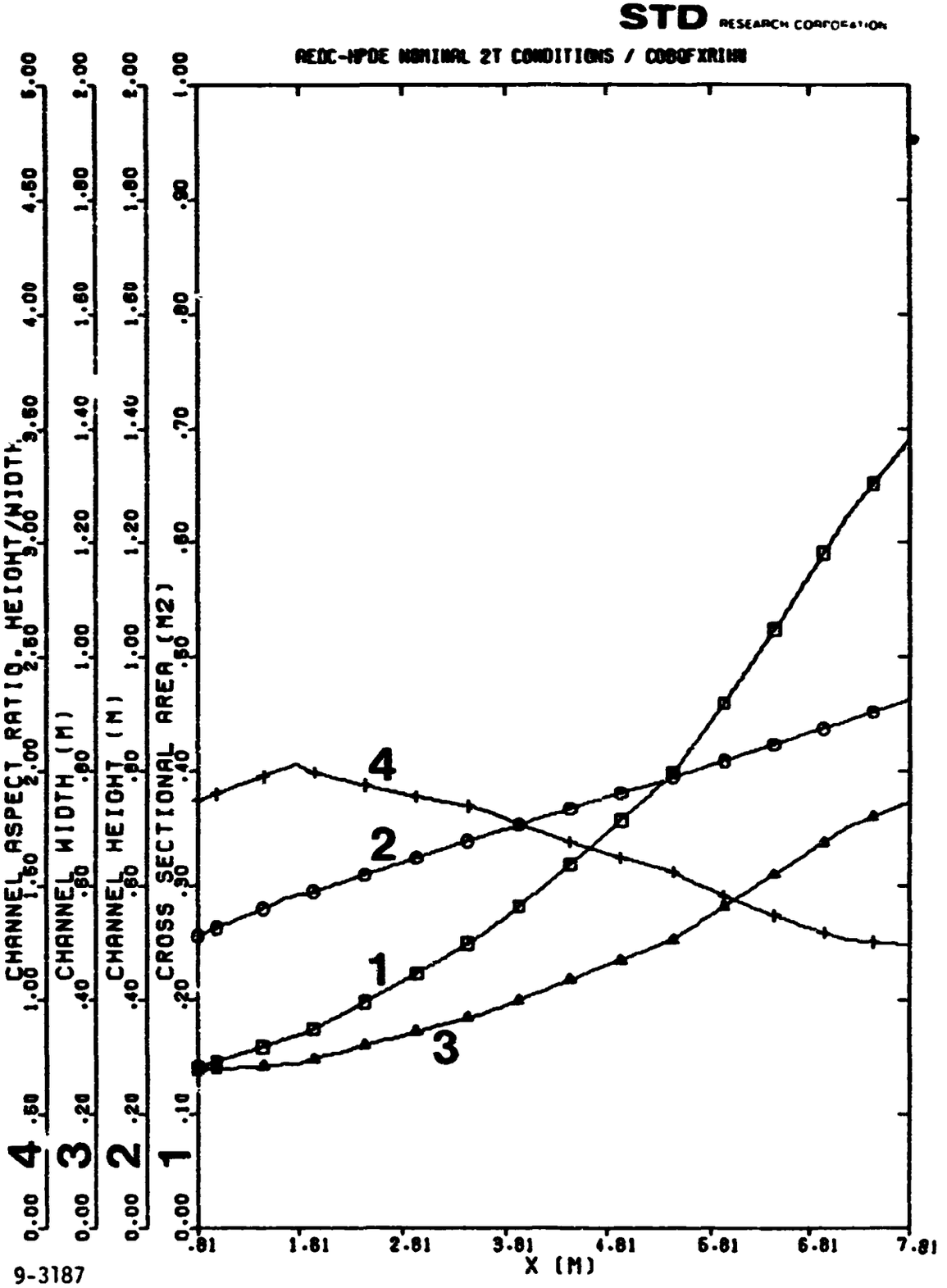

Fig. 3-12. Axial variation of the channel geometry in the AEDC/HPDE at the nominal 2 T operating conditions: Q3D calculation.

C-2

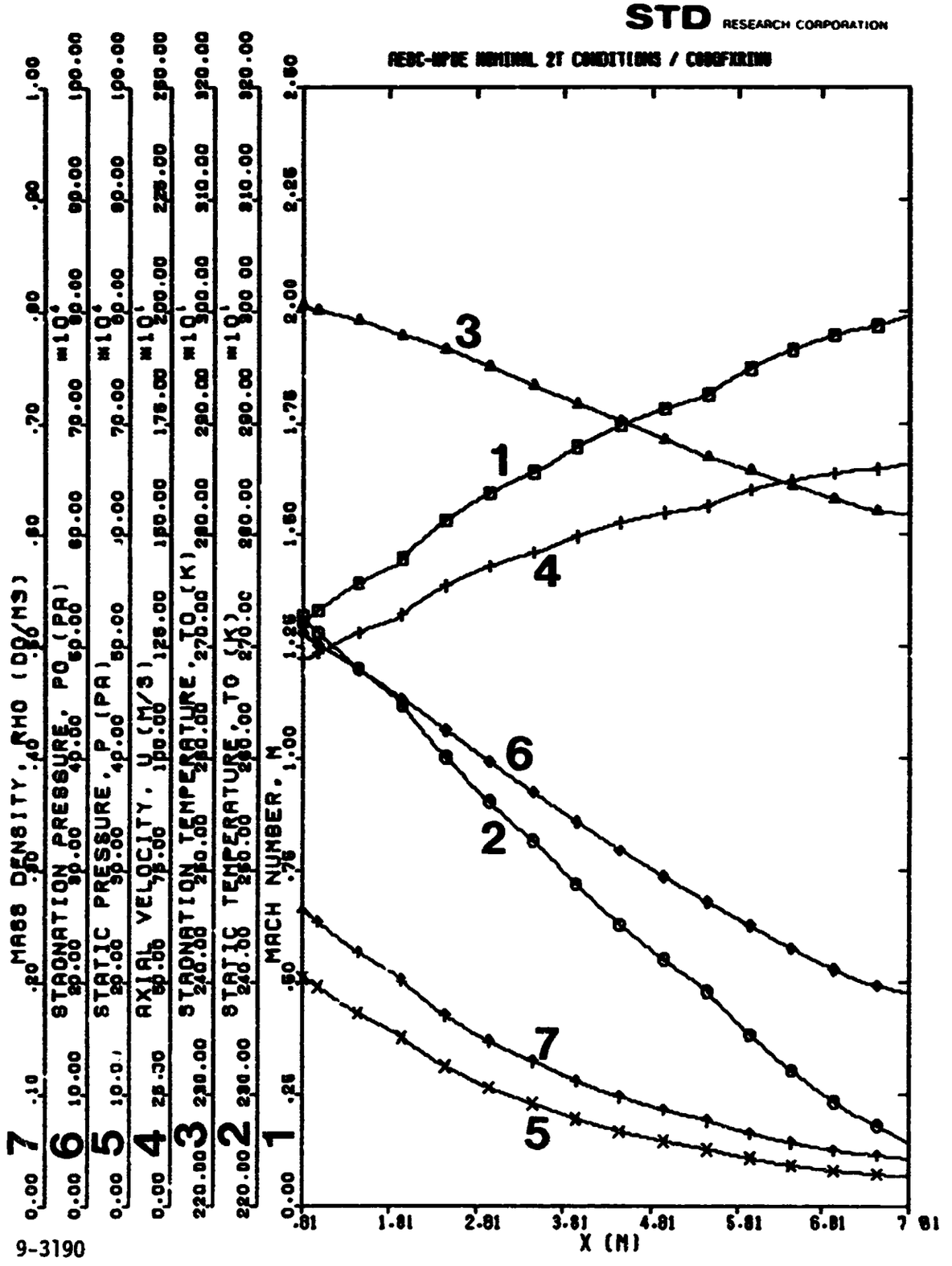

Fig. 3-13. Axial variation of the centerline gasdynamic variables in the AEDC/HPDE at the nominal 2 T operating conditions: Q3D calculation.

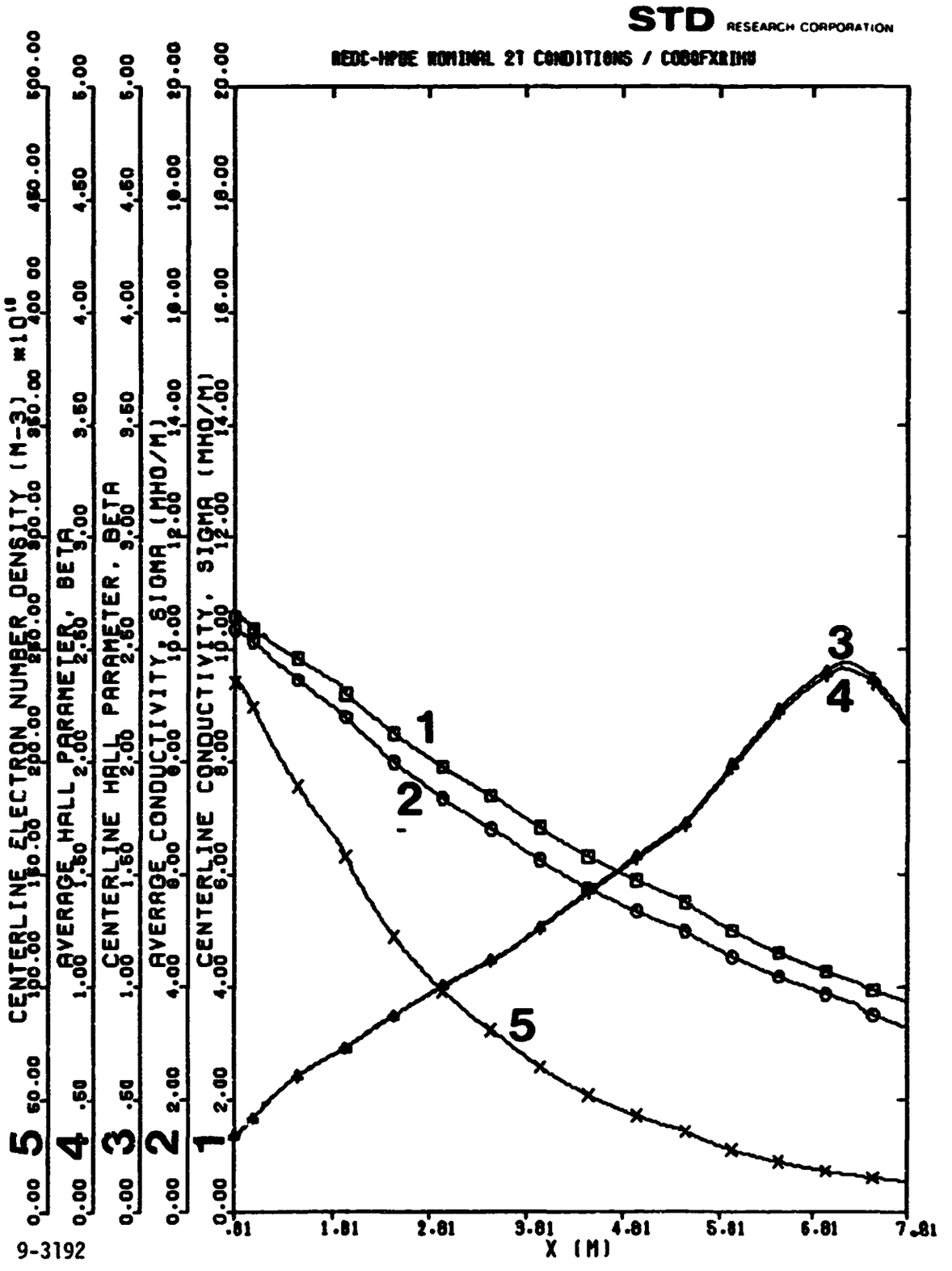

Fig. ?-14. Axial variation of the plasma parameters in the AEDC/HPDE at the nominal 2 T operating conditions: Q3D calculation.

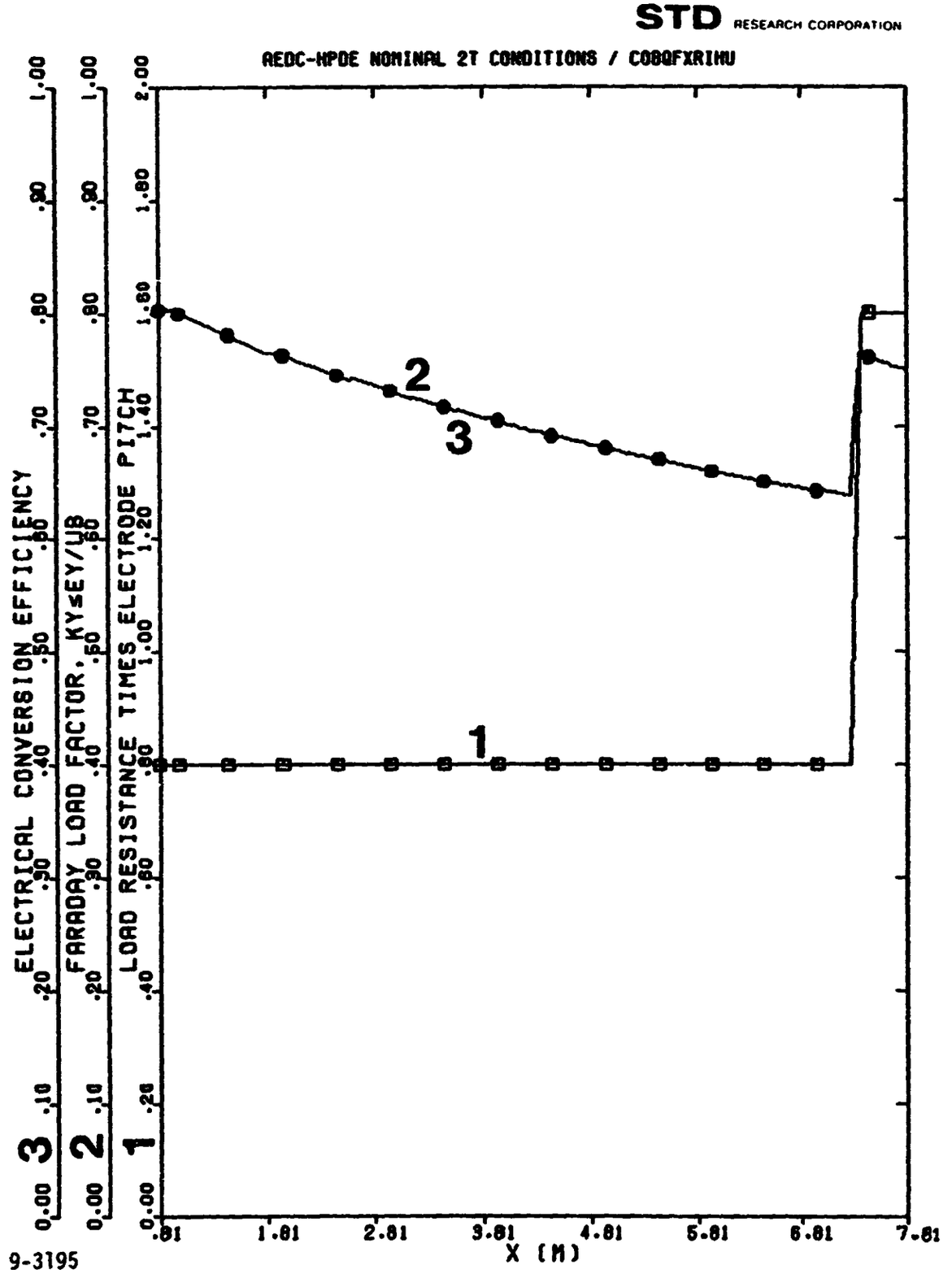

Fig. 3-15. Axial variation of the electrical loading in the AEDC/HPDE at the nominal 2 T operating conditions; Q3D calculation.

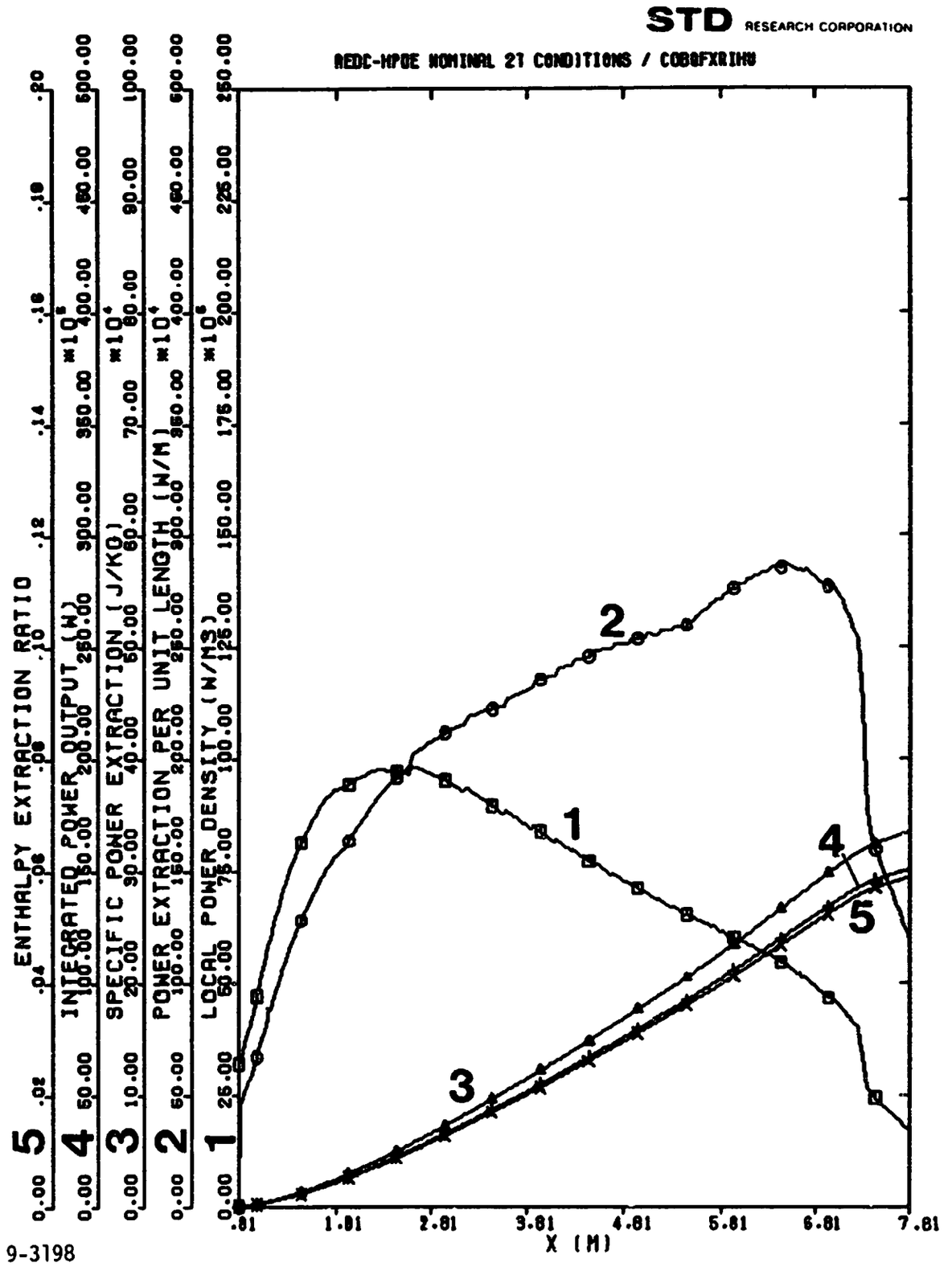

Fig. 3-16. Axial variation of the power extraction parameters in the AEDC/HPDE at the nominal 2 T operating conditions: Q3D calculation

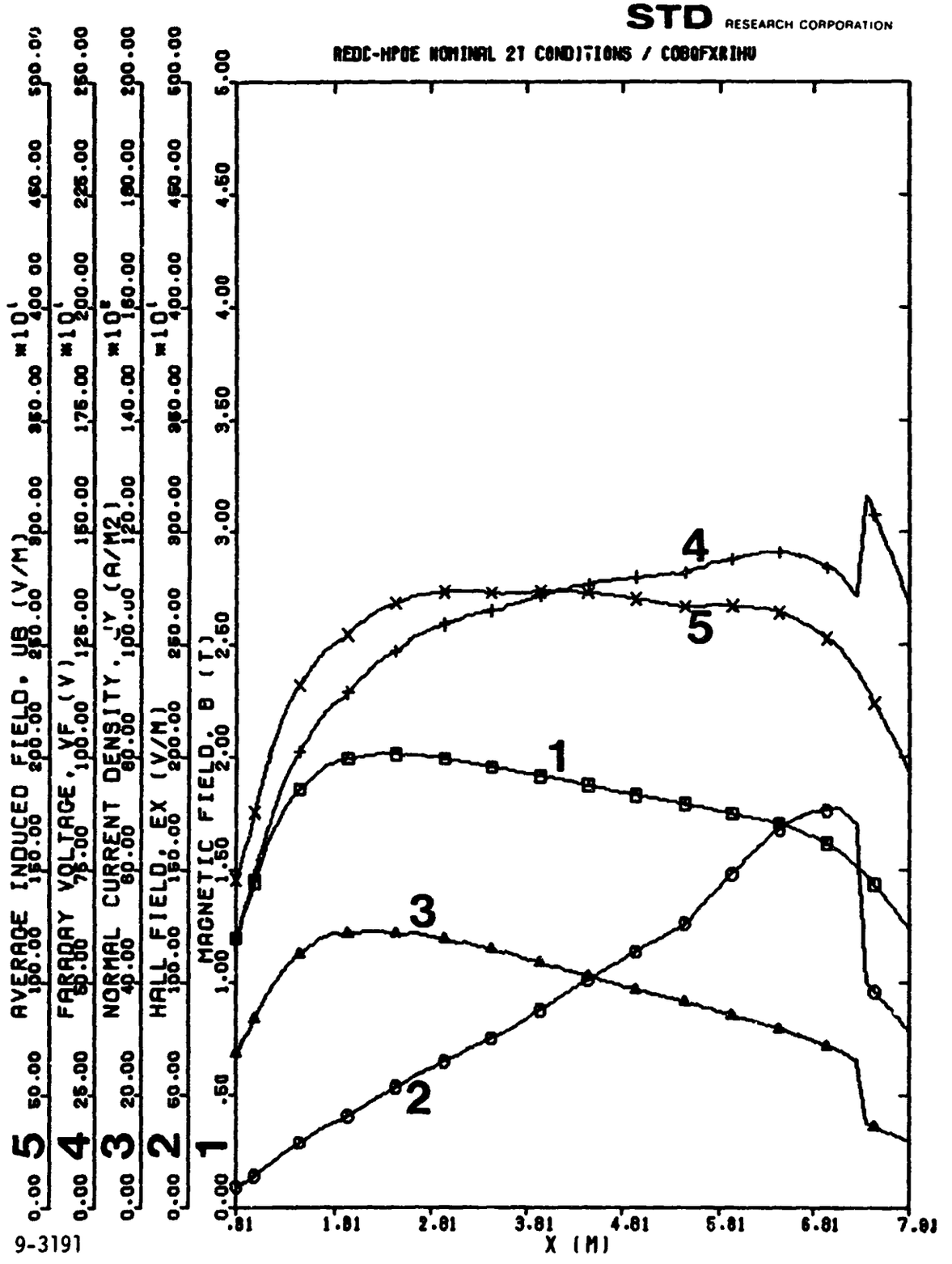

Fig. 3-17. Axial variation of the electrical field variables in the AEDC/HPDE at the nominal 2 T operating conditions: Q3D calculations.

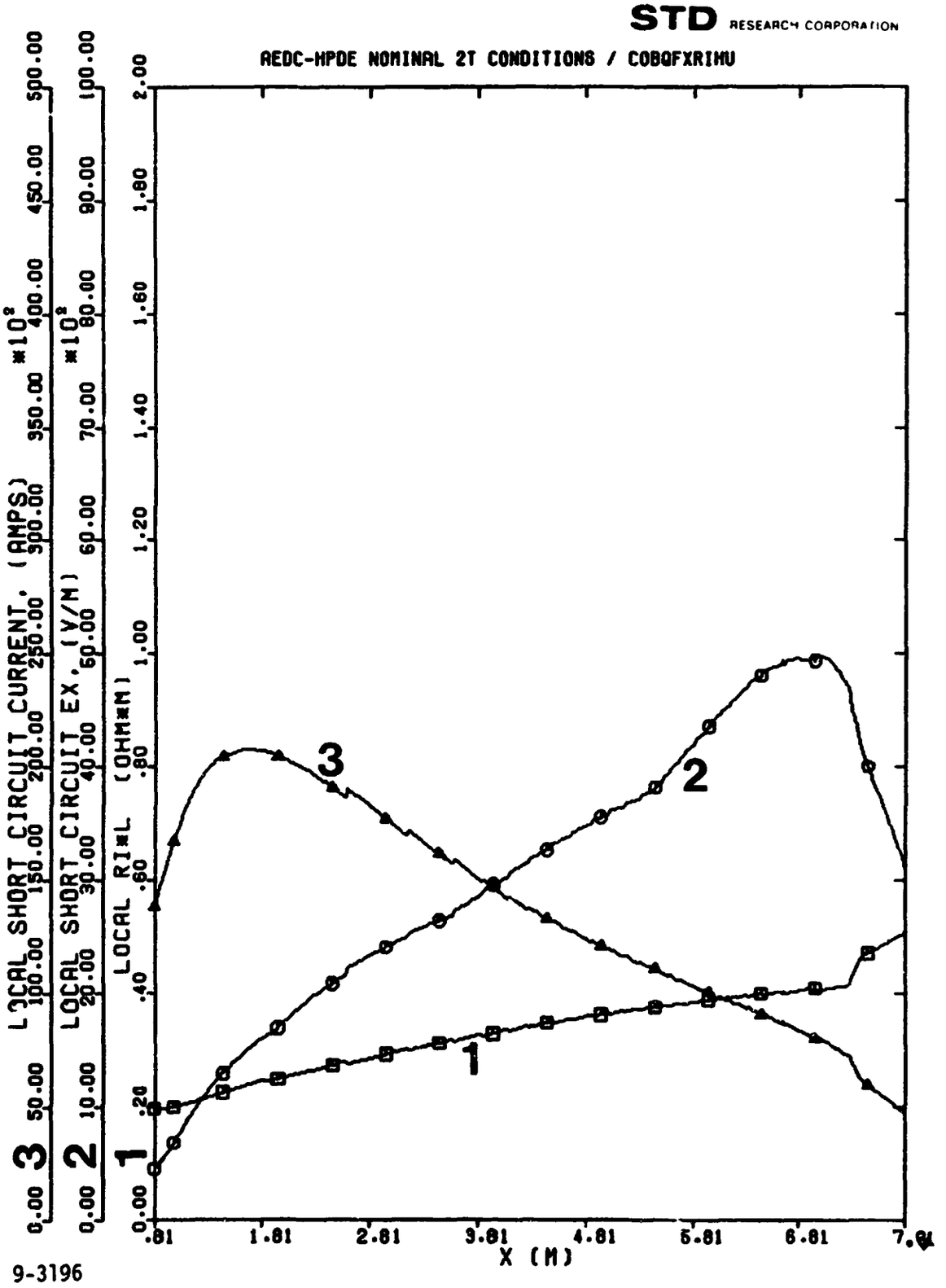

Fig. 3-18. Axial variation of the short circut fields and the local internal impedance in the AEDC/HPDE at the nominal 2 T operating conditions: Q3D calculation.

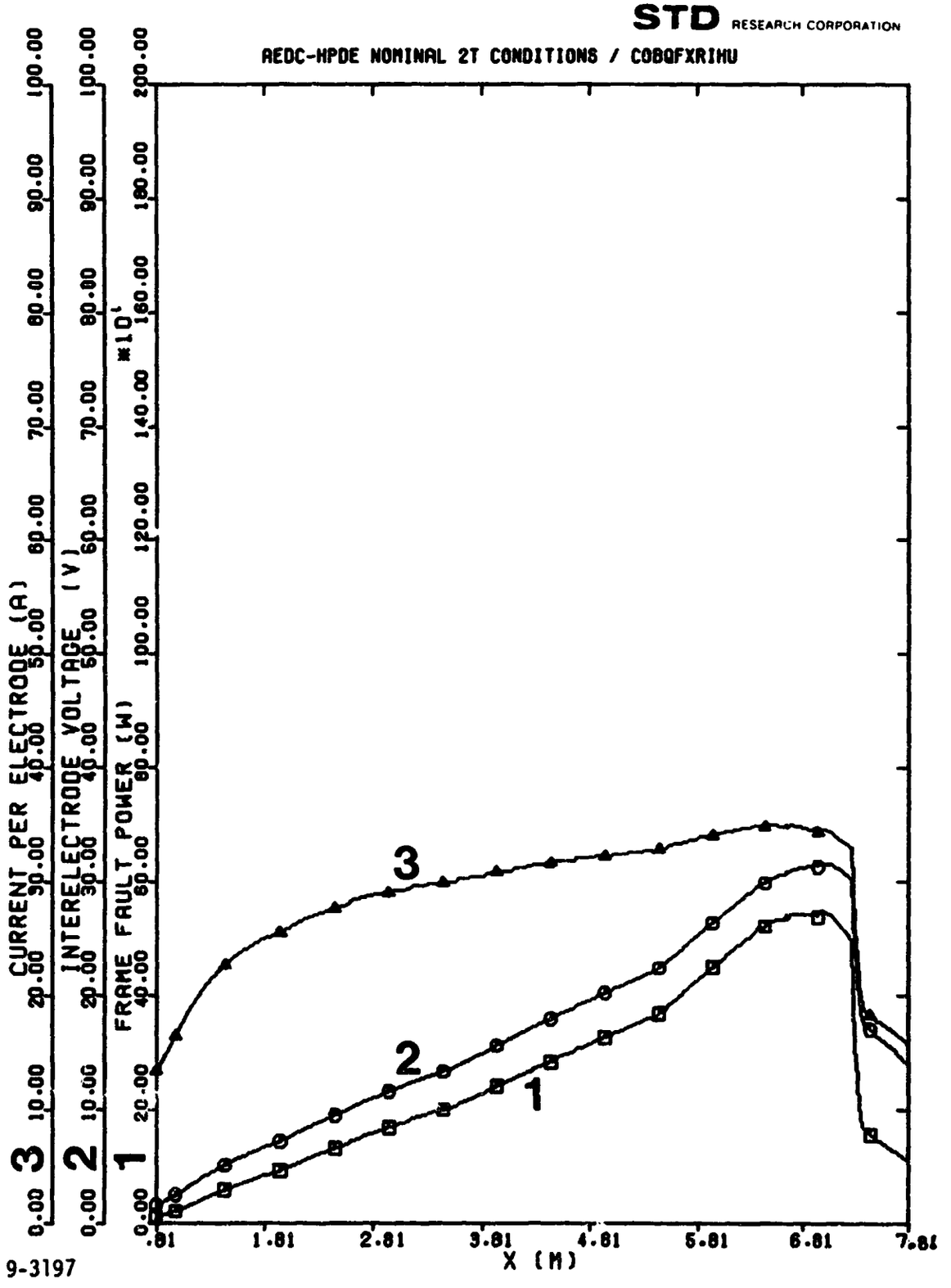

Fig. 3-19. Axial variation of the electrical stresses on the electrodes in the AEDC/HPDE at the nominal 2 T operating conditions: Q3D calculation.

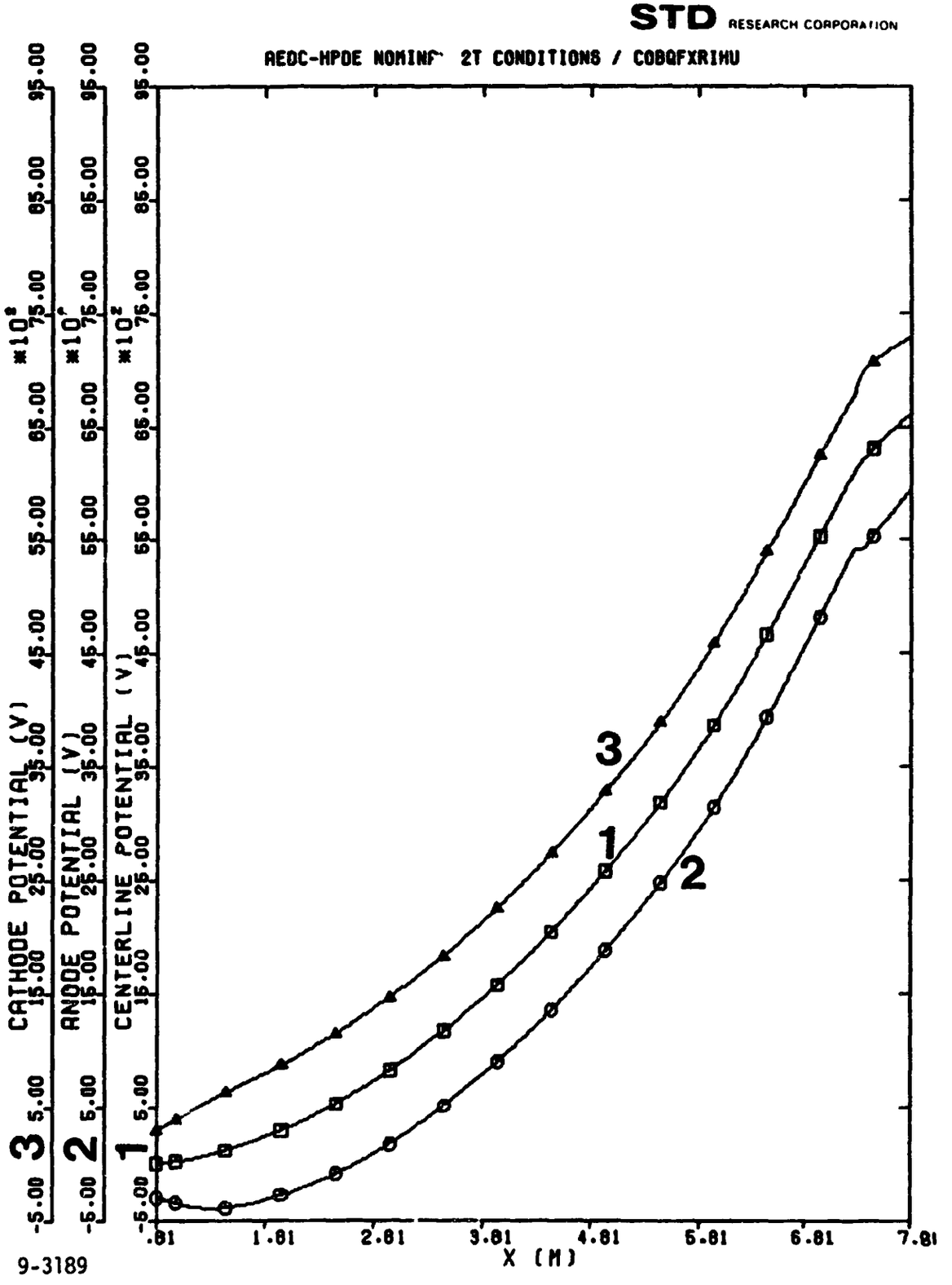

Fig. 3-20. Axial variation of the electric potential in the AEDC/HPDE at the nominal 2 T operating conditions: Q3D calculation.

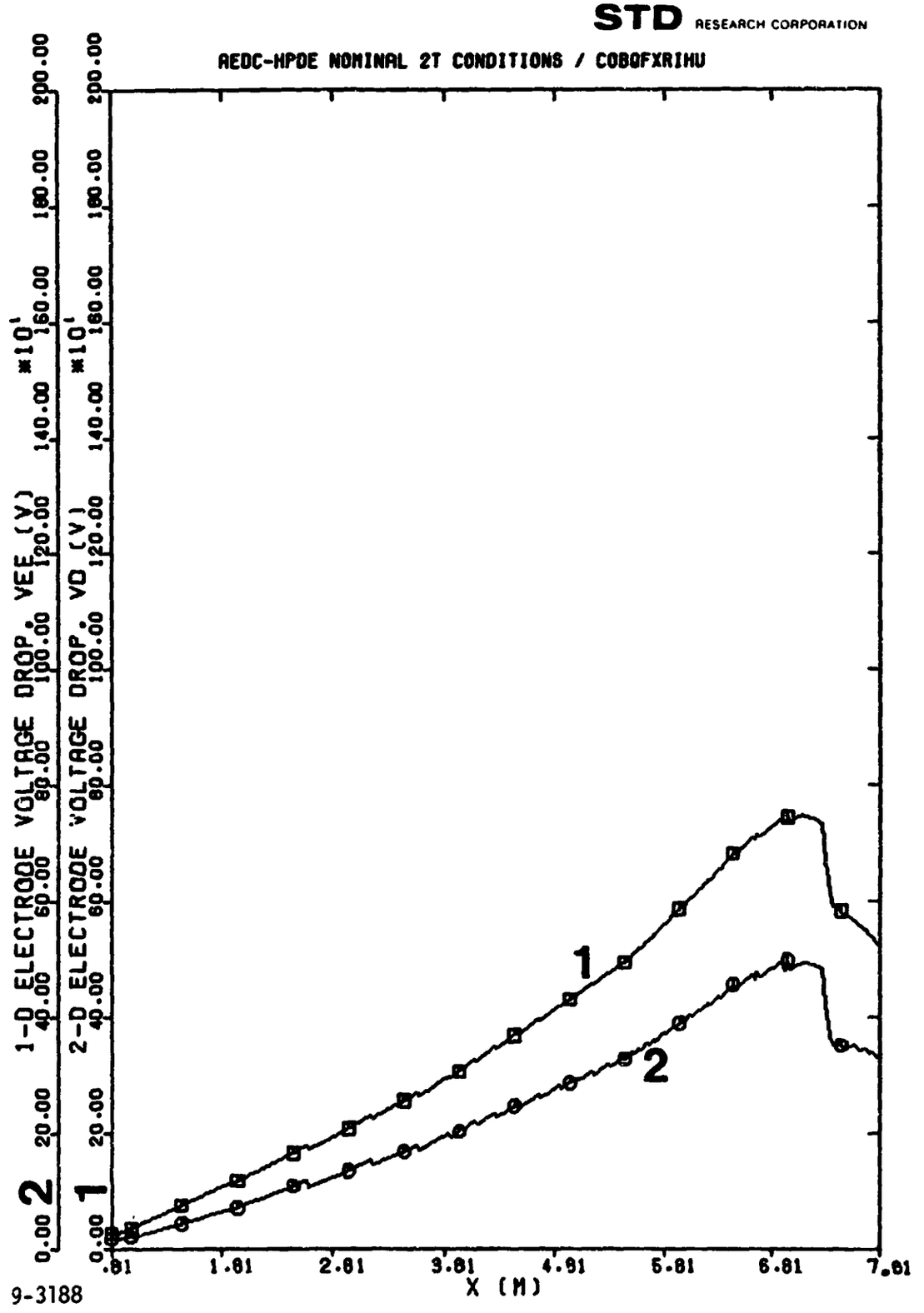

Fig. 3-21. Axial variation of the electrode voltage drops in the AEDC/HPDE at the nominal 2 T operating conditions: Q3D calculation.

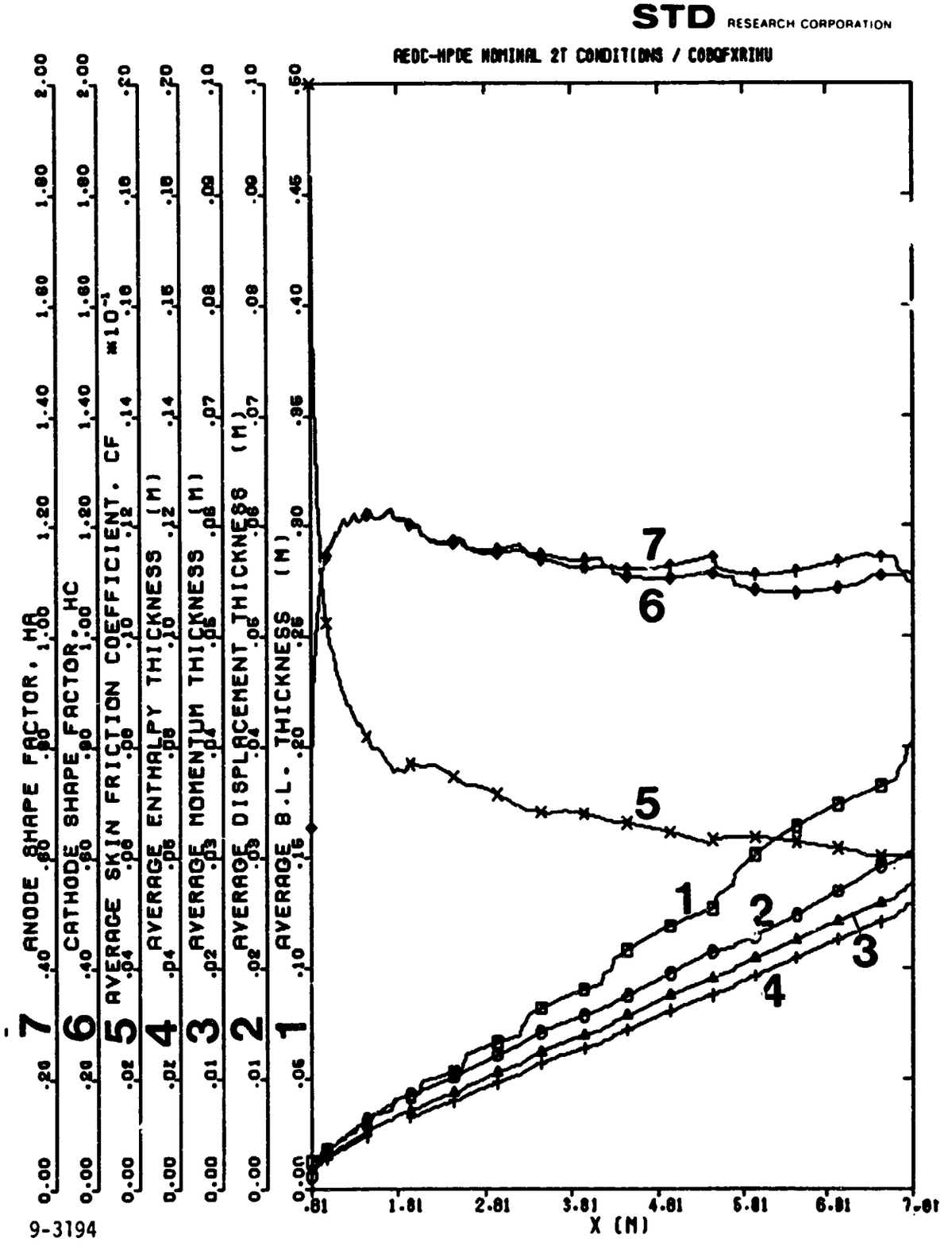

Fig. 3-22. Axial variation of the electrode boundary layer parameters in the AEDC/HPDE at the nominal 2 T operating conditions: Q3D calculation.

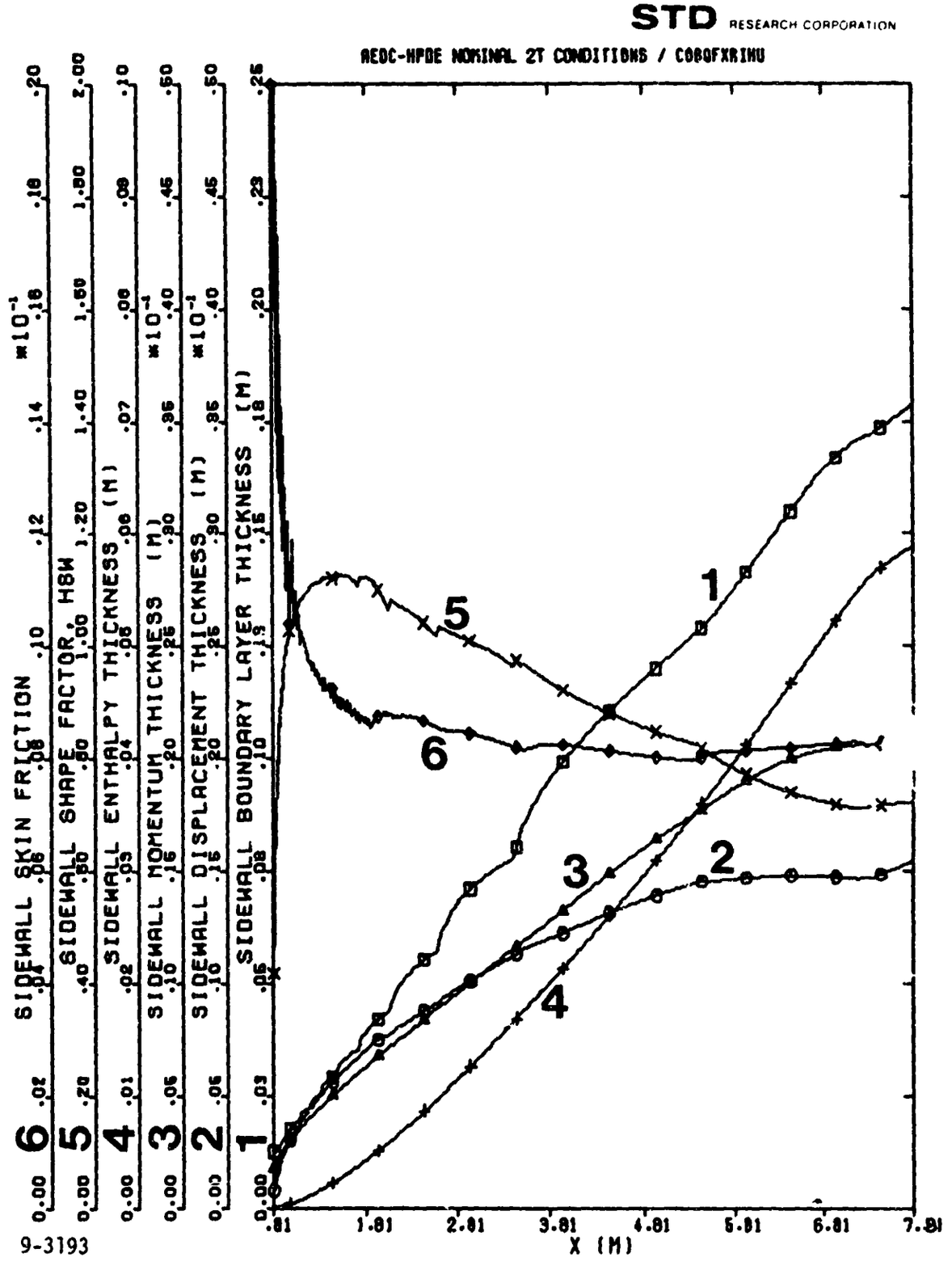

Fig. 3-23. Axial variation of the sidewall boundary layer parameters in the AEDC/HPDF at the nominal 2 T operating conditions: Q3D calculation.

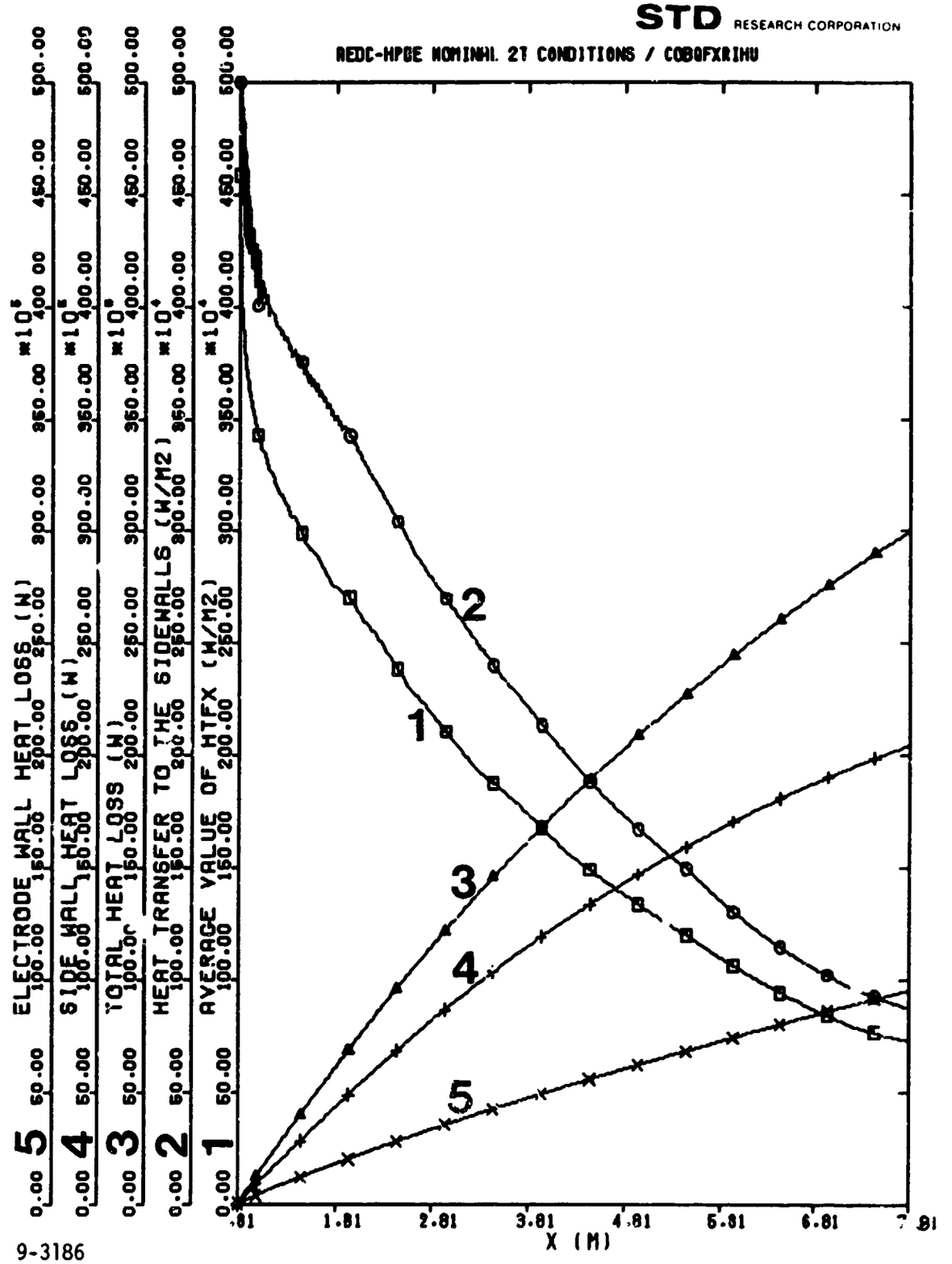

Fig. 3-24. Axial variation of the heat transfer parameters in the AEDC/HPDE at the nominal 2 T operating conditions: Q3D calculation.

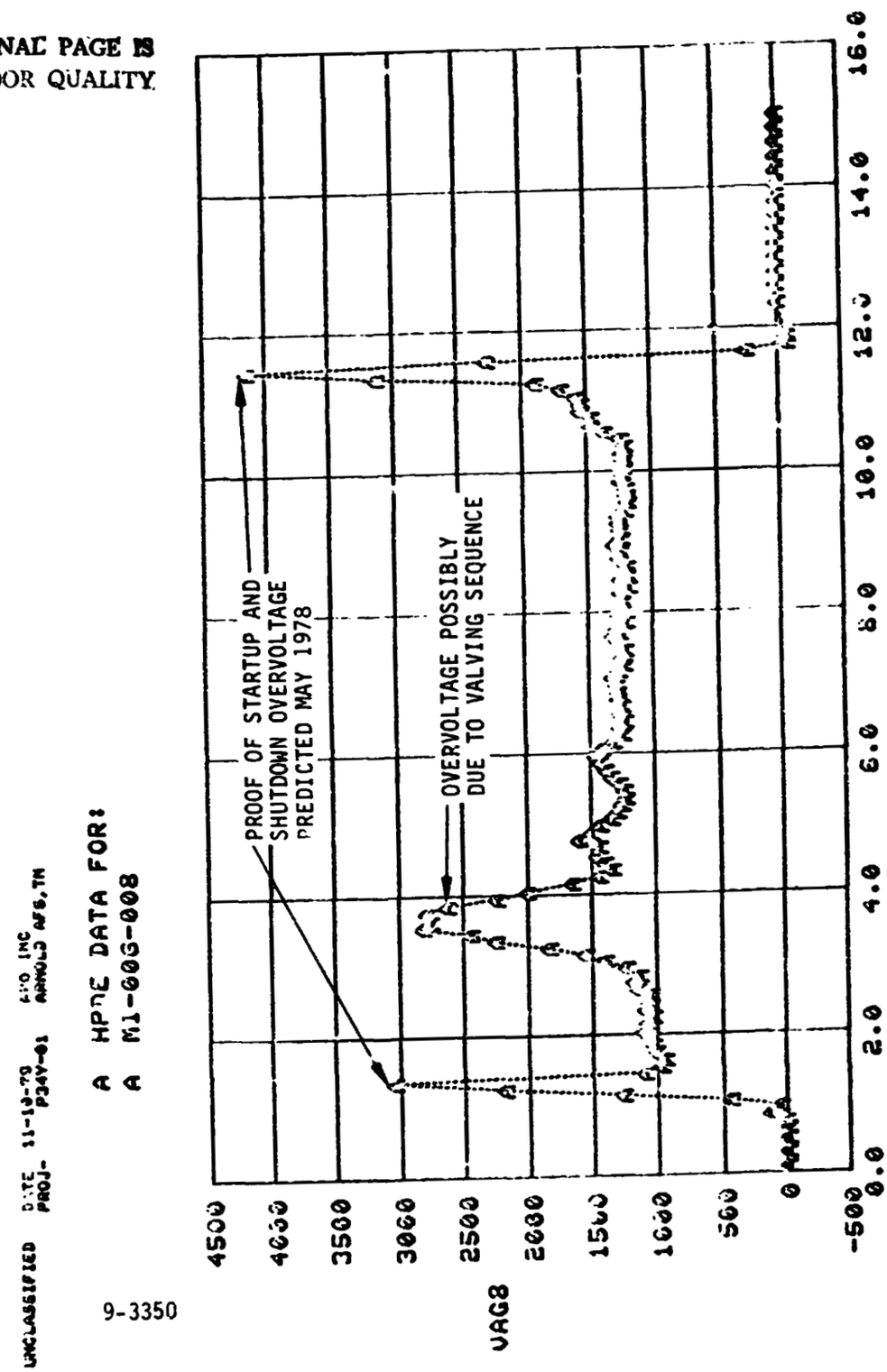

Fig. 3-25. Anode to ground voltage of electrode 336 for AEDC/HPDE run 006-008

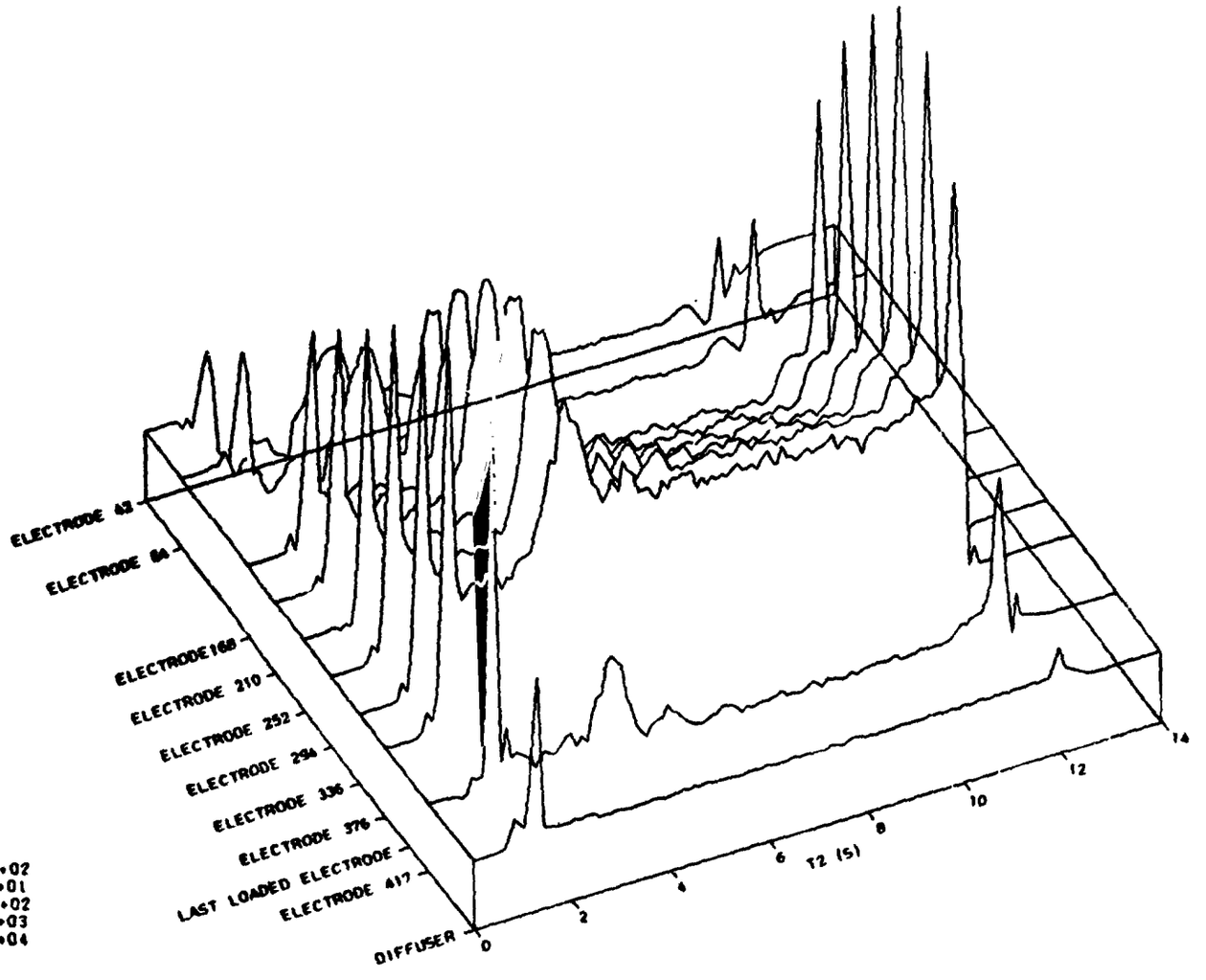

Fig. 3-26. Voltage anode to ground, HPDE Run 006-008

9-3486

STD RESEARCH CORPORATION

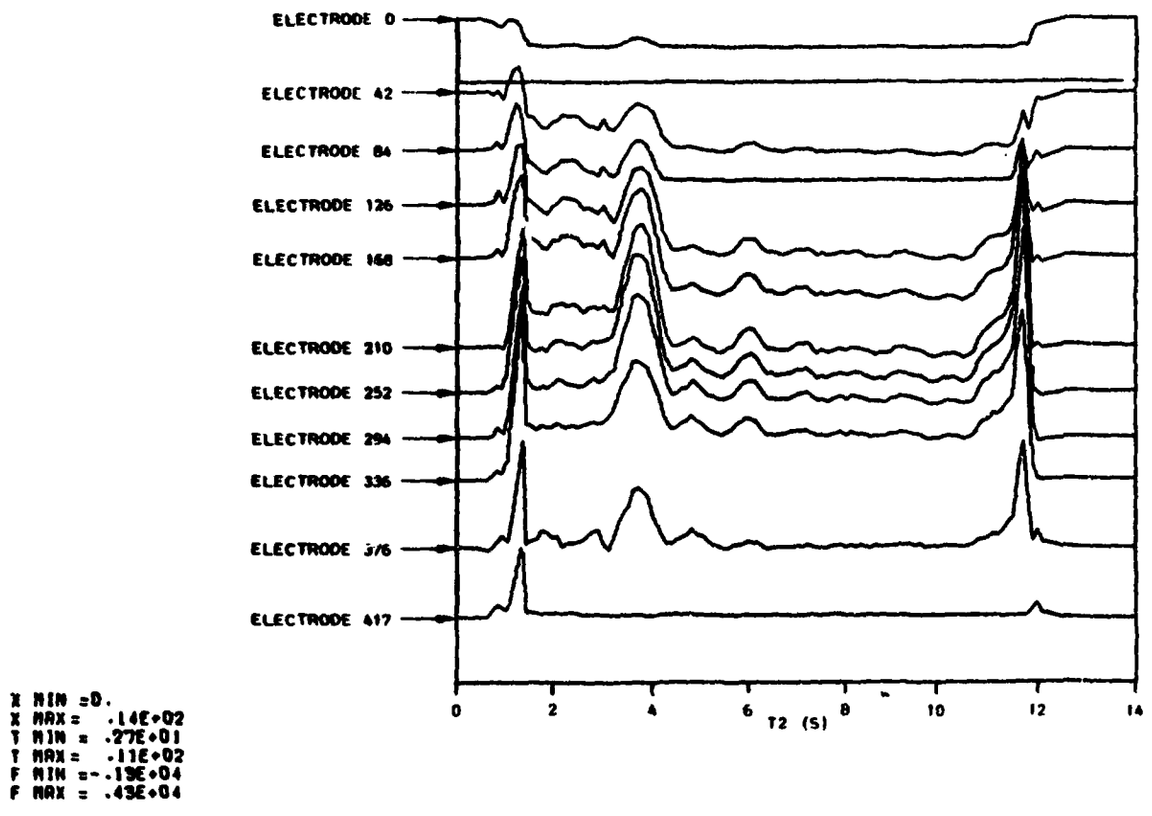

Fig. 3-27. Voltage cathode to ground, HPDE Run 006-008

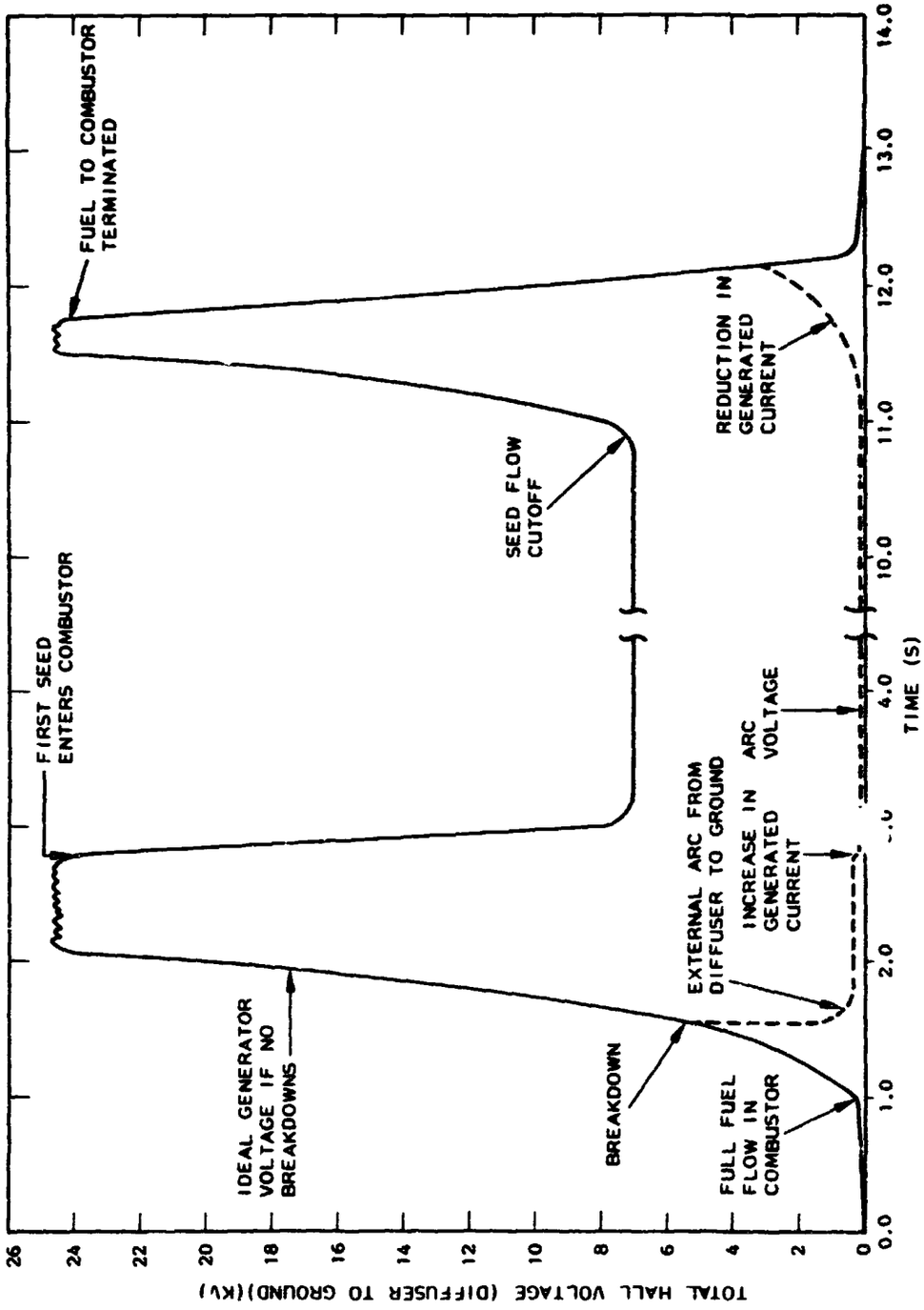

9-3404

Fig. 3-28. Total Hall voltage for AEDC/HPDE Run 006-008. (Dashed lines represent vo tage history to ground.)

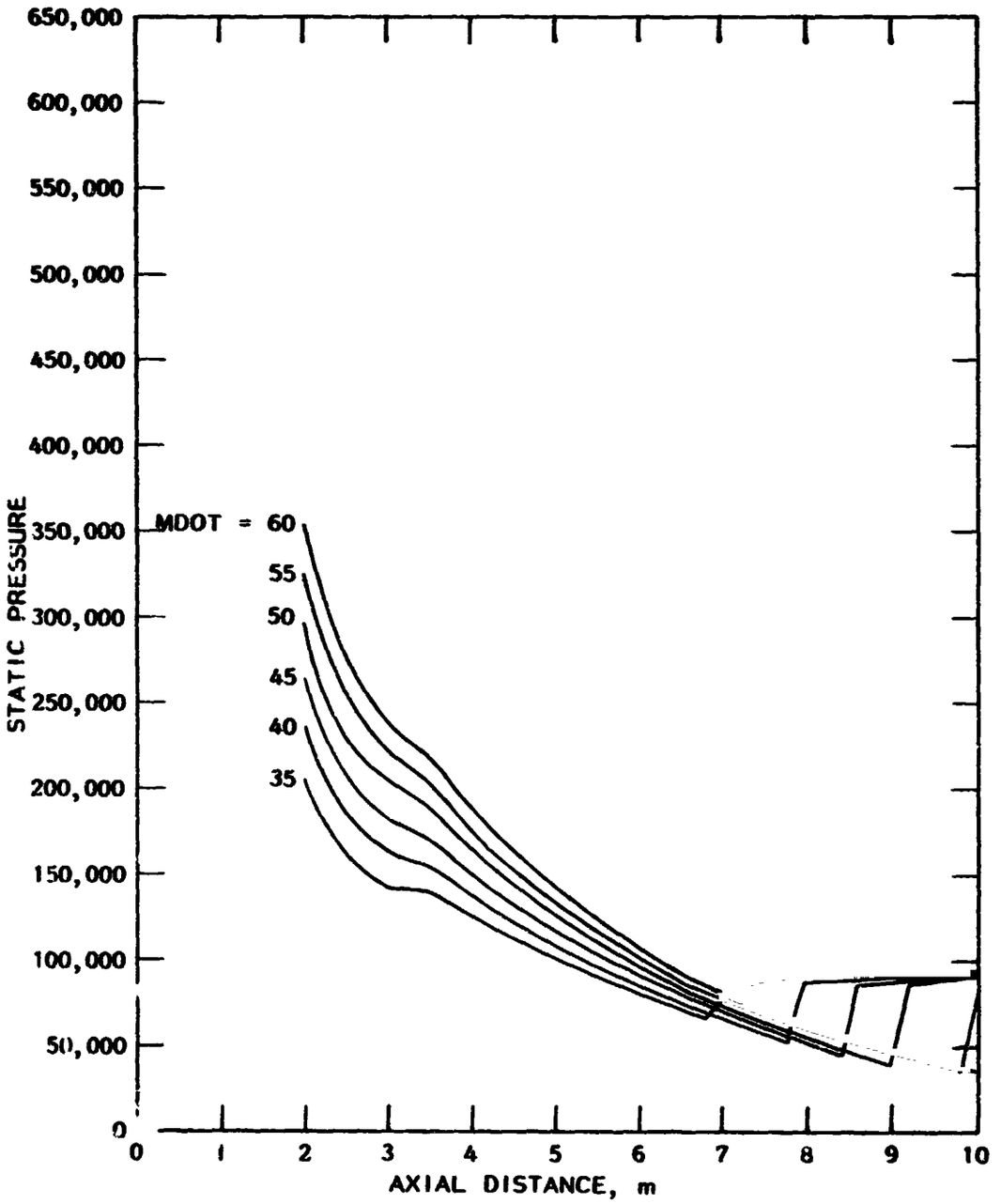

Fig. 3-29. Axial variation of static pressure for the AEDC-HPDE at the 4 Tesla nominal operating condition load resistance. TRANSIENT code family

0-4332

STD RESEARCH CORPORATION

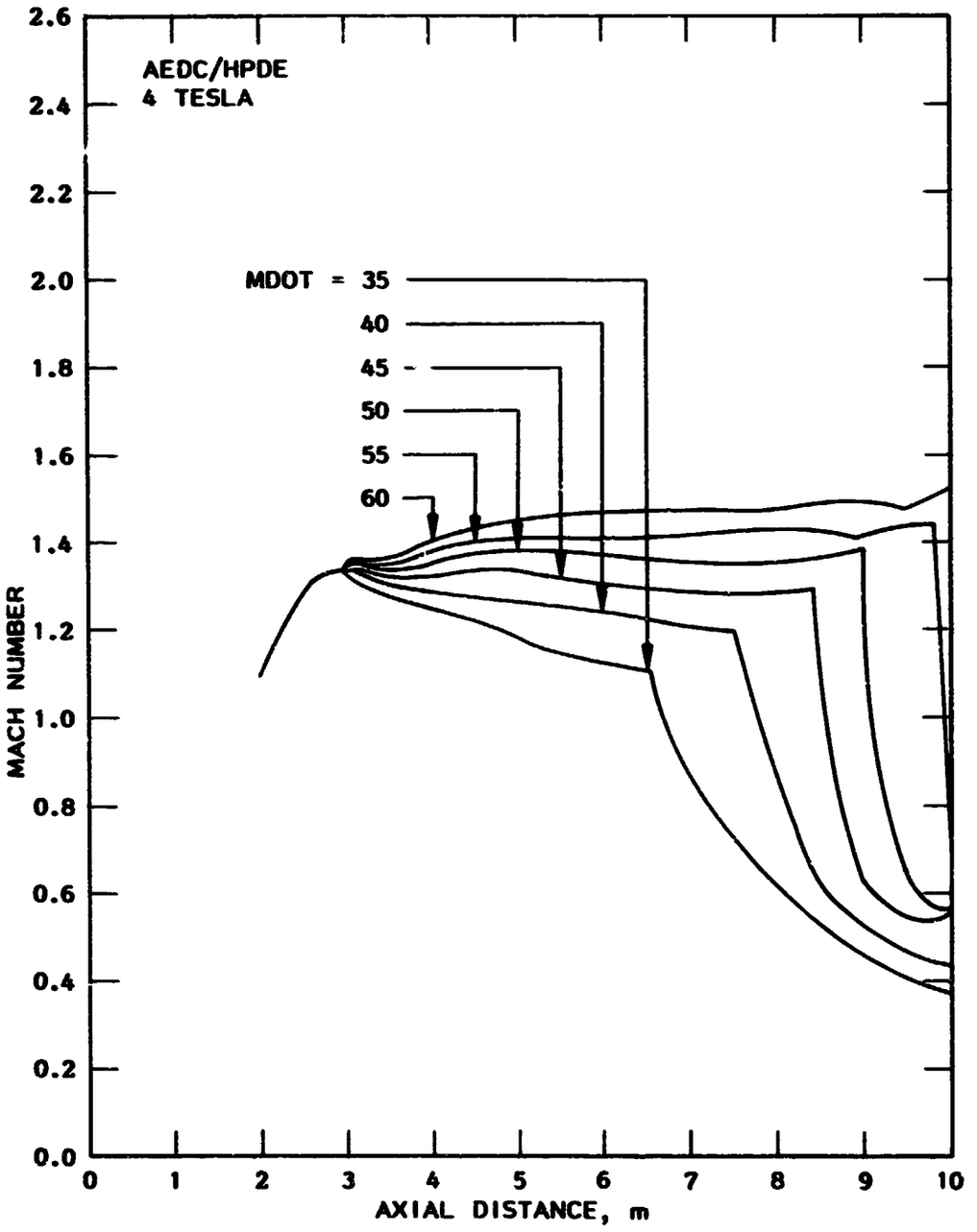

Fig. 3-30. Axial variation Mach numbers for the AEDC-HPDE at the 4 Tesla, nominal operating condition. TRANSIENT code family

0-4333

STD RESEARCH CORPORATION

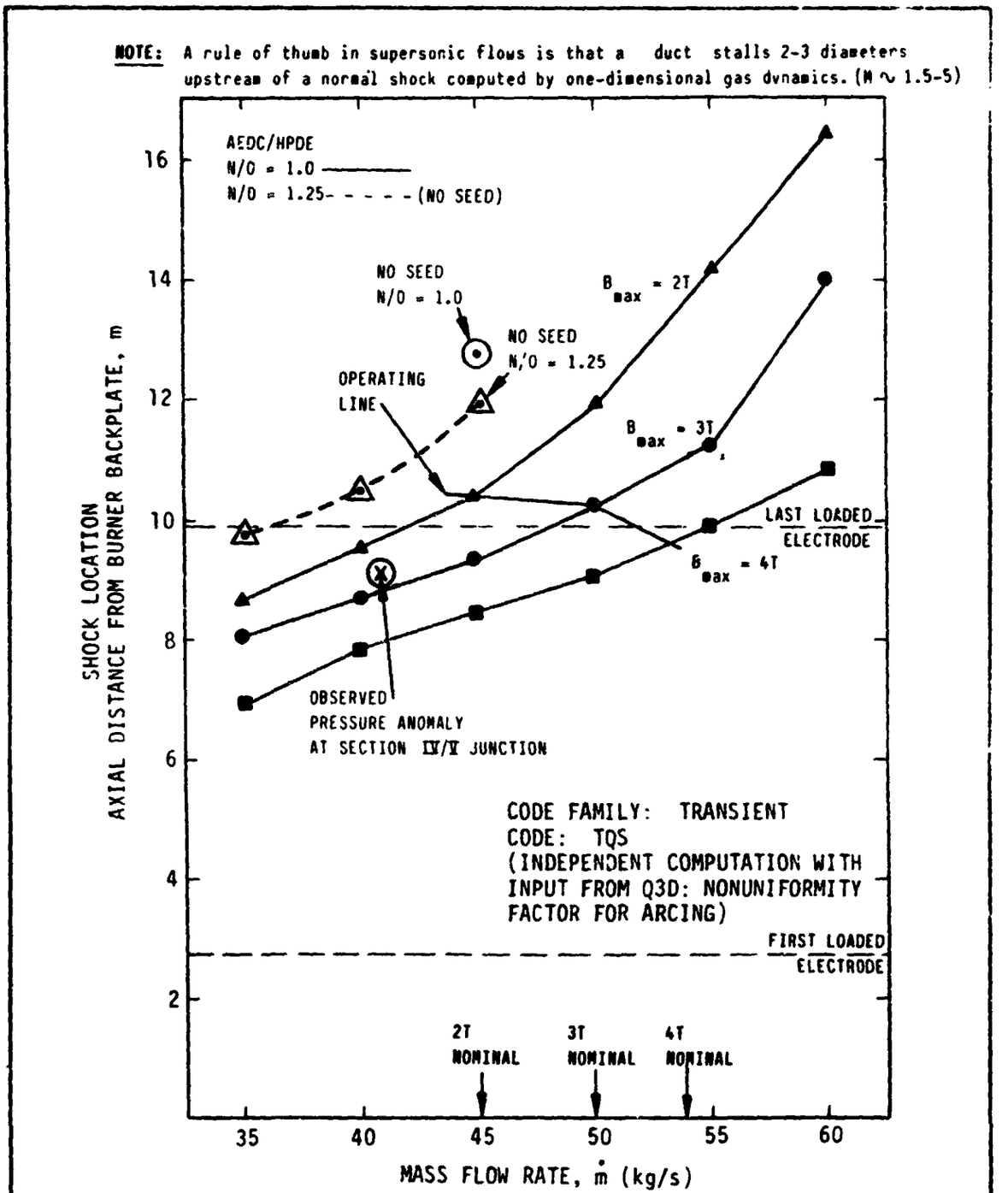

Fig. 3-31. Position of the normal shock as a function of mass flow rate and magnetic field for the nominal operating conditions of the AEDC/HPDE (except for the "NO SEED" point.) Code family: TRANSIENT. Code: TQS.

9-3218a

STD

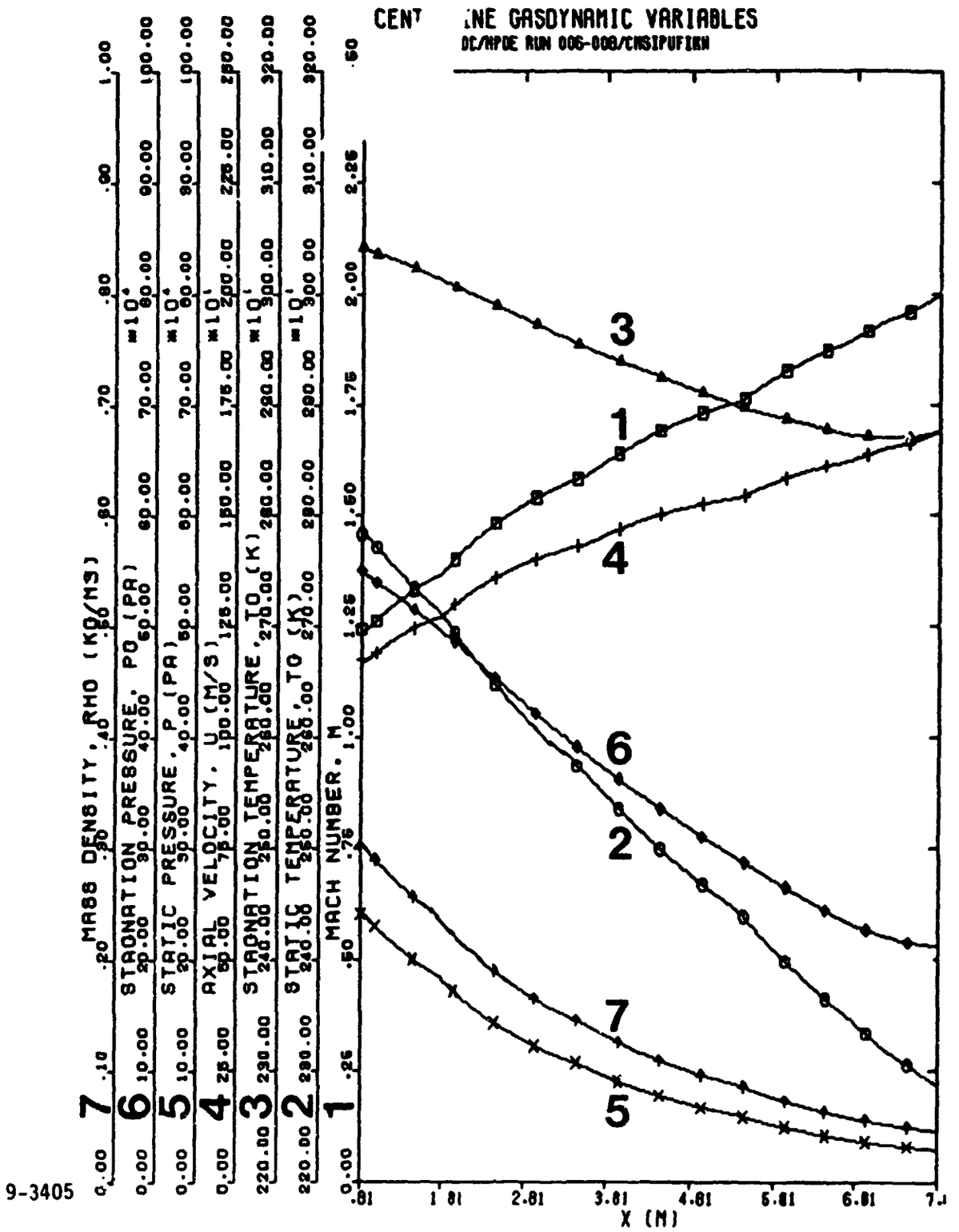

Fig. 3-32. Axial variation of the centerline gasdynamic variables from computation CMSIPUFIKW for the AEDC/HPDE.

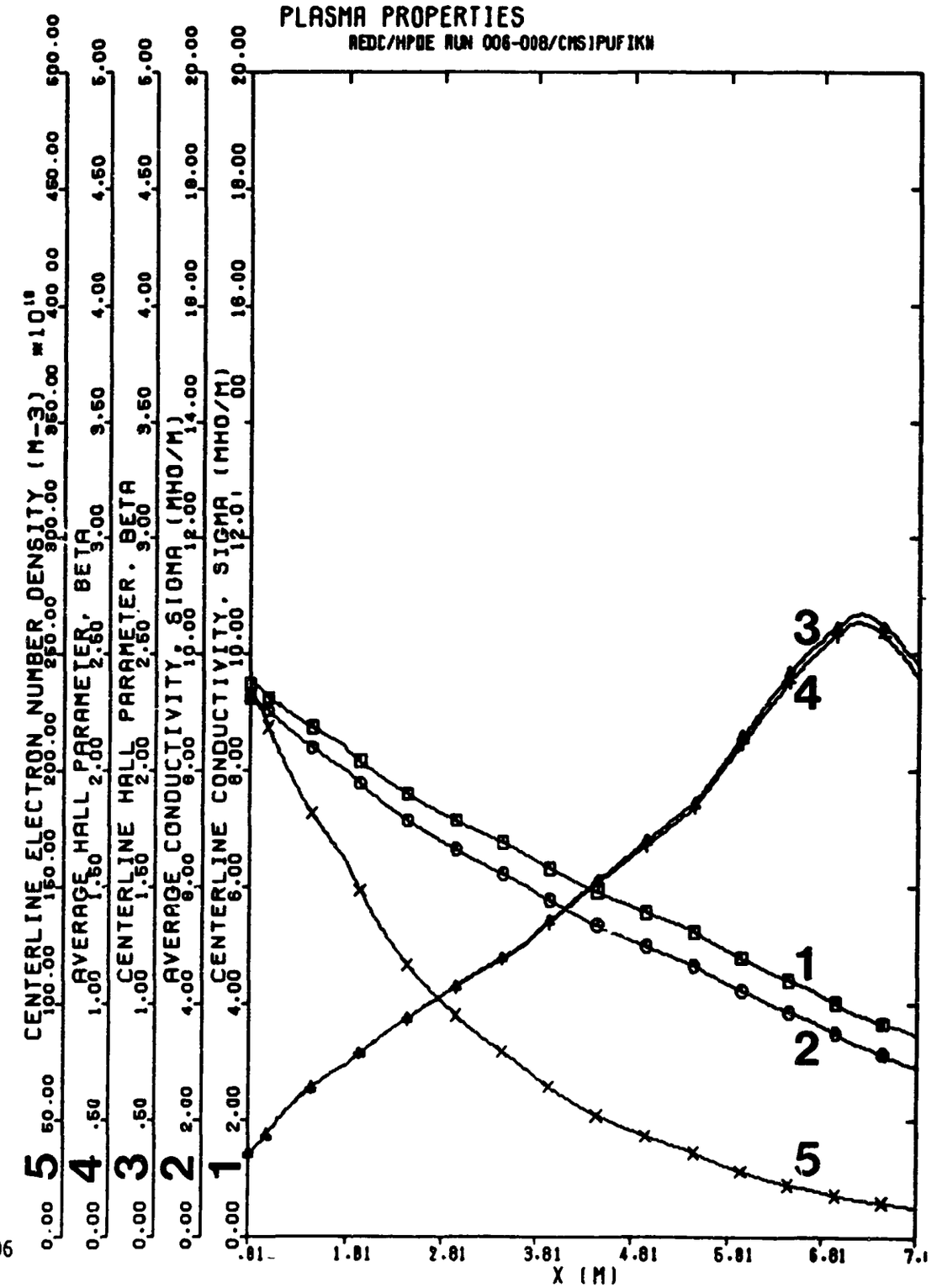

9-3406

Fig. 3-33. Axial variation of the plasma properties from computation CMSIPUFIKW for the AEDC/HPDE.

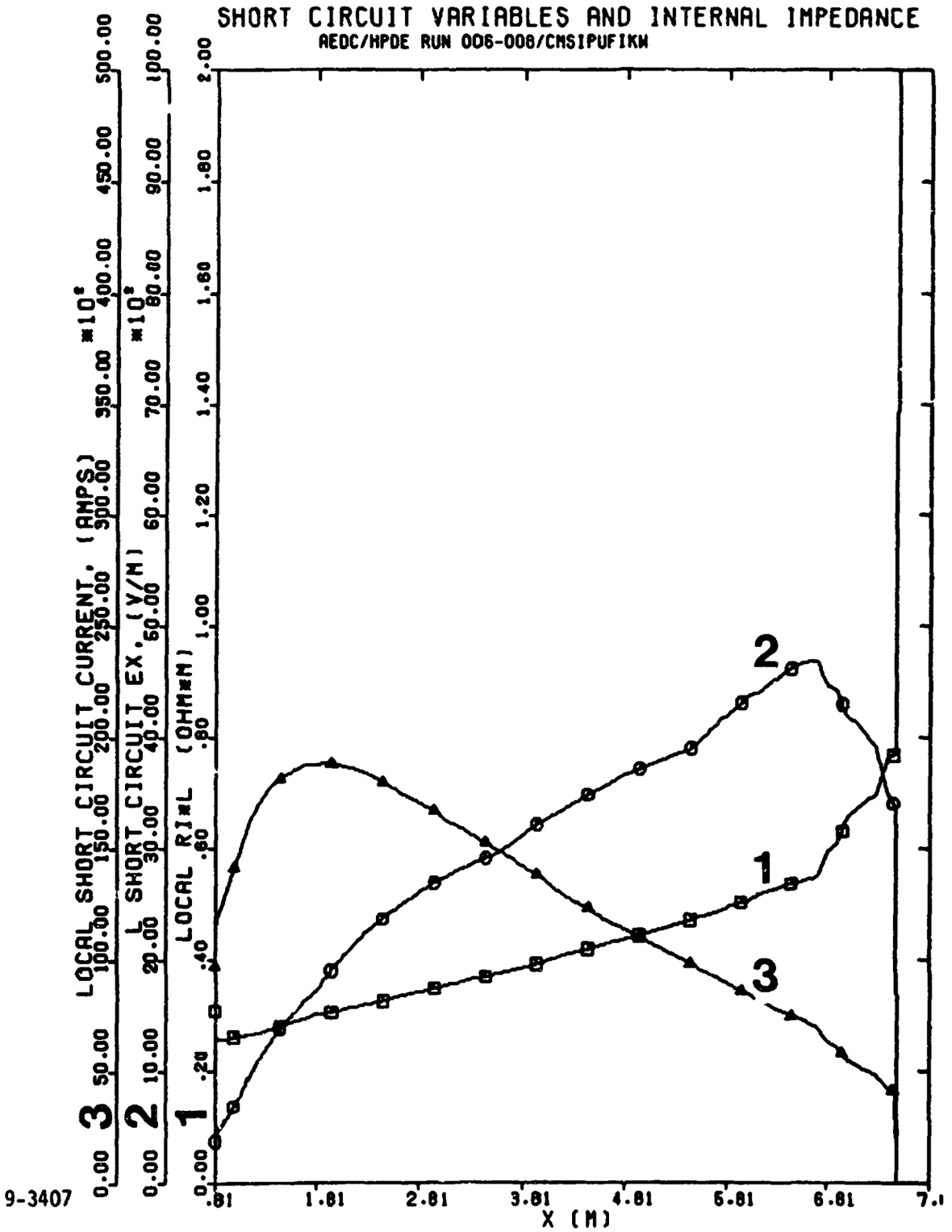

Fig. 3-34. Axial variation of the short circuit variables and internal impedance from computation CMSIPUFIKW for the AEDC/HPDE.

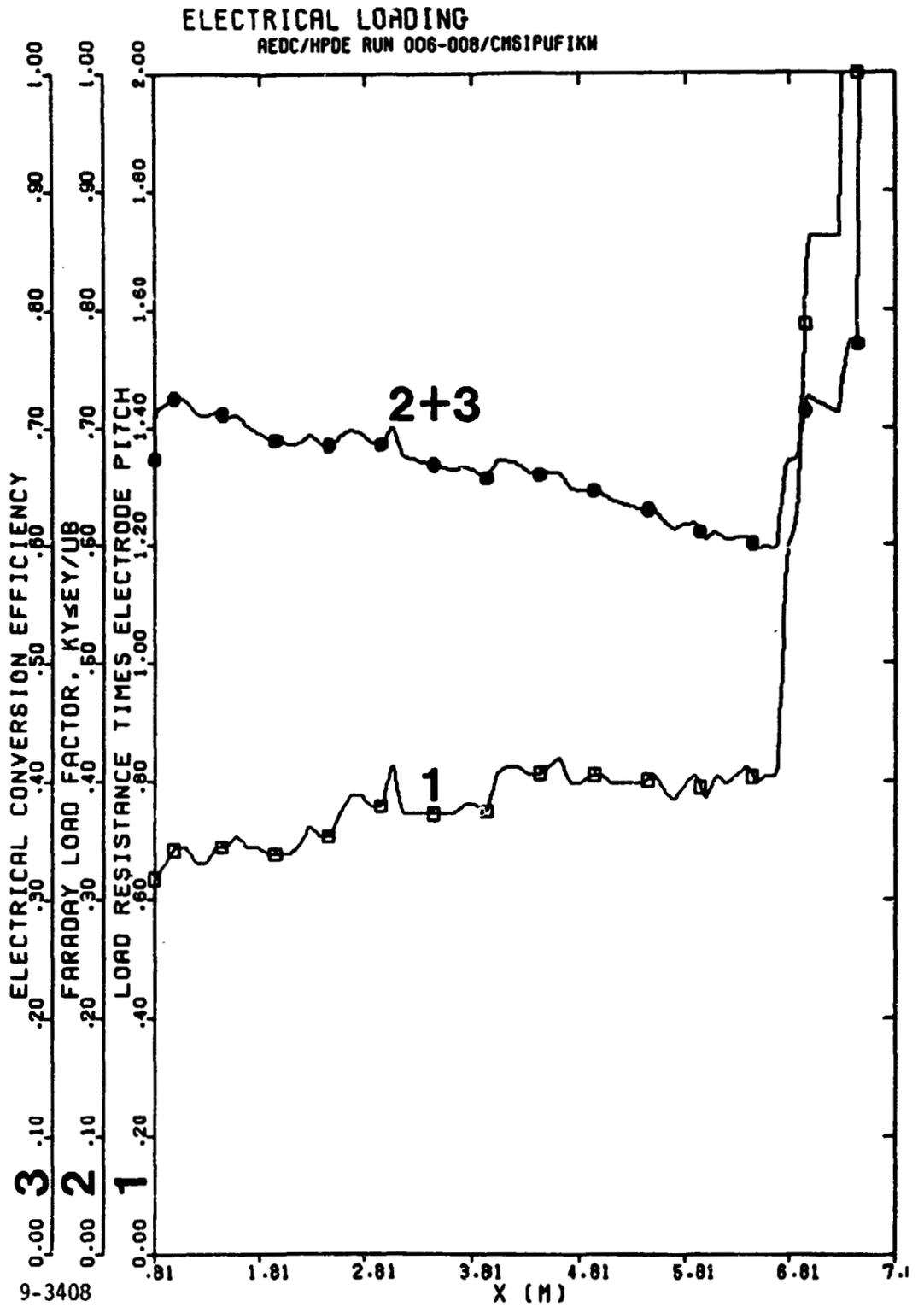

Fig. 3-35. Axial variation of the electrical loading from computation CMSIPUFIKW for the AEDC/HPDE.

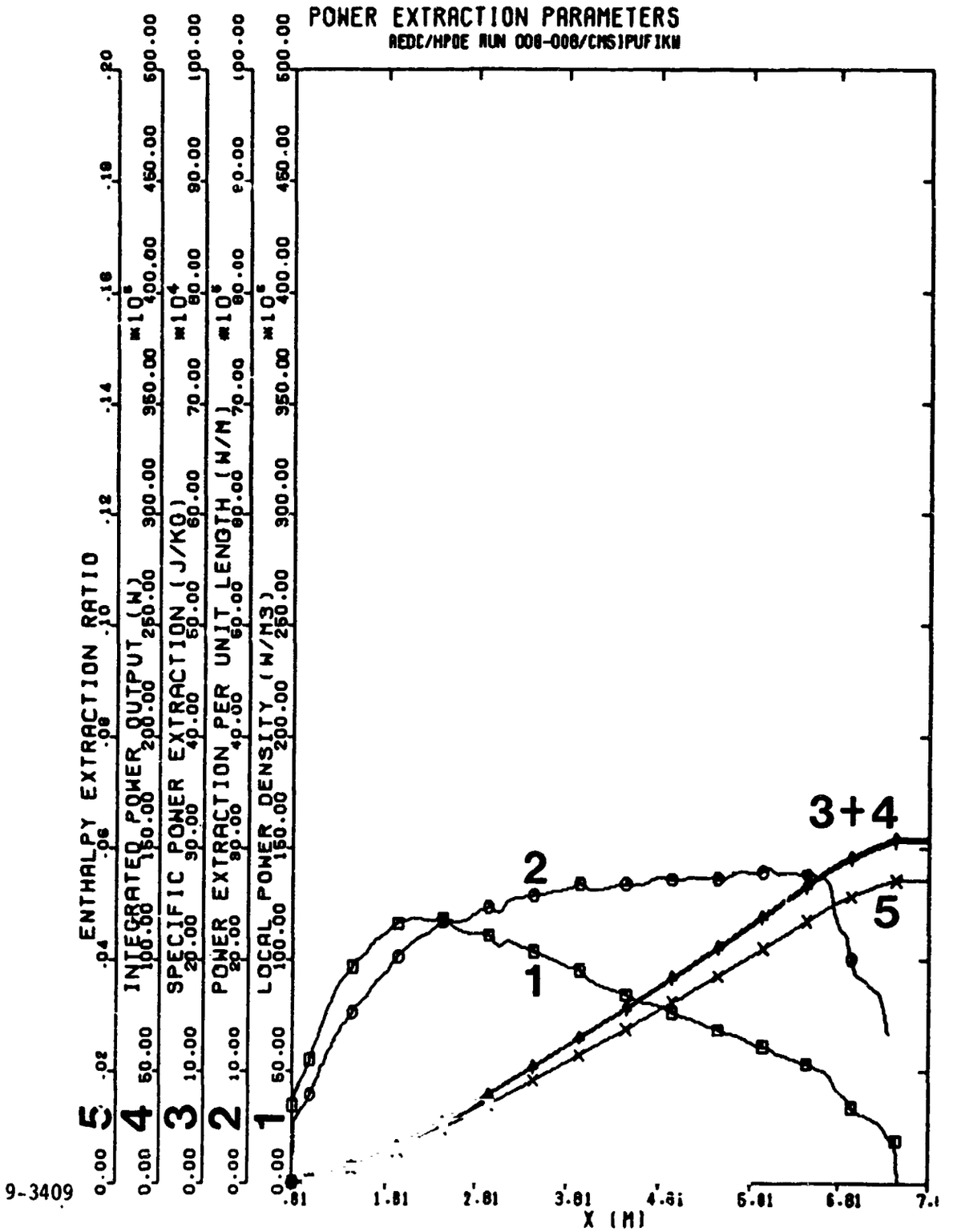

Fig. 3-36. Axial variation of the power extraction parameters from computation CMSIPUFIKW for the AEDC/HPDE.

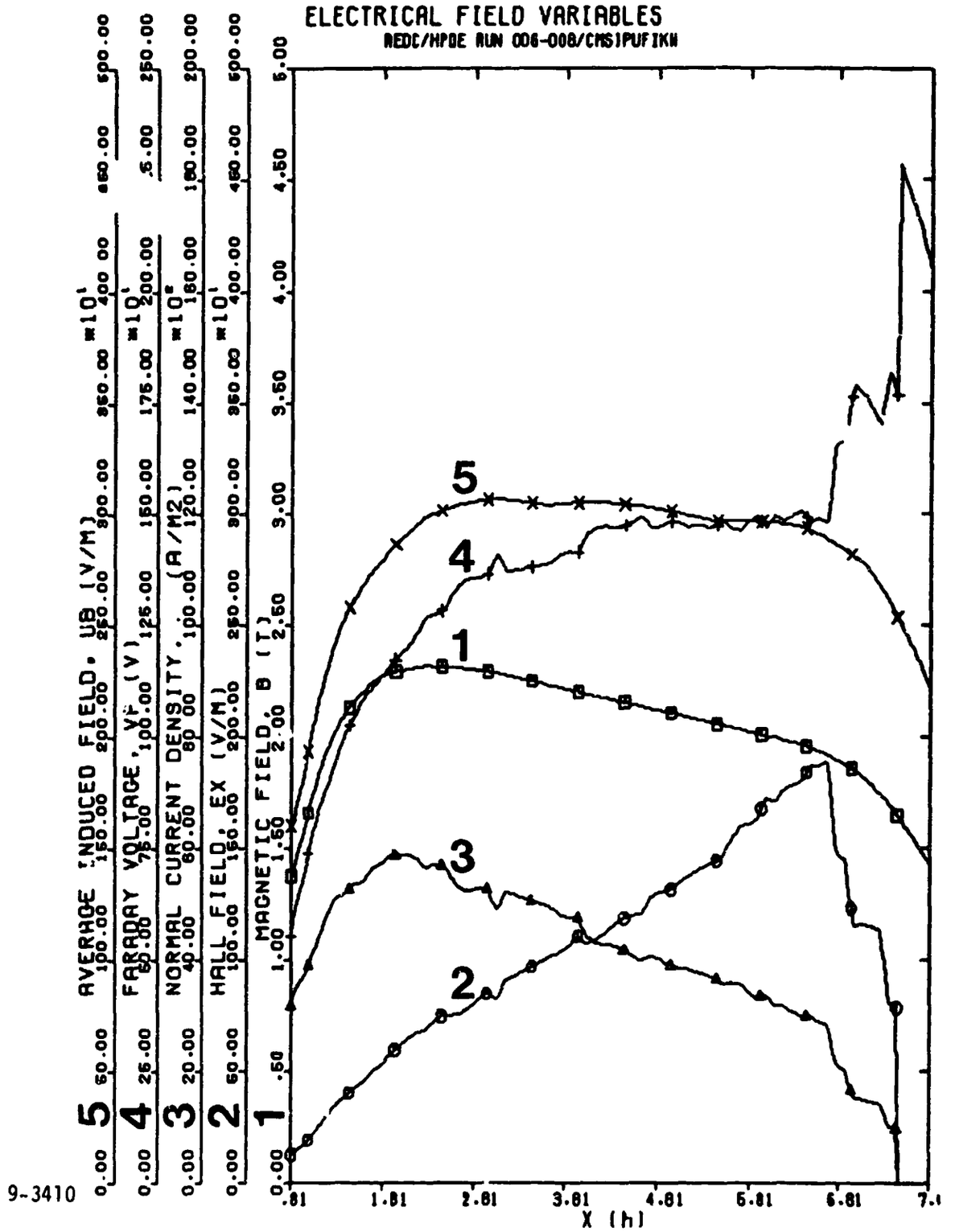

Fig. 3-37. Axial variation of the electrical field variables from computation CMSIPUFIKW for the AEDC/HPDE.

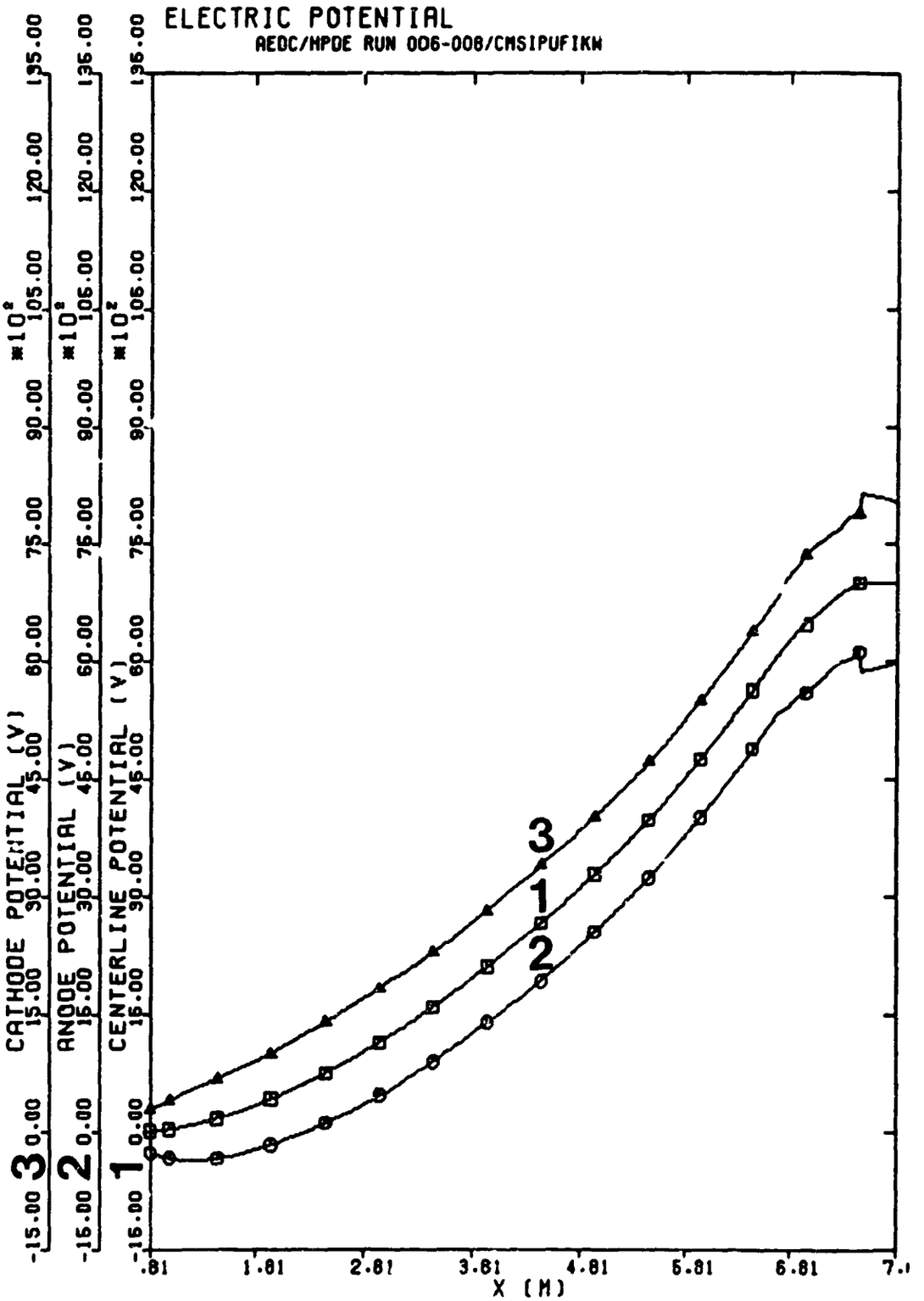

Fig. 3-38. Axial variation of the electric potential from computation CMSIPUFIKW for the AEDC/HPDE.

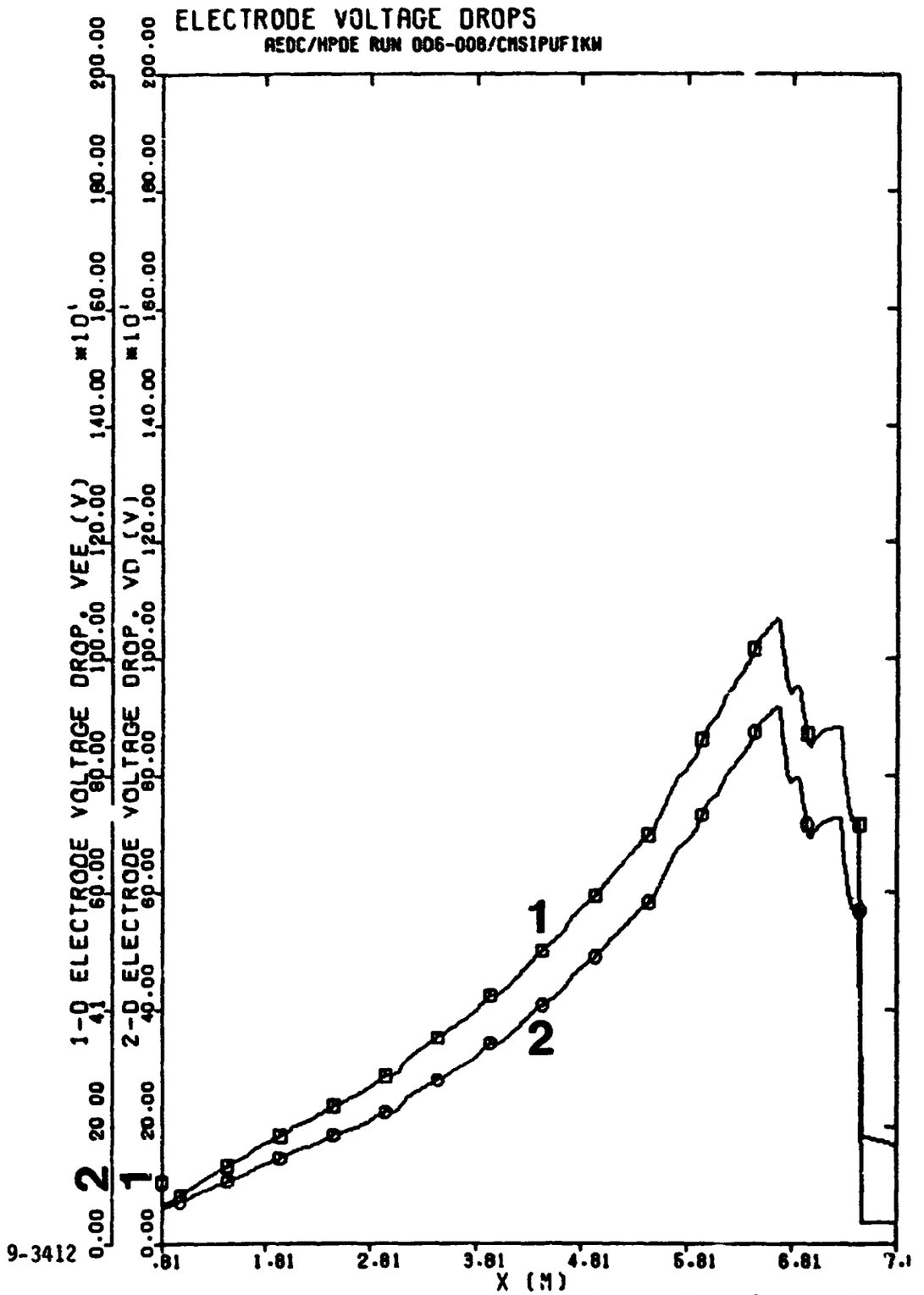

Fig. 3-39. Axial variation of the electrode voltage drops from computation SIPUFIKW for the AEDC/HPDE.

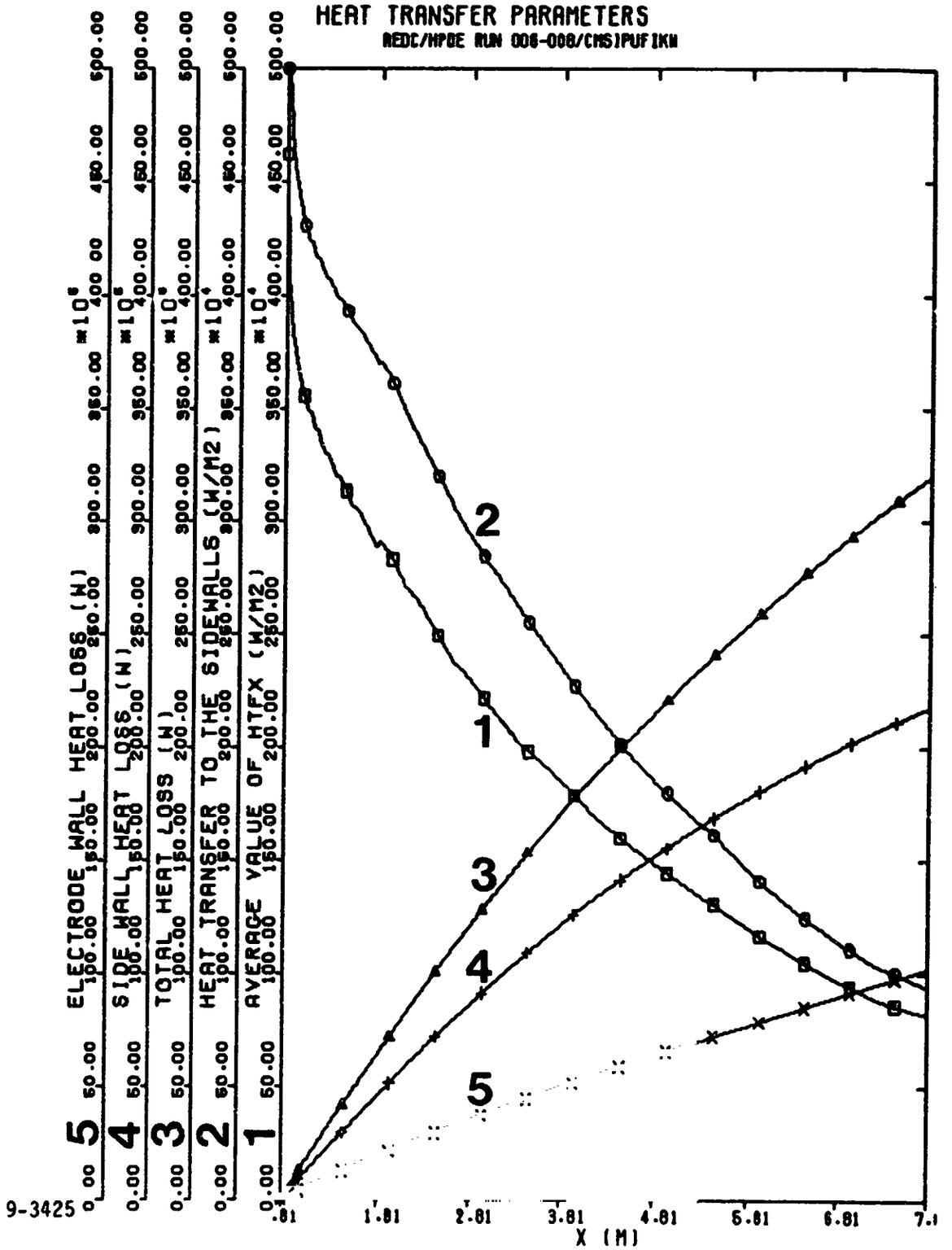

Fig. 3-40. Axial variation of the heat transfer parameters from computation CMSIPUFIKW for the AEDC/HPDE.

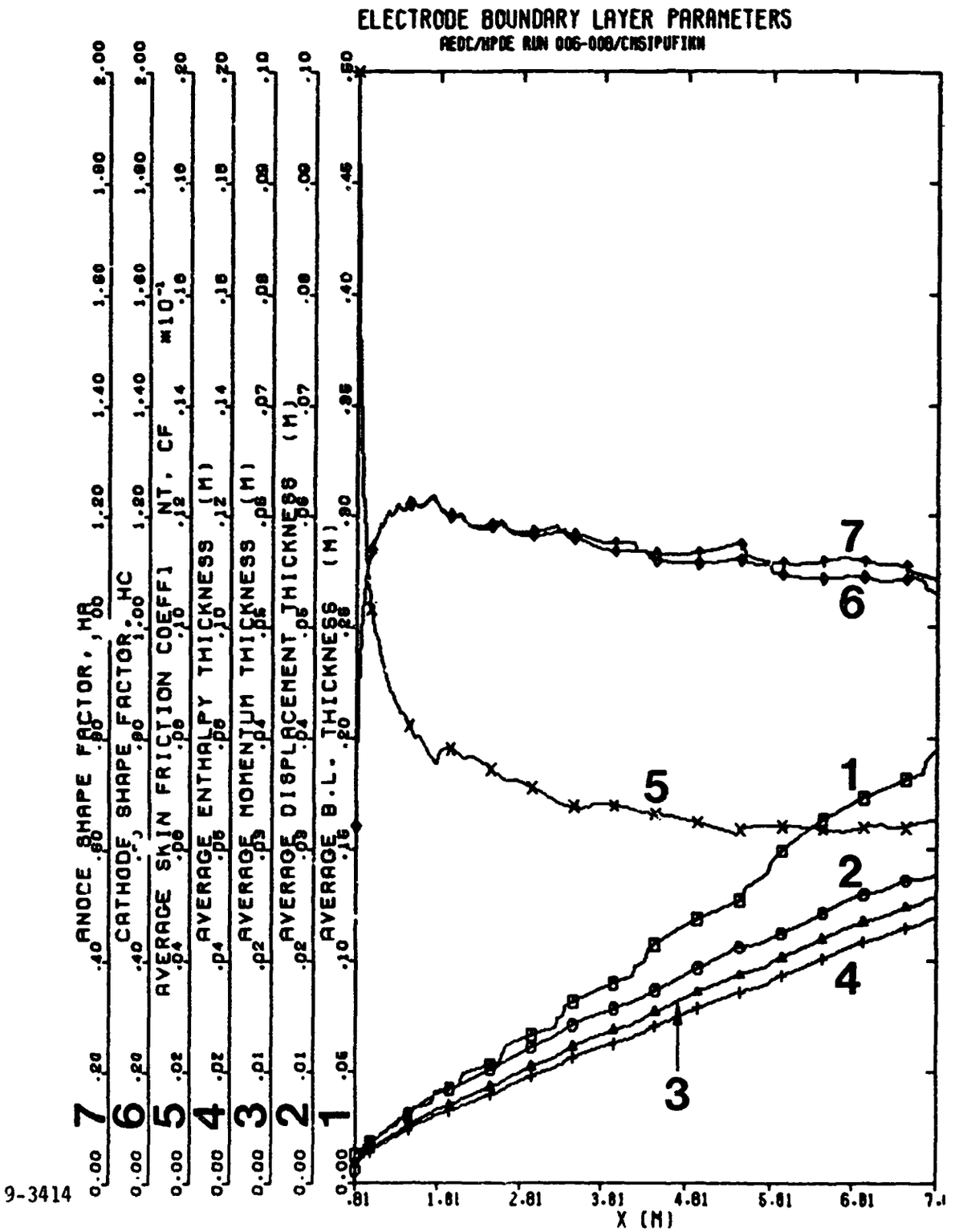

Fig. 3-41. Axial variation of the electrode boundary layer parameters from computation CMSIPUFIKW for the AEDC/HPDE.

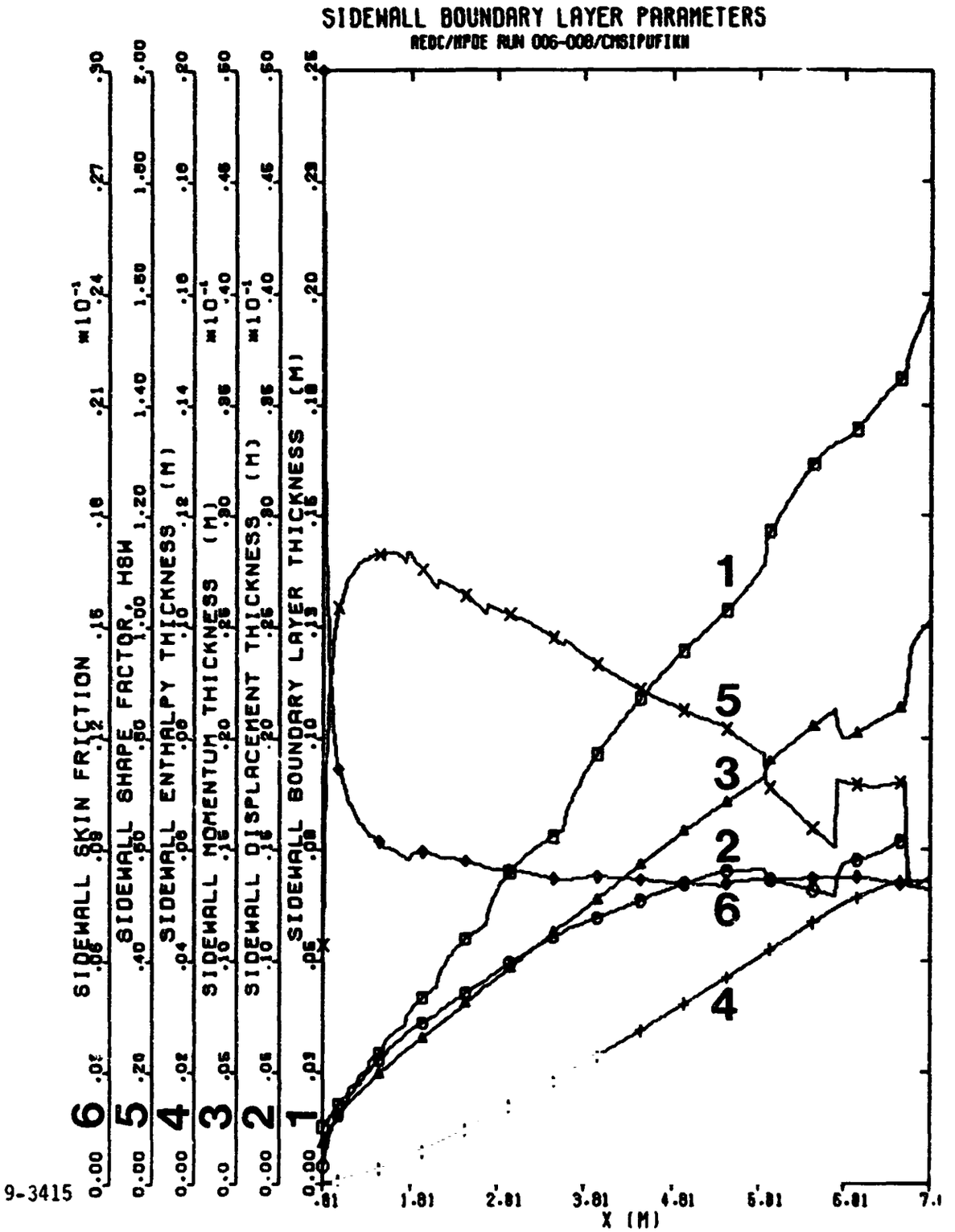

Fig. 3-42. Axial variation of the sidewall boundary layer parameters from computation CMSIPUFIKW for the AEDC/HPDE.

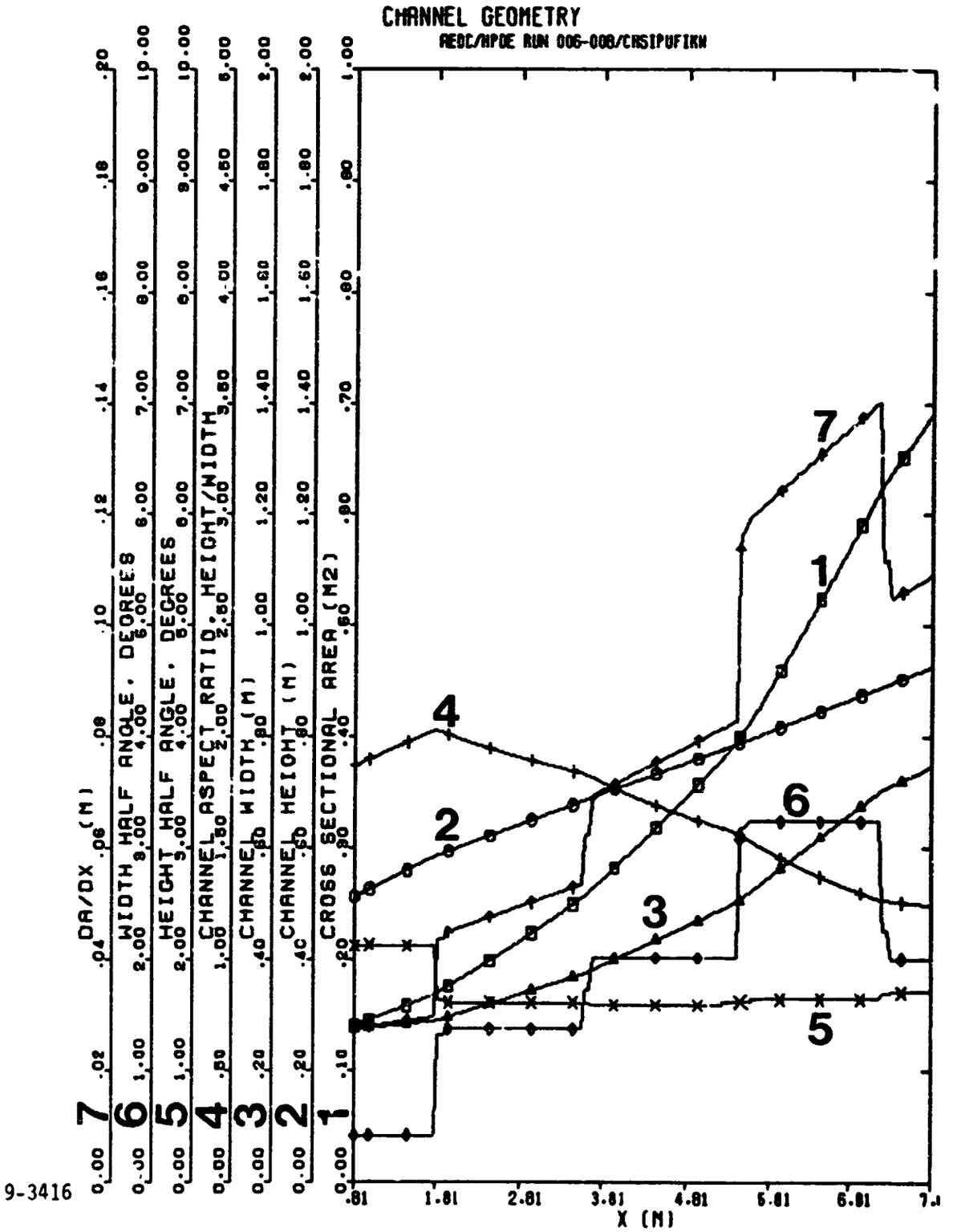

9-3416

Fig. 3-43. Axial variation of the channel geometry from computation CMSIPUFIKW for the AEDC/HPDE.

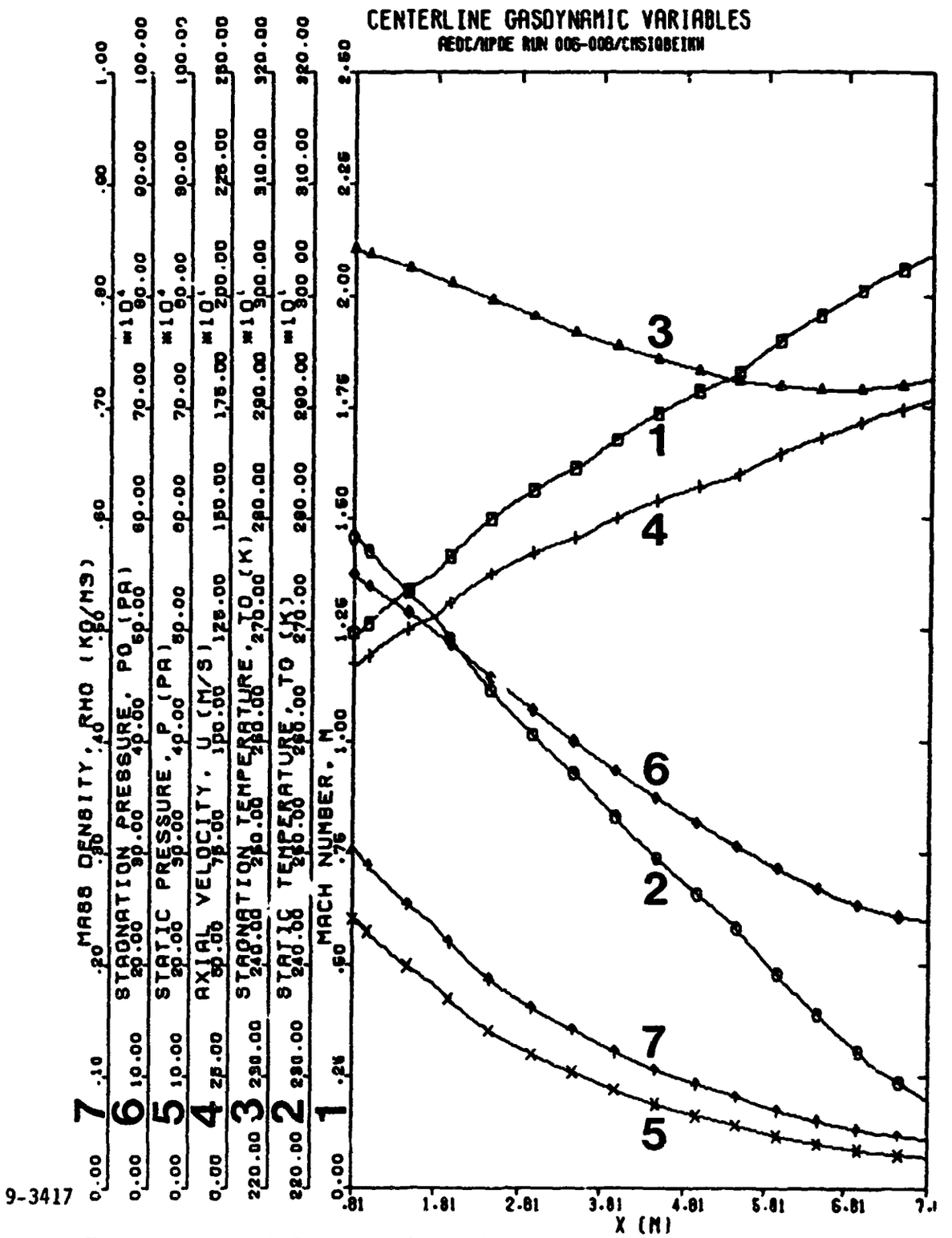

Fig. 3-44. Axial variation of the centerline gasdynamic variables from computation CMSIQBEIKW for the AEDC/HPDE.

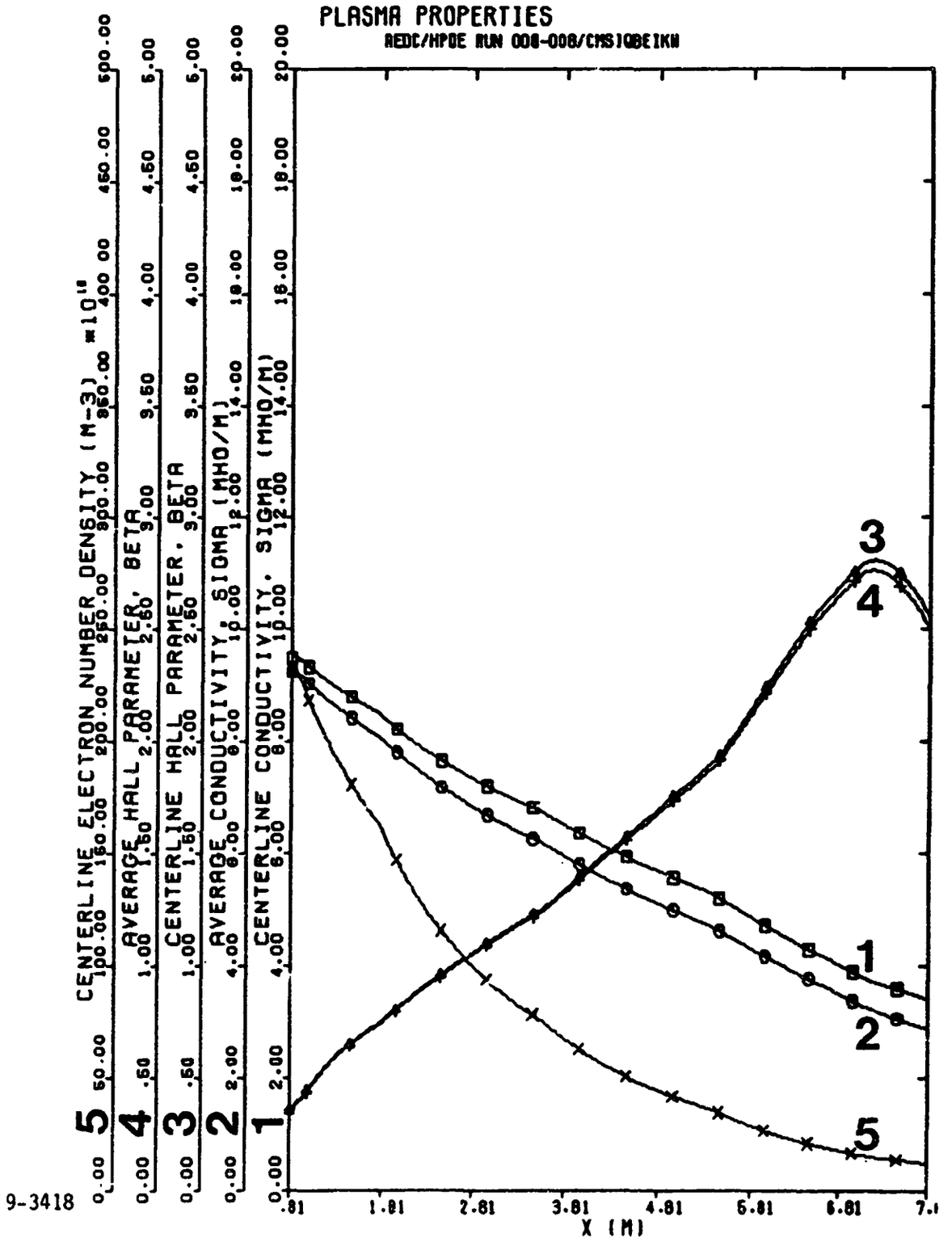

Fig. 3-45. Axial variation of the plasma properties from computation CMSIQBEIKW for the AEDC/HPDE.

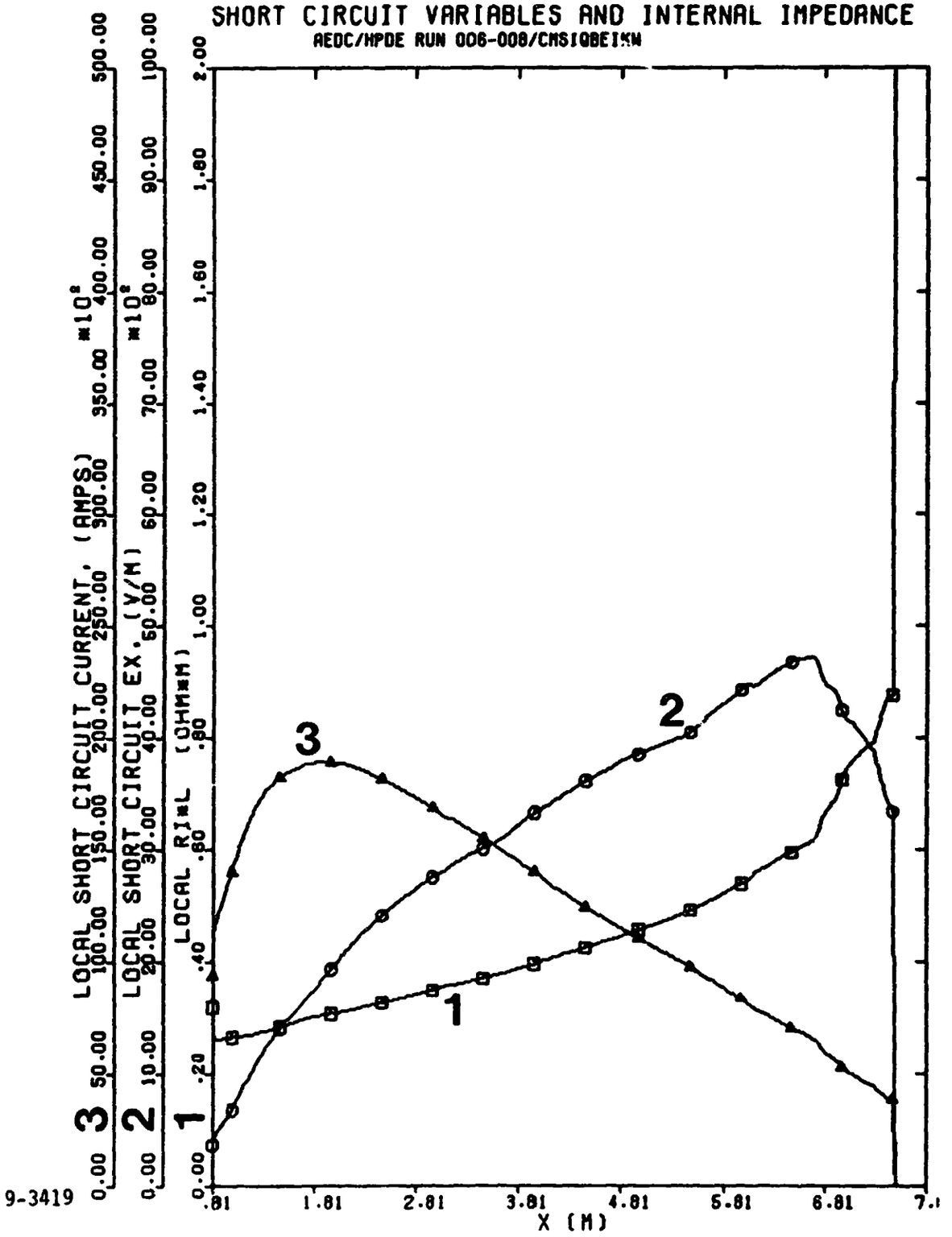

Fig. 3-46. Axial variation of the short circuit variables and internal impedance from computation CMSIQBEIKW for the AEDC/HPDE.

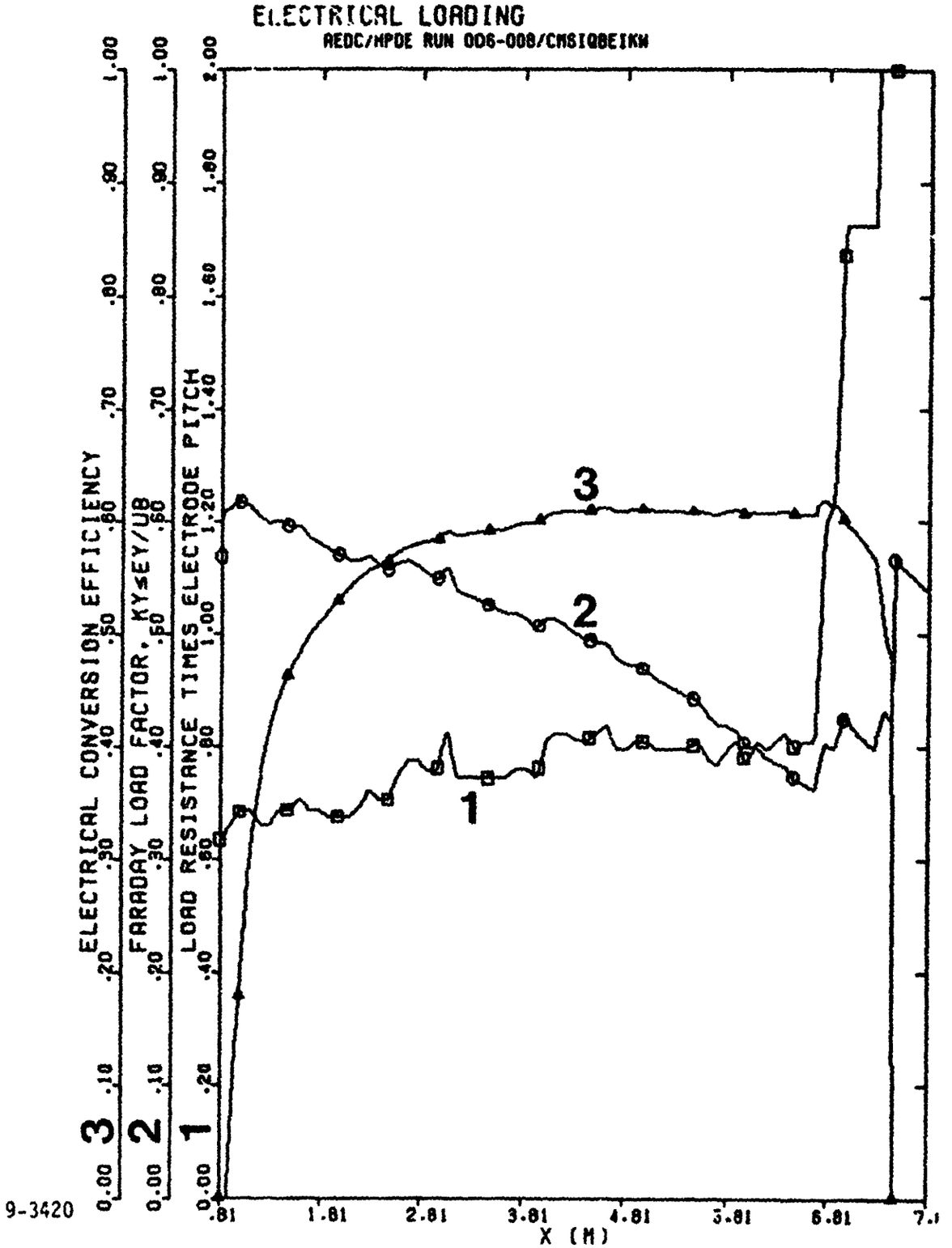

Fig. 3-47. Axial variation of the electrical loading from computation CMSIQBEIKW for the AEDC/HPDE.

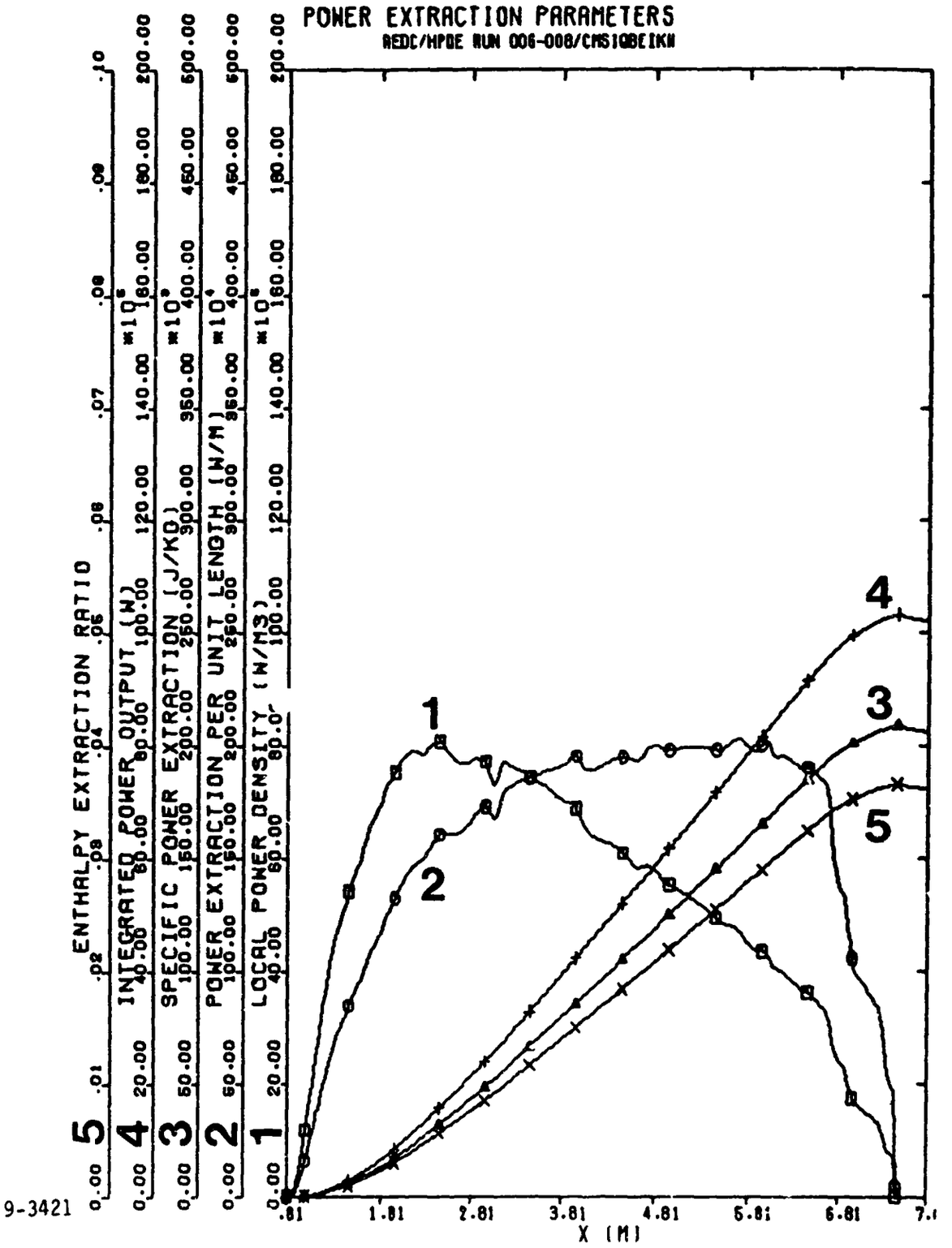

Fig. 3-48. Axial variation of the power extraction parameters from computation CMSIQBEIKW for the AEDC/HPDE.

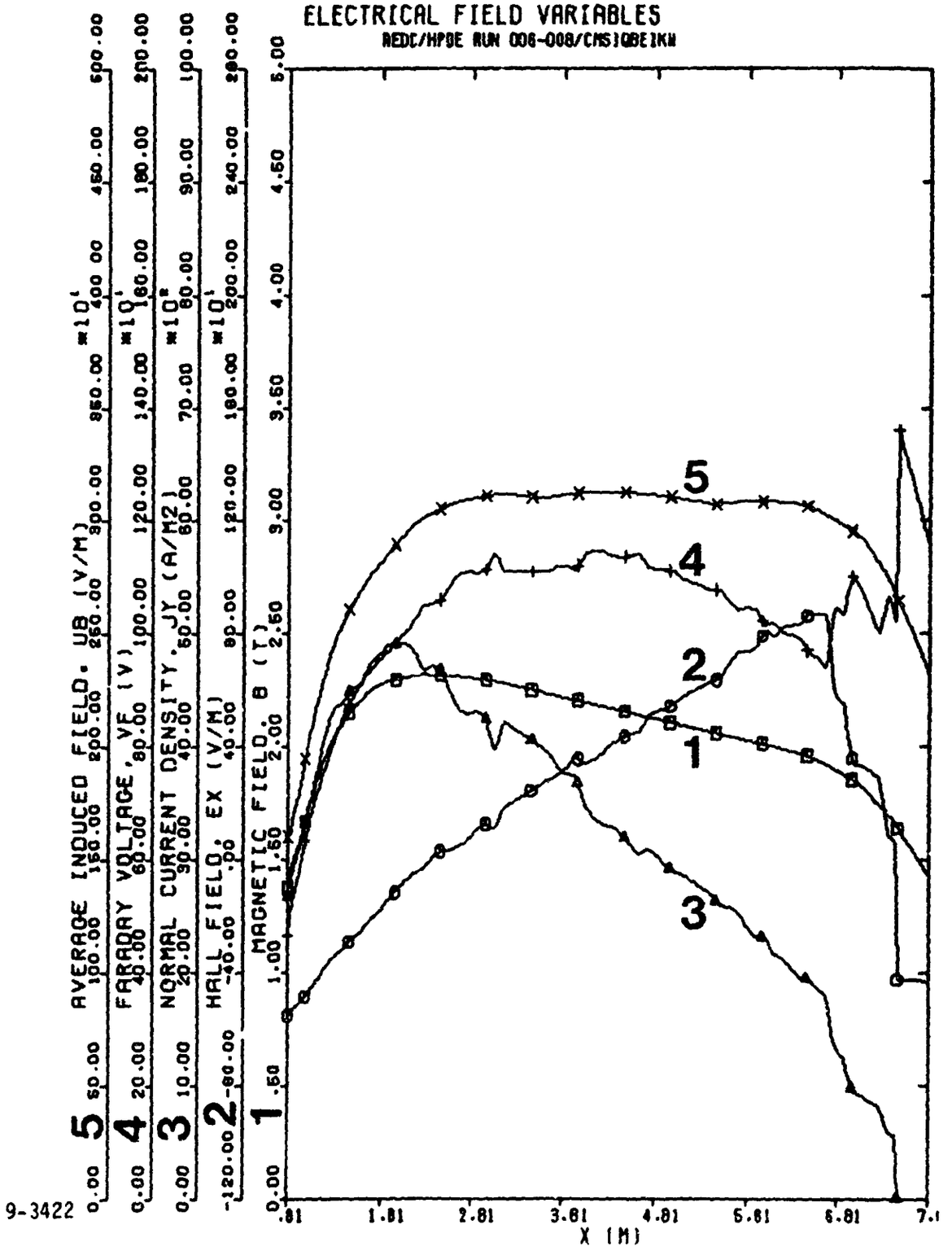

Fig. 3-49. Axial variation of the electrical field variables from computation CMSIQBEIKW for the AEDC/HPDE.

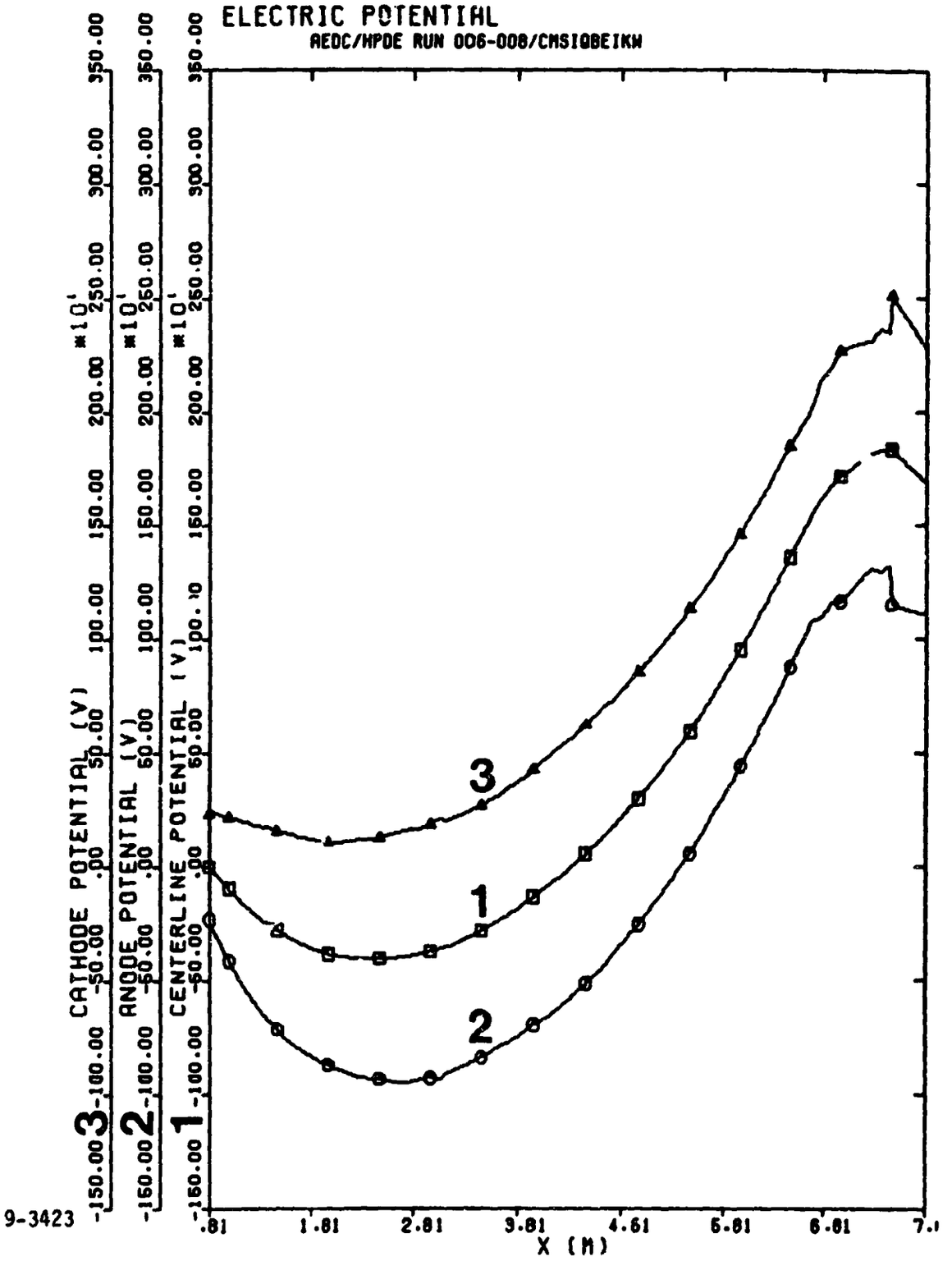

Fig. 3-50. Axial variation of the electric potential from computation CMSIQBEIKW for the AEDC/HPDE.

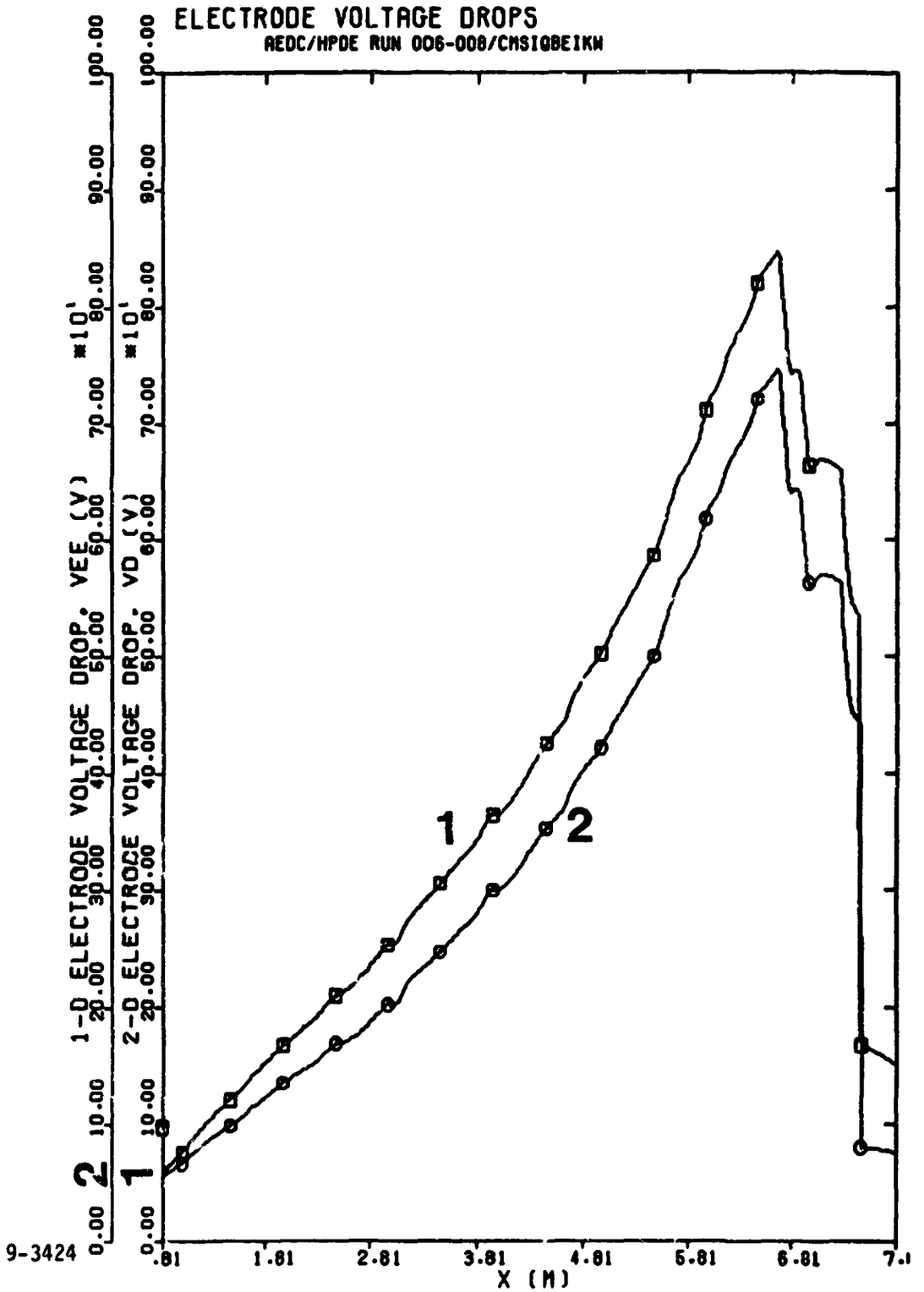

Fig. 3-51. Axial variation of the electrode voltage drops from computation CMSIQBEIKW for the AEDC/HPDE.

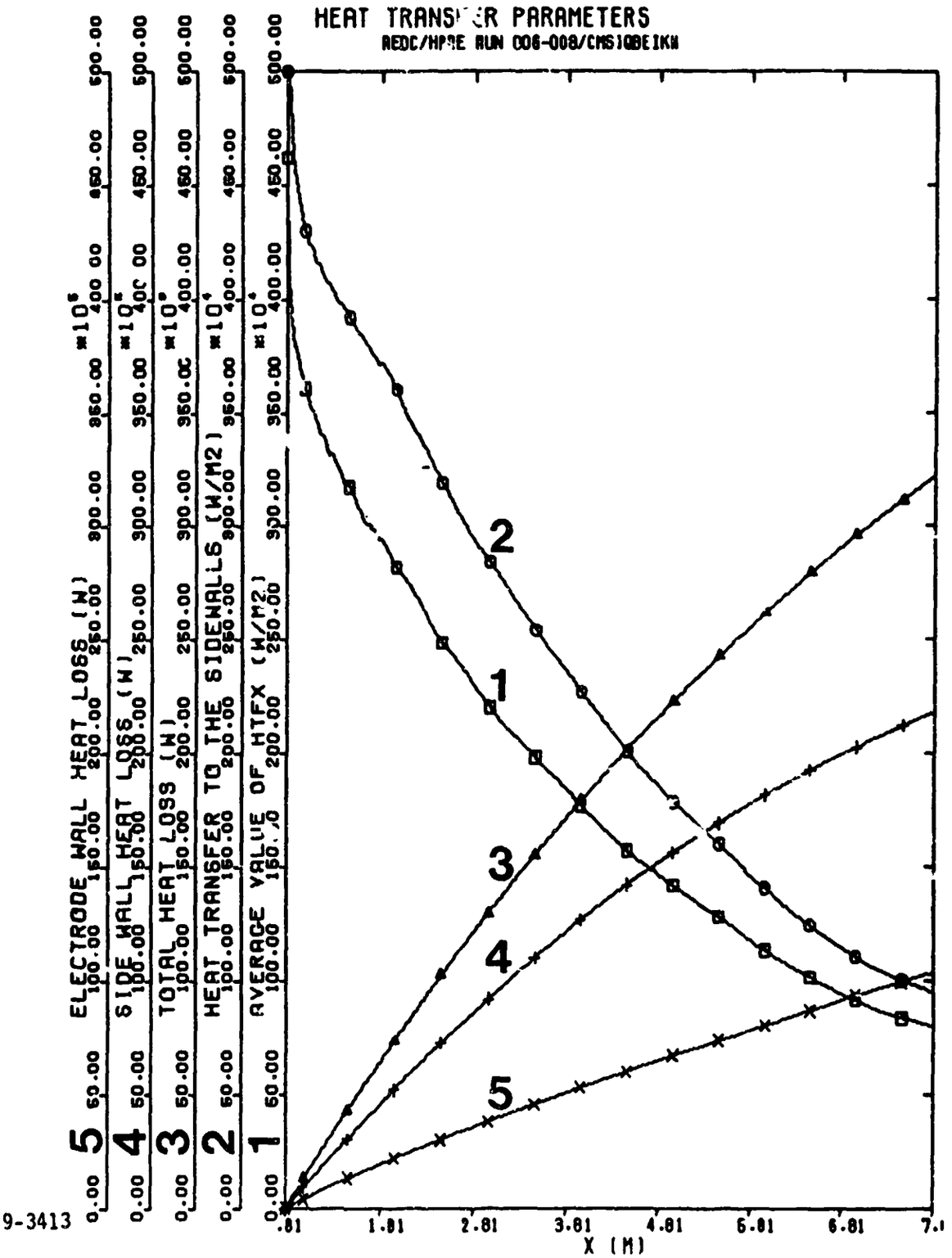

Fig. 3-52. Axial variation of the heat transfer parameters from computation CMSIQBEIKW for the AEDC/HPDE.

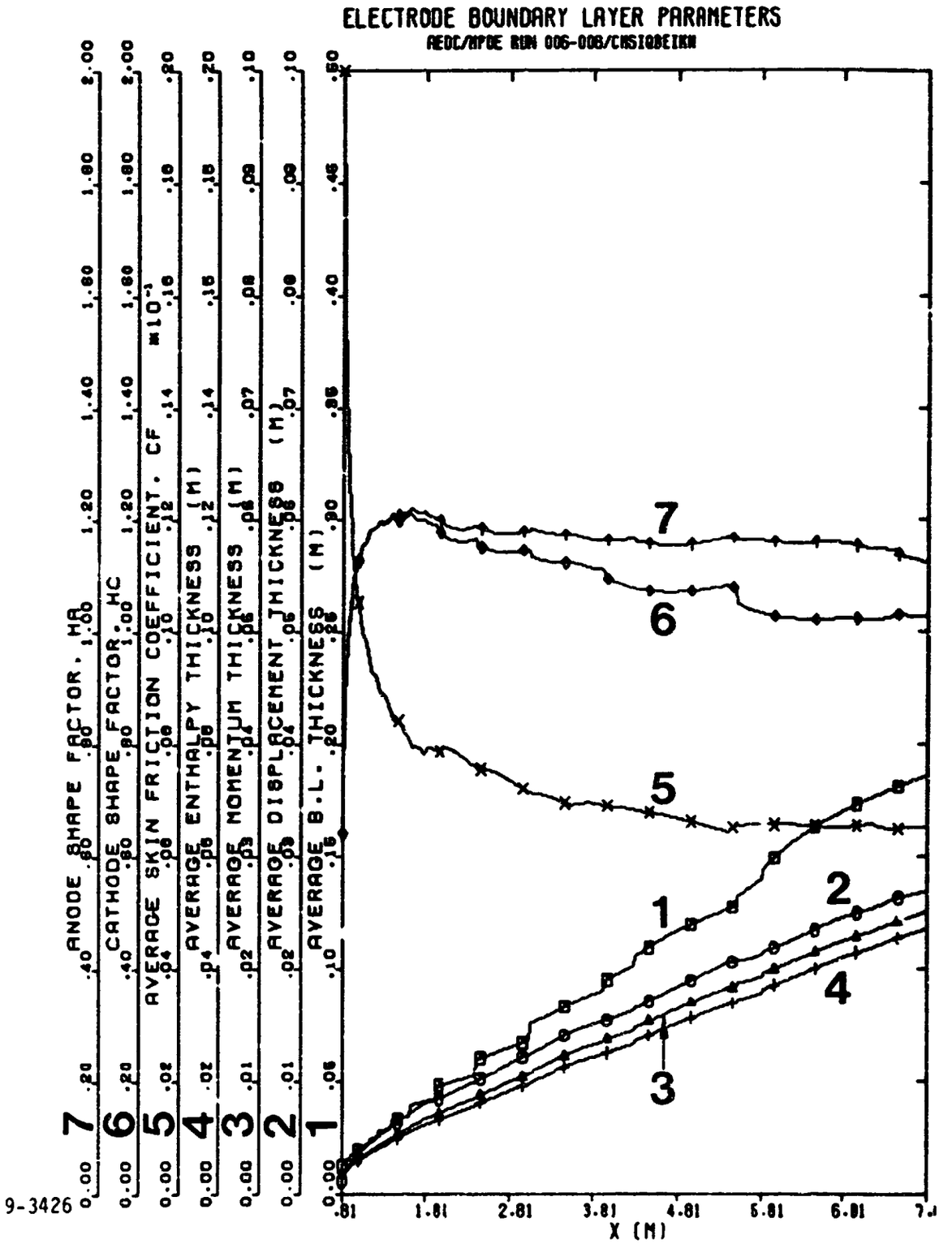

Fig. 3-53. Axial variation of the electrode boundary layer parameters from computation CMSIQBEIKW for the AEDC/HPDE.

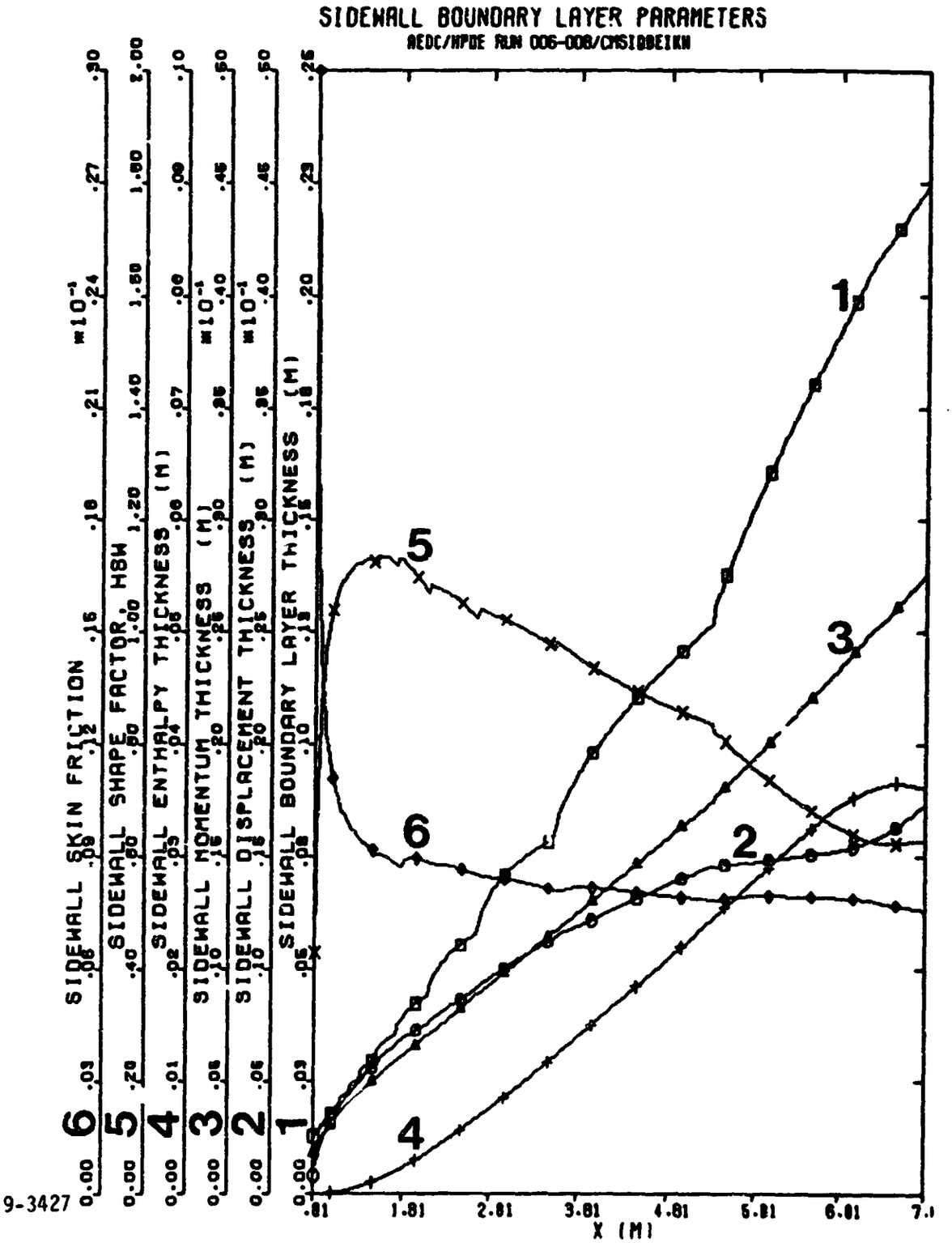

Fig. 3-54. Axial variation of the sidewall boundary layer parameters from computation CMSIQBEIKW for the AEDC/HPDE.

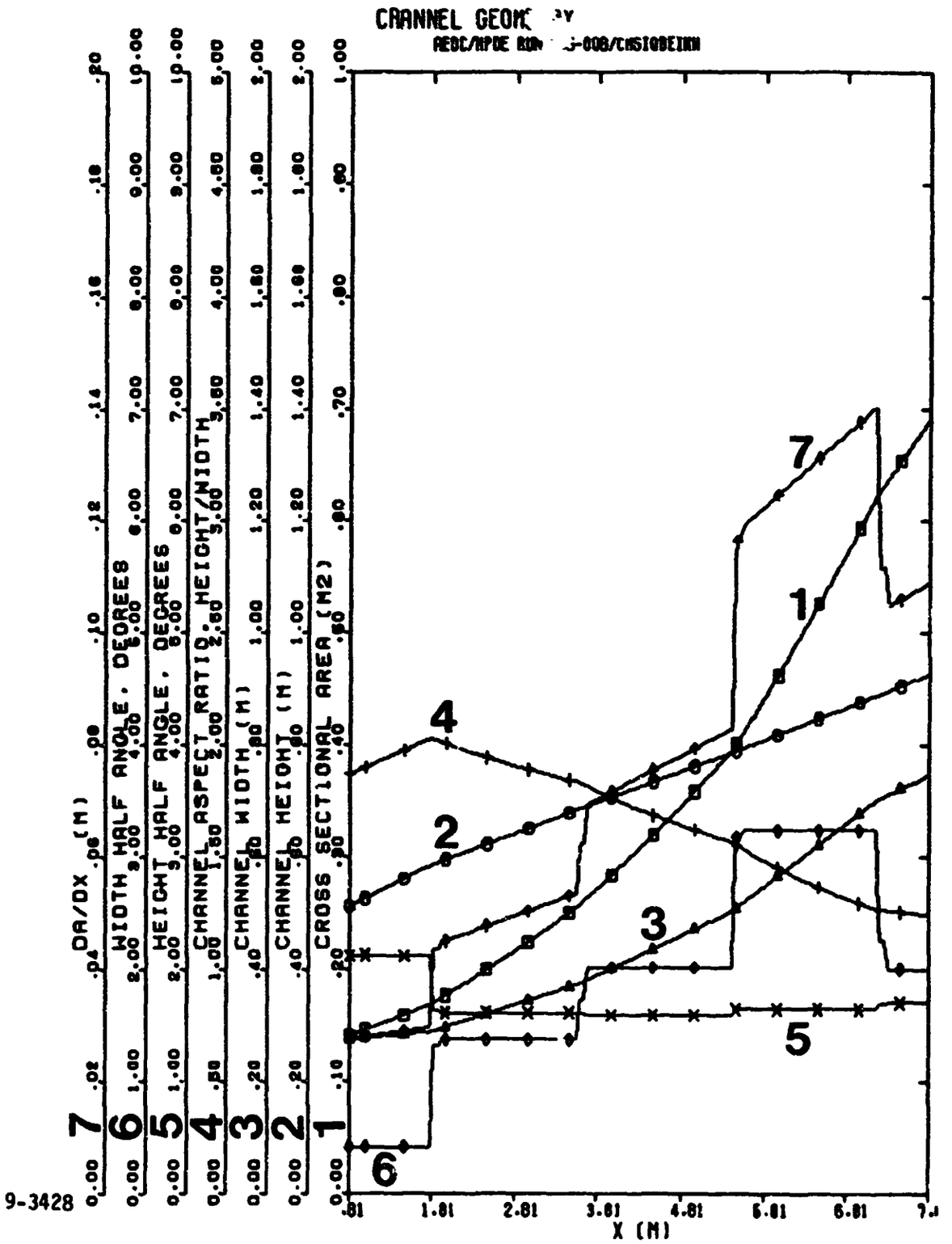

Fig. 3-55. Axial variation of the channel geometry from computation CMSIQBEIKW for the AEDC/HPDE.

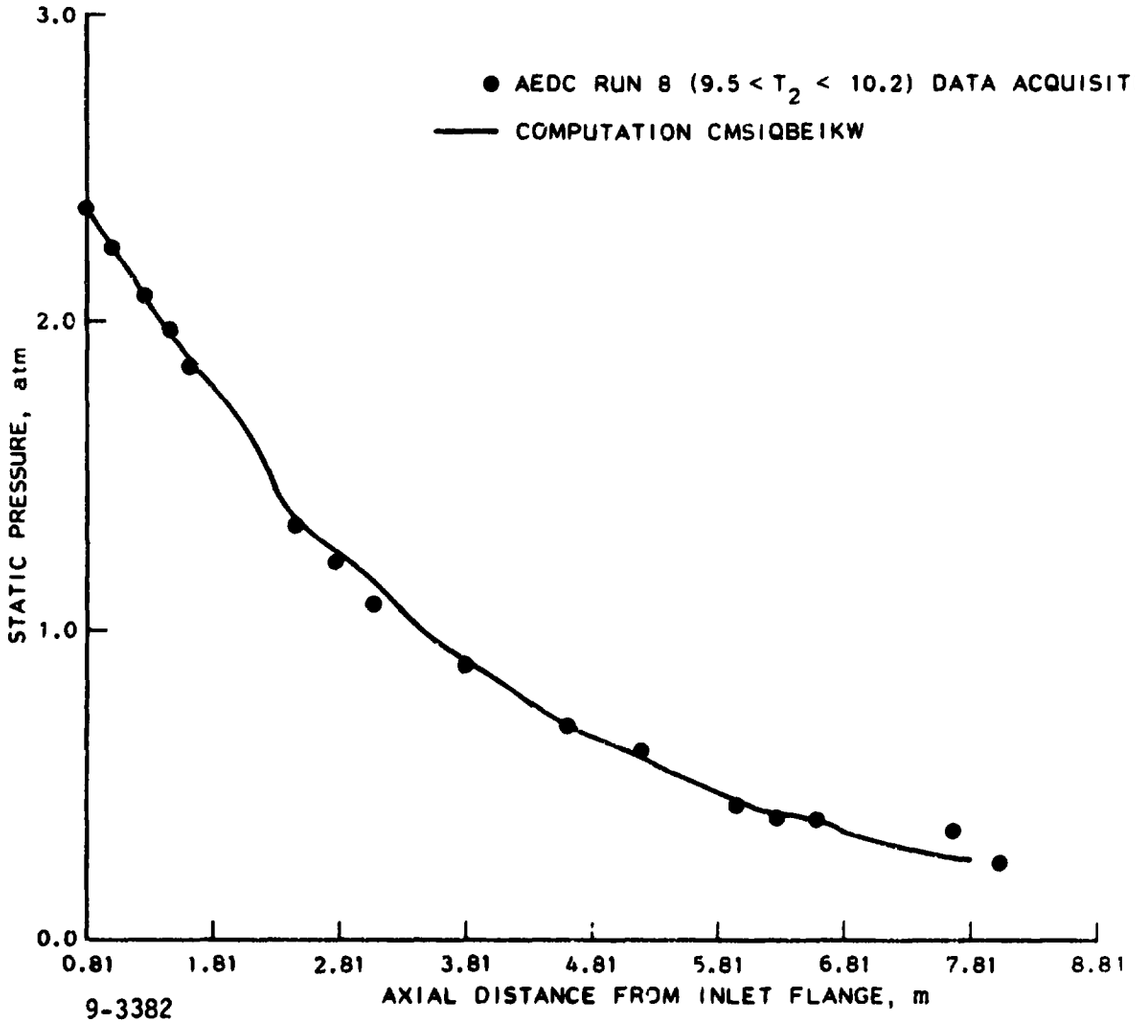

Fig. 3-56. Calculated and measured static pressure distribution in channel

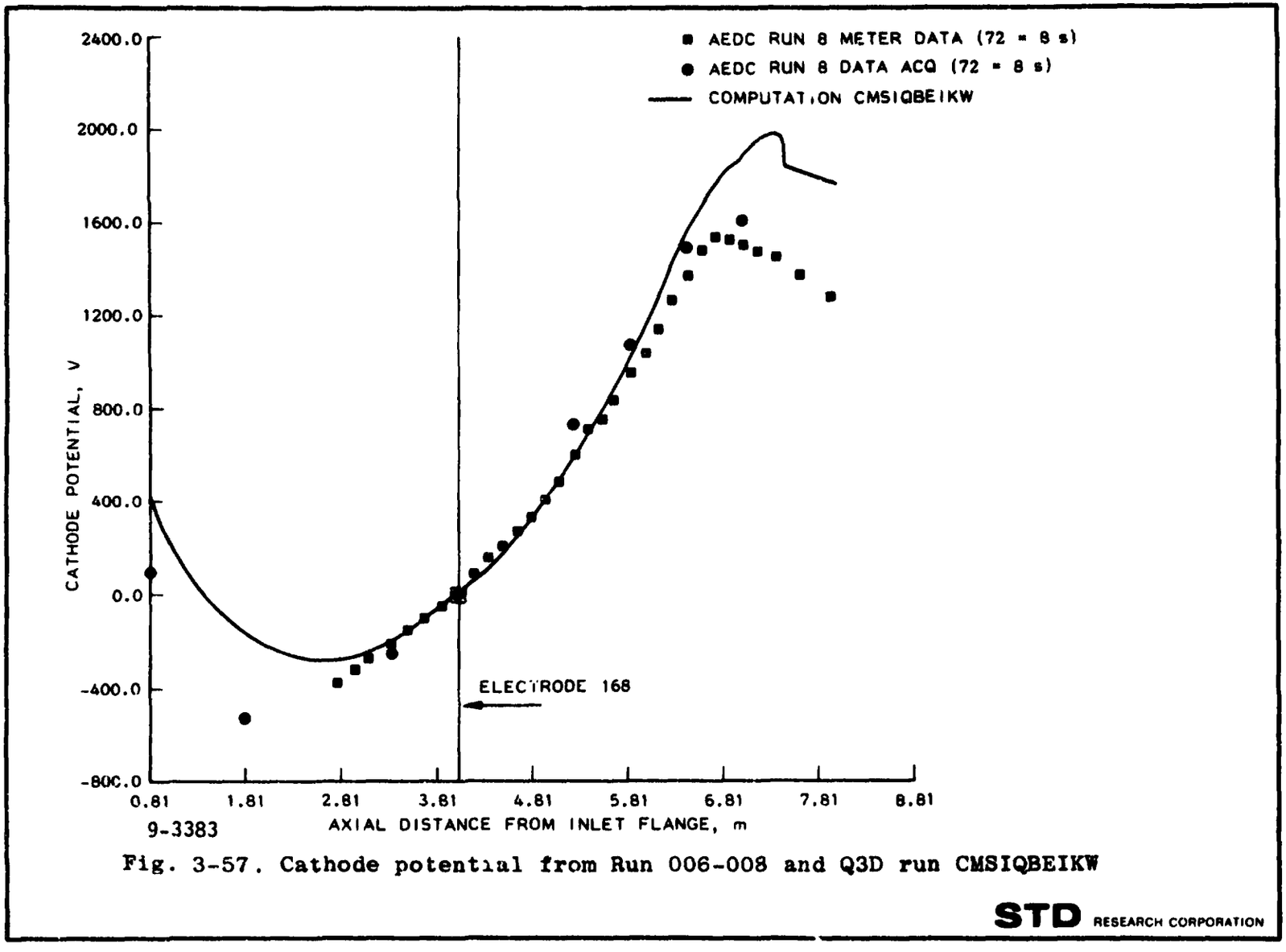

Fig. 3-57. Cathode potential from Run 006-008 and Q3D run CMSIQBEIKW

STD RESEARCH CORPORATION

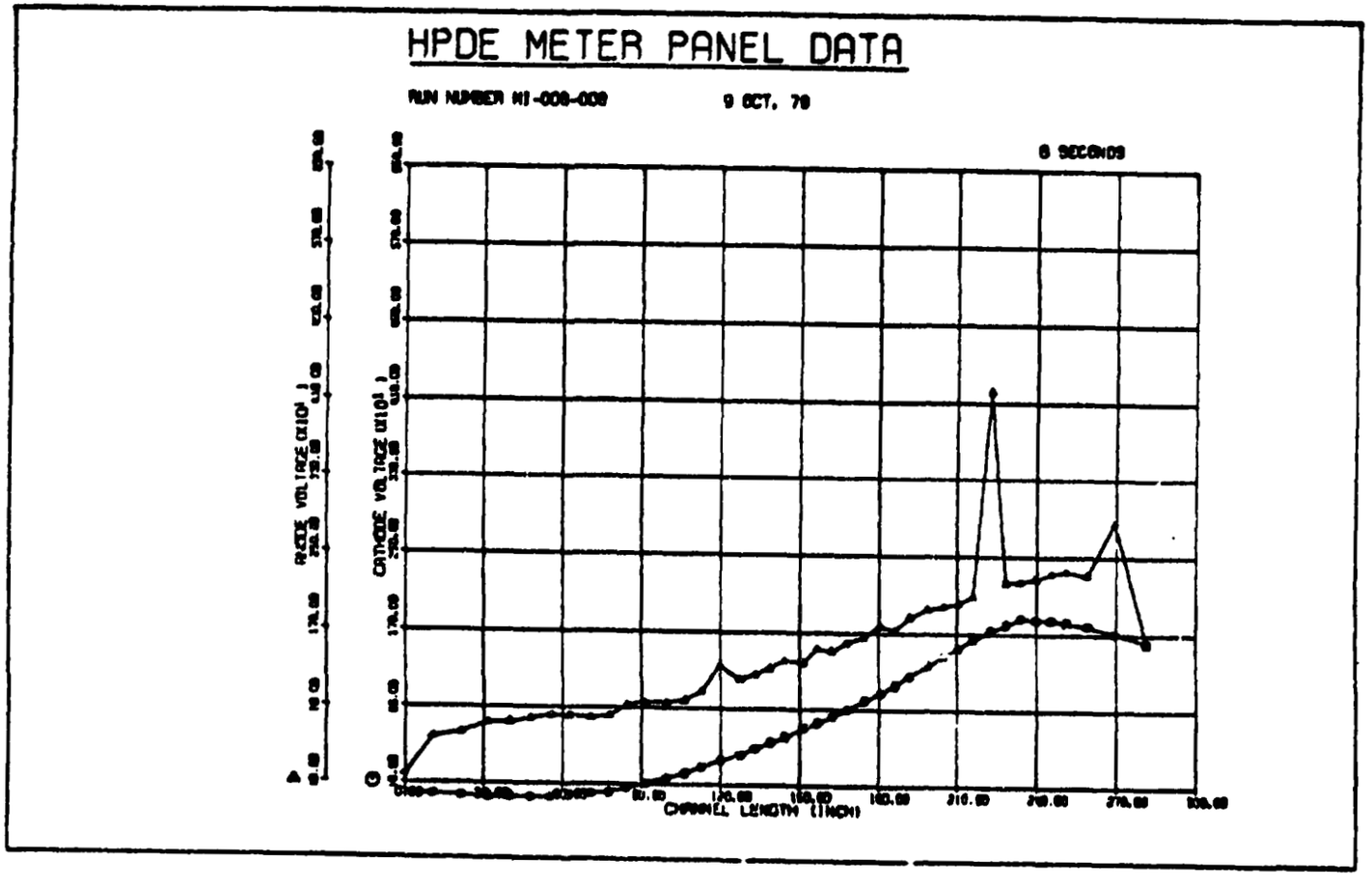

9-3384

Fig. 3-58. Anode and cathode potential Run 006-008

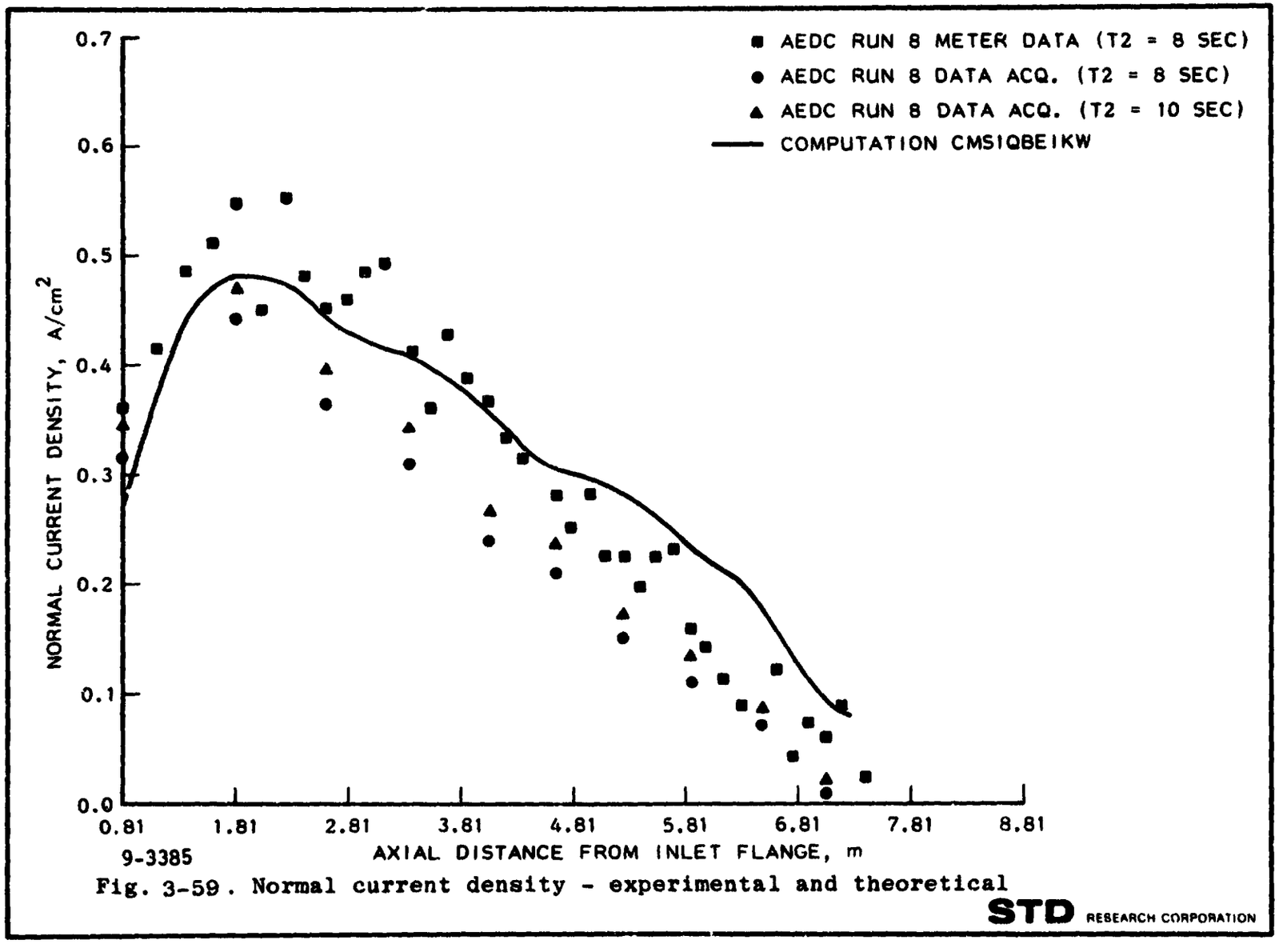

Fig. 3-59. Normal current density - experimental and theoretical

STD RESEARCH CORPORATION

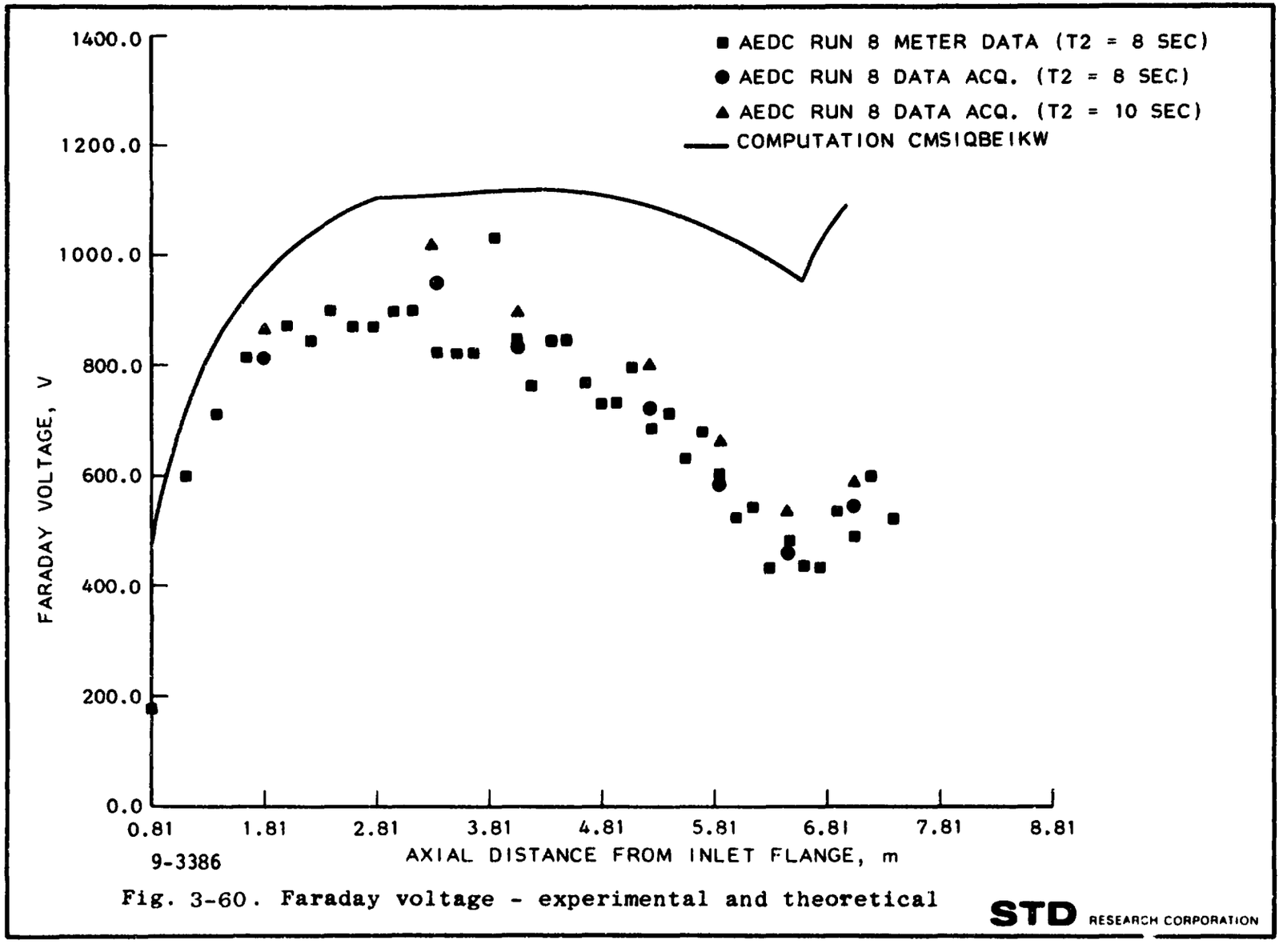

Fig. 3-60. Faraday voltage - experimental and theoretical

STD RESEARCH CORPORATION

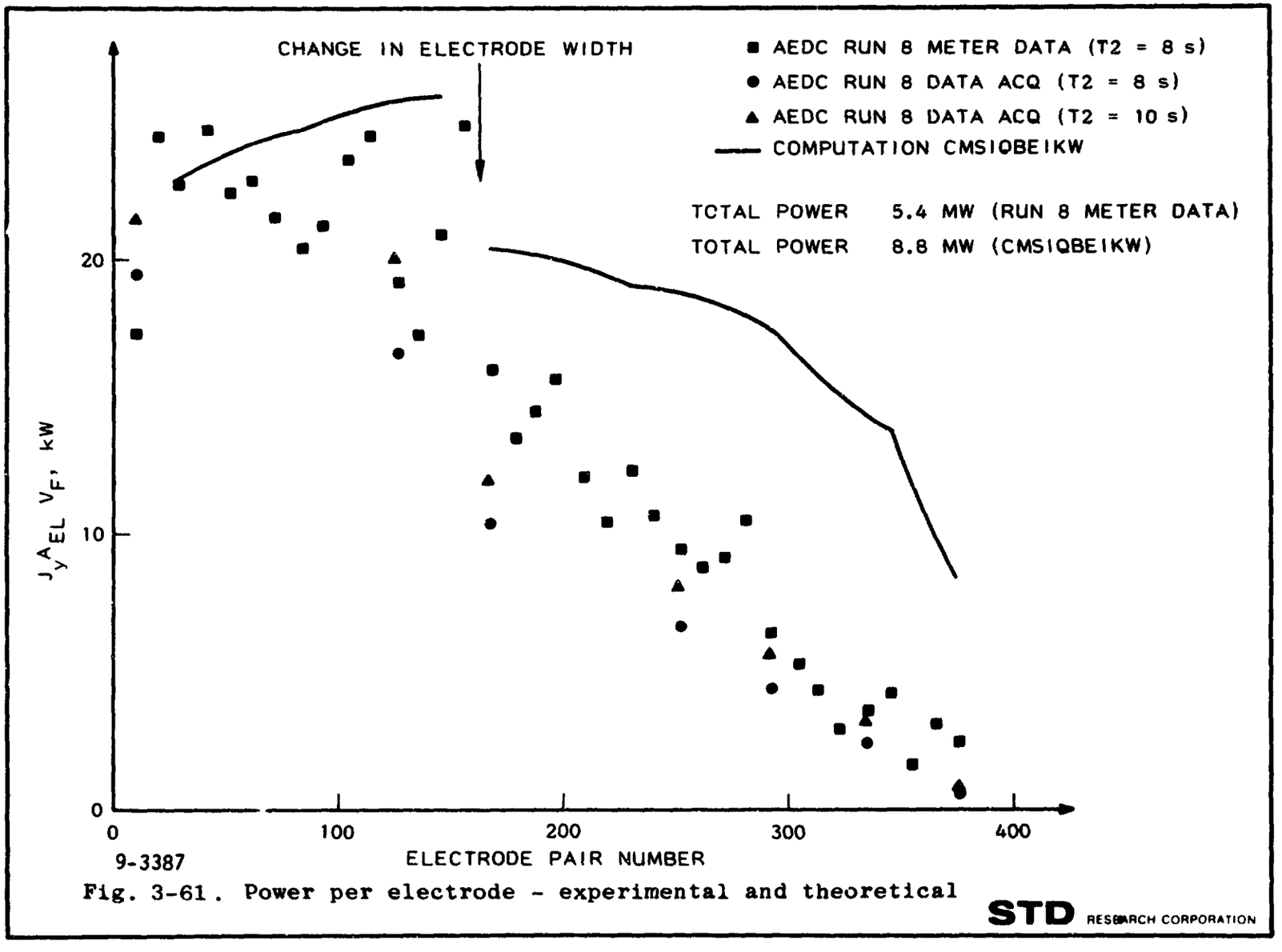

Fig. 3-61. Power per electrode - experimental and theoretical

STD RESEARCH CORPORATION

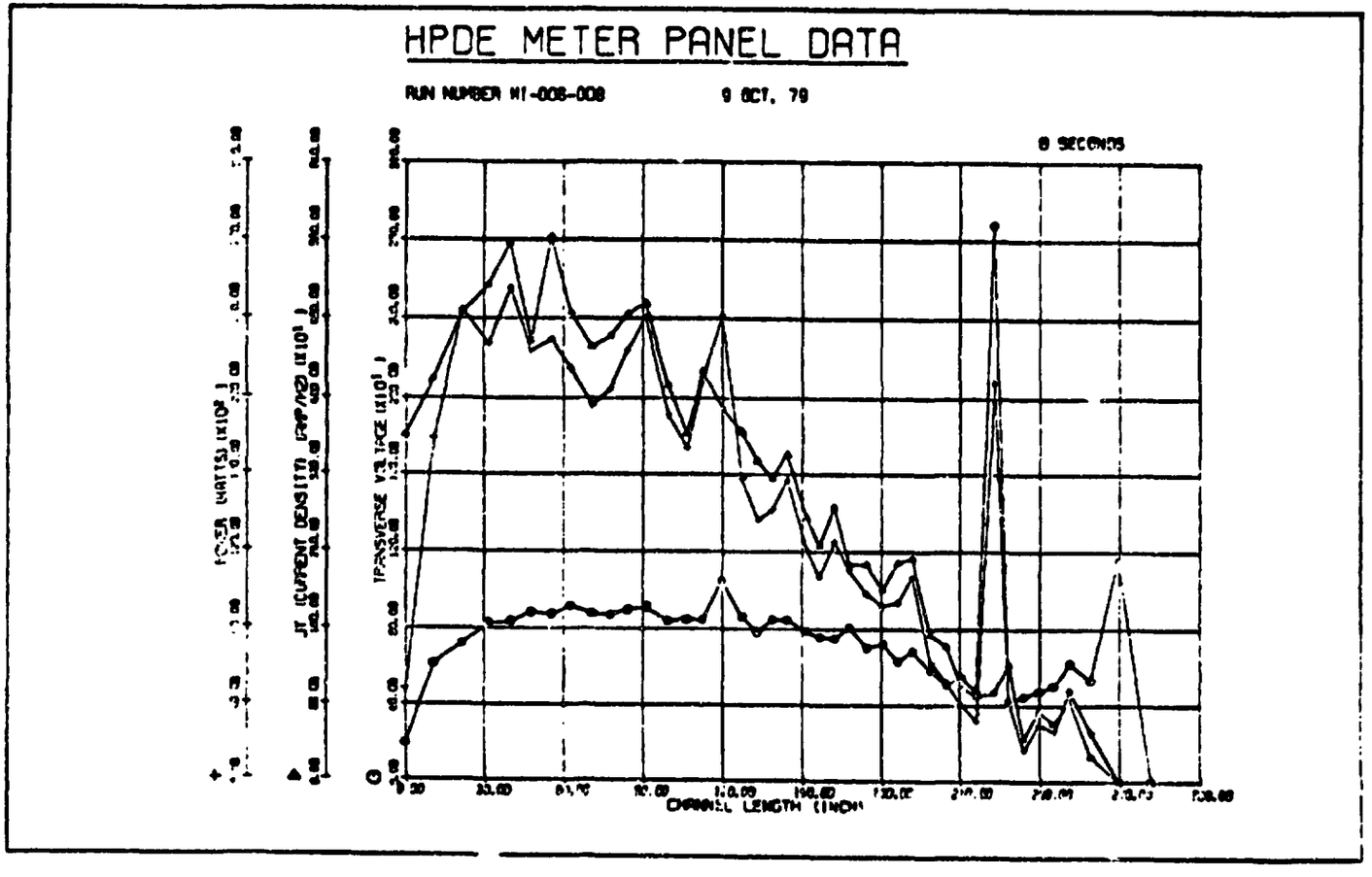

9-3388

Fig. 3-62. Faraday voltage, normal current density and power AEDC Run 006-008

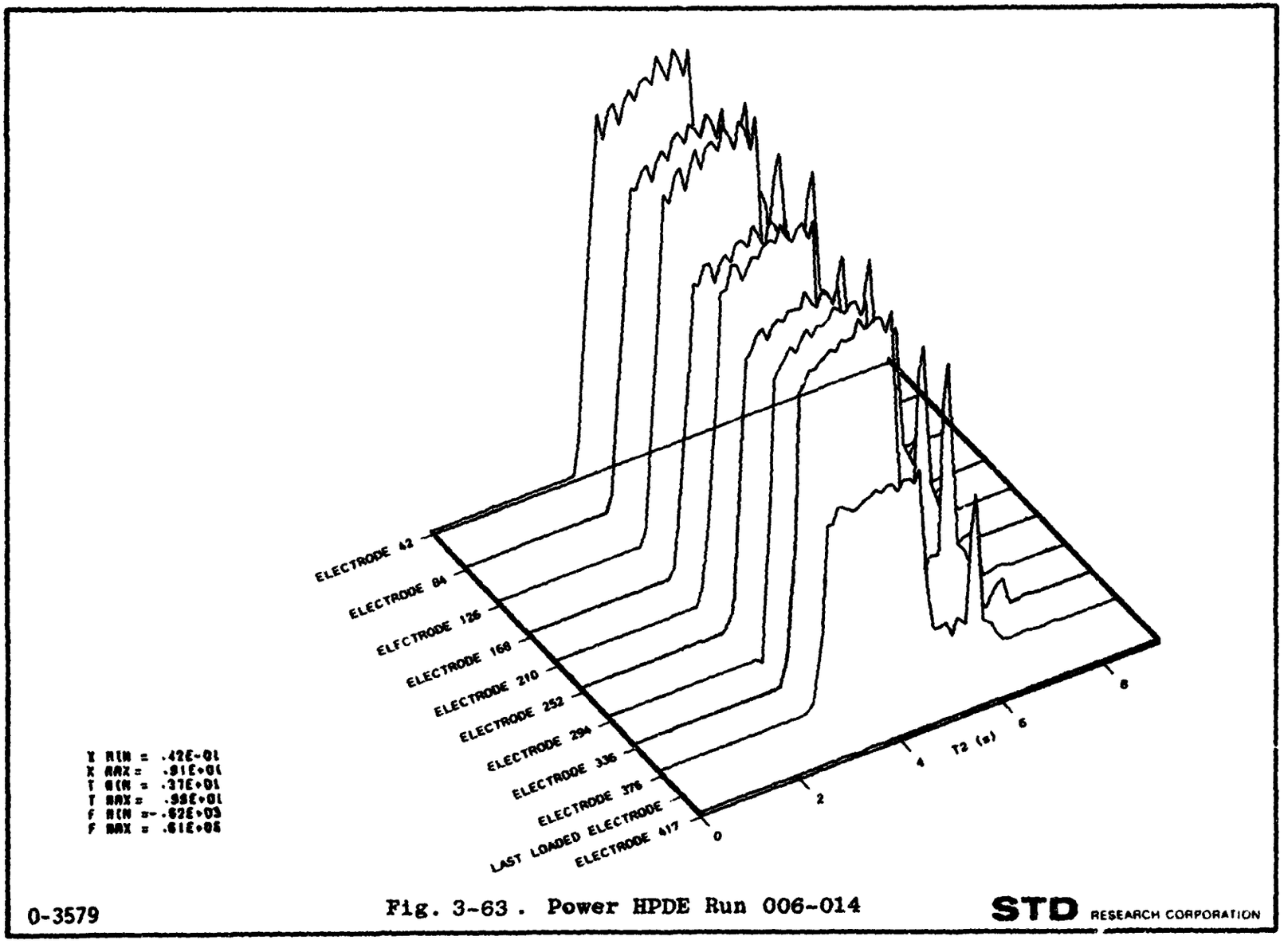

0-3579

Fig. 3-63 . Power HPDE Run 006-014

STD RESEARCH CORPORATION

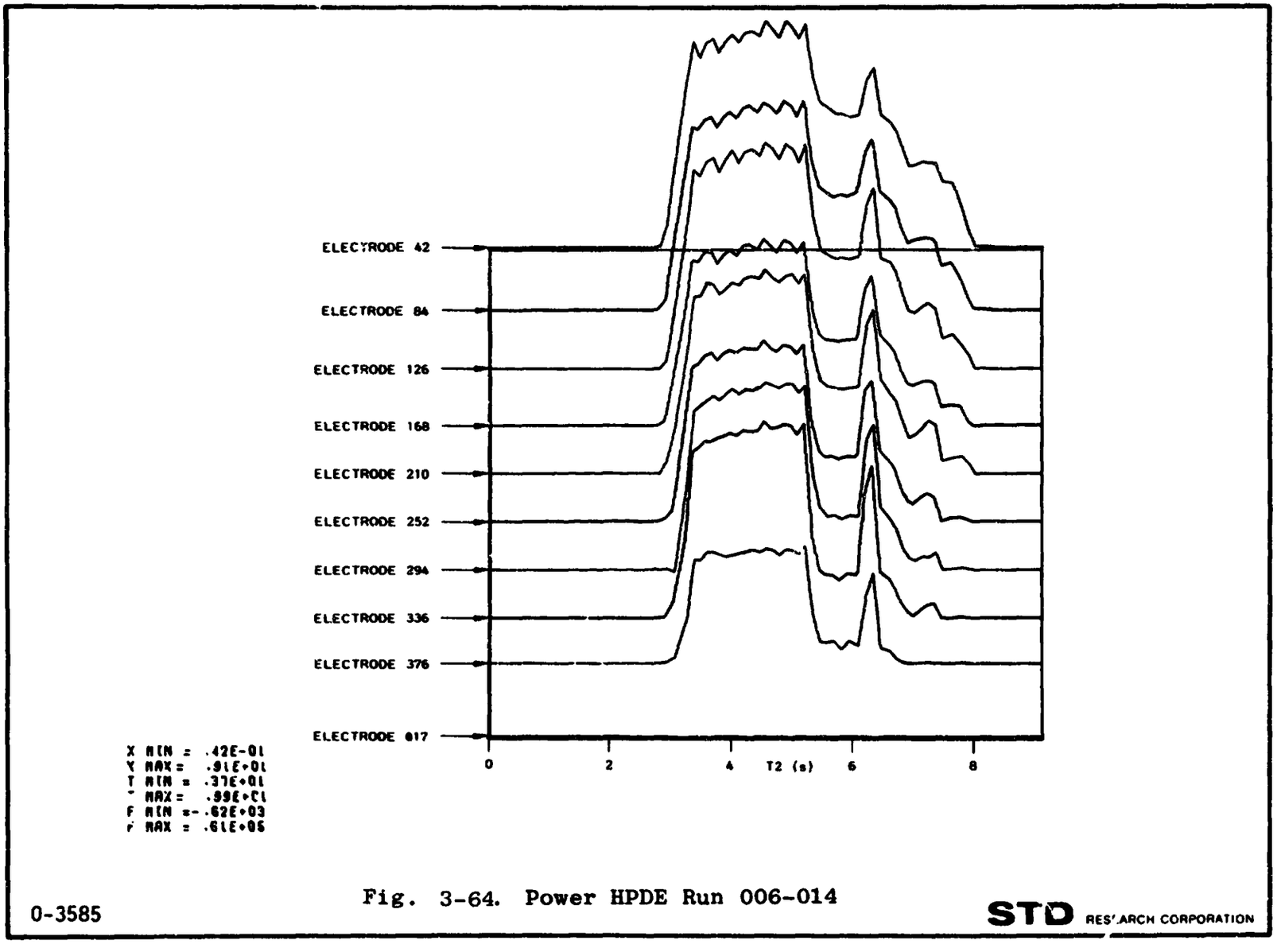

Fig. 3-64. Power HPDE Run 006-014

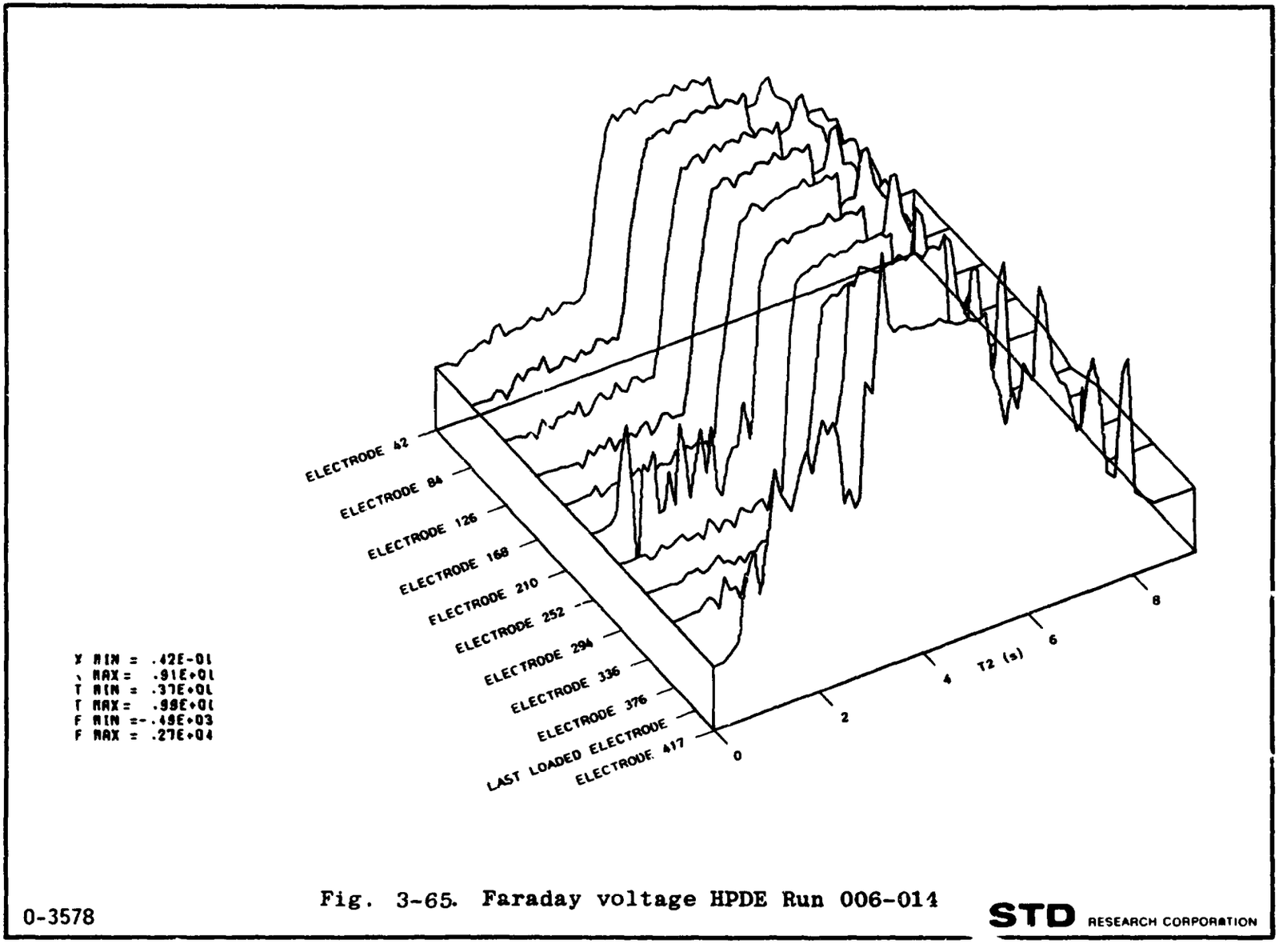

Fig. 3-65. Faraday voltage HPDE Run 006-014

0-3578

STD RESEARCH CORPORATION

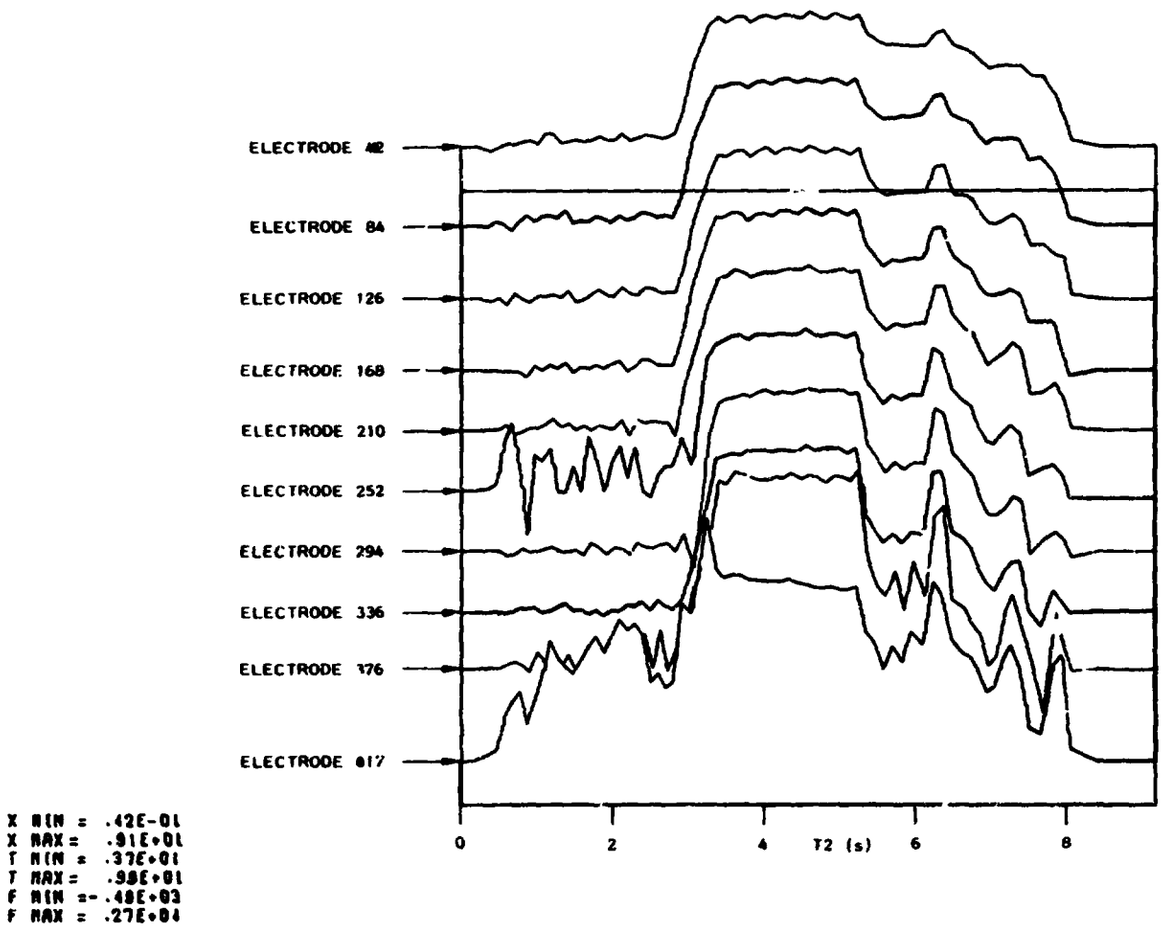

Fig. 3-66. Faraday voltage HPDE Run 006-014

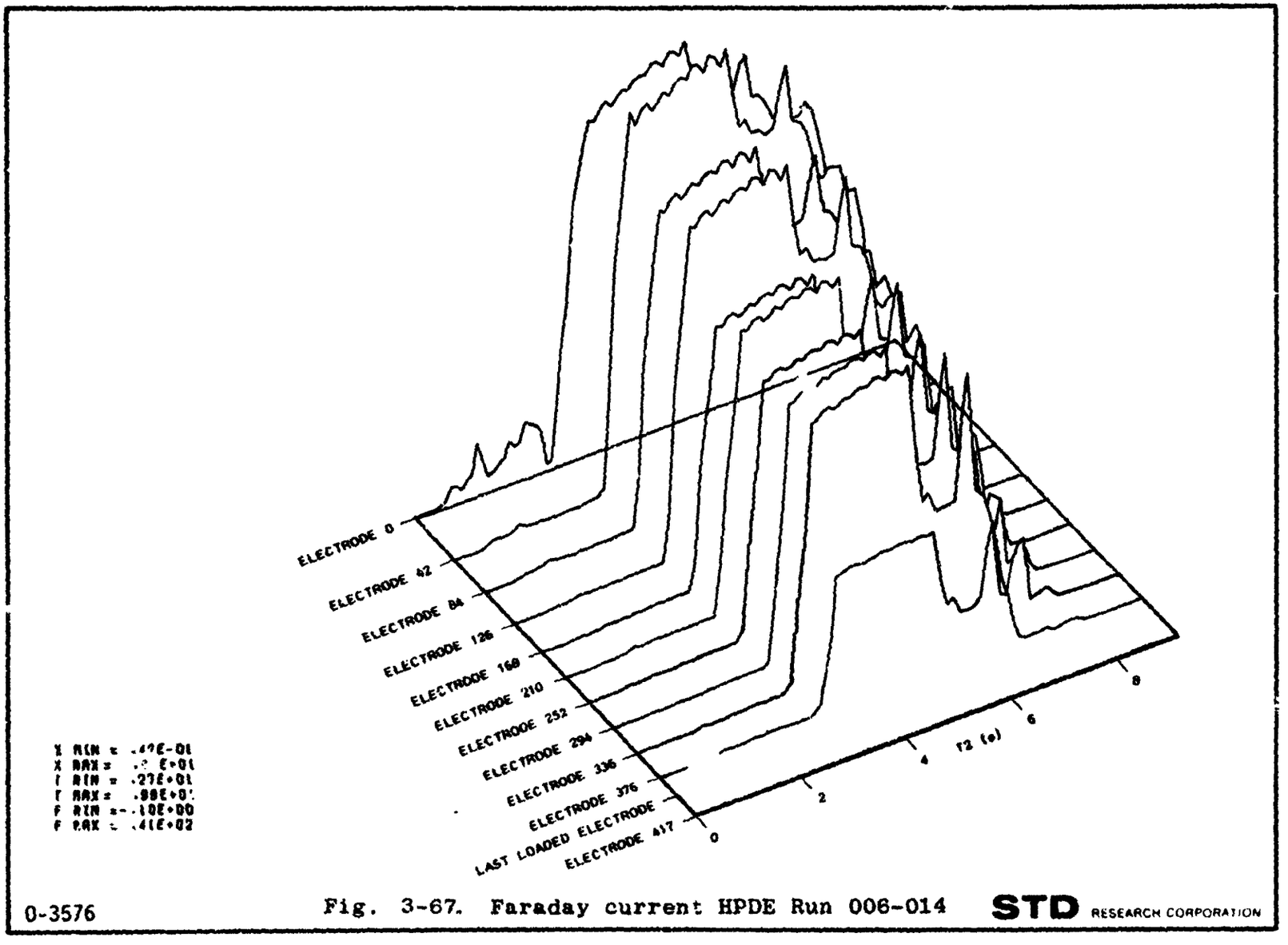

0-3576

Fig. 3-67. Faraday current HPDE Run 006-014

STD RESEARCH CORPORATION

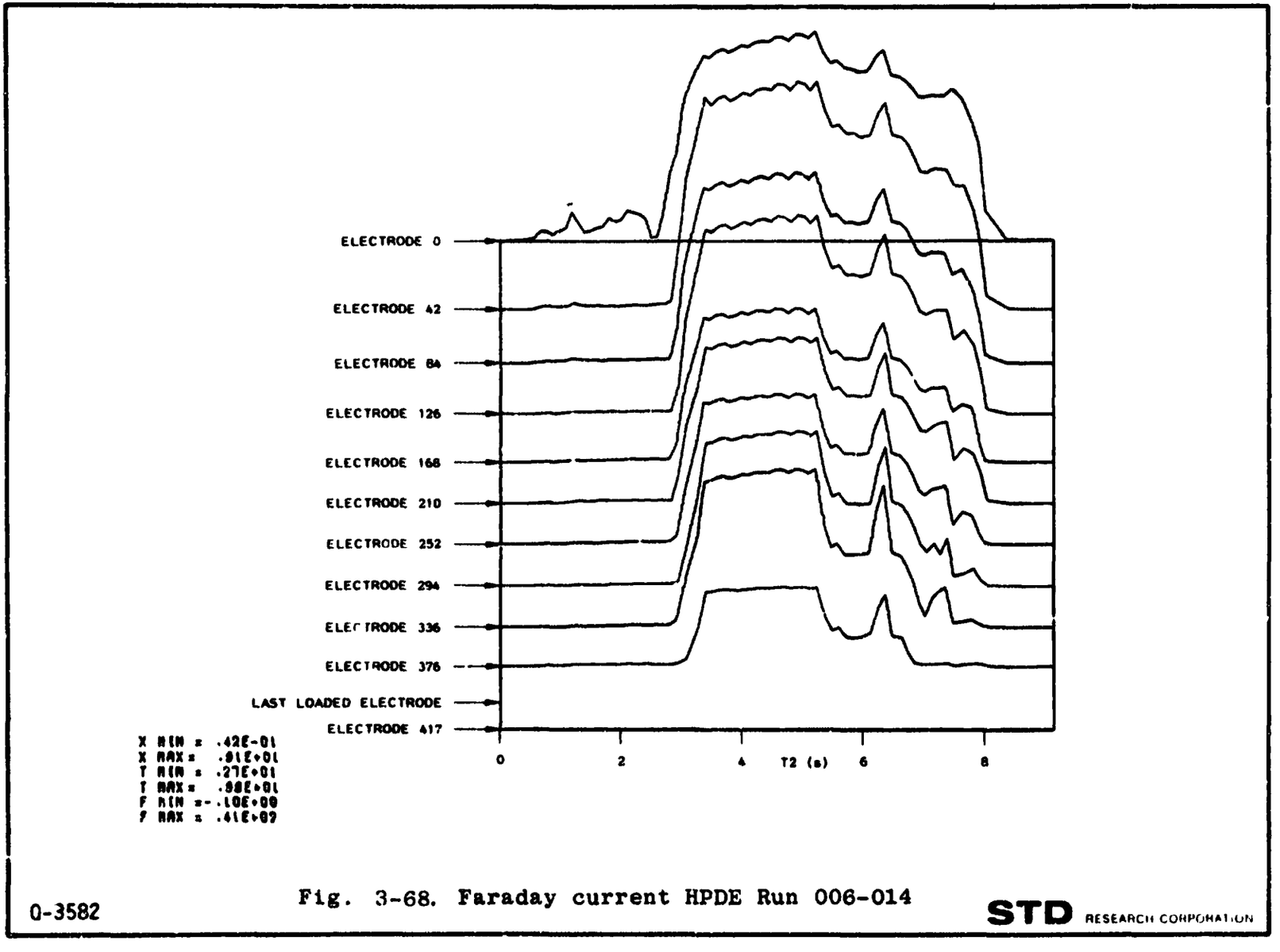

Fig. 3-68. Faraday current HPDE Run 006-014

0-3582

STD RESEARCH CORPORATION

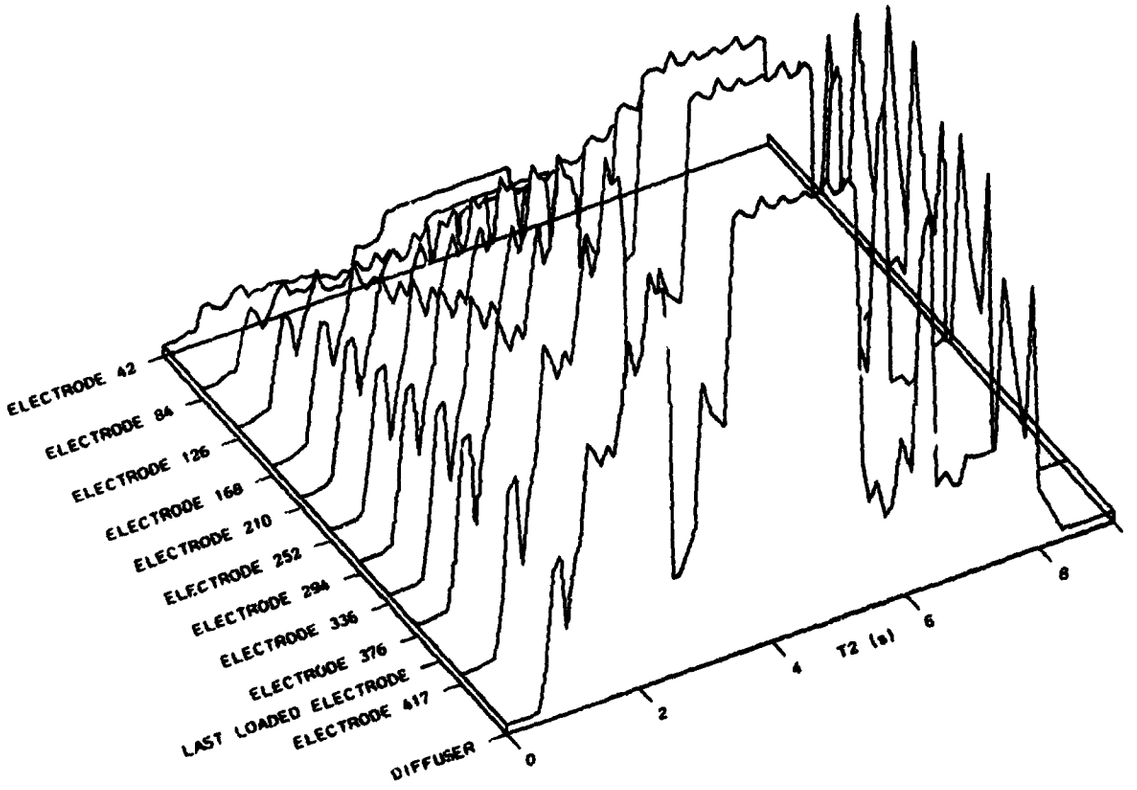

0-3574

Fig. 3-69. Voltage anode to ground HPDE Run 006-014

STD RESEARCH CORPORATION

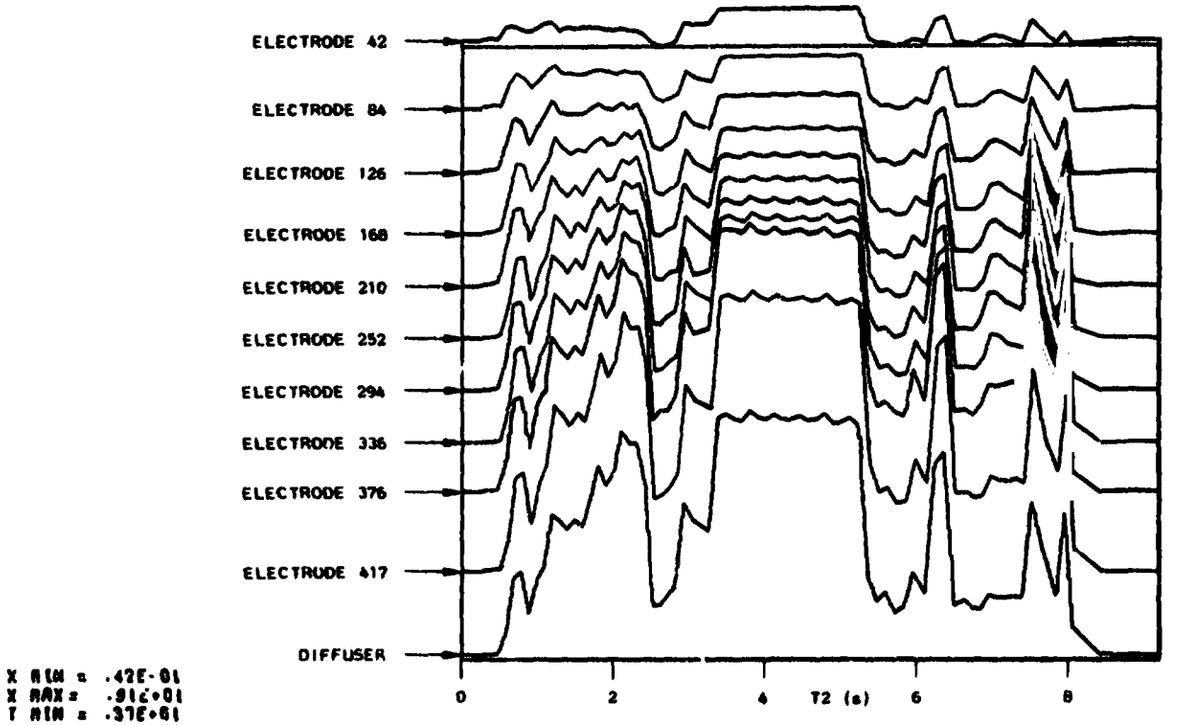

Fig. 3-7C. Voltage anode to ground HPDE Run 006-014

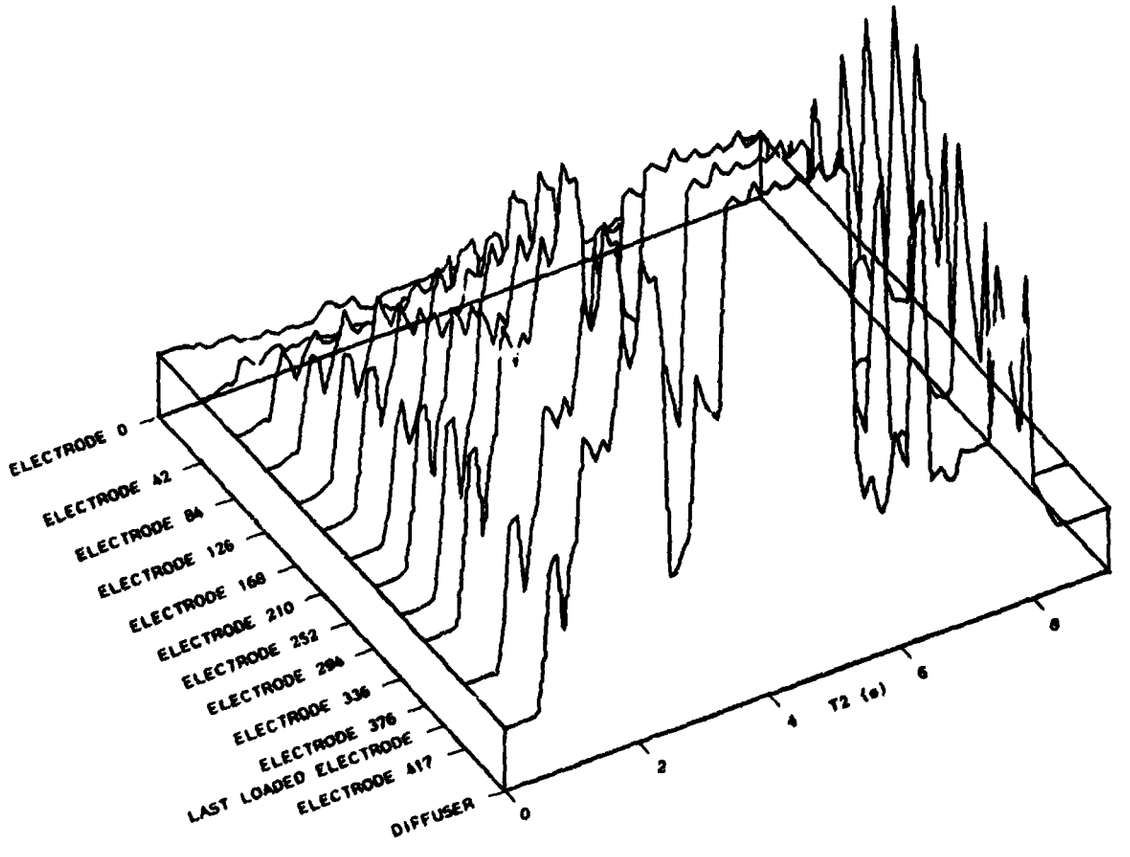

Fig. 3-71. Voltage cathode to ground HPDE Run 006-014

0-3575

STD RESEARCH CORPORATION

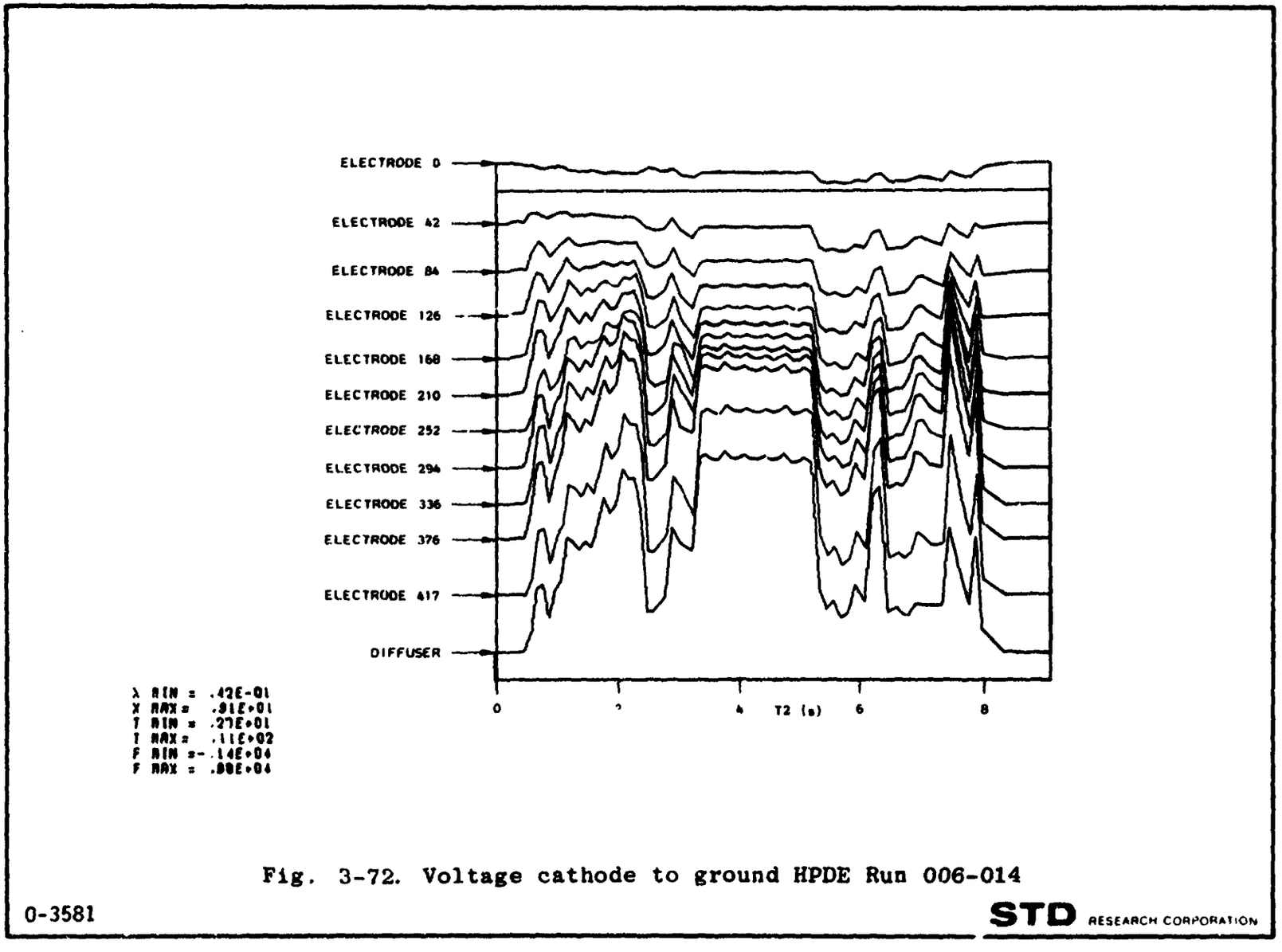

Fig. 3-72. Voltage cathode to ground HPDE Run 006-014

0-3581

STD RESEARCH CORPORATION

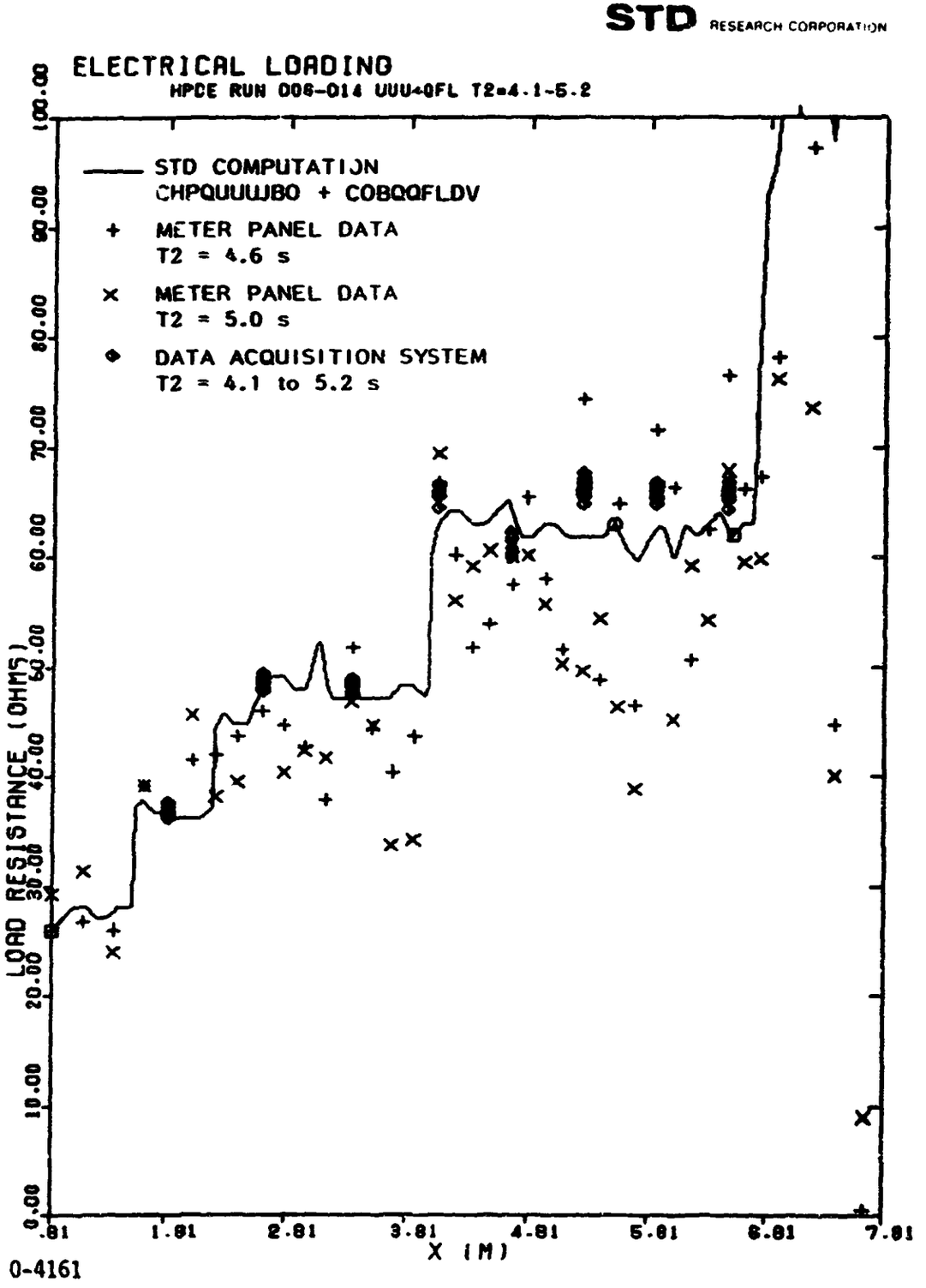

Fig. 3-73. Load resistance for HPDE Run 006-014

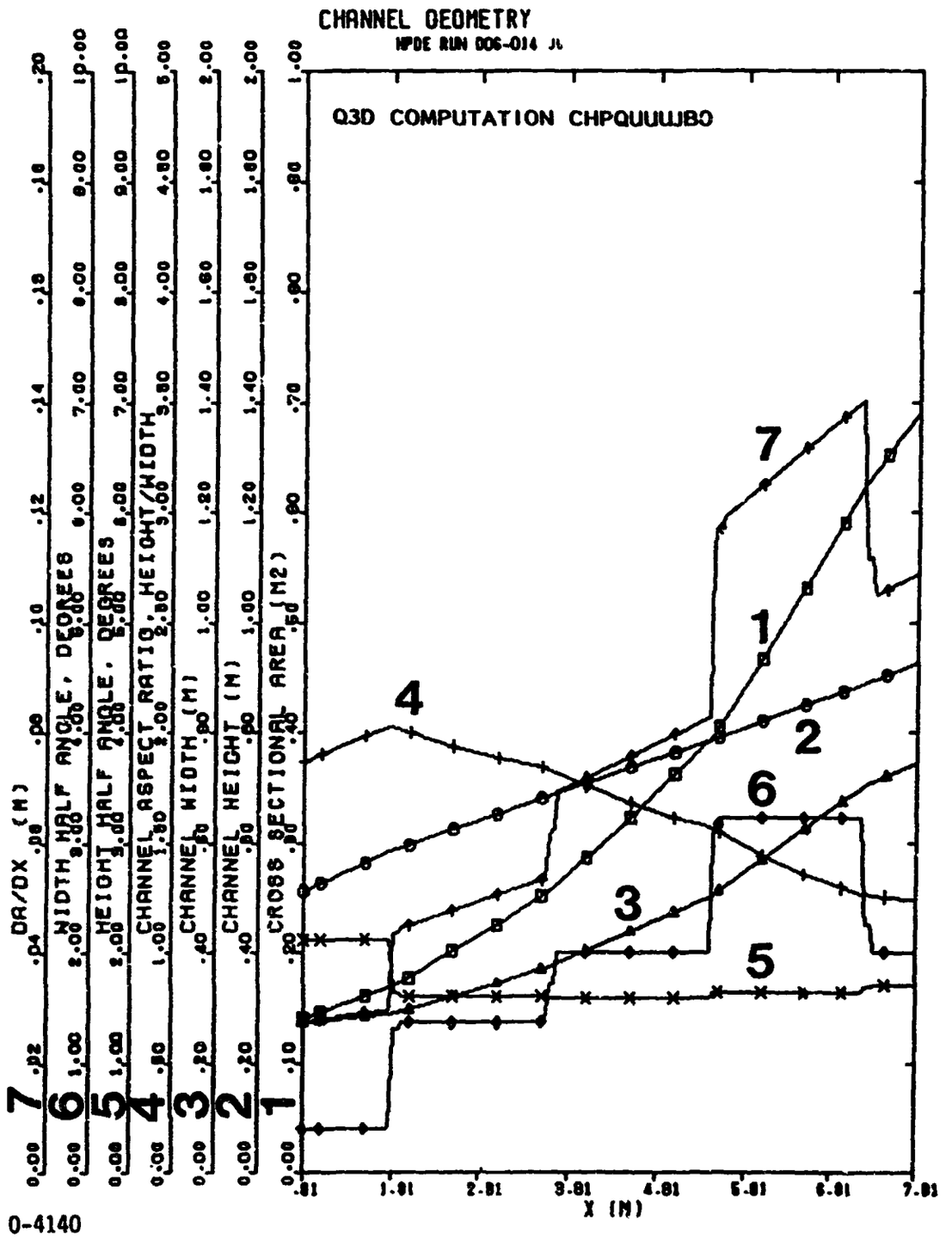

Fig. 3-74. Channel geometry HPDE Run 006-014

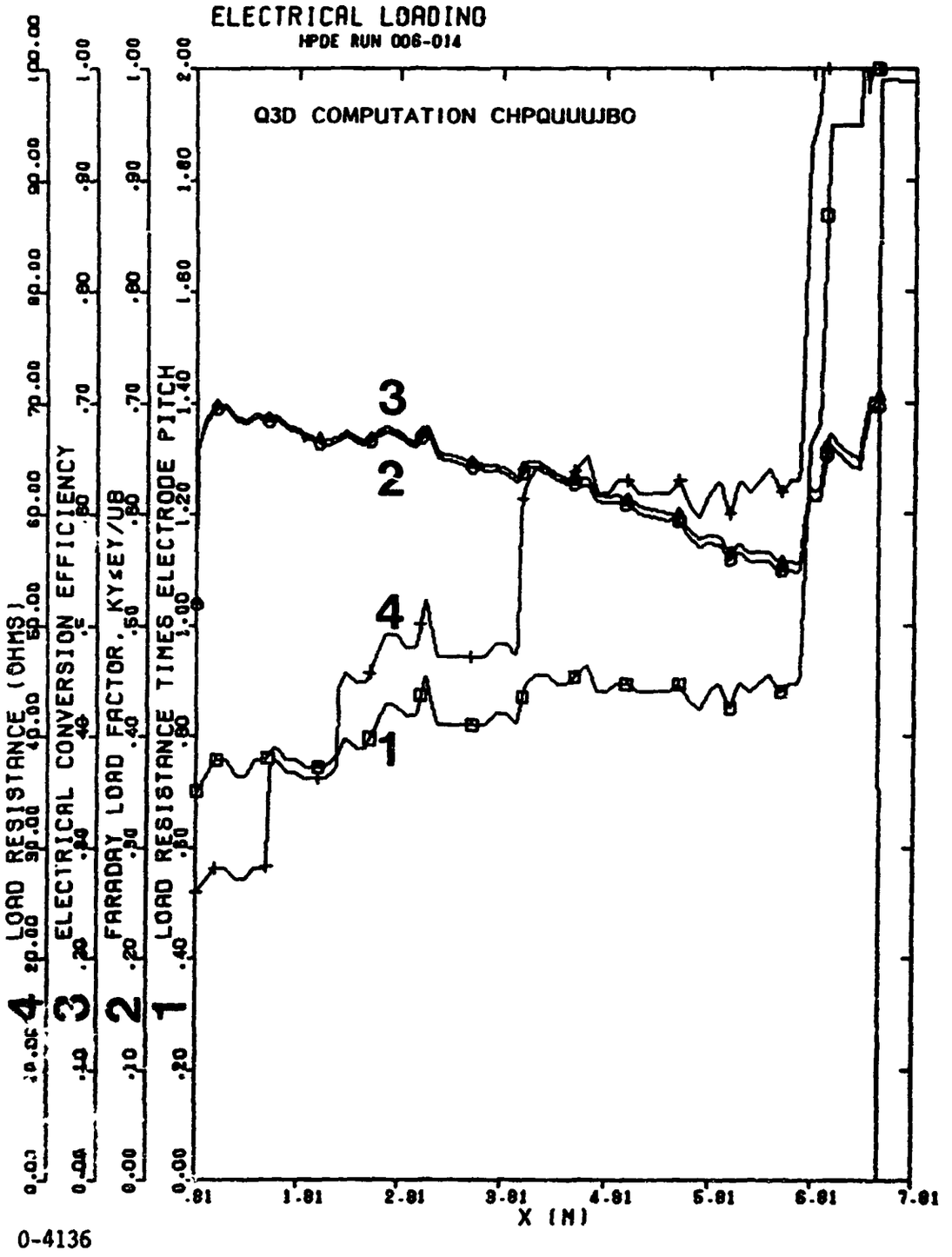

Fig. 3-75. Electrical loading HPDE Run 006-014

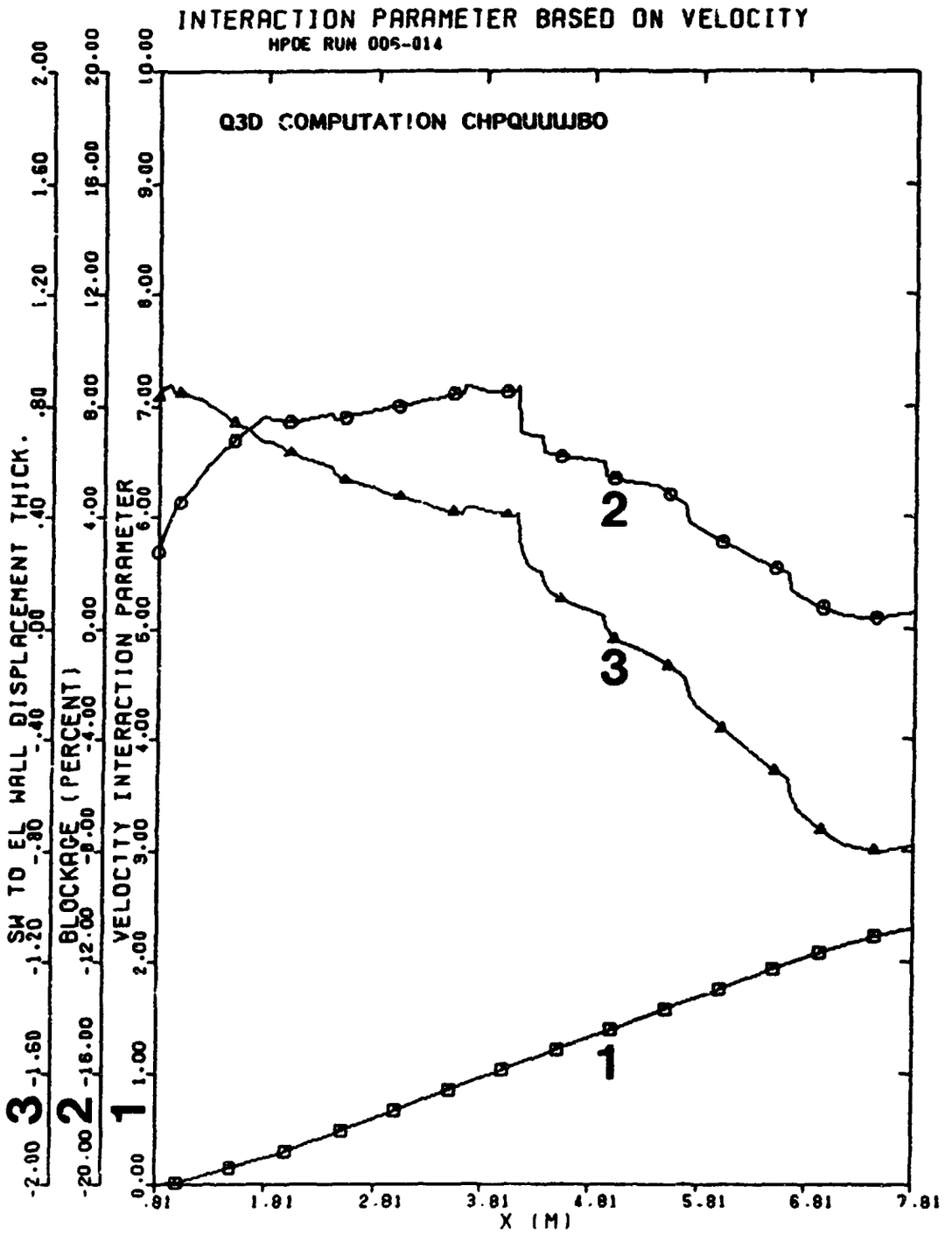

0-4149

Fig. 3-76. Interaction parameter based on velocity HPDE Run 006-014

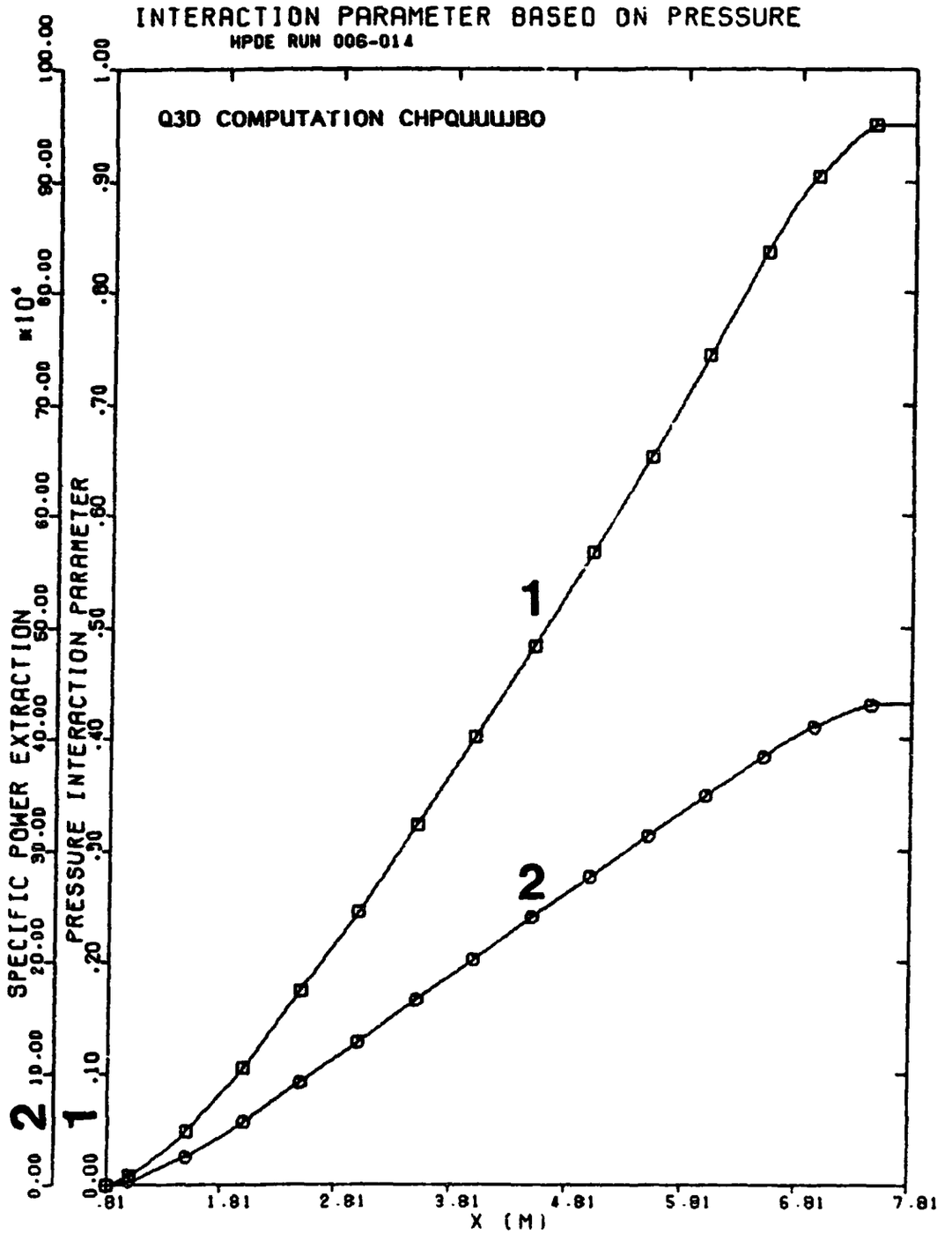

0-4150

Fig. 3-77. Interaction parameter based on pressure HPDE Run 006-014

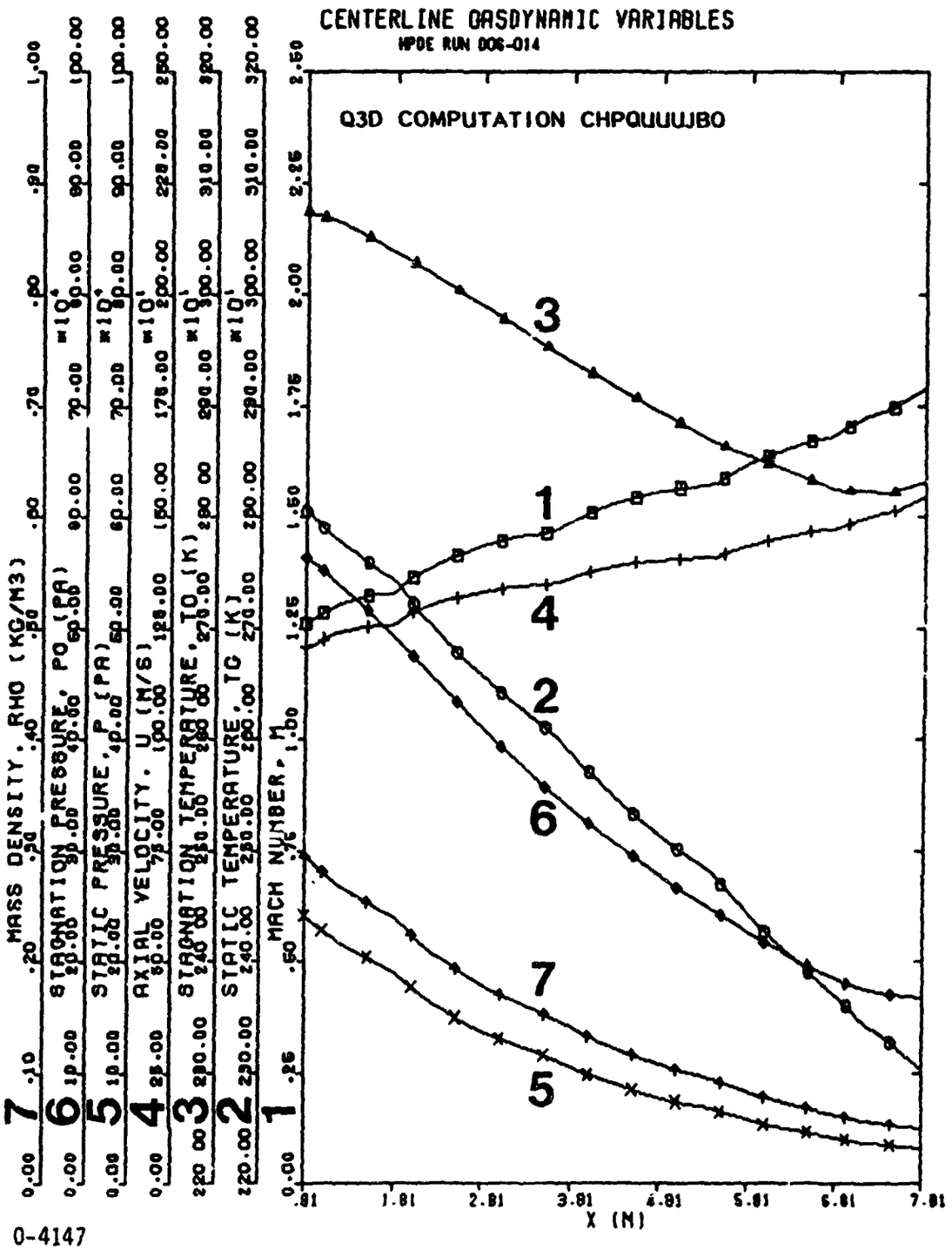

Fig. 3-78. Centerline gasdynamic variables HPDE Run 006-014

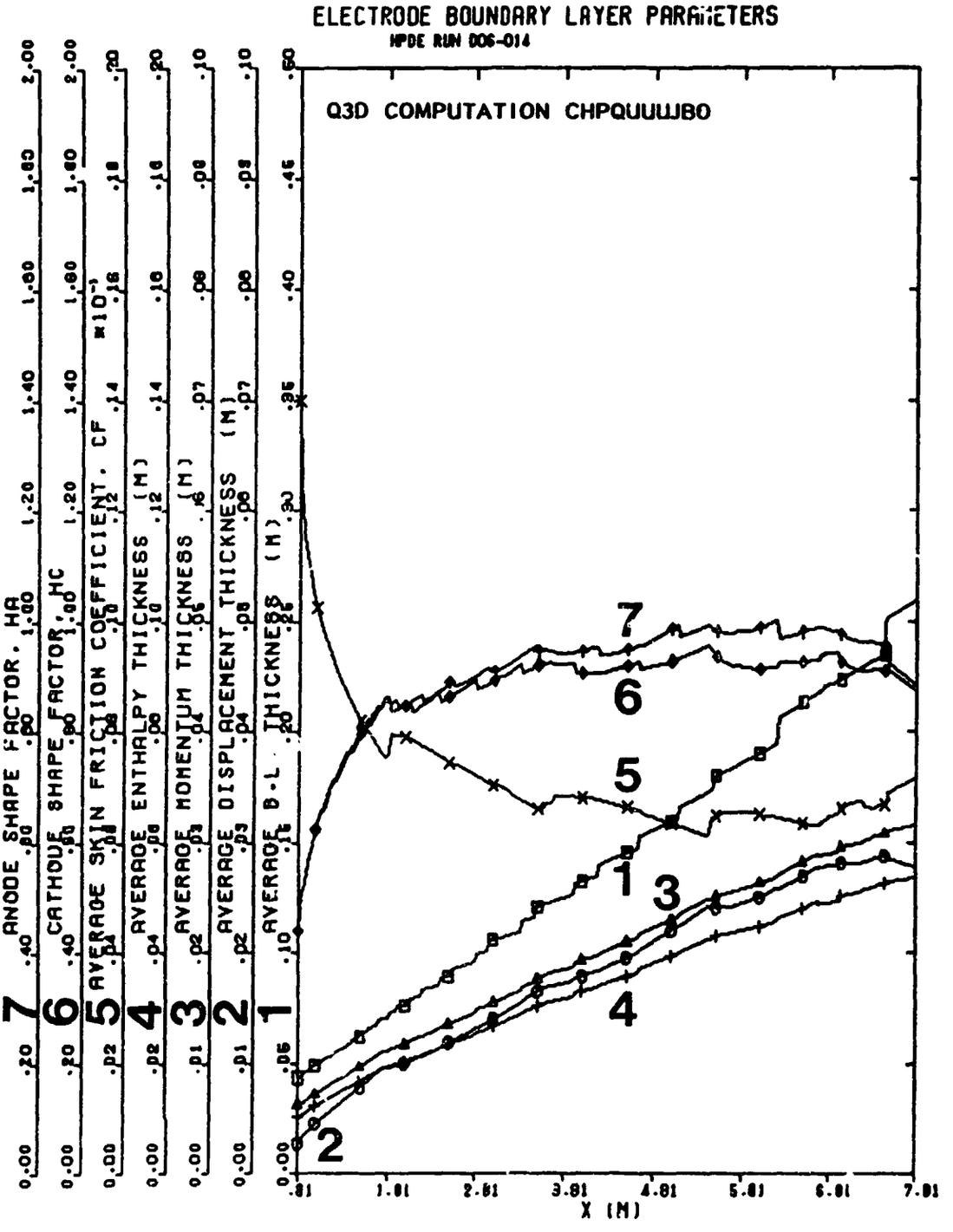

0-4137

Fig. 3-79. Electrode boundary layer parameters HPDE Run 006-014

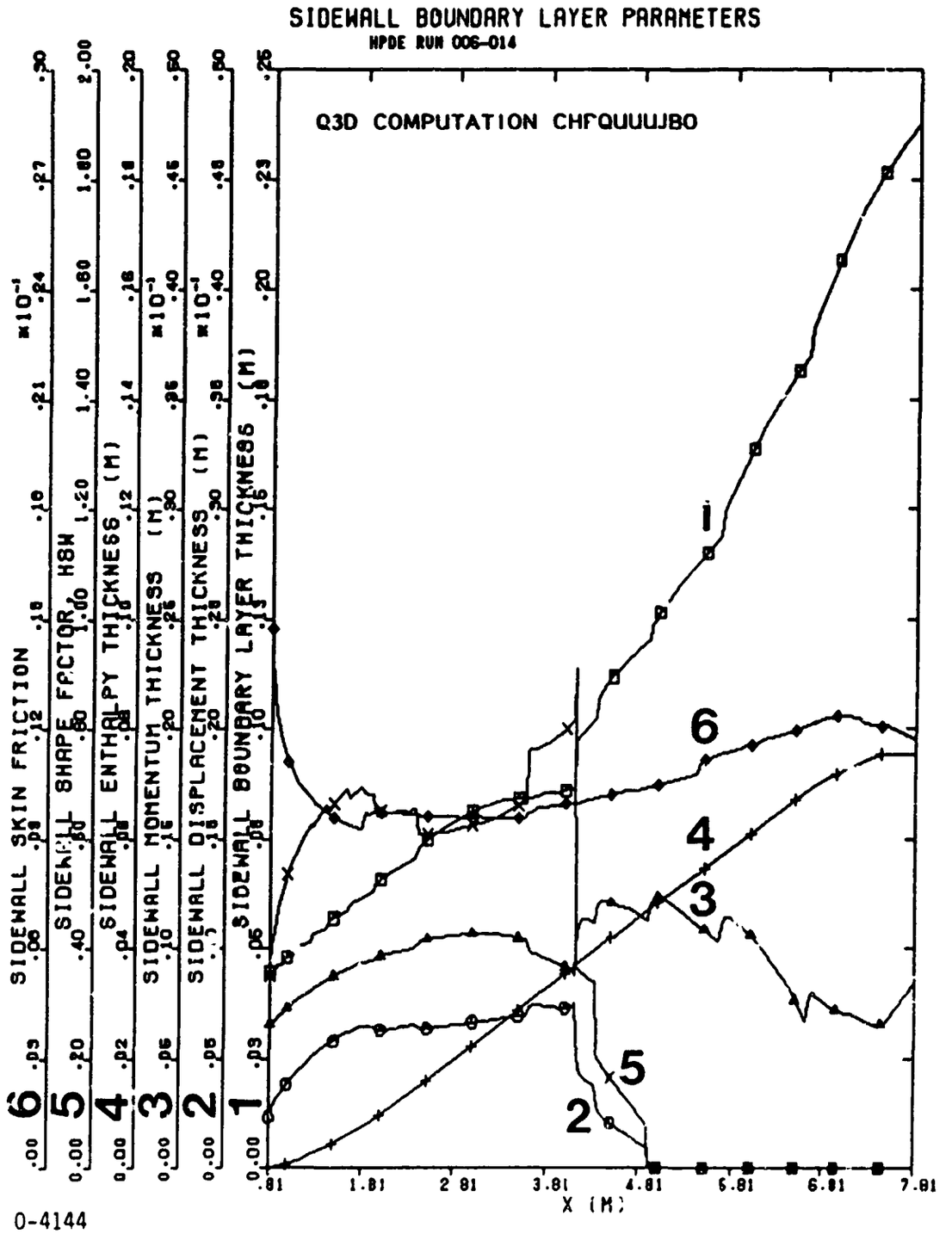

Fig. 3-8C. Sidewall boundary layer parameters HPDE Run 006-014

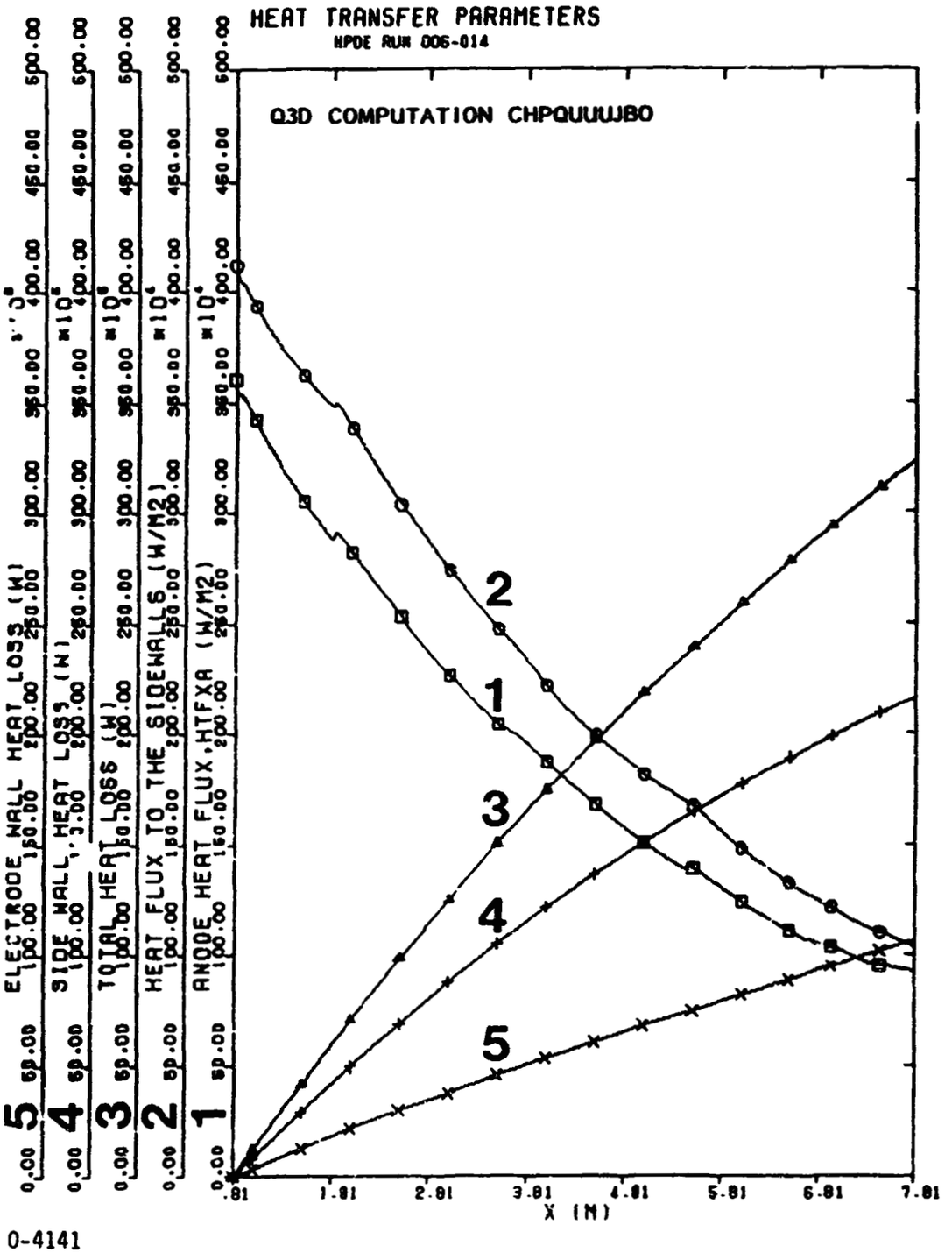

Fig. 3-81. He transfer paramters HPDE Run 006-014

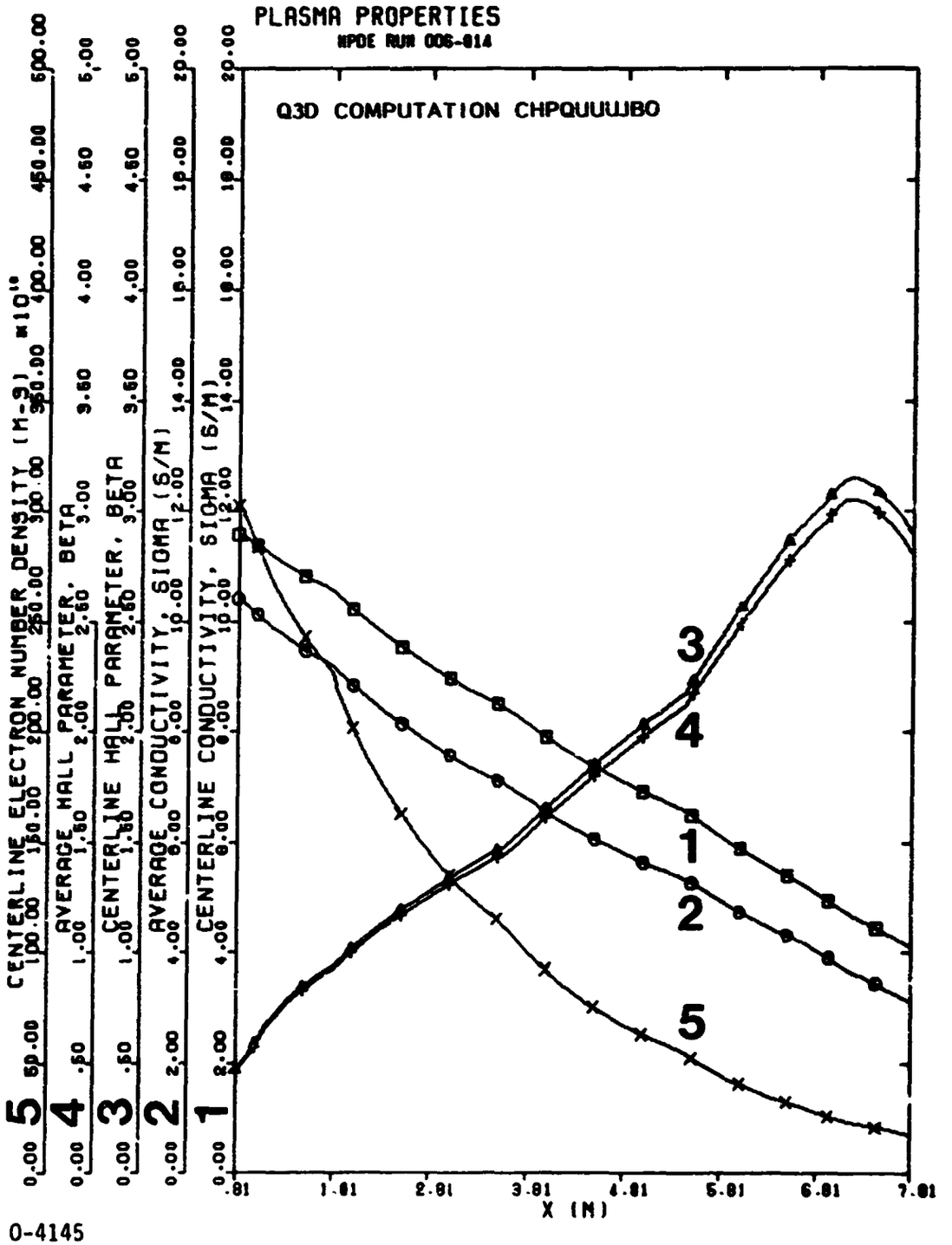

Fig. 3-82. Plasma properties HPDE Run 006-014

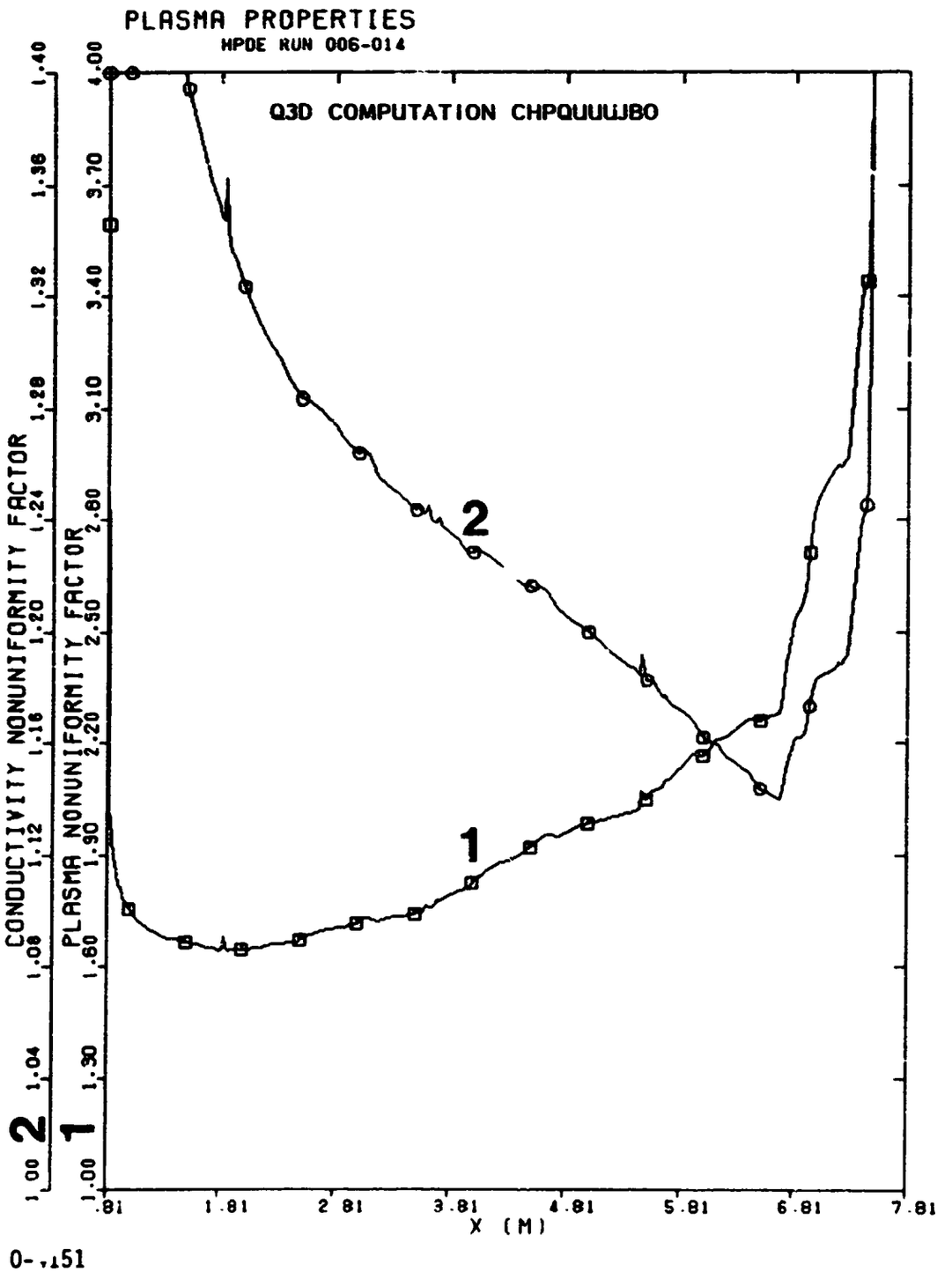

0-.151

Fig. 3-83. Nonuniformity factors HPDE Run 006-014

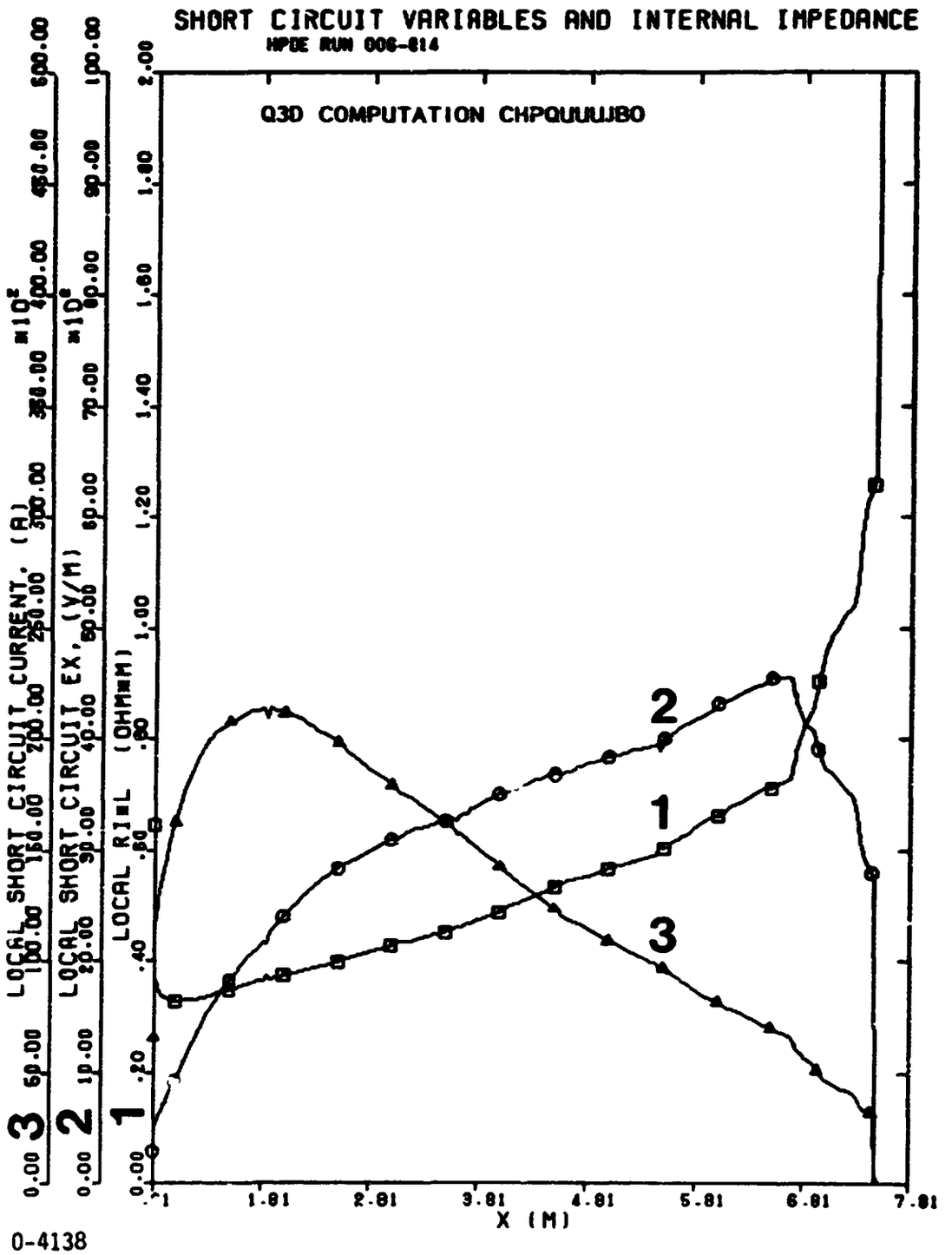

Fig. 3-84. Short circuit variables and internal impedance HPDE Run 006-014

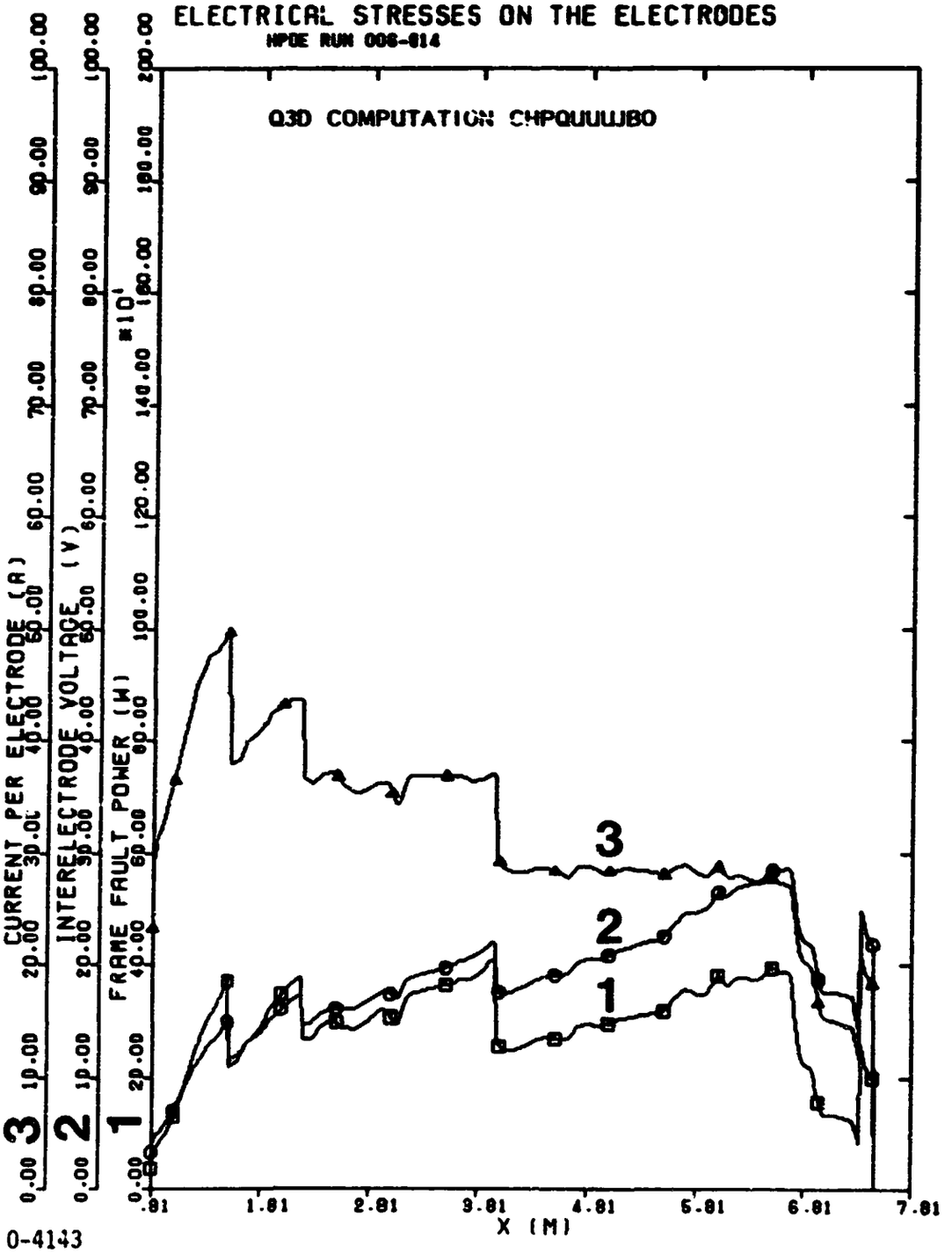

Fig. 3-85. Electrical stresses on the electrodes HPDE Rur 006-014

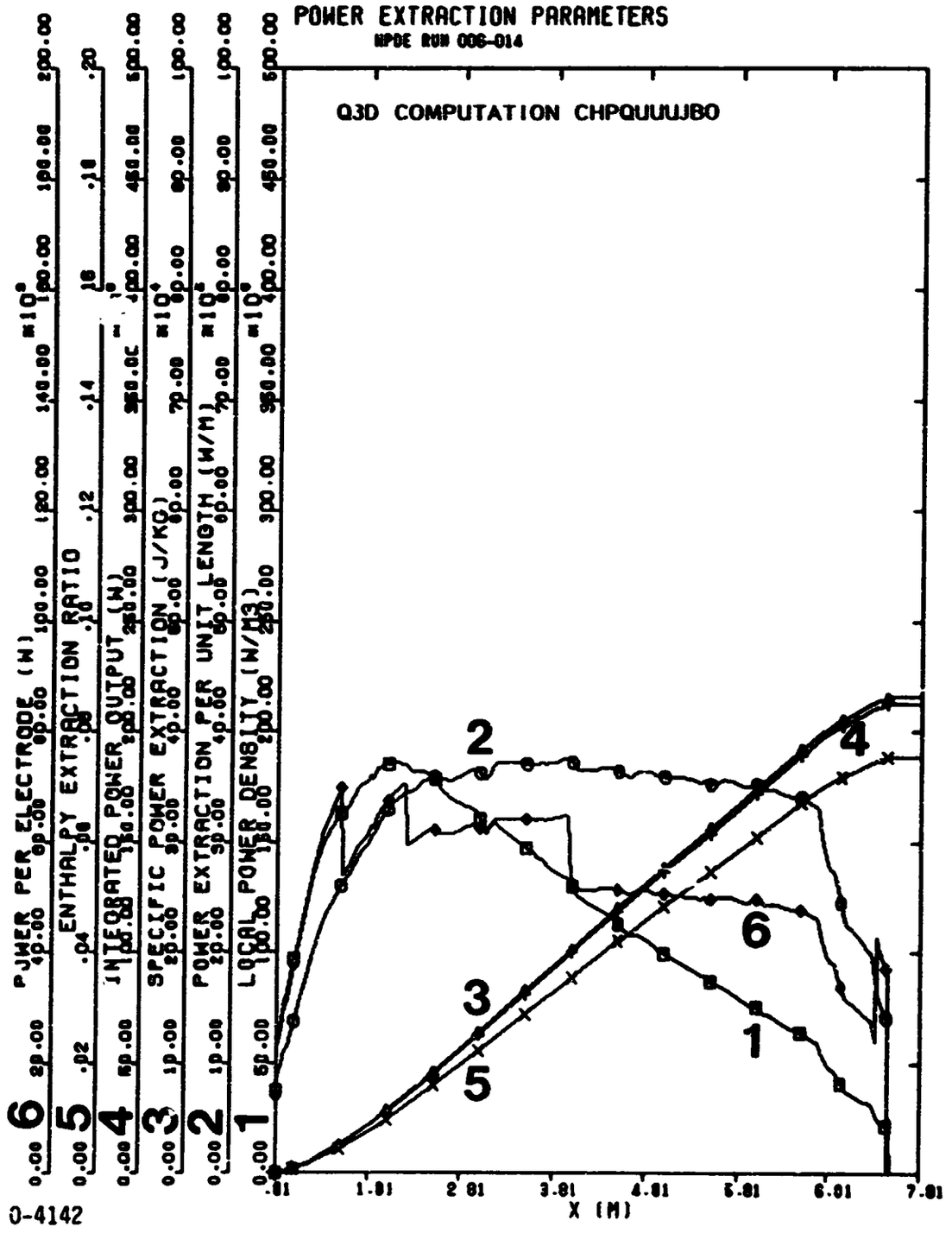

Fig. 3-86. Power extraction parameters HPDE Run 006-014

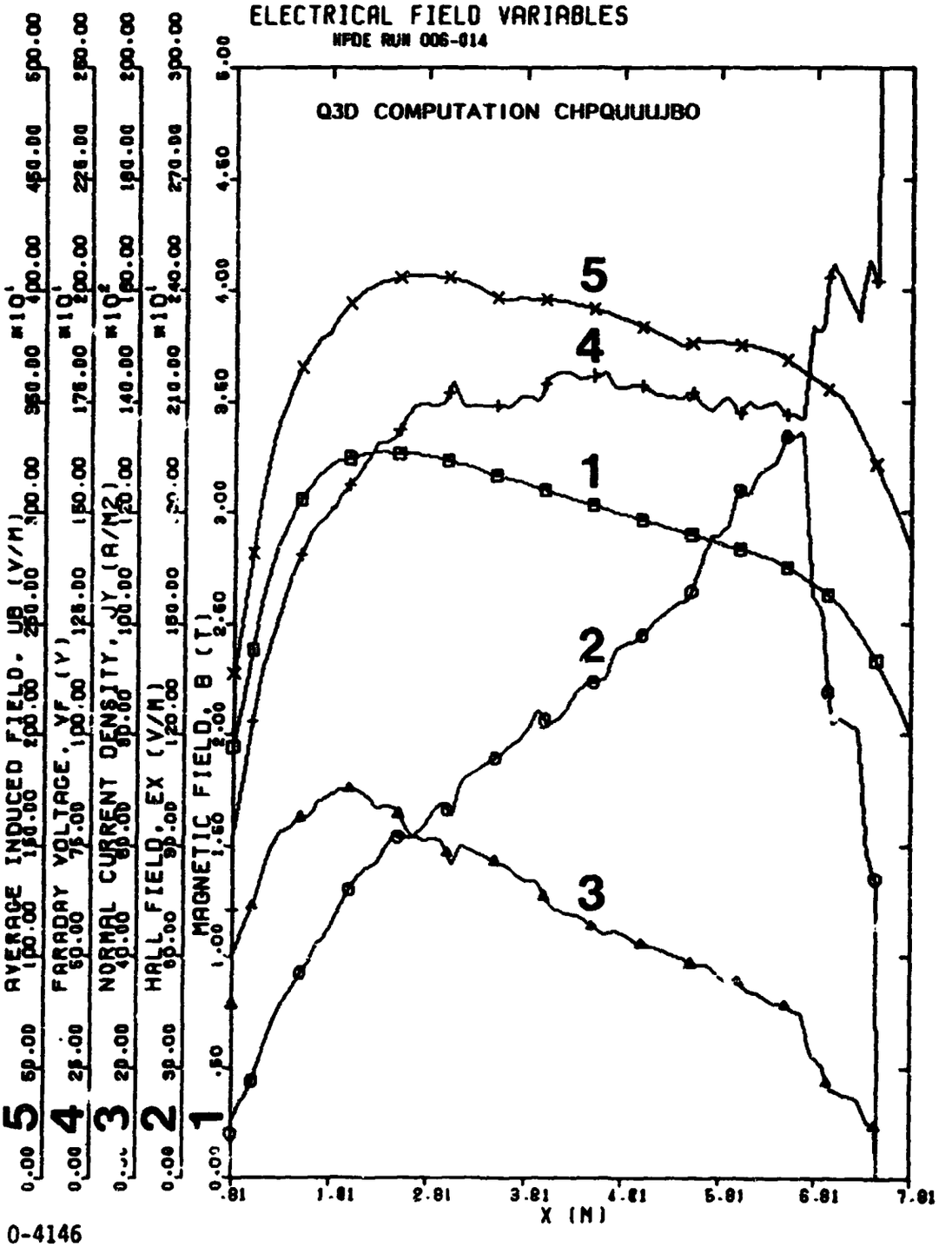

0-4146

Fig. 3-87. Electrical field variables HPDE Run 006-014

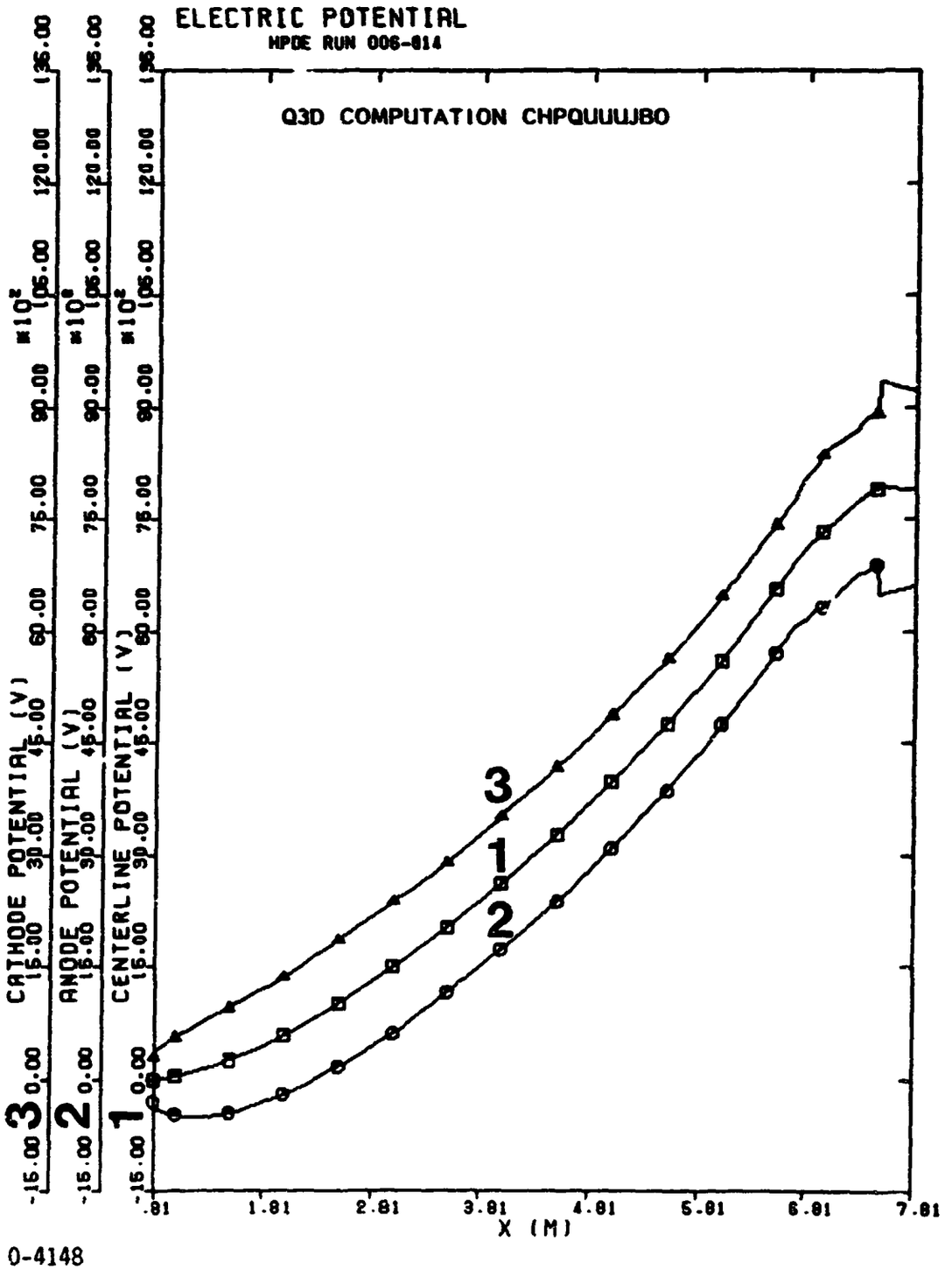

Fig. 3-88. Electric potential HPDE Run 006-014

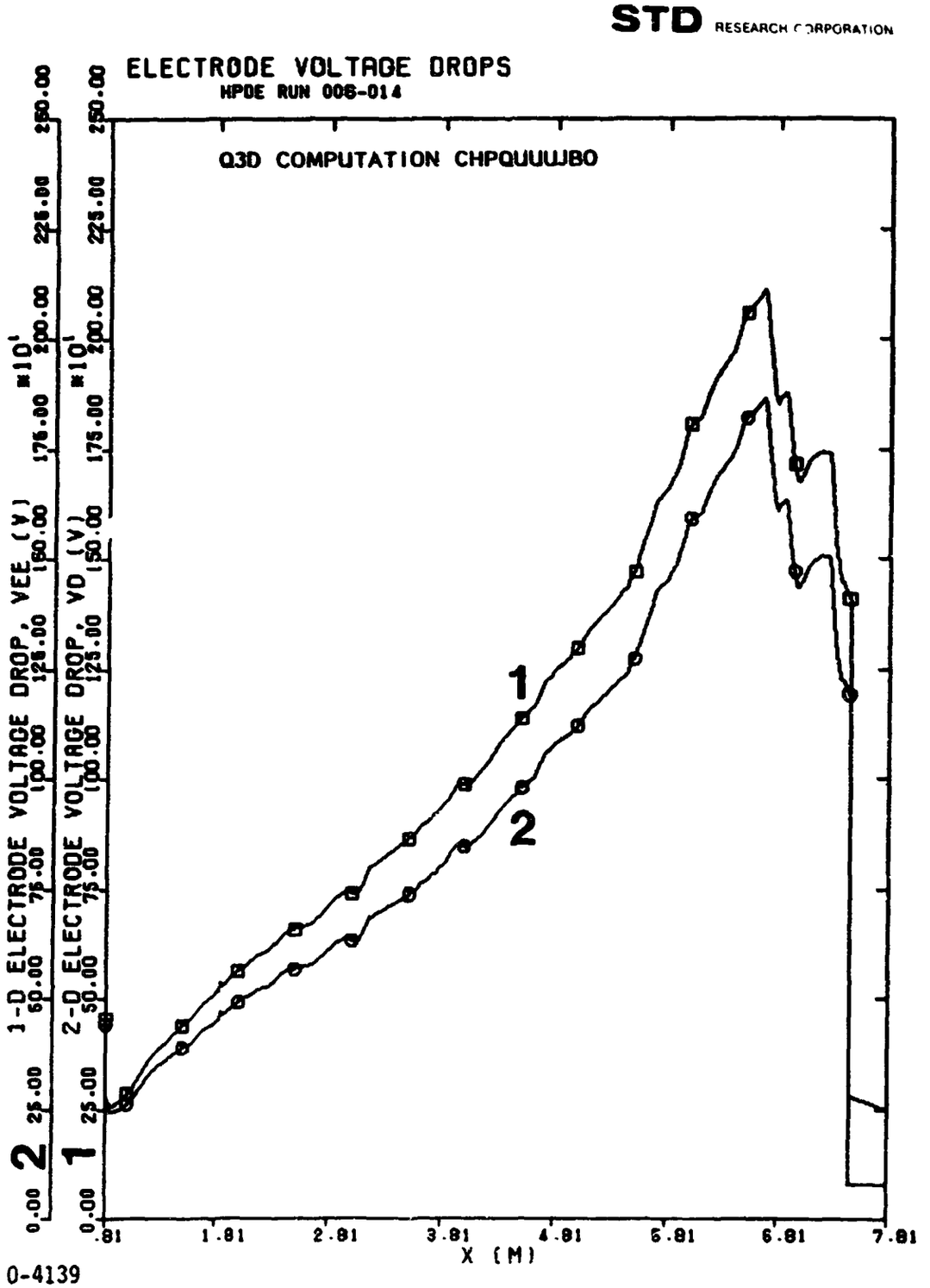

Fig. 3-89 . Electrode voltage drops HPDE Run 006-014

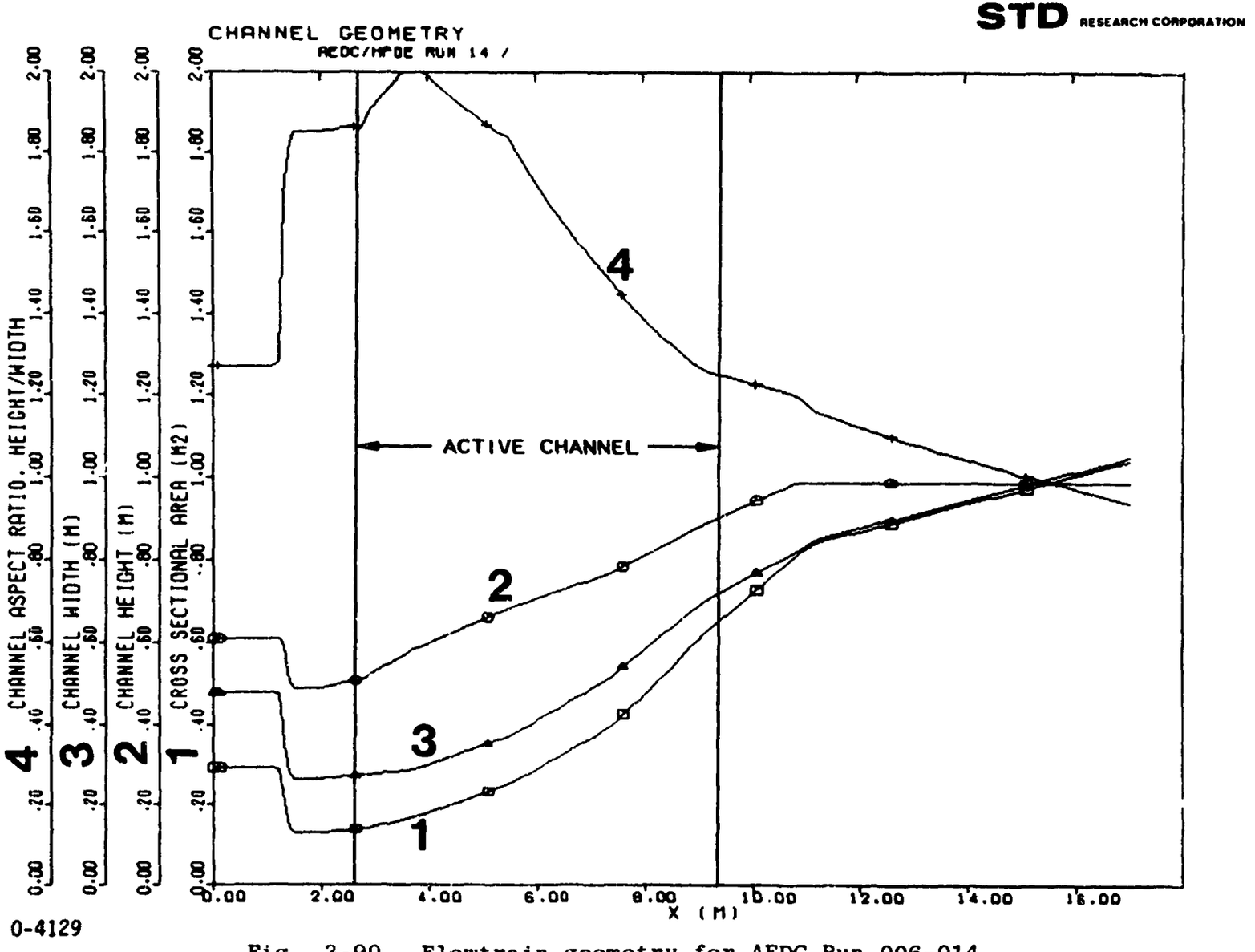

Fig. 3-90 . Flowtrain geometry for AEDC Run 006-014

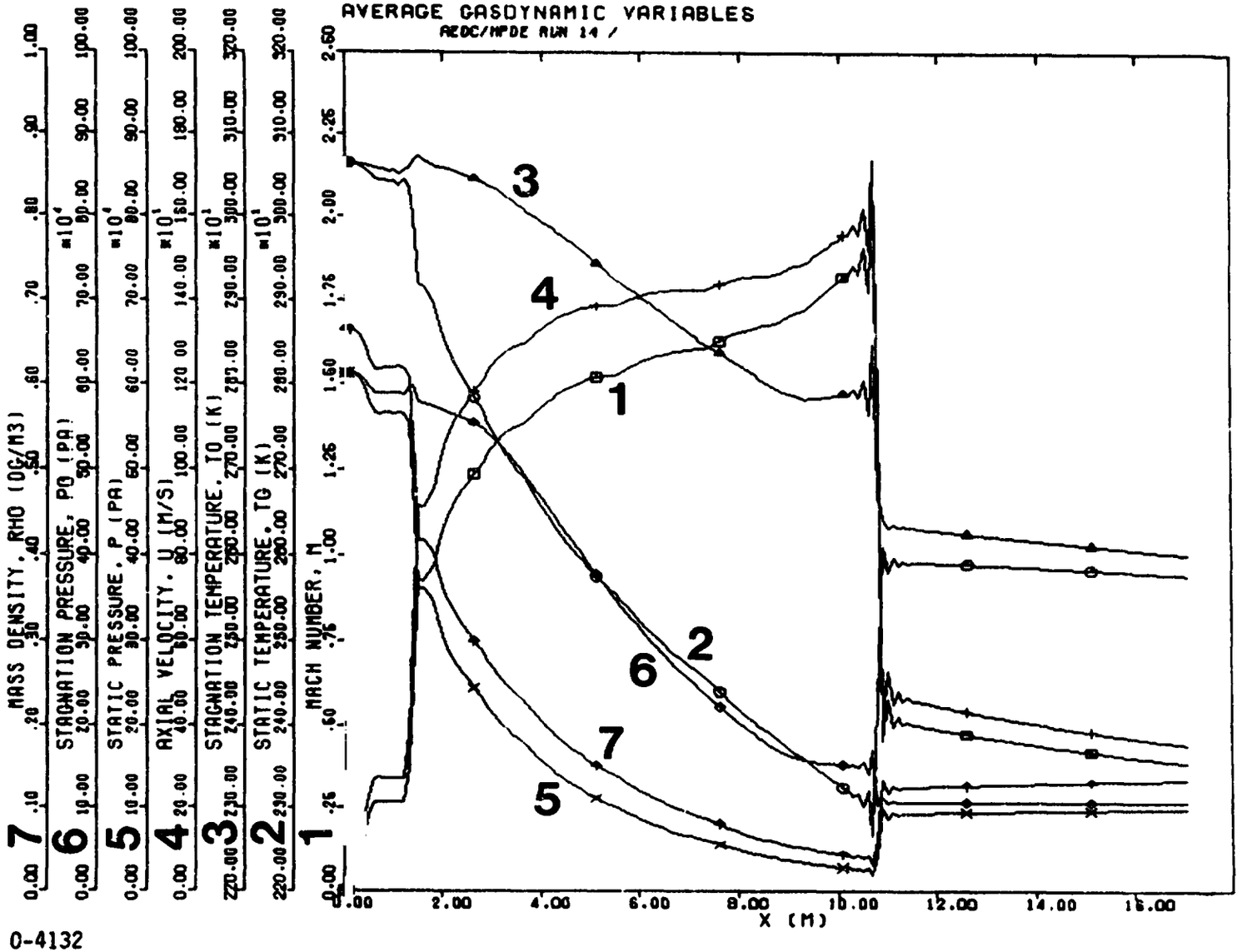

0-4132

Fig. 3-91. Axial distribution of average gasdynamic variables for AEDC Run 006-014

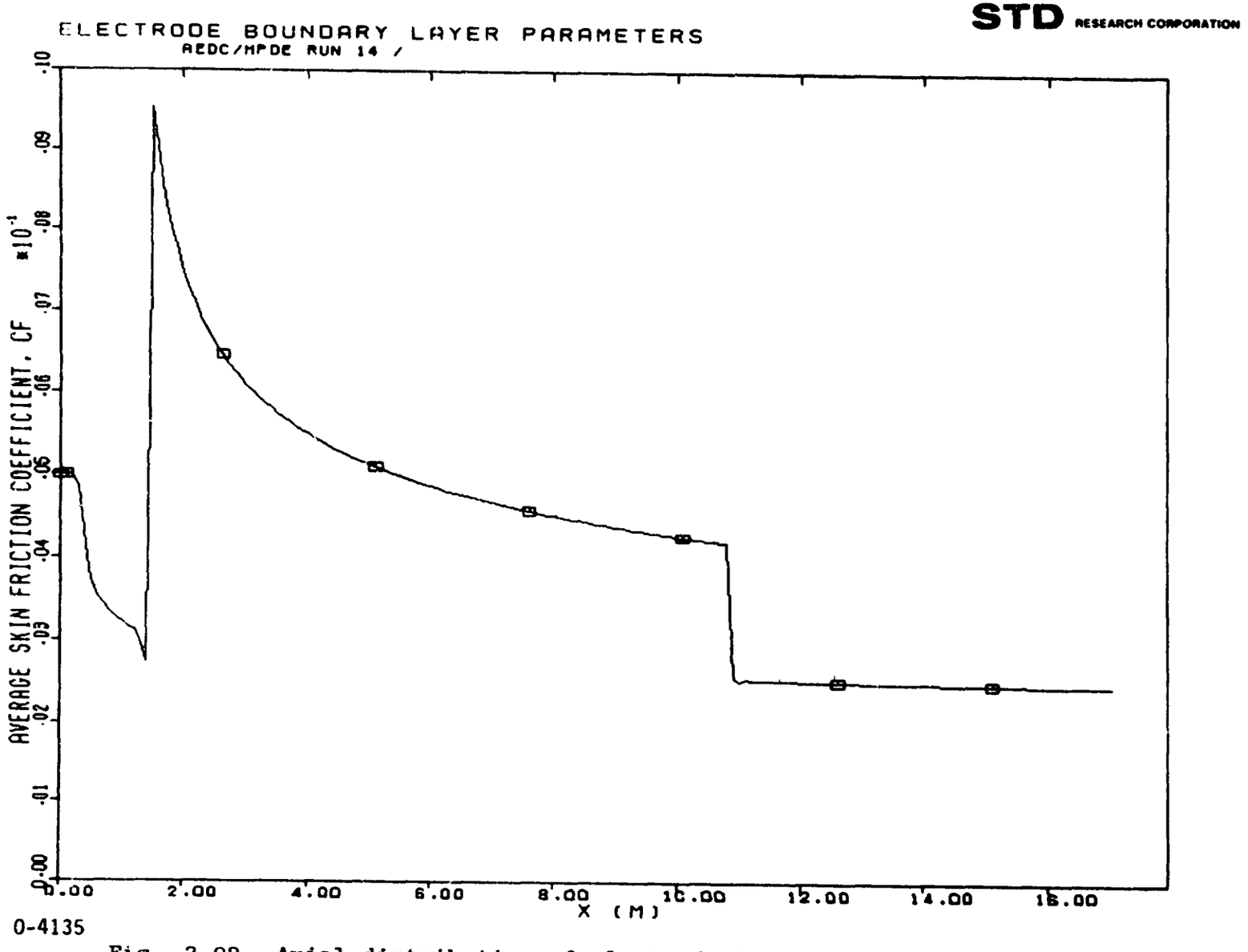

Fig. 3-92. Axial distribution of electrode boundary layer parameters for AEDC Run 006-014

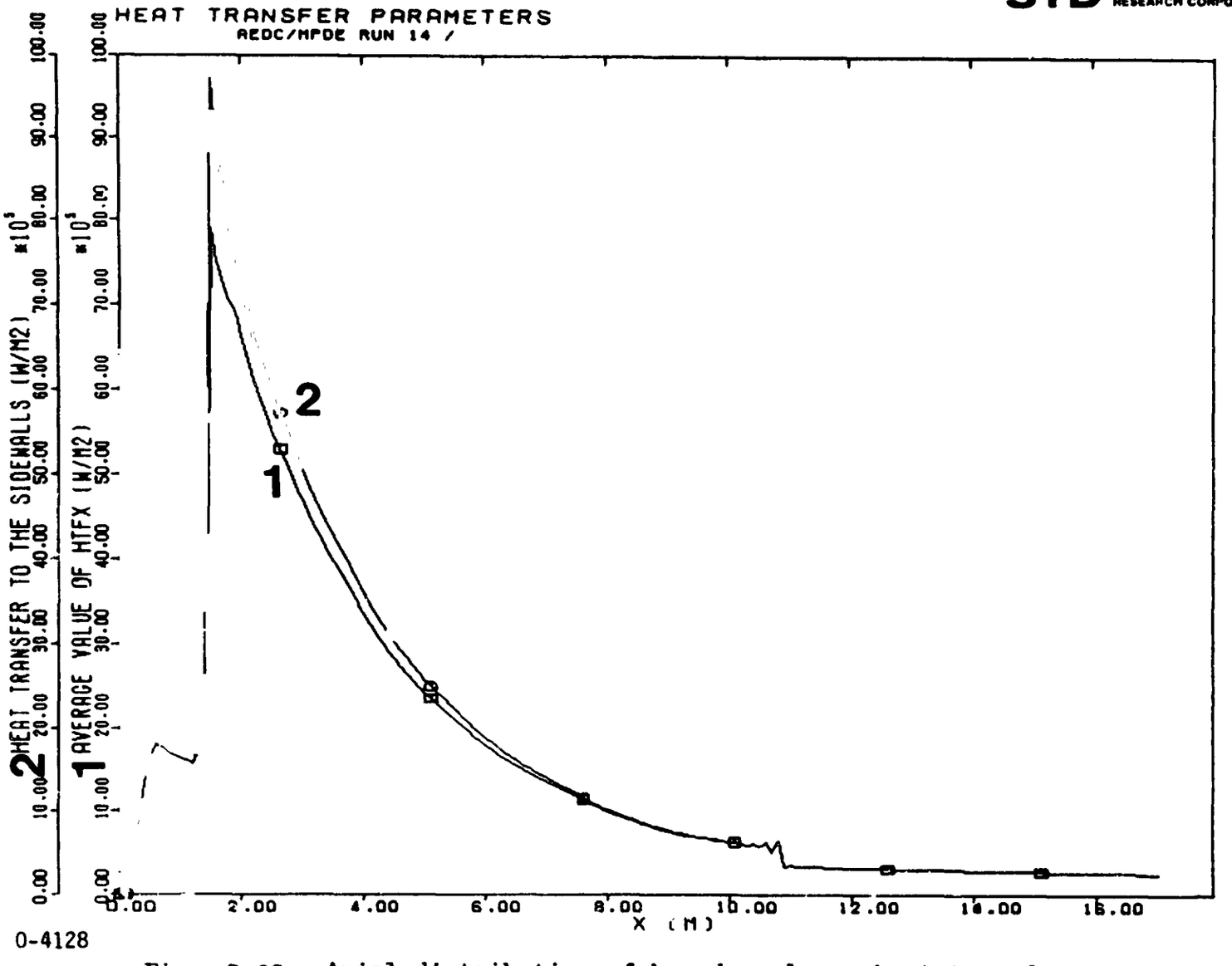

Fig. 3-93. Axial distribution of boundary layer heat transfer parameters for AEDC Run 006-014

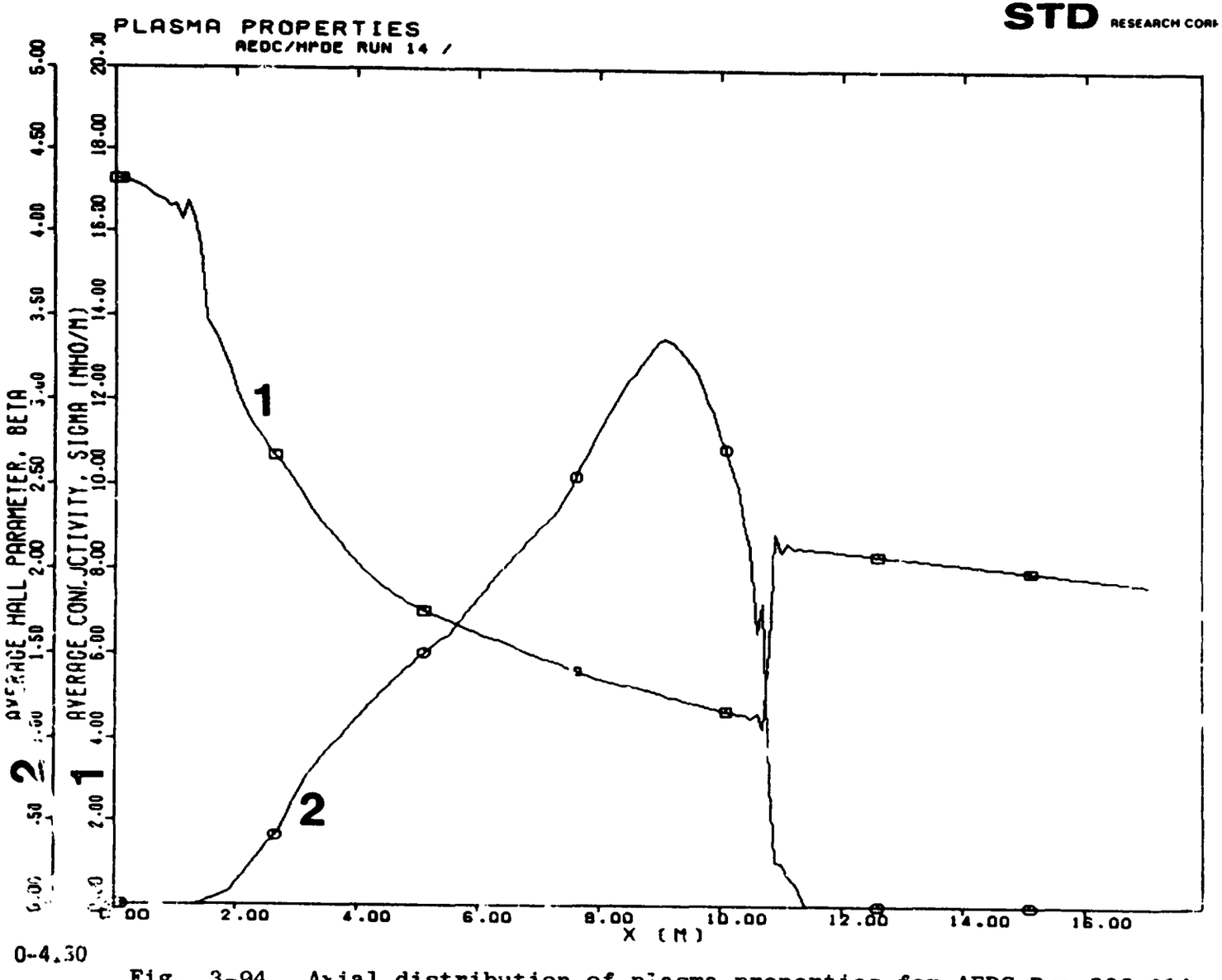

Fig. 3-94. Axial distribution of plasma properties for AEDC Run 006-014

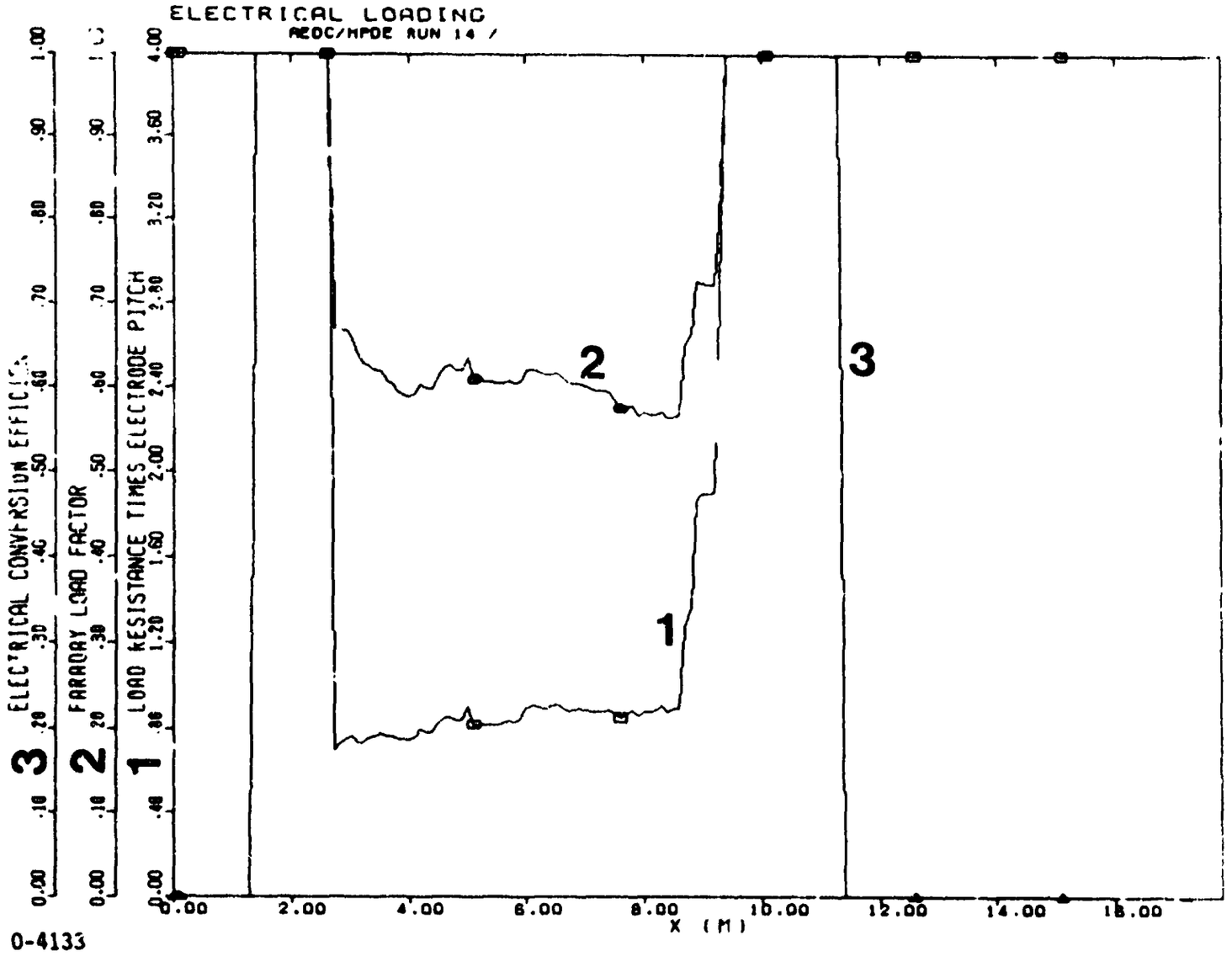

Fig. 3-95. Axial distribution of electrical loading for AEDC Run 006-014

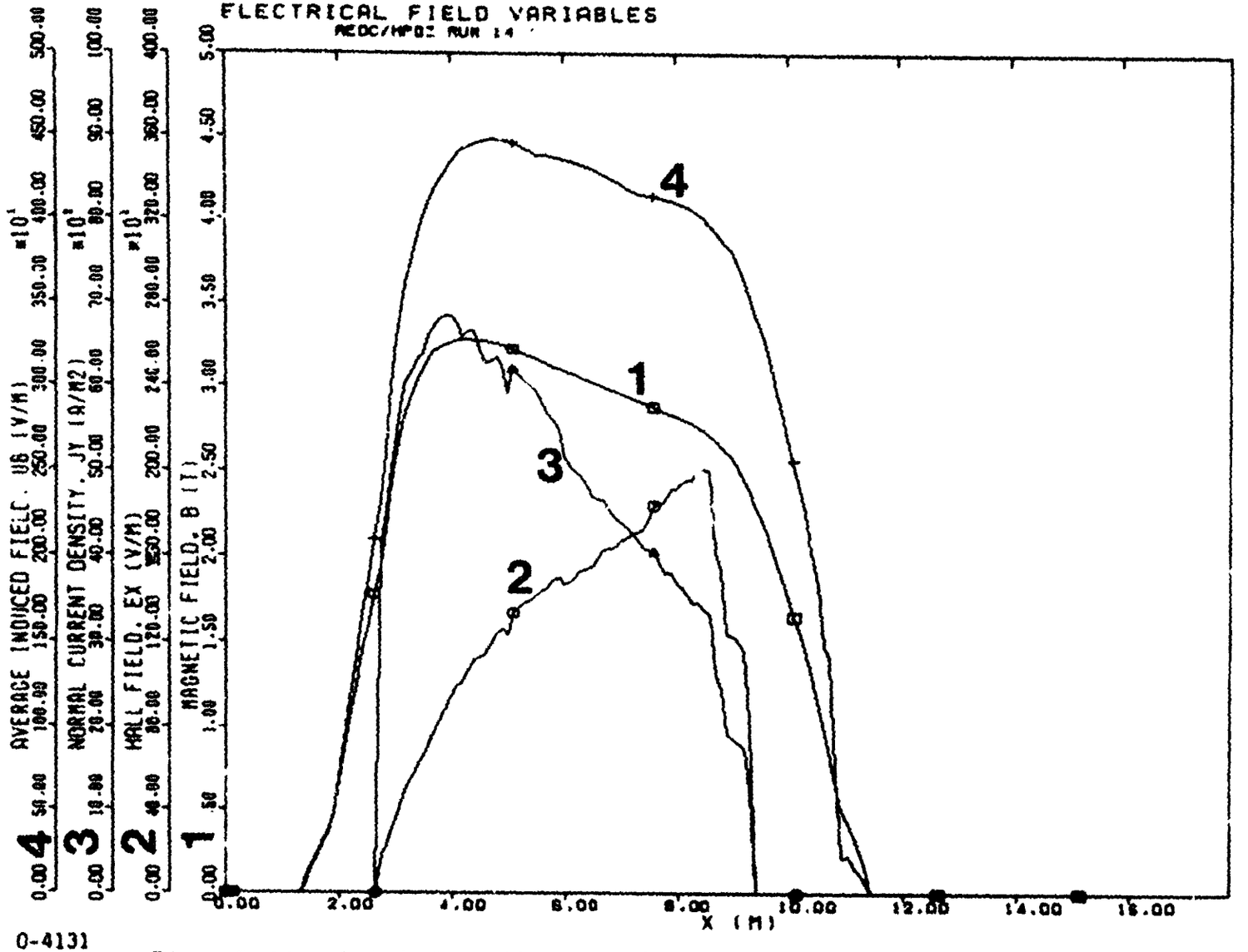

Fig. 3-96. Axial distribution of electrical field variables for AEDC Run 006-014

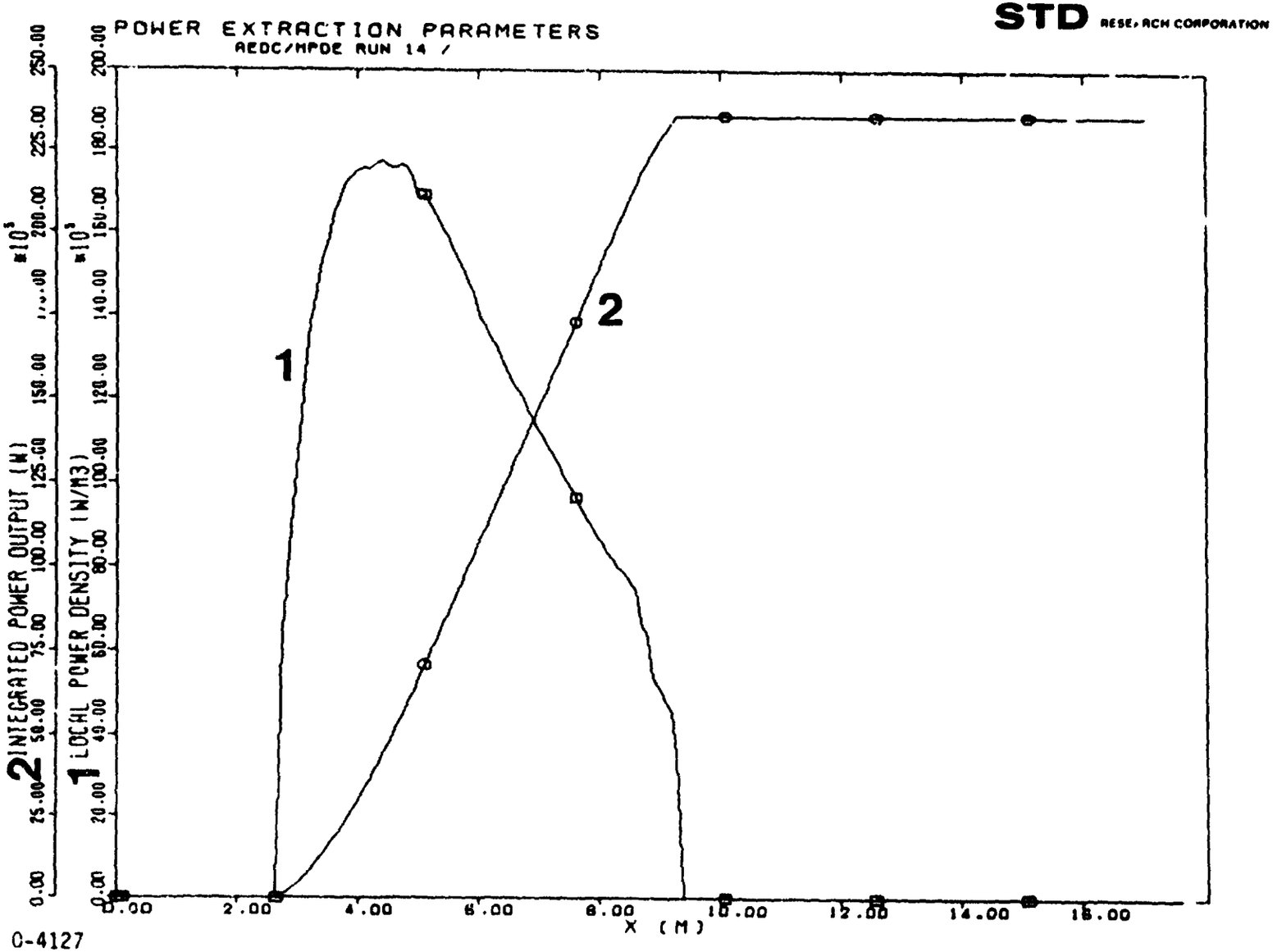

Fig. 3-97 . Axial distribution of power extraction parameters for AEDC Run 006-014

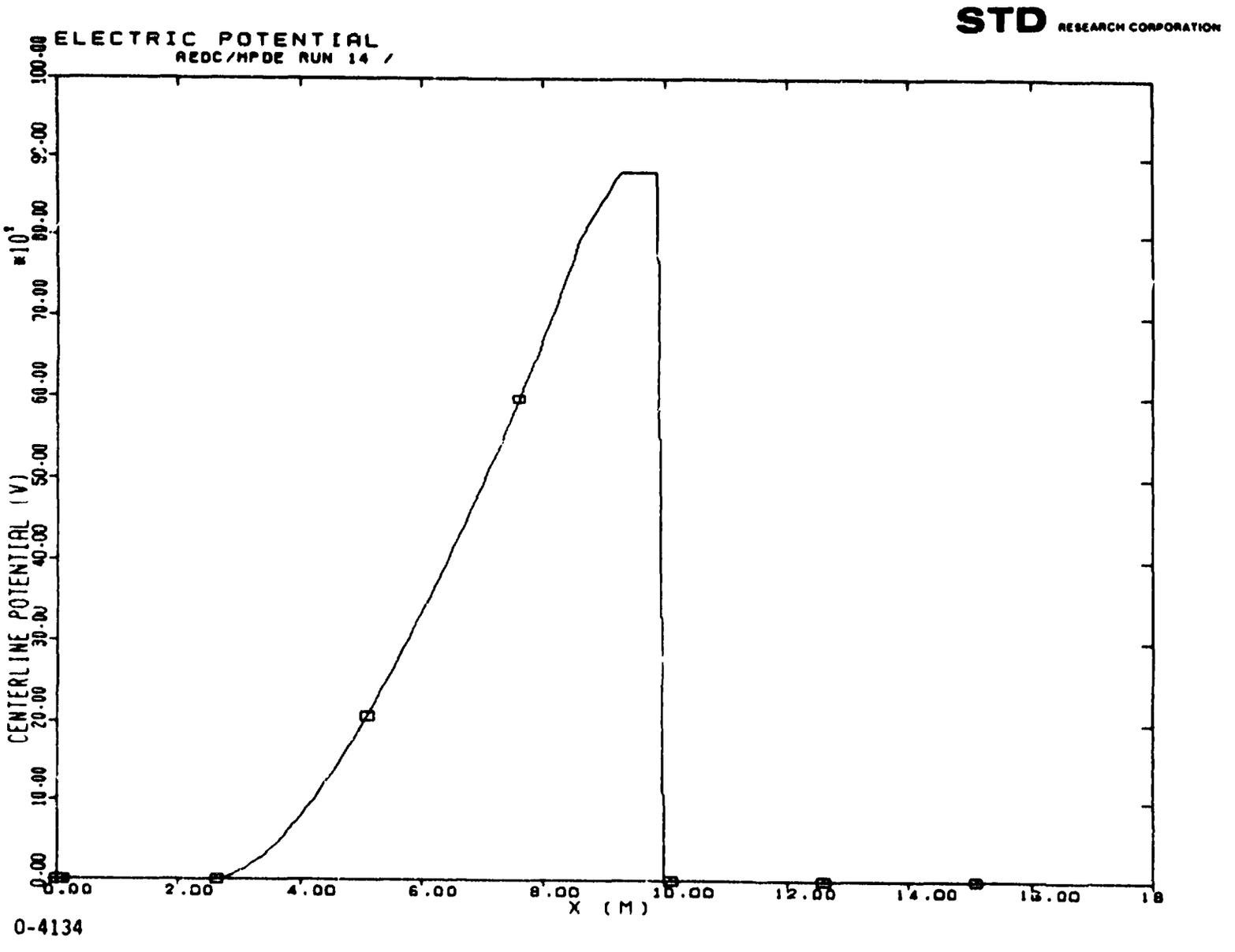

Fig. 3-98. Axial distribution of electric potential for AEDC Run 006-014

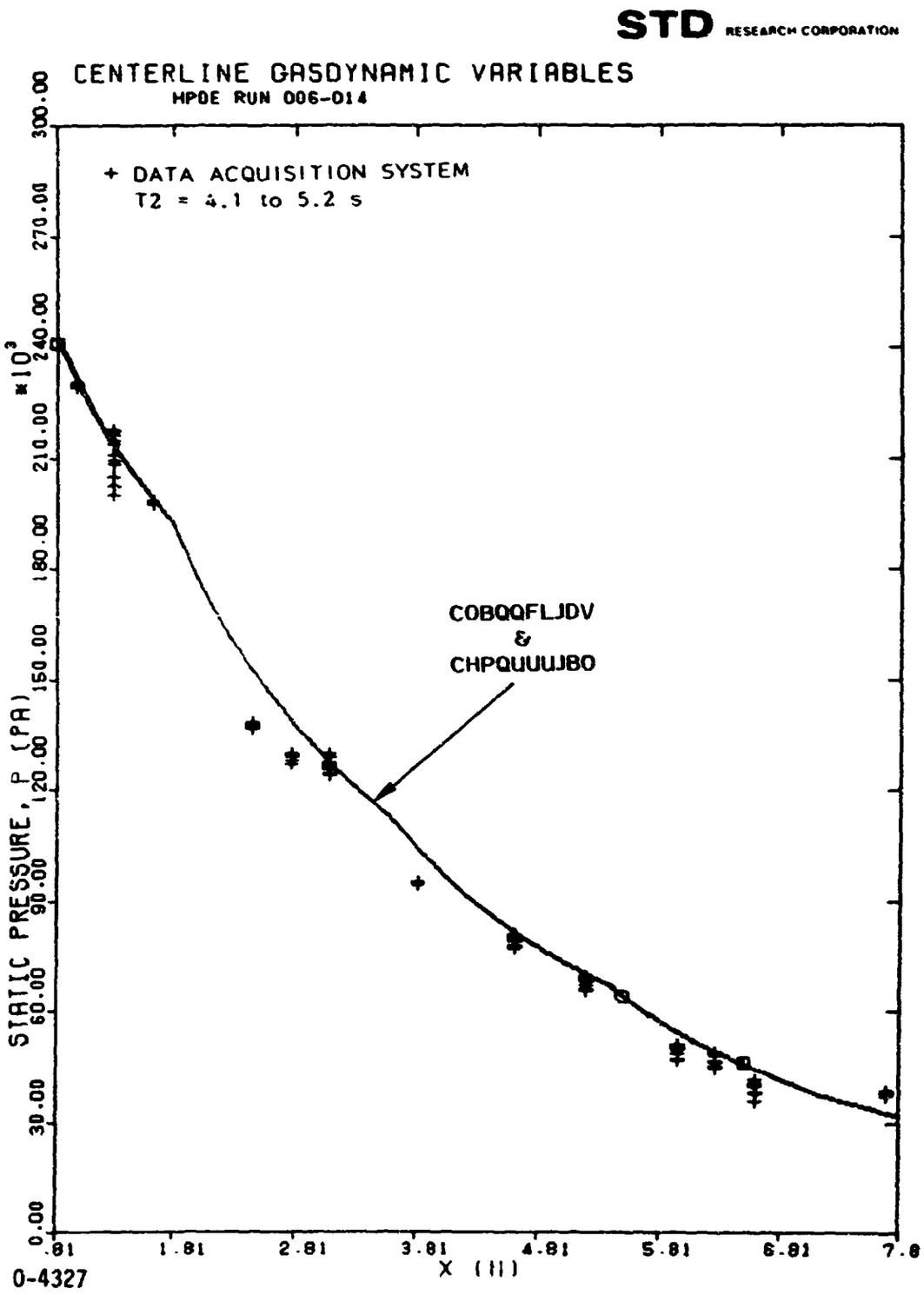

Fig. 3-99. Comparison of the axial distributions of static pressure from the data acquisition system and STD simulations of HPDE Run 006-014.

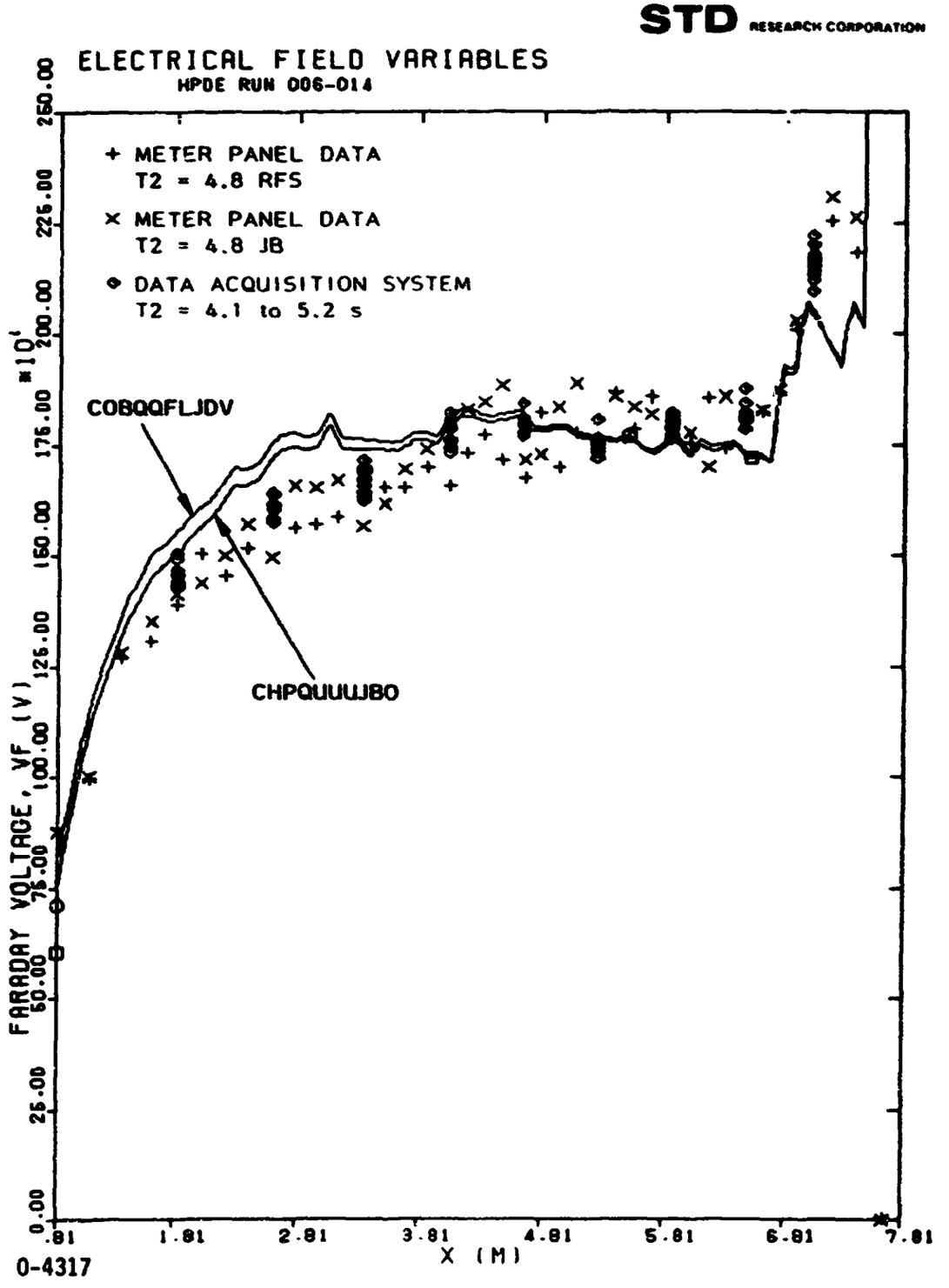

Fig. 3-100. Comparison of the axial distributions of Faraday voltage from the experimental data and from STD simulations of HPDE Run 006-014.

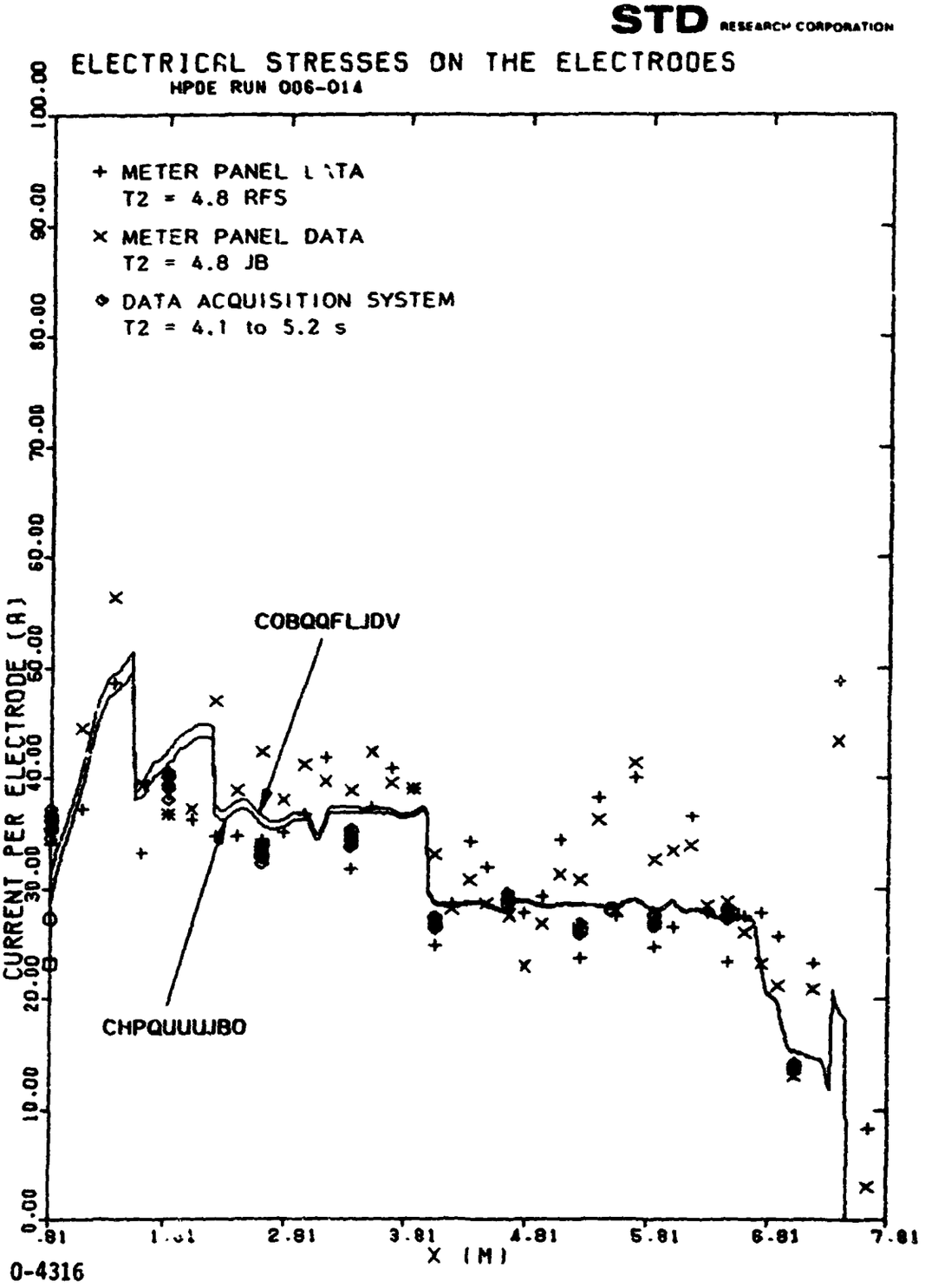

Fig. 3-101. Comparison of the axial distributions of current per electrode from the experimental data and STD simulations of HPDE Run 006-014.

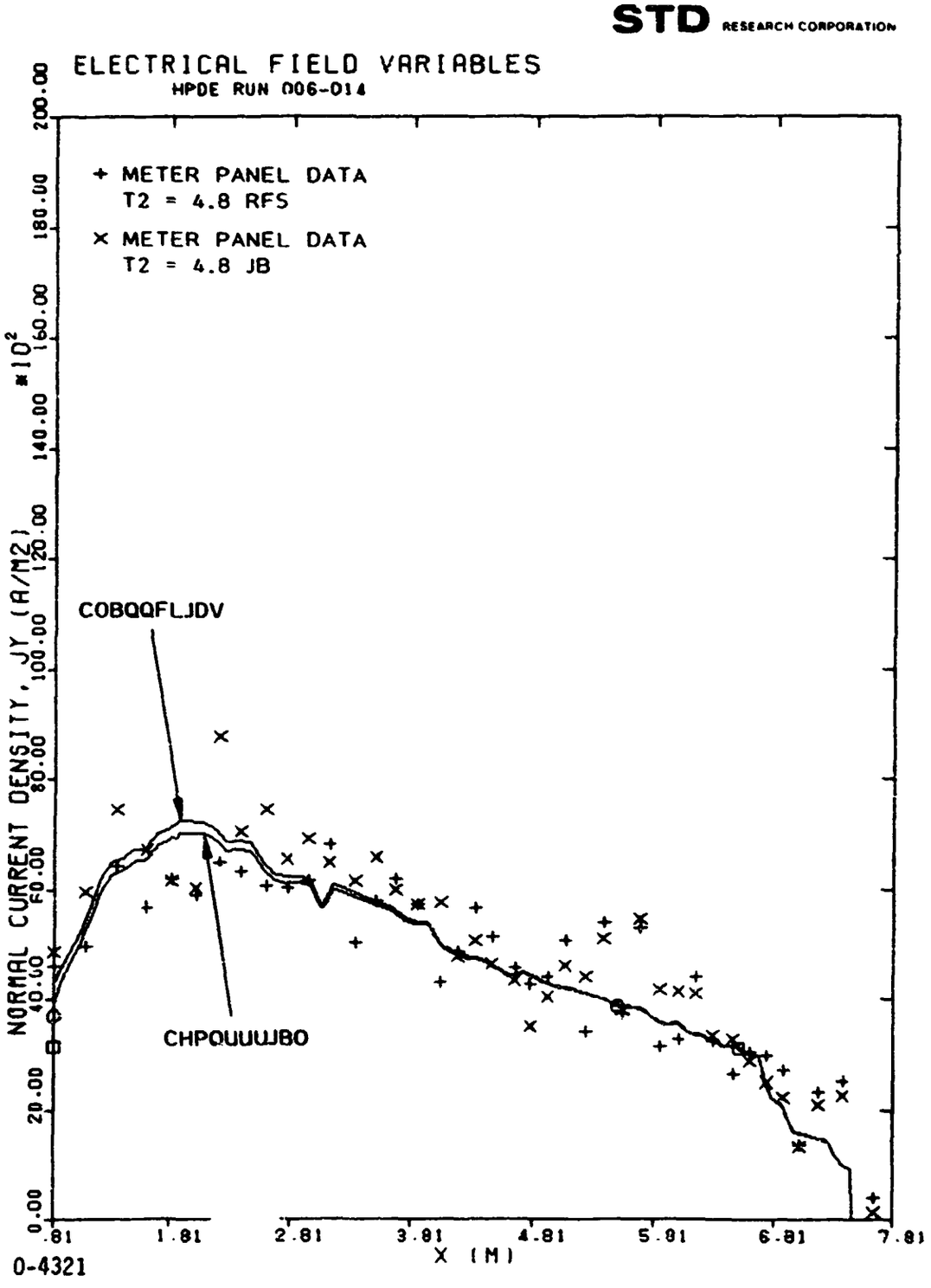

Fig. 3-102. Comparison of the axial distributions of normal current density from the experimental data and STD simulations of HPDE Run 006-014.

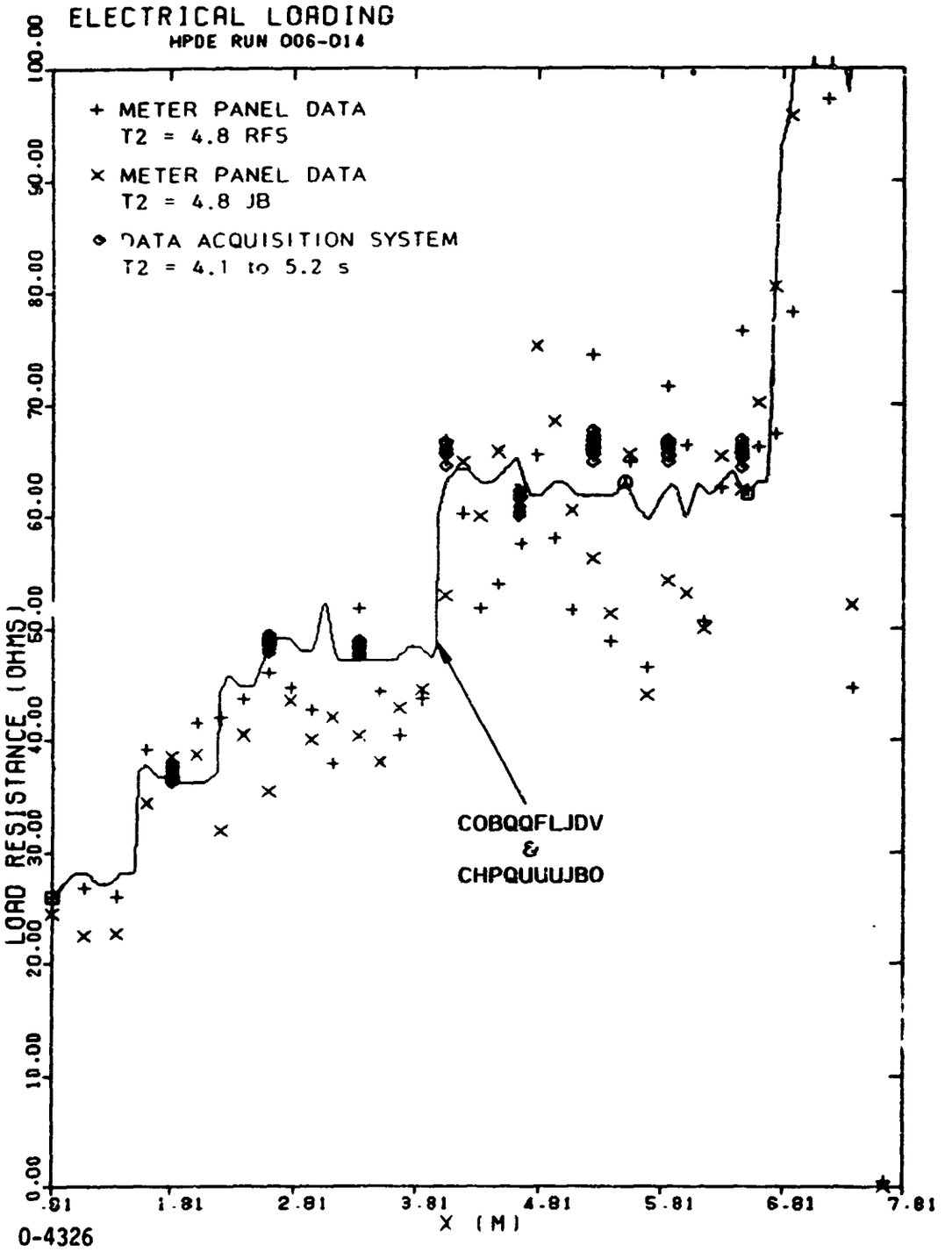

Fig. 3-103. Comparison of the axial distributions of load resistance from the experimental data and STD simulations of HPDE Run 006-014.

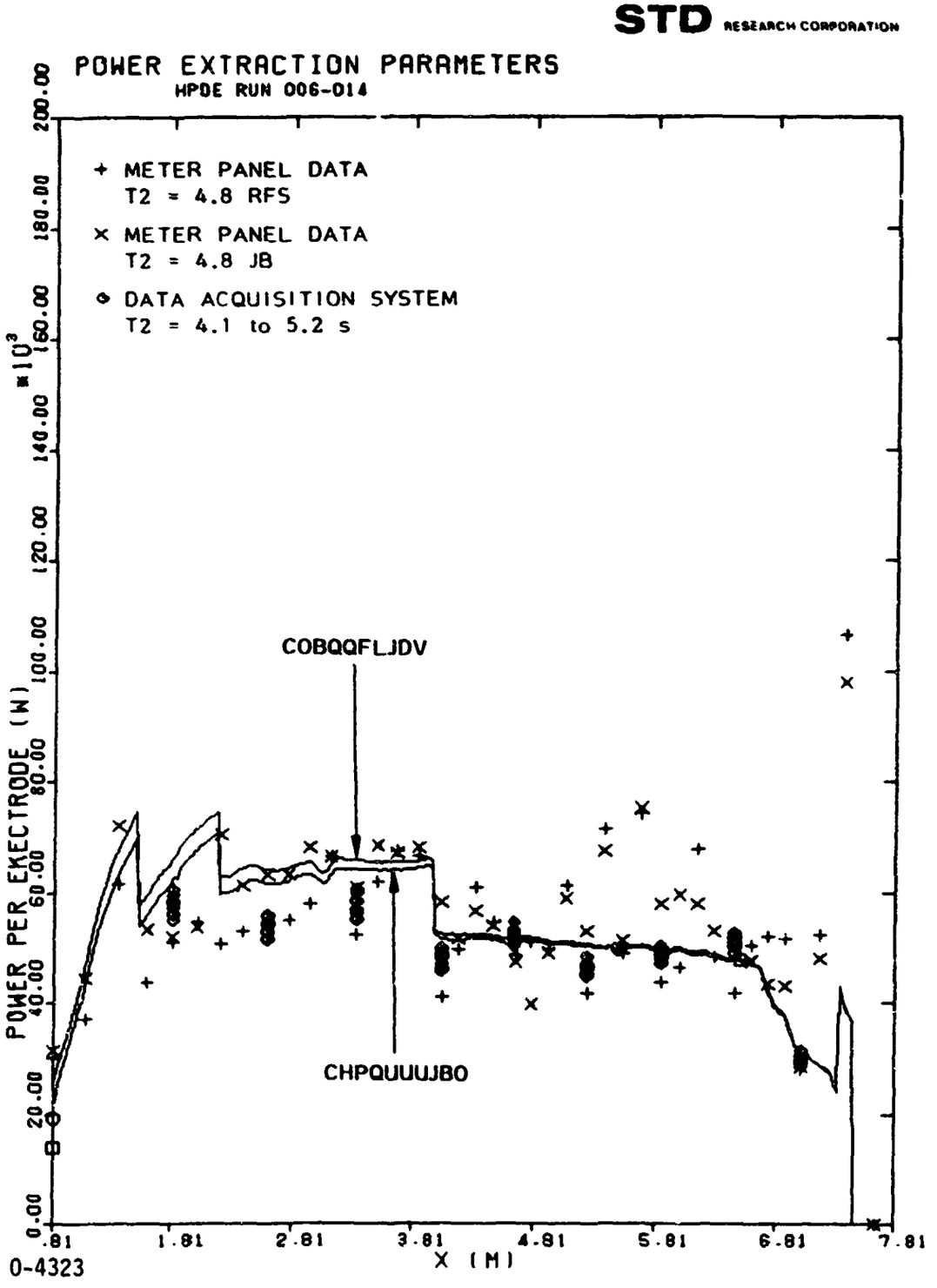

Fig. 3-104. Comparison of the axial distributions of power per electrode from the experimental data and STD simulations of HPDE Run 006-014.

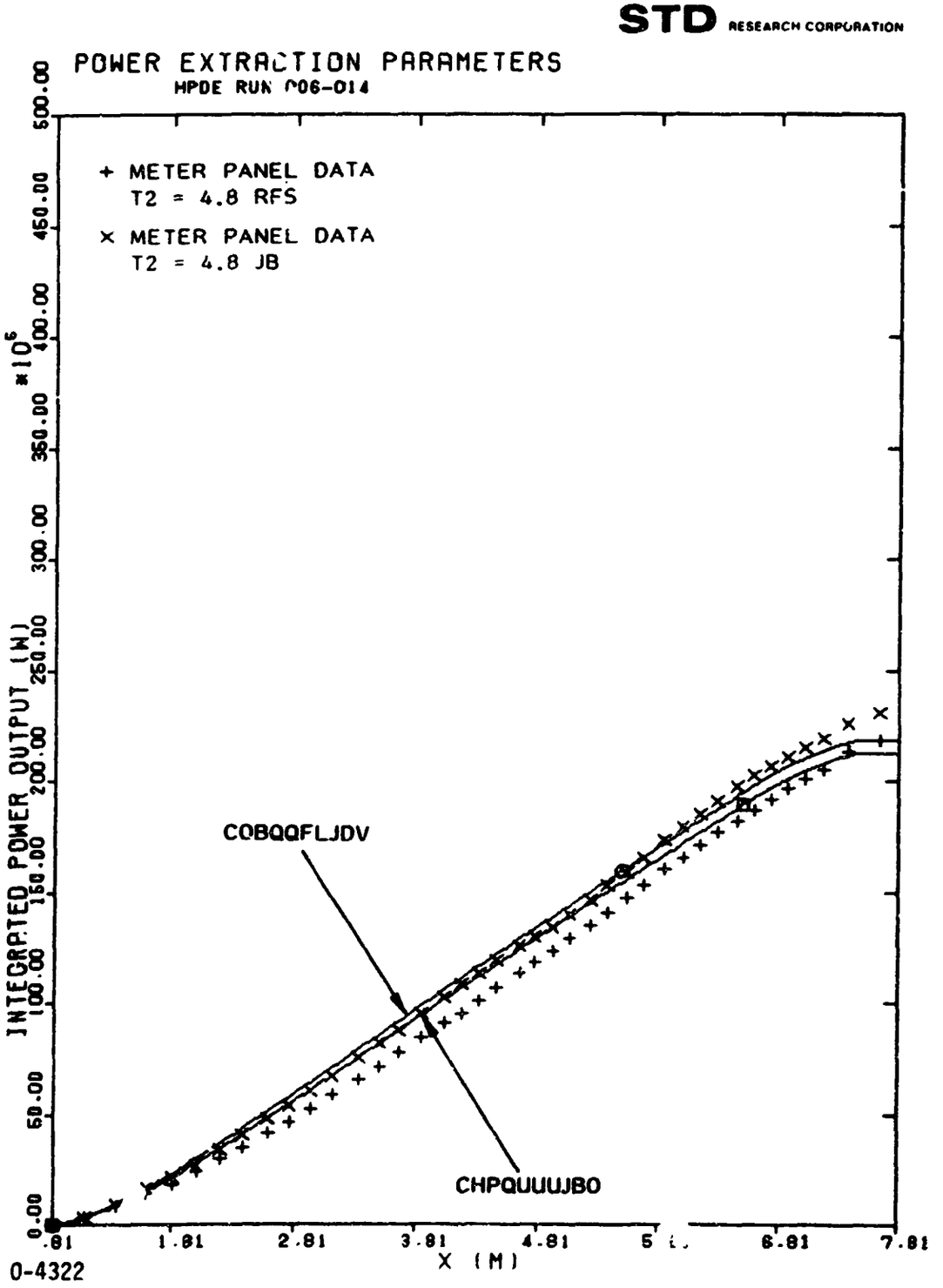

Fig. 3-105. Comparison of the axial distributions of integrated power output from the experimental data and STD simulations of HPDE Run 006-014.

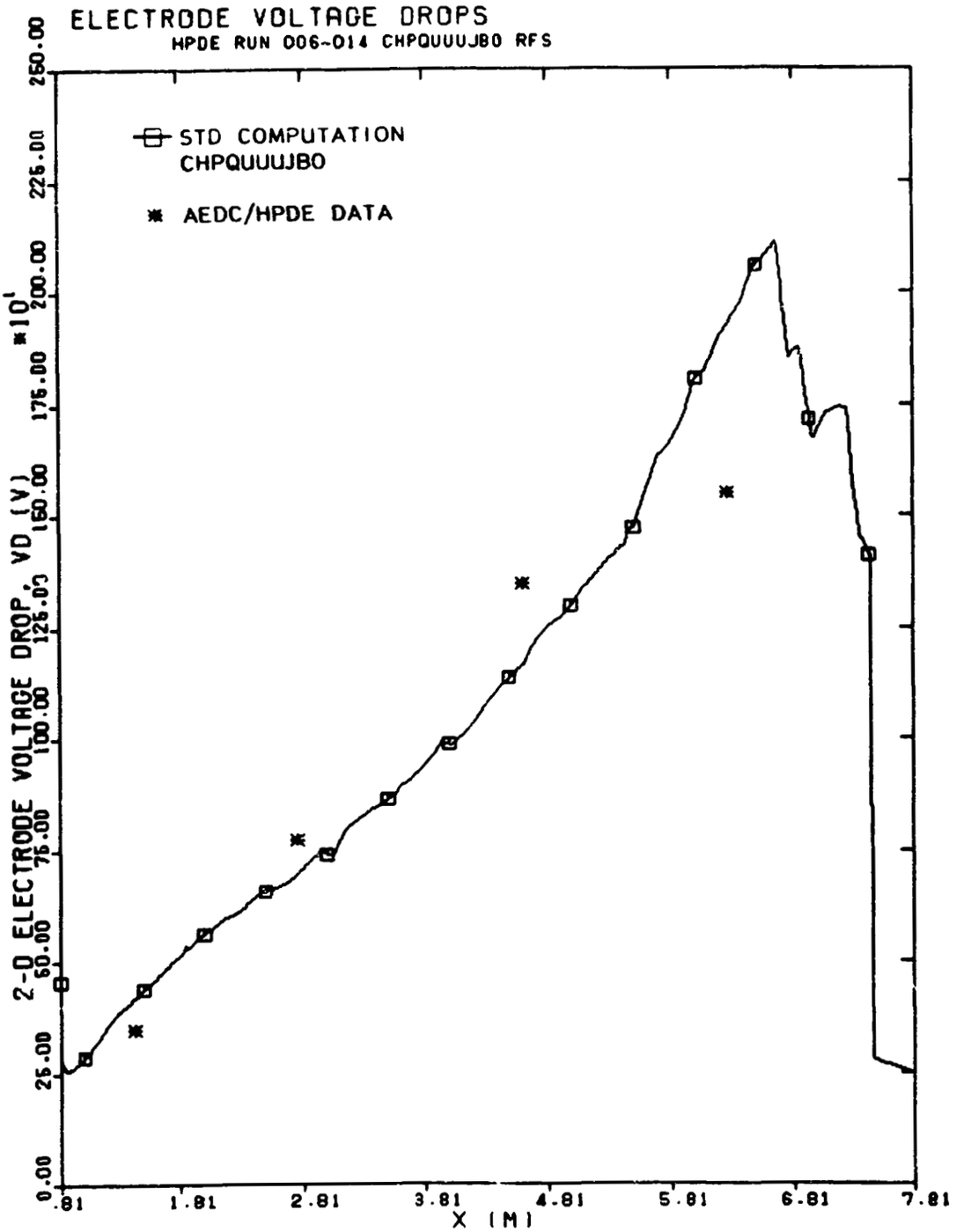

Fig. 3-106. Comparison of the axial distributions of 2-D electrode voltage drop VD(V) for HPDE run 006-014.

0-3616

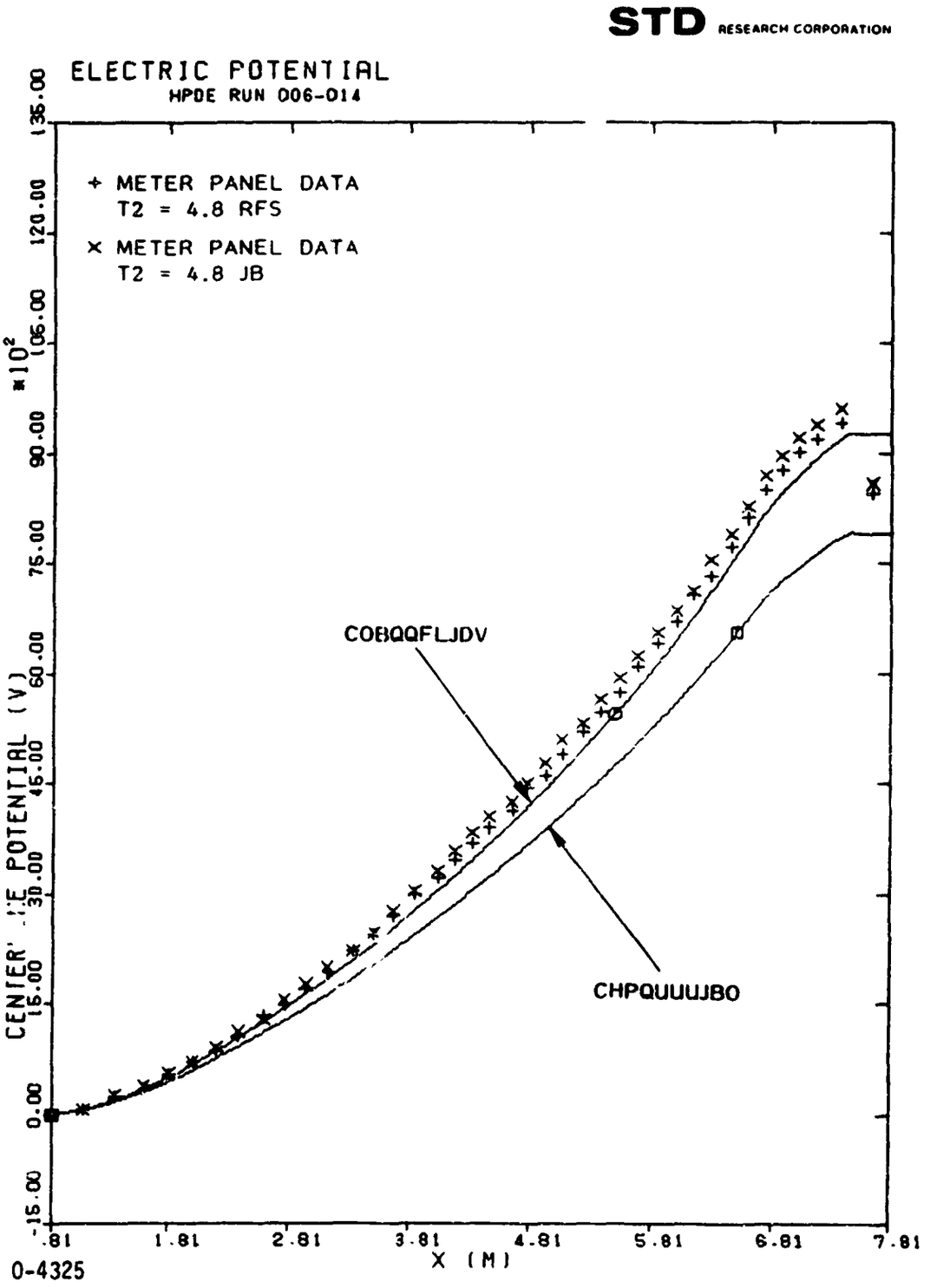

Fig. 3-107. Comparison of the axial distributions of centerline potential from the experimental data and STD simulations of HPDE Run 006-014.

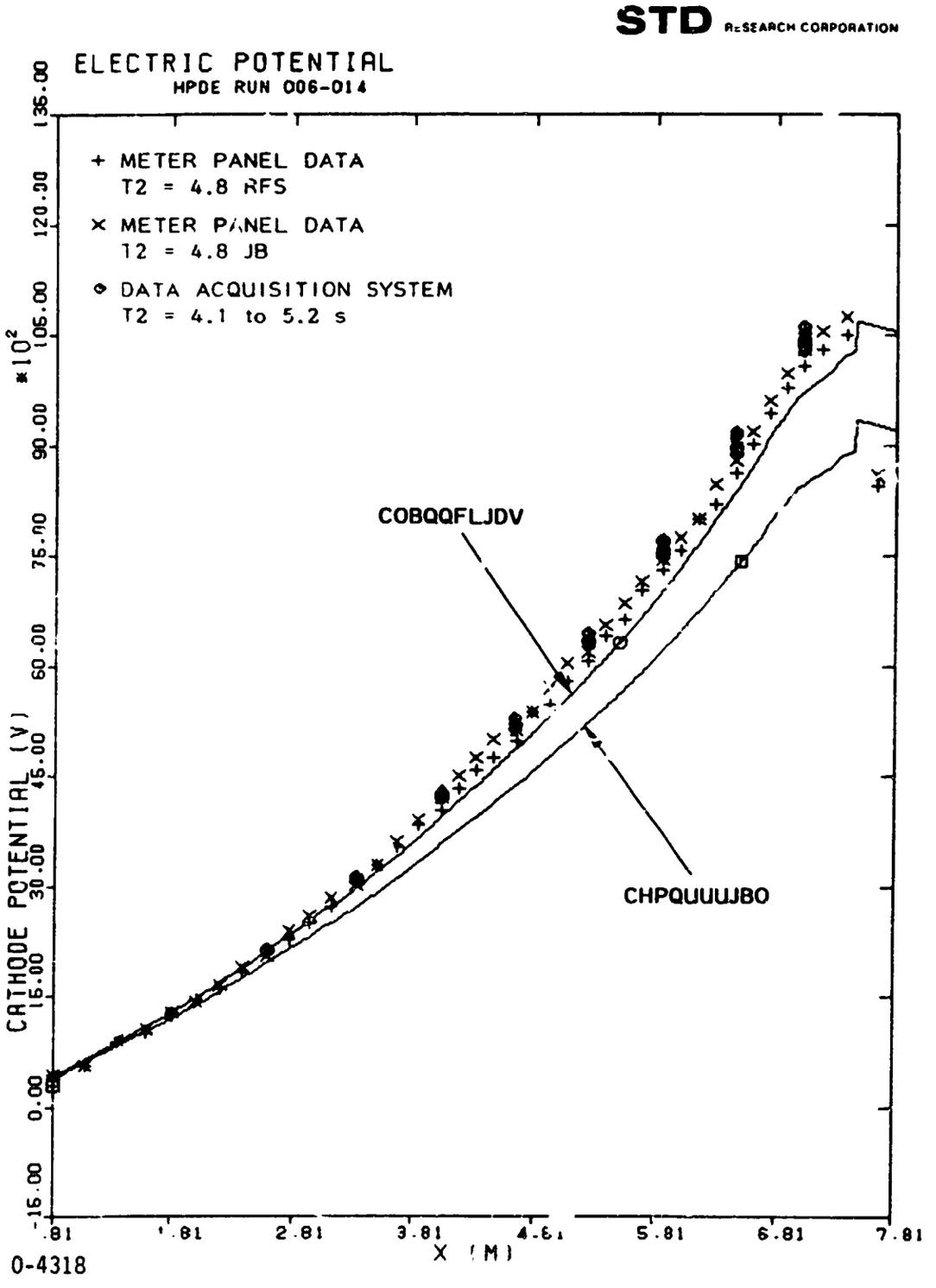

Fig. 3-108. Comparison of the axial distributions of cathode (STD ion) potential from the experimental data and STD simulations of HPDE Run 006-014.

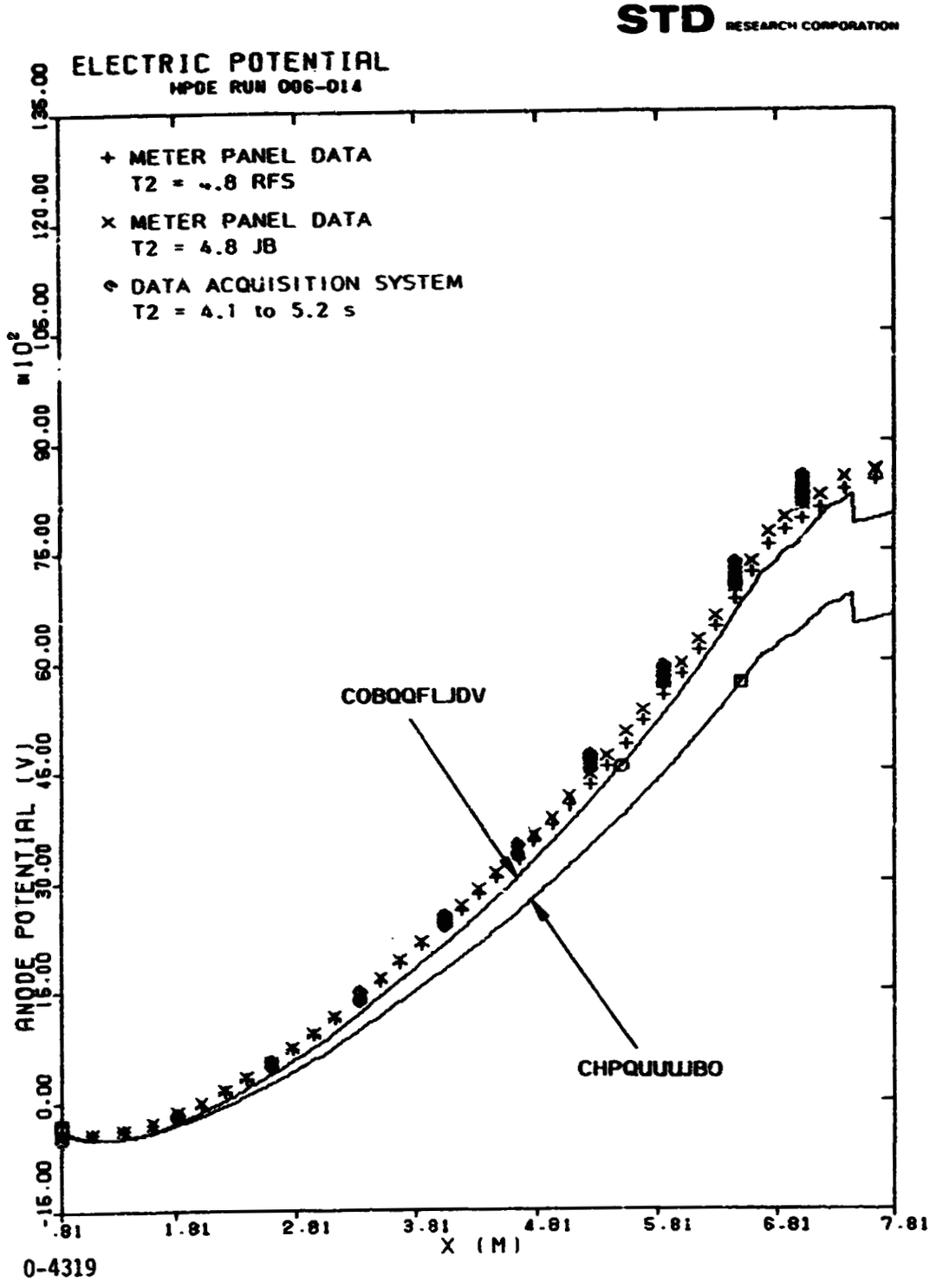

Fig. 3-109. Comparison of the axial distributions of anode (STD notation) potential from the experimental data and STD simulations of HPDE Run 006-014.

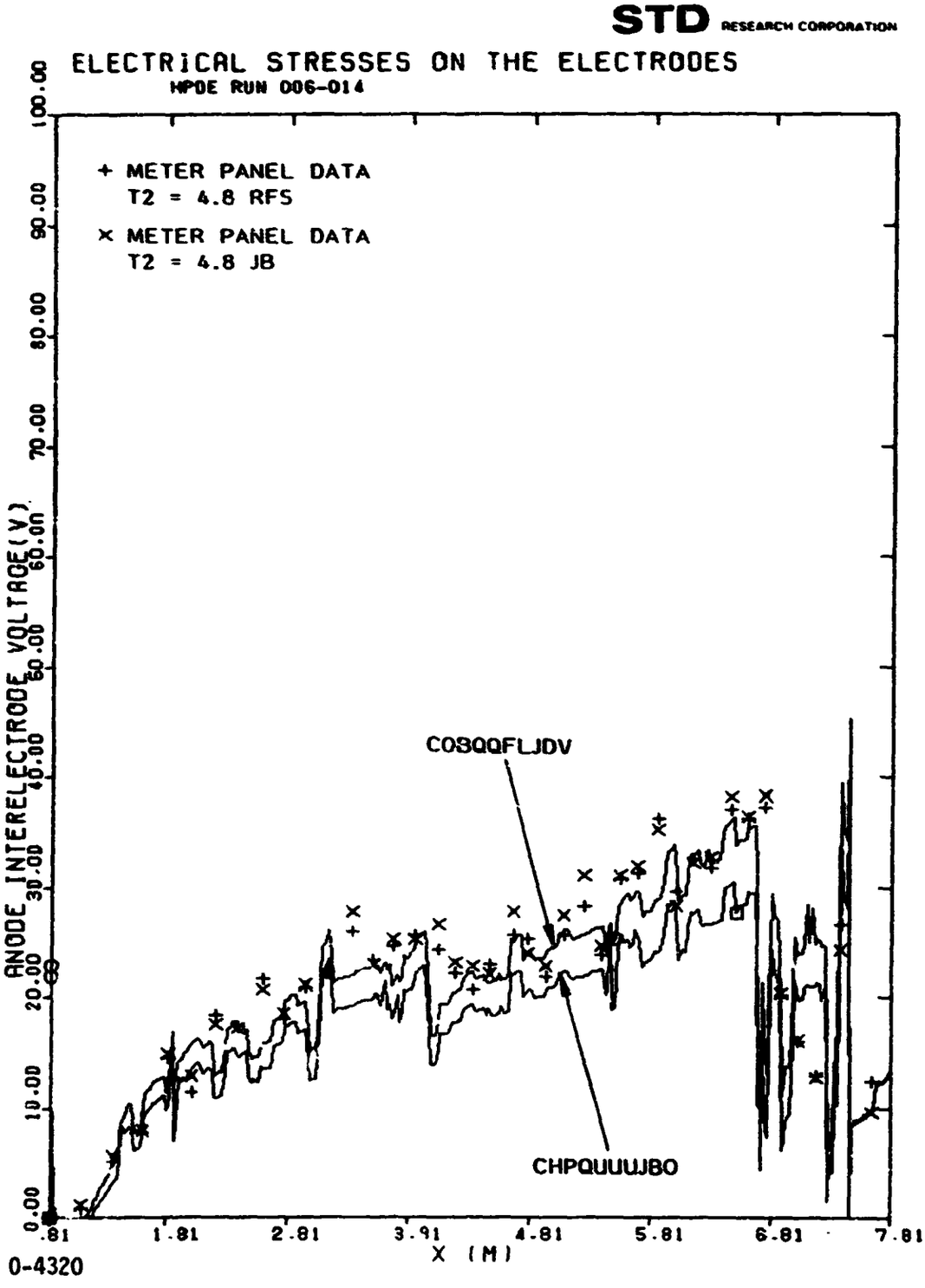

Fig. 3-110. Comparison of the axial distributions of anode interelectrode voltage from the experimental data and STD simulations of HPDE Run 006-014. Experimental data represent averages over 10 electrodes.

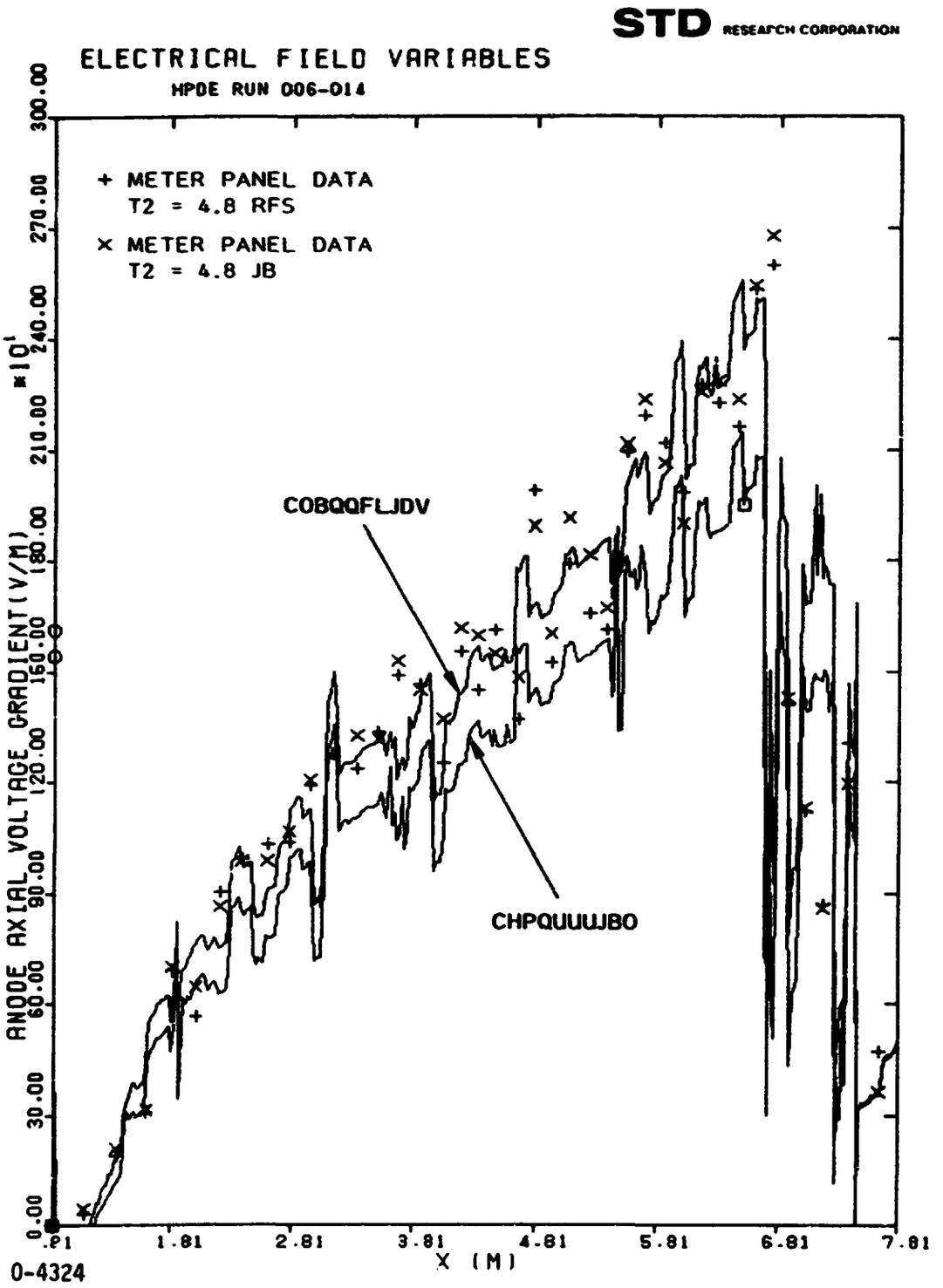

Fig. 3-111. Comparison of the axial distributions of the Anode Hall field from the experimental data and STD simulations of HPDE Run 006-014. Expermiental data represents averages over 10 electrodes.

4.0 CRITICAL PHENOMENA IN THE AEDC/HPDE

The experimental results of the AEDC/HPDE to date reveal the importance of a number of performance-controlling mechanisms in large-scale, high-interaction MHD power generators. Among these are boundary layer voltage drops and plasma nonuniformity, near-electrode phenomena including finite electrode effects, end effects, and the effects of various operating parameters on the optimization of the HPDE performance. This section is devoted primarily to the elucidation of these effects through comparisons with and parametric variations from the experimental operating conditions of HPDE Run 006-014.

4.1 PARAMETRIC VARIATIONS AROUND THE Q3D SIMULATION OF RUN 006-014

The successful completion of the Run 006-014 simulations gives an opportunity to exploit the computer models to predict performance in other operating regimes. Using the results of the detailed Q3D simulation of HPDE Run 006-014 described in Section 3.7 as a starting point, single-parameter variations in wall temperature, load factor, N/O ratio, mass flow rate, and magnetic field have been carried out. These computations demonstrate the sensitivity of HPDE performance to most of the operating conditions under the control of the experimentalists.

Fig. 4-1 presents the results of the parametric computations. All of the computations represented in Fig. 4-1 are variations from computation CHPQUUUJBO, which is the nominal, simulation of HPDE Run 006-014. The Faraday load

factor distribution was altered to a constant value of 0.55 (computation COBQFRQJEA), 0.60 (computation COBQAVWJDY), and 0.70 (computation COBQBGDJDY . The electrode wall surface temperatures were increased to a constant value of 1250 K (computation COPQRPHJBJ), to a constant value of 1500 K (computation COBQJQKJDY), and to a constant value of 1750 K (computation COBQDTBJD1). Also shown is computation COBQAIYJE1, in which the electrode wall surface temperatures were assumed to rise to "20-sec" values, which were determined by the same method applied to obtain the "5-sec" values of the nominal simulations. The peak magnetic field strength was increased to 4.02 T (computation COBQLRNJDZ) and to 4.28 T (computation COBQIJOJEA). The N/O ratio was decreased to 0.80 (computation COBQMLZJDZ) and increased to 1.00 (computation COBQIFBJEA). In contrast to the other parametric computations, the N/O variations were centered about computation COBQAVWJDY with a constant load factor of 0.60.

These new computations have shown that a constant Faraday load factor of 0.60 yields slightly better performance than the nominal simulation, which has a varying load schedule with an average load factor of approximately 0.61. A constant Faraday load factor of 0.70 yields worse performance. A load factor of 0.55 increases enthalpy extraction at the expense of isentropic efficiency.

As shown in Fig. 4-1, an increase in wall temperature to 1500 K results in higher values for both enthalpy extraction and isentropic efficiency than for the nominal simulation or the simulation with 20 second wall temperatures, but lower values than for 1750 K walls.

An increase in mass flow rate to 55 kg/s results in lower isentropic efficiency and lower enthalpy extraction ratio. While a computation with decreased mass flow rate was not carried out, it is clear that some improvement in the performance would probably be obtained by dropping the mass flow rate under the Run 006-104 conditions. The reason is that a reduction in the mass flow rate would drive the Mach number distribution toward the optimum, which in the case of the AEDC/HPDE appears to be transonic (see Sec. 4.4).

An increase in magnetic field strength (COBQLRNJDZ) results in higher values for both generator isentropic efficiency and enthalpy extraction ratio.

A variation of N/O ratio to 0.80 leads to an increase in enthalpy extraction ratio, but a decrease in isentropic efficiency. The opposite is observed with an increase in N/O ratio to 1.00.

It is important to distinguish the generator isentropic efficiency displayed in Fig. 4-1, which expresses how efficiently the generator made use of the total pressure drop across the generator, with the power train isentropic efficiency, which expresses how efficiently the generator made use of the pressure drop from the combustor to atmosphere. The latter quantity varies almost directly with the enthalpy extraction rate and is perhaps less informative than the generator efficiency. The results in Fig. 4-1 are easily interpreted if this distinction is kept in mind.

The conclusion from this survey is that, at least in the neighborhood of the Run 006-014 operating point, the pay-off from providing hot walls in this experiment is

significant and justifies a change in operating procedures or hardware to achieve elevated electrode surface temperature. It is apparent that increases of the magnetic field and electrode surface temperatures are the primary means of attaining both the enthalpy extraction and isentropic efficiency goals of the HPDE.

There are methods for mitigating the voltage drops, even in cold-wall designs (e.g., load schedule optimization). The sensitivity of the electrode voltage drops to the parameters studied thus far are described in the following section.

4.2 Parametric Dependence of Electrode Voltage Drops and Plasma Uniformity

The Q3D parametric survey of performance around the Run 006-014 conditions provides opportunity to investigate the sensitivity of the electrode voltage drops and the plasma nonuniformity to the important parameters of the experiment. In this section, the wall temperature, magnetic field, and load factor dependence of the total electrode voltage drop and two parameters, which characterize the effects of the plasma uniformity on generator performance, are examined. Before investigating the sensitivity of the total electrode voltage drop and the two nonuniformity factors to these three variables, it is useful to review the importance of the voltage drops and the nonuniformity factors in characterizing the performance of the MHD generator.

The primary importance of the electrode voltage drop is that it is a measurable quantity. The electrode voltage drop is measured by subtracting the Faraday voltage from the total transverse voltage one would obtain by extrapolating the core electric potential gradient all the way to the walls. Clearly, high electrode voltage drops correspond to reduced power production. However, there is not a simple way of relating the magnitude of the electrode voltage drops to the reduction in power output. Nevertheless, because the electrode voltage drops are measurable and give an indication of the power penalty for given operating conditions, it is a useful parameter to compute and to compare with the experimental data.

The contributing factors to the electrode voltage drop may be easily seen in the simplified MHD electrical equations. We can express the electrode voltage drop in terms of the formula for the transverse electric field E_y:

$$E_y = \frac{1+\beta^2}{\sigma} J_y + UB - \beta E_x \tag{4-1}$$

It is seen from this formula that the voltage drops are equal to the difference between the centerline value of E_y and the cross-sectional average value of E_y, since the Faraday voltage is simply the average transverse electric field, $\langle E_y \rangle$ multiplied by the transverse dimension of the channel, D. Thus the voltage drop is expressed as follows:

$$\begin{aligned} V_d &= D\left\{(E_y)_{\ell} - \langle E_y \rangle\right\} \\ &= D\left\{\left[\left(\frac{1+\beta^2}{\sigma}\right)_{\ell} - \left\langle\frac{1+\beta^2}{\sigma}\right\rangle\right] J_y + \left[(U)_{\ell} - \langle U\rangle\right] B - \left[(\beta)_{\ell} - \langle\beta\rangle\right] E_x\right\} \end{aligned} \tag{4-2}$$

It is seen from this formula that the electrode voltage drop can be considered to be composed of three components. These components are: the current density times the effective resistivity difference of the cross-section,

$$\left[\left(\frac{1+\beta^2}{\sigma}\right)_{\ell} - \left\langle\frac{1+\beta^2}{\sigma}\right\rangle\right] J_y \tag{4-3}$$

the induced field deficit in the boundary layers

$$\left[(U)_{\ell} - \langle U\rangle\right] B \tag{4-4}$$

and the variation of the Hall parameter through the electrode boundary layers due to pressure and temperature gradients in the boundary layers,

$$\left[(\beta)_{\ell} - \langle\beta\rangle\right] E_x \tag{4-5}$$

It is perhaps interesting to tabulate these components of the electrode voltage drops under various conditions. However, the variation of these expressions does not yield a great deal of insight or quantitative information about the effects of experimental parameters upon the overall performance of the generator. Again, this is because the electrode voltage drop itself is not simply related to the performance of the MHD generator. Also, because J_y and E_x are factors in these expressions which are themselves affected by the voltage drops, these expressions can hardly be called intrinsic characteristics of the channel or useful indications of the performance penalties associated with the voltage drops.

A much more useful quantity for expressing the effects of experimental parameters on the generator performance is the plasma nonuniformity factor. The plasma nonuniformity factor is defined as

$$G \equiv \langle\sigma\rangle\langle\frac{1+\beta^2}{\sigma}\rangle - \langle\beta\rangle^2 \tag{4-6}$$

where the brackets indicate cross-sectional averages of the quantities enclosed within. The concept of the plasma nonuniformity factor is a generalization of the original expression by Rosa [4-1].

In the case where variations of the Hall parameter in the cross-section are weak (usually a good assumption), the expression for the plasma nonuniformity factor can be simplified to the following expression:

$$G \simeq g + (g-1)\beta^2 \tag{4-7}$$

where

$$g \equiv \langle \sigma \rangle \langle 1/\sigma \rangle \qquad (4\text{-}8)$$

is the conductivity nonuniformity factor. Thus, the plasma nonuniformity factor, G, may be separated into contributions from the nonuniformity of the conductivity, g, and the strength of the Hall parameter, which is directly proportional to the magnetic field and approximately inversely proportional to the static pressure.

The plasma nonuniformity factor, G, is a useful parameter because it directly divides the power density at any given station in a Faraday generator ($\langle J_x \rangle = 0$)

$$\langle \vec{J} \cdot \vec{E} \rangle = \frac{\langle \sigma \rangle \langle U \rangle^2 B^2 (1-K)K}{G} \qquad (4\text{-}9)$$

The conductivity uniformity factor, g, is an intrinsic parameter which depends only on the distribution of conductivity in the channel cross-section, and not upon specific knowledge of the MHD interaction.

The scale-dependence of g has been investigated by STD Research Corporation in [4-2]. There it was shown that a number of loss mechanisms, including cold boundary layers, axial current leakage, surface voltage drops, and other effects could be summarized in this simple parameter, g. Also, as the scale of the generator increases (with fixed wall conditions), the value of g was shown to generally decline as the inverse square root of the thermal input to the generator. In most applications, the dependence of the Hall parameter in the channel cross-section is weak enough to make the parameter, g,

a very useful characterization of the potential performance of the MHD generator duct.

The following sections examine the sensitivity of V_d, G, and g to variations in the electrode wall temperature, the magnetic field strength, and the load factor. It is to be understood that the effects of Hall parameter variation, induced field deficit, and effective resistivity variations are lumped into the total electrode voltage drop, V_d in the following sections.

4.2.1 Dependence on Electrode Wall Temperature

This section compares the total electrode voltage drops and the plasma and conductivity nonuniformity factors resulting from three parametric variations in electrode wall temperature around the nominal Run 006-014 simulation. The nominal calculation has been discussed in Section 3.7. The three computations carried out with electrode wall temperature parametrically altered to constant values of 1250 K, 1500 K, and 1750 K have been described in Section 4.1. The conclusions regarding the sensitivity of electrode voltage drops and plasma uniformity presented in this Section are based upon those four computations, and apply primarily to conditions in the neighborhood of the operating conditions of Run 006-014.

To display the sensitivity of the electode voltage drops and the plasma uniformity, we have chosen to tabulate their values at four stations in the HPDE. Three of these four stations were locations at which the HPDE instrumentation provided transverse profile measurements. The fourth station, which varies about 0.1 m from computation to computation, was

the location at which the maximum electrode voltage drop occurred in each STD Q3D computation.

The location of the three voltage profile measurement stations and the approximate location of the maximum voltage drop computed by STD Research Corporation is shown in Fig. 4-2, which has been reproduced from [4-3]. Fig. 4-2 also presents a useful definition of the various coordinate systems used by STD Research Corporation and AEDC in citing positions in the channel. The lower axis in Fig. 4-2, which has been marked "STD Q3D coordinates" uses as a reference point the inlet flange of the MHD generator. The STD coordinate system also begins at the inlet flange of the MHD generator, but is expressed in metres rather than in inches. A second frame of reference has as its origin the first loaded electrode. This frame of reference in shown in the upper axis which contains the location and stations numbers, in inches, of the electrode voltage drop measurements made at the HPDE. The three stations at which the electrode voltage drops have been tabulated are, in STD coordinates, x = 1.43 m, x = 2.78 m, and x = 4.62 m. These locations correspond to STA 24.7 in., STA 77.4 in., and STA 215 in.

Fig. 4-3 illustrates the calculated variation of the total electrode voltage drop at the four stations in the MHD generator as a function of electrode surface temperature. It is noted that the maximum electrode voltage drop declines from approximately 2100 volts to approximately 1200 volts as the electrode surface temperature increases from the "5 sec" value of approximately 600 K to the assumed temperature 1750 K. At the front of the generator, x = 1.43 m, the electrode voltage

drop declines from approximately 500 volts to approximately 300 volts as the surface temperature decreases from the"5 sec"value of approximately 1000 K to the assumed wall temperature of 1750 K. The decrease in electrode voltage drop is approximately linear with temperature at each station. For comparison the experimentally measured electrode voltage drops at stations 1.43, 2.78, and 4.62 m are displayed at the same wall temperature that was assumed for the Q3D simulation of Run 006-014. The agreement between the measured and computed voltage drops appears to be within the experimental uncertainty of the measurements.

As noted above, the impact of the electrode wall surface temperature on the performance of the generator can be summarized by the value of the plasma nonuniformity factor G, which results from the nonuniformity of the conductivity field due to cold boundary layers. Fig. 4-4 presents the average value of the plasma nonuniformity factor throughout the generator as a function of the average electrode wall temperature. The error bars surrounding each average point correspond to the standard deviation of the value of wall temperature or plasma nonuniformity factor through the generator. For the "5 sec" walls conditions of the Run 006-014 simulation, the average conductivity nonuniformity factor is approximately 2. This means that any given station in the HPDE is operating with half the power density that would otherwise be obtained if the HPDE could provide perfect conductivity uniformity. Of course, doubling the local interaction at every station in the MHD generator would profoundly alter the flowfield in the generator, so that one cannot state categorically that the cold walls cause a 50% reduction in power input.

As the wall temperature increases, the average plasma nonuniformity factor declines to a value of 1.60 at 1250 K, 1.38 at 1500 K, and 1.22 at 1750 K. These reductions in the plasma nonuniformity factor correspond to potential increases in the MHD interaction in the generator of 27%, 47%, and 66%, respectively, over the "5 sec" wall temperature distribution.

The variation of the conductivity nonuniformity factor, which is an intrinsic characteristic of the channel flow, is shown in Fig. 4-5. As the wall temperature increases from the "5 sec" values to 1250, 1500, and 1750 K, the average conductivity nonuniformity factor, g, declines from 1.26 to 1.17, to 1.11, and to 1.06, respectively. As was shown in [4-2], values of this parameter implicit in the original design of the HPDE were typically on the order of 1.03, corresponding to wall temperatures between 1900 K and 2100 K. The "5 sec" wall temperature distribution is much more characteristic of small scale generators such as the Avco Mark VI and the UTSI channel.

4.2.2 Dependence on Magnetic Field

The dependence of the total electrode voltage drop upon the magnetic field is explained by two principal competing mechanisms. First, because of the increase in Hall parameter, the effects of conductivity nonuniformity are magnified by the contribution of the Hall parameter term in the plasma nonuniformity factor. Compensating this effect is the fact that an increased magnetic field creates increased current density in the electrode boundary layers. This tends to heat the boundary layers through Joule dissipation and improve somewhat the overall uniformity of the conductivity in the cross-section.

In the neighborhood of the HPDE Run 006-014 operating conditions, these two competing effects tend to slightly increase the electrode voltage drops as the magnetic field is increased to 4 T. Fig. 4-6 illustrates the almost linear dependence of the electrode voltage drop at four stations in the MHD generator as the peak magnetic field is increased from the Run 006-014 value of 3.27 T to 4.0 T and to 4.25 T.

Relative to the total induced voltage, however, the electrode voltage drop does not increase very dramatically as the magnetic field increases. Fig. 4-7 illustrates the near insensitivity of the relative voltage drop to the peak magnetic field value between 3.27 T and 4.25 T. This result suggests that one-dimensional models which rely upon a reduction in the induced field in order to represent the electrode voltage drops may be adequate in the neighborhood of the HPDE Run 006-014 conditions as long as the axial variation of the reduction factor is accounted for.

The fact that the relative voltage drop is weakly dependent on peak magnetic field is related to the fact that the plasma nonuniformity factor is essentially constant with magnetic field, as is illustrated in Fig. 4-8. Again, the competition between the declining conductivity nonuniformity factor due to Joule dissipation (shown in Fig. 4-9) and the increasing Hall parameter due to the increase in the peak magnetic field gives a nearly constant overall plasma nonuniformity factor variation.

The speculation that at high magnetic fields the voltage drops would be reduced by increased Joule dissipation in the boundary layers has not been borne out, at least in the neighborhood of the Run 006-014 operating conditions. The Hall parameter increase is an equal or even dominant effect over the g factor reduction due to Joule dissipation.

4.2.3 Dependence on Load Factor

The variation of the electrode voltage drops and the plasma uniformity with electrical load factor provides a vivid illustration of the influence of Joule dissipation in the boundary layers upon the performance of MHD generators. As the load factor increases and the generator goes more toward open circuit, the Joule dissipation in the boundary layer decreases. As the boundary layers become cooler, the plasma nonuniformity factor, G, and conductivity nonuniformity factor, g, increase substantially. In addition, with the reduction of current density associated with increasing load factor, less electron nonequilibrium can be sustained at the electrodes, so that the near electrode region becomes substantially more resistive.

The effect of increasing the Faraday load factor on the conductivity nonuniformity factor is shown in Fig. 4-10. At a load factor K = 0.55, the average conductivity nonuniformity factor g = 1.22. As the load factor increases to 0.60, g = 1.24. At the Run 006-014 simulation conditions, in which the average load factor is approximately 0.61, the average value of g increases to 1.26. When the load factor is held constant at 0.70, the magnitude of g increases to 1.34. This is an important effect for cold wall generator designs which depend on Joule dissipation to alleviate some of the thermal gradients in the electrode wall boundary layers.

The effect of increasing load factor on the overall plasma nonuniformity factor, G, is illustrated in Fig. 4-11. The increase in G is even more dramatic than the increase in g because, as the channel goes toward open circuit, the flow velocity increases and the static pressure in the generator generally decreases. Hence, as the channel is unloaded, not

only is there less Joule dissipation in the boundary layers, but the Hall parameter also tends to increase. This results in a steeply increasing plasma nonuniformity factor. The sensitivity of G to load factor reemphasizes the need for calculational procedures which can account for the Joule dissipation in the boundary layers. A calculation which assumed that the value of g and/or G was independent of B or K would clearly be incorrect for this high interaction device.

The behavior of the total electrode voltage drops as a function of load factor reveals a very interesting phenomenon associated with the accumulation of Joule heat through the MHD generator. Fig. 4-12 illustrates the values of the electrode voltage drop at four stations in the AEDC/HPDE. Four calculations are presented. The Run 006-014 simulation, CHPQUUUJBO, and three parametric variations with constant load factor throughout the generator are shown. Also shown are the data from Run 006-014, assuming that the load factor at each measurement station is as it is computed by the simulation.

The computed dependence of the electrode voltage drop on load factor is rather weak for the cases in which the load factor is held constant. (Of course, a constant voltage drop with increasing current density at lower load factors implies increased power losses.)

On the other hand, the simulation of Run 006-014, which incorporated a variable load factor (approximately 0.69 at the inlet to approximately 0.55 at the exit) deviates increasingly from the constant load factor trend lines toward the back end of the generator. The maximum voltage drop in the Run 006-014 simulation is approximately 2200 volts, whereas the maximum electrode voltage drop with constant load factors

occurs at a load factor of approximately 0.60, and has a value of approximately 1800 volts. The implication of this result is that the declining load factor profile throughout the generator in the Run 006-014 conditions cause less Joule dissipation upstream in the generator than would occur if the load factor were held constant at the average Run 006-014 values. This leads to generally colder electrode boundary layers in the downstream regions. This result suggests that the optimum load factor profile from the point of view of minimizing voltage drops would be one which begins initially lower than the average value and increases throughout the generator. While this is considered to be a second order effect on the overall performance of the device, it certainly bears further investigation for the future loading of the AEDC/HPDE.

4.3 Parametric Variations Around the Transient Simulation of Run 006-014

The response of the HPDE to parametric variations in the neighborhood of the Run 006-014 operating parameters was analyzed with the Q3D code family in the previous section. That study identified increases in the wall temperature and magnetic field as the principal means for achieving increased enthalpy extraction and isentropic efficiency of the generator. It is desirable to extend these results to the ultimate capabilities of the facility, i.e., 6 T operation. This section presents such results.

In the neighborhood of the Run 006-014 simulation studied with Q3D, the flow in the MHD generator is uniformly supersonic. Far from this neighborhood (i.e., at much higher magnetic fields or wall temperatures) the flow may become transonic or subsonic. Because of the additional expense and

effort required for Q3D computations in the transonic or subsonic modes, which require iterative matching of downstream pressure conditions, it was decided to extend the parametric studies far from the neighborhood of the Run 006-014 conditions by using the quasi-steady option of the TRANSIENT family of codes.

To make such a parametric survey meaningful, it was necessary to incorporate as much of the information from the quasi-three-dimensional calculations using the Q3D family of codes into the TRANSIENT calculations. In order to include the effects of variable wall temperature on the electrical solution in the quasi-steady TRANSIENT calculation, values of the conductivity nonuniformity factor, g, obtained from Q3D simulations, were used as input. For the parametric survey of wall temperature, the g values from Q3D Run CHPQUUUJBO were used for the "cold wall" or "5-sec" wall electrode wall conditions. Q3D calculation COBQFAVJDY was used to obtain a "hot wall" or constant 1500 K electrode wall temperature distribution of g values.

The starting point for all of the TRANSIENT parametric studies was Run BRCYTRCJEB described in Section 3.8. Utilizing the g factors corresponding to cold walls, the magnetic field distribution was increased progressively in steps from the nominal value of 3.27 T to 4 T, 5 T and then to 6 T. At each step in the magnetic field, sufficient time was provided to obtain a steady-state solution before the next increase in magnetic field was applied. Similarly, the hot wall simulation was carried out by first instantaneously modifying the g factor distribution to correspond to 1500 K walls of Q3D Run COBQFAVJDY, and then increasing the peak magnetic field

strength in steps from 3.27 T to 4 T, 5 T and then to 6 T. The results of this parametric variation in wall temperature and magnetic field are shown in Fig. 4-13. Throughout all of these parametric variations, the load schedule was fixed according to the Run 006-014 distributions, and the g distributions were held fixed at either the "hot wall" or "cold-wall" values. In view of the dependence of g on magnetic flux density discussed in the above sections, the consequence of holding g fixed is probably a slightly conservative estimate of performance.

As is clearly evident in Fig. 4-13, the reduction of the plasma nonuniformity factor due to the increase in wall temperature from the "5 sec" values to a constant 1500 K distribution makes the difference between achieving the enthalpy extraction goal of the HPDE and not achieving it. The 6 T operation of the HPDE with 1500 K walls is predicted to achieve nearly 15.5% enthalpy extraction with the Run 006-014 nominal load schedule. With "5 sec" walls the HPDE achieves less than 13% enthalpy extraction. A detailed list of the isentropic efficiency, enthalpy extraction ratio, and the exit Mach numbers are shown in Table 4-1.

It is seen from Table 4-1 that between 4 and 5 T with hot walls, there is a transition from supersonic to transonic flow with a shock in the generator. While the performance is predicted to increase despite the entry of the shock into the generator, the ramifications of operating a high-interaction MHD generator with a normal shock in the active portion of the generator remain to be investigated.

4.4 Optimal Load Schedules

The goal of the HPDE is performance, not duration. Therefore, the optimization of the loading of the HPDE should be aimed at optimizing performance without the constraints of "rule of thumb" or conventional limitations on current density, Hall field, or other parameters.

For given conditions of velocity, conductivity, and magnetic field, the most important parameter in a Faraday generator is the electrical loading factor, $K = \langle E_y \rangle / \langle UB \rangle$, which defines the operating point on the load line of a local section of the generator ($K = 1$ is open circuit, $K = 0$ is short circuit). For given conditions of conductivity, velocity, and magnetic field, the maximum enthalpy extraction per unit length is achieved at a load factor of $K = 0.5$. For maximum efficiency, the load factor is somewhat higher than 0.5.

In general, for generators of moderate and high interaction, the load-line is not linear. Changing the loading of the generator profoundly alters the distributions of conductivity and velocity in the generator, and multidimensional phenomena enhance the nonlinearity of the electrical performance. Therefore, in order to survey the performance of the device as a function of loading, the model employed must be capable of accurately predicting the interaction between the MHD forces and the fluid. For the present studies of the HPDE loading, a code from the TRANSIENT code family is used in order to facilitate rapid surveys of the impact of the loading of the generator. The nonlinear coupling between the loading and the fluid behavior is described in this section.

While sophisticated, constrained optimization procedures could be utilized for optimizing the loading schedule of the HPDE, it is felt that the variation of the load factor in the axial direction produce second order effects on the performance. The most important parameter is the average load factor. This conclusion is borne out by comparison with constant load factor calculations and variable load factor calculations, as was discussed in Section 4.2. Therefore, all of the load survey studies that have been conducted to date have been carried out with the specification of a constant load factor throughout the generator.

Many results have been presented in separate reports for the HPDE "nominal" operating conditions. Perhaps more pertinent are the results obtained when parametric variations of the load factor around the simulation of an actual high-powered run of the HPDE are calculated. Section 4.1 illustrates the load factor influence around the operating conditions simulated by Q3D for the Run 006-014. It was shown in that section that the reduction of the load factor in the Run 006-014 experiment could have improved the enthalpy extraction somewhat, but at a penalty in isentropic efficiency. In Section 4.3, the performance at various magnetic fields up to 6 T was compared with the TRANSIENT code with hot and cold wall assumptions. These studies utilized the load resistance schedule of Run 006-014.

Relative to the achievement of the performance goals of the HPDE, it was suggested that the variation in the load factor, particularly at the "hot wall", high magnetic field points in Section 4.3, might allow both the enthalpy extraction and isentropic efficiency goals to be achieved simultaneously. Consequently, the electrical load factor was varied around each

of the 4 T, 5 T and 6 T points with hot walls described in Section 4.3. The results of these load factor variations are shown in Figs. 4-14, 4-15, and 4-16 for 4 T, 5 T, and 6 T, respectively. Also shown on Figs. 4-14 through 4-16 are the points computed with the actual Run 006-014 load schedule. In each case the Run 006-014 load schedule yields slightly better performance than the maximum obtained with constant load factors. However, it is felt that there is not enough of an improvement to warrant a global optimization study with the quasi-one-dimensional TRANSIENT code. It would be more appropriate to carry out an optimization with a multidimensional code which could independently account for the boundary layer dissipation effects described in Section 4.3.3

The importance of operating the MHD generator near the optimum Mach number profile down the generator is emphasized by Figs. 4-14, 4-15 and 4-16. The flow regimes of the generator at the various load factors are indicated by the density of the trend curves. It is apparent that the enthalpy extraction of the generator optimizes in each case for 4, 5, and 6 T at transonic flow conditions. The optimum Mach number for maximum enthalpy extraction rate appears to be that load factor which provides transonic flow. At 4 T, the optimum load factor is approximately 0.65; at 5 T, it is approximately 0.72; and at 6 T, it is approximately 0.80. The meaning of this is that, as the magnetic field increases, the load factor must also increase (i.e., the generator must be less and less heavily loaded) in order to keep the flow field distribution close to the optimum design values. This concept of maintaining the flow field at or near the optimum Mach number distribution is also central to the understanding of the part load and off-design operation of generators of all scales, as is discussed in Section 7.2.

4.5 Near Electrode Phenomena with Finite Electrode Segmentation

In order to establish a basis for the Q3D current transport models, near electrode phenomena were studied under the operating conditions of the AEDC/HPDE Run 006-014. Two principal code familes were utilized for the study of near electrode effects with finite electrode segmentation. The FIN family of codes computes two-dimensional distributions of electrical and plasma transport variables in the region between a single pair of electrodes. The assumption implicit in this code family is that the variation in behavior from electrode to electrode is sufficiently weak that periodic boundary conditions can be imposed on the upstream and downstream ends of the region being computed. On the other hand, the ARRAY family of codes considers a string of electrodes without the requirement of periodicity. The upstream and downstream boundary conditions are obtained from Q3D or from the imposition of Neumann boundary conditions specifying locally invariant electrical properties.

Two FIN calculations were performed at the x = 2.77 m station in the AEDC/HPDE. Input data for gasdynamic profiles and initial conditions were obtained from the Q3D Run CHPQUUUJBO, the nominal simulation run for the HPDE Run 006-014. Two computations were carried out. Computation BRCYICLJEA utilized the option with finite reaction rates. Computation BRCYLARJD4 utilized the option for instantaneous reaction rates for electron reactions. Table 4-2 shows a comparison between the Faraday voltage, total voltage drops, Hall field, and local power density, computed by the two FIN calculations and the Q3D simulation. We note that the inclusion of finite electrode effects in the FIN calulations

results in the reduction of the Faraday voltage by 68 volts. This Faraday voltage reduction is associated with an increase in the total electrode voltage drop of 128 volts. The Hall voltage in the FIN calculations is approximately 50 V/m higher in magnitude, and the overall power density at this station is slightly decreased (4.5%) by the inclusion of the finite electrode effects. The relative small differences between the Q3D simulation CHPQUUUJBO and the FIN calculations indicates that the diffuse discharge model is suitable for simulations under the Run 006-014 conditions.

On the other hand it is possible that the inclusion of finite electrode effects and near electrode effects may explain differences between the Run 006-014 measurements and the Q3D computation CHPQUUUJPO which were discussed in Section 3.9. It is anticipated that, as the boundary layers grow and the bulk nonuniformity of the boundary layers begins to dominate the near-electrode effects on the voltage drops, the importance of near-electrode effects in the back end of the generator will be less. Insufficient resources were available to investigate the near-electrode behavior throughout the entire MHD generator under the present effort. It would be of interest to complete the analysis throughout the entire length of the generator under the Run 006-014 simulation conditions.

Two ARRAY calculations were carried out to investigate near-electrode phenomena without the requirement of periodicity. Computation BRCYYNVJEC also considered the nominal conditions of operation in the neighborhood of x = 2.77 m in the AEDC/HYPE Run 006-014. A region of 2.5 channel diameters around x = 2.77 m was chosen for simulation. An expanded view of the current pattern in the near-electrode regions computed by the ARRAY family of codes at x = 2.77 m is

shown in Figs. 4-17 and 4-18 for the cathode region and anode region. Instabilities in the near-anode region is apparent in Fig. 4-17. The operating characteristics of the electrodes at x = 2.77 m is quite comparable to the FIN results discussed above and with the measurements of Run 006-014.

Fig. 4-19 illustrates the current pattern in the entire computational region of computation BRCYYMVJEC. In this figure, the details of the near-electrode behavior is suppressed by the coarseness of the plotting grid.

Fig. 4-20 shows the corresponding equipotentials in this ARRAY computation. It is noted that the equipotentials are rather uniform. The steep inclination of the equipotential in the core in due to the relatively low Hall parameter (1.2) at this station. The curvature of the equipotentials near the walls reflects the presence of voltage drops due to the imposed gasdynamic boundary layer profiles.

The importance of relaxing the periodicity assumption is emphasized in Figs. 4-21 and 4-22. These Figures illustrate the result of calculation BRCYYQPJEC, in which the exact conditions of th previous ARRAY calculation were varied only by assuming that a single electrode pair went to short-circuit. The imposition of a short-circuit on this region causes a gross distortion of the equipotential pattern of Fig. 4-20, as shown in Fig. 4-21. Walls which normally operate at a potential difference of 1700 V or more are suddenly forced, in a very small region, to operate at the same potential. Very considerable electric fields developed due to this condition are likely to cause severe electrical breakdowns in the neighborhood of the Faraday short.

In addition, all of the power being produced in a region approximately one or two diameters upstream and downstream of the MHD generator is available to be coupled into the Faraday short. As a result, the surge current through the Faraday short increases by two orders of magnitude over the normal operating current of the electrode pair. It is evident that the increase in the current to the external load circuit would be enough to cause either mechanical or thermal damage to the load circuit connections. This and similar faults must be protected against in future HPDE operations.

The result of this "Faraday catastrophe" vividly illustrates that fine electrode segmentation is both a blessing and a curse. Fine electrode segmentation increases the overall current uniformity and decreases Hall effect reductions in the power output of the generator. On the other hand, if Faraday faults do occur, they will occur with more damaging consequences with finer electrode

4.6 Current Distribution in the End Regions

The HPDE inlet eddy currents were investigated, utilizing a two-dimensional, finite electrode, finite reaction rate code from the INLET family of codes. The operating conditions were specified from the outputs of the Run 006-014 simulation by Q3D (CHPQUUUJBO). The presence of open circuit electrodes in the magnetic field gradient of the end regions of the HPDE leads to internal circulating currents in the plasma. These are depicted in Fig. 4-23 for the computation BRCYZGGJEC. Because the passage of current in the downstream end of the current loops is through a higher magnetic field than the return current through the upstream portion of the loops, there is a net reduction in the total pressure of the power train.

This loss of pressure does not produce useful work. Under the Run 006-014 operating conditions, it is estimated, based on this computation, that this pressure drop is of the order of 0.07 atmospheres.

Fig. 4-24 shows the equipotentials associated with the current pattern in Fig. 4-23. It is interesting to note that the lack of current through the upstream boundary layers make these boundary layers very good insulators. The cold upstream boundary layers effectively shield the core from the open-circuit electrodes, which serve as insulators, and promote the circulation of current inside the plasma. It is noted that the voltage in the core at the first loaded electrode persists for a considerable distance upstream of the generator.

REFERENCES

[4-1] R.J. Rosa, Magnetohydrodynamic Power Generation, McGraw-Hill, New York, 1968.

[4-2] C.D. Maxwell, S.T. Demetriades, D.A. Oliver, A.A. Vetter, T.F. Swean, "Scale-up of Advanced MHD Generators", AIAA 18th Aerospace Sciences Meeting, Paper No. AIAA=80=0179, Pasadena, California, January 1980.

[4-3] R.L. Lowery, "High Performance Demonstration Experiment Supersonic Faraday Performance Evaluation", Data Package: Propulsion Wind Tunnel Facility, Arnold Engineering Development Center; Preliminary Data: Run MI-006-006, September 1979.

TABLE 4-1

Results of TRANSIENT Computations Performed for Task I
Nominal Loading from HPDE Run 006-014
and Combustor Thermal Input of 303.2 MW

Run	B_{max} (T)	M_{exit}	Wall Temp (K)	Power (MW)	Enthalpy Extraction (%)	Efficiency (%)
BRCYTRCJEB	3.274	1.794	"5 s"	23.60	8.24	37.46
	4.0	1.648	"5 s"	28.95	10.11	40.72
	5.0	0.651	"5 s"	34.17	11.94	42.25
	6.0	0.654	"5 s"	36.39	12.71	45.11
BRCYUXWJEB	4.0	1.124	1500	36.80	12.83	43.88
	5.0	0.650	1500	41.75	14.56	51.56
	6.0	0.699	1500	44.39	15.48	53.81

0-4361

TABLE 4-2

Electrical Performance Parameters at x = 2.77 m in the AEDC/HPDE Run 006-014: Comparison Between FIN Calculation BRCYICLJEA and Q3D Calculation CHPQUUUJBO

Quantity	FIN	Q3D
Run No.	BRCYICLJEA	CHPQUUUJBO
Total Electrode Voltage Drop, V	830	702
Faraday Voltage, V	1676	1743
Centerline Hall Field, V/m	984	959
Local Power Density, MW/m^3	16.05	16.78

0-4362

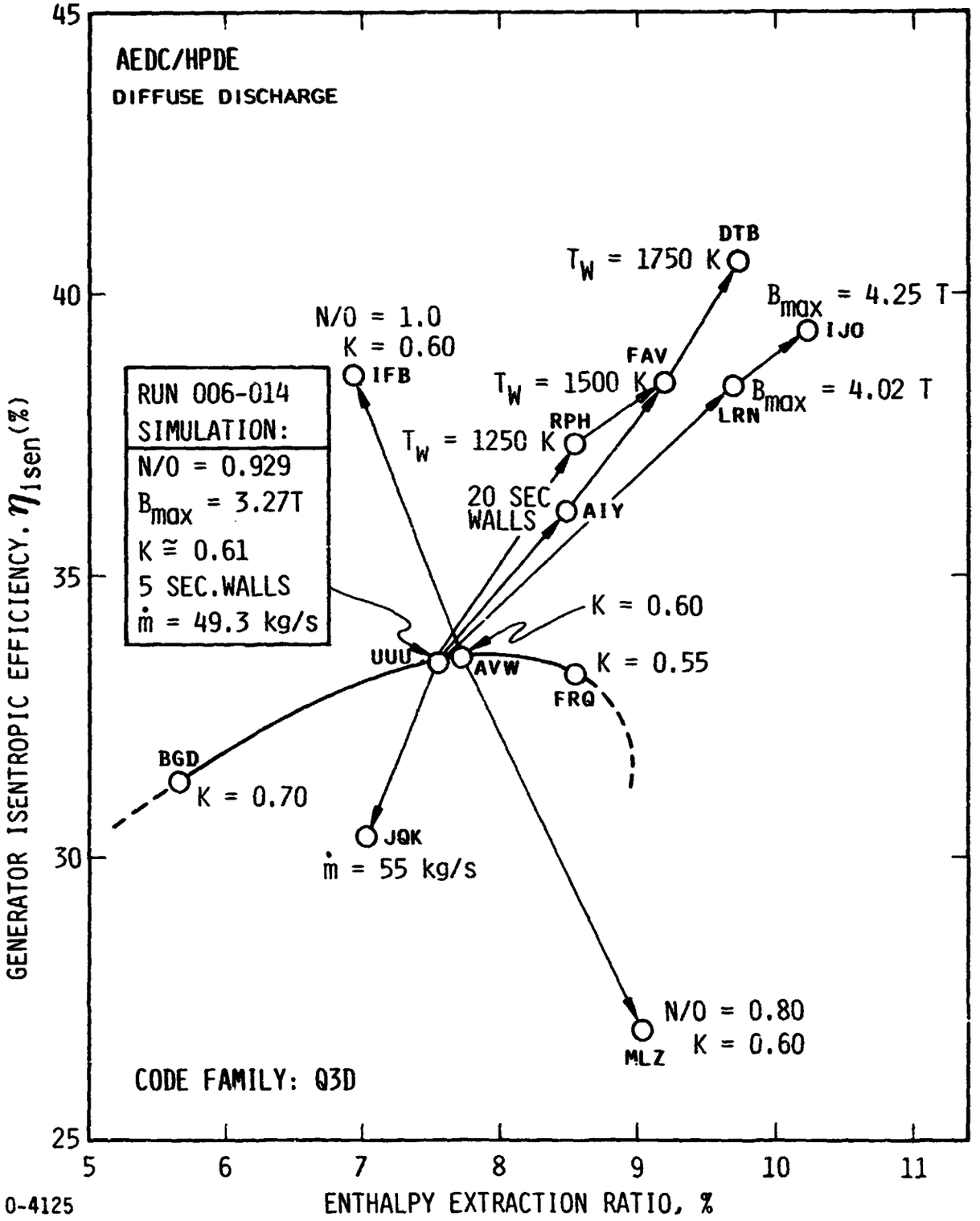

0-4125

Fig. 4-1. Generator isentropic efficiency vs. enthalpy extraction ratio for simulation of HPDE Run 006-014 and simulations with variations in the conditions from those of Computation CHPQUUUJBO. Three-letter code by each point is the abbreviated STD Computation number.

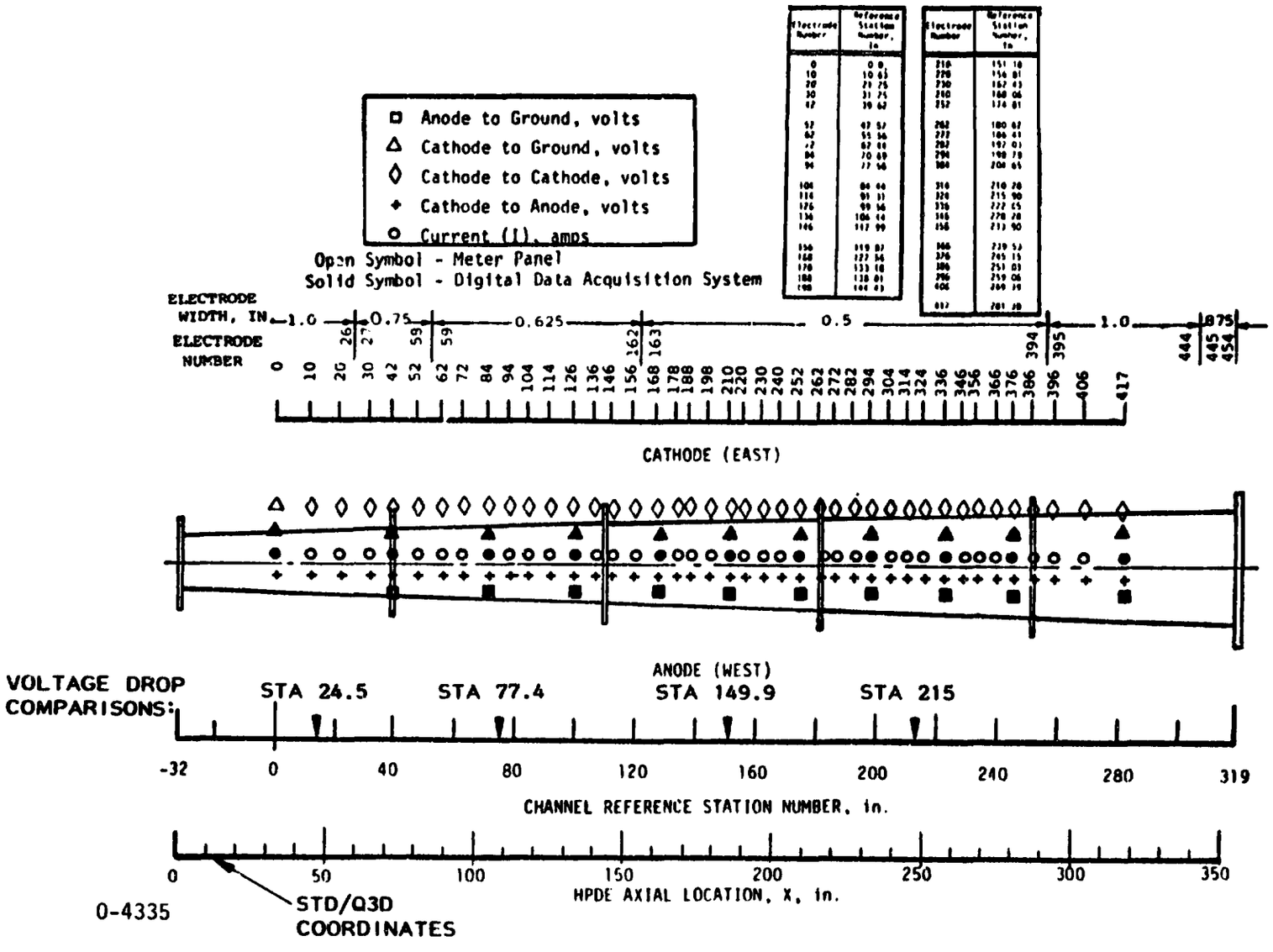

Fig. 4-2. Coordinate systems and stations at which total voltage drops are measured and computed voltage drops are tabulated.

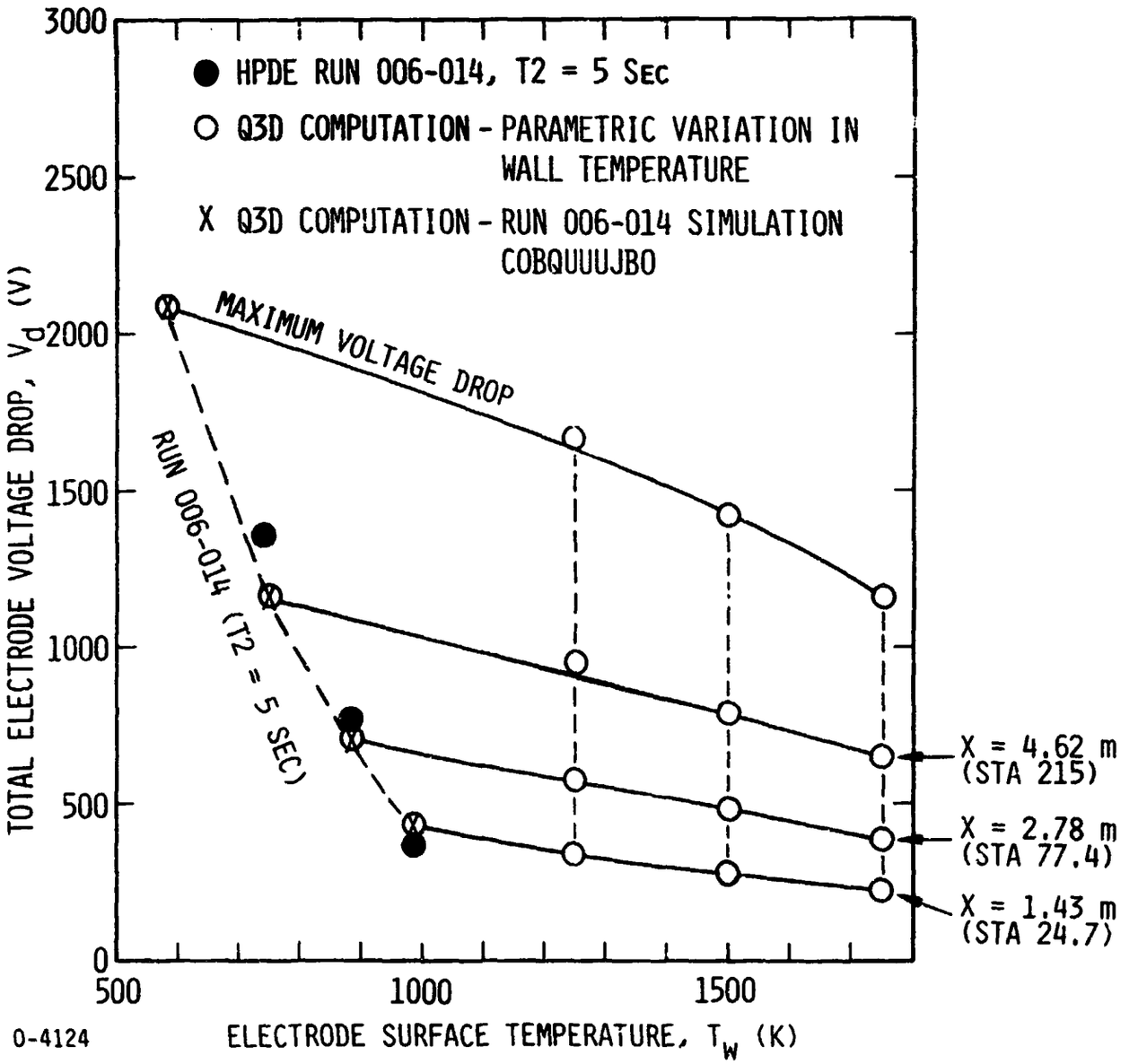

Fig. 4-3. Variation of total (anode + cathode) electrode voltage drop with electrode surface temperature under the conditions of the Q3D simulation COBQUUUJBO of the HPDE Run 006-014.

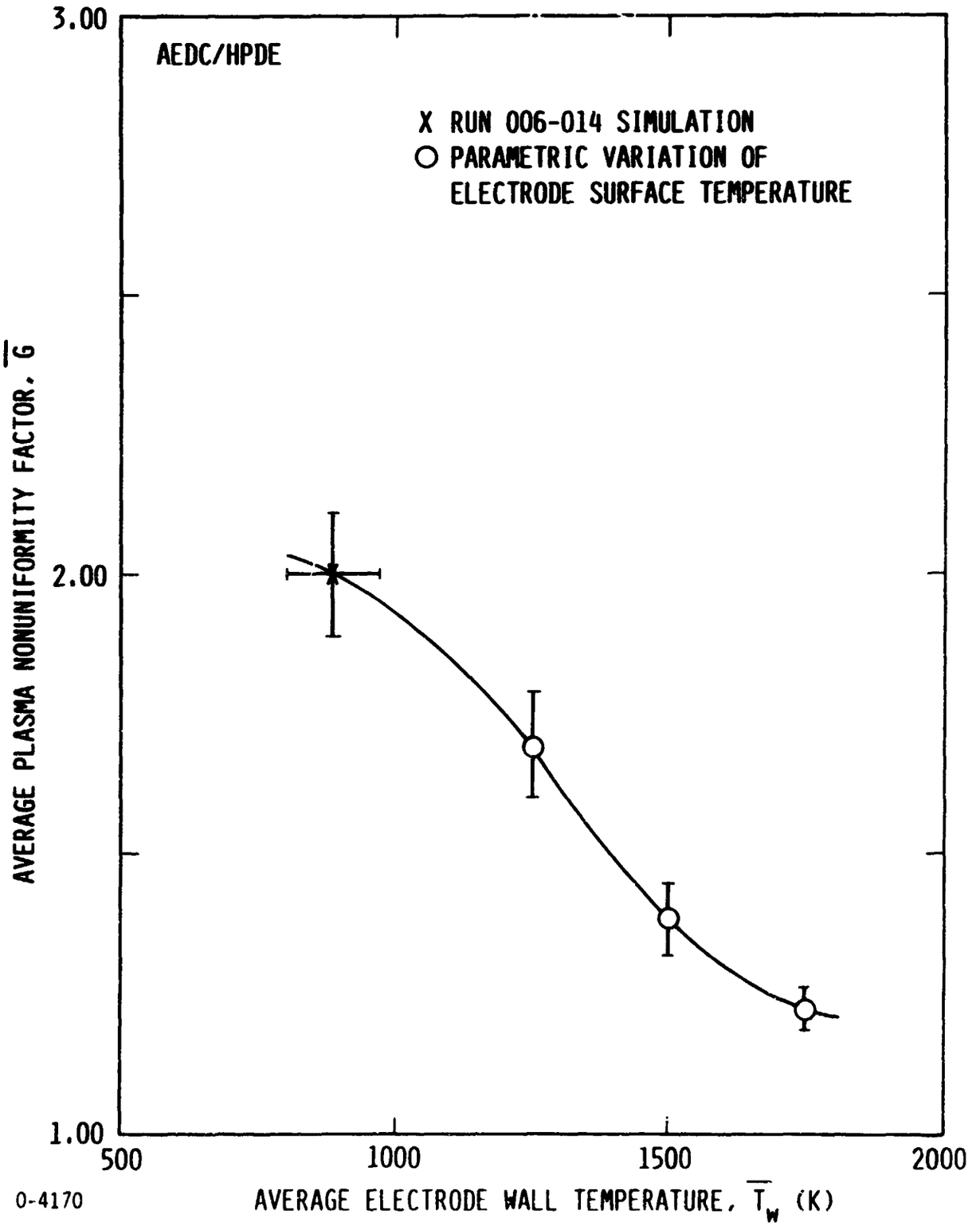

Fig. 4-4. Variation of the plasma nonuniformity factor G with electrode wall temperature: Parametric variations around the AEDC/HPDE Run 006-014 simulation conditions.

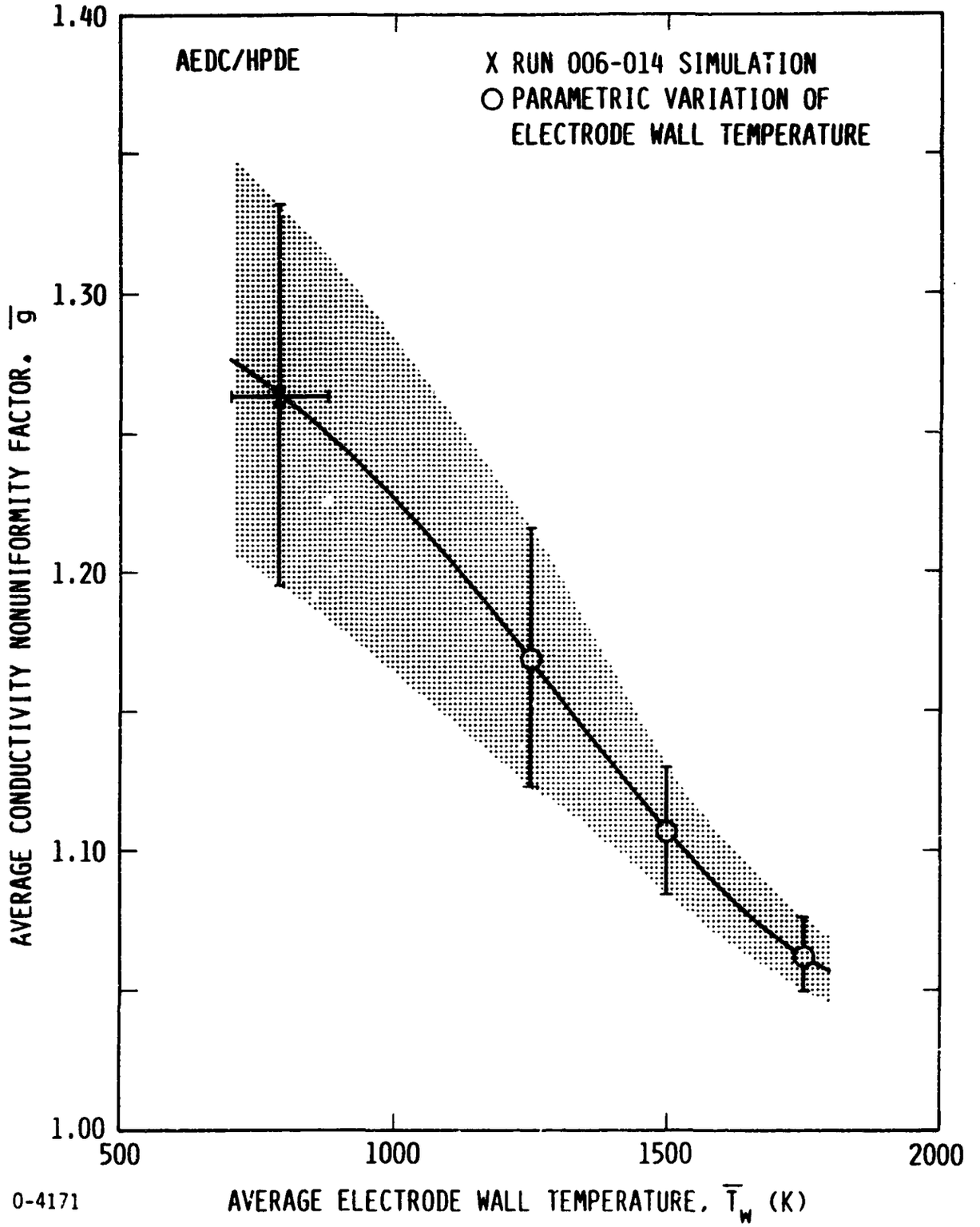

Fig. 4-5. Variation of the conductivity nonuniformity factor with electrode wall temperature: Parametric variations around the AEDC/HPDE Run 006-014 simulation conditions.

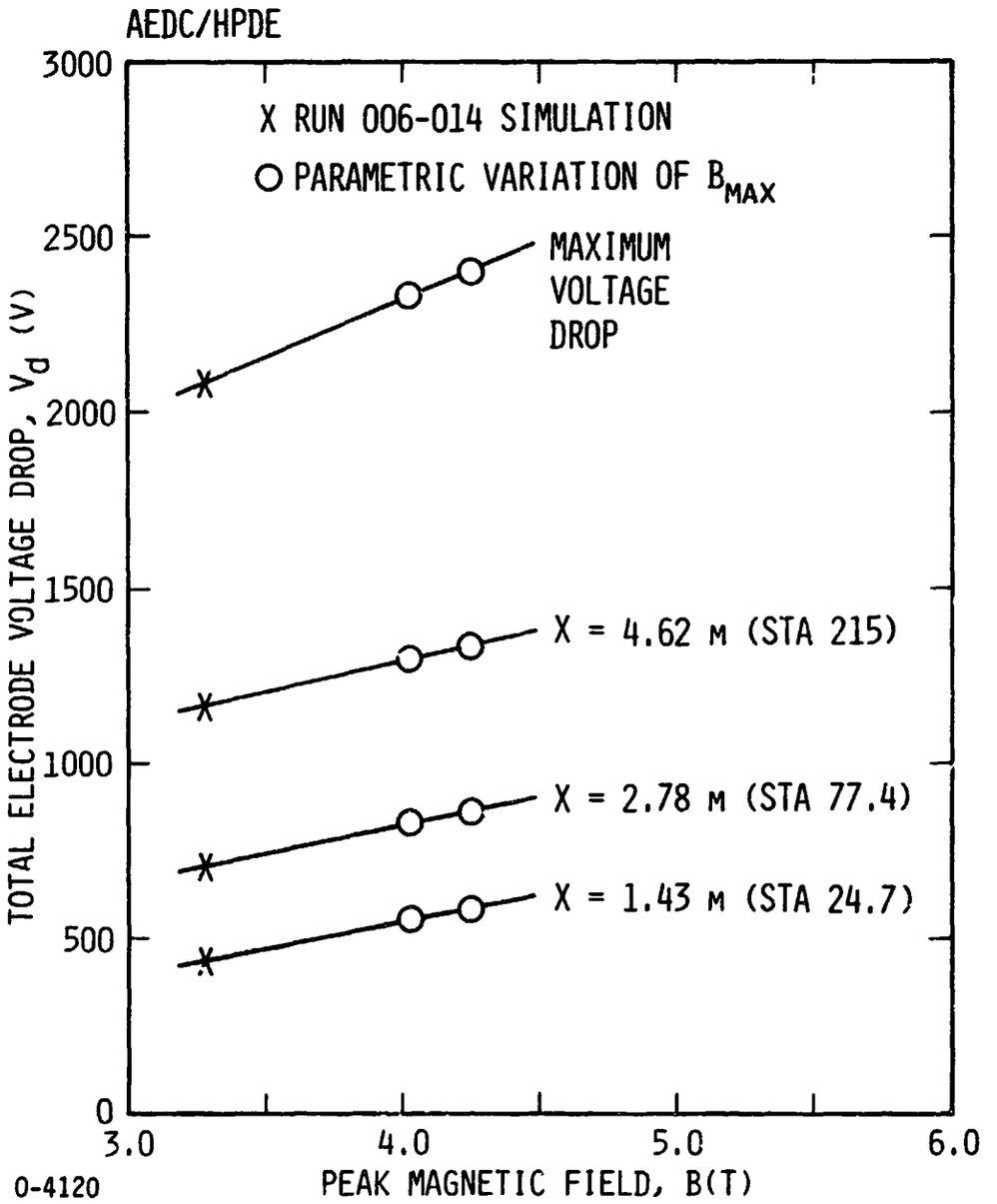

Fig. 4-6. Variation of the total electrode voltage drop with peak magnetic field at various stations in the AEDC/HPDE; parametric variations around the Q3D simulation of the HPDE Run 006-014

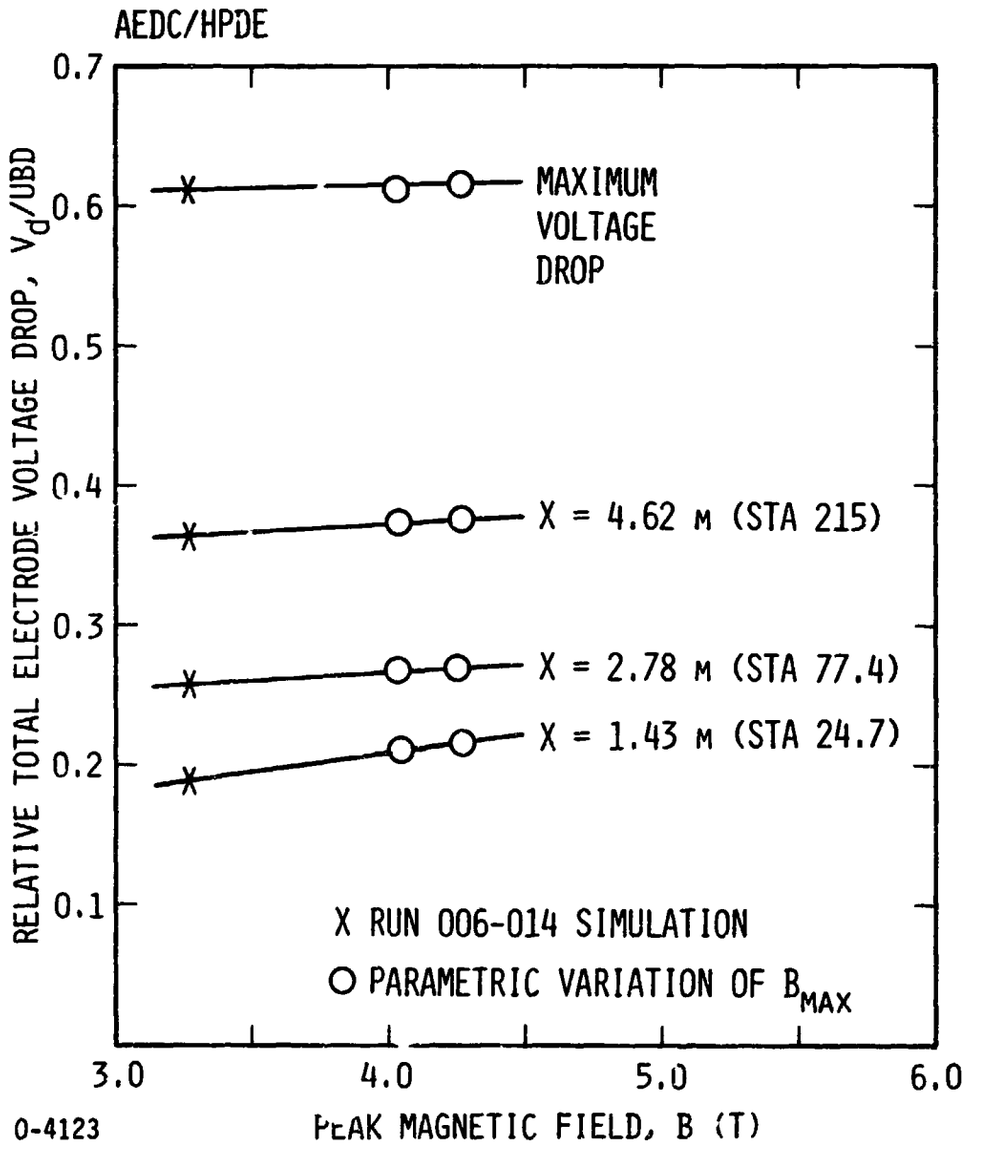

Fig. 4-7. Variation of the relative electrode voltage drops with peak magnetic field at various stations in the AEDC/HPDE: parametric variations around the Q3D simulation of the HPDE Run 006-014

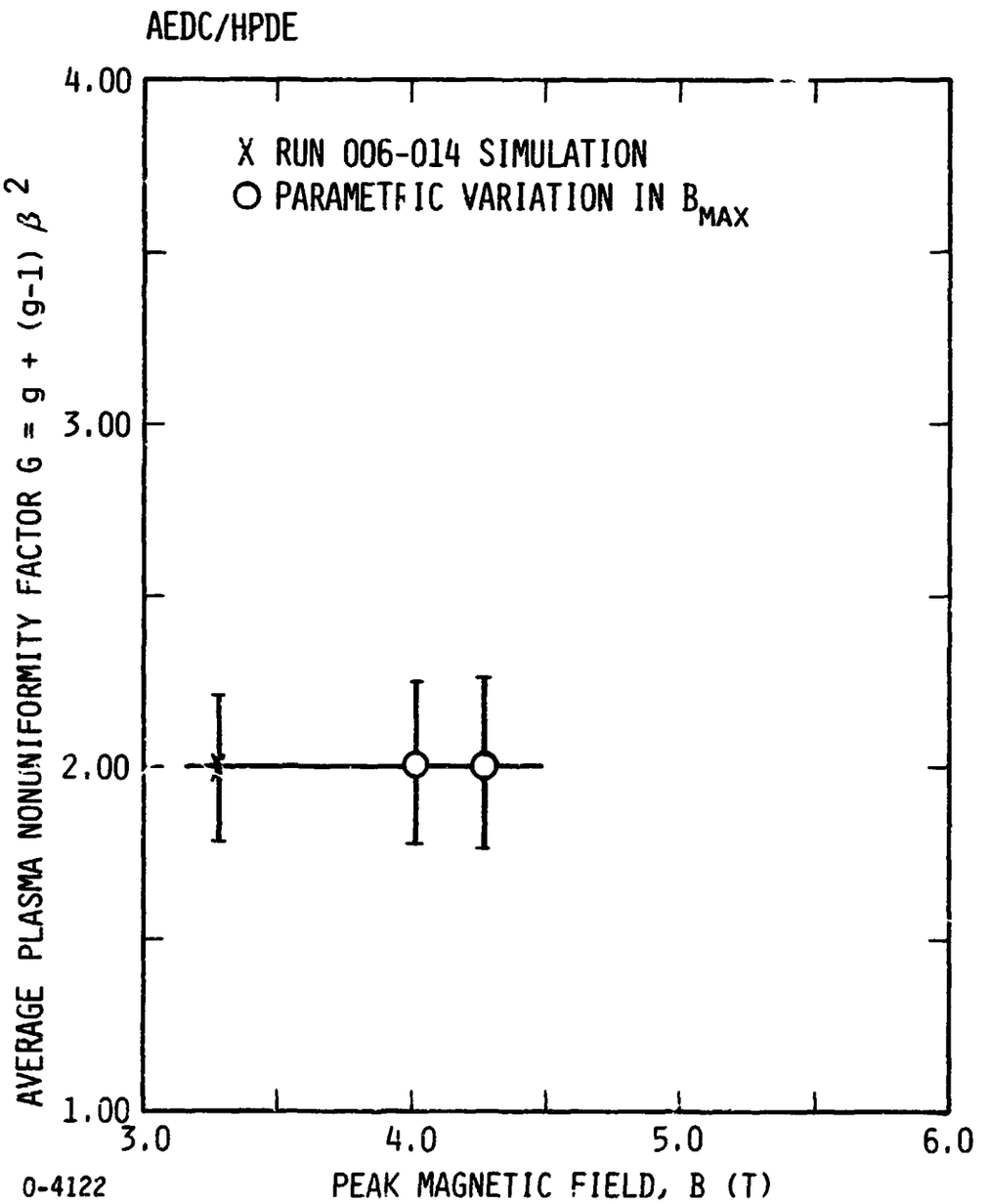

Fig. 4-8. Variation of the plasma nonuniformity factor with peak magnetic field in the AEDC/HPDE: parametric variations around the Q3D simulation of the HPDE Run 006-014

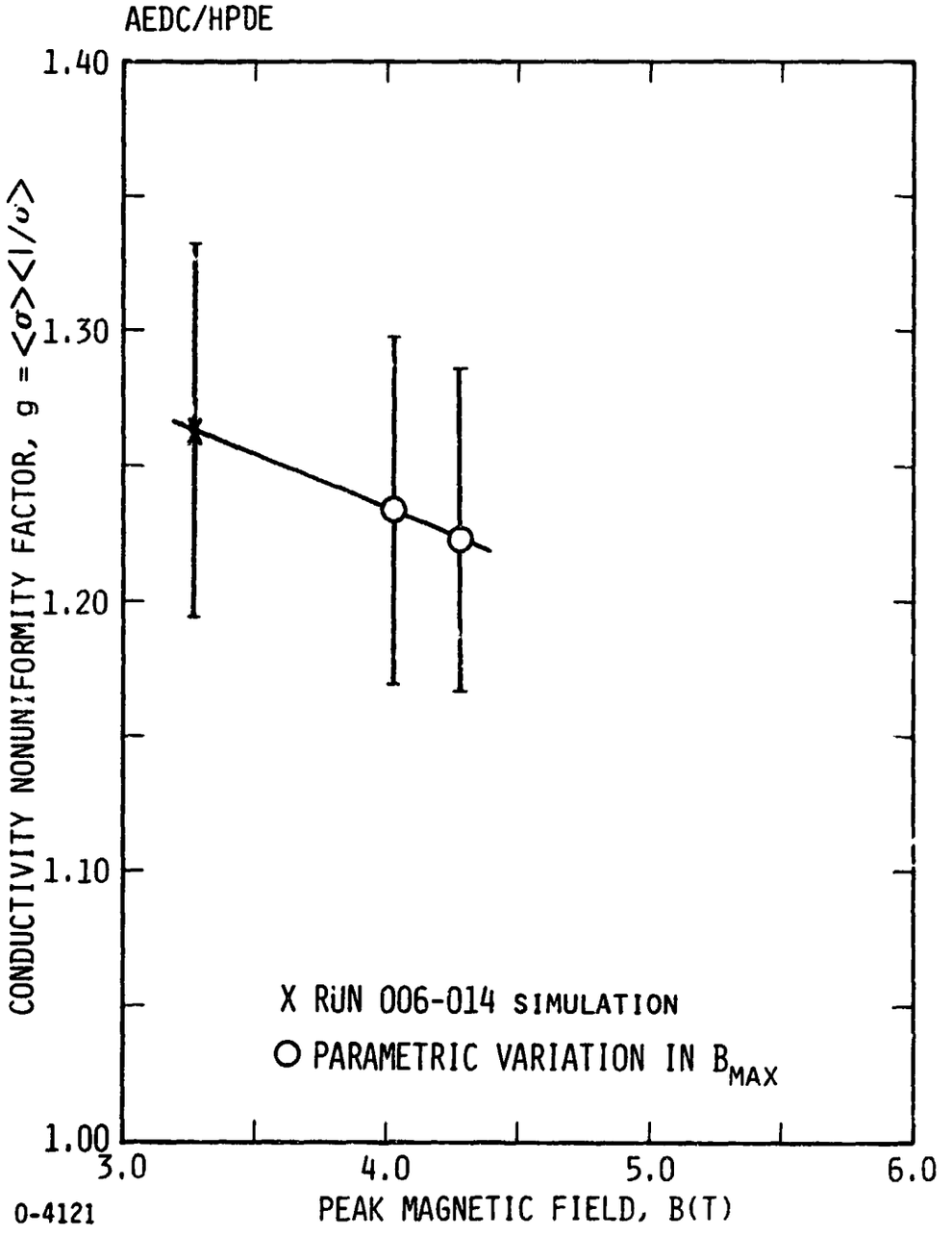

Fig. 4-9. Variation of the conductivity nonuniformity factor with peak magnetic field in the AEDC/HPDE: parametric variations around the Q3D simulation of the HPDE Run 006-014

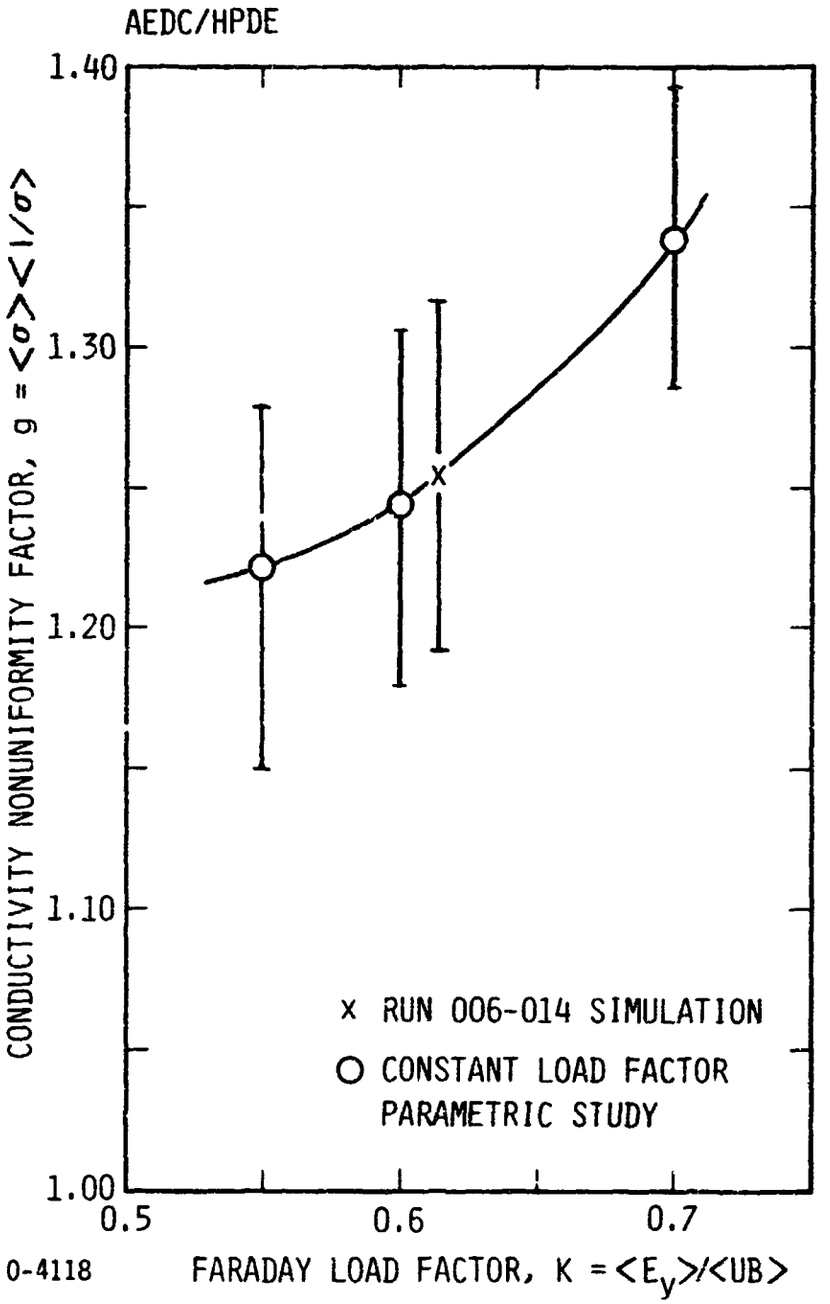

Fig. 4-10. Variation of the conductivity nonuniformity factor with Faraday load factor; parametric variations around the Q3D simulation of the AEDC/HPDE Run 006-014.

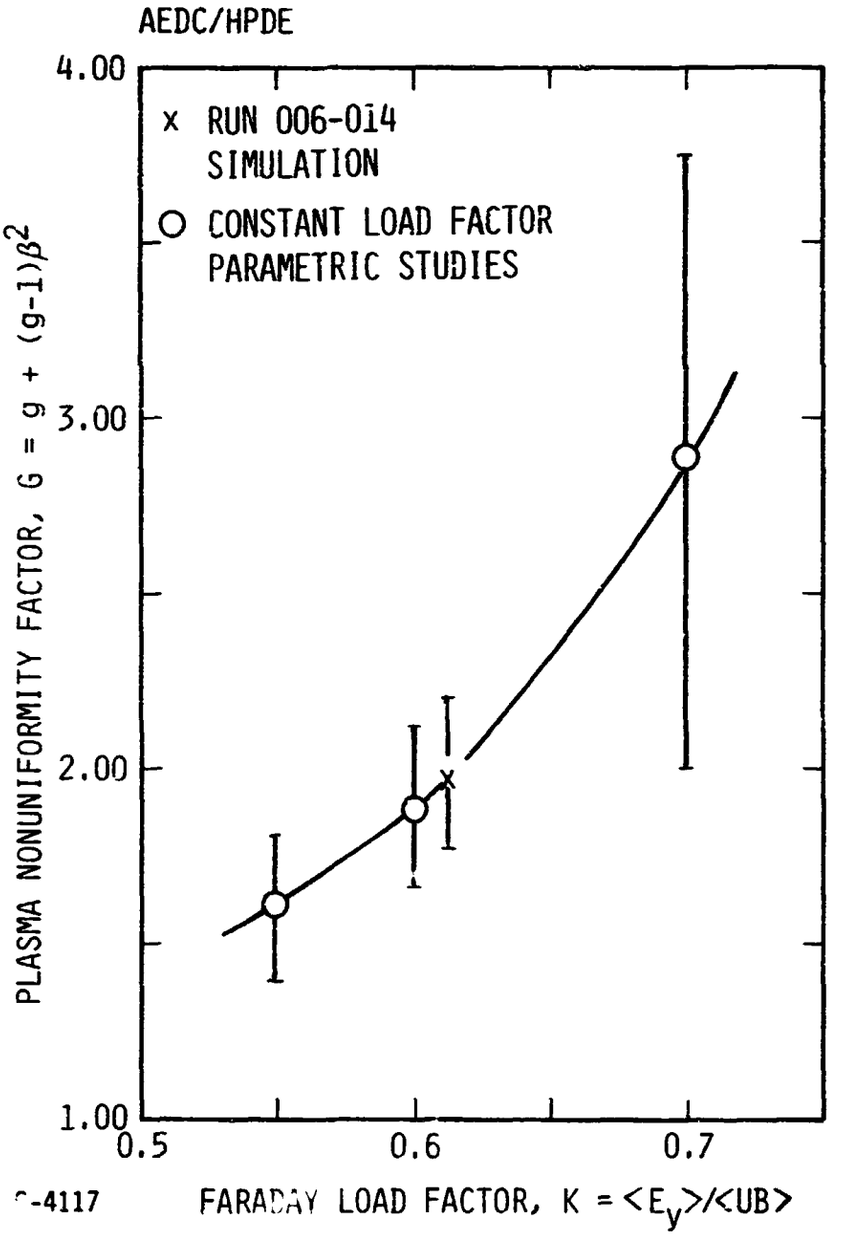

Fig. 4-11. Variation of the plasma nonuniformity factor with Faraday load factor: parametric variations around the Q3D simulation of the AEDC/HPDE Run 006-014.

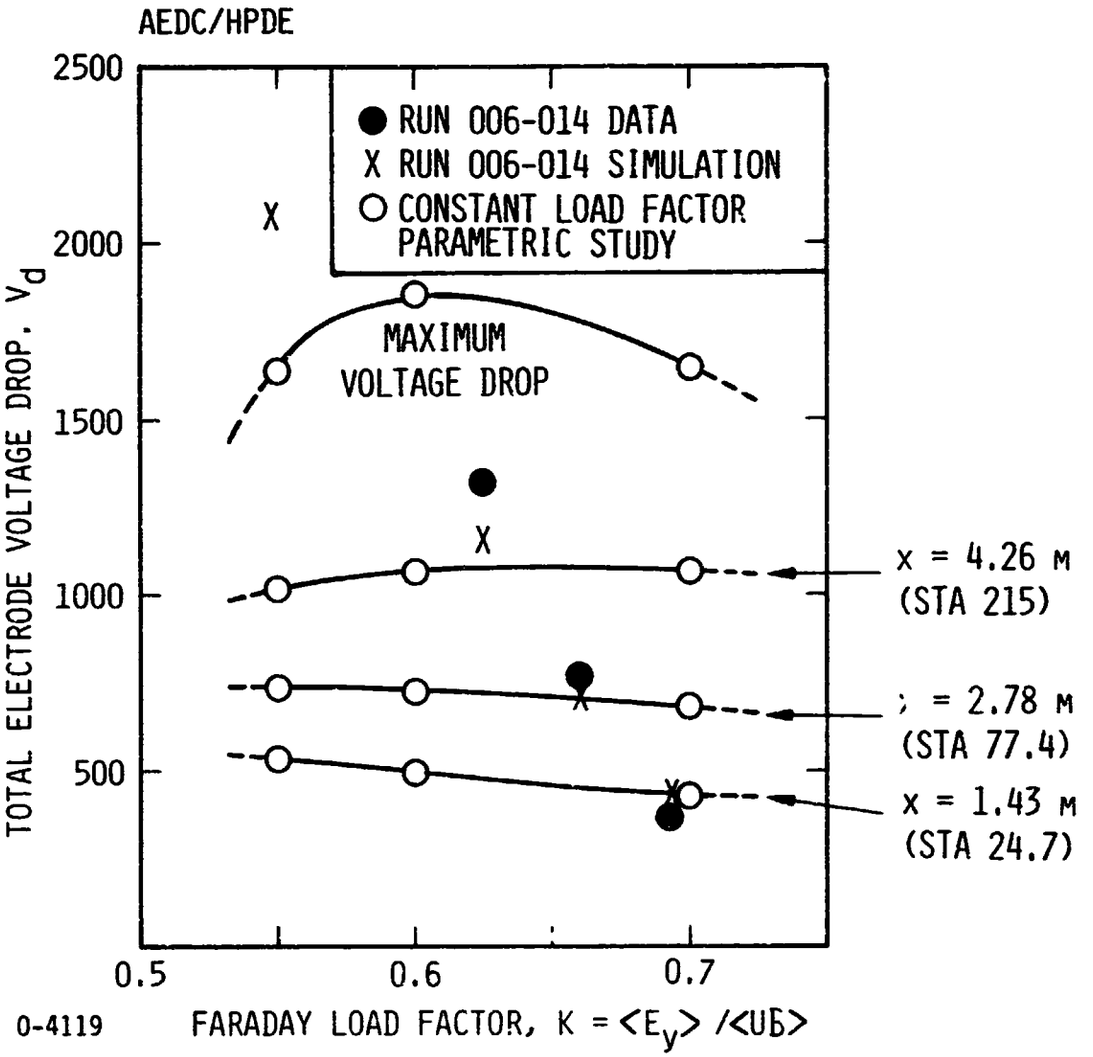

Fig. 4-12. Variation of total electrode voltage drop at various stations in the AEDC/HPDE with Faraday load factor: parametric variations around the Q3D simulation of Run 006-014.

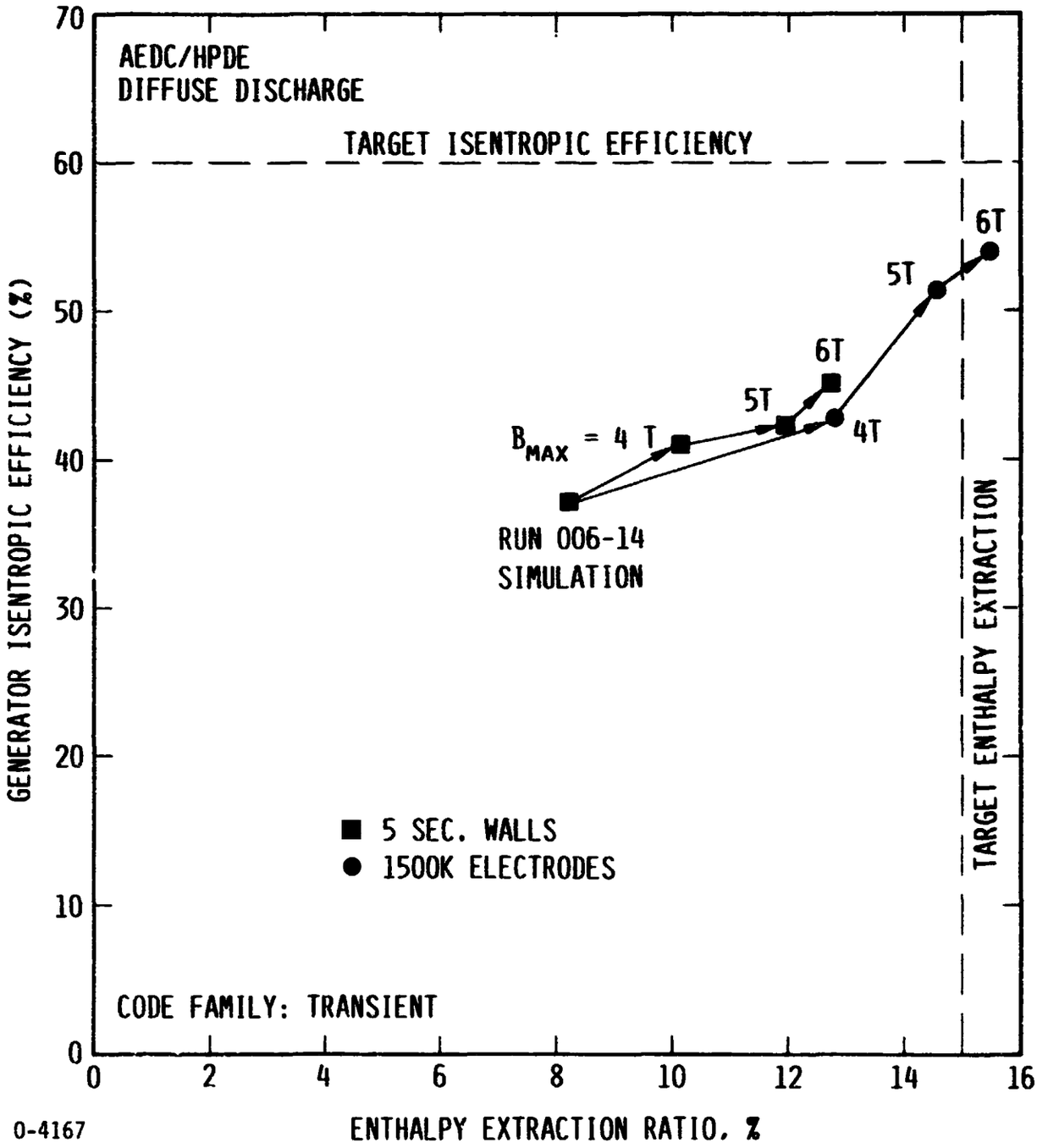

Fig. 4-13. Generator isentropic efficiency vs. enthalpy extraction ratio for simulation of HPDE Run 006-014 and simulations with variations in the magnetic field and wall temperature distribution

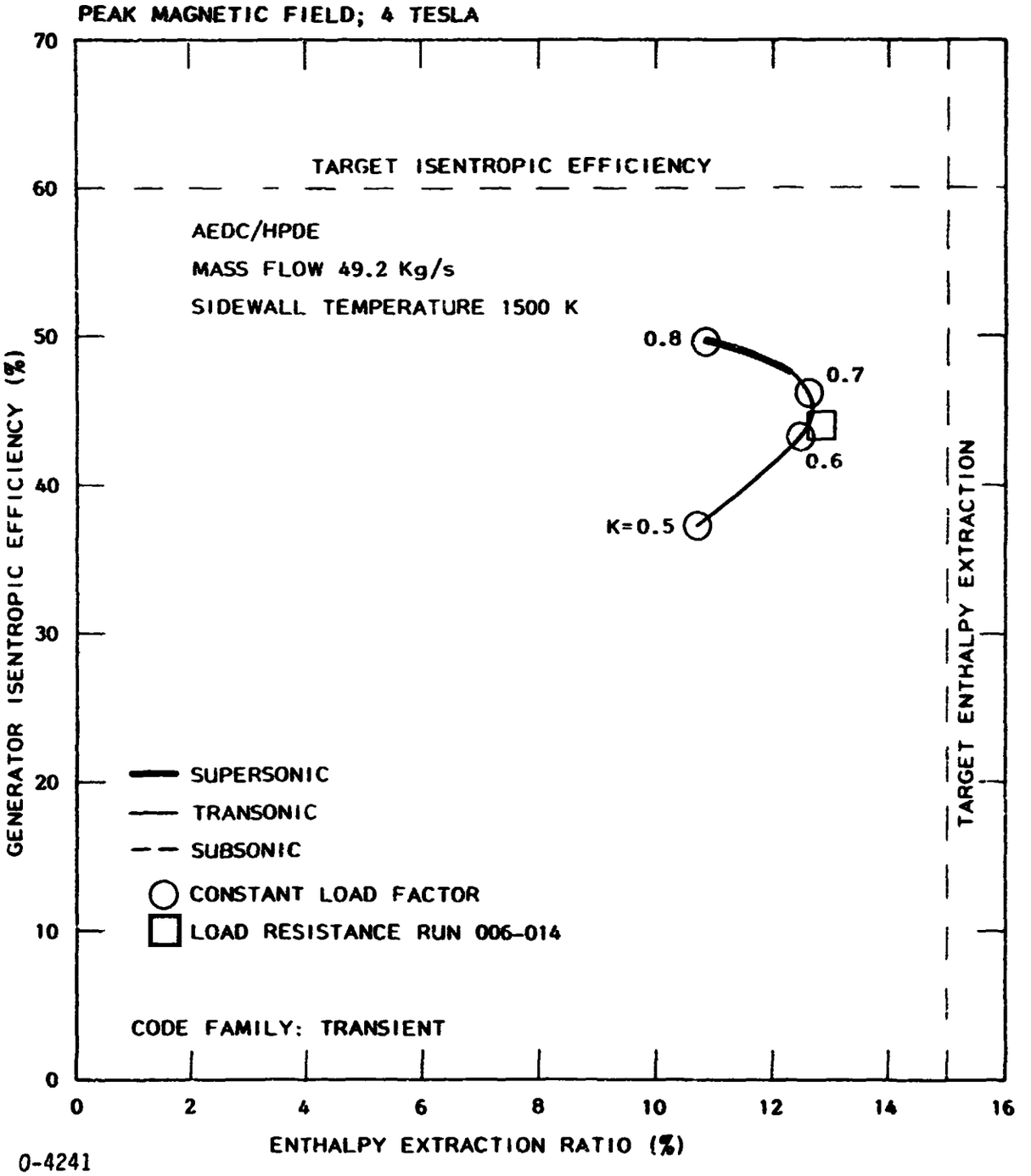

Fig. 4-14. Generator isentropic efficiency vs. enthalpy extraction ratio for simulation of AEDC/HPDE Run 006-014 with variations in load factor and a magnetic field of 4 tesla

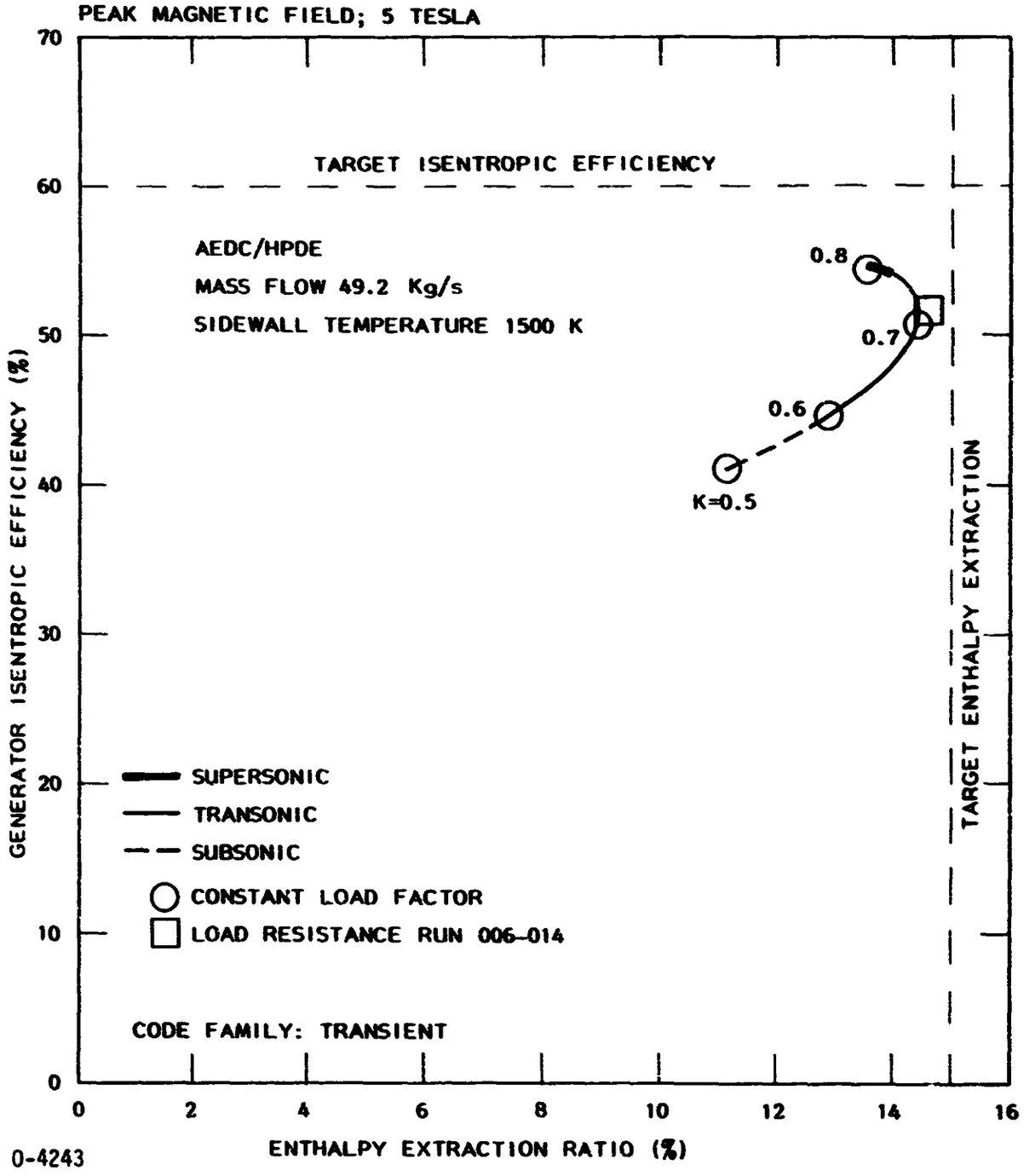

Fig. 4-15. Generator isentropic efficiency vs. enthalpy extraction ratio for simulation of AEDC/HPDE Run 006-014 with variations in load factor and a magnetic field of 5 tesla

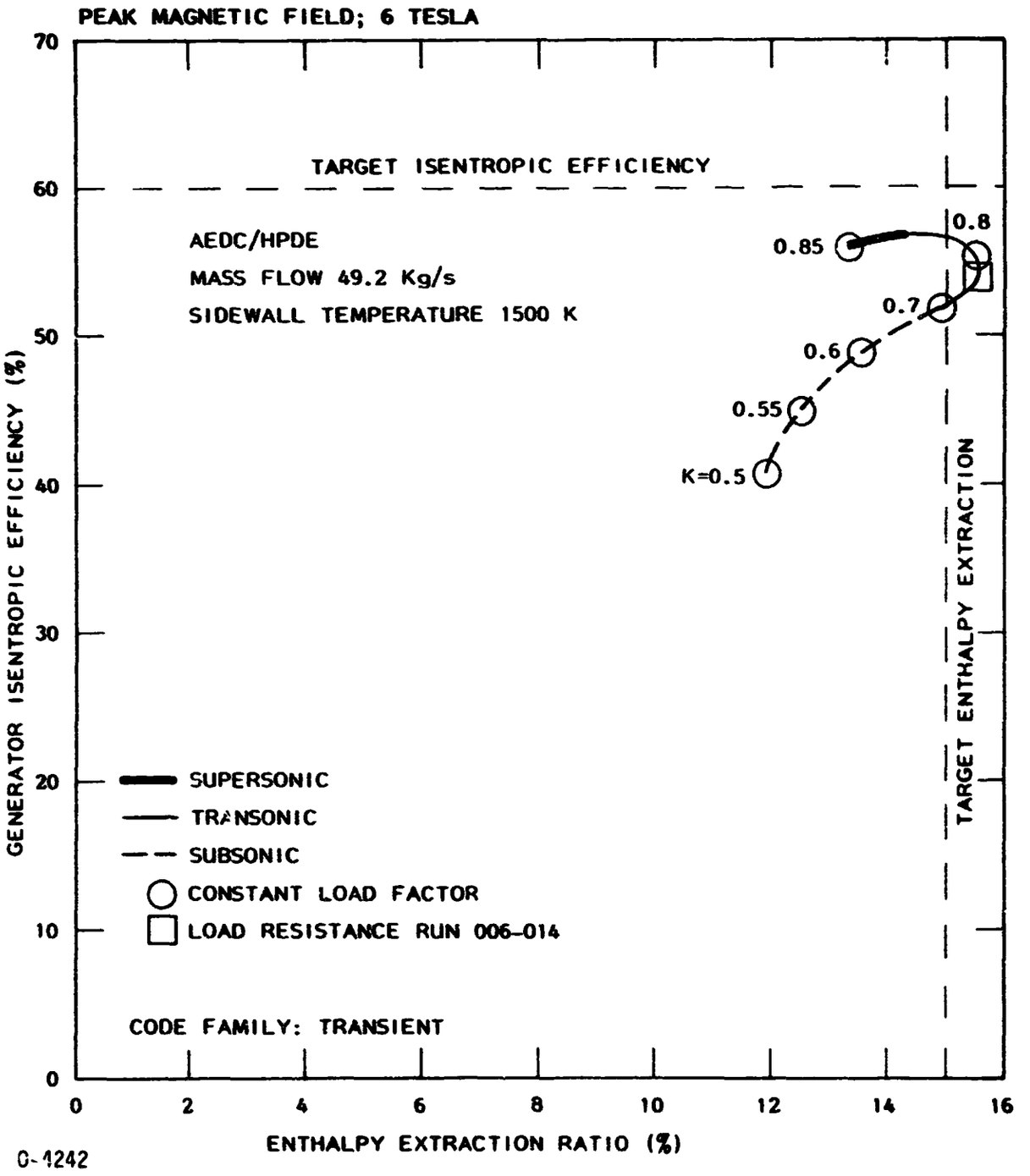

Fig. 4-16. Generator isentropic efficiency vs. enthalpy extraction ratio for simulation of AEDC/HPDE Run 006-014 with variations in load factor and a magnetic field of 6 tesla

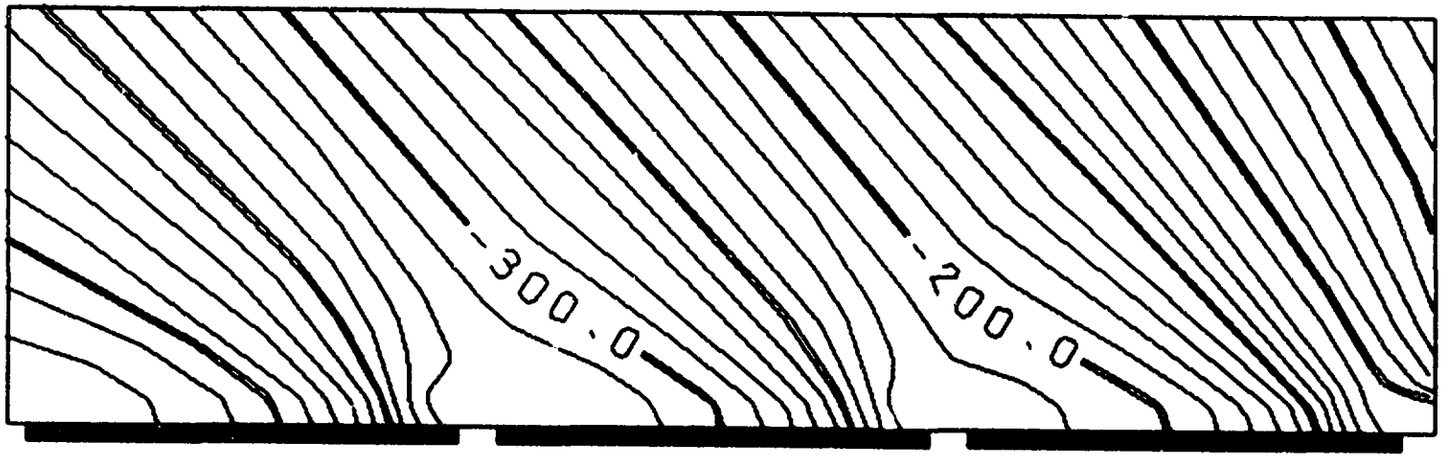

Fig. 4-17. AEDC/HPDE RUN 006-014 SIMULATION - CODE FAMILY: ARRAY. CURRENT STREAMLINES IN THE NEAR-CATHODE REGION AT STATION 77.4 (x = 2.779 M FROM INLET FLANGE)

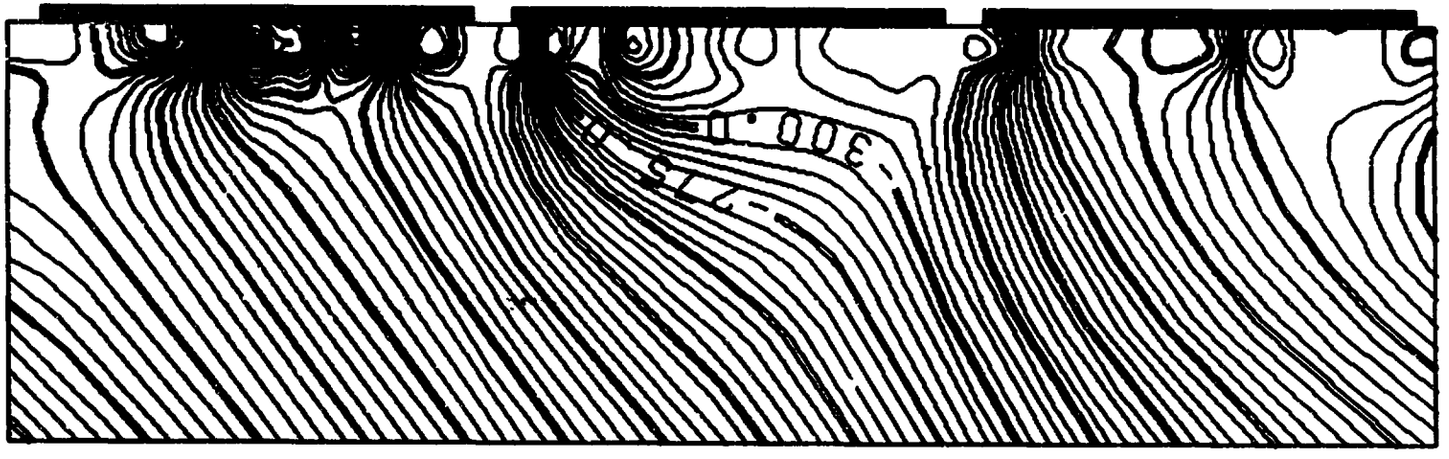

0-4163

Fig. 4-18. AEDC/HPDE RUN 006-014 SIMULATION - CODE FAMILY: ARRAY. CURRENT STREAMLINES IN THE NEAR-ANODE REGION AT STATION 77.4 (x = 2.779 M FROM INLET FLANGE)

ANODE WALL

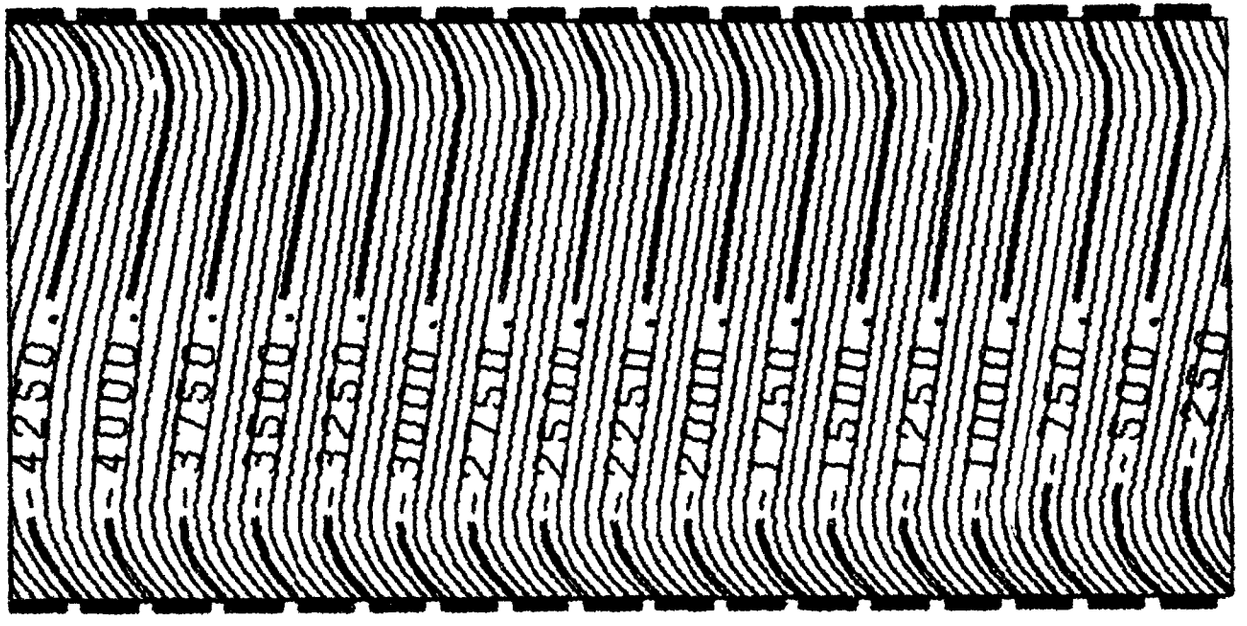

CATHODE WALL

Fig. 4-19. AEDC/HPDE RUN J06-014 SIMULATION - CODE FAMILY: INLET
CURRENT STREAMLINES IN MIDCHANNEL
NO SHORTED LOADS
CONTOUR INTERVAL: 50A/m

0-4177

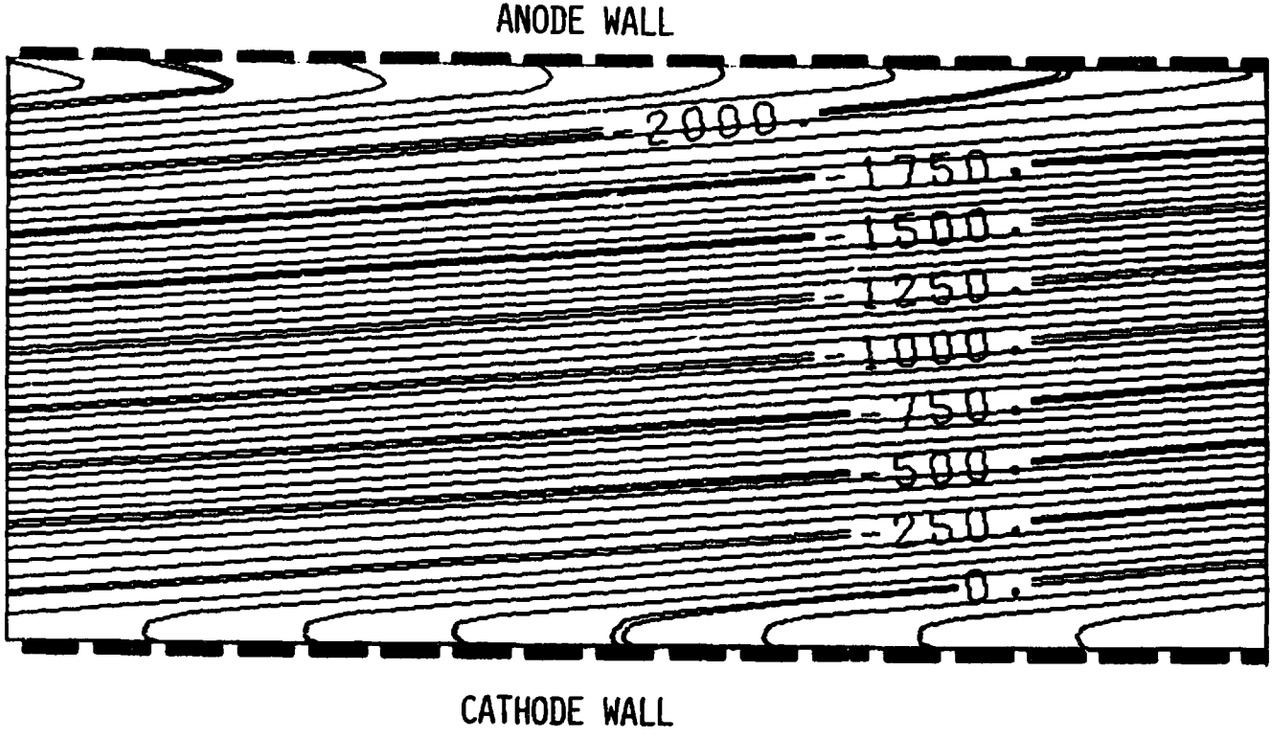

Fig. 4-20. AEDC/HPDE RUN 006/014 SIMULATION - CODE FAMILY: INLET
EQUIPOTENTIALS IN MIDCHANNEL
NO SHORTED LOADS
CONTOUR INTERVAL: 50V

0-4179

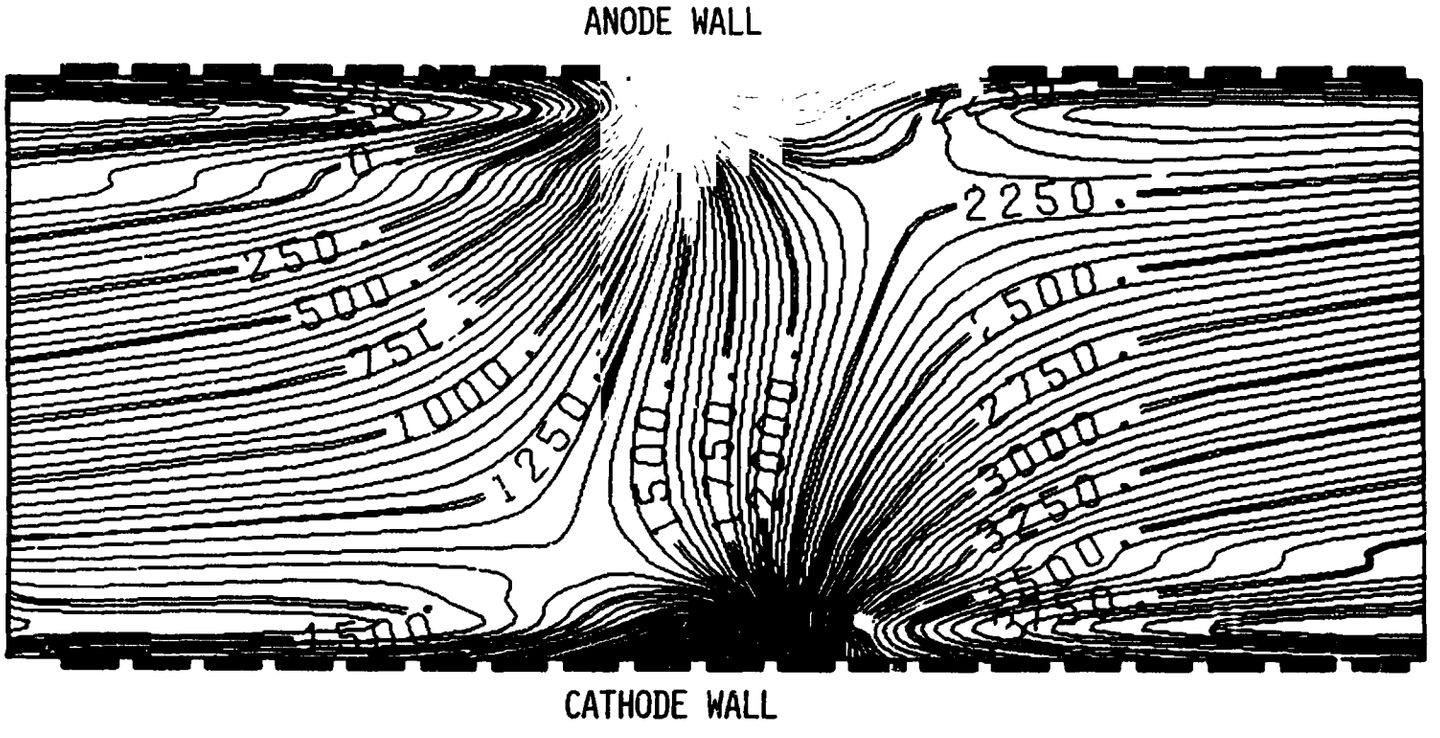

Fig. 4-21. AEDC/HPDE RUN 006-014 SIMULATION - CODE FAMILY: INLET
EQUIPOTENTIALS IN MIDCHANNEL
SINGLE-PAIR FARADAY SHORT
CONTOUR INTERVAL: 50V

0-4178

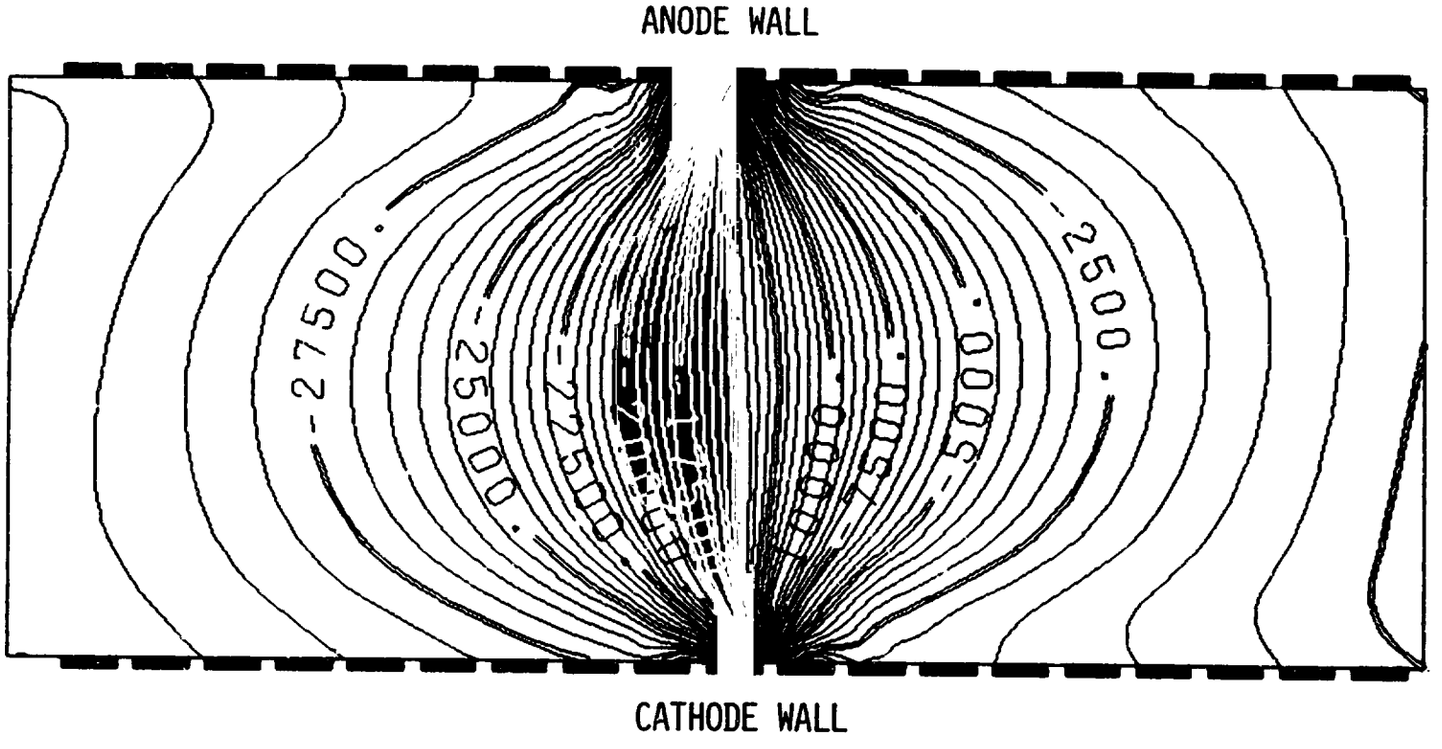

Fig. 4-22. AEDC/HPDE RUN 006-014 SIMULATION - CODE FAMILY: INLET
CURRENT STREAMLINES IN MIDCHANNEL
SINGLE-PAIR FARADAY SHORT
CONTOUR INTERVAL: 500A/m

0-4175

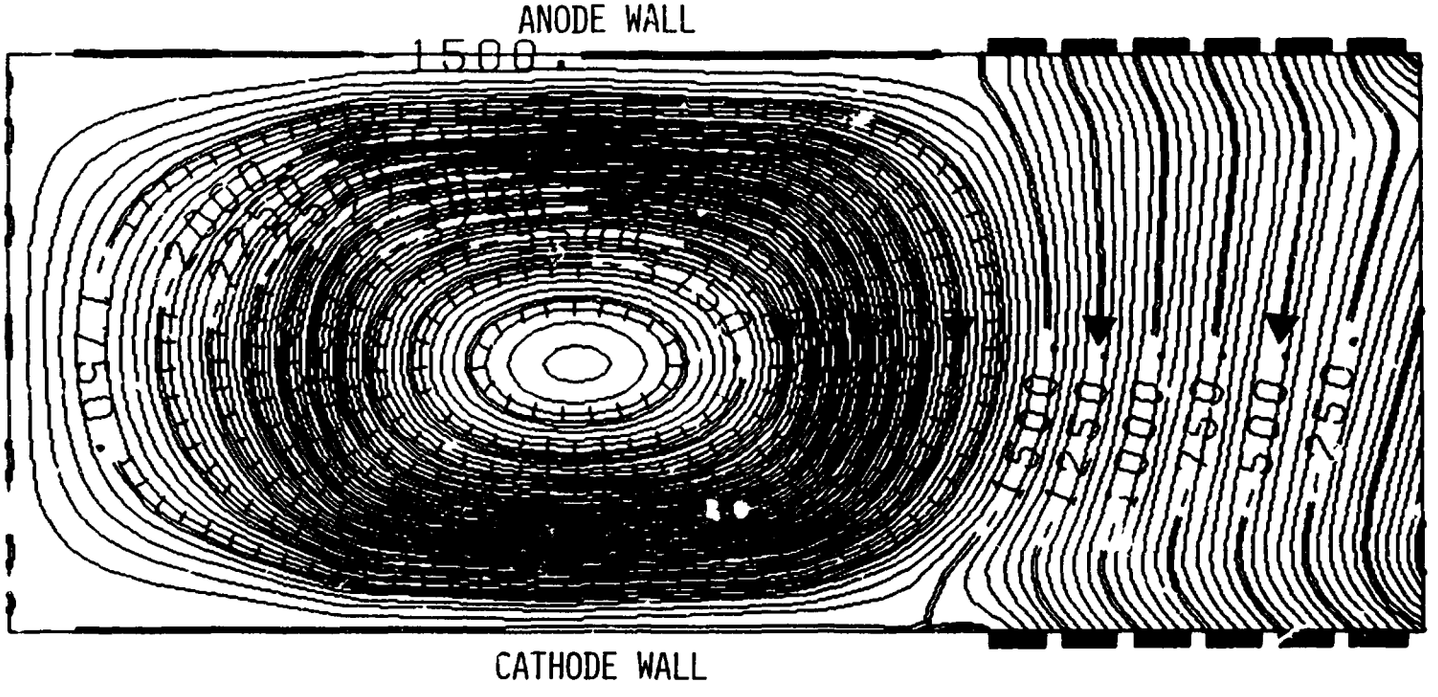

Fig. 4-23. AEDC/HPDE RUN 006-014 SIMULATION - CODE FAMILY: INLET
INLET REGION CURRENT STREAMLINES
CONTOUR INTERVAL: 50A/m

0-4176

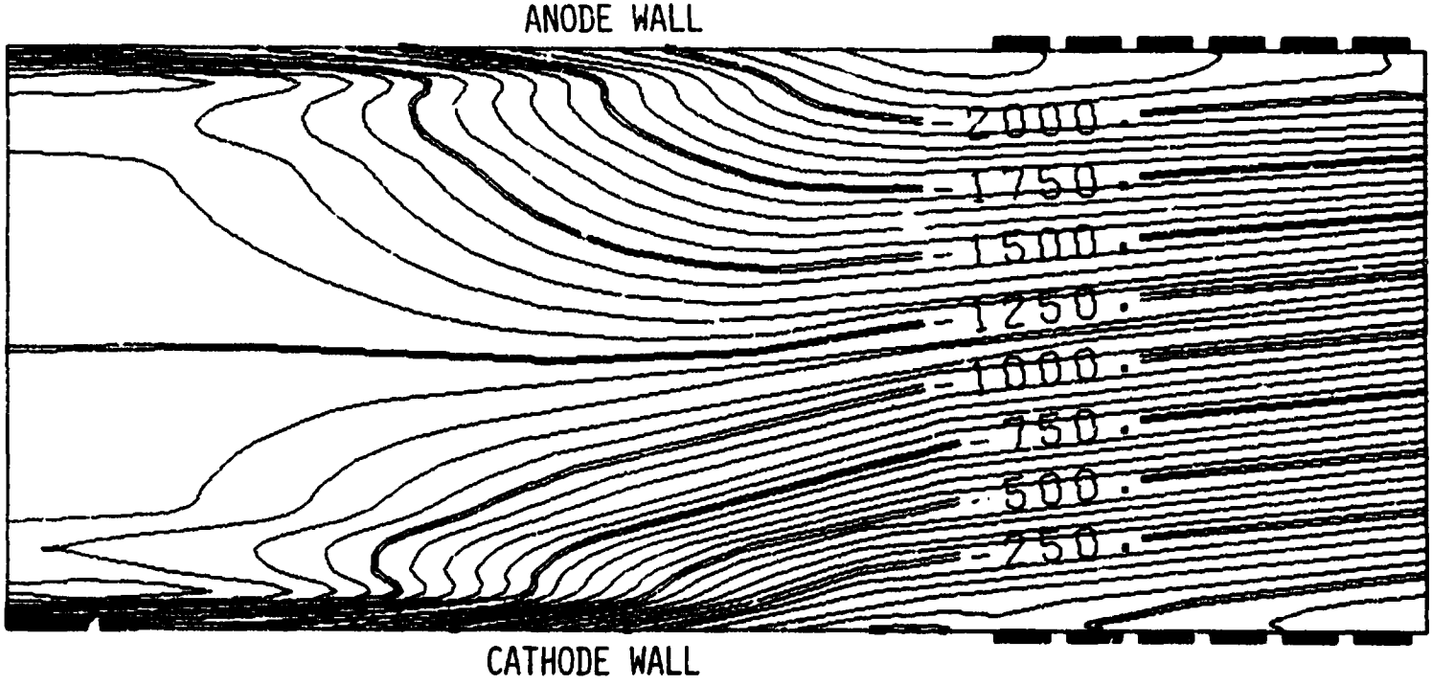

Fig. 4-24. AEDC/HPDE RUN 006-014 SIMULATION - CODE FAMILY: INLET
INLET REGION EQUIPOTENTIALS
CONTOUR INTERVAL: 50V

0-4164

5.0 CRITICAL PHENOMENA FOR THE U.S. U-25 EXPERIMENT

An MHD generator for installation in the Soviet U-25 facility was designed and fabricated in the United States as part of the joint U.S./U.S.S.R. cooperative MHD Program. STD has simulated the "as built" performance of the U.S. U-25 channel to determine the nominal operating performance and to analyze the critical phenomena of this experiment.

5.1 Channel Characterization: U-25 Nominal Operating Conditions

The values of the physical and nominal operating parameters used for simulations of the U.S. U-25 channel are discussed in this section.

5.1.1 Geometry

The major components of the flow train sections of the U.S. U-25 experiment are the KS-3 combustor (Soviet design and fabrication), the U.S. U-25 nozzle and channel assembly, and the U.S. U-25 diffuser assembly. The KS-3 combustor is a cylindrical unit with an inside diameter of 1.7 m [5-1]. It is connected to the main oxidant feed line, which is of 1.5 m inside diameter, by a short conical diffuser section. The combustion zone lies entirely within the conical divider, which is perforated to meter the oxidant flow to the upstream and downstream parts of the combustion zone. The combustion zone and the first exit transition piece is of circular section (1.2 m in diameter) at the inlet and of rectangular section (640 mm by 760 mm) at the exit. The nozzle of the U.S. U-25 flow train assembly is connected directly to the flange at the exit of the first transition piece. The nozzle inlet plan section is 624 mm by 744 mm [5-2]. The nozzle contours are defined by the

753.7 mm tangent radius on the sidewall contour and a straight taper from 744 mm at inlet to 730 mm at nozzle exit on the electrode wall contour. The exit of the nozzle mates directly with the inlet of the channel.

The channel frame number, width, height and diagonalization angle are given as functions of axial distance in Table 5-1 [5-3]. The origin of the axial distance coordinate is the 0-0 station, which corresponds to the front vertical edge of the magnet pole. This coordinate runs through the center of the channel, midway between both the electrode walls and the sidewalls. The U.S. U-25 generator is rectangular along its entire length.

5.1.2 Magnetic Field

The axial distribution of the magnetic flux density is given in Table 5-2 [5-4].

5.1.3 Loading

The U.S. U-25 experiment is planned to be run with a single load at a nominal load current of 2840 A [5-5]. The loading is connected with distributed current collection through diodes (International Rectifier 501VFR200) on frames 1 through 67 on the front end and diodes (International Rectifier 501VFR200) on frames 366 through 432 in the back end [5-3].

5.1.4 Working Fluid

The working fluid for the U.S. U-25 experiment is defined in this section. The mass flow rate for the nominal conditions is 50 kg/s [5-3].

The composition of the fuel is given by volume as [5-4], [5-6]:

CH_4	92.4 - 94.5%
C_2H_6	3.33 - 2.11%
C_3H_8	1.38 - 0.87%
C_4H_{10}	0.36 - 0.14%
CO_2	0.70 - 0.70%
N_2	1.5 - 1.5%
O_2	0.3 - 0.2%

The fuel has a lower heating value of 45.98 to 46.51 MJ/kg and is supplied to the combustor in the gaseous phase at ambient temperature [5-4].

The oxidizer is composed of air enriched with oxygen so that the total oxygen in the mixture is 40% by weight of the combined weight of the air and added oxygen [5-5]. The oxygen for enrichment is assumed to be pure O_2 [5-5]. The air is taken from the atmosphere and has a nominal moisture content of 0.89% by volume (equivalent to 50% relative humidity at 10°C) [5-5]. The total oxidizer flow is preheated to 1200°C before it enters the combustor [5-3], [5-5].

The seed is potassium carbonate in purified water solution [5-5]. The concentration of K_2CO_3 in the water is 1:1 by weight [5-5]. The flow rate of seed is such that K_2CO_3 is 2% of the total mass flow rate [5-5]. The seed solution is injected at ambient temperature [5-5].

For the nominal conditions the combustion is stoichiometric [5-3], [5-5].

5.1.5 Wall Conditions

The combustor wall temperature is 1773 K for all surfaces [5-5]. The nozzle, channel and diffuser wall temperatures are 644 [5-5], 644 to 672 [5-5], and 514 K [5-3], respectively, for each wall and for the entire length of each section. The wall roughness is characterized by an equivalent sand roughness height of 3 mm in the combustor and channel and smooth walls in the nozzle and diffuser.

5.1.6 Channel Inlet Conditions

The conditions at the inlet of the U.S. U-25 are determined by the total mass flow rate, the thermodynamics of the working fluid, the inlet dimensions, and the enthalpy flux. The enthalpy flux was determined by assuming complete combustion and applying a 4.0% heat loss [5-1] for the combustor.

5.1.7 Other Conditions and Assumptions

The design value of the diffuser recovery coefficient is 0.45. The pressure at the end of the diffuser is 2 to 3 kPa below atmospheric [5-5].

5.2 Steady-State Performance for Nominal Design

The U-25 steady-state performance for the nominal design was simulated with the TRANSIENT code family in the quasi-steady mode of operation. The initial computations were performed under the optimistic condition of an assumed conductivity nonuniformity factor of 1.06. This value was taken from preliminary U-25 calculations with the Q3D family of codes performed previously to this contract and corresponds to arc-mode current transport with a critical field of 12 kV/m. Definitions of arc-mode current transport and critical electric field are given in Section 3.3. For the cold walls of the nominal operating conditions, the arc-mode current transport assumption is likely to yield the highest estimate of power output.

Under the nominal conditions, transonic flow is predicted for the U.S. U-25 experiment by computation BRCYKDXJGJ. The axial distributions of the gasdynamic and plasma property variables for the U-25 under the nominal conditions are given in Figs. 5-1 through 5-10. The variables displayed in these figures are grouped into the following classifications: (1) open and short circuit variables; (2) electrical loading, (3) plasma properties; (4) electrical field variables; (5) average gasdynamic variables; (6) electric potential; (7) channel geometry; (8) heat transfer parameters; (9) power extraction parameters; and (10) optimization variables. The origin of the axial coordinate in these figures is the upstream end of the KS-3 combustor. For this axial coordinate system, station 0-0 is located at an axial distance of 2.789 m, the upstream end of the nozzle is located at an axial distance of 2.100 m, the end of the channel is located at an axial distance of 9.851 m, and the end of the diffuser is located at an axial distance of 12.827 m.

Experience with simulations of the HPDE indicate a higher conductivity nonuniformity factor for cold wall channels than was utilized in computation BRCYKDXJGJ. Computation BRCYEHZJGK used the nominal conditions and, in addition, had an assumed conductivity nonuniformity factor of 1.24, which was established from simulations of the HPDE under cold wall conditions. The results of computation BRCYEHZJGK are presented in Figs. 5-11 through 5-20. The variables presented in Figs. 5-11 through 5-20 correspond to the same variables presented in Figs. 5-1 through 5-10. The flow remains transonic and the power output decreases to 7.74 MW (BRCYEHZJGK) from 10.97 MW (BRCYKDXJGJ).

By decreasing the load current to obtain maximum power output, some of the power difference can be recovered. Computation BRCYJCGJGK assumed a conductivity nonuniformity factor of 1.24 and also assumed a load current of 2128 A. The results of computation BRCYJCGJGK are presented in Figs. 5-21 through 5-30. The flow remains transonic, but the power increases to 9.44 MW, which is only slightly below the goal of 10 MW.

The isentropic efficiency is shown in Fig. 5-31 as a function of the gross channel power for these three simulations. This figure illustrates that of these three simulations of the nominal operating conditions only computation BRCYKDXJGJ predicts an output power above the goal of the experiment, but that simulation BRCYJCGJGK, with higher conductivity nonuniformity factor and lower load current, predicts that the output power will be very close to the goal.

5.3 Quasi-Steady Performance as a Function of Mass Flow Rate

A series of five preliminary performance calculations with the nominal conditions, except for mass flow rate, were carried out with the TRANSIENT code family in the quasi-steady mode of operation. The range of mass flow rates was taken to be from 35 to 55 kg/s. The performance of the U-25 over this mass flow rate range was evaluated with an assumed conductivity nonuniformity factor of 1.06. This value was taken from previous preliminary U-25 calculations with the Q3D family of codes and is typical of values obtained with the assumption of arc-mode current transport with a 12 kV/m breakdown criterion in the U-25. The arc-mode current transport assumption is likely to be the most favorable current transport mechanism for cold wall channels and is likely to yield the highest estimate of power output.

The five computations in this series are: A5MYISTIKM, 50 kg/s; A5MYNEPIKN, 45 kg/s; A5MYNGCIKN, 55 kg/s; A5MYONTIKN, 40 kg/s; and A5MYRAWIKN, 35 kg/s.

The transonic flow predicted by these calculations for all mass flow rates above 40 kg/sec is illustrated by Fig. 5-32. Fig. 5-32 shows that the flow chokes from 3.2 m to 6.6 m downstream of the combustor backplate (the origin of axial coordinate for these STD computations) and recovers to atmospheric pressure through a normal shock in the diffuser. Because the power extraction and MHD interaction in these computations are near maximum, it is expected that more conservative assumptions for the wall current transport mechanism will lead to even more supersonic flow conditions.

The power output computed in these preliminary calculations is presented in Fig. 5-33. It is significant that

these prelim nary calculations predict that power output in excess of 10 MW might be achieved even at a mass flow rate of 40 kg/s. It must be reemphasized, however, that these calculations are based on the assumption of the most favorable current transport mechanism for this cold wall channel.

The isentropic efficiency is given as a function of mass flow rate in Fig. 5-34. The maximum value of isentropic efficiency calculated was nearly 40% from A5MYNEPIKN. As is shown in Fig. 5-32, the shock enters the channel for the nominal conditions and for mass flow rates less than 44 kg/s. The decrease in isentropic efficiency caused by the shock entering the active channel is seen in Fig. 5-34.

REFERENCES

[5-1] A. F. Sheindlin, The U-25 MHD Pilot Plant: Major Components and the Long-Duration R-Channel, Institute of High Temperature, Moscow (1975)

[5-2] MEPPSCO Drawing U-25 SOD Channel Rev. N. attached to letter EET/ECP-369, dated 6 July 1979, from E. Doss (ANL) to D. Oliver (STD)

[5-3] Letter EET/ECP-369 and attachments thereto, dated 6 July 1979 from E. Doss (ANL) to D. Oliver (STD)

[5-4] Letter EET/ECP-386, dated 20 July 1979, from E. Doss (ANL) to D. Oliver (STD

[5-5] Coordination Meeting between ANL, NASA LeRC, and STD personnel held at ANL 3 October 1979

[5-6] Letter ENG/PE/4354, dated 1 November 1979 from K. D. Kuczen (ANL) to B. Phillips (NASA LeRC)

TABLE 5-1. Design Data for the U.S. U-25 MHD Generator

FRAME NUMBER	AXIAL DISTANCE (m)	WIDTH (m)	HEIGHT (m)	DIAGONALIZATION ANGLE (radians)
1	-0.10831	0.35507	0.73000	0.39158
2	-0.08873	0.35515	0.73000	0.39812
3	-0.07510	0.35584	0.73000	0.40405
4	-0.06145	0.35624	0.73000	0.41115
5	-0.04774	0.35665	0.73000	0.41764
6	-0.03401	0.35707	0.73000	0.42411
7	-0.02023	0.35751	0.73000	0.43056
8	-0.00641	0.35795	0.73000	0.43699
9	0.00745	0.35840	0.73000	0.44340
10	0.02136	0.35886	0.73000	0.44979
11	0.03530	0.35933	0.73000	0.45617
12	0.04929	0.35981	0.73000	0.46252
13	0.06332	0.36030	0.73000	0.46885
14	0.07739	0.36081	0.73000	0.47516
15	0.09152	0.36133	0.73000	0.48145
16	0.10568	0.36185	0.73000	0.48772
17	0.11990	0.36239	0.73000	0.49397
18	0.13416	0.36294	0.73000	0.50020
19	0.14847	0.36350	0.73000	0.50641
20	0.16283	0.36408	0.73000	0.51259
21	0.17724	0.36466	0.73000	0.51876
22	0.19170	0.36525	0.73000	0.52490
23	0.20621	0.36586	0.73000	0.53102
24	0.22077	0.36647	0.73000	0.53712
25	0.23539	0.36711	0.73000	0.54319
26	0.25005	0.36775	0.73000	0.54925
27	0.26478	0.36840	0.73000	0.55528
28	0.27955	0.36906	0.73000	0.56129
29	0.29438	0.36973	0.73000	0.56728
30	0.30928	0.37041	0.73000	0.57324
31	0.32422	0.37112	0.73000	0.57918
32	0.33922	0.37183	0.73000	0.58510
33	0.35429	0.37255	0.73000	0.59099
34	0.36941	0.37328	0.73000	0.59686
35	0.38459	0.37403	0.73000	0.60271
36	0.39983	0.37479	0.73000	0.60853
37	0.41513	0.37557	0.73000	0.61433
38	0.43050	0.37635	0.73000	0.62011
39	0.44593	0.37715	0.73000	0.62586
40	0.46142	0.37797	0.73000	0.63159
41	0.47698	0.37880	0.73000	0.63729
42	0.49260	0.37965	0.73000	0.64298
43	0.50829	0.38050	0.73000	0.64863
44	0.52404	0.38137	0.73000	0.65427
45	0.53986	0.38224	0.73000	0.65987
46	0.55576	0.38311	0.73000	0.66545
47	0.57172	0.38398	0.73000	0.67101
48	0.58775	0.38486	0.73000	0.67655
49	0.60386	0.38574	0.73000	0.68206
50	0.62003	0.38662	0.73000	0.68754
51	0.63627	0.38750	0.73000	0.69301
52	0.65260	0.38839	0.73000	0.69844
53	0.66899	0.38928	0.73000	0.70386
54	0.68546	0.39017	0.73000	0.70925
55	0.70200	0.39106	0.73000	0.71461
56	0.71863	0.39195	0.73000	0.71994
57	0.73533	0.39285	0.73000	0.72525
58	0.75211	0.39375	0.73000	0.73054
59	0.76896	0.39465	0.73000	0.73580
60	0.78590	0.39555	0.73000	0.74104

9-3336

STD RESEARCH CORPORATION

TABLE 5-1. Design Data for the U.S. U-25 MHD Generator (cont)

FRAME NUMBER	AXIAL DISTANCE (m)	WIDTH (m)	HEIGHT (m)	DIAGONALIZATION ANGLE (radians)
61	0.80292	0.39605	0.73000	0.74025
62	0.82002	0.39736	0.73000	0.75144
63	0.83720	0.39826	0.73000	0.75859
64	0.85447	0.39917	0.73000	0.76173
65	0.87182	0.40009	0.73000	0.76685
66	0.88925	0.40100	0.73000	0.77195
67	0.90677	0.40192	0.73000	0.77700
68	0.92439	0.40284	0.73000	0.78203
69	0.94208	0.40350	0.73048	0.78497
70	0.95912	0.40381	0.73152	0.78540
71	0.97547	0.40401	0.73270	0.78540
72	0.99181	0.40421	0.73388	0.78540
73	1.00816	0.40442	0.73506	0.78540
74	1.02451	0.40462	0.73623	0.78540
75	1.04085	0.40483	0.73741	0.78540
76	1.05720	0.40503	0.73859	0.78540
77	1.07354	0.40524	0.73977	0.78540
78	1.08988	0.40545	0.74094	0.78540
79	1.10623	0.40566	0.74212	0.78540
80	1.12257	0.40587	0.74330	0.78540
81	1.13892	0.40608	0.74448	0.78540
82	1.15526	0.40629	0.74565	0.78540
83	1.17161	0.40650	0.74683	0.78540
84	1.18795	0.40672	0.74801	0.78540
85	1.20429	0.40693	0.74919	0.78540
86	1.22064	0.40715	0.75036	0.78540
87	1.23698	0.40736	0.75154	0.78540
88	1.25333	0.40758	0.75272	0.78540
89	1.26967	0.40780	0.75390	0.78540
90	1.28601	0.40802	0.75508	0.78540
91	1.30236	0.40824	0.75625	0.78540
92	1.31870	0.40846	0.75743	0.78540
93	1.33505	0.40868	0.75861	0.78540
94	1.35139	0.40891	0.75978	0.78540
95	1.36773	0.40913	0.76096	0.78540
96	1.38408	0.40935	0.76214	0.78540
97	1.40042	0.40958	0.76332	0.78540
98	1.41677	0.40981	0.76450	0.78540
99	1.43311	0.41003	0.76567	0.78540
100	1.44946	0.41026	0.76685	0.78540
101	1.46580	0.41050	0.76803	0.78540
102	1.48214	0.41073	0.76921	0.78540
103	1.49849	0.41097	0.77038	0.78540
104	1.51483	0.41120	0.77156	0.78540
105	1.53118	0.41144	0.77274	0.78540
106	1.54752	0.41168	0.77392	0.78540
107	1.56386	0.41192	0.77509	0.78540
108	1.58021	0.41216	0.77627	0.78540
109	1.59655	0.41240	0.77745	0.78540
110	1.61290	0.41264	0.77863	0.78540
111	1.62924	0.41288	0.77980	0.78540
112	1.64558	0.41313	0.78098	0.78540
113	1.66193	0.41337	0.78216	0.78540
114	1.67827	0.41362	0.78334	0.78540
115	1.69462	0.41386	0.78451	0.78540
116	1.71096	0.41411	0.78569	0.78540
117	1.72731	0.41436	0.78687	0.78540
118	1.74365	0.41461	0.78805	0.78540
119	1.75999	0.41486	0.78922	0.78540
120	1.77634	0.41511	0.79040	0.78540

TABLE 5-1. Design Data for the U.S. U-25 MHD Generator (cont)

FRAME NUMBER	AXIAL DISTANCE (m)	WIDTH (m)	HEIGHT (m)	DIAGONALIZATION ANGLE (radians)
181	1.79268	0.41536	0.79158	0.78540
182	1.80903	0.41562	0.79276	0.78540
183	1.82537	0.41587	0.79393	0.78540
184	1.84171	0.41613	0.79511	0.78540
185	1.85806	0.41638	0.79629	0.78540
186	1.87440	0.41664	0.79747	0.78540
187	1.89075	0.41690	0.79864	0.78540
188	1.90709	0.41716	0.79982	0.78540
189	1.92343	0.41742	0.80100	0.78540
190	1.93978	0.41768	0.80218	0.78540
191	1.95612	0.41795	0.80335	0.78540
192	1.97247	0.41821	0.80453	0.78540
193	1.98881	0.41848	0.80571	0.78540
194	2.00516	0.41874	0.80689	0.78540
195	2.02150	0.41901	0.80806	0.78540
196	2.03784	0.41928	0.80924	0.78540
197	2.05419	0.41955	0.81042	0.78540
198	2.07053	0.41982	0.81160	0.78540
199	2.08688	0.42009	0.81277	0.78540
200	2.10322	0.42036	0.81395	0.78540
201	2.11956	0.42064	0.81513	0.78540
202	2.13591	0.42091	0.81631	0.78540
203	2.15225	0.42119	0.81748	0.78540
204	2.16860	0.42146	0.81866	0.78540
205	2.18494	0.42174	0.81984	0.78540
206	2.20128	0.42202	0.82102	0.78540
207	2.21763	0.42230	0.82219	0.78540
208	2.23397	0.42258	0.82337	0.78540
209	2.25032	0.42287	0.82455	0.78540
210	2.26666	0.42315	0.82573	0.78540
211	2.28301	0.42344	0.82691	0.78540
212	2.29935	0.42371	0.82808	0.78540
213	2.31569	0.42399	0.82926	0.78540
214	2.33204	0.42427	0.83044	0.78540
215	2.34838	0.42456	0.83161	0.78540
216	2.36473	0.42485	0.83279	0.78540
217	2.38107	0.42513	0.83397	0.78540
218	2.39741	0.42542	0.83515	0.78540
219	2.41376	0.42571	0.83632	0.78540
220	2.43010	0.42600	0.83750	0.78540
221	2.44645	0.42630	0.83868	0.78540
222	2.46279	0.42659	0.83986	0.78540
223	2.47913	0.42689	0.84103	0.78540
224	2.49548	0.42718	0.84221	0.78540
225	2.51182	0.42748	0.84339	0.78540
226	2.52817	0.42778	0.84457	0.78540
227	2.54451	0.42808	0.84574	0.78540
228	2.56086	0.42838	0.84692	0.78540
229	2.57720	0.42869	0.84810	0.78540
230	2.59354	0.42899	0.84928	0.78540
231	2.60989	0.42929	0.85045	0.78540
232	2.62623	0.42960	0.85163	0.78540
233	2.64258	0.42991	0.85281	0.78540
234	2.65892	0.43022	0.85399	0.78540
235	2.67526	0.43053	0.85516	0.78540
236	2.69161	0.43084	0.85634	0.78540
237	2.70795	0.43115	0.85752	0.78540
238	2.72430	0.43147	0.85870	0.78540
239	2.74064	0.43178	0.85987	0.78540
240	2.75698	0.43210	0.86105	0.78540

TABLE 5-1. Design Data for the U.S. U-25 MHD Generator (cont)

FRAME NUMBER	AXIAL DISTANCE (m)	WIDTH (m)	HEIGHT (m)	DIAGONALIZATION ANGLE (radians)
1A1	2.77333	0.43272	0.86223	0.78540
1A2	2.78967	0.43274	0.86341	0.78540
1A3	2.80602	0.43306	0.86458	0.78540
1A4	2.82236	0.43338	0.86576	0.78540
1A5	2.83871	0.43371	0.86694	0.78540
1A6	2.85505	0.43403	0.86812	0.78540
1A7	2.87139	0.43436	0.86929	0.78540
1A8	2.88774	0.43469	0.87047	0.78540
1A9	2.90408	0.43501	0.87165	0.78540
100	2.92043	0.43534	0.87283	0.78540
101	2.93677	0.43568	0.87400	0.78540
102	2.95311	0.43601	0.87518	0.78540
103	2.96946	0.43635	0.87636	0.78540
104	2.98580	0.43668	0.87754	0.78540
105	3.00215	0.43702	0.87871	0.78540
106	3.01849	0.43736	0.87989	0.78540
107	3.03483	0.43770	0.88107	0.78540
108	3.05118	0.43804	0.88225	0.78540
109	3.06752	0.43839	0.88343	0.78540
200	3.08387	0.43873	0.88460	0.78540
201	3.10021	0.43908	0.88578	0.78540
202	3.11656	0.43942	0.88696	0.78540
203	3.13290	0.43977	0.88814	0.78540
204	3.14924	0.44012	0.88931	0.78540
205	3.16559	0.44047	0.89049	0.78540
206	3.18193	0.44083	0.89167	0.78540
207	3.19828	0.44118	0.89285	0.78540
208	3.21462	0.44154	0.89402	0.78540
209	3.23096	0.44190	0.89520	0.78540
210	3.24731	0.44226	0.89638	0.78540
211	3.26365	0.44262	0.89756	0.78540
212	3.28000	0.44298	0.89873	0.78540
213	3.29634	0.44335	0.89991	0.78540
214	3.31268	0.44371	0.90109	0.78540
215	3.32903	0.44408	0.90227	0.78540
216	3.34537	0.44445	0.90344	0.78540
217	3.36172	0.44482	0.90462	0.78540
218	3.37806	0.44519	0.90580	0.78540
219	3.39441	0.44556	0.90698	0.78540
220	3.41075	0.44594	0.90815	0.78540
221	3.42709	0.44631	0.90933	0.78540
222	3.44344	0.44669	0.91051	0.78540
223	3.45978	0.44707	0.91169	0.78540
224	3.47613	0.44745	0.91286	0.78540
225	3.49247	0.44783	0.91404	0.78540
226	3.50881	0.44821	0.91522	0.78540
227	3.52516	0.44860	0.91640	0.78540
228	3.54150	0.44899	0.91757	0.78540
229	3.55785	0.44939	0.91875	0.78540
230	3.57419	0.44979	0.91993	0.78540
231	3.59053	0.45018	0.92111	0.78540
232	3.60688	0.45058	0.92228	0.78540
233	3.62322	0.45098	0.92346	0.78540
234	3.63957	0.45138	0.92464	0.78540
235	3.65591	0.45178	0.92582	0.78540
236	3.67225	0.45219	0.92699	0.78540
237	3.68860	0.45260	0.92817	0.78540
238	3.70494	0.45300	0.92935	0.78540
239	3.72129	0.45342	0.93053	0.78540
240	3.73763	0.45383	0.93170	0.78540

9-3338

STD RESEARCH CORPORATION

TABLE 5-1. Design Data for the U.S. U-25 MHD Generator (cont)

FRAME NUMBER	AXIAL DISTANCE (m)	WIDTH (m)	HEIGHT (m)	DIAGONALIZATION ANGLE (radians)
2a1	3.75398	0.45424	0.93288	0.78540
2a2	3.77632	0.45466	0.93400	0.78540
2a3	3.78666	0.45508	0.93524	0.78540
2a4	3.80301	0.45550	0.93641	0.78540
2a5	3.81935	0.45592	0.93759	0.78540
2a6	3.83570	0.45634	0.93877	0.78540
2a7	3.85204	0.45676	0.93995	0.78540
2a8	3.86838	0.45719	0.94112	0.78540
2a9	3.88473	0.45761	0.94230	0.78540
2a0	3.90107	0.45804	0.94348	0.78540
2b1	3.91742	0.45848	0.94466	0.78540
2b2	3.93376	0.45891	0.94583	0.78540
2b3	3.95010	0.45933	0.94701	0.78540
2b4	3.96645	0.45977	0.94819	0.78540
2b5	3.98279	0.46021	0.94937	0.78540
2b6	3.99914	0.46064	0.95055	0.78540
2b7	4.01547	0.46108	0.95172	0.78540
2b8	4.03182	0.46151	0.95290	0.78540
2b9	4.04817	0.46197	0.95408	0.78540
2b0	4.06450	0.46241	0.95525	0.78540
2c1	4.08086	0.46286	0.95643	0.78540
2c2	4.09720	0.46331	0.95761	0.78540
2c3	4.11354	0.46376	0.95879	0.78540
2c4	4.12989	0.46421	0.95996	0.78540
2c5	4.14622	0.46467	0.96114	0.78540
2c6	4.16257	0.46512	0.96232	0.78540
2c7	4.17892	0.46558	0.96350	0.78540
2c8	4.19526	0.46604	0.96467	0.78540
2c9	4.21161	0.46650	0.96585	0.78540
2c0	4.22795	0.46697	0.96703	0.78540
2d1	4.24429	0.46743	0.96821	0.78540
2d2	4.26064	0.46790	0.96938	0.78540
2d3	4.27698	0.46837	0.97056	0.78540
2d4	4.29332	0.46884	0.97174	0.78540
2d5	4.30967	0.46931	0.97292	0.78540
2d6	4.32601	0.46979	0.97409	0.78540
2d7	4.34236	0.47027	0.97527	0.78540
2d8	4.35870	0.47075	0.97645	0.78540
2d9	4.37504	0.47123	0.97763	0.78540
2d0	4.39139	0.47171	0.97880	0.78540
2e1	4.40773	0.47220	0.97998	0.78540
2e2	4.42407	0.47269	0.98116	0.78540
2e3	4.44042	0.47318	0.98234	0.78540
2e4	4.45676	0.47367	0.98351	0.78540
2e5	4.47312	0.47416	0.98469	0.78540
2e6	4.48945	0.47466	0.98587	0.78540
2e7	4.50579	0.47515	0.98705	0.78540
2e8	4.52214	0.47565	0.98822	0.78540
2e9	4.53848	0.47615	0.98940	0.78540
2e0	4.55482	0.47666	0.99058	0.78540
2f1	4.57117	0.47717	0.99176	0.78540
2f2	4.58751	0.47768	0.99293	0.78540
2f3	4.60387	0.47819	0.99411	0.78540
2f4	4.62020	0.47870	0.99529	0.78540
2f5	4.63656	0.47921	0.99647	0.78540
2f6	4.65289	0.47972	0.99764	0.78540
2f7	4.66923	0.48025	0.99882	0.78540
2f8	4.68559	0.48077	1.00000	0.78540
2f9	4.70192	0.48131	1.00118	0.78540
2f0	4.71826	0.48185	1.00235	0.78540

TABLE 5-1. Design Data for the U.S. U-25 MHD Generator (cont)

FRAME NUMBER	AXIAL DISTANCE (m)	WIDTH (m)	HEIGHT (m)	DIAGONALIZATION ANGLE (radians)
301	4.73402	0.48237	1.00353	0.78540
302	4.75096	0.48293	1.00471	0.78540
303	4.76731	0.48347	1.00589	0.78540
304	4.78364	0.48401	1.00706	0.78540
305	4.79999	0.48455	1.00824	0.78540
306	4.81634	0.48510	1.00942	0.78540
307	4.83268	0.48564	1.01060	0.78540
308	4.84903	0.48621	1.01177	0.78540
309	4.86537	0.48677	1.01295	0.78540
310	4.88171	0.48733	1.01413	0.78540
311	4.89806	0.48789	1.01531	0.78540
312	4.91440	0.48846	1.01648	0.78540
313	4.93074	0.48902	1.01766	0.78540
314	4.94709	0.48960	1.01884	0.78540
315	4.96343	0.49017	1.02002	0.78540
316	4.97978	0.49075	1.02120	0.78540
317	4.99612	0.49133	1.02237	0.78540
318	5.01246	0.49192	1.02355	0.78540
319	5.02881	0.49251	1.02473	0.78540
320	5.04515	0.49311	1.02591	0.78540
321	5.06149	0.49371	1.02709	0.78540
322	5.07855	0.49435	1.02831	0.78363
323	5.09629	0.49502	1.02959	0.78008
324	5.11390	0.49569	1.03087	0.77653
325	5.13157	0.49637	1.03213	0.77297
326	5.14913	0.49706	1.03340	0.76940
327	5.16661	0.49775	1.03466	0.76583
328	5.18405	0.49845	1.03591	0.76224
329	5.20141	0.49915	1.03717	0.75865
330	5.21873	0.49985	1.03841	0.75505
331	5.23598	0.50056	1.03965	0.75145
332	5.25318	0.50128	1.04089	0.74783
333	5.27031	0.50200	1.04213	0.74421
334	5.28739	0.50274	1.04336	0.74057
335	5.30441	0.50348	1.04458	0.73693
336	5.32138	0.50423	1.04581	0.73328
337	5.33829	0.50497	1.04703	0.72963
338	5.35514	0.50573	1.04824	0.72597
339	5.37194	0.50648	1.04945	0.72230
340	5.38868	0.50725	1.05065	0.71863
341	5.40538	0.50801	1.05186	0.71495
342	5.42202	0.50878	1.05306	0.71125
343	5.43860	0.50956	1.05425	0.70755
344	5.45513	0.51035	1.05544	0.70384
345	5.47162	0.51114	1.05663	0.70013
346	5.48804	0.51193	1.05781	0.69641
347	5.50442	0.51273	1.05899	0.69268
348	5.52074	0.51354	1.06017	0.68895
349	5.53702	0.51435	1.06135	0.68521
350	5.55324	0.51516	1.06251	0.68145
351	5.56942	0.51598	1.06368	0.67770
352	5.58555	0.51677	1.06484	0.67396
353	5.60163	0.51759	1.06600	0.67018
354	5.61766	0.51843	1.06715	0.66639
355	5.63364	0.51925	1.06830	0.66261
356	5.64957	0.52009	1.06945	0.65881
357	5.66546	0.52093	1.07059	0.65501
358	5.68131	0.52177	1.07173	0.65121
359	5.69710	0.52263	1.07287	0.64739
360	5.71285	0.52347	1.07413	0.64357

9-3341

STD RESEARCH CORPORATION

TABLE 5-1. Design Data for the U.S. U-25 MHD Generator (cont)

FRAME NUMBER	AXIAL DISTANCE (m)	WIDTH (m)	HEIGHT (m)	DIAGONALIZATION ANGLE (radians)
3e1	5.72859	0.52542	1.07941	0.63575
3e2	5.74422	0.52684	1.07668	0.63591
3e3	5.75983	0.52830	1.07795	0.63207
3e4	5.77540	0.52973	1.07923	0.62823
3e5	5.79094	0.53116	1.08049	0.62437
3e6	5.80642	0.53259	1.08175	0.62051
3e7	5.82186	0.53401	1.08301	0.61664
3e8	5.83726	0.53542	1.08427	0.61277
3e9	5.85261	0.53684	1.08552	0.60888
3f0	5.86793	0.53825	1.08677	0.60499
3f1	5.88320	0.53965	1.08801	0.60110
3f2	5.89843	0.54106	1.08925	0.59720
3f3	5.91363	0.54246	1.09049	0.59329
3f4	5.92879	0.54385	1.09172	0.58938
3f5	5.94390	0.54525	1.09296	0.58546
3f6	5.95897	0.54663	1.09418	0.58154
3f7	5.97400	0.54802	1.09541	0.57760
3f8	5.98901	0.54940	1.09664	0.57366
3f9	6.00396	0.55077	1.09785	0.56972
3g0	6.01887	0.55215	1.09907	0.56577
3g1	6.03374	0.55352	1.10028	0.56181
3g2	6.04861	0.55488	1.10149	0.55785
3g3	6.06341	0.55625	1.10269	0.55387
3g4	6.07818	0.55761	1.10390	0.54990
3g5	6.09291	0.55896	1.10511	0.54592
3g6	6.10762	0.56032	1.10630	0.54194
3g7	6.12228	0.56167	1.10750	0.53794
3g8	6.13691	0.56302	1.10869	0.53394
3g9	6.15151	0.56437	1.10987	0.52994
3h0	6.16607	0.56570	1.11106	0.52593
3h1	6.18059	0.56704	1.11224	0.52192
3h2	6.19507	0.56838	1.11343	0.51789
3h3	6.20950	0.56971	1.11461	0.51386
3h4	6.22390	0.57104	1.11578	0.50984
3h5	6.23826	0.57236	1.11695	0.50580
3h6	6.25272	0.57368	1.11812	0.50176
3h7	6.26705	0.57500	1.11929	0.49771
3h8	6.28135	0.57632	1.12045	0.49366
3h9	6.29561	0.57763	1.12162	0.48960
4g0	6.30985	0.57894	1.12278	0.48554
4g1	6.32406	0.58025	1.12394	0.48147
4g2	6.33822	0.58156	1.12509	0.47739
4g3	6.35237	0.58286	1.12624	0.47331
4g4	6.36648	0.58416	1.12739	0.46923
4g5	6.38056	0.58546	1.12854	0.46515
4g6	6.39462	0.58675	1.12968	0.46105
4g7	6.40865	0.58805	1.13083	0.45695
4g8	6.42265	0.58933	1.13196	0.45285
4g9	6.43662	0.59062	1.13311	0.44875
4h0	6.45057	0.59190	1.13425	0.44464
4h1	6.46448	0.59318	1.13538	0.44052
4h2	6.47836	0.59446	1.13651	0.43640
4h3	6.49222	0.59574	1.13764	0.43228
4h4	6.50606	0.59701	1.13877	0.42815
4h5	6.51987	0.59828	1.13990	0.42402
4h6	6.53365	0.59955	1.14102	0.41988
4h7	6.54741	0.60082	1.14214	0.41574
4h8	6.56114	0.60208	1.14326	0.41160
4h9	6.57485	0.60335	1.14437	0.40744
4i0	6.58855	0.60461	1.14549	0.40329

9-3342

STD RESEARCH CORPORATION

TABLE 5-1. Design Data for the U.S. U-25 MHD Generator (cont)

FRAME NUMBER	AXIAL DISTANCE (m)	WIDTH (m)	HEIGHT (m)	DIAGONALIZATION ANGLE (radians)
451	6.00219	0.60586	1.14660	0.39914
452	6.01502	0.60712	1.14772	0.39498
453	6.02943	0.60859	1.14883	0.39081
454	6.04302	0.60962	1.14993	0.38665
455	6.05658	0.61088	1.15104	0.38248
456	6.07012	0.61212	1.15214	0.37830
457	6.08364	0.61337	1.15324	0.37412
458	6.09714	0.61461	1.15434	0.36994
459	6.71061	0.61585	1.15544	0.36576
460	6.72406	0.61709	1.15654	0.36157
461	6.73749	0.61832	1.15763	0.35738
462	6.75091	0.61956	1.15872	0.35319
463	6.76429	0.62079	1.15981	0.34899
464	6.77765	0.62202	1.16090	0.34479
465	6.79101	0.62325	1.16199	0.34059
466	6.80433	0.62448	1.16307	0.33639
467	6.81764	0.62570	1.16416	0.33218
468	6.83092	0.62693	1.16525	0.32797
469	6.84419	0.62815	1.16633	0.32375
460	6.85745	0.62937	1.16741	0.31954
461	6.87068	0.63059	1.16848	0.31532
462	6.88389	0.63180	1.16956	0.31110
463	6.89709	0.63302	1.17063	0.30688
464	6.91027	0.63414	1.17166	0.30265
465	6.92342	0.63514	1.17262	0.29843
466	6.93656	0.63615	1.17356	0.29420
467	6.94969	0.63706	1.17449	0.28997
468	6.96280	0.63801	1.17543	0.28575
469	6.9759[illegible]	0.63897	1.17636	0.28150
470	6.98697	0.63993	1.17729	0.27726
471	7.00203	0.64088	1.17822	0.27302
472	7.01508	0.64187	1.[illegible]	0.26878
473	7.02811	0.64278	1.1806	0.26454
474	7.04112	0.64373	1.18101	0.26030
475	7.05411	0.64467	1.18199	0.25605

9-3343

STD RESEARCH CORPORATION

TABLE 5-2

The U.S. U-25 1-D Magnetic Field Distribution

X(m)	B(T)	X(m)	B(T)
-1.5	0.1	5.1	1.99
-1.4	0.11	5.2	1.98
-1.3	0.12	5.3	1.96
-1.2	0.14	5.4	1.92
-1.1	0.18	5.5	1.88
-1.0	0.23	5.6	1.85
-0.9	0.3	5.7	1.75
-0.8	0.39	5.8	1.62
-0.7	0.52	5.9	1.48
-0.6	0.68	6.0	1.38
-0.5	0.83	6.1	1.22
-0.4	0.97	6.2	1.12
-0.3	1.13	6.3	1.0
-0.2	1.28	6.4	0.92
-0.1	1.4	6.5	0.86
0.0	1.55	6.6	0.79
0.1	1.72	6.7	0.73
0.2	1.81	6.8	0.66
0.3	1.88	6.9	0.6
0.4	1.9	7.0	0.54
0.5	1.94	7.1	0.5
0.6	1.97	7.2	0.45
0.7	1.98	7.3	0.41
0.8	1.99	7.4	0.36
0.9-5.0	2.0	7.5	0.33

0-4303

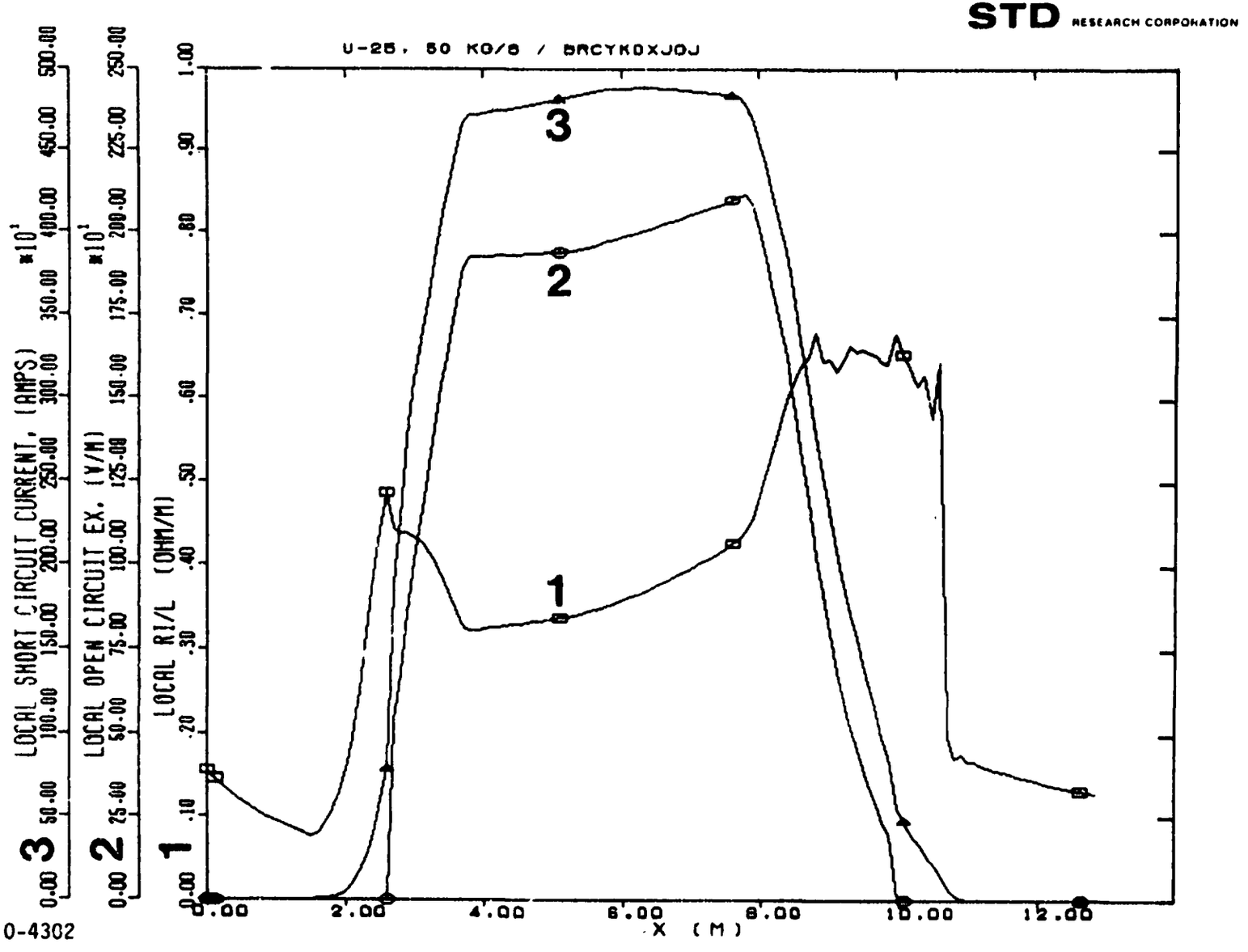

Fig.3-1. Axial variation of open and short circuit variables in the U-25 at 50 kg/s operating conditions. STD computation BRCYKDXJGJ

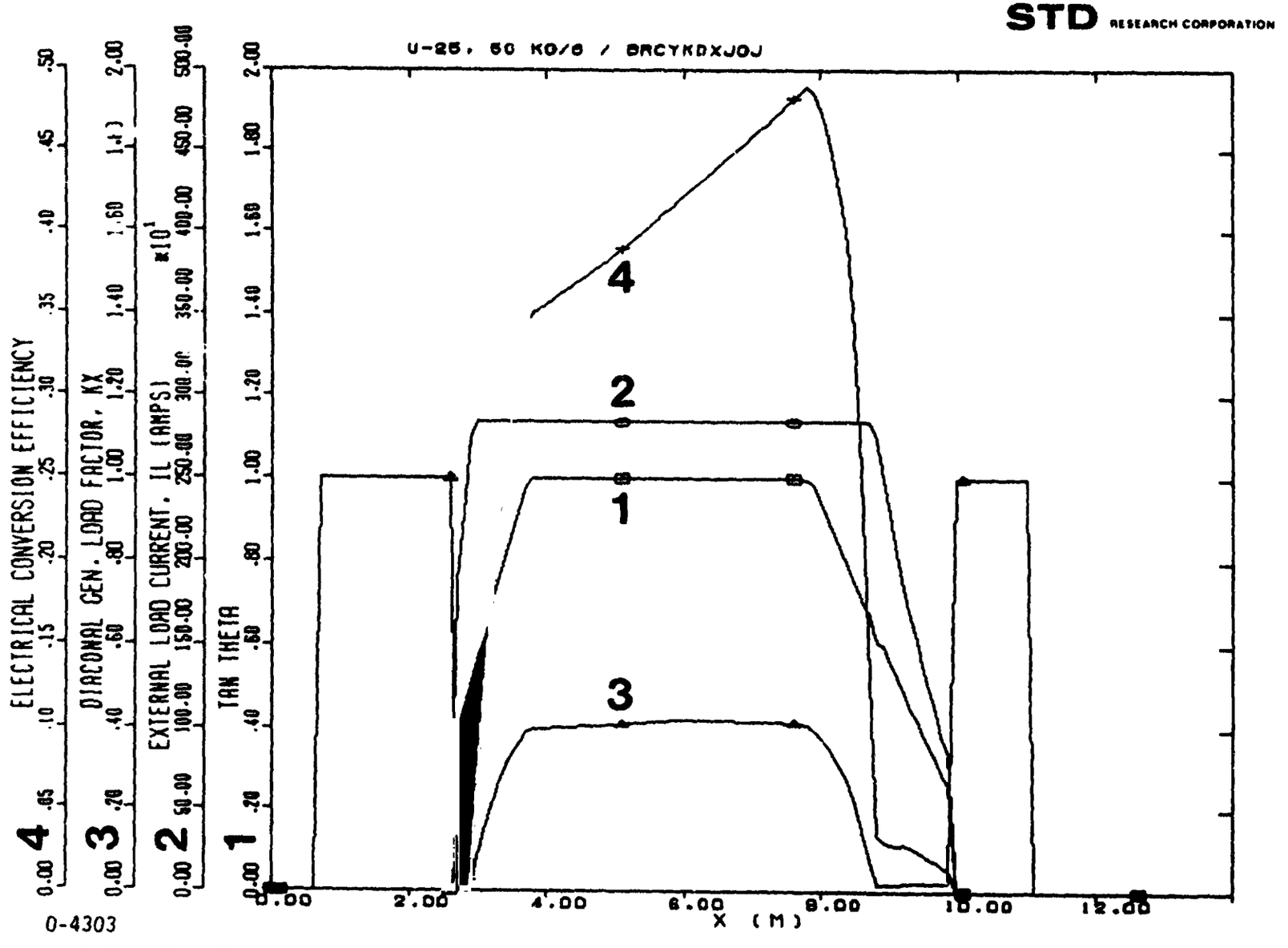

Fig. 5-2. Axial variation of the electrical loading in the U-25 at 50 kg/s operating conditions. STD computation BRCYKDXJGJ

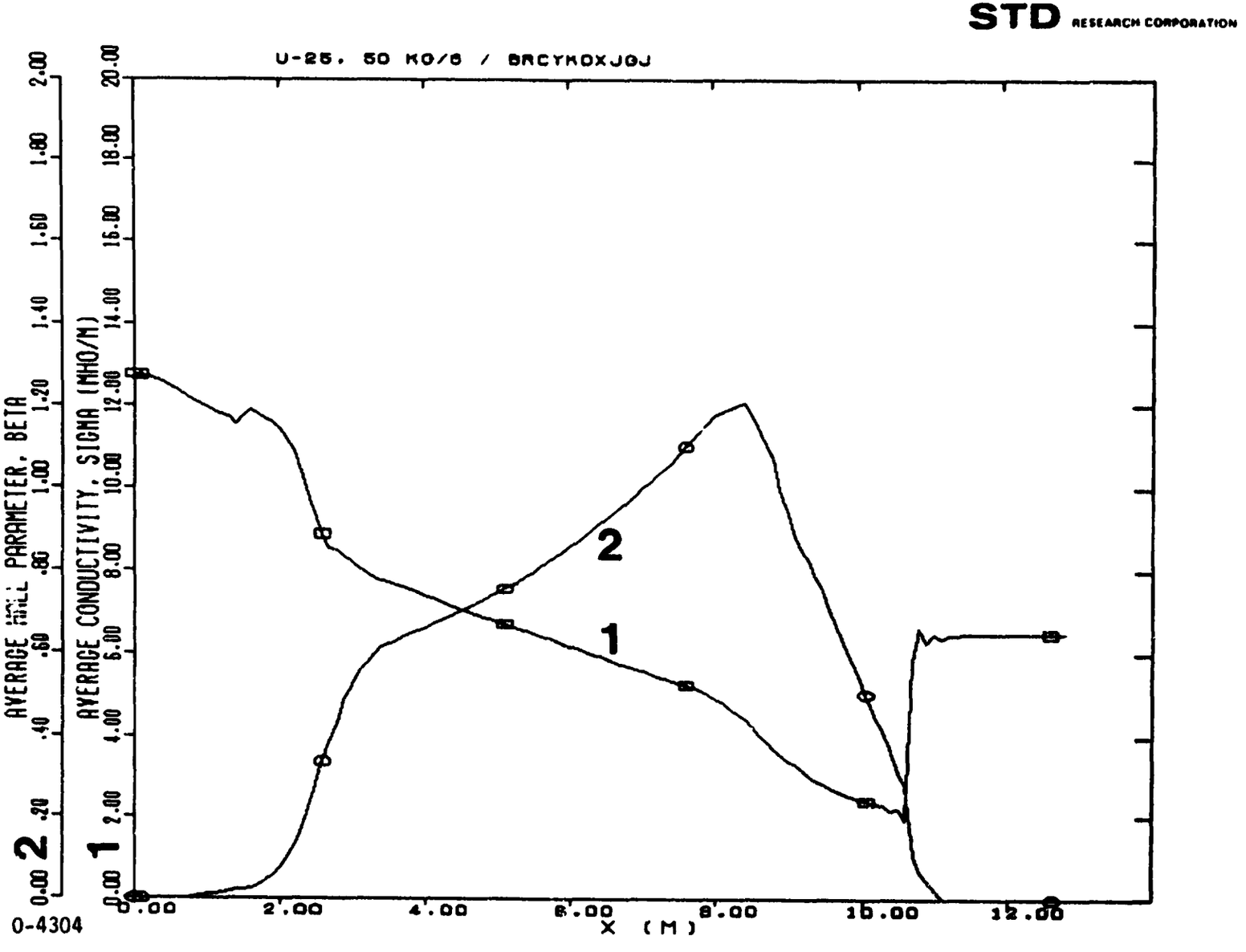

Fig. 5-3. Axial variation of the plasma properties in the U-25 at 50 kg/s operating conditions. STD computation BRCYKDXJGJ

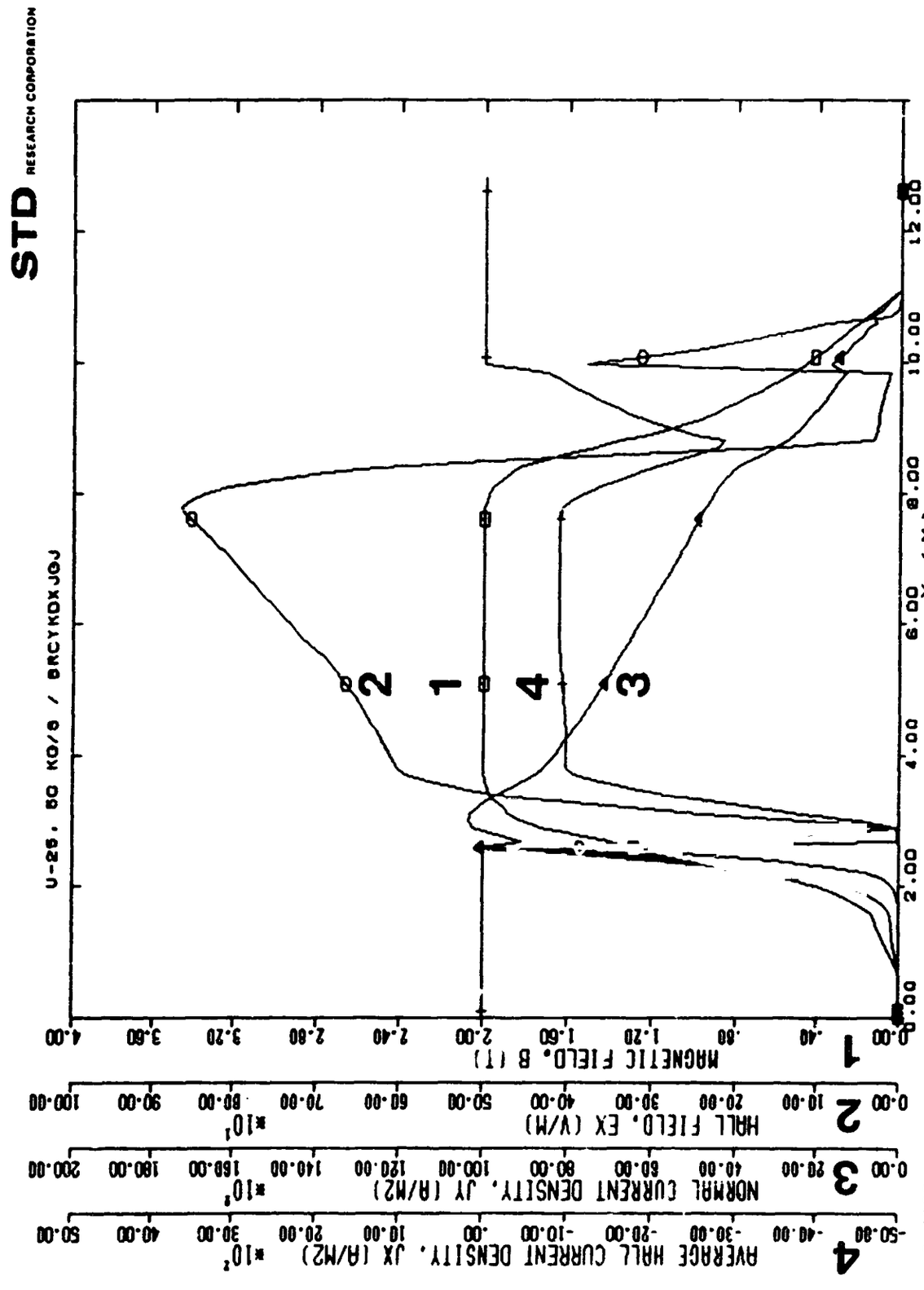

Fig. 5-4. Axial variation of electrical field variables in the U-25 at 50 kg/s operating conditions. STD computation BRCYKDXJGJ

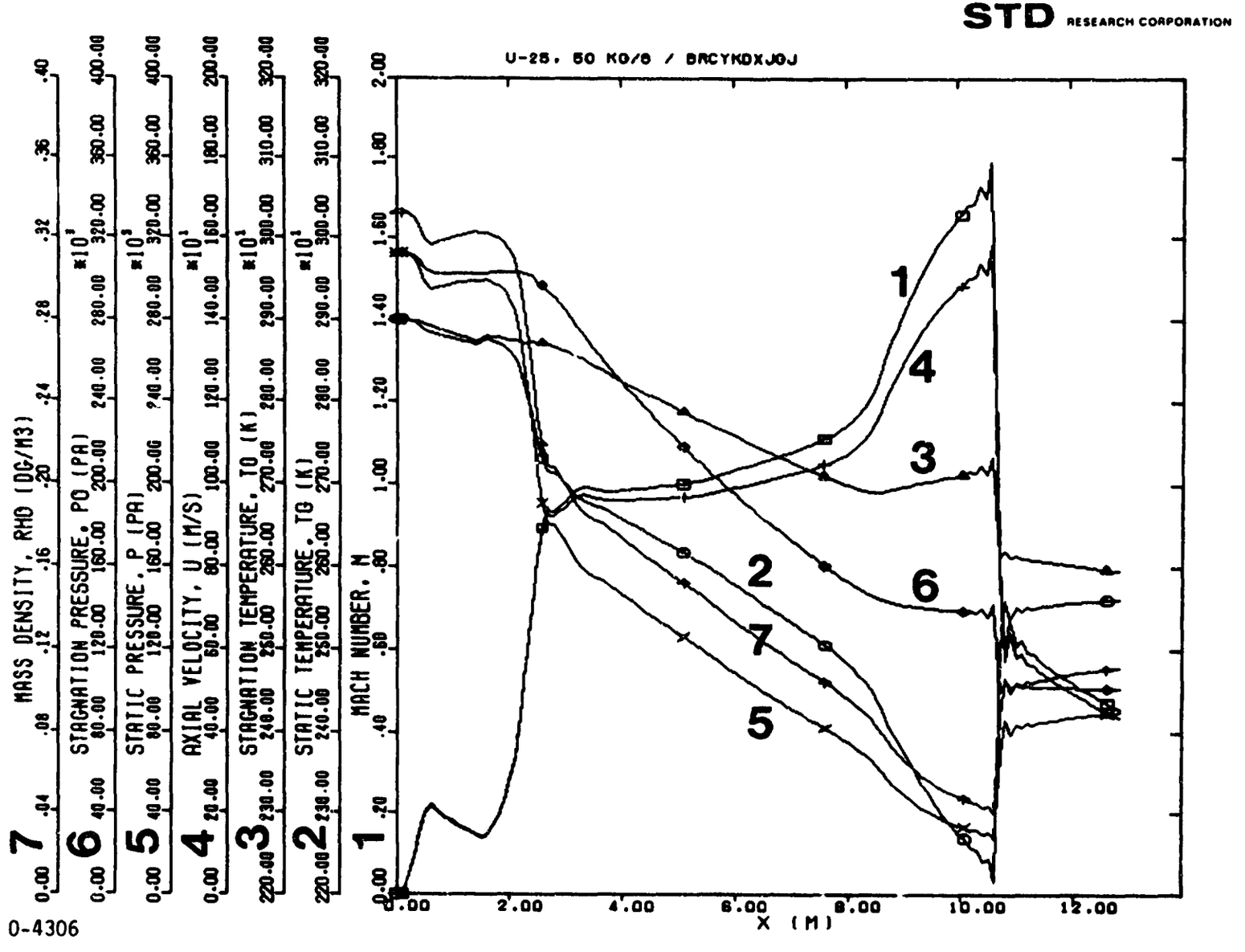

Fig. 5-5. Axial variation of the average gasdynamic variables in the U-25 at 50 kg/s operating conditions. STD computation BRCYKDXJGJ

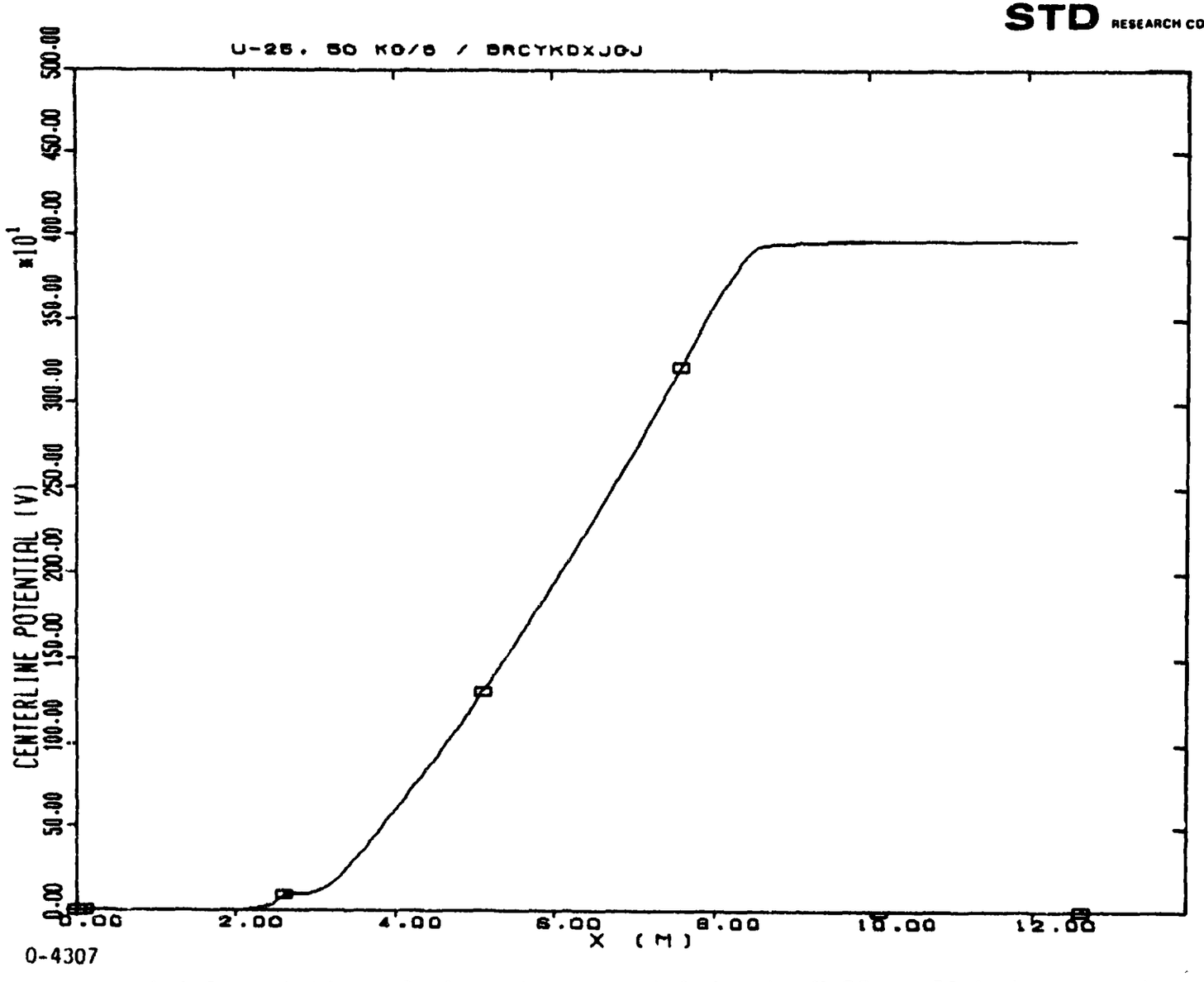

Fig. 5-6. Axial variation of electric potential in the U-25 at 50 kg/s operating conditions. STD computation BRCYKDXJGJ

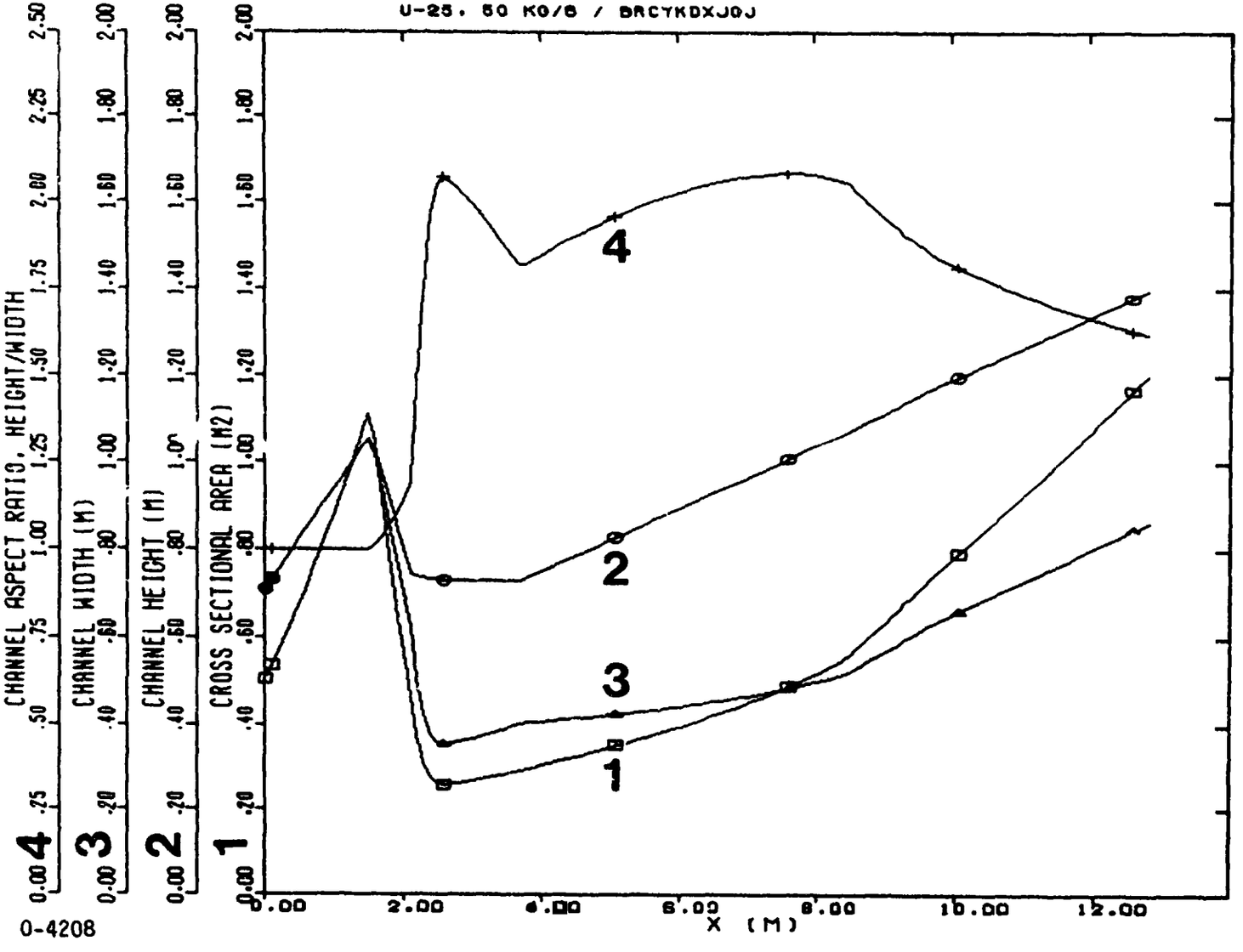

Fig. 5-7. Axial variation of the channel geometry in the U-25 at 50 kg/s operating conditions. STD computation BRCYKDXJGJ

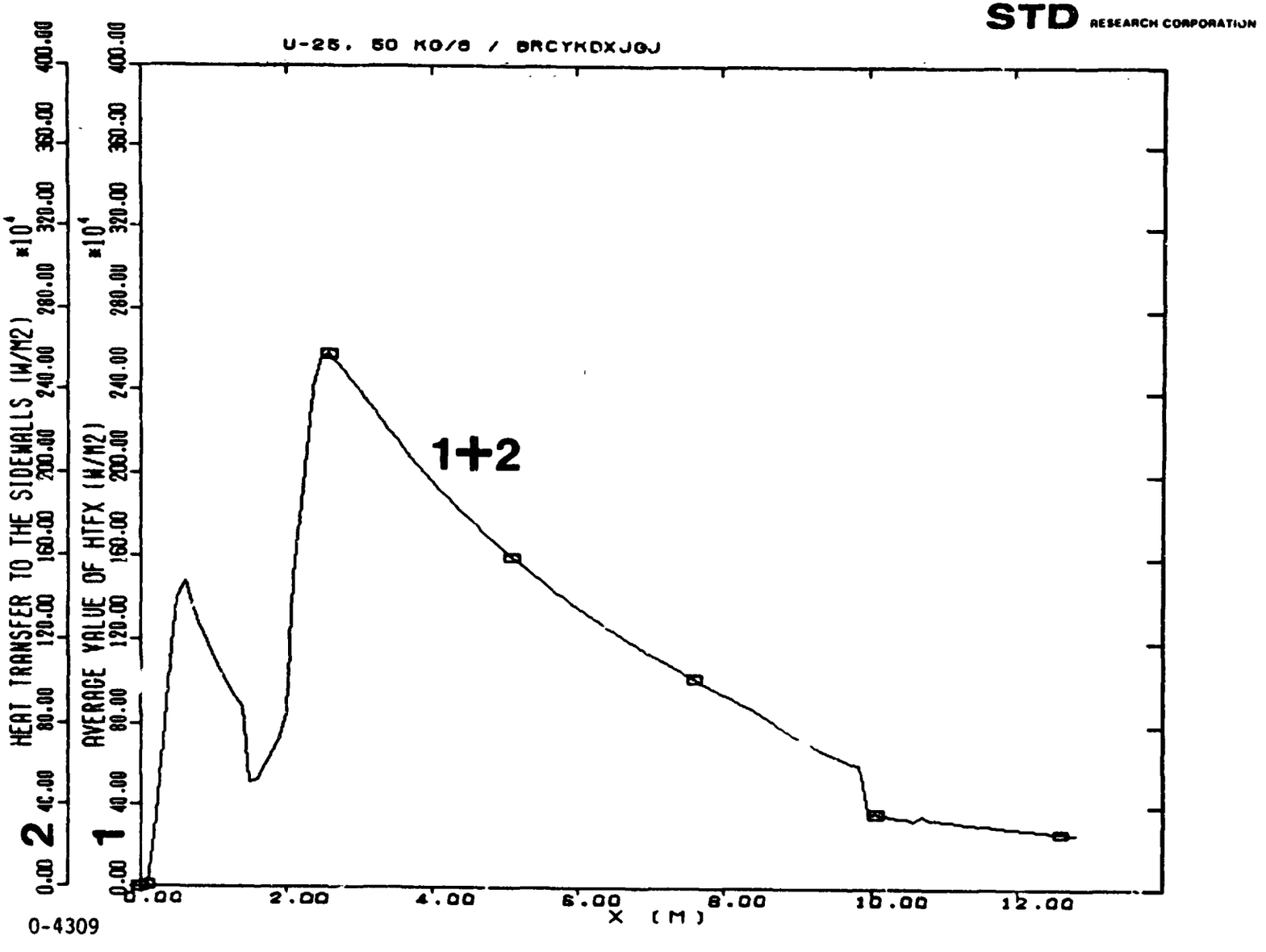

Fig. 5-8. Axial variation of the heat transfer parameters in the U-25 at 50 kg/s operating conditions. STD computation BRCYKDXJGJ

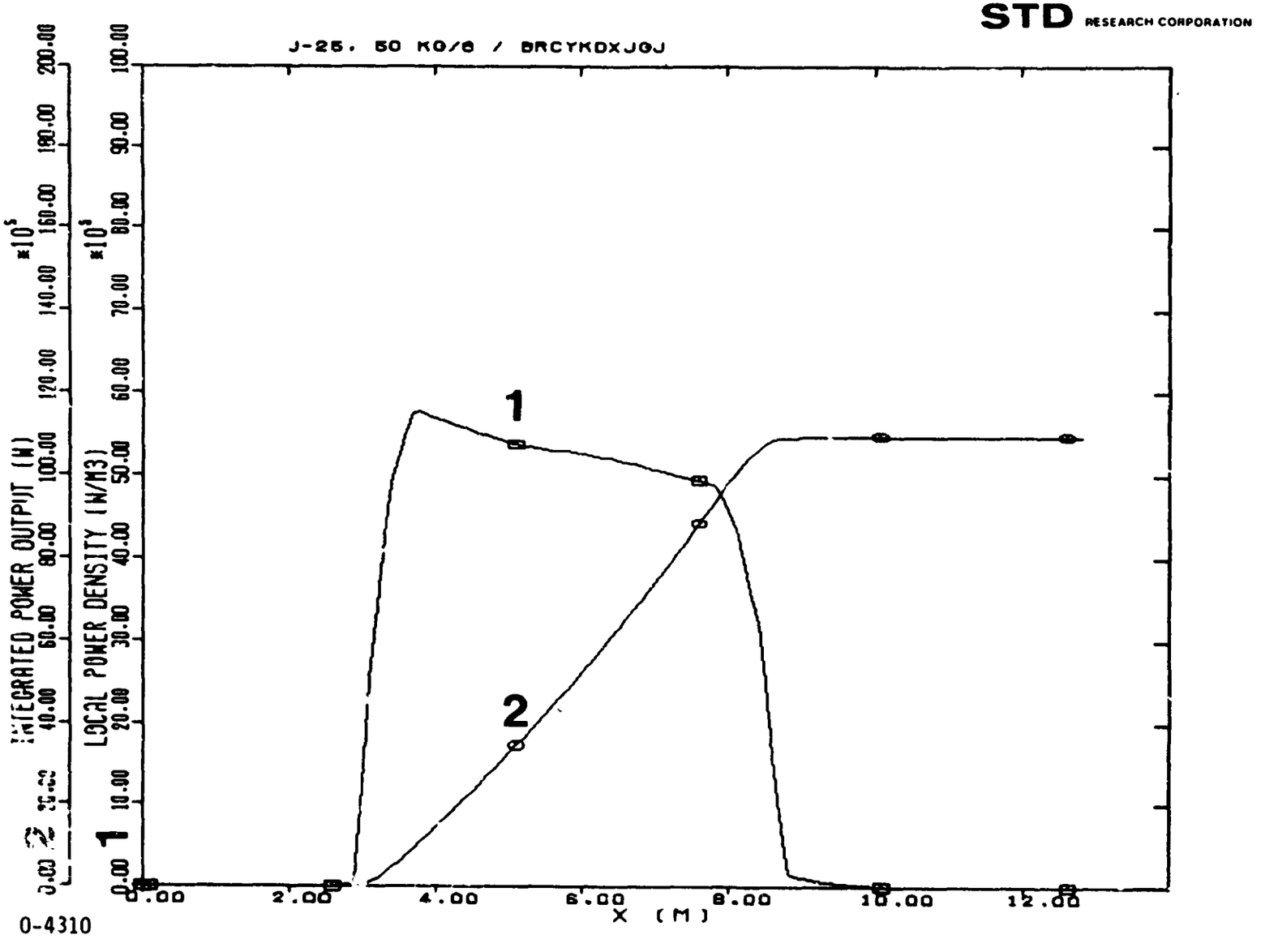

Fig. 5-9. Axial variation of the power extraction parameters in the U-25 at 50 kg/s operating conditions. STD computation BRCYKDXJGJ

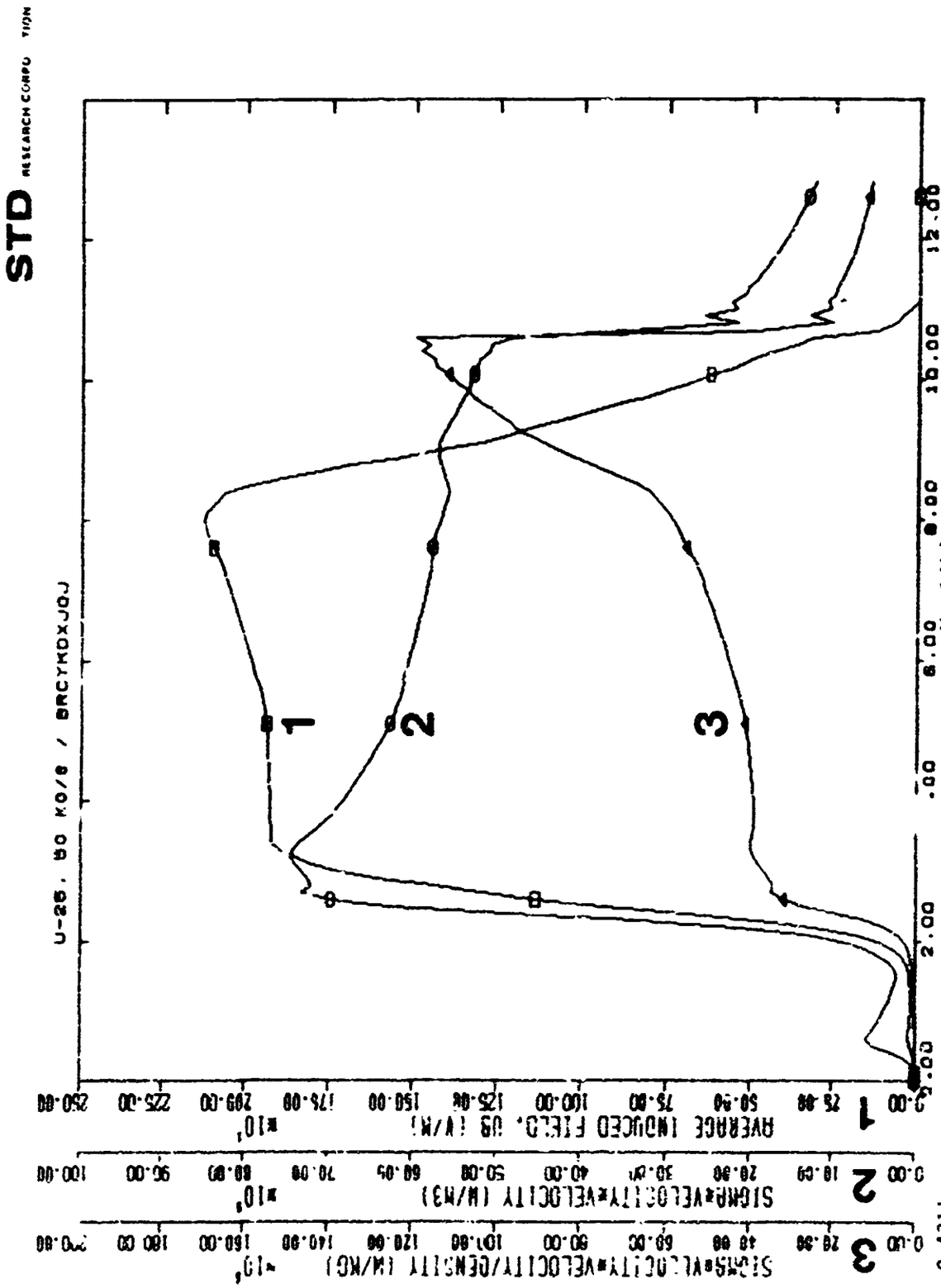

Fig. 5-10. Axial variation of the optimization variables in the U-25 at 50 kg/s operating conditions. STD computation BRCYKDXJGJ

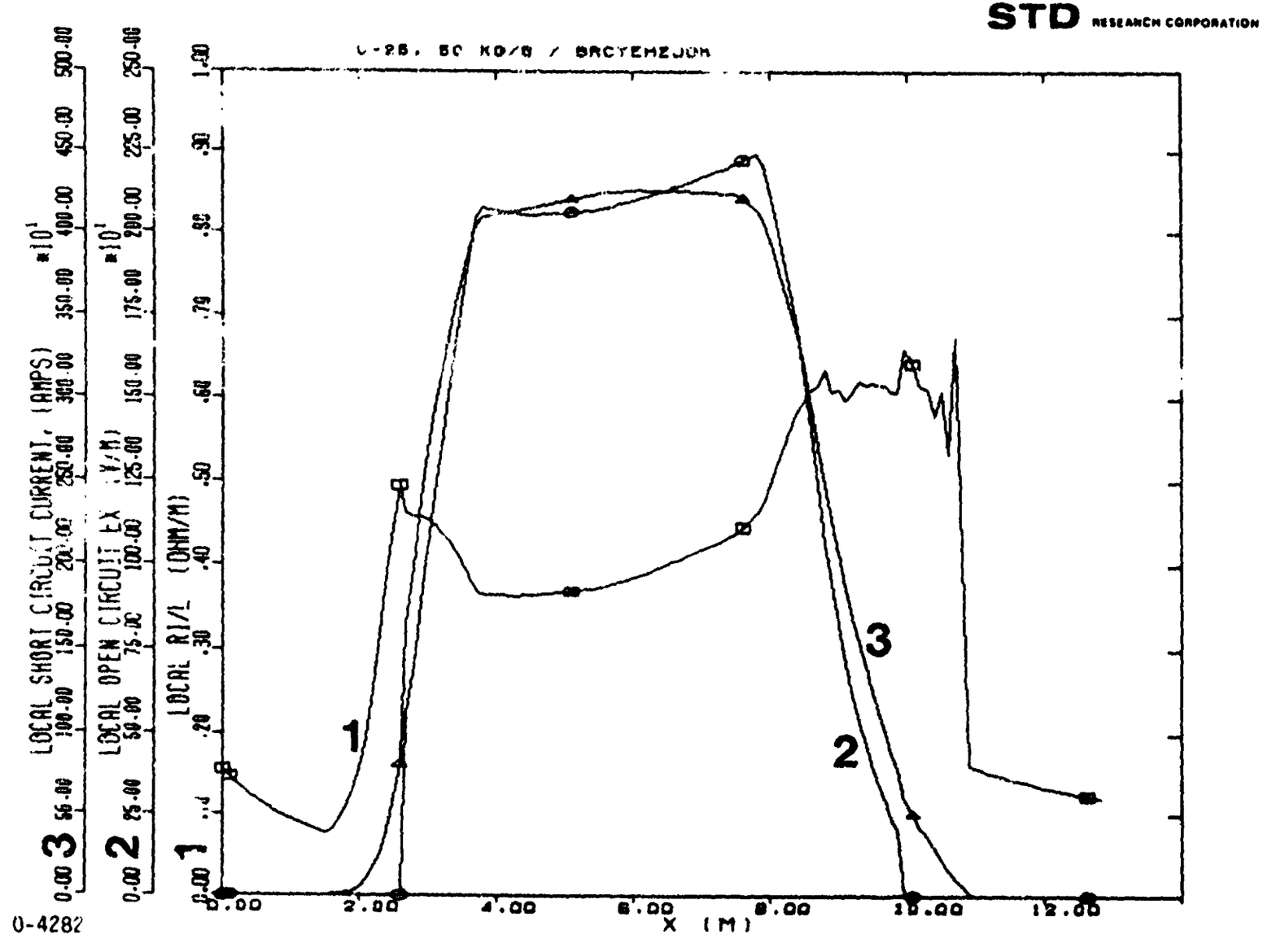

Fig. 5-11. Axial variation of open and short circuit variables in the U-25 at 50 kg/s operating conditions. STD computation BRCYEHZJGK

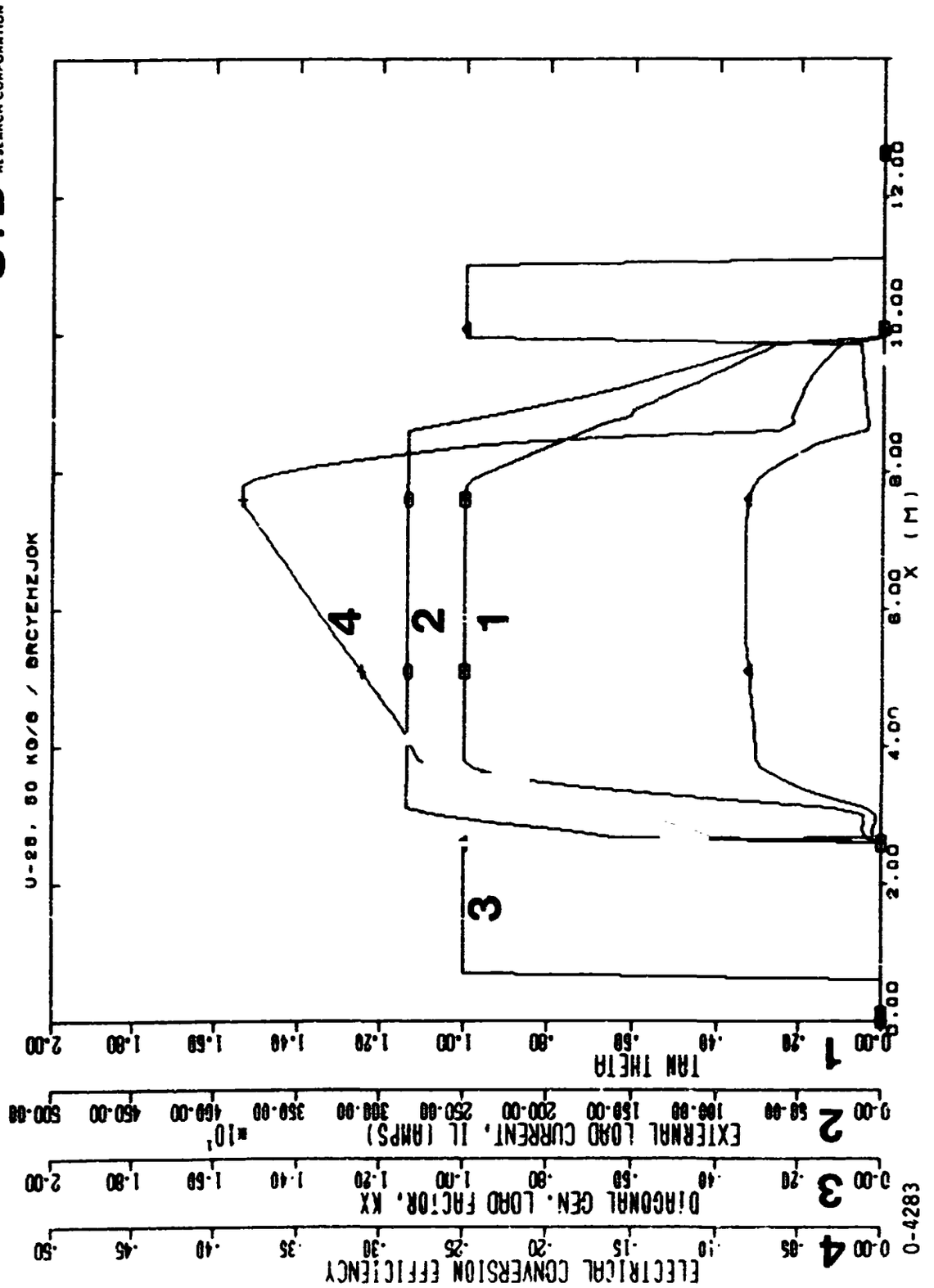

Fig. 5-12. Axial variation of the electrical loading in the U-25 at 50 kg/s operating conditions. STD computation BRCYEHZJGK

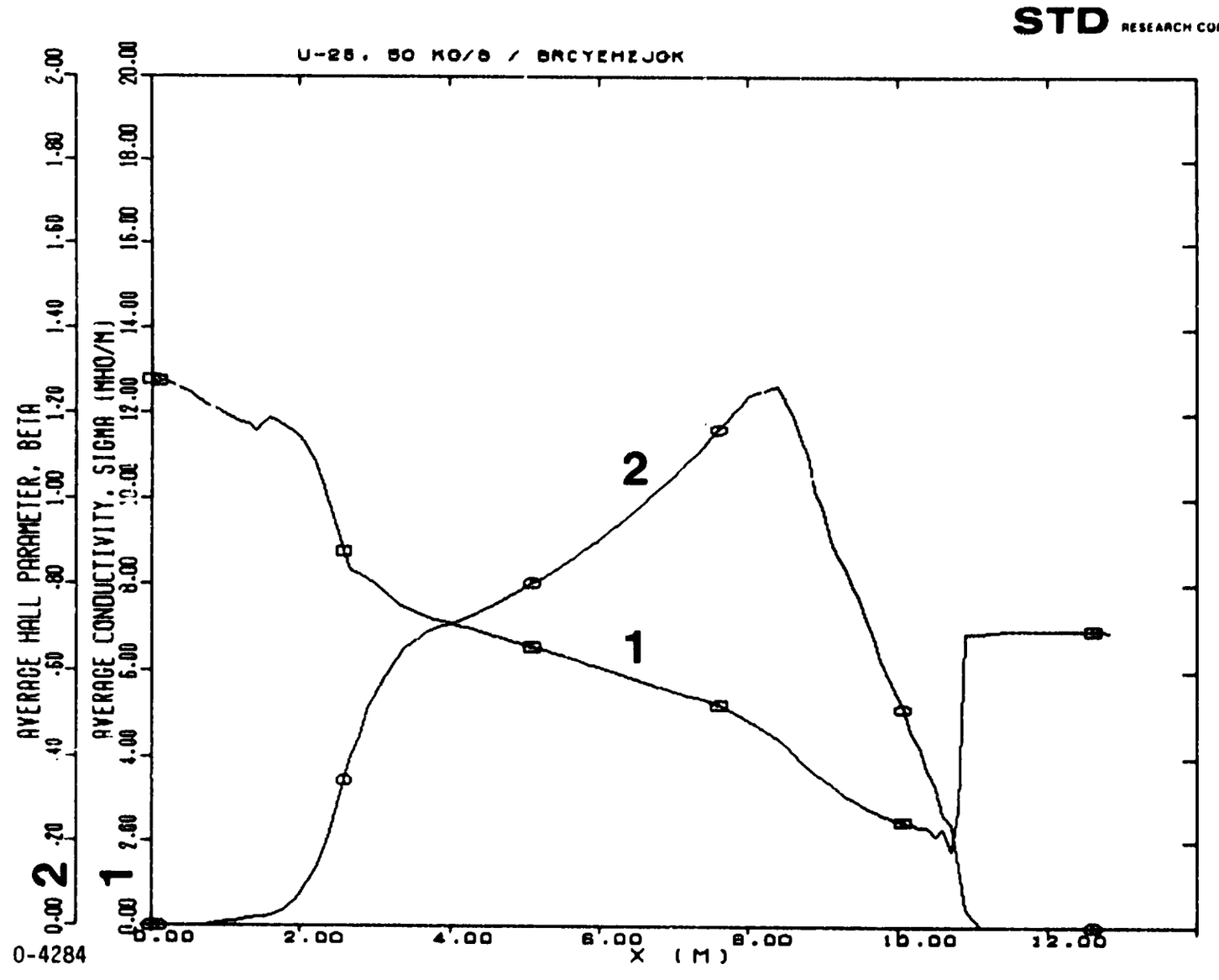

Fig. 5-13. Axial variation of the plasma properties in the U-25 at 50 kg/s operating conditions. STD computation BRCYEHZJGK

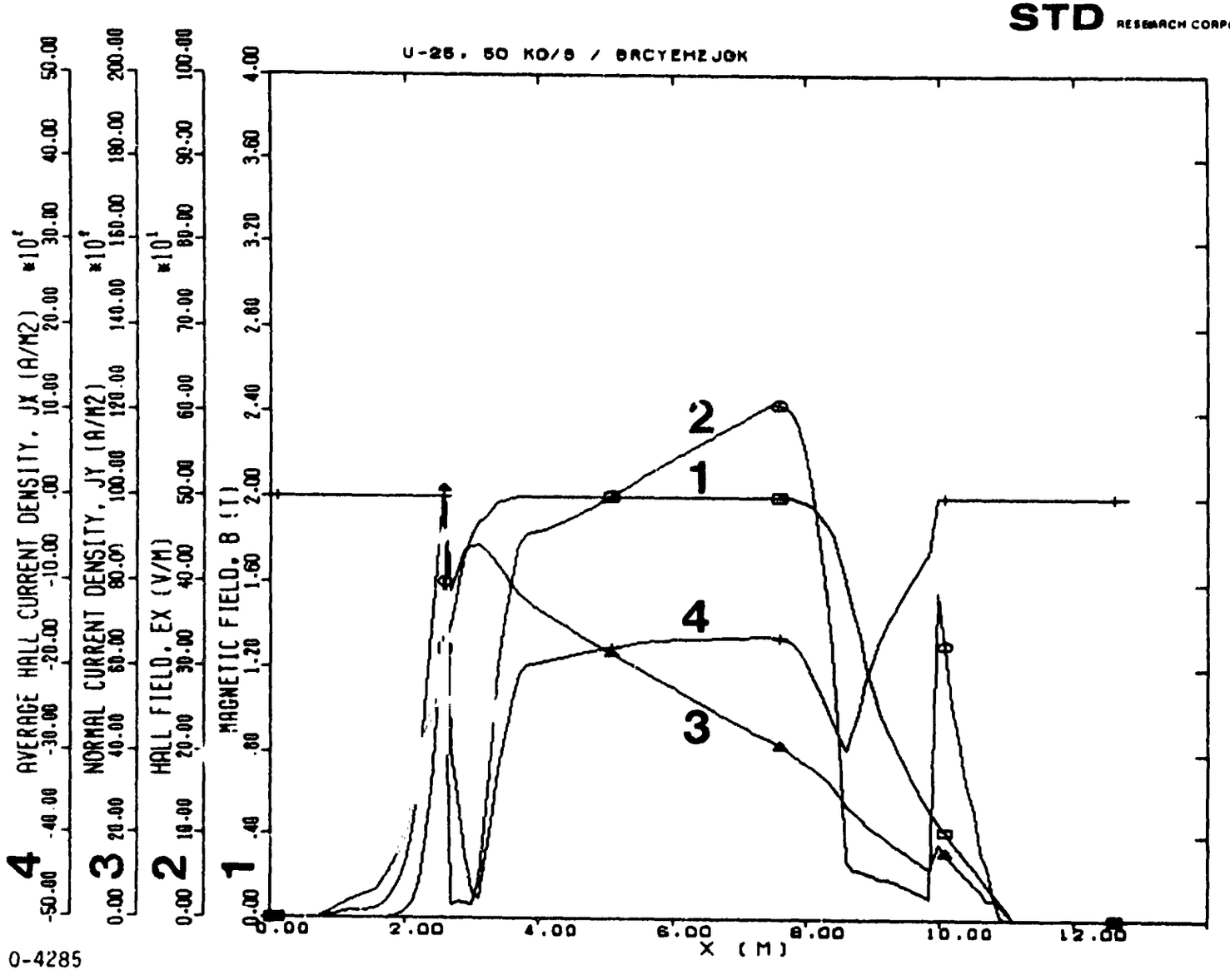

Fig. 5-14. Axial variation of electrical field variables in the U-25 at 50 kg/s operating conditions. STD computation BRCYEHZJGK

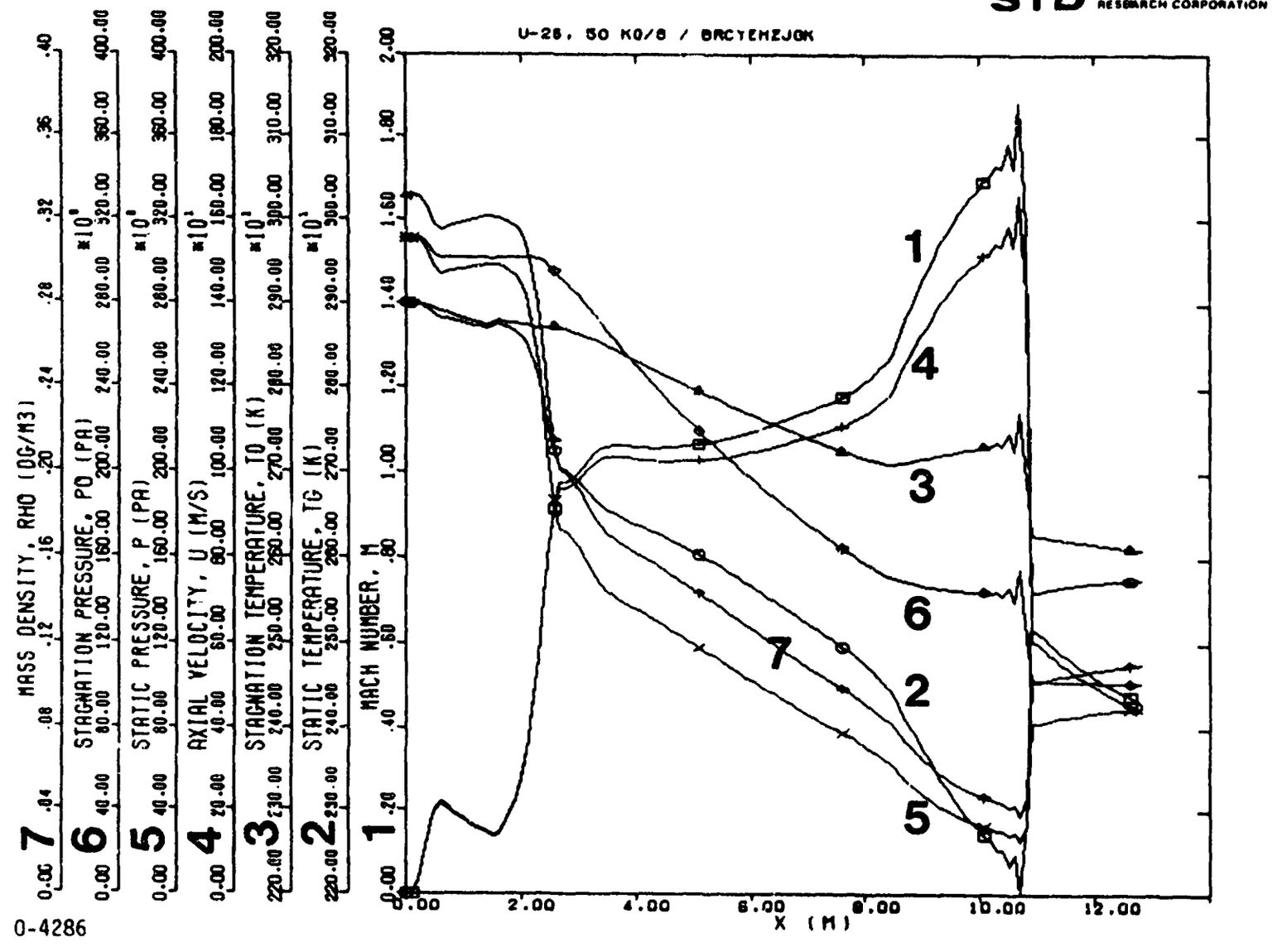

Fig. 5-15. Axial variation of the average gasdynamic variables in the U-25 at 50 kg/s operating conditions. STD computation BRCYEHZJGK

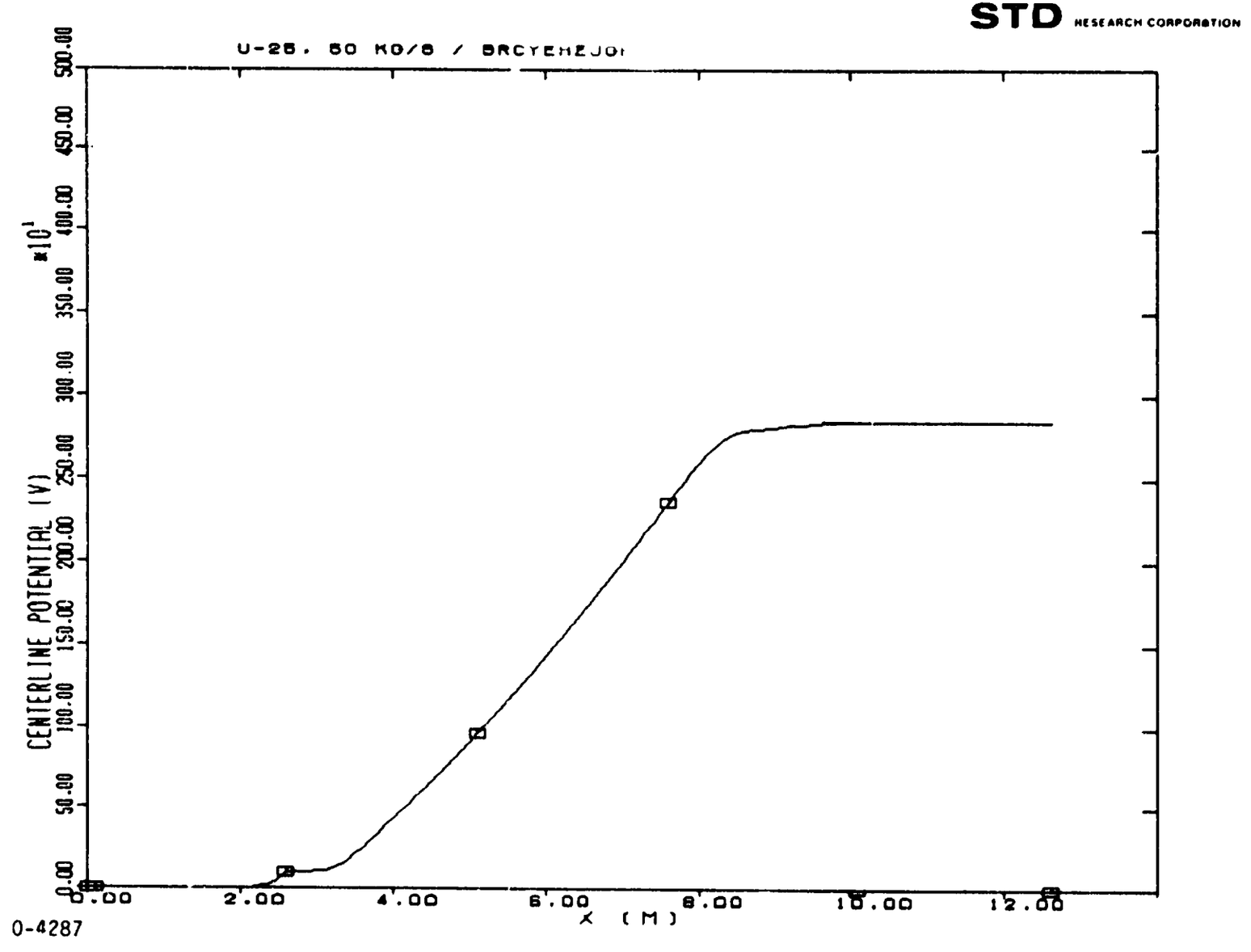

Fig. 5-16. Axial variation of electrical potential in the U-25 at 50 kg/s operating conditions. STD computation BRCYEHZJGK

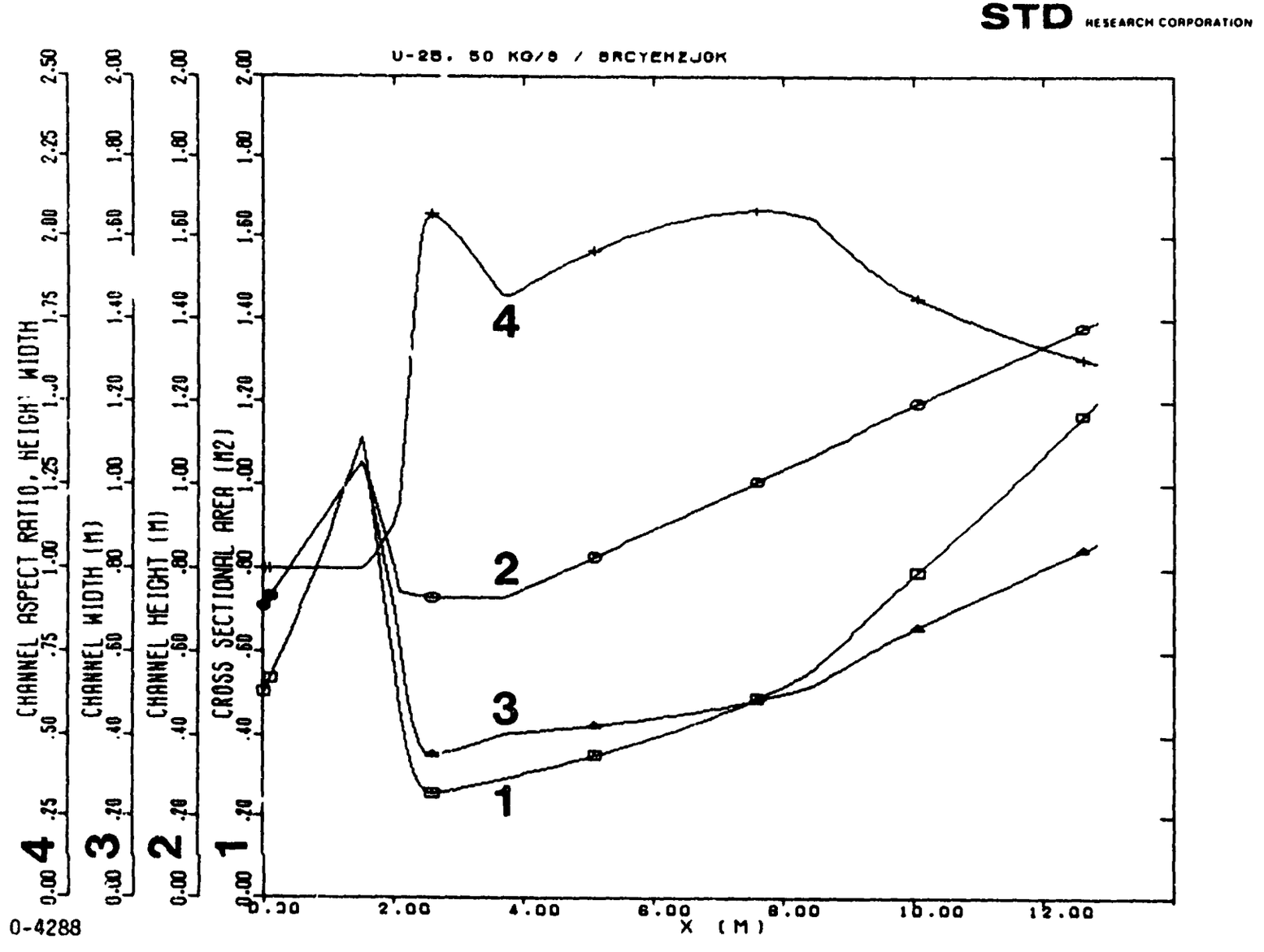

Fig. 5-17. Axial variation of the channel geometry in the U-25 at 50 kg/s operating conditions. STD computation BRCYEHZJGK

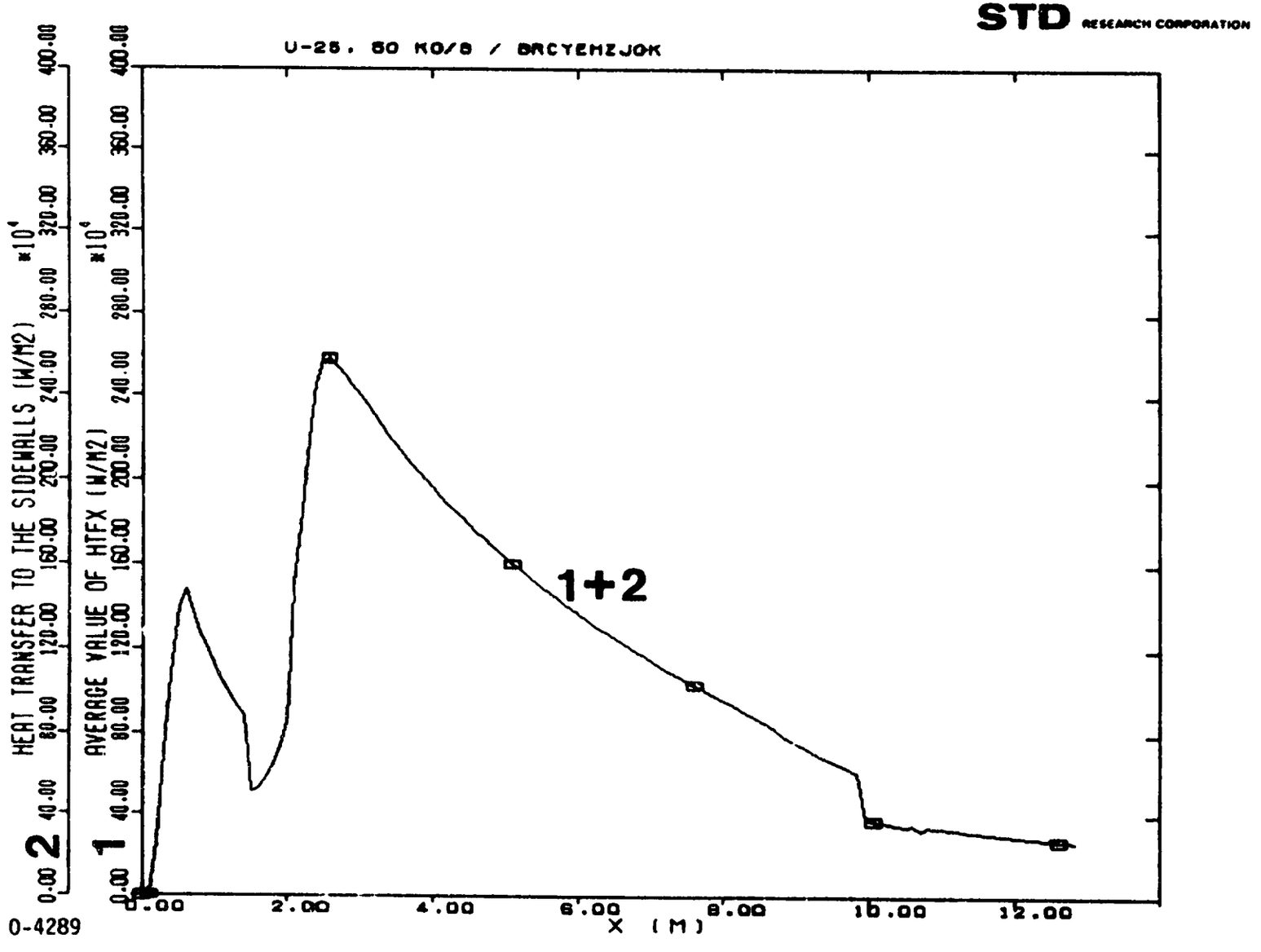

Fig. 5-18. Axial variation of the heat transfer parameters in the U-25 at 50 kg/s operating conditions. STD computation BRCYEHZJGK

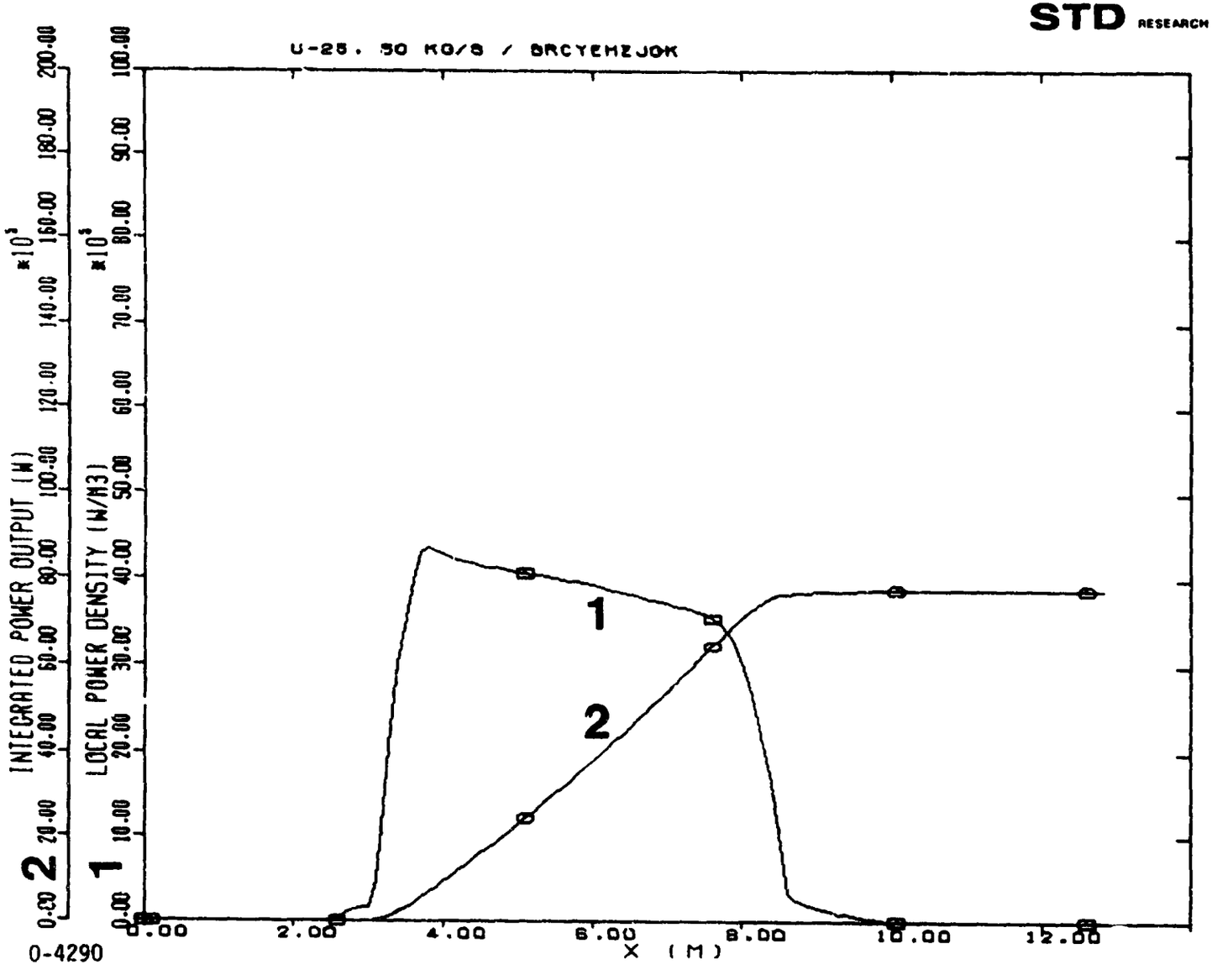

Fig. 5-19. Axial variation of power extraction parameters in the U-25 at 50 kg/s operating conditions. STD computation BRCYEHZJGK

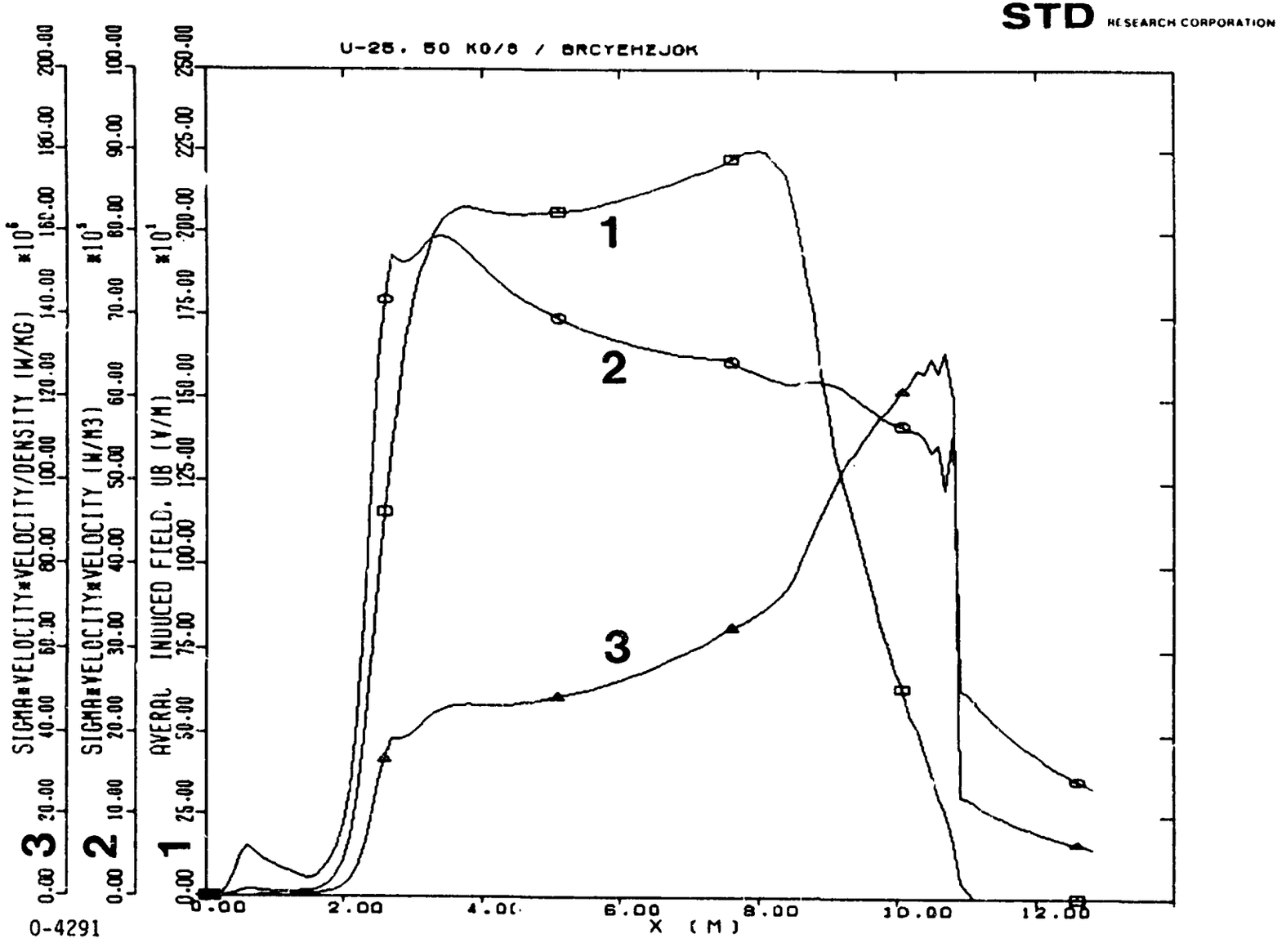

Fig. 5-20. Axial variation of the optimization variables in the U-25 at 50 kg/s operating conditions. STD computation BRCYEHZJGK

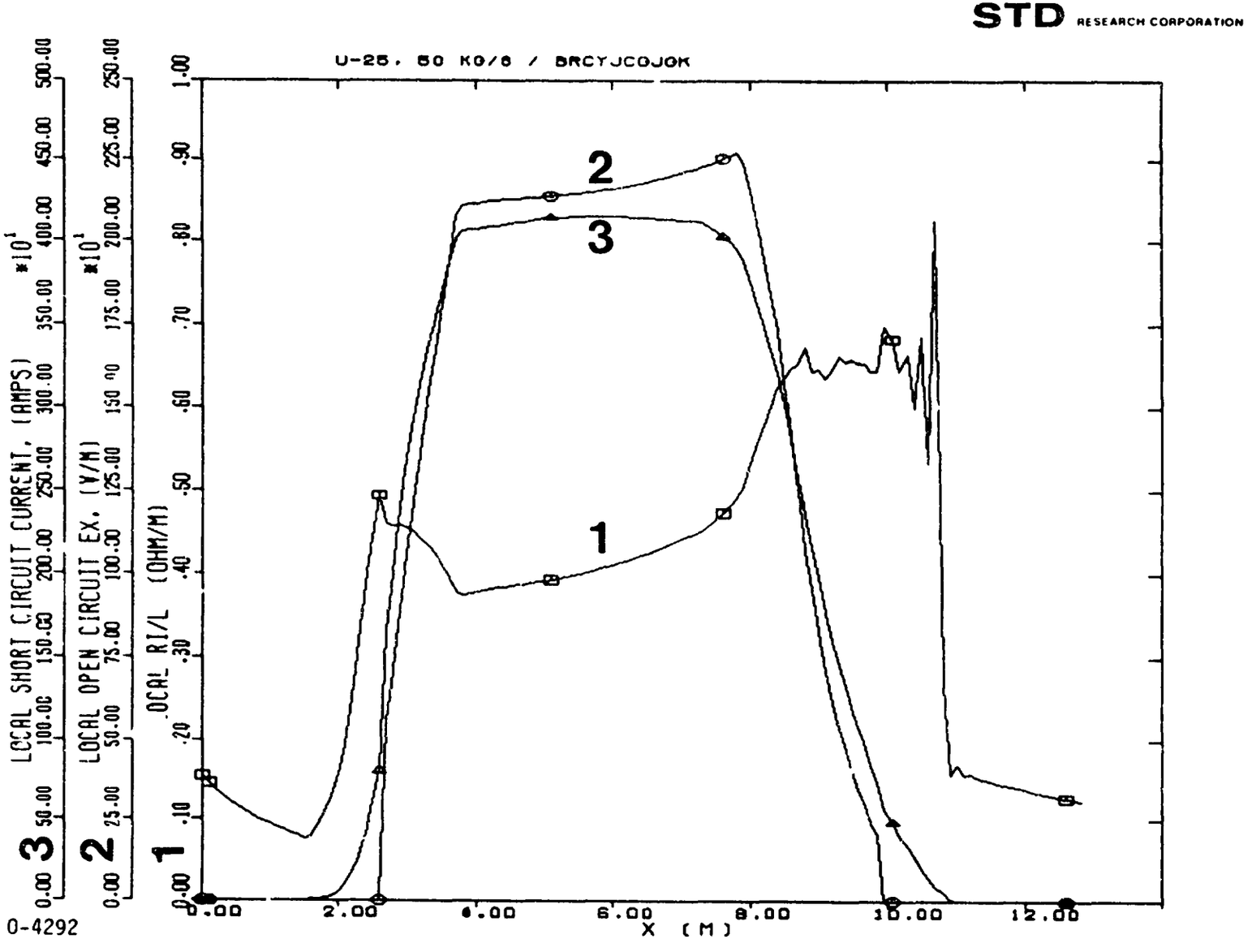

Fig. 5-21. Axial variation of open and short circuit variables in the U-25 at 50 kg/s operating conditions. STD computation BRCYJCGJGK

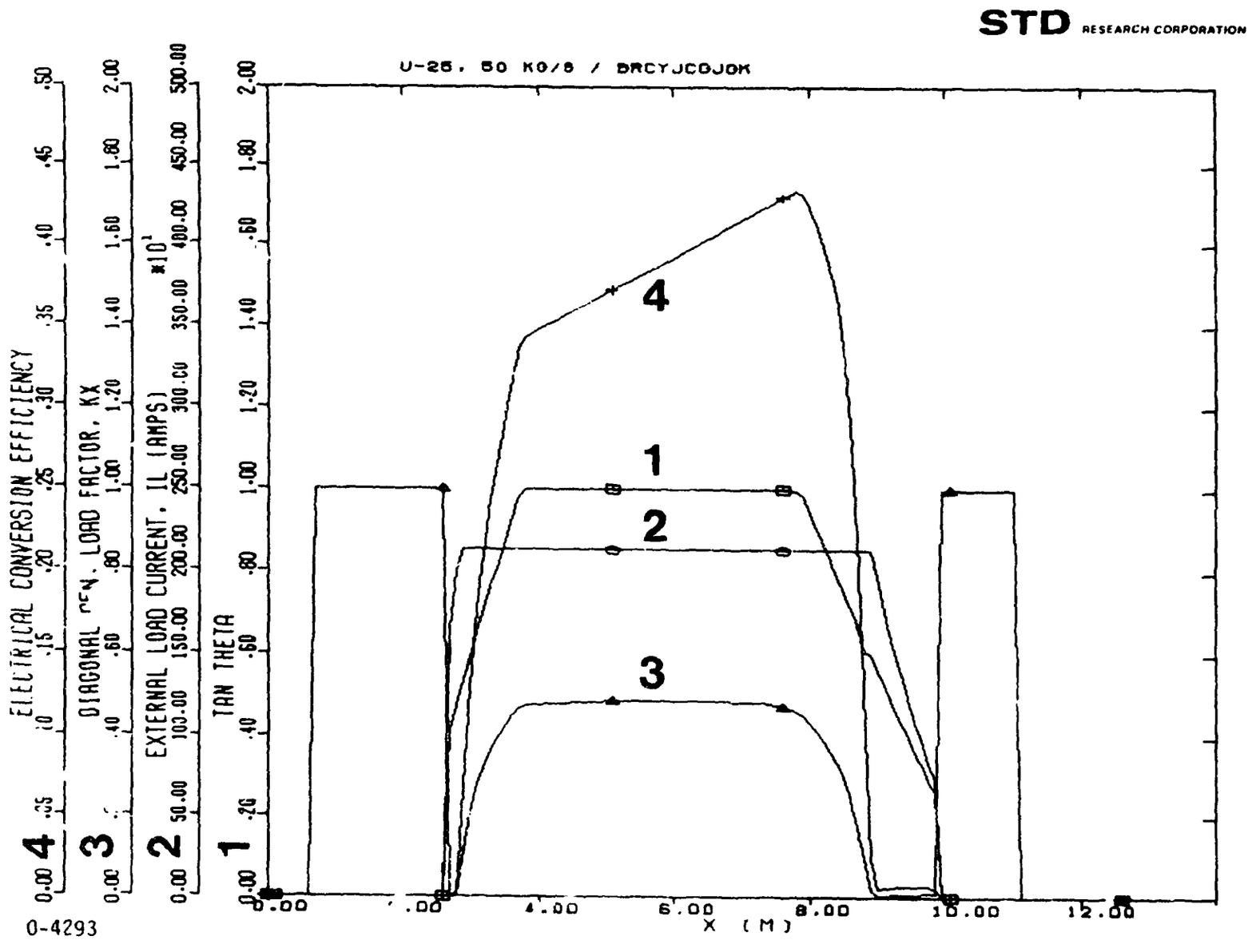

Fig. 5-22. Axial variation of the electrical loading in the U-25 at 50 kg/s operating conditions. STD compu ation BRCYJCGJGK

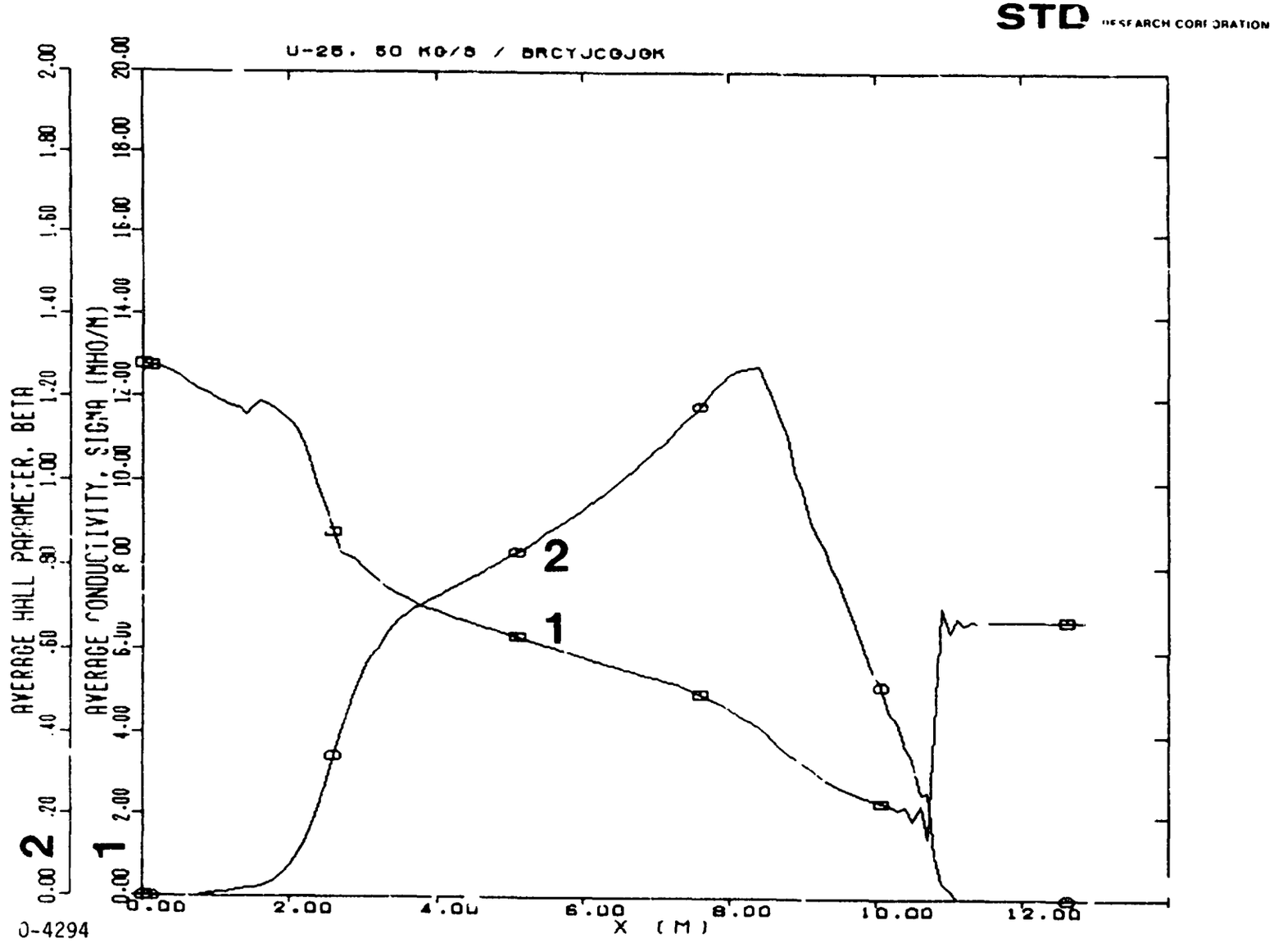

Fig. 5-23. Axial variation of the plasma properties in the U-25 at 50 kg/s operating conditions. STD computation BRCYJCGJGK

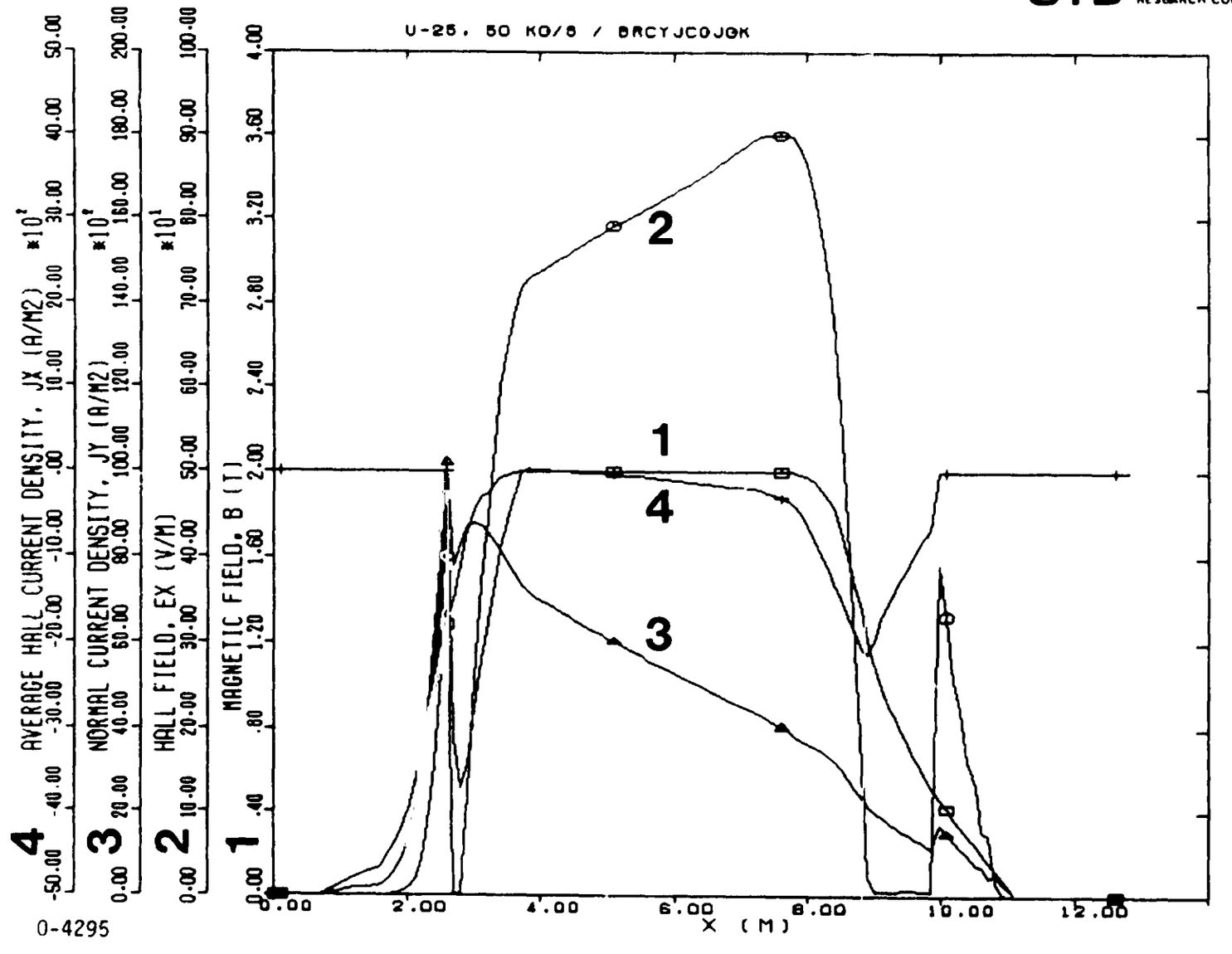

Fig. 5-24. Axial variation of electrical field variables in the U-25 at 50 kg/s operating conditions. STD computation BRCYJCGJGK

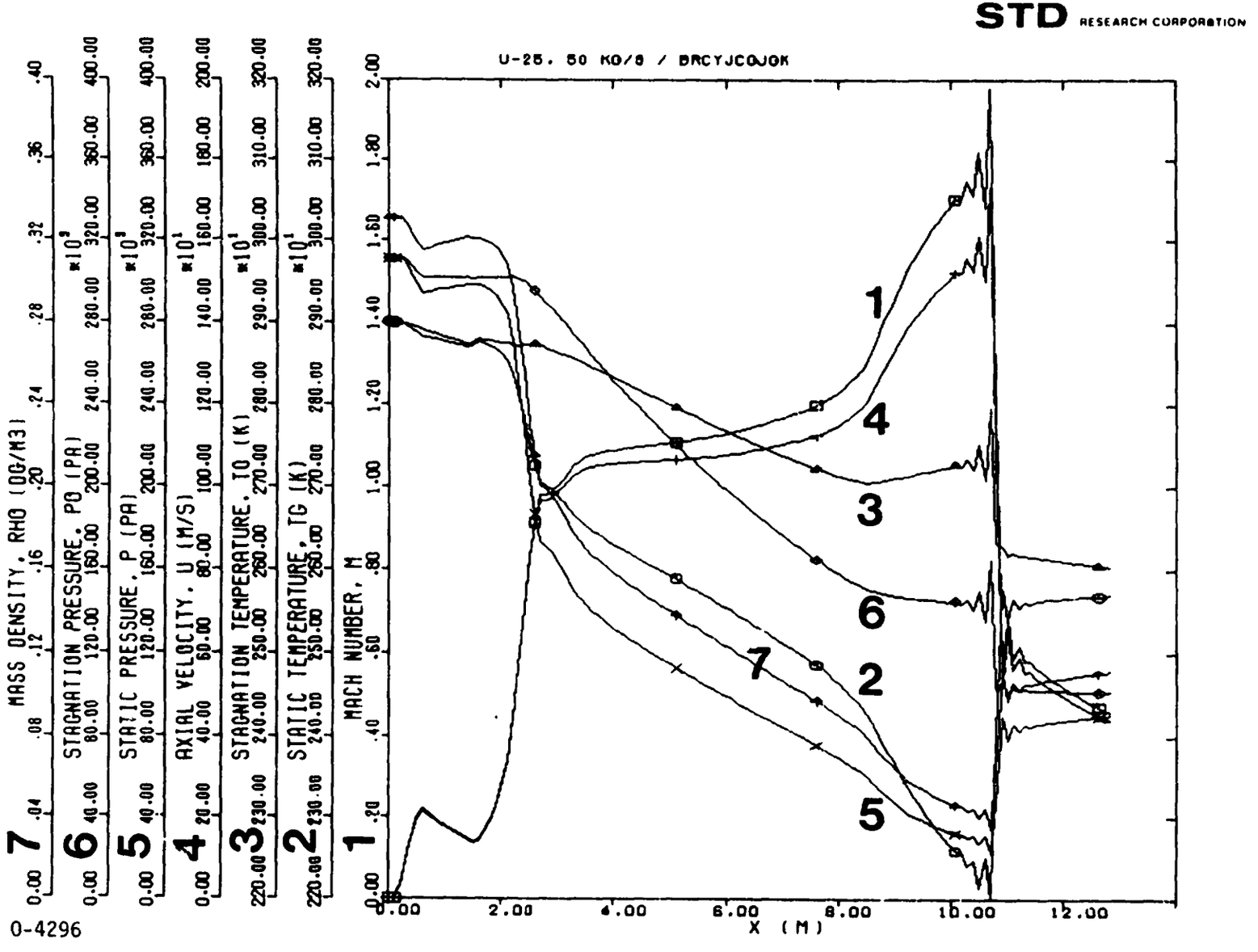

Fig. 5-25. Axial variation of the average gasdynamic variables in the U-25 at 50 kg/s operating conditions. STD computation BRCYJCGJGK

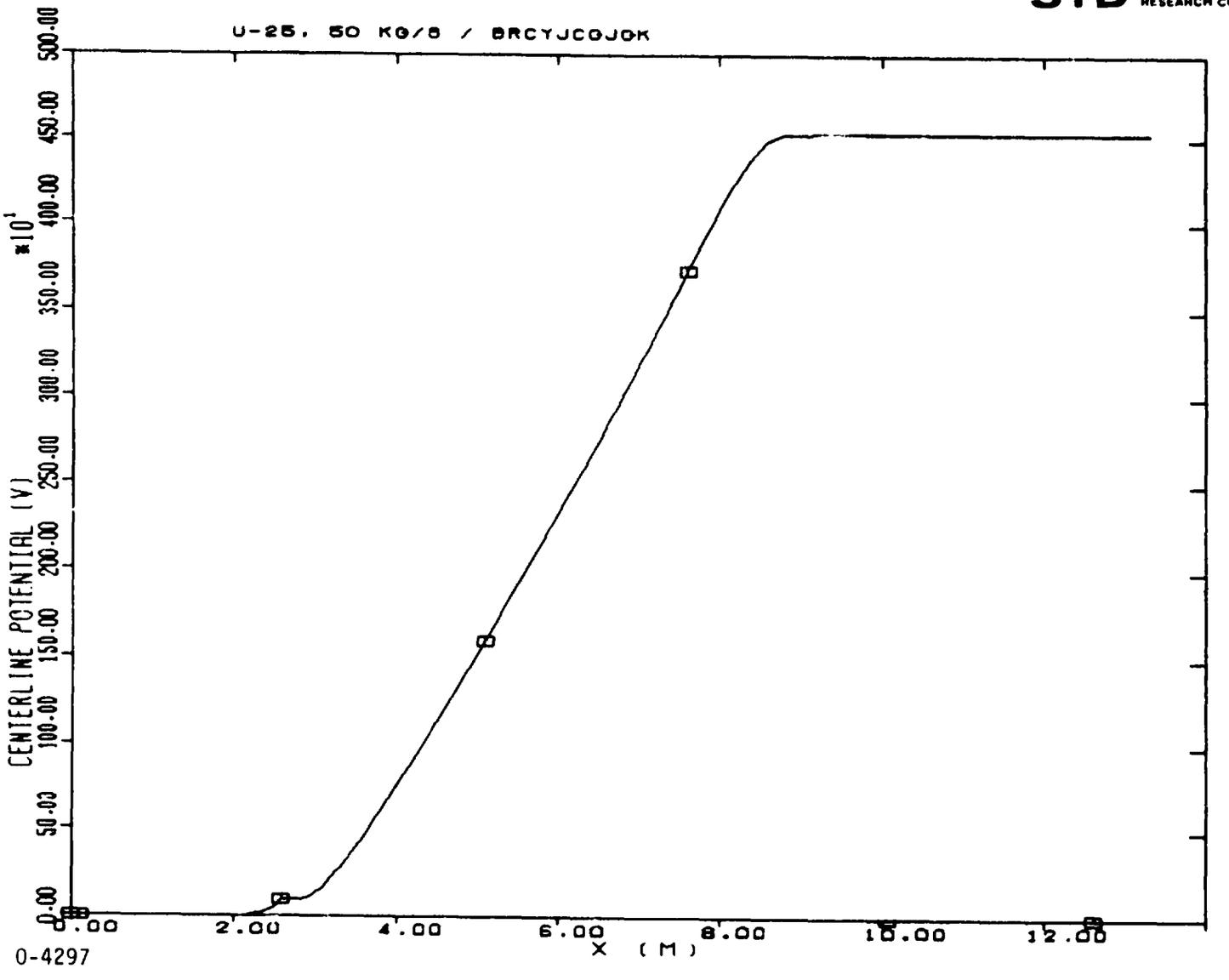

Fig. 5-26. Axial variation of electric potential in the U-25 at 50 kg/s operating conditions. STD computation BRCYJCGJGK

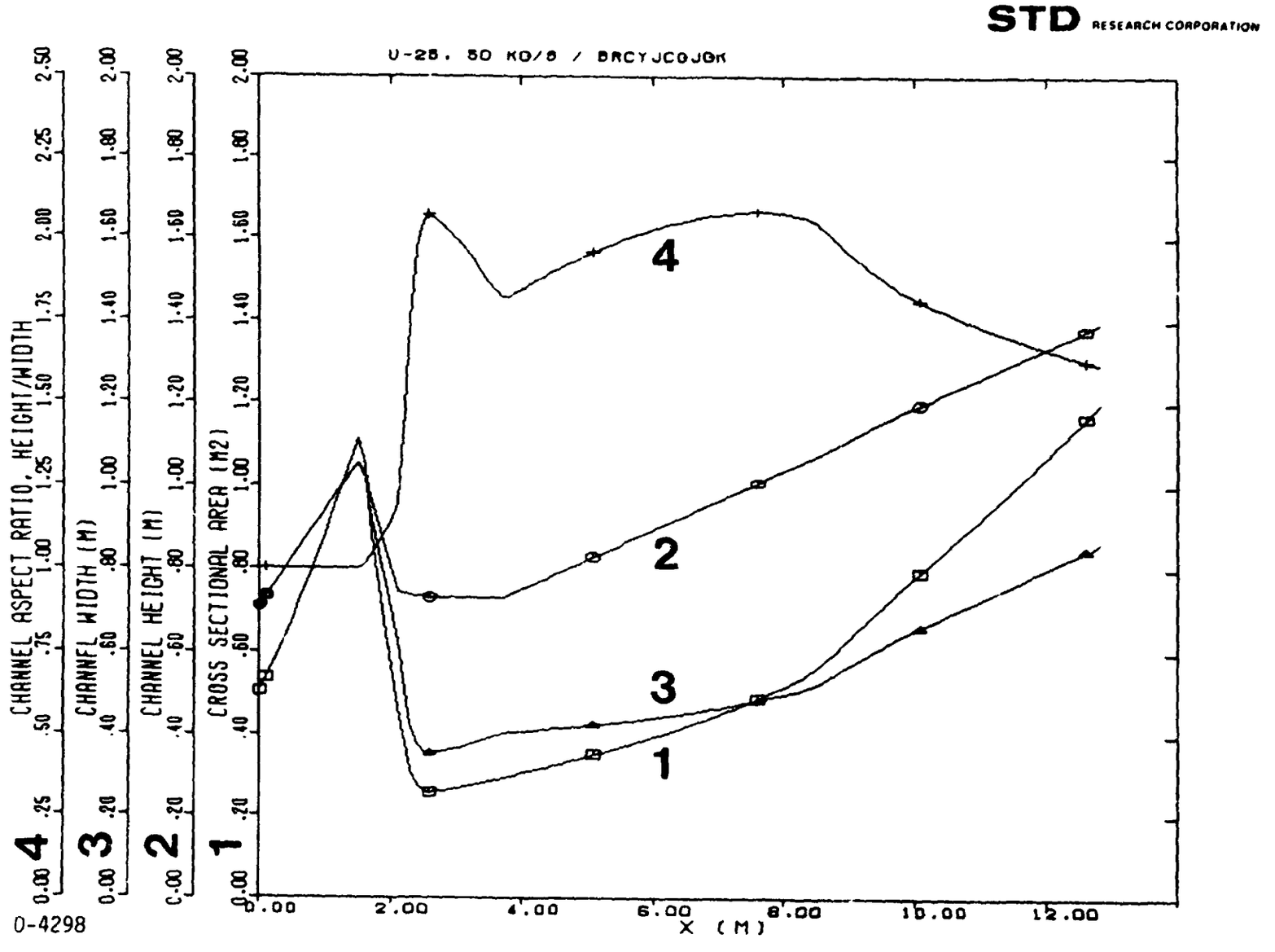

Fig. 5-27. Axial variation of the channel geometry in the U-25 at 50 kg/s operating conditions. STD computation BRCYJCGJGK

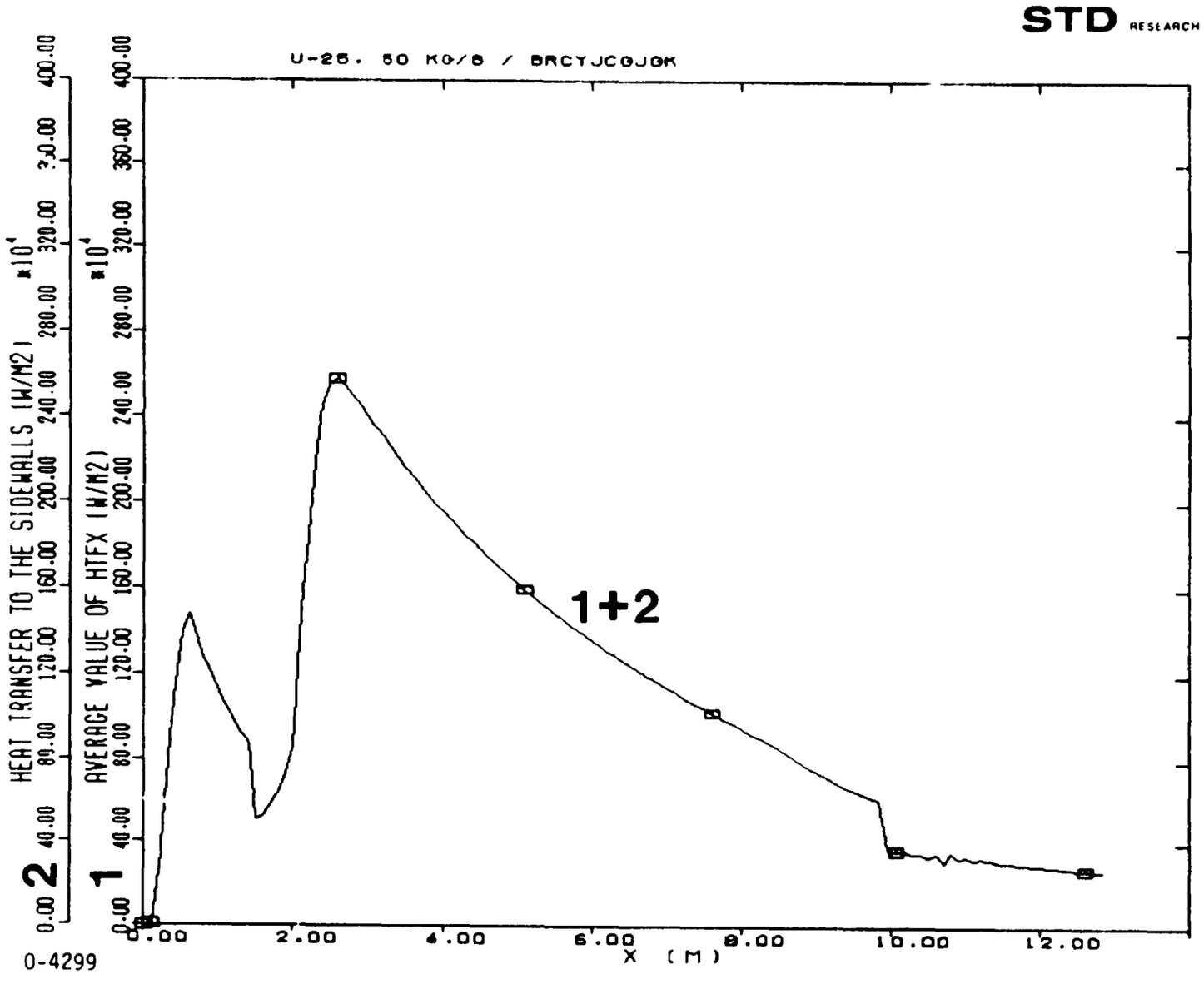

Fig. 5-28. Axial variation of the heat transfer parameters in the U-25 at 50 kg/s operating conditions. STD computation BRCYJCGJGK

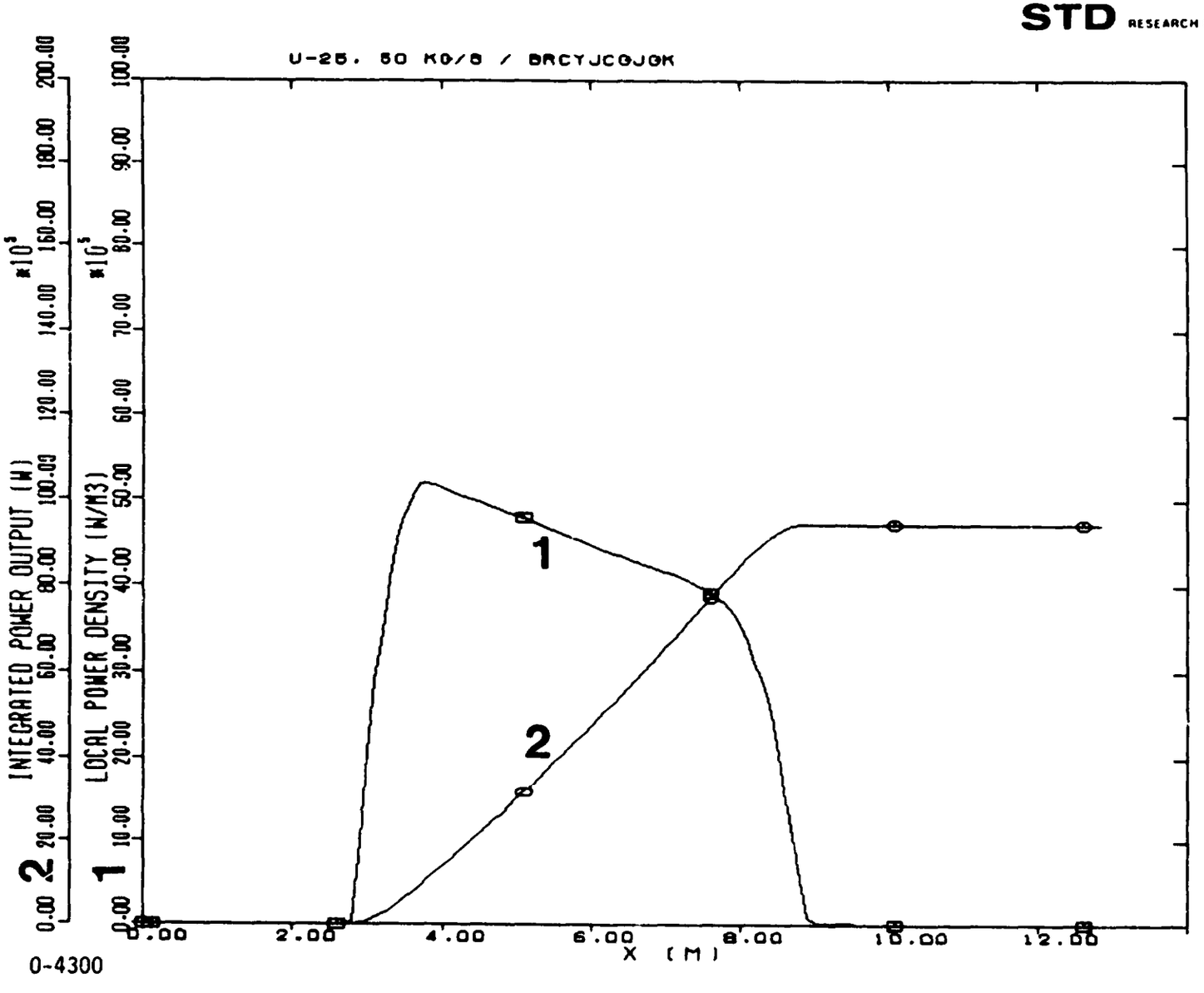

Fig. 5-29. Axial variation of power extraction parameters in the U-25 at 50 kg/s operating conditions. STD computation BRCYJCGJGK

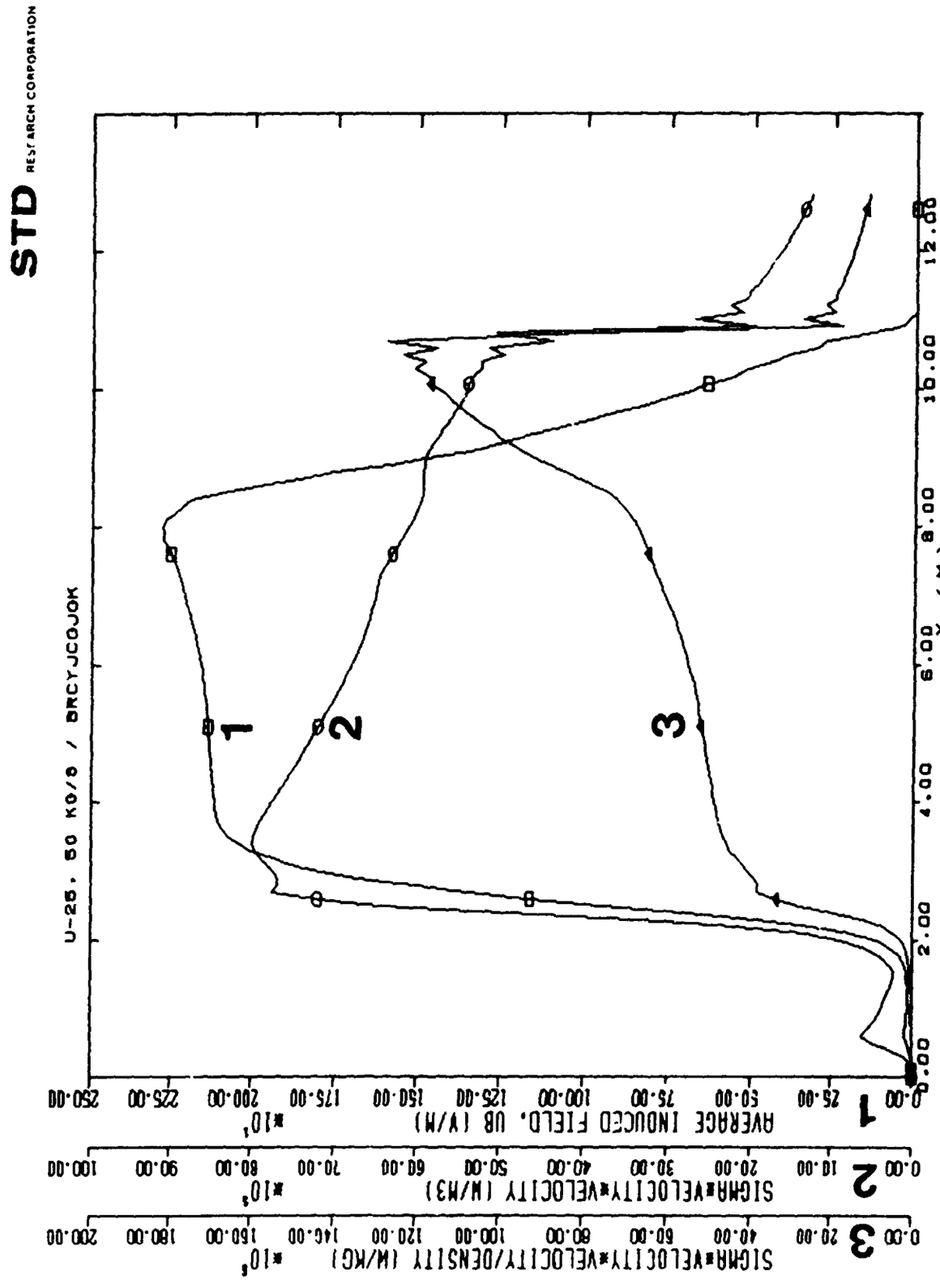

Fig. 5-30. Axial variation of the optimization variables in the U-25 at 50 kg/s operating conditions. STD computation BRCYJCGJGK

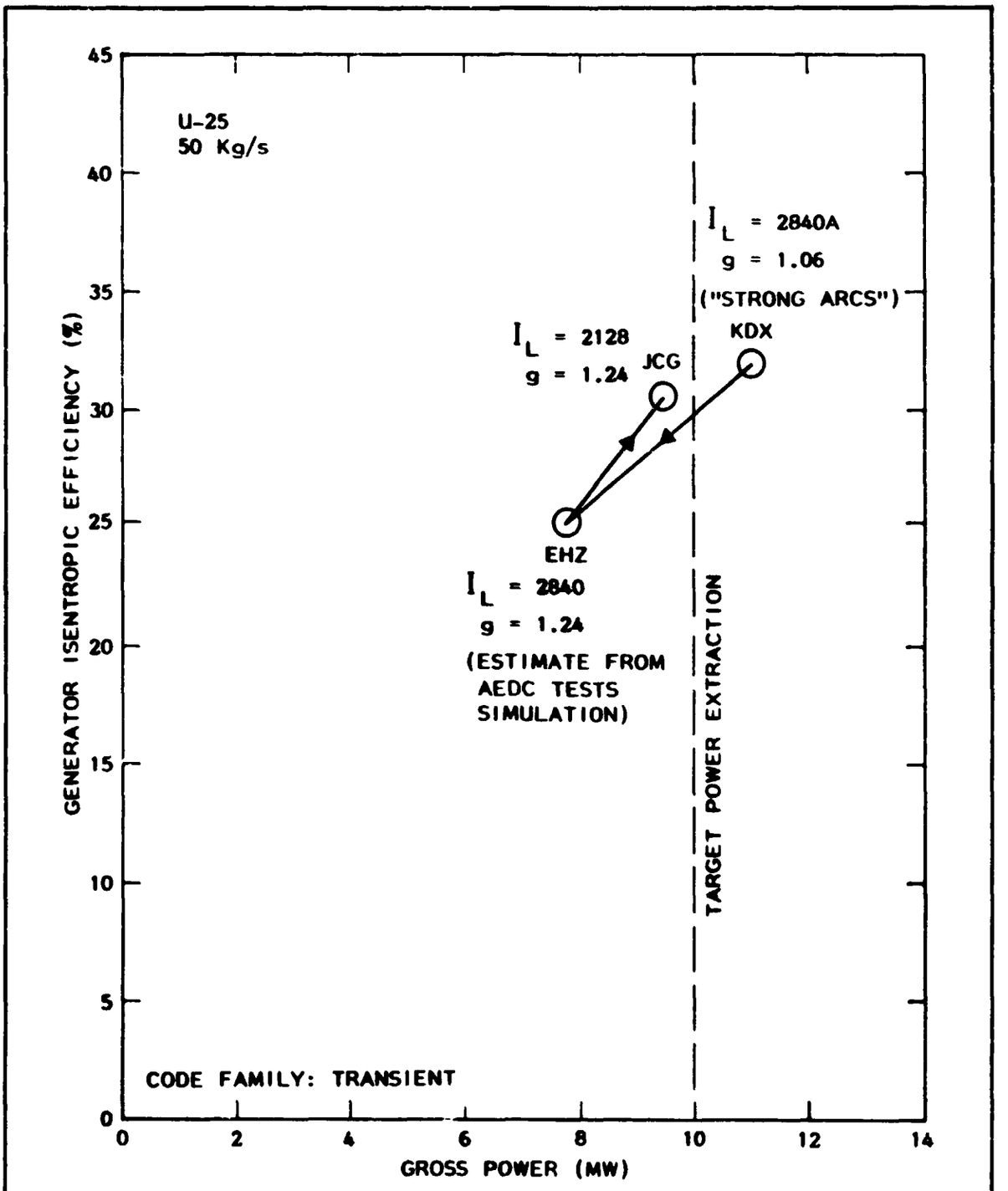

Fig. 5-31. Generator isentropic efficiency vs. gross power for simulation of U-25 with hot and cold walls.

0-4314

STD RESEARCH CORPORATION

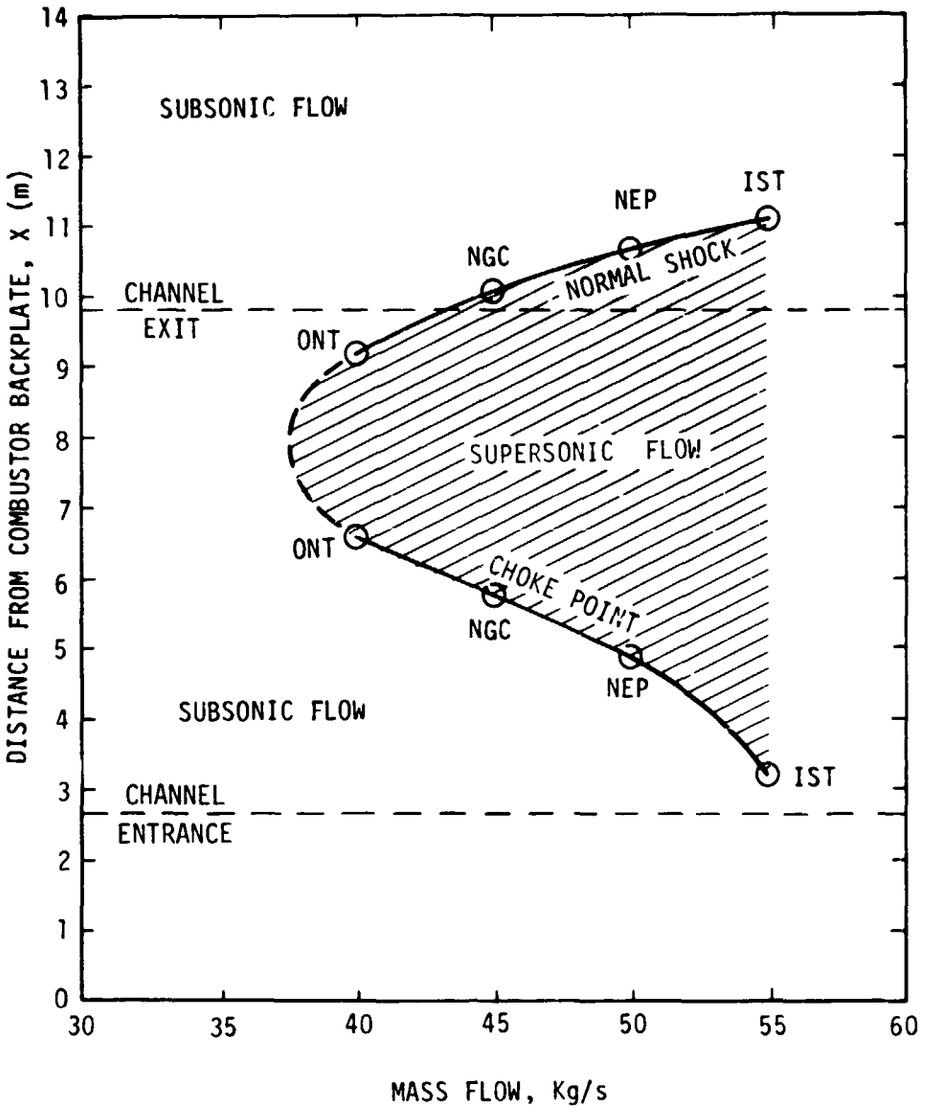

9-3354

Fig. 5-32. Shock location and choke points as a function of mass flowrate for the U-25 channel

STD RESEARCH CORPORATION

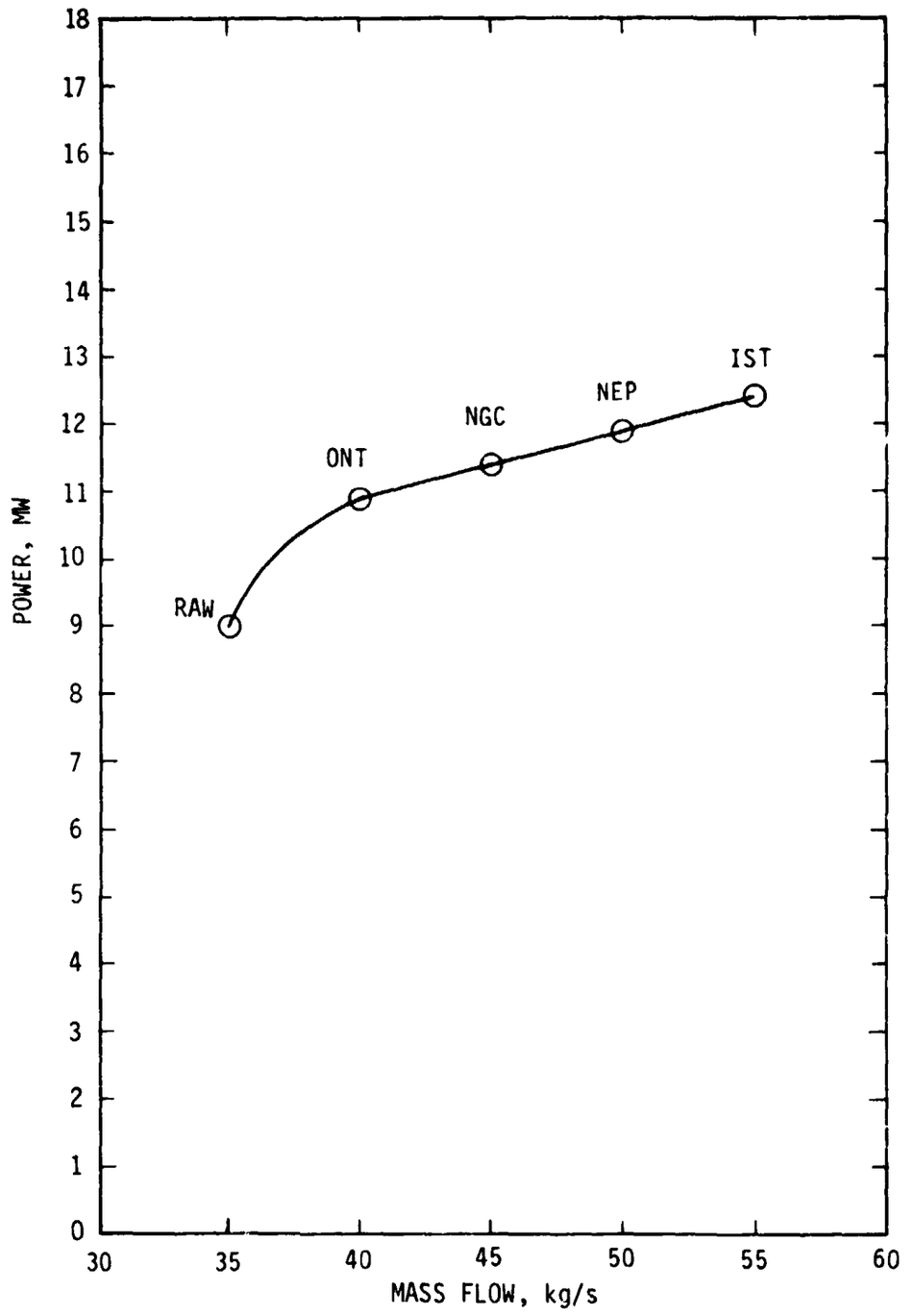

Fig. 5-33. Output power as a function of mass flowrate for the U-25 channel

9-3355

STD RESEARCH CORPORATION

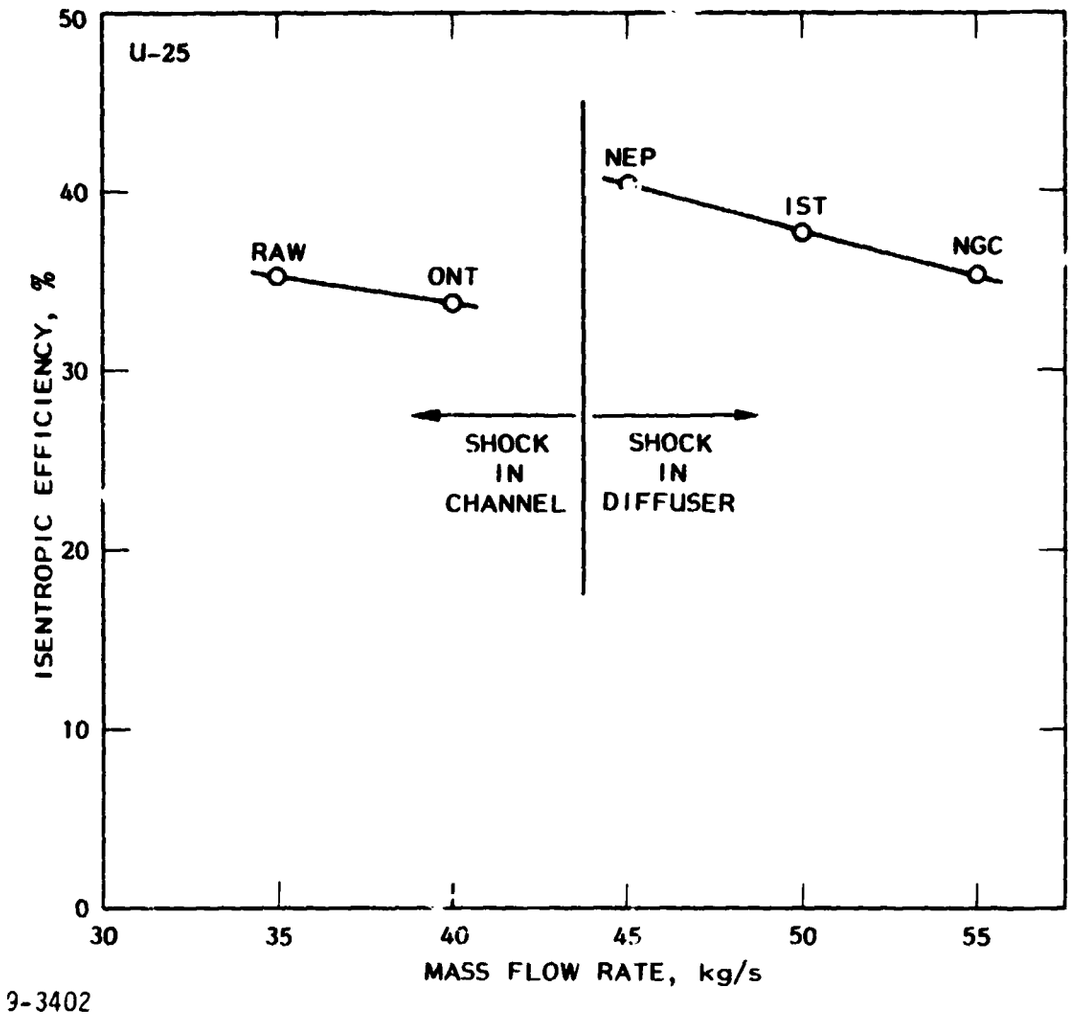

Fig. 5-34. Enthalpy extraction as a function of mass flow rate for the U-25 experiment.

6.0 PERFORMANCE OF NASA-SPECIFIED 500 MW(th) MHD GENERATOR

6.1 Channel Characterization

The full load operating characteristics of the NASA-specified 500 MW(th) MHD channel are given in Table 6-1. The generator is defined to be square, i.e. rectangular with aspect ratio of 1.0, from inlet to exit. The axial distribution of magnetic flux density increases from 4 T at the inlet to 6 T at 2.5 m from the inlet, then decreases linearly to 4.6 T at the exit of the generator. A list of the thermodynamic data to define the working fluid for this NASA-specified 500 MW(th) MHD channel are given in Table 6-2. The specifications contained in Tables 6-1 and 6-2 may not be consistent, i.e., it is possible that not all of these specifications can be attained simultaneously.

6.2 Generator Inlet Plane Electrical Conductivity Calculations

The specifictions of the working fluid and inlet thermodynamic and fluid mechanical conditions, given in Tables 6-1 and 6-2, were reduced to species inlet mole ratio, listed in Table 6-3, and inlet thermodynamic conditions. The thermodynamic conditions are inlet static temperature of 2710 K and inlet static pressure of 4.35 atm.

The inlet transport and thermodynamic properties for the NASA-specified 500 MW(th) MHD generator have been computed with a zero-dimensional, equilibrium method using the STDNASP code from the STD THERMODYNAMICS family of codes. For these conditions, the inlet thermodynamic and transport data are electron concentration of 2.71×10^{20} electrons/m^3 and electrical conductivity of 6.83 S/m.

Even with equilibrium chemistry, the conductivity in the inlet plane is more realistically a function of the distribution of static temperatures and pressures and also a function of the distribution of current. Since the electrical conductivity is approximately an exponential function of temperature and the electrical current raises the electron temperature, both of these two important effects will raise the value of average electrical conductivity in the inlet plane above that computed with the zero-dimensional, equilibrium code.

For example, at the 0.813 m station (inlet plane) of the HPDE the average electrical conductivity from computation CHPQUUUJBO is 10.4 S/m, and the electrical conductivity calculated for the average static temperature and average static pressure is 9.46 S/m. Thus, for this example, the multidimensional, nonequilibrium code computes an average inlet conductivity which is 10.6% higher than would be calculated by a zero-dimensional method. In another example, taken from the inlet plane of the Mark VI-C simulation STD68830HI, the average conductivity is 12.4 S/m and the zero-dimensional conductivity at the average static pressure and average static temperature is 12.2 S/m, a difference of only 2.0%.

TABLE 6-1

Full Load Operating Characteristics
For a NASA-Specified 500 MW(th) MHD Channel

1. Channel mass flow rate: 97.5 kg/s
2. Channel inlet average stagnation pressure: 6.5 atm
3. Channel inlet average stagnation temperature: 2837 K
4. Channel inlet height: 0.51 m
5. Channel inlet width: 0.51 m
6. Channel length. 14.8 m
7. Faraday load factor: 0.85
8. Channel inlet average mach number: 0.85
9. Burner and nozzle heat loss: 21 MW
10. Slag heat loss: 3.7 MW

0-4364

TABLE 6-2

Thermodynamic Data to Define the Working Fluid
For a NASA-Specified 500 MW(th) MHD Channel

1. Coal and Ash Analysis

A. Proximate analysis, weight percent

Moisture	22.7
Volatiles	29.4
Fixed Carbon	39.2
Ash	8.7

B. Ultimate Analysis, weight percent

Hydrogen	6.0
Carbon	52.1
Nitrogen	0.79
Oxygen	31.5
Sulfur	0.85

C. Ash analysis, weight percent

SiO_2	37.6
Al_2O_3	17.3
Fe_2O_3	5.1
TiO_2	0.7
P_2O_5	0.4
CaO	11.0
MgO	4.0
Na_2O	3.1
K_2O	0.5
SO_3	17.5 (assumed redundant)

0-4365

TABLE 6-2 (Continued)

D. Heating values

wet	20.73 MJ/kg
dry	26.87 MJ/kg

E. Coal dried to 5.0% moisture

F. Coal injected at 300 K

G. Coal carrier gas: none

2. Oxidizer

A. Air composition of 300 K, 0.0132 kg H_2O/kg dry air

B. Oxygen enriched to 35% O_2 by volume

C. Preheat to 922 K

3. Seed

A. 1% K by weight of channel mass flow rate

B. 0% by weight K_2SO_4

C. 100% by weight K_2CO_3

D. Anhydrous K_2CO_3

E. Seed temperature at 300 K

F. Seed injected downstream of ash removal

G. Seed carrier fluid: none

4. Combustor

A. Ash removal of 65%

B. Oxidizer/Fuel stoichiometric ratio of 0.90

5. Pilot

A. None

0-4366

TABLE 6-3

List of Species Used to Define the Working Fluid
at the Inlet of the NASA-specified 500 MW(th) Generator

Species	Mole Ratio
$C_{5.3302}$ $H_{4.2192}$ $N_{0.0693}$ $S_{0.0326}$ $O_{0.8716}$	1.0000
SiO_2	0.0269
Al_2O_3	0.0064
MgO	0.0037
TiO_2	0.00033
CaO	0.0074
Fe_2O_3	0.0012
P	0.00022
Na_2O	0.0019
K_2CO_3	0.0708
SO_3	0.0082
N_2	9.6694
O_2	5.3397
H_2O	0.542

0-4367

7.0 SCALE-UP CONSIDERATIONS FOR MHD POWER TRAINS

In order to put the critical phenomena and the performance obtained to date in the power trains discussed above into the context of the overall development program for MHD power generation, it is necessary to consider the scale dependence of the performance and behavior of MHD power trains. In [7-1], STD Research Corporation outlined convenient interaction parameters for correlating the performance and behavior of high interaction MHD power trains. These interaction parameters and the appropriate measures of power train performance are defined in Table 7-1. Case E of [7-1] is the original "Revision 7-C" design conditions of the U-25 generator. Case F of [7-1] pertained to the "Revision 4", "hot wall" design conditions of the AEDC/HPDE. The scale dependence of the performance of these two devices, relative to power trains ranging from the smallest (UTSI) to the largest commercial scale power train (the "STD Benchmark Power Train"), are depicted in Figs. 7-1 through 7-4 and 7-6 through 7-8, which are reproduced from [7-1].

In addition to the quasi-three-dimensional calculations discussed in [7-1], STD Research Corporation, under U.S. Department of Energy Contract AC-01-79ET15501 performed a series of calculations for cases B, C, F, and G in order to elucidate the scale dependence of other critical phenomena besides those considered in [7-1]. These phenomena included quantitative calculations of the scale dependence of secondary flows transient behavior, part load operation, and the effects of alternate cross-sectional shapes on channel performance. While the results of these additional investigations into the scale dependence of these phenomena did not generally yield as

simple and as elegant correlations as were obtained in [7-1], a number of interesting and important relationships were observed which will be described in the present section.

This section reviews the AEDC/HPDE performance to date in the context of the scaling parameters presented in Figs. 7-1 through 7-8 and reviews the additional investigations carried out under Contract AC-01-15501.

7.1 AEDC/HPDE Performance to Date

Figs. 7-1, 7-2, 7-3, and 7-4 summarize the electrical performance obtained by the AEDC/HPDE to date. It is observed that, at a magnetic field of 3.27 T, the HPDE has achieved approximately half of its original design goals. The enthalpy extraction rate is approximately 8% instead of 16%. The isentropic efficiency is approximately 37% rather than approximately 60%. The specific energy extraction is approximately 0.45 MJ/kg versus approximately 0.86 MJ/kg. The interaction parameter based on pressure obtained to date is approximately 0.99, which is the highest interaction parameter based on pressure achieved in modern experiments aimed at commercial power generation. This interaction parameter is compared to the original design interaction parameter of approximately 1.8.

Fig. 7-5 shows the development of the axial velocity profiles between the electrode walls and between the sidewalls in the Run 006-014 Q3D simulation CHPQUUUJBO. (The first three profiles are offset from the main channel outline due to a plotter error.) The development of the 15% sidewall overshoots at the exit of this generator are consistent with the interaction parameter based on velocity, S_u, of approximately

2.2, which is obtained in this experiment. (As pointed out in [7-1], supersonic generators have lower interaction parameters based on velocity for a given interaction parameter based on pressure. The design value of interaction parameter based on velocity is in excess of 10, because the original design was based on subsonic flow.) The ratio of the sidewall displacement thickness to the average electrode wall displacement thickness is exhibited in Fig. 7-6. It is clear that the AEDC/HPDE experiment has already achieved negative displacement thickness at the exit of the generator, according to the Q3D simulation. If properly instrumented with pressure probes, the experiment should be able to observe velocity overshoots under the Run 006-014 conditions. Fig. 7-7 shows the dependence of total channel blockage at the exit of the generator. It is seen that the AEDC generator performance to date has nearly passed the milestone of zero blockage at the exit of the channel. Finally, the average skin friction coefficient throughout the generator is exhibited in Fig. 7-8 as a function of the interaction parameter based on velocity. It is seen that the sidewall friction, while greater than the electrode wall skin friction, has not reached the steep part of the curve associated with very strong velocity overshoots on the sidewalls.

It is evident that the AEDC/HPDE offers an early opportunity to study multidimensional phenomena in high interaction MHD devices. Many of the effects which are predicted by the STD/MHD codes will become important as the interaction level of the AEDC/HPDE is increased from its present levels.

7.2 Optimum Mach Number Distribution and Its Effect on Part-Load and Transient Behavior

The Mach number distribution determines performance because the power density falls dramatically on either side of an optimum Mach number value. The optimum Mach number is determined by the thermodynamic and transport properties of the working fluid and the stagnation conditions at each generator station. A series of part-load and off-design calculations performed by STD illustrate the impact of the Mach number distribution on generator performance.

Critical phenomena related to the optimum Mach number distribution and its effect on part-load and transient behavior were deduced by analyses and evaluation of computations with the TRANSIENT family of codes which were completed under Contract AC-01-79ET15501. A diagram which schematically presents the logic of the variations of the part-load and unsteady cases which were completed with the TRANSIENT code family under is given as Fig. 7-9. For each of four channels with thermal inputs of 20 MW, 50 MW, 300 MW, and 2000 MW, a nominal steady-state solution was computed. These steady-state solutions were the starting point of the following variations: (1) 5% step reduction in mass flow, (2) $\pm$ 5% sine wave input in mass flow; (3) 30% quasi-steady mass flow reduction; and (4) 30% instantaneous load reduction. The electrical connection of each channel was then redesigned from Faraday to diagonal or diagonal to Faraday and the 30% quasi-steady mass flow reduction cases were calculated. A list of the final computations performed for these cases is presented in Table 7-2.

The Mach number distributions for these channels during mass flow rate reduction are displayed in Figs. 7-10 through 7-17 for both the nominal electrical connections and the alternate electrical connections. For the 300 MW Faraday connected channel, the mass flow linearly decreases from 100% to 70% over the 300 ms time range of the computation, as shown in Fig. 7-14. For this case, the flow starts out almost entirely subsonic. As the mass flow rate decreases, the small supersonic region becomes subsonic and the Mach number at each station in the entire flow field decreases.

The Mach number distribution for the 50 MW Faraday connected channel is shown in Fig. 7-13. This channel is initially completely supersonic with a shock near the end of the diffuser. As the mass flow rate decreases to 70% of its initial value, the Mach number throughout the channel decreases. The Mach number at the channel entrance decreases only 0.3% but the Mach number at the channel exit decreases by 12.5%.

A correlation of the normalized gross power to normalized mass flow rate for the four channels is shown in Figs. 7-18 and 7-19. The reduction in power follows very closely the reduction in mass flow, except in the case of the 50 MW(th) channel. The power output of the 50 MW(th) channel remains high as the mass flow decreases because its profile does not go far from optimum.

As the mass flow rate varies, so does the combustor pressure and the required compressor power. The combustor pressure is given as a function of normalized mass flow rate for the 20, 50, 300, and 2000 MW(th) flow trains in Fig. 7-20 for the nominal electrical hookup and in Fig. 7-21 for the

alternate electrical hookup. The net power is given as a function of normalized mass flow rate for the 20 and 50 MW(th) flow trains in Figs. 7-22 and 7-23. The normalized net power is given as a function of the normalized mass flow rate for the 300 and 2000 MW(th) flow trains in Figs. 7-24 and 7-25.

The relationships between gross power per unit mass flow rate (specific energy extraction) and the product of interaction parameter and electrical efficiency are shown in Figs. 7-26 and 7-27. For each channel, a trace is shown which describes the result of linearly decreasing the mass flow from its nominal value to 70% of the nominal. For the two subsonic channels, nominally 300 MW(th) and 2000 MW(th), both the specific energy extraction and the interaction decrease as the mass flow rate is reduced. This is attributed to the departure of the channel Mach number distribution further from the optimum distribution. Conversely, for the two supersonic channels, nominally 20 MW(th) and 50 MW(th), the specific energy extraction and the interaction increase with decreasing mass flow. This effect is attributed to the fact that the Mach number distribution for the supersonic designs of the small channels approaches the optimum Mach number distribution as the mass flow rate is reduced. These results point to the maintenance of the optimum Mach number distribution as an important consideration for MHD generator load following.

The relationship between power output and the specified mass flow which varies sinusoidally with a $\pm$ 5% amplitude, is given for the nominal 20 MW(th), Faraday-connected case in Fig. 7-28 and for the nominal 300 MW(th), Faraday-connected case in Fig. 7-29. These figures show both the relative amplitudes and the phase difference between the mass fluctuation and the resulting power fluctuations.

7.3 Effect of Alternate Cross-Sectional Shapes on Channel Performance

The effects of alternate cross-sectional shapes on c l performance were deduced by analysis and evaluation of com ations completed under Contract AC-01-79ET15501 with codes from the Q3DYZ of the Q3D Family of codes. A diagram which represents schematically the variations of the cases which were completed is presented as Fig. 7-30. For each of four channels with nominal thermal inputs of 20 50 MW, 300 MW, and 2000 MW, three axial stations were chosen analysis. These three axial stations were chosen to be representative of the front end, middle, and the back end of the channels. At each of these stations and for each channel, three different cross-sectional shapes, rectangular, hexagonal, and elliptical, were considered. Therefore, there were 36 cases completed. A list of these computations is given in Table 7-3.

The Q3DYZ code has been applied to analyze Faraday, diagonal-conducting-wall, and insulating-wall-diagonal channels. For the computations listed in Table 7-3, the 20 MW and 2000 MW generators are Faraday-connected, the 50 MW(th) generator is a diagonal-conducting-wall generator, and the 300 MW generator is an insulating-wall-diagonal.

At each station in each channel, the load factor, enthalpy flux, magnetic field strength, average static pressure, wall temperature, anode-center boundary layer thickness, cathode-center boundary layer thickness, sidewall-center boundary layer thickness, electrode center wall temperature, and sidewall-center wall temperature were the same for each different geometry. At each station in the 20, 50 and 300 MW(th) channels, the cross-sectional area and aspect ratio were also the same for each geometry.

The geometrical definitions used for the hexagonal, rectangular, and elliptical shapes of these computations are given in Fig. 7-31. For all hexagonal shaped channels the included electrode angle was 120 degrees. For the 20, 50, and 300 MW(th) channels, the angles subtended by the electrodes for the elliptical shapes were the same angles, as measured from the center point in the channel, as for the corresponding rectangular shapes. For the 2000 MW(th) channel, the hexagonal cases were regular hexagons and the elliptical cases had aspect ratios of unity (i.e., circular).

The data which have been compiled for the 36 cases are listed in Tables 7-4, 7-5, 7-6, and 7-7 for the 20, 50, 300, and 2000 MW(th) channels, respectively. The data which are listed in these Tables are run identifier, shape, axial location, magnetic field, load factor, diagonalization angle (for the diagonally-connected channel), aspect ratio, cross-sectional area, cross-section perimeter, enthalpy flow, enthalpy flux, average static pressure, average static temperature, core static temperature, average axial velocity, core axial velocity, average electrical conductivity, core electrical conductivity, average Hall parameter, electrode wall temperature, sidewall temperature, anode boundary layer thickness, cathode boundary layer thickness, sidewall boundary layer thickness, Hall field, Faraday voltage, load current, power output, internal resistance, plasma nonuniformity factor, and two power production parameters, C_{25} and C_{26}. The power production parameter C_{25} is defined as the power divided by the product of load factor, one minus the load factor, core electrical conductivity, magnetic field squared, core axial velocity squared, and the cross-sectional area, and this parameter represents the performance at the station relative to an ideal channel with no thermal or velocity gradients. The power production parameter C_{26} is defined as the power divided

by the product of load factor, one minus the load factor, average electrical conductivity, magnetic field squared, average axial velocity squared, and the cross-sectional area; this parameter represents the performance at the station relative to a simplified one-dimensional model.

The analyses and interpretations of the computations with alternate cross-sections have resulted in the following implications:

(1) Some of the inefficiency caused by conductivity nonuniformity can be removed by appropriate choice of a channel cross-section. The larger the nonuniformity factor in a particular rectangular channel, the larger the potential gain which can be obtained with a nonrectangular geometry. As the nonuniformity factor increases with axial distance down the channel, the improvement in power obtained from nonrectangular geometry should also increase with axial distance.

In order to obtain the potential increase in performance, it is necessary to choose a geometry so that the boundary layer voltage drop is minimized, but not a geometry which causes the power producing core to become shorted out. An incorrect choice of geometry for a particular case can result in none of the potential gain from being exploited. In most cases, the potential loss from an inappropriate choice of geometry is much greater than the potential gain from an appropriate choice.

An example of the reduction of the boundary layer voltage drop is given with assistance from Figs. 7-32 through 7-35. The isopotentials and current streamlines for the 2 m axial station of the nominal 50 MW(th) channel are given for the rectangular cross-section in Figs. 7-32 and 7-33,

respectively. The isopotentials and current streamlines for the corresponding elliptical cross-section are shown in Figs. 7-34 and 7-35, respectively. The region of voltage drop near the anode and cathode is much larger for the rectangular case, Fig. 7-32, than for the elliptical case, Fig. 7-34. The peak potential (at the zero field point) for the cathode region in the rectangular case is 32 V, and the peak potential for the cathode region in the elliptical case is 17 V. That is a difference of about a factor of two.

(2) The geometry (cross-sectional shape) that improves the performance of one particular channel can yield poorer performance than the rectangular geometry for a different channel.

The optimum geometric shape is a complex function of many parameters (boundary layer thicknesses, wall temperatures, Hall parameter, to name a few) and the substitution of this shape into a different channel with different values for these important parameters will yield different results. An illustration of this can be found with the hexagonal shapes for the 20 MW(th) and 300 MW(th) channels. For each of the stations for the 20 MW(th) channel, the hexagonal case had better performance than the corresponding rectangular case, but for each of the stations for the 300 MW(th) channel, the hexagonal case had worse performance than the corresponding rectangular case.

(3) As shown by the results for the 50 MW(th) channel cases, compared to the results from the three other channels, the electrical performance of a completely diagonal-conducting-wall channel is not as strong a function of cross-sectional shape as for the insulating wall Faraday-connected channel. Since the diagonal-conducting-wall channel has all walls as

conductors, the current can enter the walls where it is most efficient for the particular geometry and distributions of plasma properties. However, this does not say that the DCW channel is better than a Faraday-connected channel.

(4) Geometries which have less surface-to-area ratios and larger hydraulic diameters than the rectangular cross-sectional shape, but have the same area, have smaller losses due to heat transfer to the walls, wall shear stresses, and viscous effects. For particular cases, each of these three losses can be simultaneously decreased by over 10%.

(5) Geometries which allow the current to enter the electrodes parallel to the magnetic field have a lower internal plasma impedance. The lower internal plasma impedance can be utilized to improve the performance of the channel.

An example of the effect of lower plasma impedance is given with assistance from Figs. 7-36 through 7-39. The isopotentials and current streamlines for the 1 m station of the nominal 20 MW(th) channel are given for the rectangular cross-section case in Figs. 7-36 and 7-37, respectively. The isopotentials and current streamlines for the corresponding hexagonal cross-sections are shown in Figs. 7-38 and 7-39, respectively. As shown on Fig. 7-37, the current enters the electrode nearly perpendicular to the magnetic field for the rectangular case and, as shown on Fig. 7-39, the current enters the electrode nearly parallel to the magnetic field for the hexagonal case. The internal resistance of the hexagonal case, illustrated by Figs. 7-38 and 7-39, is 32% less than that for the rectangular case. At the same Faraday load factor of 0.5 (for maximum power production), the Faraday voltage is 13% lower for the hexagon, but the load current is 28% higher, so

that the power output is 12% higher for the hexagon than for the rectangle.

Although the cases represented in Table 7-3 and Fig. 7-30 define a systematic approach to analysis of the effects of cross-sectional geometry, the detailed analyses performed to date have not resulted in complete and unambiguous interpretations which are applicable in all cases. These calculations of performance with variable cross-sectional shapes did not include sufficient parametric variation and were applied over too great a range of conditions to obtain regular trends with scale and position in the channel. It is probable that many of the elliptical or hexagonal cross-sections with lower performance than the rectangular design values could be optimized to outperform the rectangle when additional systematic parametric variations are considered. In addition, other cross-sectional shapes (e.g., octagonal) may provide better performance than any of the three shapes considered.

REFERENCES

[7-1] C.D. Maxwell, S.T. Demetriades, D.A. Oliver, A.A. Vetter, T.F. Swean, "Scale-up of Advanced MHD Generators", AIAA 18th Aerospace Sciences Meeting, Paper No. AIAA-80-0179, Pasadena, California, January 1980.

TABLE 7-1

Interaction Parameters and Performance Indices for Evaluation of MHD Generator Performance Scaling

Interaction parameter based on pressure

$$I_p \equiv \int_0^L \frac{J_y B}{p}\, dx$$

Interaction parameter based on velocity

$$S_u \equiv L \frac{\sigma B^2}{\rho U}$$

Generalized nonuniformity factor

$$G \approx g + (g-1(\beta^2))$$

where

$$g = \langle \sigma \rangle \langle 1/\sigma \rangle$$

Electrical conversion efficiency

$$\eta_e = \frac{\vec{J} \cdot \vec{E}}{\vec{J} \cdot (\vec{U} \times \vec{B})}$$

Isentropic efficiency

$$\frac{\mathbb{P}}{(\Delta H)_{isentropic}}$$

Enthalpy extraction ratio

$$\frac{\mathbb{P}}{mH_0} \quad \frac{\text{power out}}{\text{thermal power in}}$$

Specific energy extraction

$\frac{\mathbb{P}}{\dot{m}}$: power per unit mass flow rate

0-4354

TABLE 7-2

List of Final TRANSIENT Computations Performed Under Contract AC-01-79ET15501

Case	Run	Date	Nominal Thermal Flux (MW)	Electrical Connection	Identification
1.1.1	A5MYUDMIE4	5/30/79	20	Faraday	benchmark run
1.1.2	A5MYGWJIE5	5/31/79	20	Faraday	5% step reduction in mass flow
1.1.3	A5MYEWMIE5	5/31/79	20	Faraday	5% ripple in mass flow
1.1.4/1.1.5	A5MYFALIE5	5/31/79	20	Faraday	10%/30% quasi-steady mass flow and power reduction
1.1.6	A5MYFDQIE5	5/31/79	20	Faraday	30% instantaneous load reduction
1.1.7	A5MYHJDIE5	5/31/79	20	Diagonal	benchmark run
1.1.8/1.1.9	A5MYSHSIFA	6/1/79	20	Diagonal	10%/30% quasi-steady mass flow and power reduction
2.1.1	CHTQPENIFA	6/1/79	50	Diagonal	benchmark run
2.1.2	A5MYSKDIFA	6/1/79	50	Diagonal	5% step reduction in mass flow
2.1.3	A5MYFZPIFD	6/4/79	50	Diagonal	5% ripple in mass flow
2.1.4/2.1.5	A5MYCJGIFE	6/5/79	50	Diagonal	10%/30% quasi-steady mass flow and power reduction
2.1.6	A5MYCLTIFE	6/5/79	50	Diagonal	30% instantaneous load reduction
2.1.1	A5MYHSZIEY	5/25/79	50	Faraday	benchmark run
2.1.8/2.1.9	A5MYJIKIEY	5/25/79	50	Faraday	10%/30% quasi-steady mass flow and power reduction
3.1.1	A5MYDFJIDI	4/9/79	300	Faraday	benchmark run
3.1.2	A5MYBBEIEM A5MYBEWIEM	5/13/79	300	Faraday	5% instantaneous mass flow reduction
3.1.3	A5MYBFRIEM	5/13/79	300	Faraday	5% mass flow ripple
3.1.4/3.1.5	A5MYBGNIEM	5/13/79	300	Faraday	10%/30% quasi-steady mass flow and power reduction
3.1.6	A5MYBILIEM	5/13/79	300	Faraday	30% instantaneous load reduction
3.1.7	A5MYRIYIFA	6/1/79	300	Diagonal	benchmark run

TABLE 7-2

List of Final TRANSIENT Computations Performed Under Contract AC-01-79ET15501
(continued)

Case	Run	Date	Nominal Thermal Flux (MW)	Electrical Connection	Identification
3.1.8/3.1.9	A5MYFUGIFD	6/4/79	300	Diagonal	10%/30% quasi-steady mass flow and power reduction
4.1.1	BRCYKKRIEE	5/5/79	2000	Faraday	benchmark run
4.1.2	A5MYCHZIEN	5/14/79	2000	Faraday	5% instantaneous mass flow reduction
4.1.3	A5MYEWRIEN/ A5MYBTMIET	5/14/79/ 5/20/79	2000	Faraday	5% mass flow ripple
4.1.4/4.1.5	A5MYCXGIEN	5/14/79	2000	Faraday	10%/30% quasi-steady mass flow and power reduction
4.1.6	A5MYDEEIEN	5/14/79	2000	Faraday	30% instantaneous load reduction
4.1.7	A5MYRMYIFA	6/1/79	2000	Diagonal	benchmark run
4.1.8/4.1.9	BRCYKPSIFS	6/19/79	2000	Diagonal	10%/30% quasi-steady mass flow and power reduction

TABLE 7-3

List of Final Q3DYZ Computations Performed Under Contract AC-01-79ET15501

Run	Date	Nominal Thermal Flux (MW)	Cross-Sectional Shape	Axial Location (m)
BRCYCHPIFQ	17 June 1979	20	rectangle	0.50
BRCYCJAIFQ	17 June 1979	20	rectangle	1.00
BRCYCJCIFQ	17 June 1979	20	rectangle	1.49
BRCYCISIFQ	17 June 1979	20	hexagon	0.50
BRCYCIUIFQ	17 June 1979	20	hexagon	1.00
BRCYCJKIFQ	17 June 1979	20	hexagon	1.49
BRCYCIQIFQ	17 June 1979	20	ellipse	0.50
BRCYCIWIFQ	17 June 1979	20	ellipse	1.00
BRCYCJFIFQ	17 June 1979	20	ellipse	1.49
BRCYBIEIFQ	17 June 1979	50	rectangle	1.00
BRCYBIIIFQ	17 June 1979	50	rectangle	2.00
BRCYBIQIFQ	17 June 1979	50	rectangle	3.00
BRCYBHFIFQ	17 June 1979	50	hexagon	1.00
BRCYBILIFQ	17 June 1979	50	hexagon	2.00
BRCYBIMIFQ	17 June 1979	50	hexagon	3.00
BRCYBHQIFQ	17 June 1979	50	ellipse	1.00
BRCYBRNIFQ	17 June 1979	50	ellipse	2.00
BRCYBIOIFQ	17 June 1979	50	ellipse	3.00
BRCYBGLIFQ	17 June 1979	300	rectangle	2.00
BRCYBGBIFQ	17 June 1979	300	rectangle	3.50
BRCYBFZIFQ	17 June 1979	300	rectangle	5.00
BRCYBGHIFQ	17 June 1979	300	hexagon	2.00
BRCYBGFIFQ	17 June 1979	300	hexagon	3.50
BRCYBFLIFQ	17 June 1979	300	hexagon	3.00
BRCYBGJIFQ	17 June 1979	300	ellipse	2.00
BRCYBGDIFQ	17 June 1979	300	ellipse	3.50
BRCYBFXIFQ	17 June 1979	300	ellipse	5.00
CHRQBUEIF3	29 June 1979	2000	rectangle	4.00
CHRQLNIIF3	29 June 1979	2000	rectangle	7.50
CHRQBVFIF3	29 June 1979	2000	rectangle	11.00
CHRQEHRIF3	29 June 1979	2000	hexagon	4.00
BRCYEHPIF3	29 June 1979	2000	hexagon	7.50
CHRQBXJIF3	29 June 1979	2000	hexagon	11.00
CHRQDWBIF2	28 June 1979	2000	ellipse	4.00
BRCYHQJIF2	28 June 1979	2000	ellipse	7.50
BRCYINQIF2	28 June 1979	2000	ellipse	11.00

0-4368

TABLE 7-4

Data from Q3DYZ Computations Performed under
Contract AC-01-79ET15501 from the Nominal 20 MW(th) Channel

Run	Shape	x	B	K_F	H/W	A	P	$\dot{H}$	H_{flux}	<p>	<T>	T_c	<U>	U_c	<σ>	σ_c
		m	T			m^2	m	MW	MW/m^2	kPa	K	K	m/s	m/s	S/m	S/m
BRCYCHPIFQ	rect.	0.498	2.66	0.500	1.855	0.015	0.510	15.25	1032.7	85.85	2655	2728	1454	1592	12.26	15.61
BRCYCISIFQ	hex.	0.498	2.66	0.500	1.855	0.015	0.472	15.25	1032.7	85.85	2656	2731	1452	1594	12.42	15.87
BRCYCIQIFQ	ellip.	0.498	2.66	0.500	1.855	0.015	0.470	15.22	1032.7	85.85	2659	2737	1449	1598	12.69	16.31
BRCYCJAIFQ	rect.	0.996	2.76	0.500	1.578	0.020	0.586	14.71	721.5	58.39	2572	2658	1484	1669	10.92	14.93
BRCYCIJIFQ	hex.	0.996	2.76	0.500	1.578	0.020	0.542	14.71	721.5	58.39	2573	2663	1482	1673	11.11	15.32
BRCYCIWIFQ	ellip.	0.996	2.76	0.500	1.578	0.020	0.524	14.67	721.5	58.34	2575	2666	1480	1675	11.24	15.48
BRCYCJCIFQ	rect.	1.494	2.34	0.500	1.399	0.027	0.662	14.18	531.7	43.37	2508	2602	1482	1698	9.78	14.10
BRCYCJKIFQ	hex.	1.494	2.34	0.500	1.399	0.027	0.612	14.18	531.7	43.37	2511	2610	1479	1703	9.99	14.63
BRCYCJFIFQ	ellip.	1.494	2.34	0.500	1.399	0.027	0.590	14.15	531.7	43.37	2511	2609	1478	1702	10.03	14.53

TABLE 7-4

Data from Q3DYZ Computations Performed under
Contract AC-01-79ET15501 from the Nominal 20 MW(th) Channel
(continued)

Run	Shape	x	<β>	T_{we}	T_{ws}	δ_c	δ_a	δ_s	E_x	V_F	I_L	Power	R_I	C_{25}	C_{26}	G
		m		K	K	mm	mm	mm	V/m	V	kA/m	MW/m	Ω·m			
BRCYCHPIFQ	rect.	0.498	1.608	1750	1750	14.9	13.6	15.6	-2516	-332	-1.704	0.565	-194.8	0.545	0.833	1.20
BRCYCISIFQ	hex.	0.498	1.608	1750	1750	14.9	13.6	15.6	-2726	-297	-2.015	0.598	-147.4	0.566	0.872	1.15
BRCYCIQIFQ	ellip.	0.498	1.609	1750	1750	14.9	13.6	15.6	-2577	-322	-1.819	0.586	-177.0	0.537	0.840	1.19
BRCYCJAIFQ	rect.	0.996	2.369	1750	1750	24.3	21.8	24.1	-3537	-383	-1.860	0.712	-205.9	0.441	0.762	1.31
BRCYCIJIFQ	hex.	0.996	2.370	1750	1750	24.3	21.8	24.1	-4046	-335	-2.377	0.797	-140.9	0.478	0.841	1.19
BRCYCIWIFQ	ellip.	0.996	2.371	1750	1750	24.3	21.8	24.1	-3638	-371	-1.996	0.741	-185.9	0.439	0.775	1.29
BRCYCJCIFQ	rect.	1.494	2.631	1750	750	31.1	31.4	32.4	-3314	-350	-1.716	0.600	-204.0	0.405	0.767	1.30
BRCYCJKIFQ	hex.	1.494	2.632	1750	1750	31.1	31.4	32.4	-3795	-301	-2.226	0.671	-135.2	0.434	0.843	1.19
BRCYCJFIFQ	ellip.	1.494	2.633	1750	1750	31.1	31.4	32.4	-3300	-340	-1.765	0.600	-192.6	0.391	0.752	1.33

TABLE 7-5

Data from Q3DYZ Computations Performed under
Contract AC-01-79ET15501 from the Nominal 50 MW(th) Channel

Run	Shape	x	B	tanθ	K_x	H/W	A	P	$\dot{H}$	H_{flux}	⟨P⟩	⟨T⟩	T_c	⟨U⟩	U_c	⟨σ⟩	σ_c
		m	T				m^2	m	MW	MW/m^2	kPa	K	K	m/s	m/s	S/m	S/m
BRCYBIEIFQ	rect.	1.0	2.96	0.9823	0.500	1.829	0.034	0.770	44.37	1311	129.3	2630	2714	1332	1490	8.190	11.05
BRCYBHFIFQ	hex.	1.0	2.96	0.9823	0.500	1.829	0.034	0.713	44.36	1311	129.3	2630	2717	1330	1493	8.307	11.26
BRCYBHQIFQ	ellip.	1.0	2.96	0.9823	0.500	1.829	0.034	0.696	44.28	1311	129.3	2634	2724	1327	1497	8.549	11.65
BRCYBIIIFQ	rect.	2.0	2.94	0.9225	0.500	1.501	0.046	0.879	42.57	919	94.4	2556	2656	1294	1490	7.209	10.66
BRCYBILIFQ	hex.	2.0	2.94	0.9225	0.500	1.501	0.046	0.812	42.56	919	94.4	2557	2662	1292	1494	7.330	10.99
BRCYBRNIFQ	ellip.	2.0	2.94	0.9225	0.500	1.501	0.046	0.785	42.48	919	94.4	2559	2664	1290	1496	7.455	11.10
BRCYBIQIFQ	rect.	3.0	2.78	0.8661	0.500	1.294	0.060	0.988	40.95	683	76.0	2490	2602	1224	1433	6.084	9.65
BRCYBIMIFQ	hex.	3.0	2.78	0.8661	0.500	1.294	0.060	0.914	40.95	683	76.0	2491	2610	1222	1438	6.184	10.06
BRCYBIOIFQ	ellip.	3.0	2.78	0.8661	0.500	1.294	0.060	0.877	10.87	683	76.0	2493	2608	1221	1437	6.254	9.96

TABLE 7-5

Data from Q3DYZ Computations Performed under
Contract AC-01-79ET15501 from the Nominal 50 MW(th) Channel
(continued)

Run	Shape	x	⟨β⟩	T_{we}	T_{ws}	δ_c	δ_a	δ_s	E_x	V_F	I_L	Power	R_I/L	C_{25}	C_{26}	G
		m		K	K	mm	mm	mm	V/m		A	MW/m	Ω·m			
BRCYBIEIFQ	rect.	1.0	1.172	1750	1750	28.7	28.4	28.8	-2136	-522.1	487.3	1.041	4.383	0.572	0.966	1.035
BRCYBHFIFQ	hex.	1.0	1.172	1750	1750	28.7	28.4	28.8	-2128	-566.7	492.1	1.047	4.324	0.563	0.961	1.040
BRCYBHQIFQ	ellip.	1.0	1.173	1750	1750	28.7	28.4	28.8	-2169	-598.0	512.3	1.111	4.234	0.576	0.998	1.002
BRCYBIIIFQ	rect.	2.0	1.544	1750	1750	43.8	48.2	42.0	-2481	-603.6	460.1	1.142	5.392	0.482	0.945	1.058
BRCYBILIFQ	hex.	2.0	1.544	1750	1750	43.8	48.2	42.0	-2469	-668.4	465.9	1.148	5.310	0.468	0.938	1.066
BRCYBRNIFQ	ellip.	2.0	1.546	1750	1750	43.8	48.2	42.0	-2519	-691.4	477.9	1.204	5.271	0.485	0.972	1.029
BRCYBIQIFQ	rect.	3.0	1.760	1750	1750	64.5	64.2	51.5	-2468	-595.5	395.4	0.976	6.242	0.425	0.924	1.082
BRCYBIMIFQ	hex.	3.0	1.760	1750	1750	64.5	64.2	51.5	-2448	-670.0	399.8	0.979	6.123	0.406	0.915	1.093
BRCYBIOIFQ	ellip.	3.0	1.762	1750	1750	64.5	64.2	51.5	-2498	-680.1	407.2	1.017	6.135	0.428	0.943	1.060

TABLE 7-6

Data from Q3DYZ Computations Performed under
Contract AC-01-79ET15501 from the Nominal 300 MW(th) Channel

Run	Shape	x	B	K	H/W	A	P	$\dot{H}$	H_{flux}	$\langle p \rangle$	$\langle T \rangle$	T_c	$\langle U \rangle$	U_c	$\langle \sigma_1 \rangle$	σ_2
		m	T			m^2	m	MW	MW/m^2	kPa	K	K	m/s	m/s	S/m	S/m
BRCYBGLIFQ	rect.	2.0	6.02	0.500	1.938	0.212	1.945	245.0	1154.0	24.64	2669	2745	728.2	758.7	9.418	11.14
BRCYBGHIFQ	hex.	2.0	6.02	0.500	1.938	0.212	1.805	245.0	1154.5	4.64	2666	2744	728.5	758.3	9.373	11.08
BRCYBGJIFQ	ellip.	2.0	6.02	0.500	1.938	0.211	1.761	244.0	1154.5	24.64	2673	2752	726.4	761.0	9.686	11.52
BRCYBGBIFQ	rect.	3.5	5.73	0.500	1.738	0.303	2.286	228.4	853.9	15.89	2523	2614	758.7	782.6	6.695	8.30
BRCYBGFIFQ	hex.	3.5	5.73	0.500	1.738	0.303	2.117	228.4	753.9	15.89	2519	2610	759.4	781.4	6.591	8.17
BRCYBGDIFQ	ellip.	3.5	5.73	0.500	1.738	0.302	2.055	227.3	753.8	15.89	2527	2620	757.1	784.6	6.873	8.56
BRCYBFZIFQ	rect.	5.0	5.44	0.500	1.497	0.438	2.701	213.5	487.5	10.18	2370	2463	787.8	793.8	4.060	5.29
BRCYBFLIFQ	hex.	5.0	5.44	0.500	1.497	0.438	2.498	213.5	487.5	10.18	2361	2457	789.4	791.3	3.885	5.10
BRCYBFXIFQ	ellip.	5.0	5.44	0.500	1.497	0.436	2.407	212.5	487.5	10.18	2373	2468	786.6	795.4	4.156	5.42

TABLE 7-6

Data from Q3DYZ Computations Performed under
Contract AC-01-79ET15501 from the Nominal 300 MW(th) Channel
(continued)

Run	Shape	x	$\langle \beta \rangle$	T_{we}	T_{ws}	δ_c	δ_a	δ_s	E_x	V_F	I_L	Power	R_J	C_{25}	C_{26}	G
		m		K	K	mm	mm	mm	V/m	V	kA/m	MW/m	$\Omega \cdot m$			
BRCYCHPIFQ	rect.	2.0	1.423	2058	850	50.1	50.9	49.5	-2802	-1426	-6.019	8.584	-236.9	0.696	0.893	1.120
BRCYBGHIFQ	hex.	2.0	1.422	2058	850	50.1	50.9	49.5	-2746	-1321	-6.172	8.152	-214.0	0.665	0.852	1.174
BRCYBGJIFQ	ellip.	2.0	1.425	2058	850	50.1	50.9	49.5	-2778	-1390	-6.056	8.421	-229.5	0.659	0.861	1.161
BRCYBGBIFQ	rect.	3.5	1.984	2025	756	82.5	84.2	73.7	-3465	-1581	-4.740	7.493	-333.5	0.592	0.781	1.280
BRCYBGFIFQ	hex.	3.5	1.980	2025	756	82.5	84.2	73.7	-3178	-1477	-4.513	6.664	-327.3	0.537	0.705	1.418
BRCYBGDIFQ	ellip.	3.5	1.987	2025	756	82.5	84.2	73.7	-3430	-1555	-4.789	7.448	-324.7	0.571	0.763	1.311
BRCYBFZIFQ	rect.	5.0	2.751	1993	575	114.8	118.3	117.3	-4135	-1710	-3.205	5.481	-533.5	0.507	0.671	1.490
BRCYBFLIFQ	hex.	5.0	2.739	1993	575	114.8	118.3	117.3	-3606	-1584	-2.835	4.491	-558.7	0.434	0.572	1.743
BRCYBFXIFQ	ellip.	5.0	2.755	1993	575	114.8	118.3	117.3	-4094	-1689	-3.233	5.462	-522.4	0.493	0.658	1.520

TABLE 7-7

Data from Q3DYZ Computations Performed under
Contract AC-01-79ET15501 from the Nominal 2000 MW(th) Channel

Run	Shape	x	B	k_F	H/W	A	P	$\dot{H}$	H_{flux}	$\langle p \rangle$	$\langle T \rangle$	T_c	$\langle U \rangle$	U_c	$\langle \sigma \rangle$	σ_c
		m	T			m^2	m	MW	MW/m^2	kPa	K	K	m/s	m/s	S/m	S/m
CHRQBUEIF3	rect.	4.0	6.00	0.500	0.978	2.016	5.680	2556	1268	296.5	2513	2535	820.6	860.9	4.783	5.165
CHRQEHRIF3	hex.	4.0	6.00	0.500	1.153	2.380	5.742	3018	1268	296.5	2515	2537	820.4	861.8	4.810	5.210
CHRQDWBIF2	circle	4.0	6.00	0.500	1.000	2.057	5.080	2608	1268	296.5	2515	2537	820.0	861.7	4.820	5.210
CHRQLNIIF3	rect.	7.5	6.00	0.500	0.940	2.950	6.874	2395	812	192.5	2386	2408	823.5	865.8	3.489	3.816
BRCYEHPIF3	hex.	7.5	6.00	0.500	1.155	3.601	7.064	2923	812	192.5	2387	2409	823.5	866.3	3.494	3.841
BRCYHQJIF2	circle	7.5	6.00	0.500	1.000	3.112	6.248	2526	812	192.5	2388	2409	823.0	866.5	3.489	3.848
CHRQBUFIF3	rect.	11.0	5.72	0.500	0.953	4.587	8.569	2219	484	116.6	2239	2256	826.7	864.5	2.204	2.401
CHCQBXJIF3	hex.	11.0	5.72	0.500	1.155	5.554	8.773	2687	484	116.6	2237	2256	826.9	864.2	2.185	2.394
BRCYINQIF2	circle	11.0	5.72	0.500	1.000	4.800	7.760	2322	484	116.6	2240	2258	826.3	865.1	2.222	2.420

TABLE 7-7

Data from Q3DYZ Computations Performed under
Contract AC-01-79ET15501 from the Nominal 2000 MW(th) Channel
(continued)

Run	Shape	x	$\langle \beta \rangle$	T_{we}	T_{ws}	δ_c	δ_a	δ_s	E_x	V_F	I_L	Power	R_I	C_{25}	C_{26}	G
		m		K	K	mm	mm	mm	V/m	V	kA/m	MW/m	Ω·m			
CHRQBUEIF3	rect.	4.0	1.481	2100	2100	113.0	125.2	71.3	-3493	-3490	-16.19	56.51	-215.6	0.715	0.967	1.034
CHRQEHRIF3	hex.	4.0	1.481	2100	2100	113.0	125.2	71.3	-3691	-3401	-19.11	65.00	-178.0	0.784	0.937	1.067
CHRQDWBIF2	circle	4.0	1.481	2100	2100	113.0	125.2	71.3	-3222	-3533	-14.90	52.64	-237.1	0.735	0.944	1.059
CHRQLNIIF3	rect.	7.5	2.185	2100	2100	198.0	205.2	10.8	-5101	-4157	-14.38	59.78	-289.1	0.785	0.952	1.050
BRCYEHPIF3	hex.	7.5	2.185	2100	2100	198.0	205.2	10.8	-5332	-4250	-17.00	72.24	-250.0	0.770	0.941	1.063
BRCYHQJIF2	circle	7.5	2.186	2100	2100	198.0	205.2	10.8	-4540	-4333	-12.86	55.71	-337.0	0.690	0.842	1.188
CHRQBUFIF3	rect.	11.0	3.253	2100	2100	300.2	306.2	17.4	-7366	-4953	-10.04	54.20	-452.6	0.805	0.959	1.043
CHRQBXJIF3	hex.	11.0	3.251	2100	2100	300.2	306.2	17.4	-7515	-5089	-12.59	64.08	-404.2	0.790	0.944	1.059
BRCYINQIF2	circle	11.0	3.254	2100	2100	300.2	306.2	17.4	-6171	-5118	-9.27	47.46	-551.9	0.665	0.797	1.255

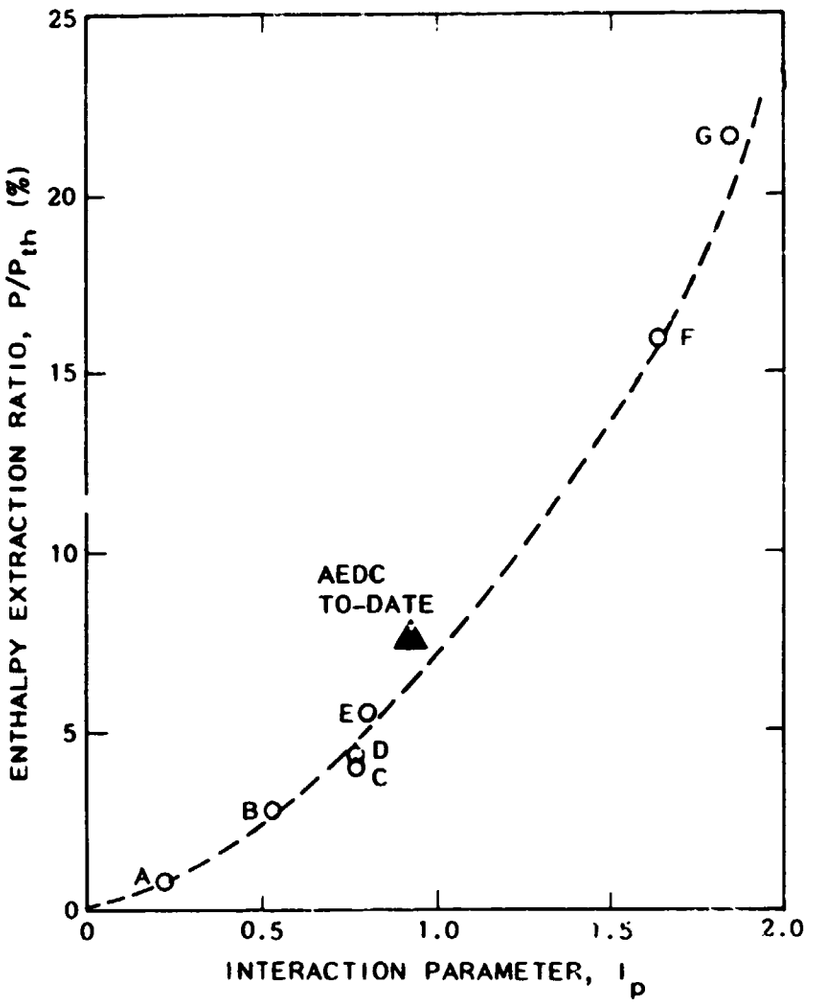

Fig. 7-1. Variation of enthalpy extraction rate with the interaction parameter based on pressure.

0-3633a

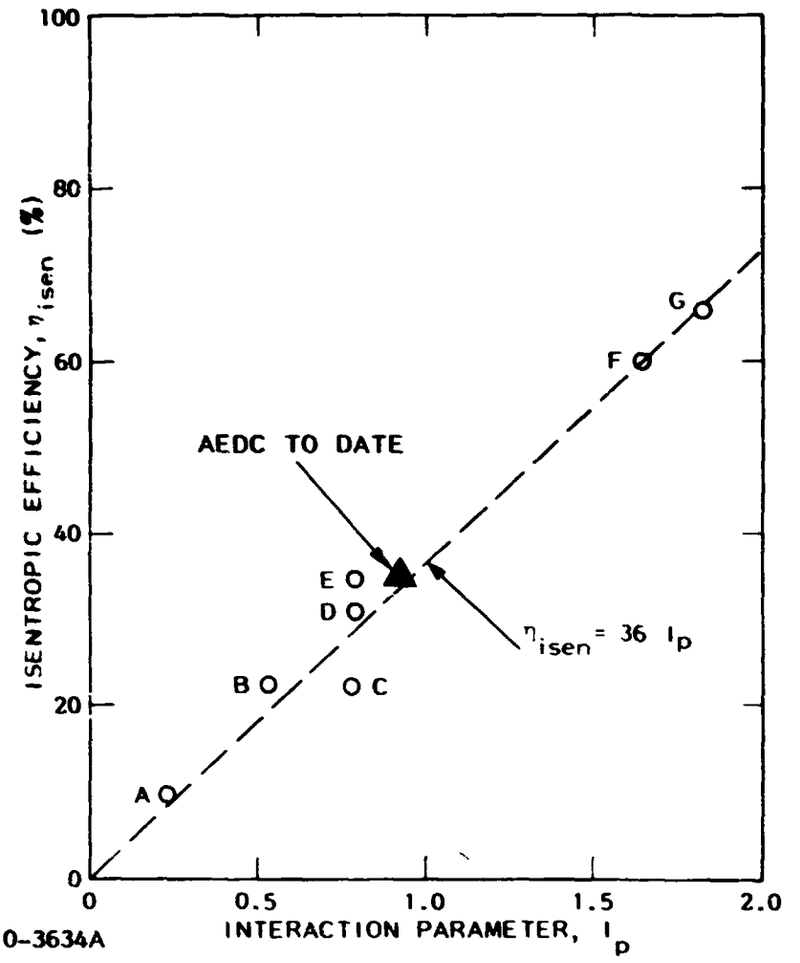

Fig. 7-2. Variation of isentropic efficiency with interaction parameter based on pressure.

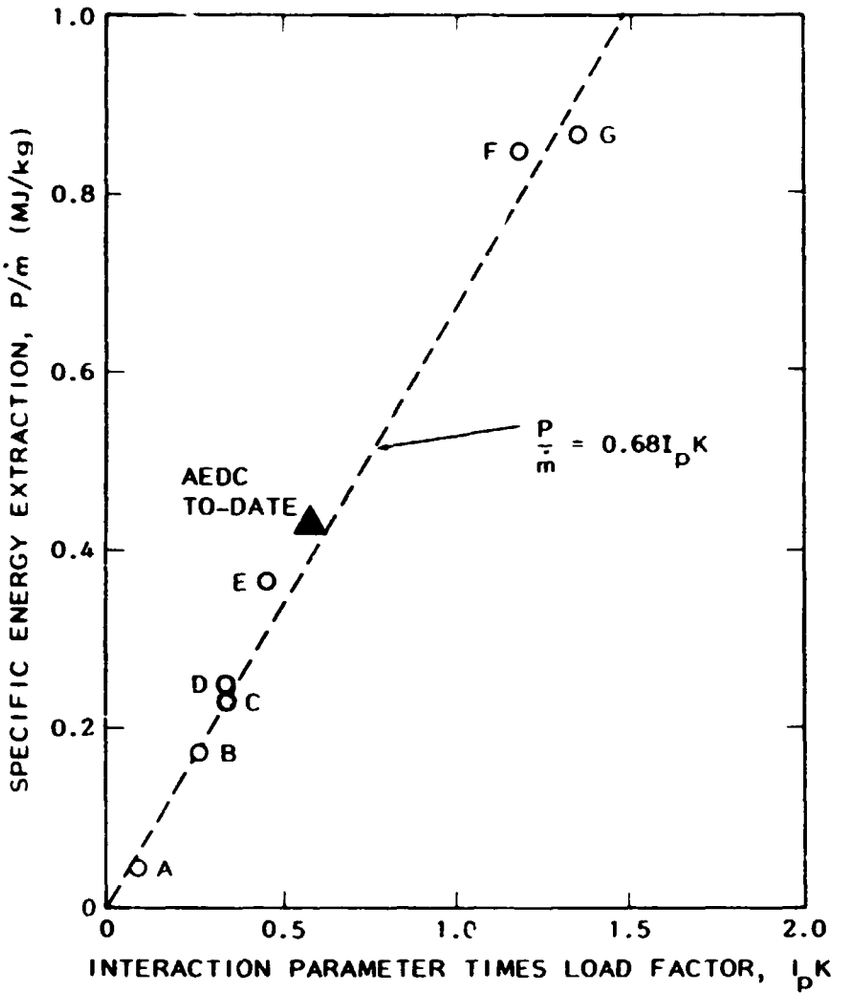

Fig. 7-3. Variation of specific energy extraction with the product of interaction parameter based on pressure and the Faraday load factor K or diagonal generator electrical conversion efficiency η_e.

U-3632a

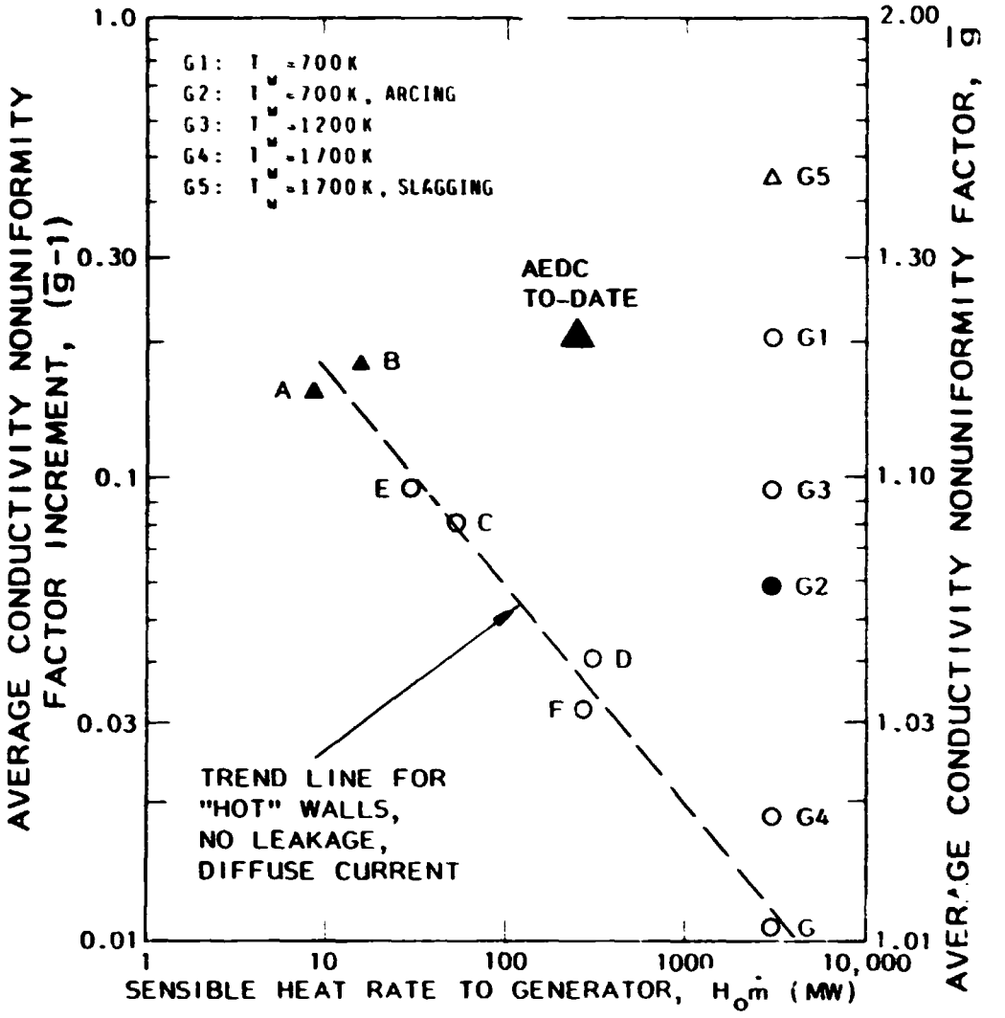

Fig. 7-4. Variation of conductivity nonuniformity factor g, averaged over the channel length, with sensible heat rate or thermal input to the MHD generator. Solid symbols denote arc-mode current transport, and triangles denote slagging walls.

0-3635a

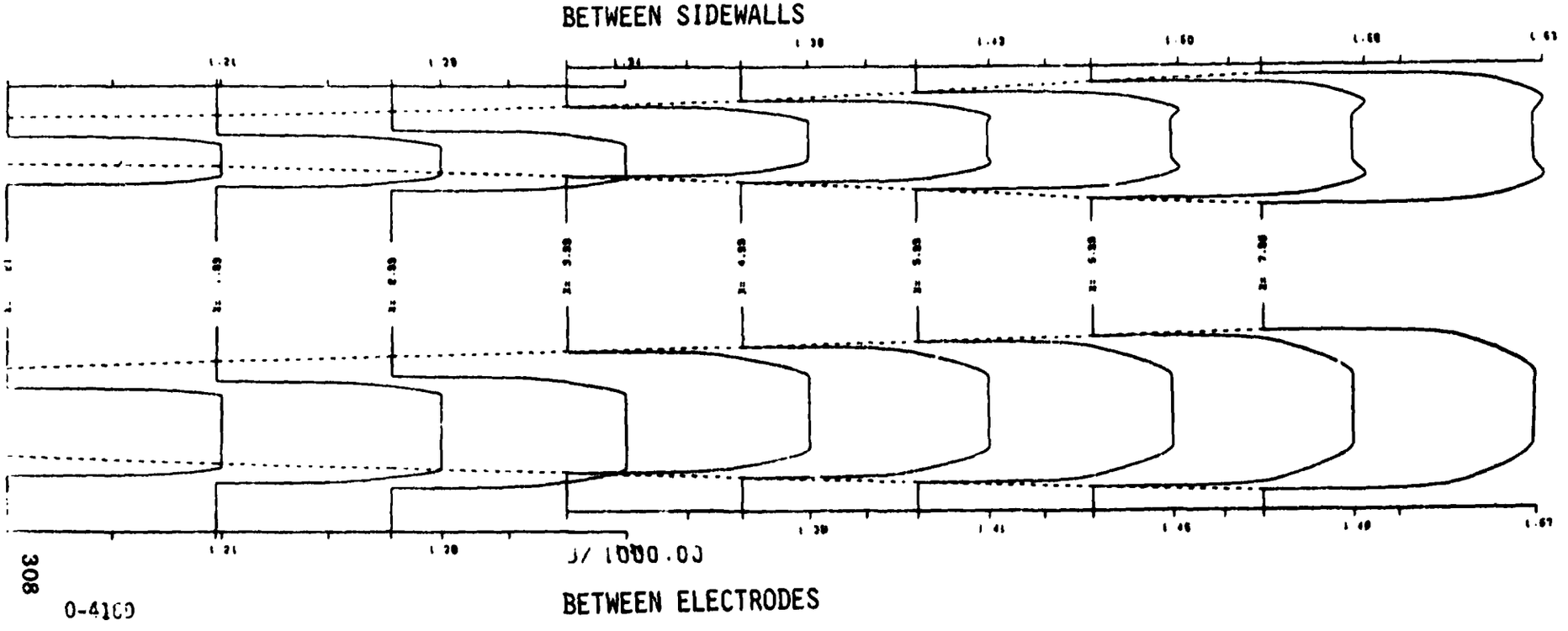

Fig. 7-5. Development of the axial velocity profiles in the Q3D simulation CHPQUUUJB0 of the AEDC/HPDE Run 006-014.

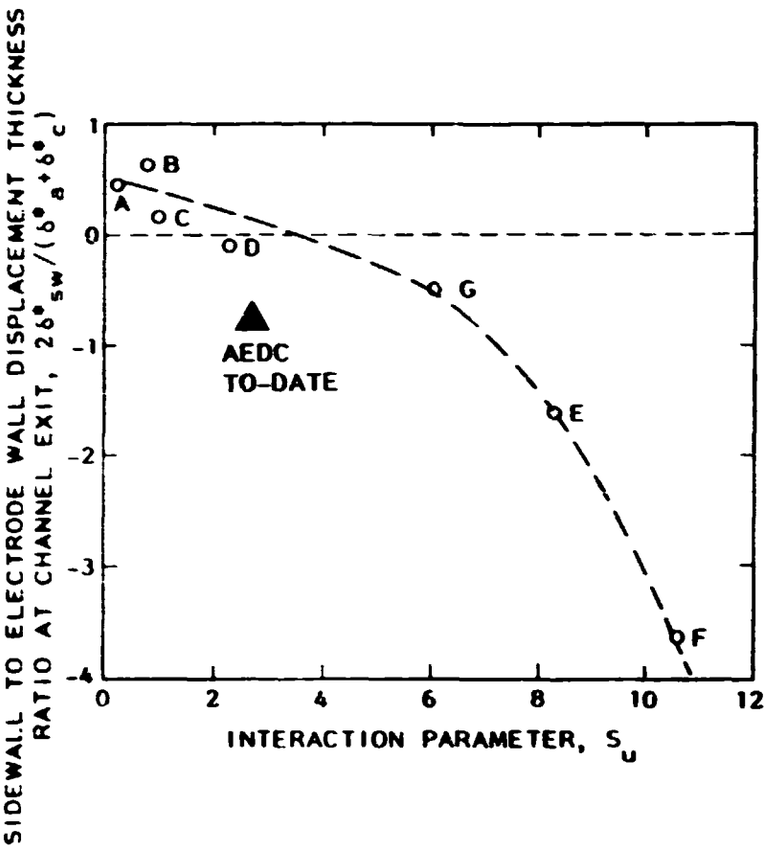

Fig. 7-6. Variation of the ratio of sidewall to average electrode wall displacement thickness with the interaction parameter based on velocity.

0-3630a

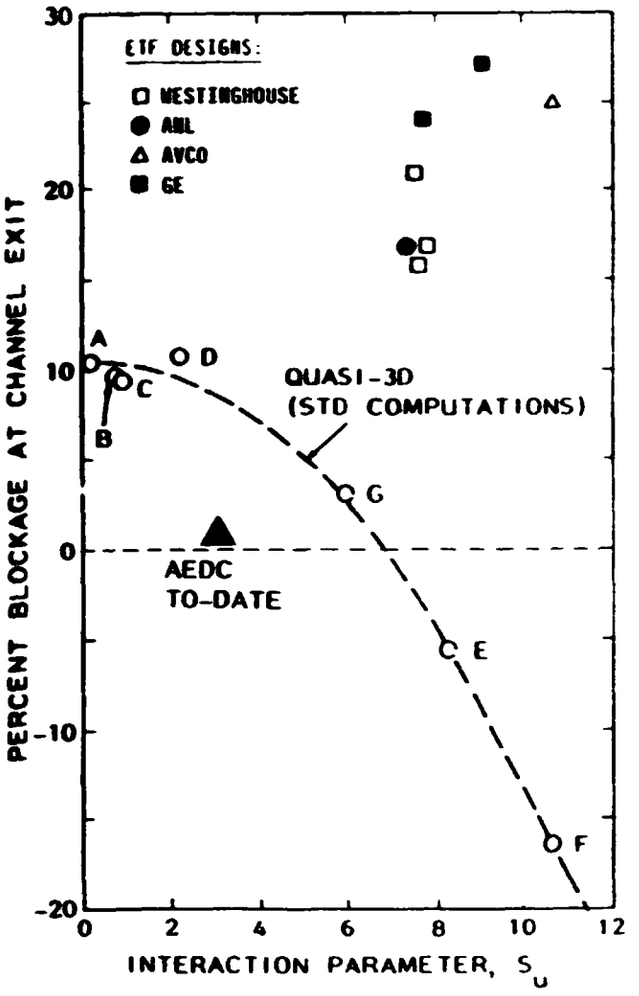

Fig. 7-7. Variation of the MHD generator exit blockage with interaction parameter based on velocity. The STD computational Cases A-G are compared with the estimates used by the ETF conceptual design contractors and the AEDC performance to date.

0-3631a

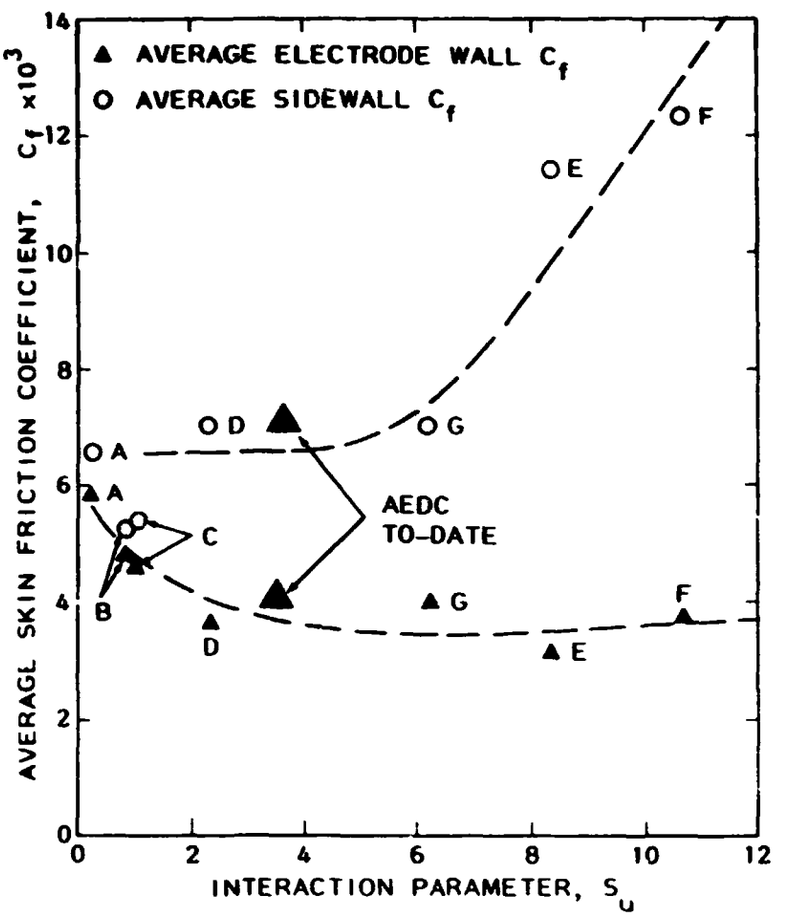

Fig. 7-8. Average skin friction coefficient on the electrode walls and sidewalls as a function of the interaction parameter based on velocity.

0-3629 a

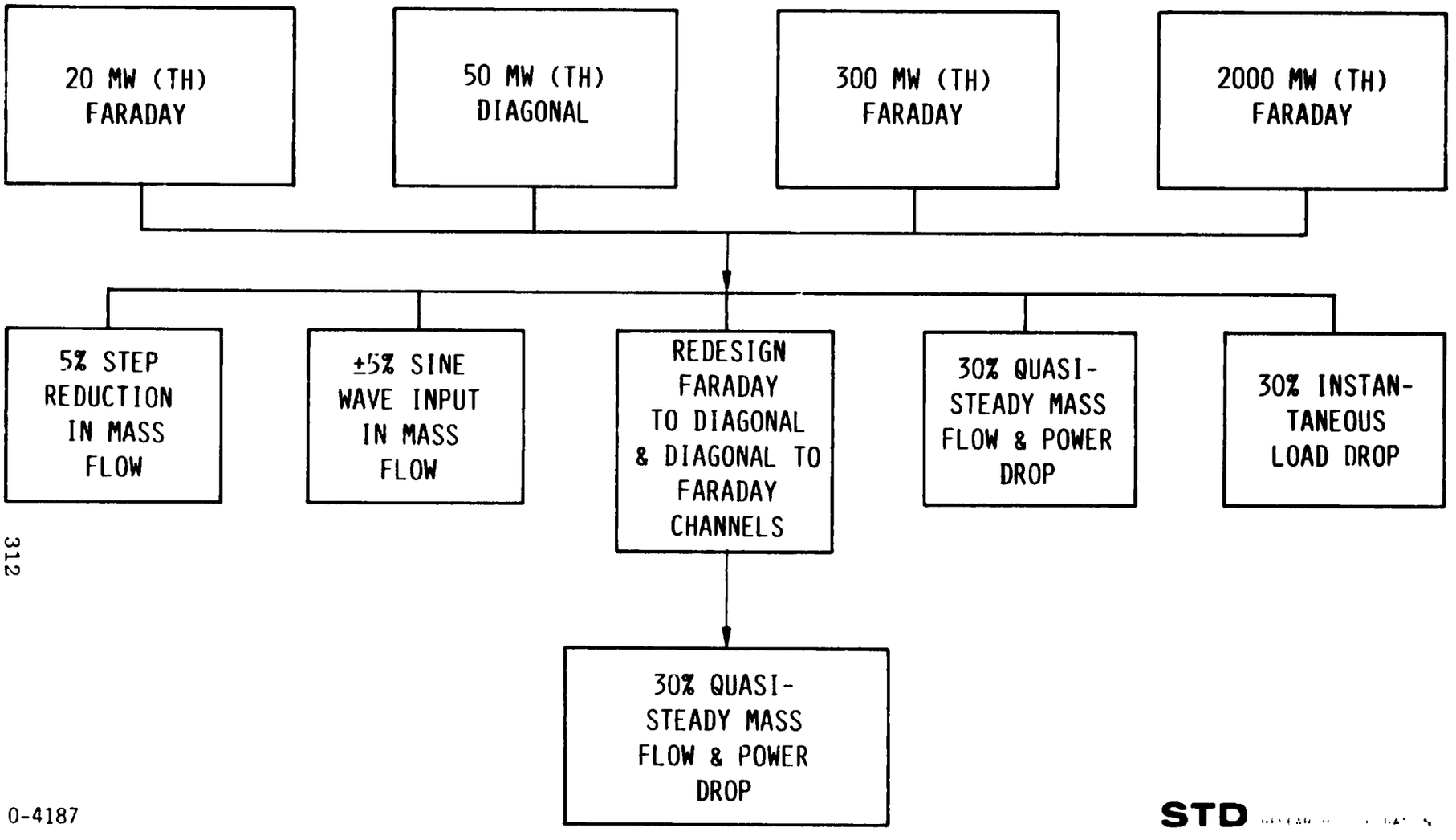

Fig. 7-9. Schematic diagram representing the cases which were completed with the TRANSIENT code under contract AC-01-79ET15501.

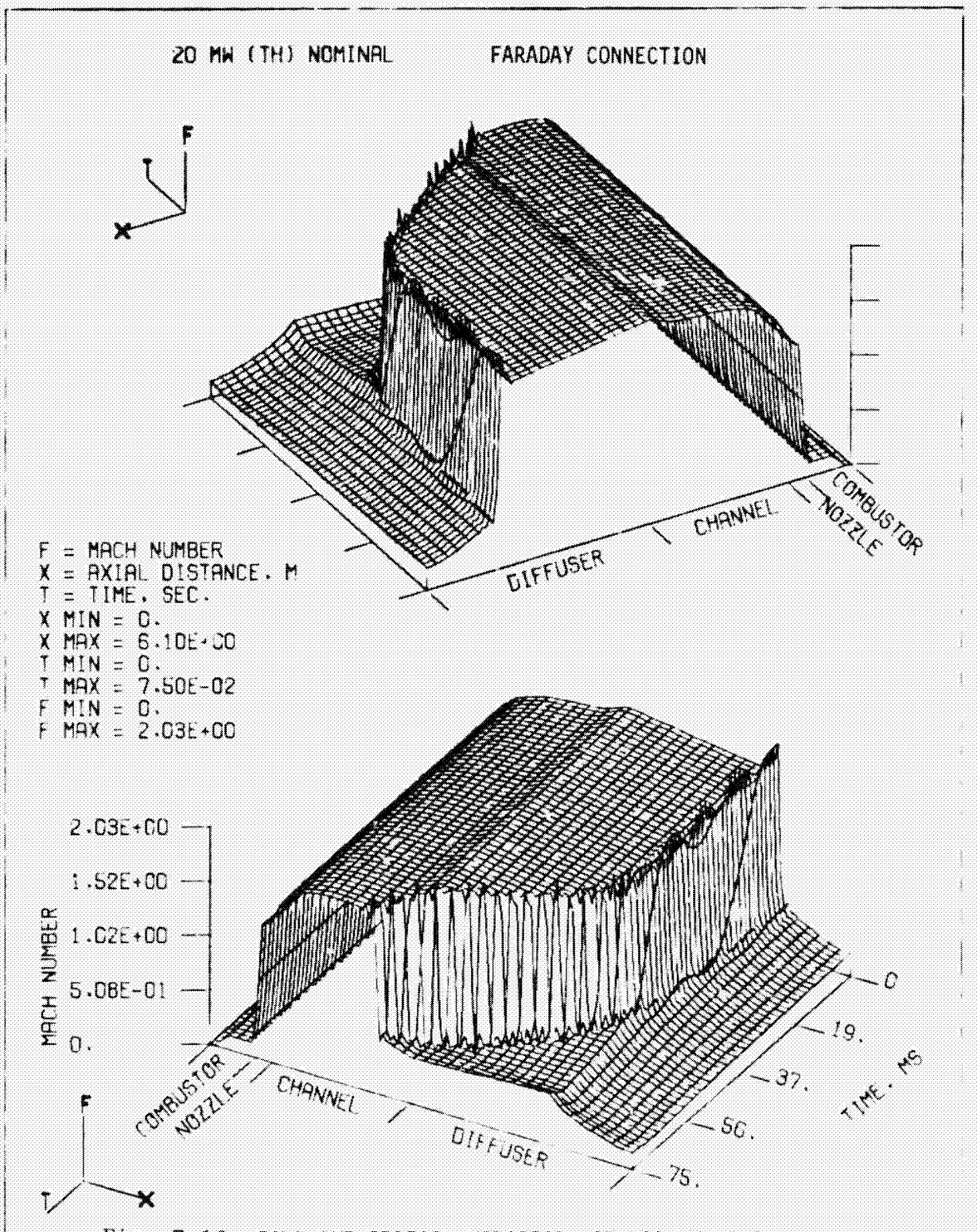

Fig. 7-10. TIME AND SPATIAL VARIATION OF MACH NUMBER FOR CASE 1.1.5, 30% QUASI-STEADY MASS FLOW AND POWER REDUCTION FROM STD COMPUTATION NO. A5MYFALIE5

0-3851

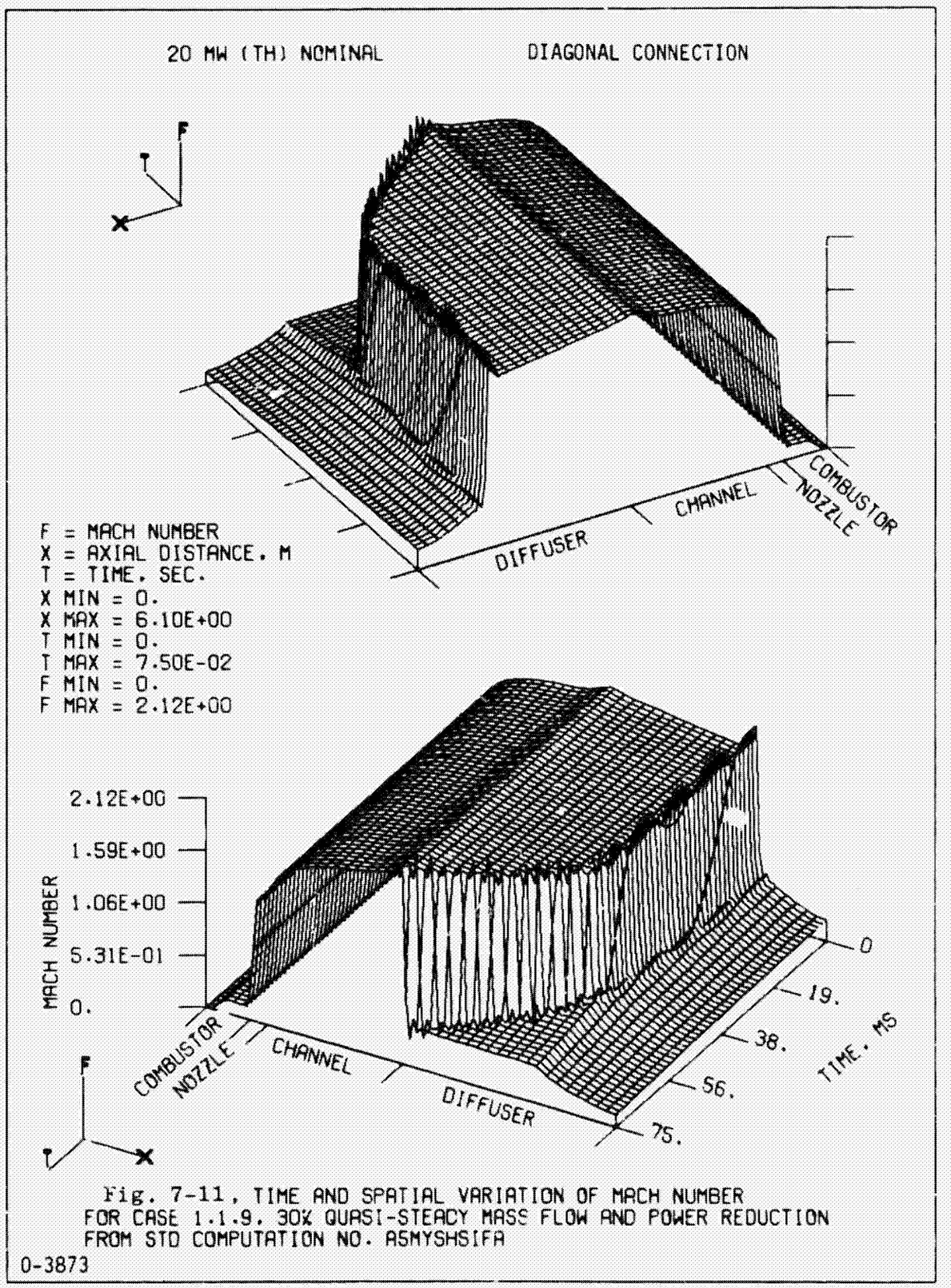

Fig. 7-11, TIME AND SPATIAL VARIATION OF MACH NUMBER FOR CASE 1.1.9. 30% QUASI-STEADY MASS FLOW AND POWER REDUCTION FROM STD COMPUTATION NO. A5MYSHSIFA

0-3873

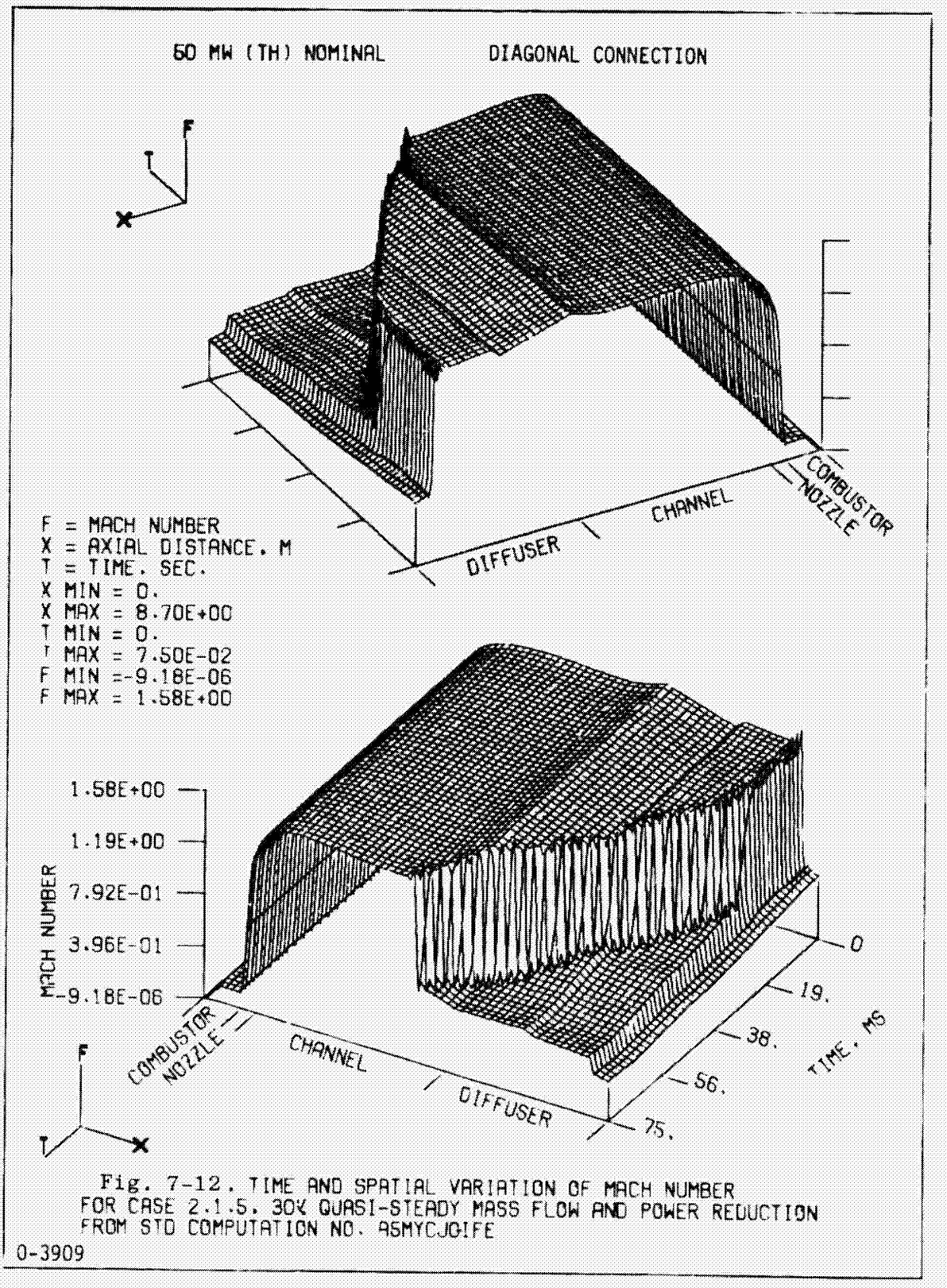

Fig. 7-12. TIME AND SPATIAL VARIATION OF MACH NUMBER FOR CASE 2.1.5, 30% QUASI-STEADY MASS FLOW AND POWER REDUCTION FROM STD COMPUTATION NO. ASMYCJGIFE

0-3909

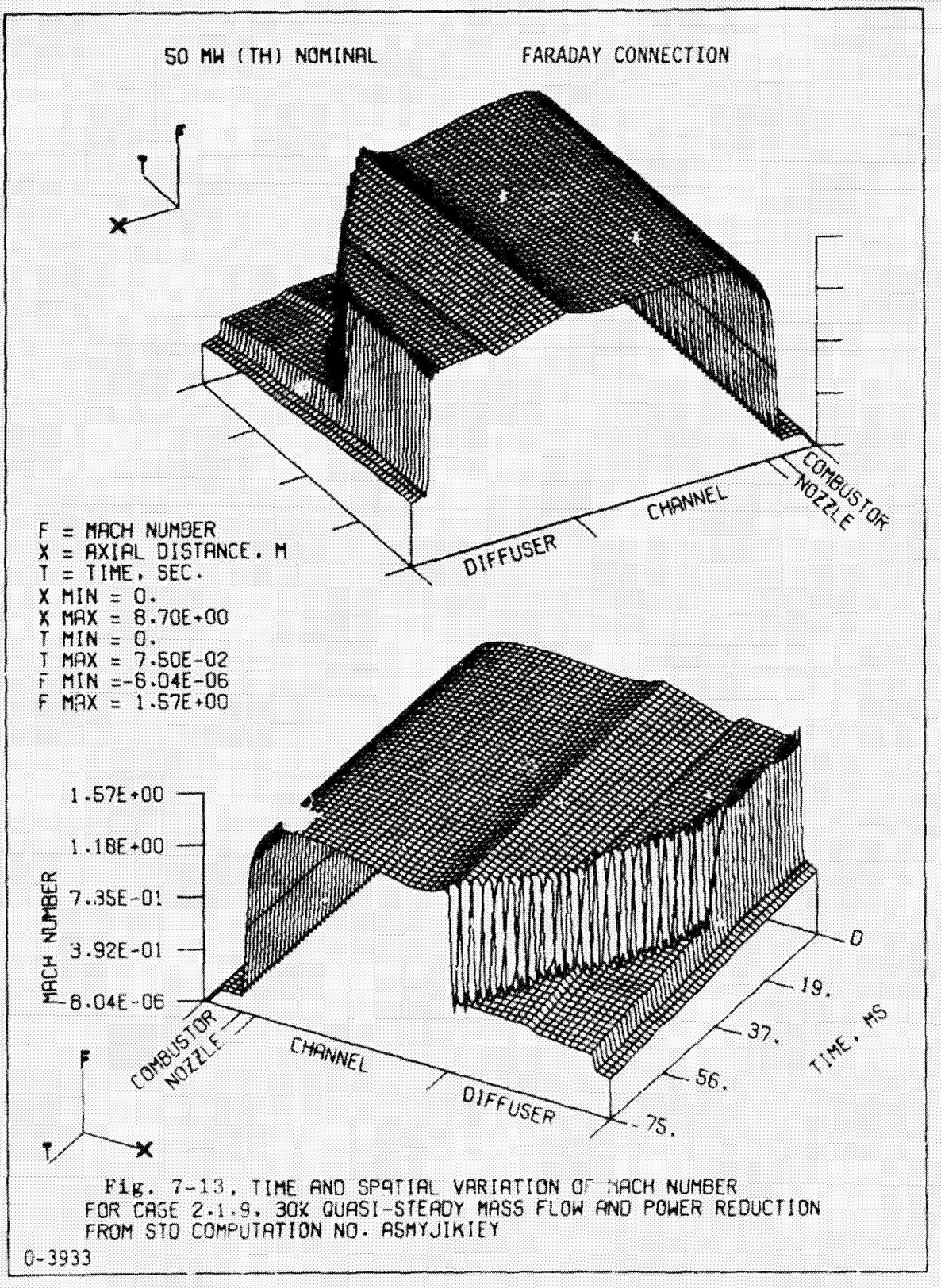

Fig. 7-13. TIME AND SPATIAL VARIATION OF MACH NUMBER FOR CASE 2.1.9, 30% QUASI-STEADY MASS FLOW AND POWER REDUCTION FROM STD COMPUTATION NO. ASMYJIKIEY

0-3933

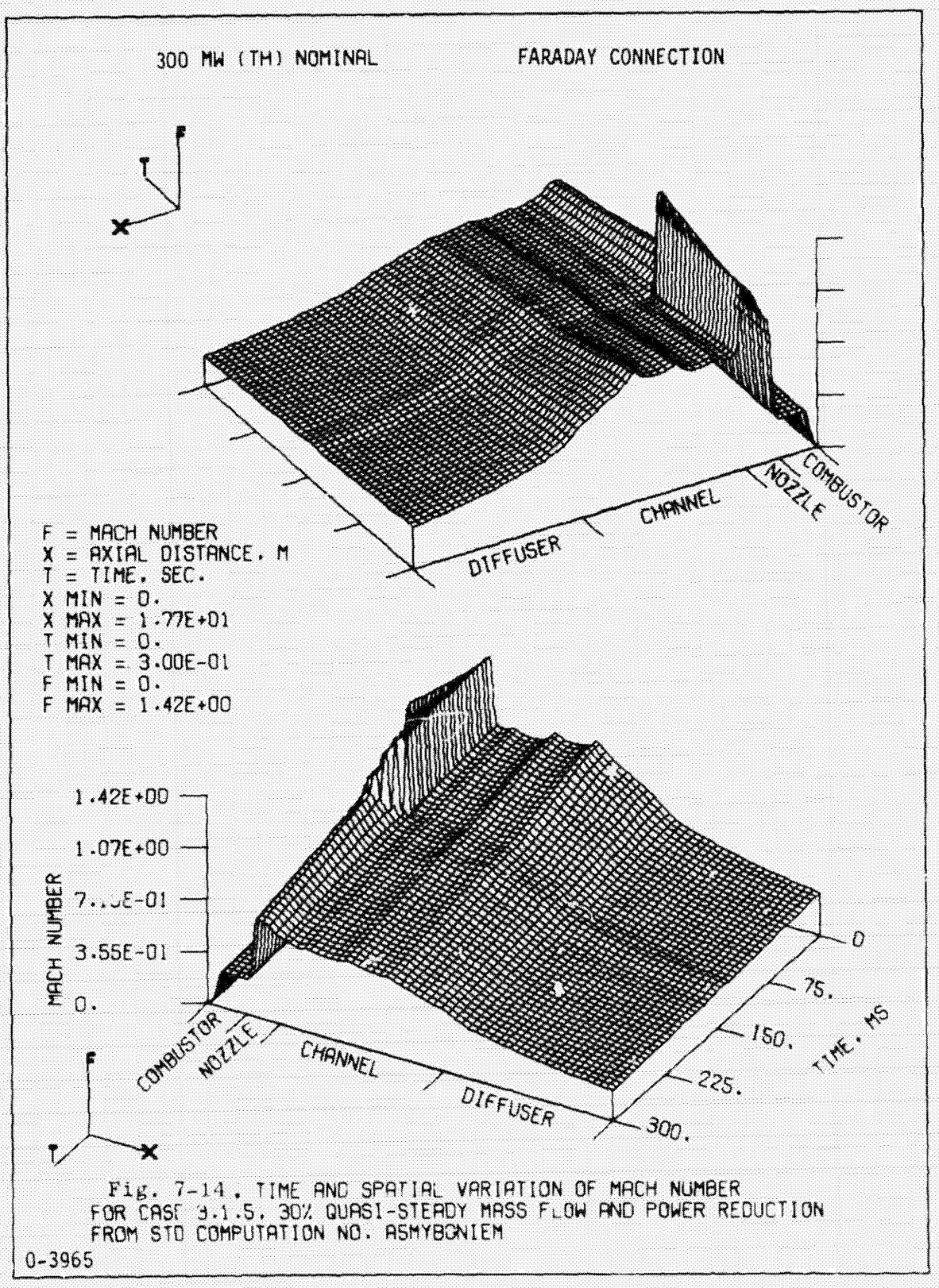

Fig. 7-14. TIME AND SPATIAL VARIATION OF MACH NUMBER FOR CASE 3.1.5, 30% QUASI-STEADY MASS FLOW AND POWER REDUCTION FROM STD COMPUTATION NO. A5MYBGNIEM

0-3965

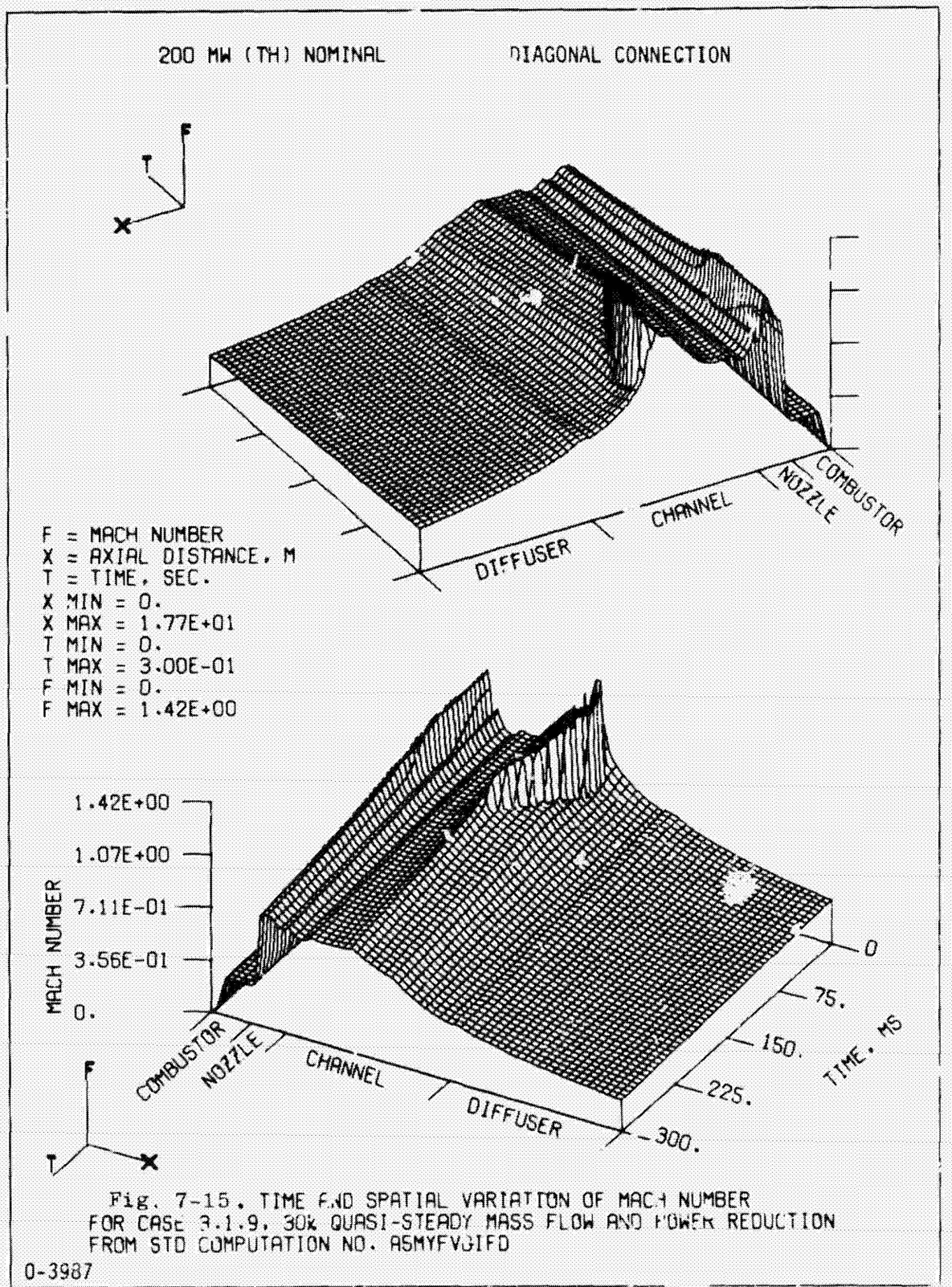

Fig. 7-15. TIME AND SPATIAL VARIATION OF MACH NUMBER FOR CASE 3.1.9, 30% QUASI-STEADY MASS FLOW AND POWER REDUCTION FROM STD COMPUTATION NO. A5MYFVGIFD

0-3987

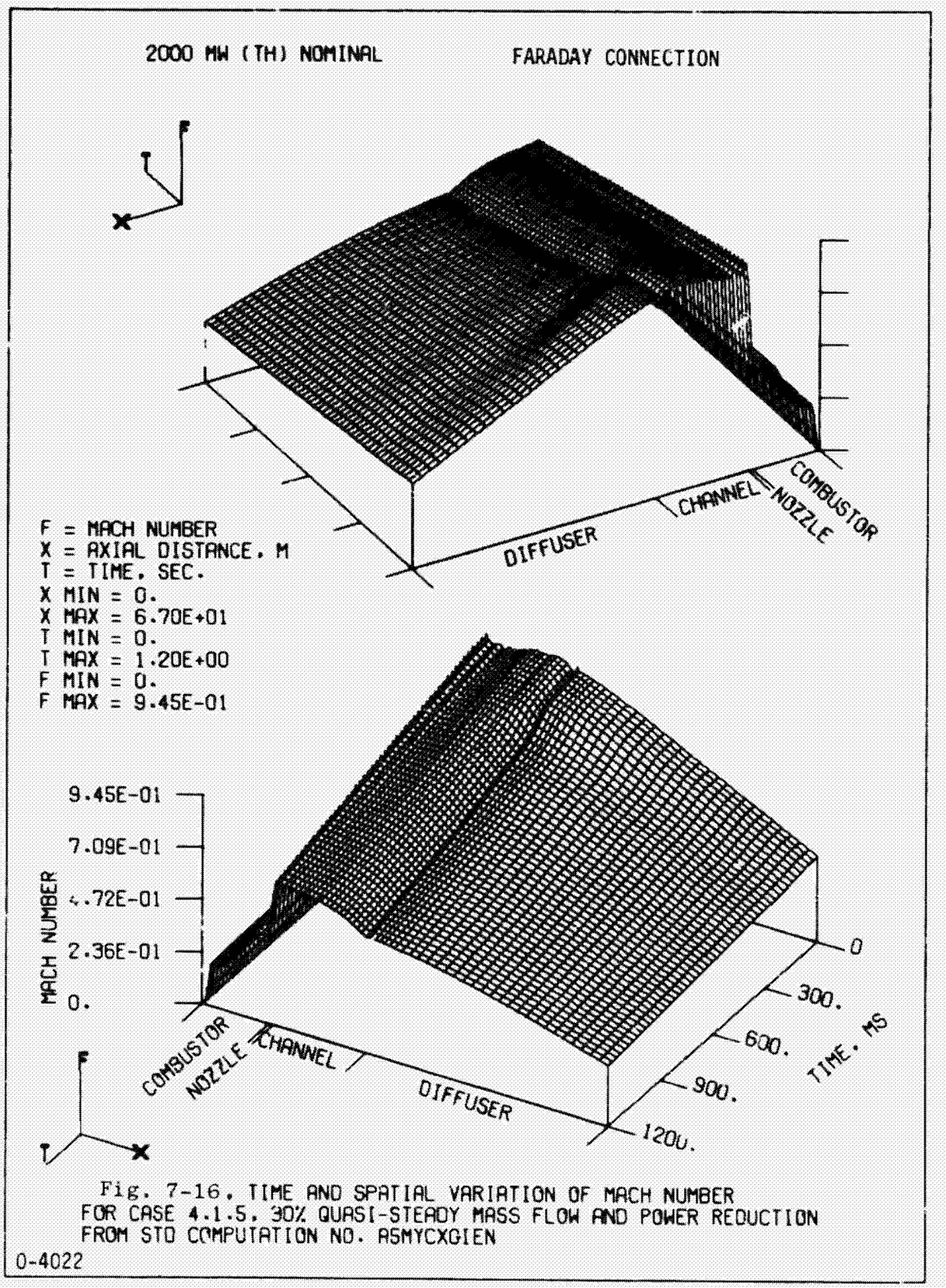

Fig. 7-16. TIME AND SPATIAL VARIATION OF MACH NUMBER FOR CASE 4.1.5, 30% QUASI-STEADY MASS FLOW AND POWER REDUCTION FROM STD COMPUTATION NO. A5MYCXGIEN

0-4022

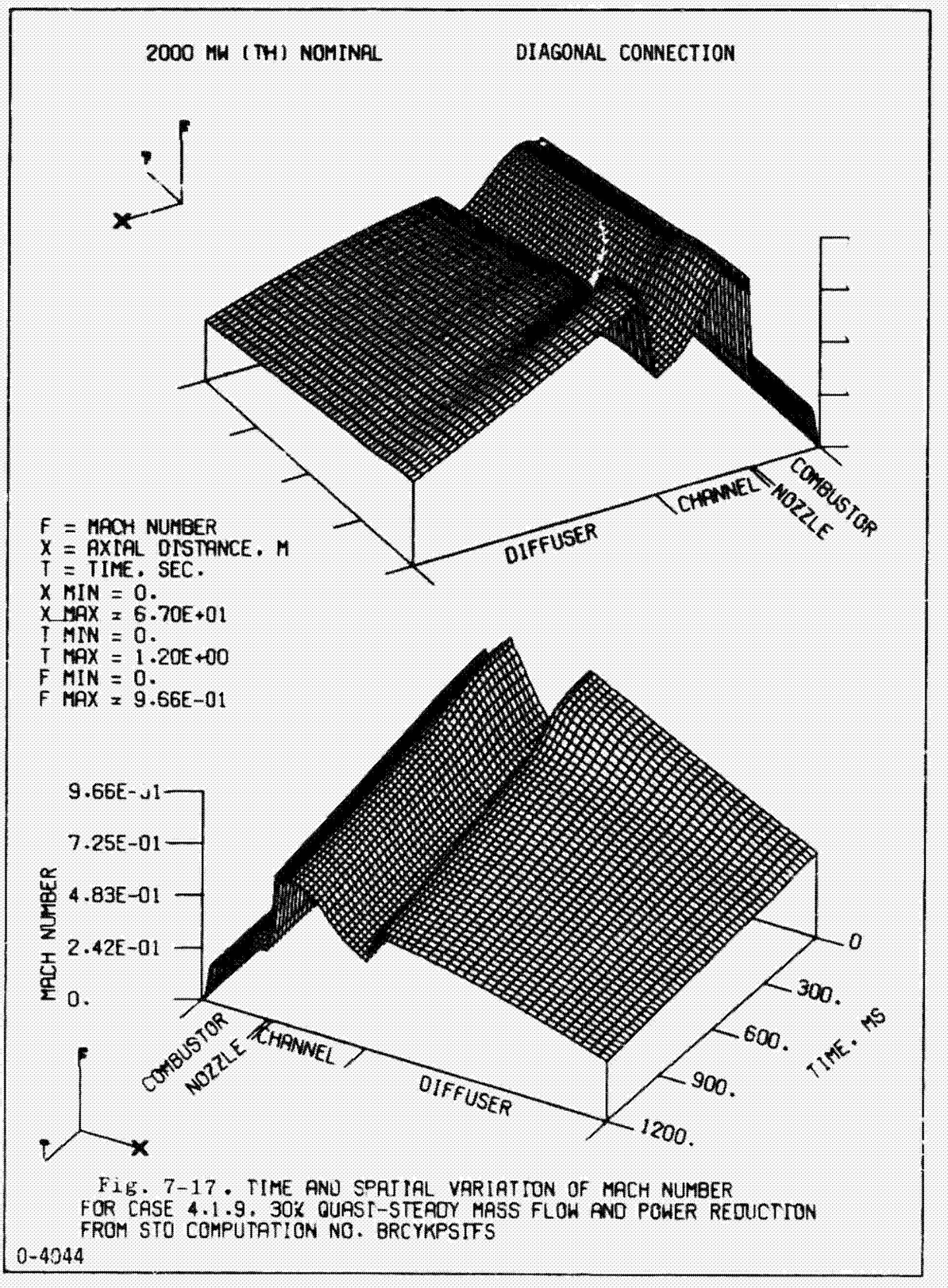

Fig. 7-17. TIME AND SPATIAL VARIATION OF MACH NUMBER FOR CASE 4.1.9. 30% QUASI-STEADY MASS FLOW AND POWER REDUCTION FROM STD COMPUTATION NO. BRCYKPSIFS

0-4044

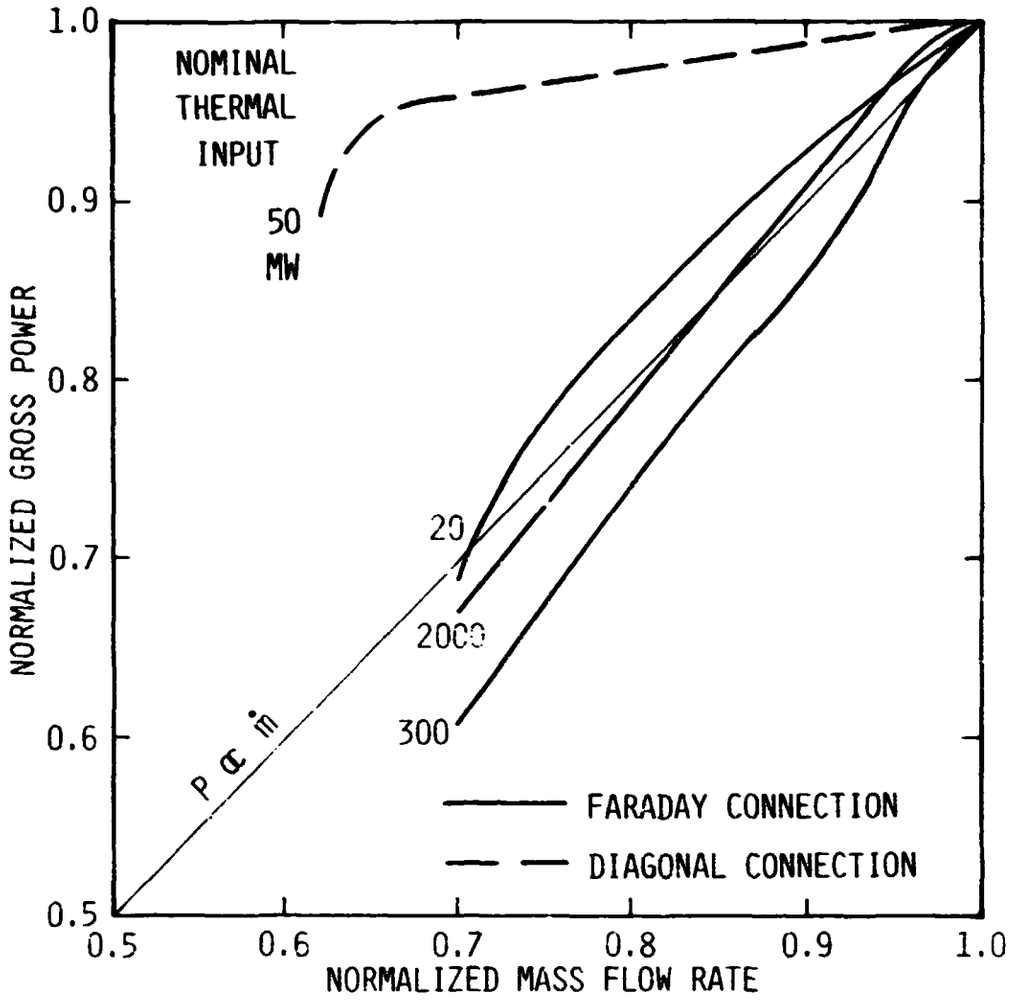

CHANNEL	MASS FLOW kg/sec	POWER MW
20 MWth	2.49	0.423
50 MWth	8.00	1.819
300 MWth	50.0	39.91
2000 MWth	705.1	602.9

0-4114

Fig. 7-18 Normalized gross power vs. normalized mass flow rate for channels with their nominal electrical hook-up.

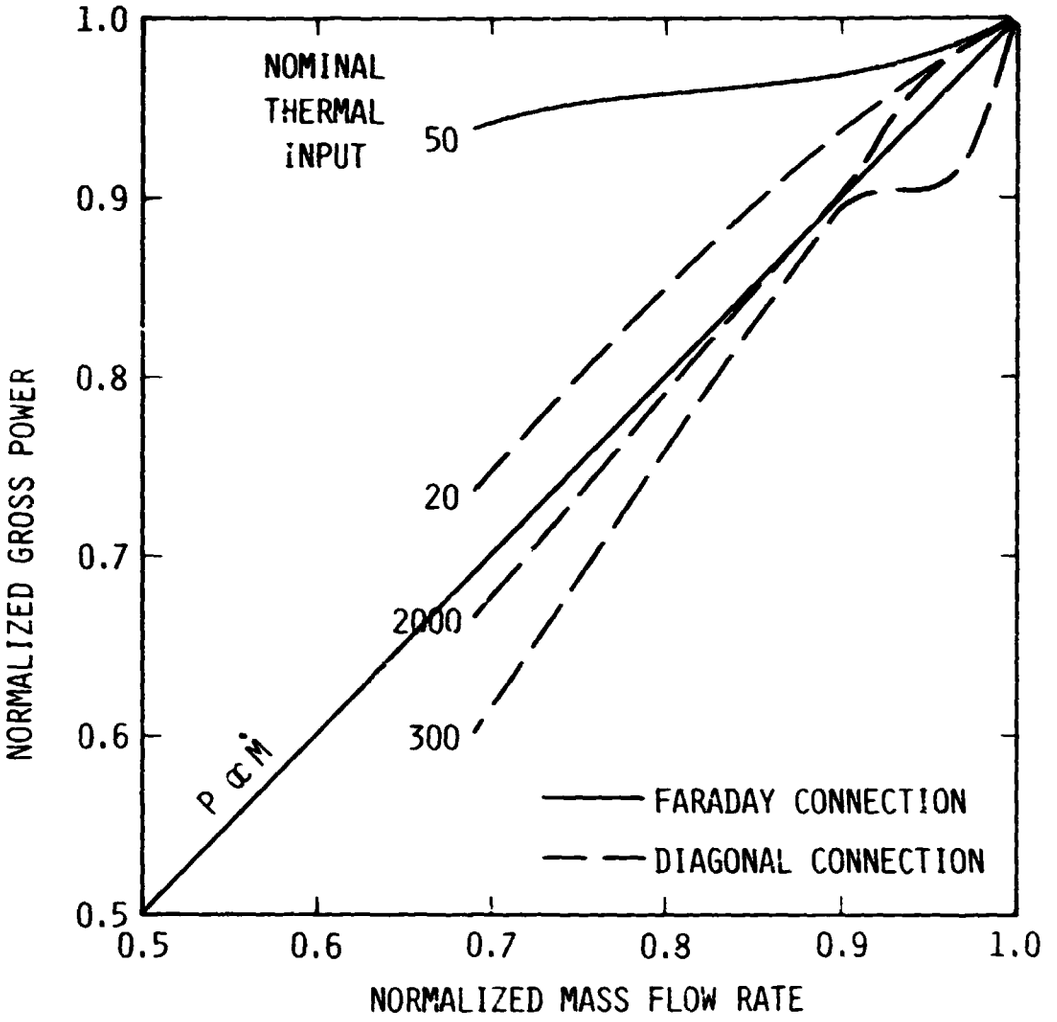

CHANNEL	MASS FLOW kg/sec	POWER
20 MWth	2.49	0.502
50 MWth	8.00	1.777
300 MWth	50.0	36.67
2000 MWth	705.9	522.9

0-4111

Fig. 7-19 Normalized gross power vs. normalized mass flow rate for 4 channels with their alternate electrical hook-up.

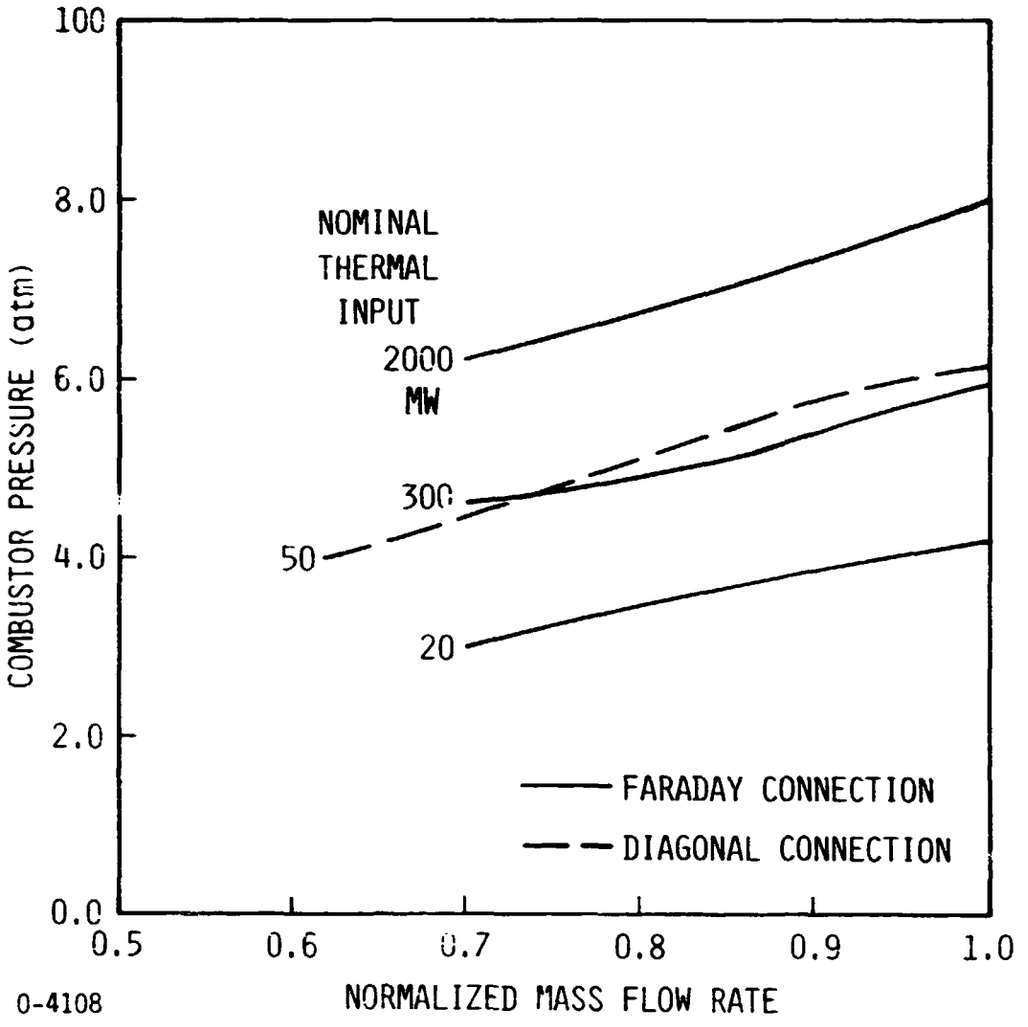

Fig. 7-20. Combustor stagnation pressure vs. normalized mass flow rate for different size generators with mass flow varying between 70% and 100% at nominal design value.

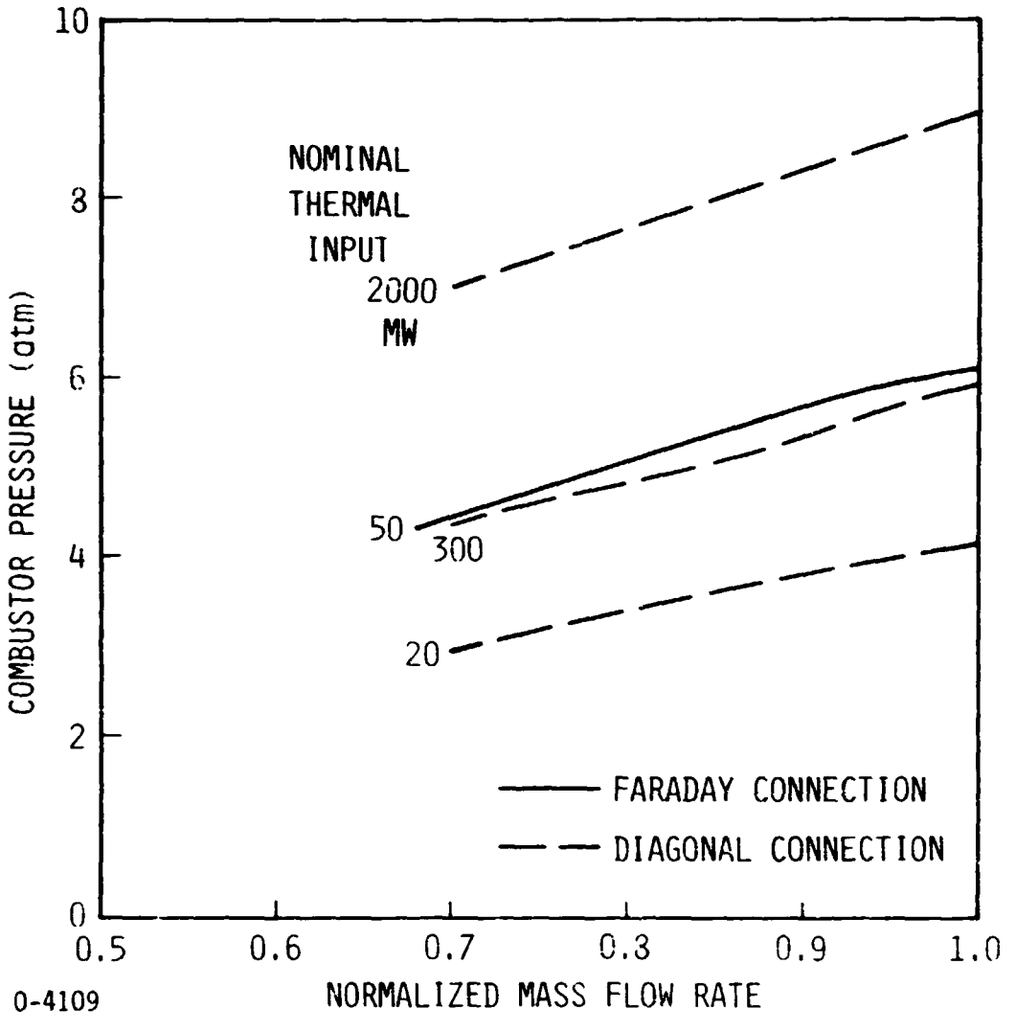

Fig. 7-21 . Combustor stagnation pressure vs. normalized mass flow rate for different size generators with mass flow varying between 70% and 100% of nominal design value.

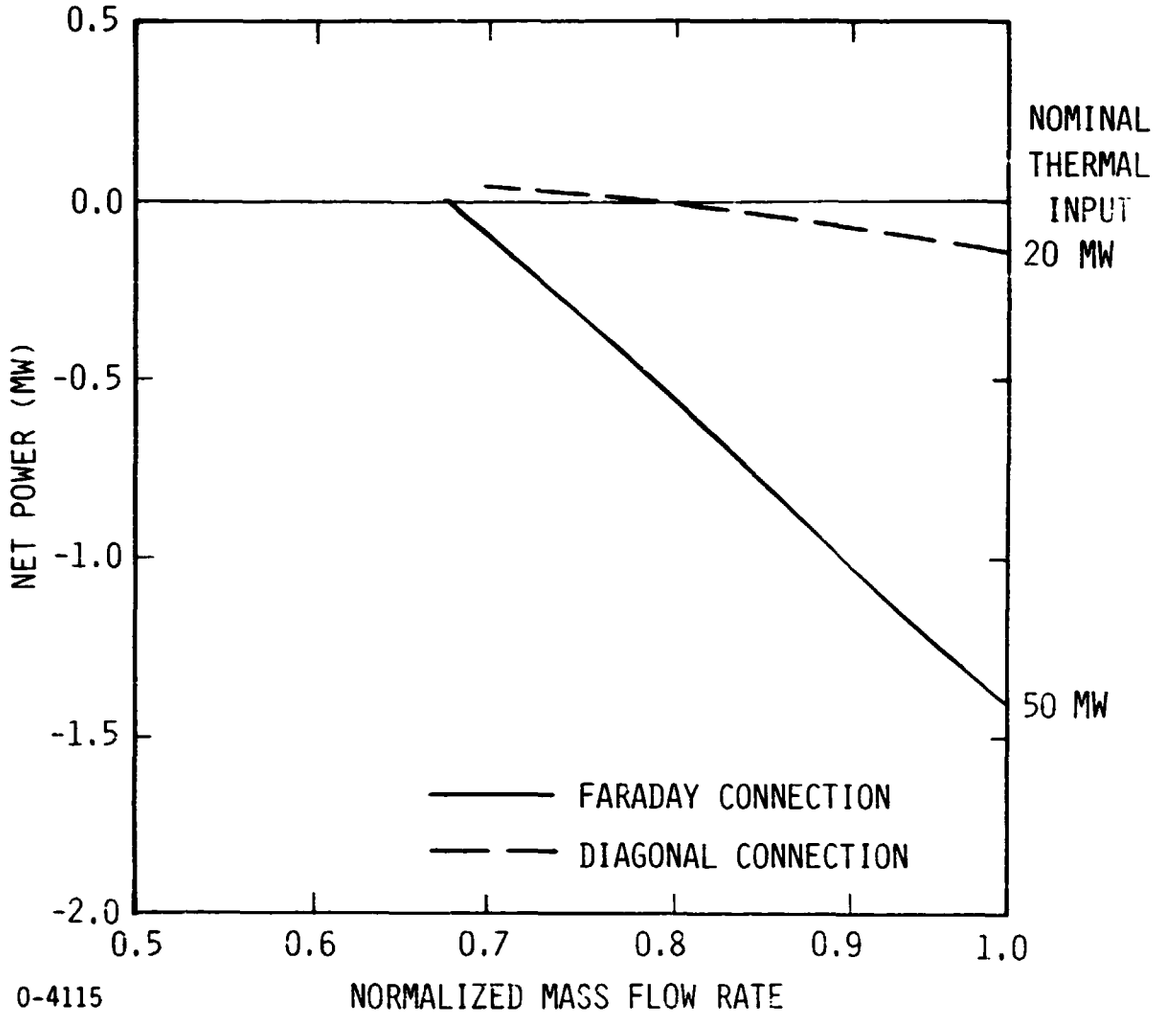

Fig. 7-22. Net power vs. normalized mass flow rate for two generators with mass flow varying between 70% to 100% of nominal design value.

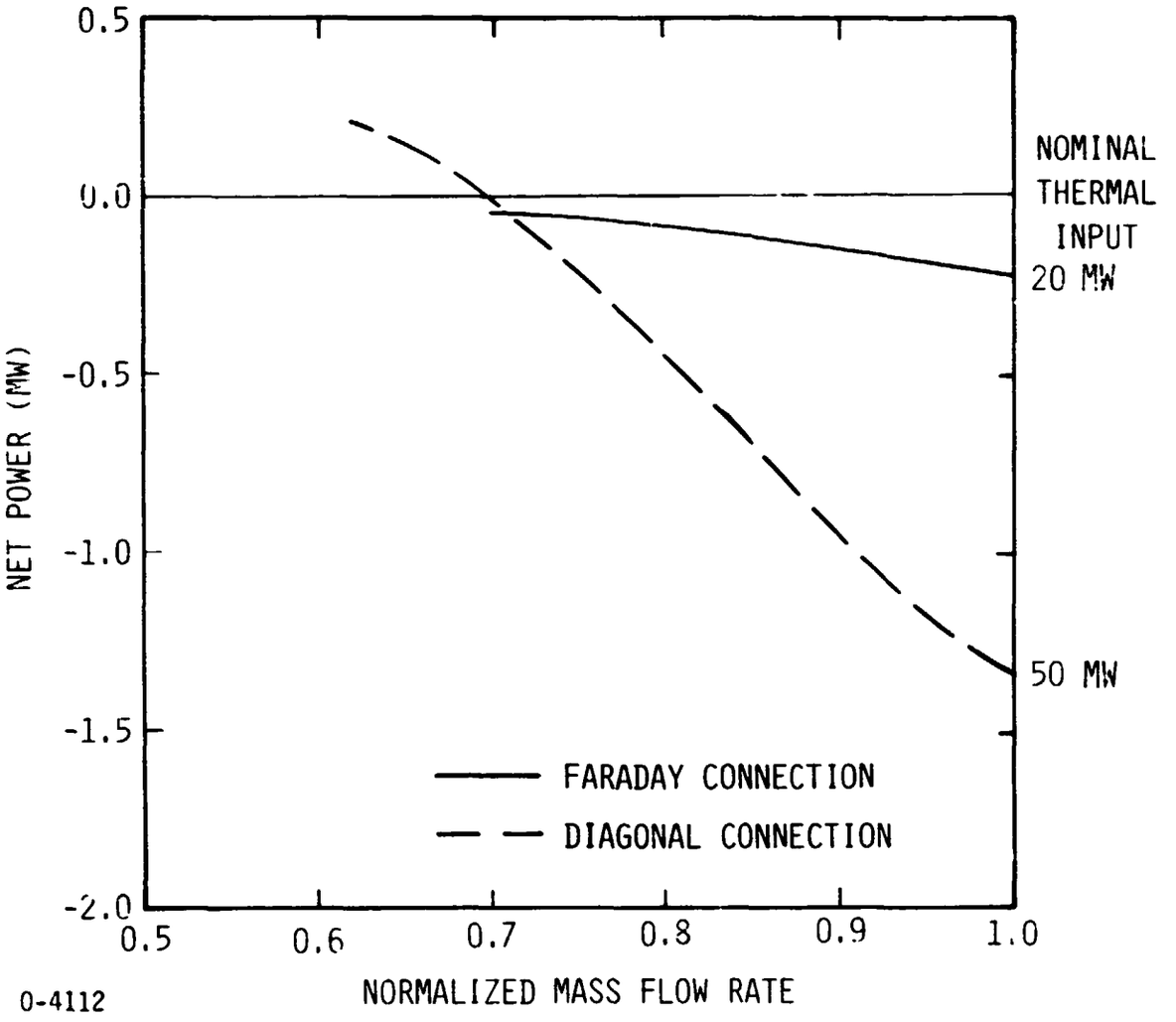

Fig. 7-23. Net power vs. normalized mass flow rate for two generators with mass flow varying between 70% to 100% of nominal design value.

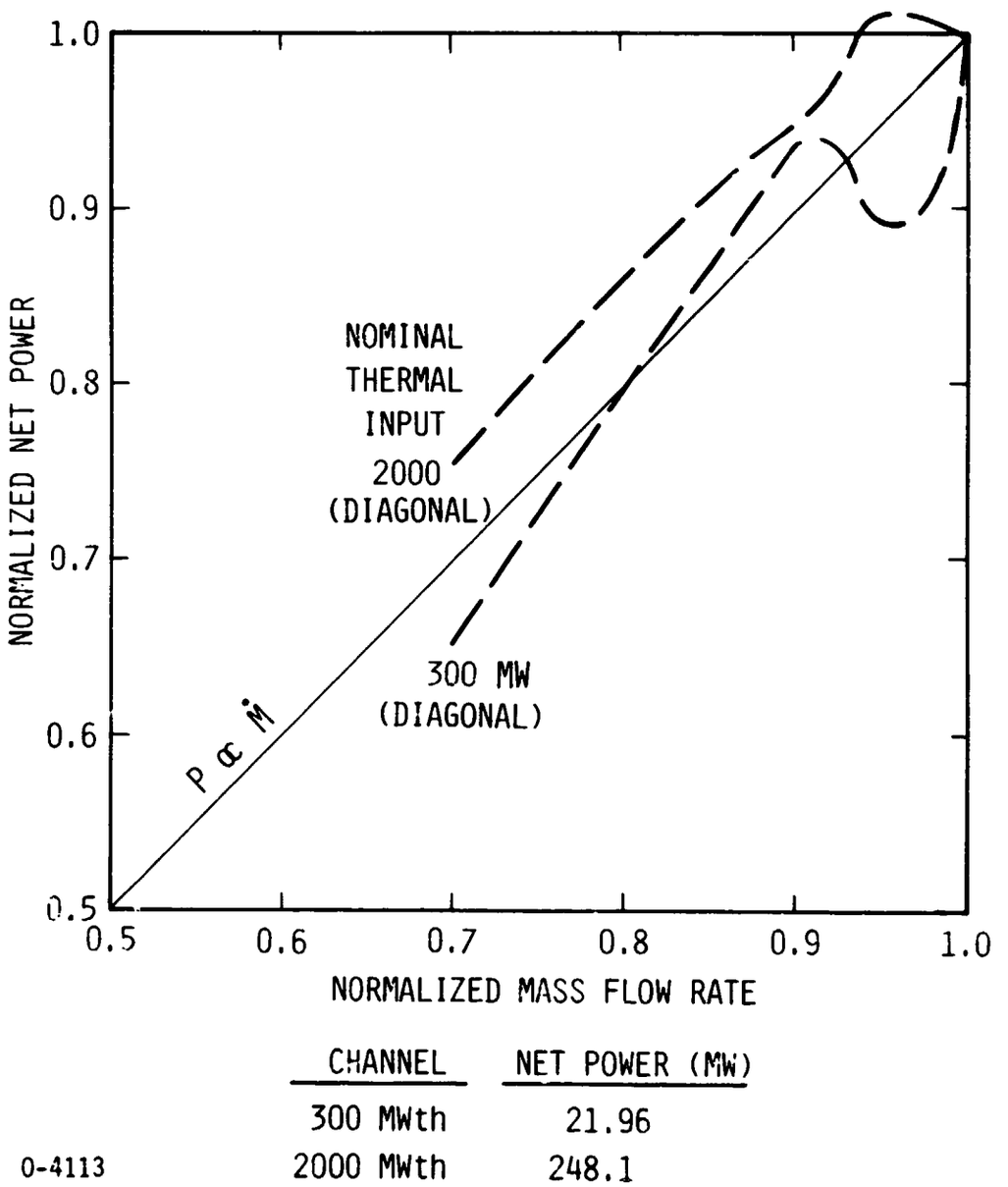

Fig. 7-24. Normalized net power vs. normalized mass flow rate for two generators with mass flow varying between 70% and 100% of nominal design value.

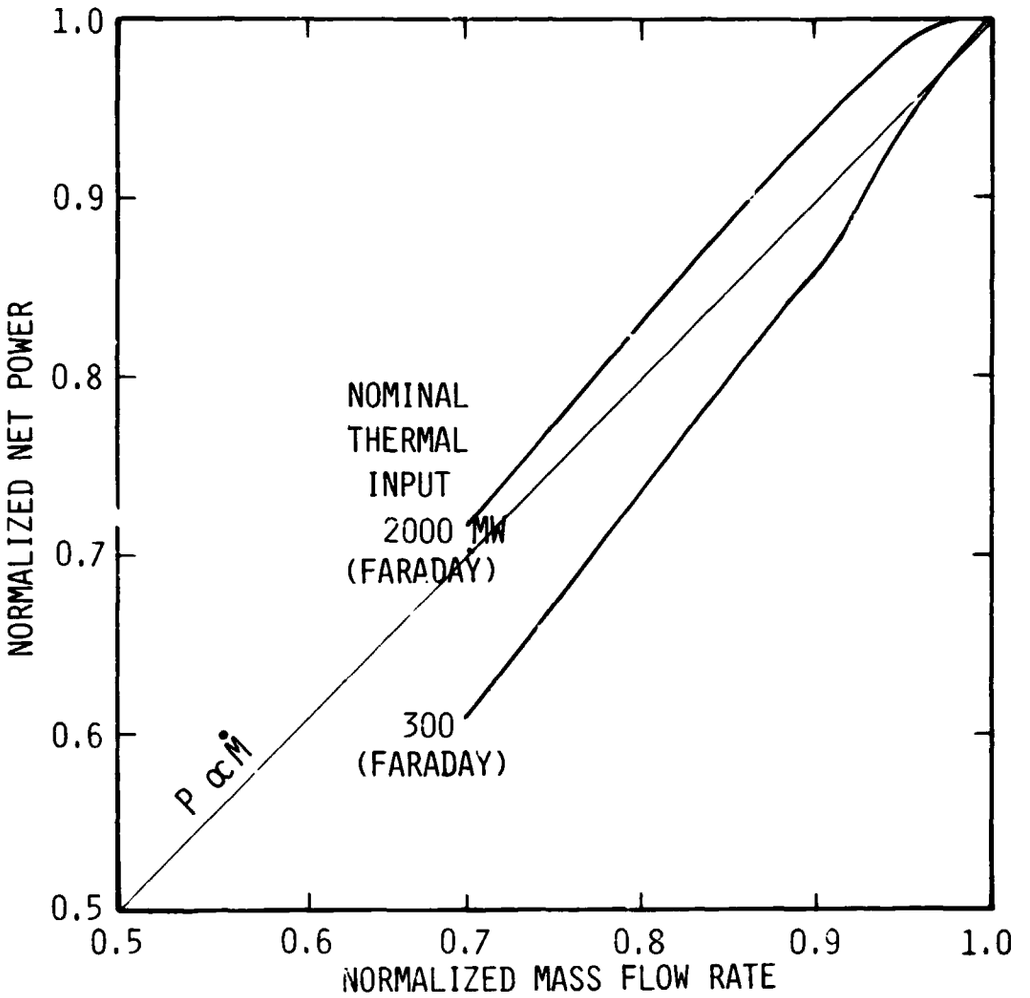

CHANNEL	NET POWER (MW)
300 MWth	25.18
2000 MWth	350.8

0-4116

Fig. 7-25. Normalized net power vs. normalized mass flow rate for two generators with mass flow varying between 70% and 100% of the nominal design value.

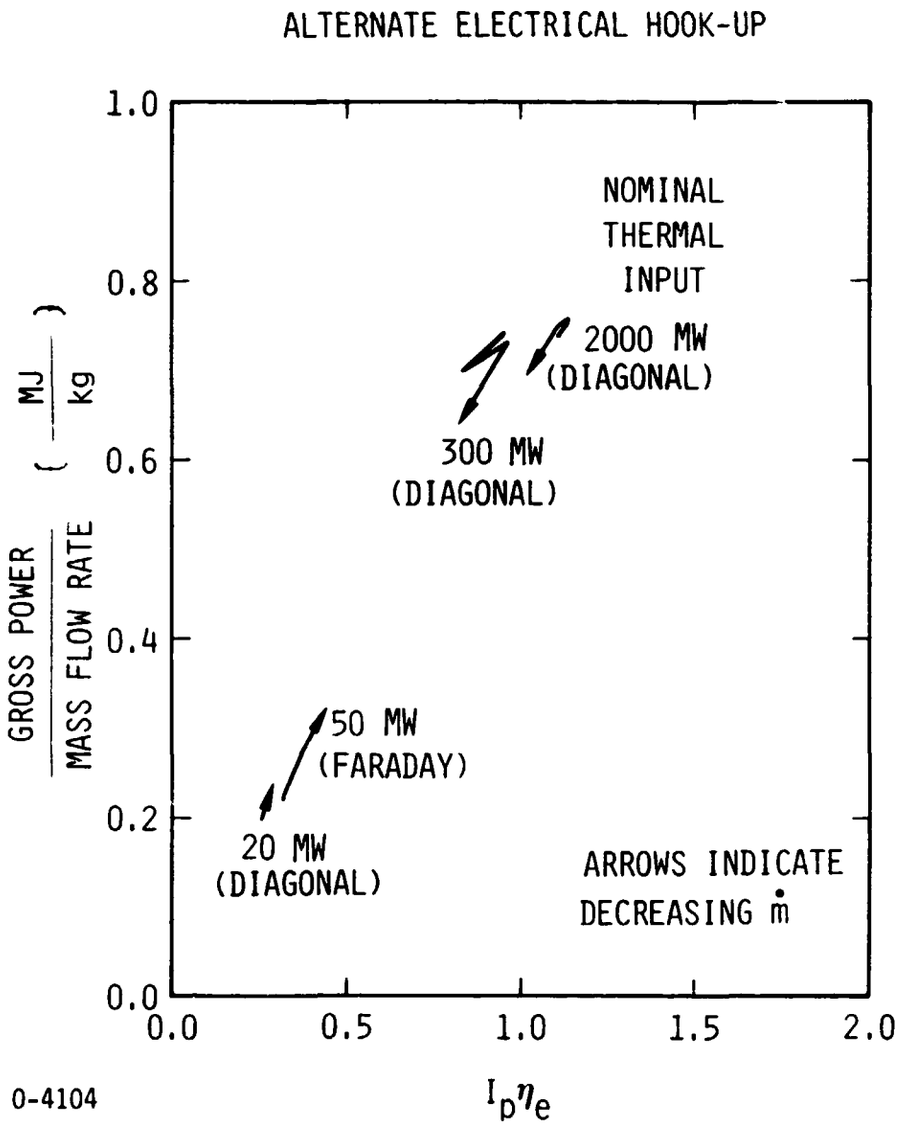

Fig. 7-26 . Gross power/mass flow rate vs. interaction parameter times electrical efficiency for four different size channels with mass flow varying from design to 70% of design.

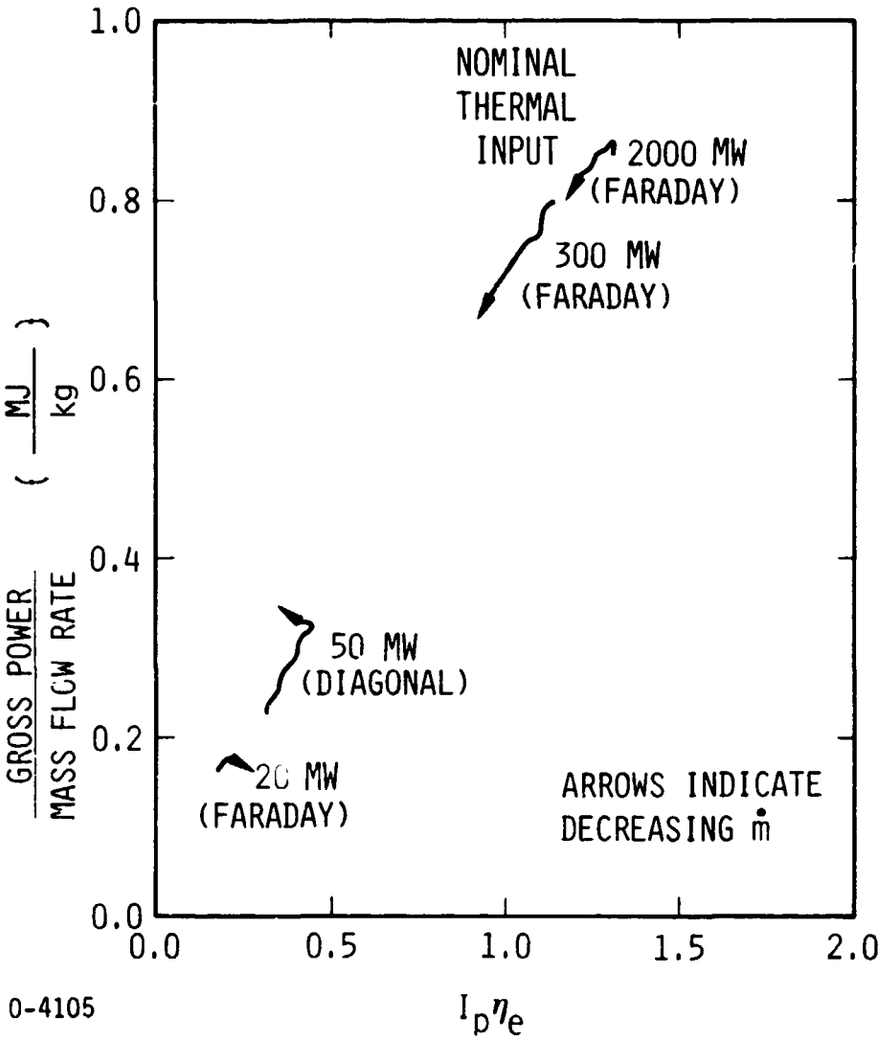

Fig. 7-27. Gross power/mass flow rate vs. interaction parameter times electrical efficiency for four different size channels with mass flow varying from design to 70% of design.

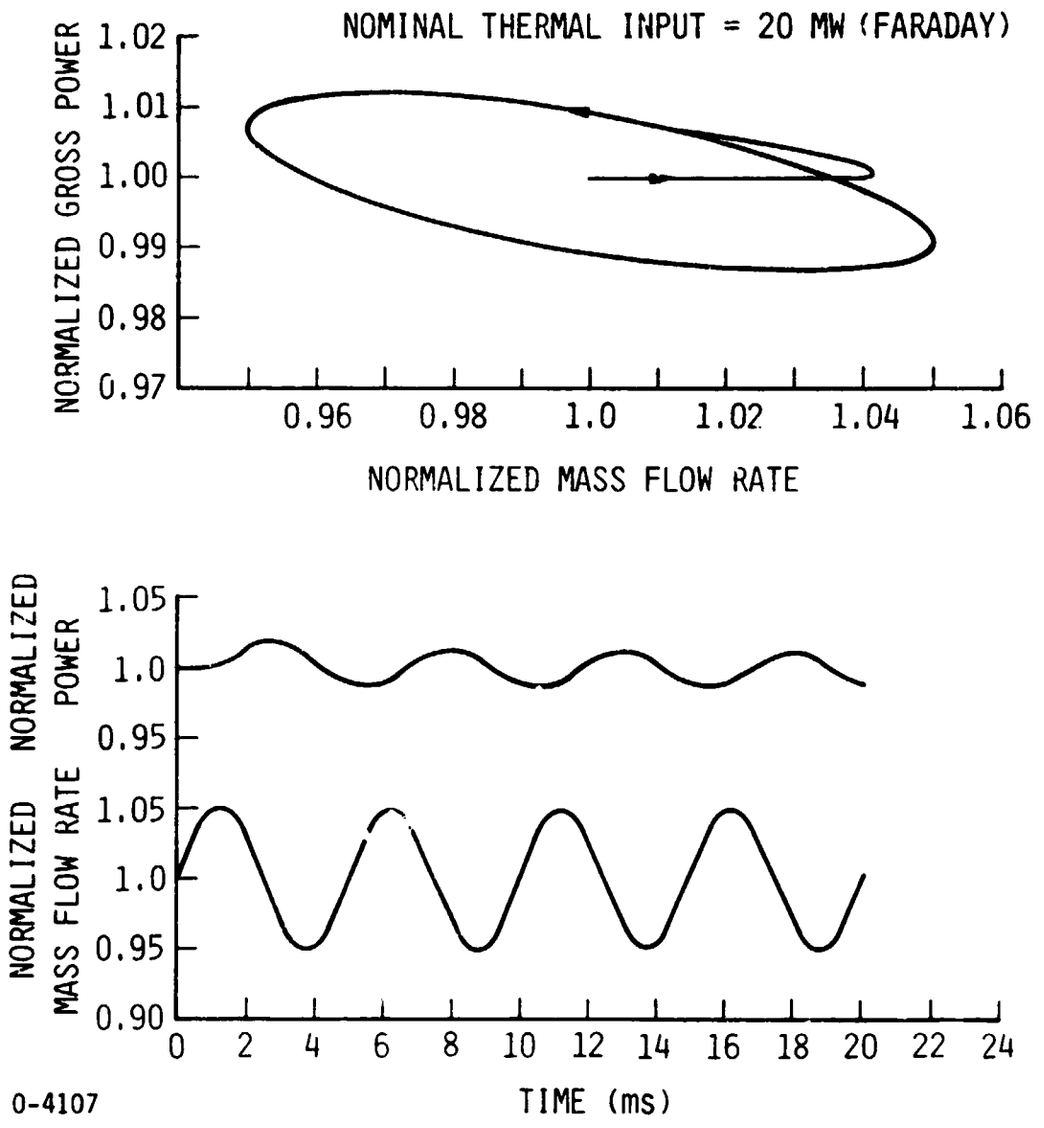

Fig. 7-28. Normalized gross power and normalized mass flow rate for an inputted ±5% sine wave in mass flow for a 20 MWth channel with Faraday connection.

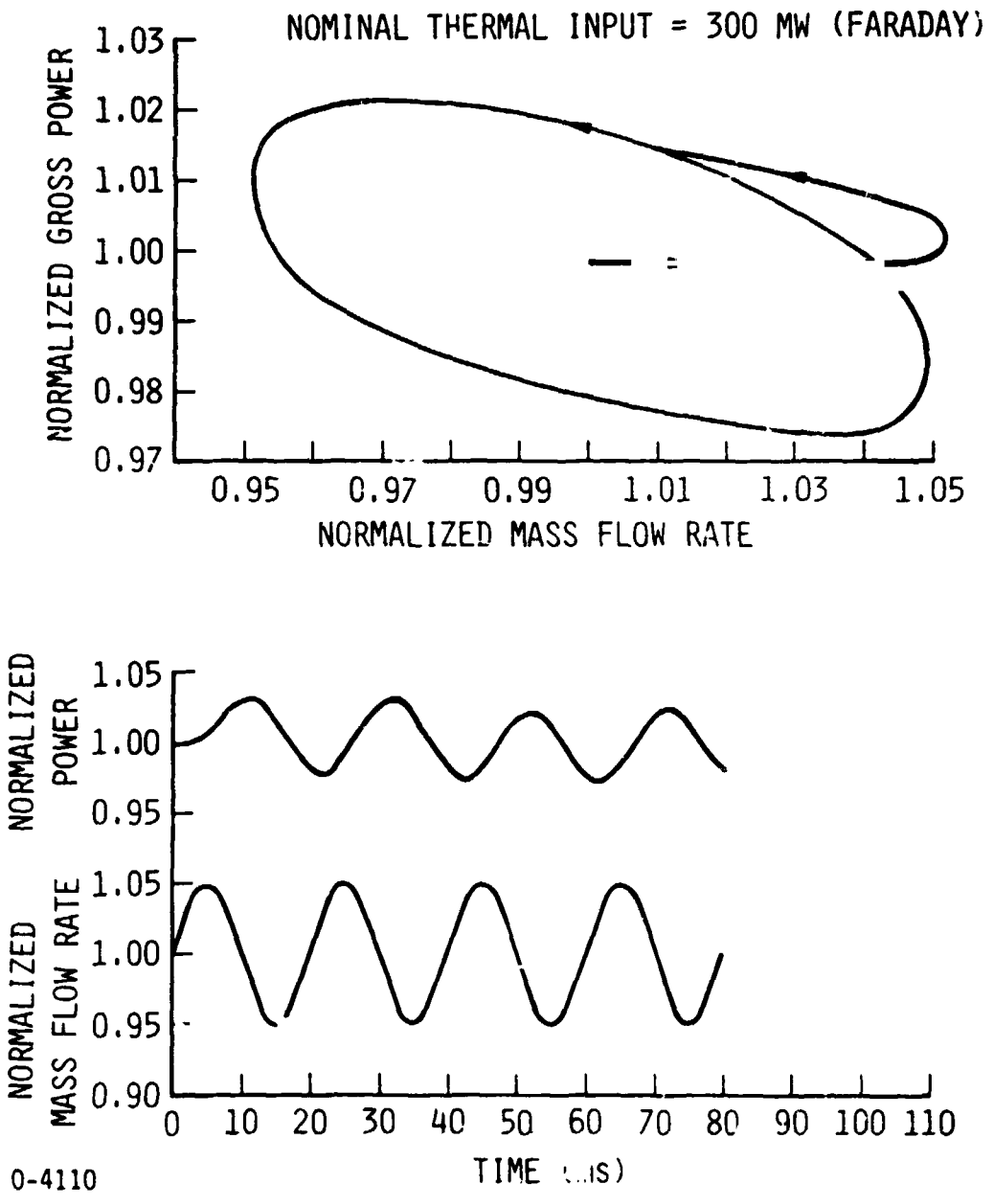

Fig. 7-29. Normalized gross power and normalized mass flow rate for an inputted ± 5% sine wave in mass flow for a 300 MWth channel with Faraday connection.

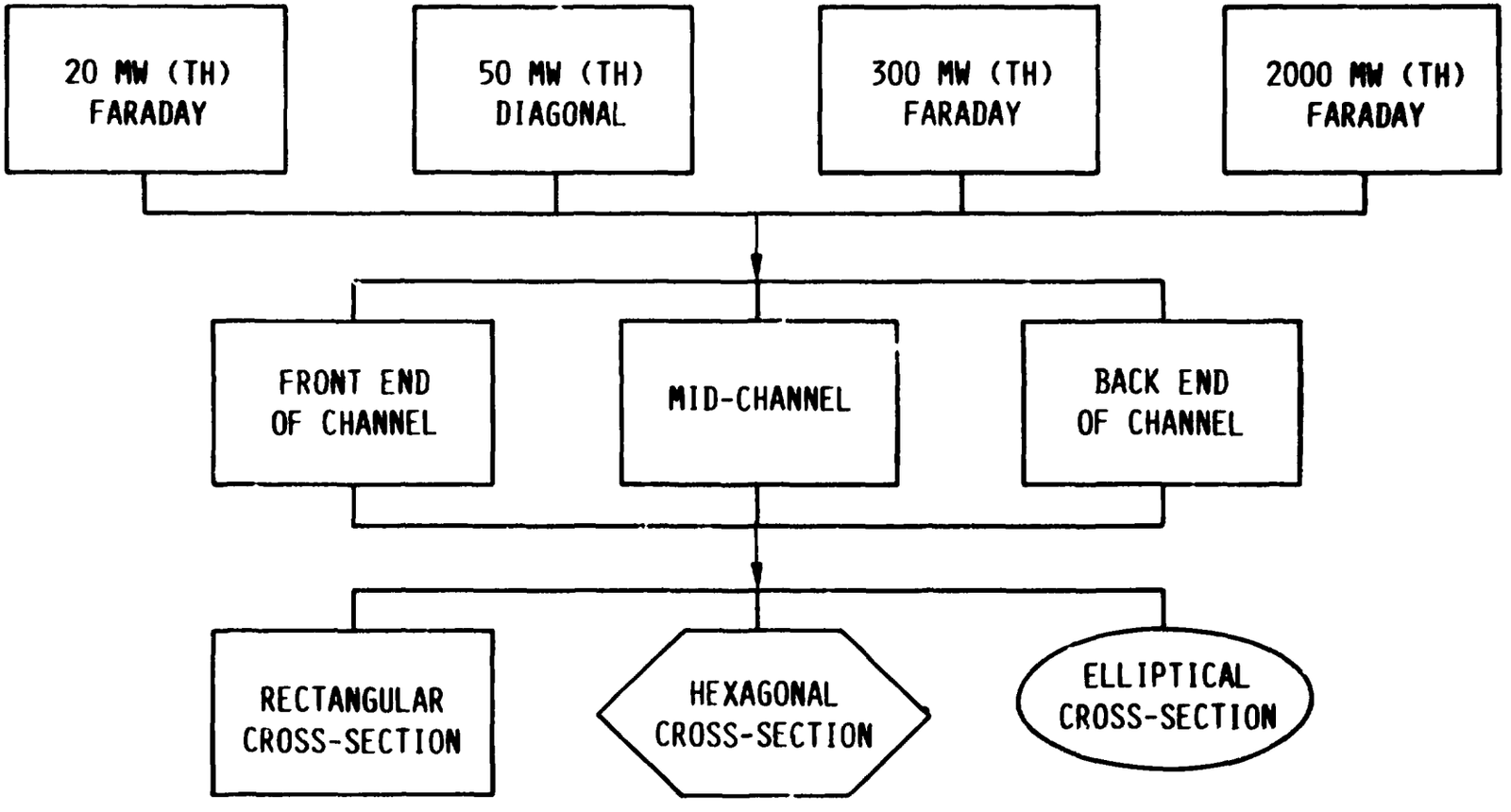

0-4165

STD RESEARCH CORPORATION

Fig. 7-30. Schematic diagram representing the cases which were completed with the Q3DYZ code under contract AC-01-79ET15501.

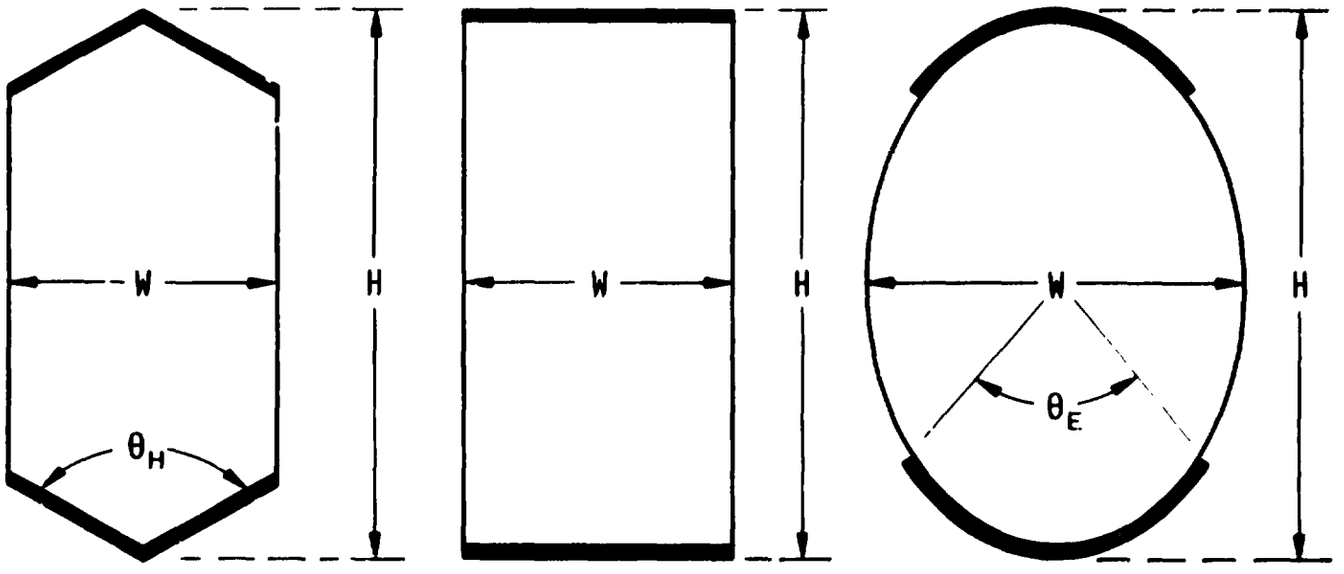

Fig. 7-31. Schematic diagrams of the hexagonal, rectangular, and elliptical geometries used for MHD channel cross-sections. The electrically conducting walls are noted by thick boundaries while insulating walls are indicated by thin boundaries

0-4315

STD RESEARCH CORPORATION

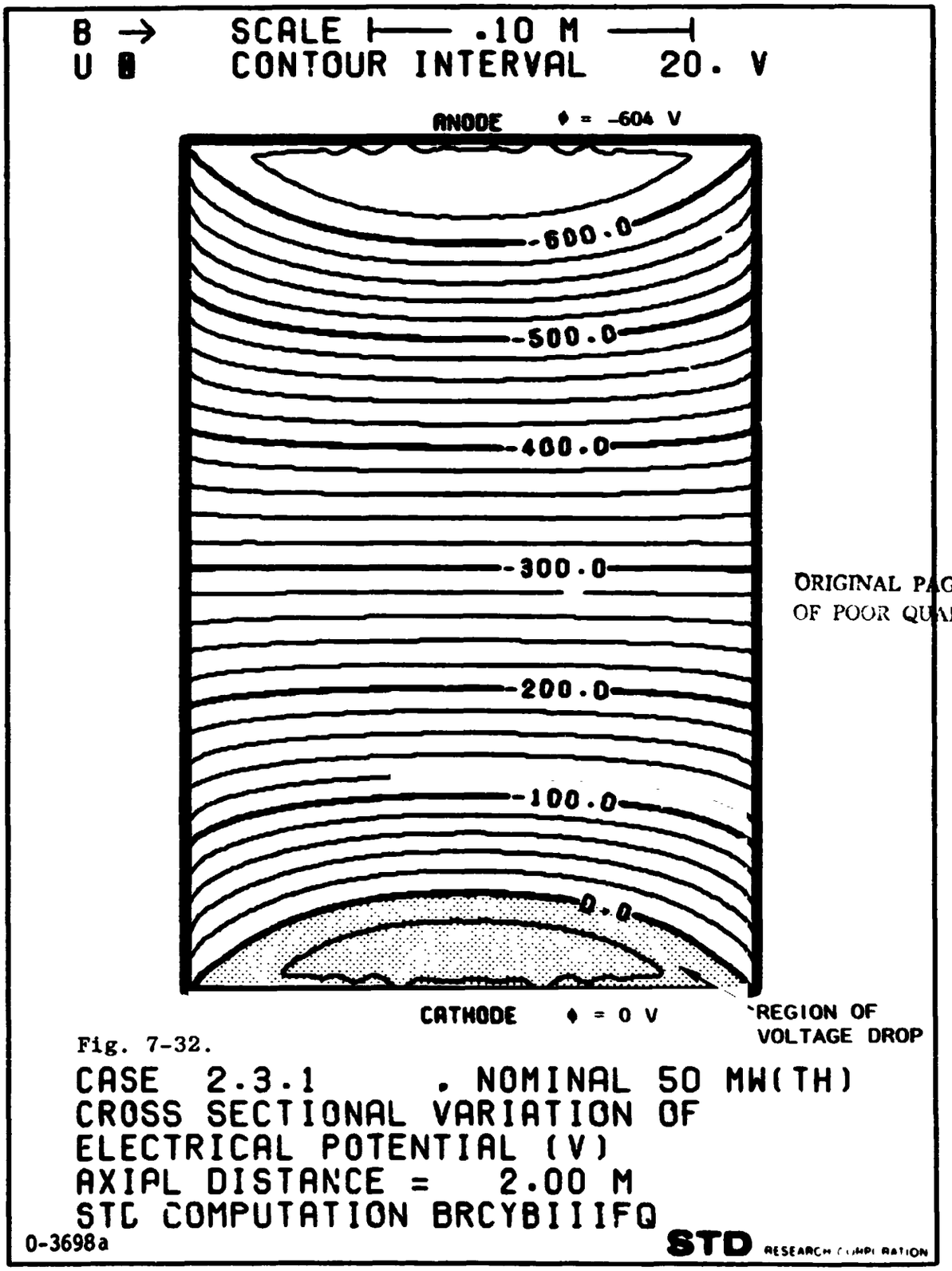

Fig. 7-32.

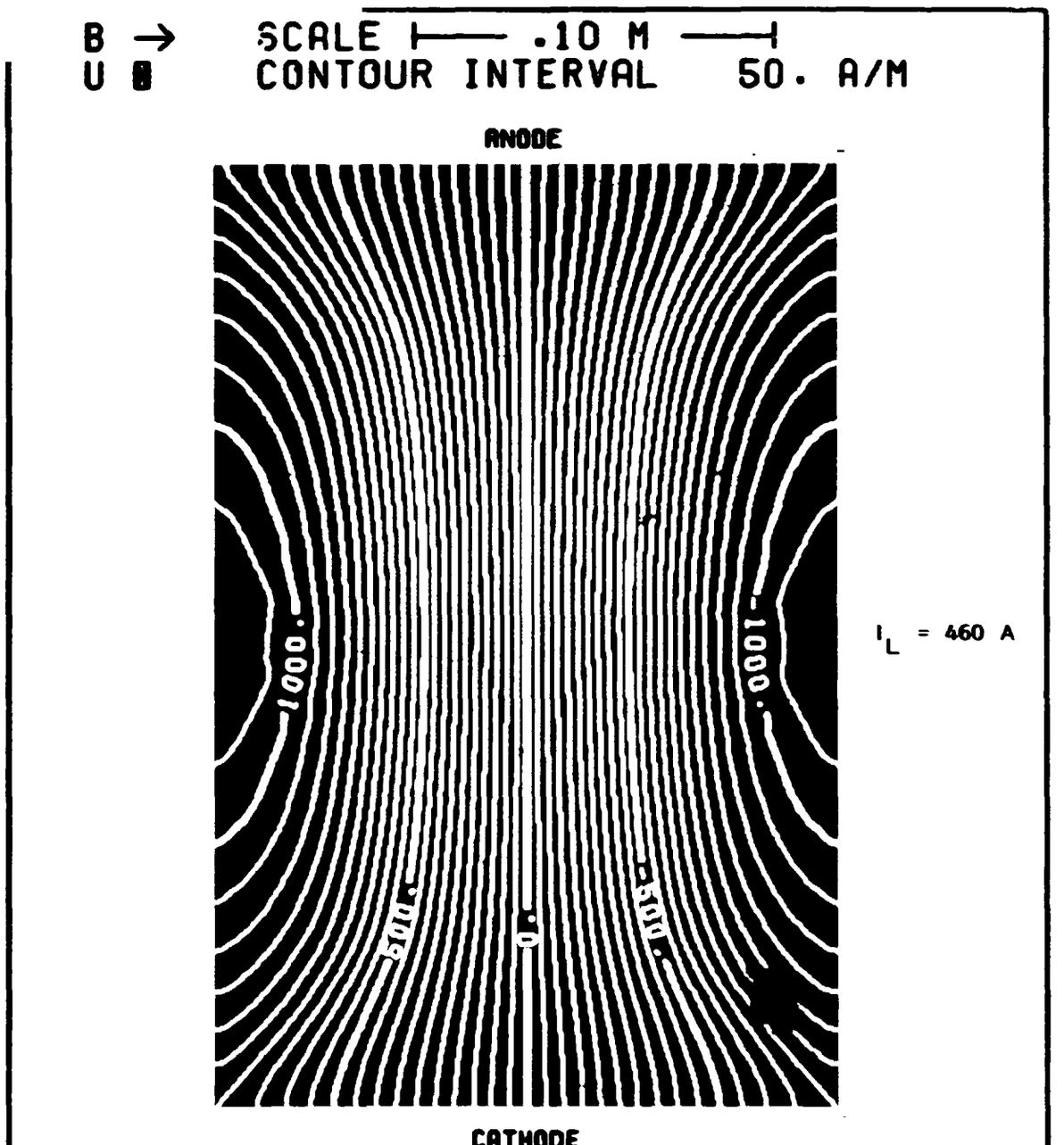

Fig. 7-33.

CASE 2.3.1 . NOMINAL 50 MW(TH)
CROSS SECTIONAL VARIATION OF
CURRENT STREAMFUNCTION (A/M)
AXIAL DISTANCE = 2.00 M
STD COMPUTATION BRCYBIIIFQ

0-3699a

STD RESEARCH CORPORATION

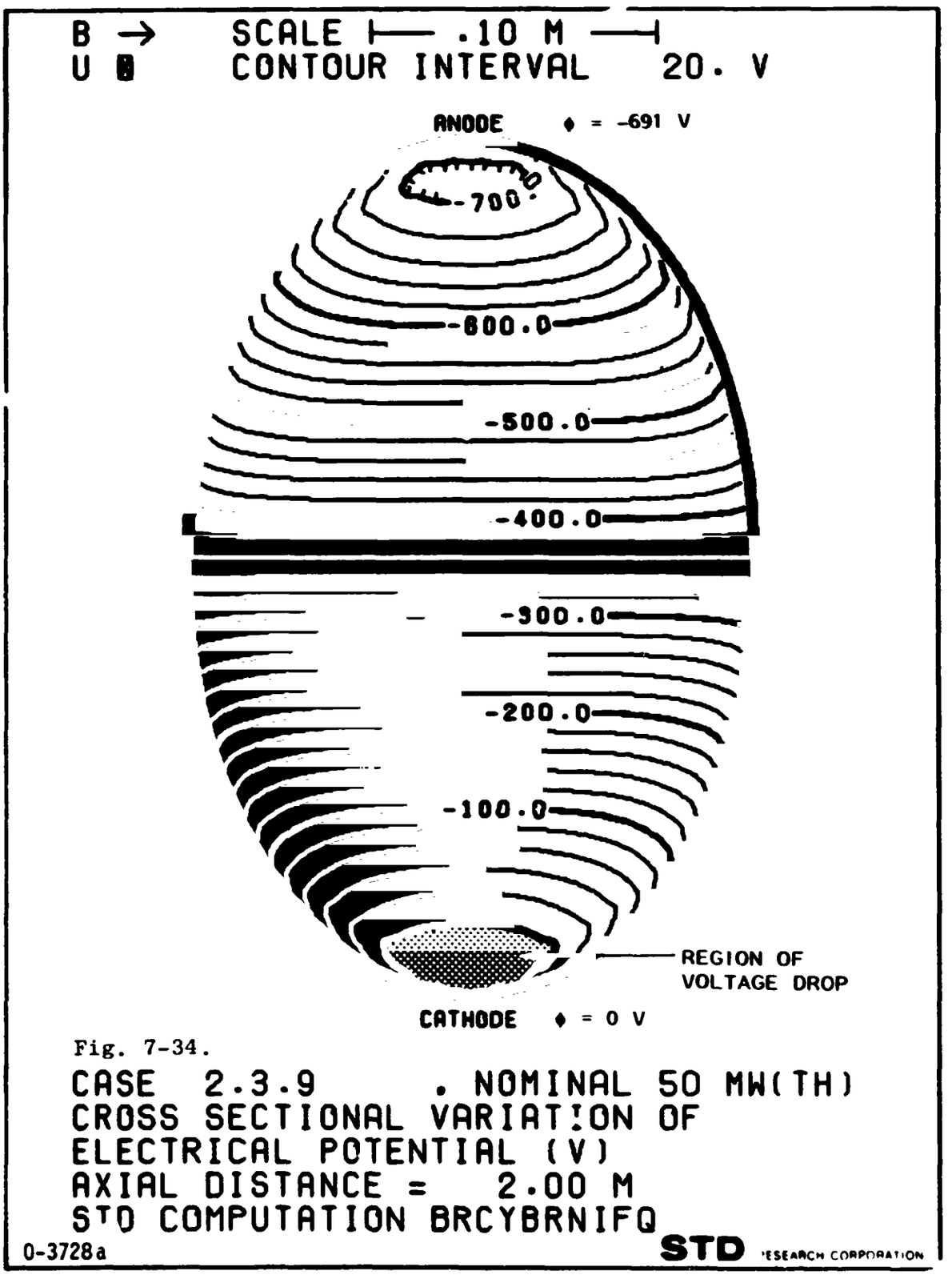

Fig. 7-34.

CASE 2.3.9 . NOMINAL 50 MW(TH)
CROSS SECTIONAL VARIATION OF
ELECTRICAL POTENTIAL (V)
AXIAL DISTANCE = 2.00 M
STD COMPUTATION BRCYBRNIFQ

0-3728a

STD RESEARCH CORPORATION

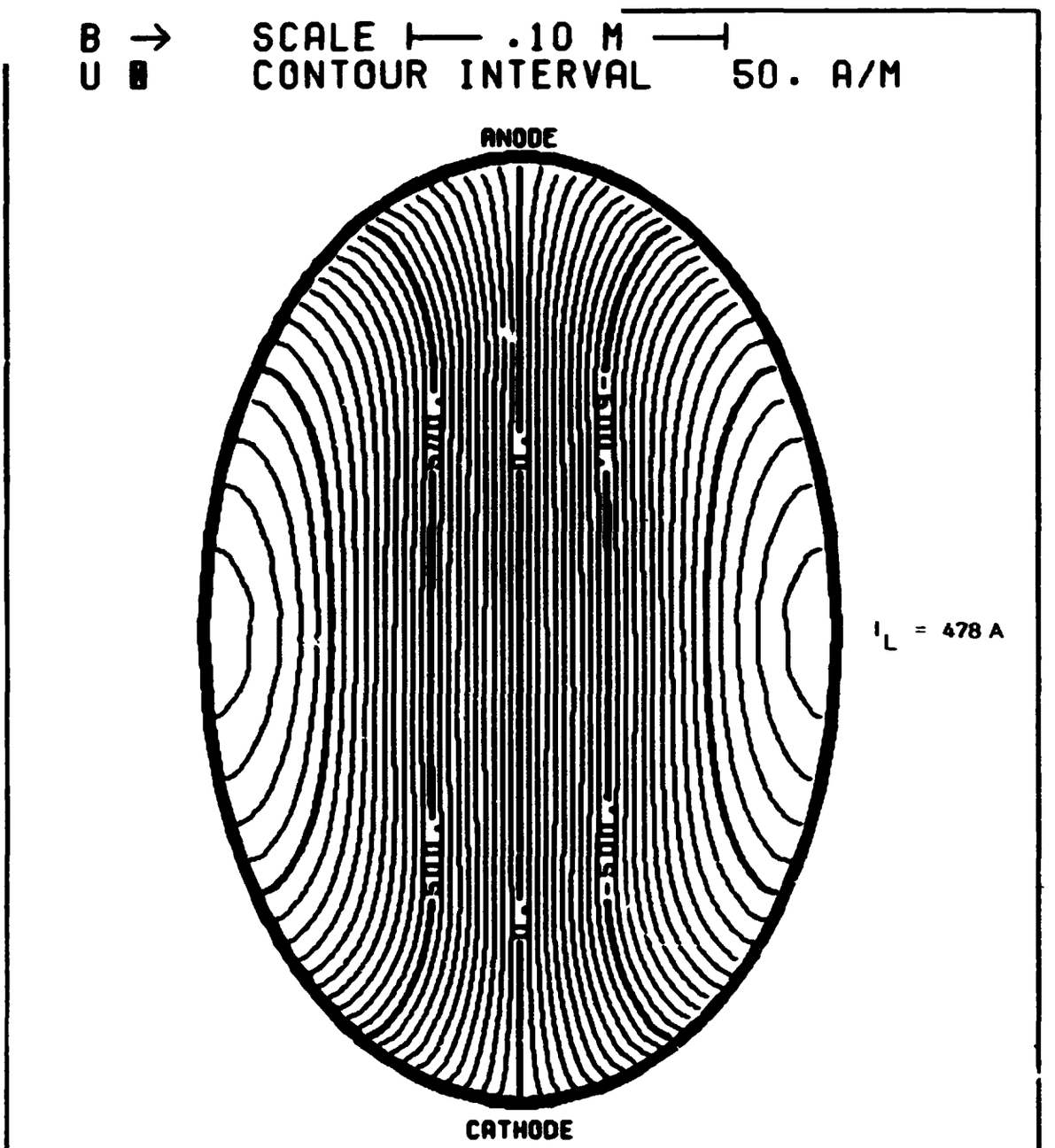

Fig. 7-35.
CASE 2.3.9 . NOMINAL 50 MW(TH)
CROSS SECTIONAL VARIATION OF
CURRENT STREAMFUNCTION (A/M)
AXIAL DISTANCE = 2.00 M
STD COMPUTATION BRCYBRNIFQ

0-3729a

STD RESEARCH CORPORATION

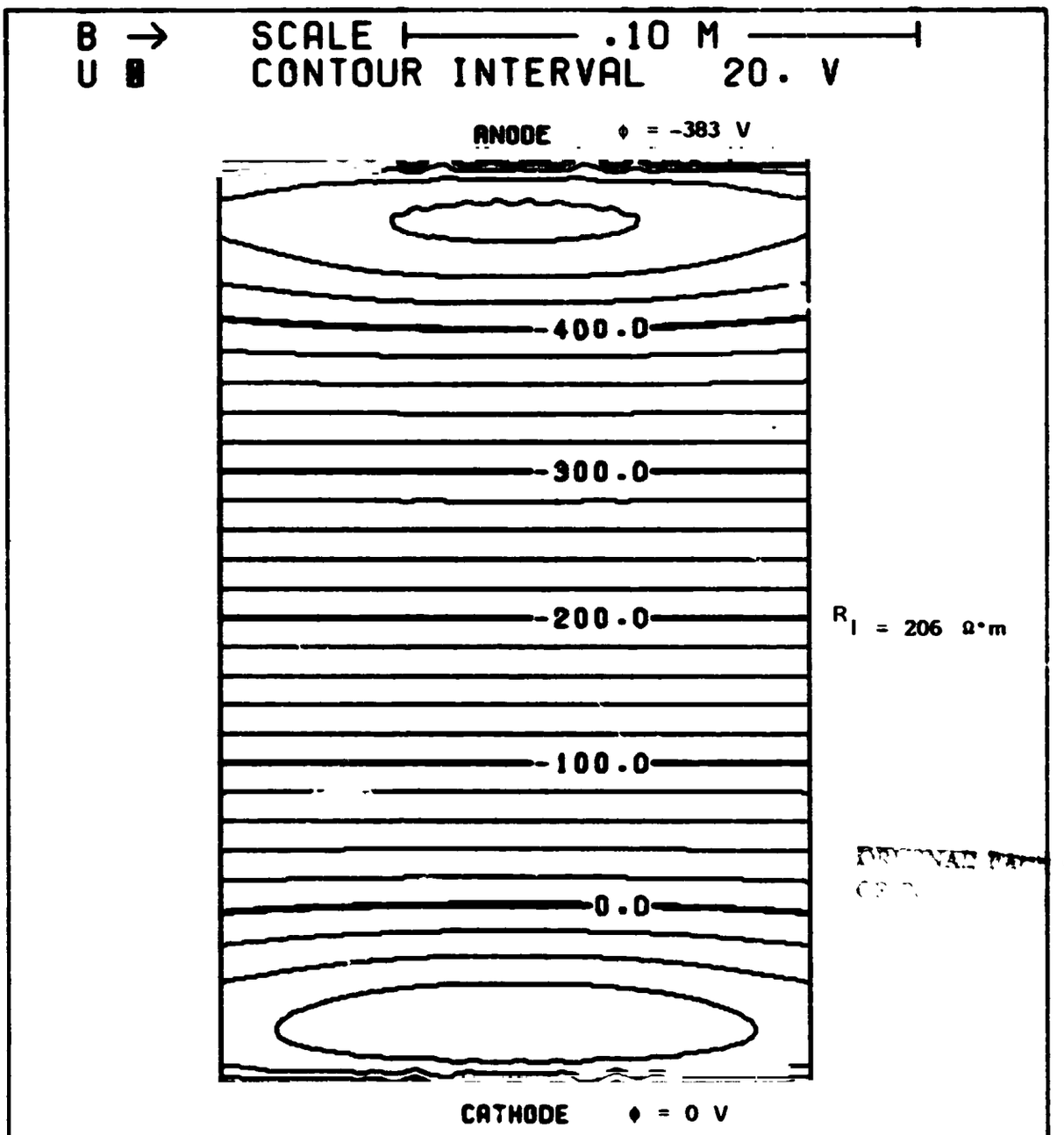

Fig. 7-36.

CASE 1.3.1 NOMINAL 20 MW(TH)
CROSS SECTIONAL VARIATION OF
ELECTRICAL POTENTIAL (V)
AXIAL DISTANCE = 1.00 M
STD COMPUTATION BRCYCJAIFQ

0-3648a

STD RESEARCH CORPORATION

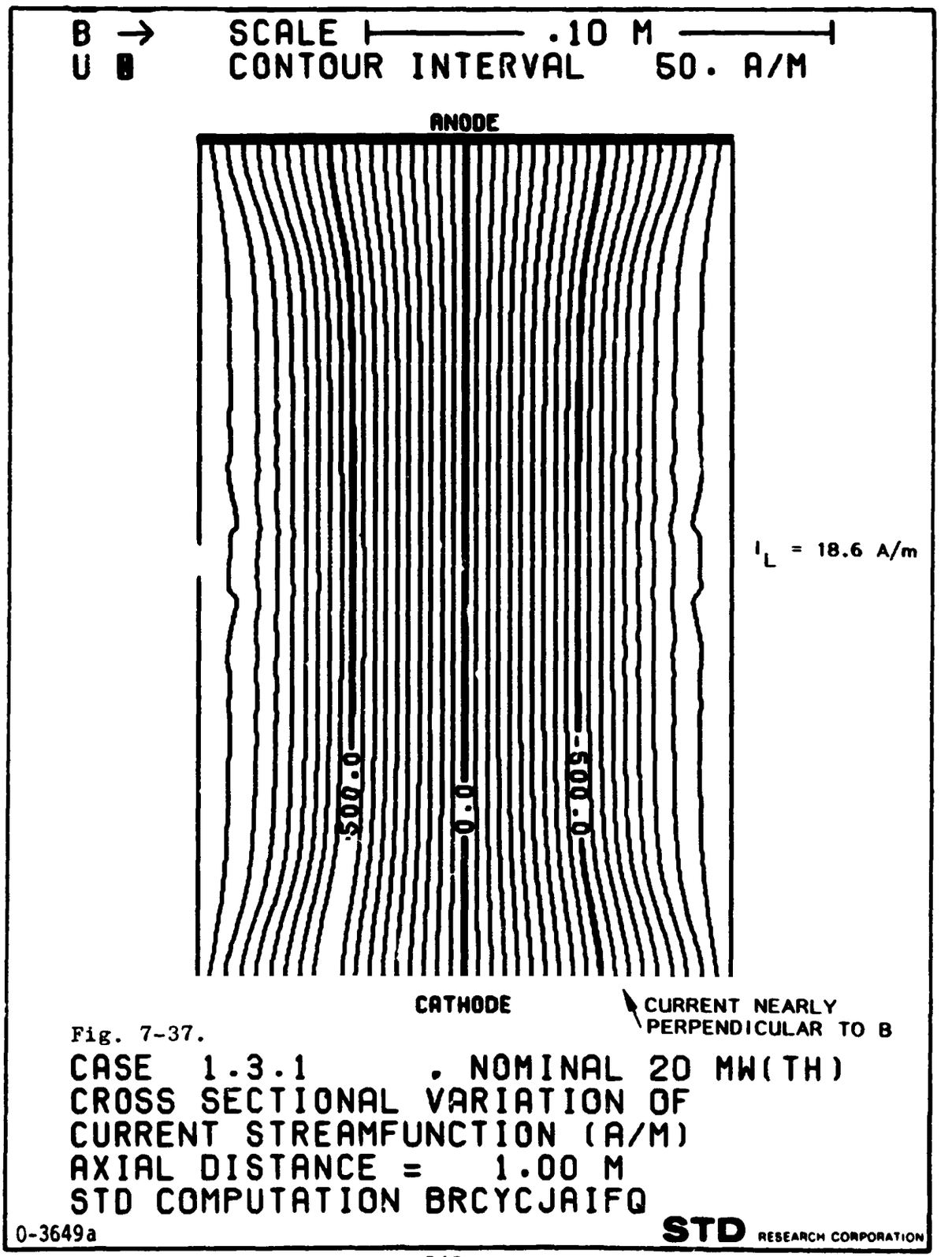
B →
U
SCALE .10 M
CONTOUR INTERVAL 50. A/M
ANODE
500.0
0.0
-500.0
I_L = 18.6 A/m
CATHODE
CURRENT NEARLY PERPENDICULAR TO B
CASE 1.3.1 . NOMINAL 20 MW(TH)
CROSS SECTIONAL VARIATION OF
CURRENT STREAMFUNCTION (A/M)
AXIAL DISTANCE = 1.00 M
STD COMPUTATION BRCYCJAIFQ
0-3649a
STD RESEARCH CORPORATION

Fig. 7-37.

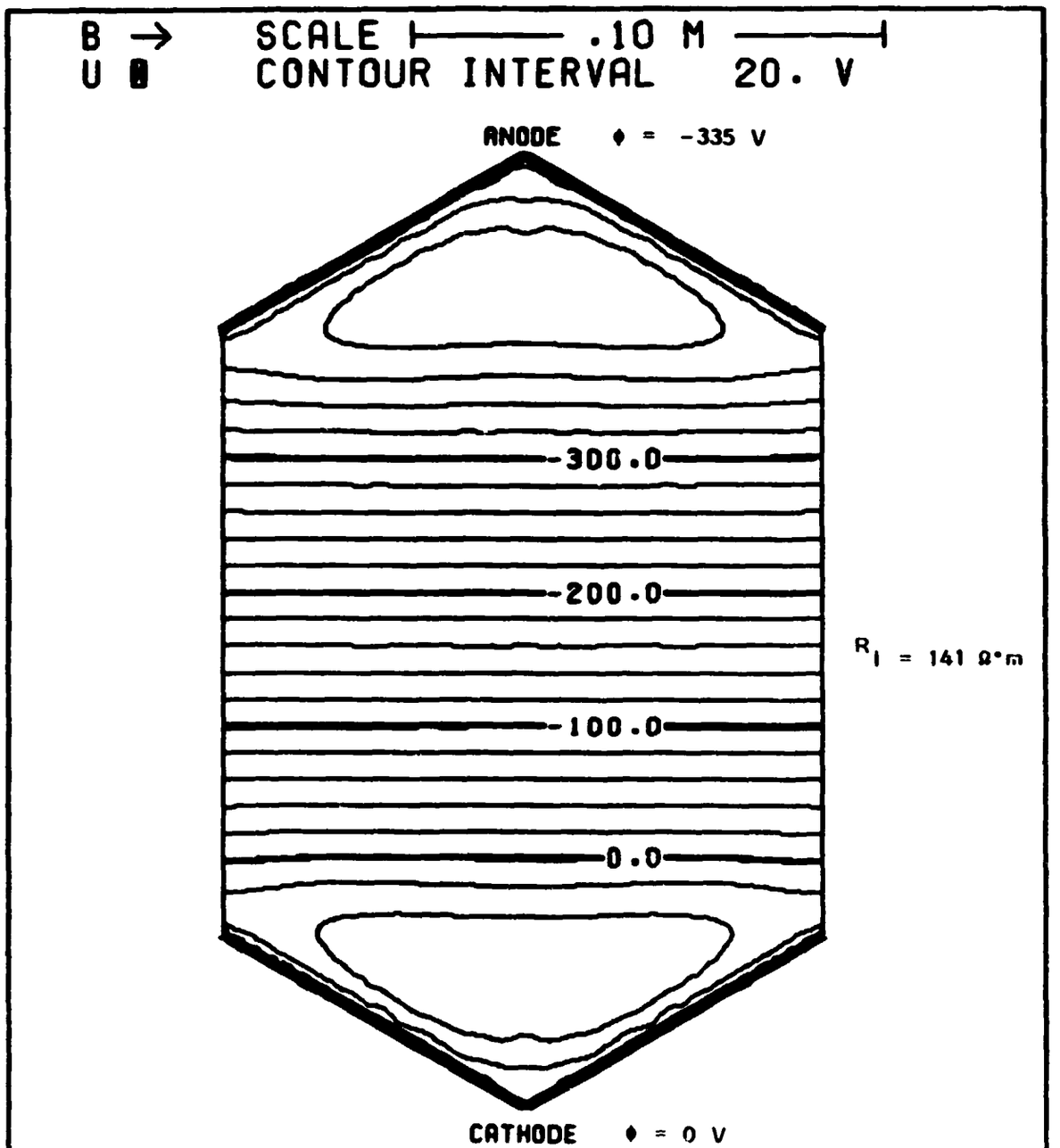

Fig. 7-38.
CASE 1.3.5 NOMINAL 20 MW(TH)
CROSS SECTIONAL VARIATION OF
ELECTRICAL POTENTIAL (V)
AXIAL DISTANCE = 1.00 M
STD COMPUTATION BRCYCIUIFQ

0-3667a

STD RESEARCH CORPORATION

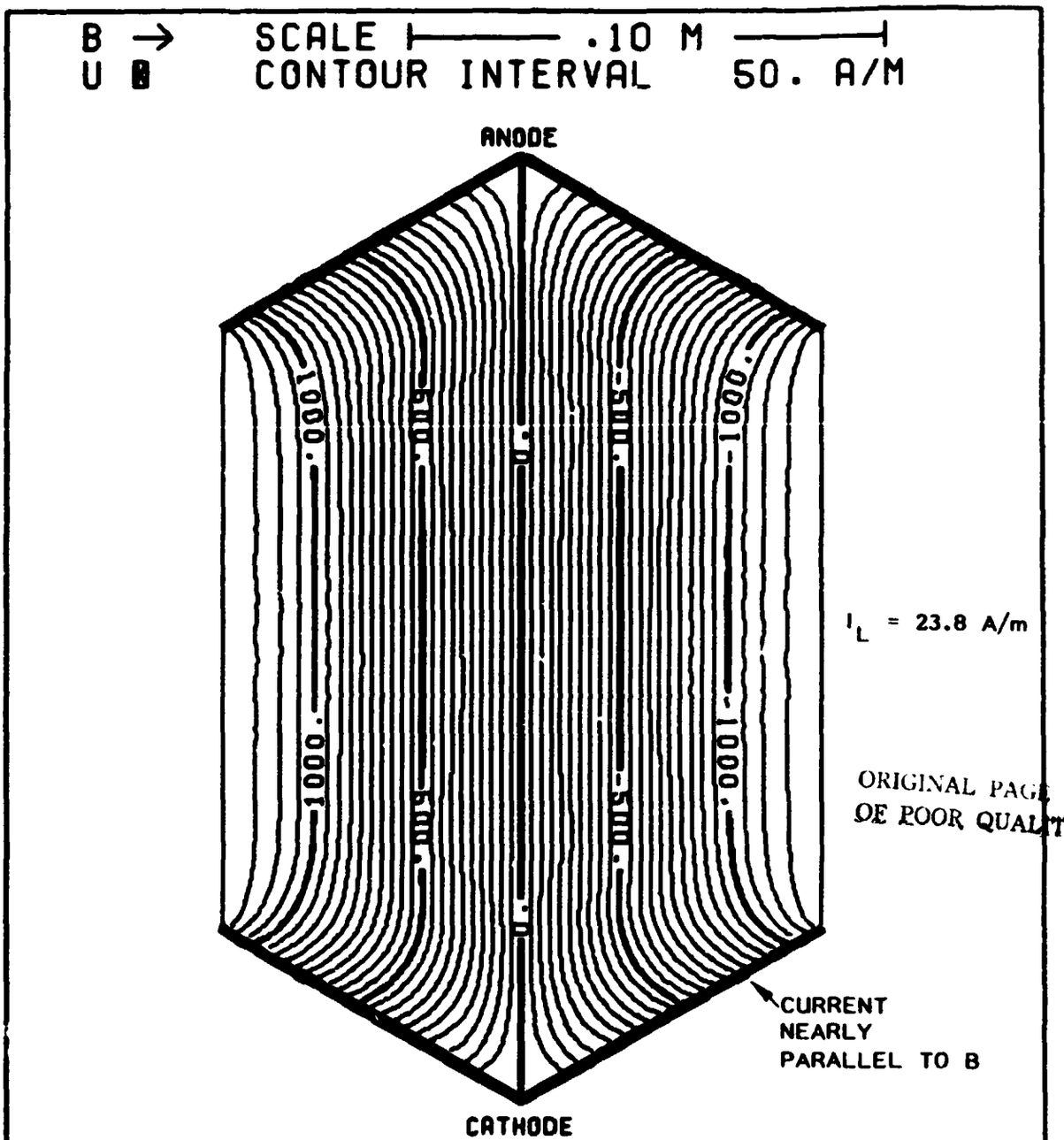

Fig. 7-39.

CASE 1.3.5 . NOMINAL 20 MW(TH)
CROSS SECTIONAL VARIATION OF
CURRENT STREAMFUNCTION (A/M)
AXIAL DISTANCE = 1.00 M
STD COMPUTATION BRCYCIUIFQ

0-3668a

STD RESEARCH CORPORATION

8.0 SUMMARY AND CONCLUSIONS

This section summarizes the major conclusions derived from the studies described in this report.

8.1 AEDC/HPDE Data Analysis and Interpretation

Attention has been concentrated on the data from two power producing runs of the AEDC/HPDE (Runs 006-008 and 006-014). Calculations have been performed with codes from the Q3D and TRANSIENT families in order to compare theory and experiment where possible.

The comparison of theory and experiment for Run 006-008 is incomplete because the experimental data were inadequate to accurately define the conditions that existed during the operation of that run. Nevertheless, the qualitative agreement is sufficiently good to presume that if the Hall voltage across the channel were known, the discharge current could have been accurately determined and the comparison would have been excellent.

The comparison between theory and experiment was much better for Run 006-014. The data from the two recording systems were much more consistent for this run and are more reliable. On the whole, the predictions are well within the scatter for the data.

8.2 Critical Phenomena in the AEDC/HPDE

The power dissipation in the thermal boundary layers of the HPDE is much more important than was originally assumed in the design of the HPDE. However, the enthalpy extraction

goal of the experiment can be met without providing the original design values of electrode wall temperatures (2100 K - 1950 K). On the basis of the calculations performed to-date, provision of a uniform 1500 K wall temperature would be sufficient to meet the enthalpy extraction goal of the experiment.

Under the operating conditions of Run 006-014, which represents the best-diagnosed, high-power run of the HPDE to date, the principal operational parameters available to increase the HPDE performance toward the goals of the experiment are the electrode surface temperature and magnetic field.

The central role of the Mach number distribution in achieving the performance goals of the experiment is demonstrated by the calculations performed to date. The optimum Mach number distribution in the AEDC/HPDE appears to be transonic.

Finite electrode and near electrode effects appear to have a four to five percent impact on the performance of the MHD generator under the operating conditions of Run 006-014. The experimental data therefore are perhaps not sufficiently refined to discriminate between the differences calculated with some models for near electrode effects (small arcs vs. diffuse mode transport), and electrode segmentation. The data to date do appear to rule out the existence of very strong arcs and suggest that the severe losses associated with seed condensation on the electrodes and seed depletion in the boundary layers are not controlling mechanisms.

The AEDC/HPDE computations performed to date indicate that the fluid mechanical behavior of the generator is approaching the interesting regime of zero blockage and measurable sidewall velocity oversnoots. The data thus far are not sufficiently complete to detect these effects. However, the general agreement with the pressure predictions and the other electrical and gasdynamic predictions with the multidimensional Q3D calculations suggests that the inclusion of these effects in the computations may be necessary. As the performance of the MHD generator improves, and the interaction level increases, the differences between simplified and sophisticated models of the flow field will become more and more apparent. The AEDC/HPDE should be afforded additional instrumentation with which to diagnose the local fluid phenomena which are predicted by the analyses.

The unconventional fluid behavior will be magnified when the generator is operated in the subsonic mode. It would be possible, under conditions similar to HPDE Run 006-014, to achieve an interaction parameter based on velocity sufficient to exhibit many of the secondary flow and velocity overshoot effects predicted by the STD/MHD codes, if the mass flow rate were reduced sufficiently to provide subsonic flow throughout the generator. While this may not be the optimum enthalpy extraction and isentropic efficiency point, it would be possible, neverthess, to simulate conditions in a large, subsonic, baseload MHD generator, if the appropriate interaction parameter based on velocity is provided.

The inlet pressure loss was calculated fo one operating condition to be approximately 1.5% of the total pressure entering the generator. Such a pressure loss in the inlet and exit regions of the generator would not present a

substantial penalty to the overall performance of an MHD plant operating with an MHD generator of the type represented by the AEDC/HPDE. The exit region pressure loss remains to be evaluated.

The electrode voltage drops are sensitive not only to the wall temperature but also to the amount of Joule dissipation heat deposited in the boundary layers. Second order improvement in performance may be achieved by tailoring the load factor distribution to achieve high dissipation in the inlet regions of the generator. Analytical models which fail to account for Joule dissipation effects in the electrode boundary layers will fail to predict the electrode voltage drops with accuracy.

8.3 Critical Phenomena in the U.S. U-25 Experiment

The nominal conditions of the U.S. U-25 are predicted to yield transonic behavior with a shock located in the channel. Even under these nonideal conditions, the U.S. U-25 experiment is predicted to be able to reach or come very close to the goal of 10 MW power output. The operation of this experiment can be altered by changing the mass flow rate, but simultaneous attainment of both fully subsonic flow and at least 10 MW power output was not predicted under the nominal operating conditions.

8.4 Electrical Conductivity Calculations in Coal Flames

The calculation of electrical conductivity of the products of coal combustion is a subject of considerable uncertainty due to the lack of sufficiently accurate compositional and thermochemical data. Even for equilibrium

calculations, the elemental composition of the products of combustion is dependent upon history of the combustion, particularly for the treatment of ash and slag. In addition, for MHD generators the nonequilibrium effects of boundary layers, current transport, radiation transport, condensation, and chemical kinetics must be taken into account.

Even when the coal composition is defined (defined for computational purposes), the values of the transport and thermodynamic properties at the inlet to the generators is dependent upon the conditions in the combustor, separator, throat, nozzle, and mating sections of the flow train. It is particularly important to know the distributions of heat flux and slag removal in these sections of the flow train in order to define the inlet conditions.

For example, there are many ways of modeling slag removal: (a) all of the liquid and solid slag species can be removed at the flame temperature, (b) the slag that is removed can be assumed to have the same composition as for the ash analysis; (c) the condensed phase slag can be removed at the equilibrium composition of the gas-phase, condensed-phase interface temperature; or (d) any combination of these, i.e., some slag removed at one condition and some removed at another. Since condensed phase matter is removed to the walls continuously along each section of the flow train, the model of slag removal must be applied as a function of axial distance and for conditions which are functions of location in the flow train.

1. REPORT NO.	2. GOVERNMENT ACCESSION NO.	3. RECIPIENT'S CATALOG NO.
NASA CR-165143		

4. TITLE AND SUBTITLE	5. REPORT DATE
ANALYTICAL INVESTIGATION OF CRITICAL PHENOMENA IN MHD POWER GENERATORS	31 July 1980
	6. PERFORMING ORGANIZATION CODE
7. AUTHOR(S)	8. PERFORMING ORG. REPORT NO. STDR-80-22
	10. WORK UNIT NO.
9. PERFORMING ORGANIZATION NAME AND ADDRESS STD Research Corporation P.O. Box "C" Arcadia, CA 91006	11. CONTRACT OR GRANT NO. DEN3-179
	13. TYPE OF REPORT Contractor Report
12. SPONSORING AGENCY NAME AND ADDRESS U.S. Department of Energy Office of Magnetohydrodynamics Washington, D.C. 20545	14. SPONSORING AGENCY REPORT NO. DOE/NASA/0179-1

15. SUPPLEMENTARY NOTES
Final Report. Prepared under Interagency Agreement EC-77-AA-012674.
Project Manager, Bert Phillips, Wind and Stationary Power Division,
NASA Lewis Research Center, Cleveland, OH 44133

16. ABSTRACT

Critical phenomena in the Arnold Engineering Development Center (AEDC) High Performance Demonstration Experiment (HPDE) and the U.S. U-25 Experiment, are analyzed. Also analyzed are the performance of a NASA-specified 500 MW(th) flow train and computations carried out by STD Research under Contract AC-01-79ET15501 concerning critical issues for the scale-up of MHD generators.

Critical phenomena analyzed include Hall voltage overshoots, optimal load schedules, parametric dependence of the electrode voltage drops, boundary layer behavior, near electrode phenomena with finite electrode segmentation, current distribution in the end regions, scale-up rules, optimum Mach number distribution, and the effects of alternative cross-sectional shapes.

17. KEY WORDS (SUGGESTED BY AUTHOR(S))	18. DISTRIBUTION STATEMENT
Magnetohydrodynamics	Unclassified - Unlimited Star Category 44 DOE Category UC-90g

19. SECURITY CLASSIF. OF REPORT	20. SECURITY CLASSIF. OF THIS PAGE	21. NO. OF PP.	22. PRICE *
Unclassified	Unclassified	[illegible]	

* FOR SALE BY THE NATIONAL TECHNICAL INFORMATION SERVICE, SPRINGFIELD, VA 22161

USGPO 1980 [illegible]